JAAVSO

Volume 48
Number 2
2020

The Journal of the American Association of Variable Star Observers

Exoplanets for Everyone

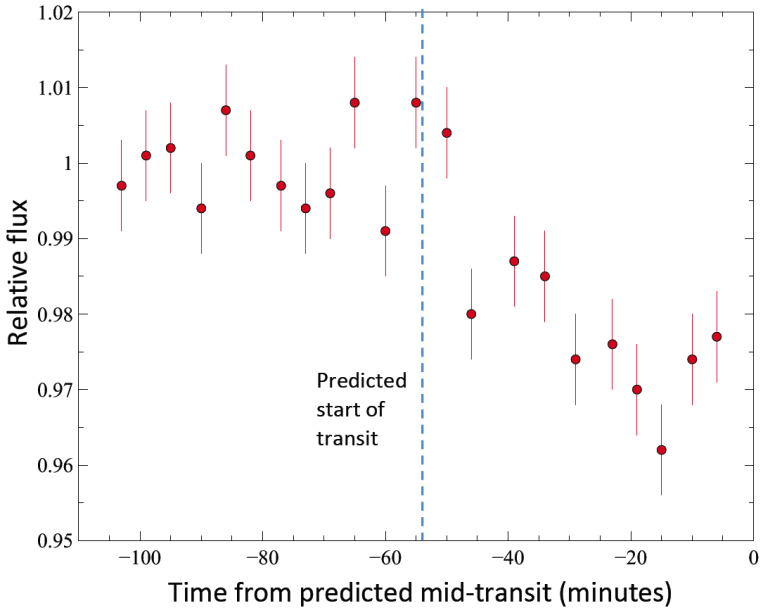

Individual HD 189733b data points obtained from 40-second integration on variable star, comparison star, and sky background.

Also in this issue...

Complete table of contents inside...

The American Association of Variable Star Observers
49 Bay State Road, Cambridge, MA 02138, USA

The Journal of the American Association of Variable Star Observers

Editor-in-Chief
Nancy D. Morrison
Professor of Astronomy Emerita
Department of Physics and Astronomy
The University of Toledo, Toledo, Ohio

Associate Editor
Elizabeth O. Waagen

Production Editor
Michael Saladyga

Editorial Board
Geoffrey C. Clayton
Louisiana State University
Baton Rouge, Louisiana

Kosmas Gazeas
University of Athens
Athens, Greece

Laszlo L. Kiss
Konkoly Observatory
Budapest, Hungary

Katrien Kolenberg
Universities of Antwerp and of Leuven, Belgium
and Harvard-Smithsonian Center for Astrophysics
Cambridge, Massachusetts

Kristine Larsen
Department of Geological Sciences, Central Connecticut State University,
New Britain, Connecticut

Vanessa McBride
IAU Office of Astronomy for Development; South African Astronomical Observatory; and University of Cape Town, South Africa

Ulisse Munari
INAF/Astronomical Observatory of Padua
Asiago, Italy

Karen Pollard
Director, Mt. John Observatory, University of Canterbury,
Christchurch, New Zealand

Nikolaus Vogt
Universidad de Valparaiso
Valparaiso, Chile

The Board of the American Association of Variable Star Observers 2019–2020

Executive Director and CEO	Stella Kafka
President	Gordon Myers
Past President	Kristine Larsen
1st Vice President	Bill Stein
2nd Vice President	Richard Berry
Secretary	Kristine Larsen
Treasurer	Robert Stephens

Board Members

Robert Buchheim	Ken Hudson
Michael Cook	Bob Massey
David Cowall	Gregory R. Sivakoff
Joyce A. Guzik	Brad Vietje

ISSN 0271-9053 (print)
ISSN 2380-3606 (online)

JAAVSO

The Journal of
The American Association
of Variable Star Observers

Volume 48
Number 2
2020

ISSN 0271-9053 (print)
ISSN 2380-3606 (online)

AAVSO
49 Bay State Road
Cambridge, MA 02138
USA

Publication Schedule

The Journal of the American Association of Variable Star Observers is published twice a year, June 15 (Number 1 of the volume) and December 15 (Number 2 of the volume). The submission window for inclusion in the next issue of JAAVSO closes six weeks before the publication date. A manuscript will be added to the table of contents for an issue when it has been fully accepted for publication upon successful completion of the referee process; these articles will be available online prior to the publication date. An author may not specify in which issue of JAAVSO a manuscript is to be published; accepted manuscripts will be published in the next available issue, except under extraordinary circumstances.

Page Charges

Page charges are waived for Members of the AAVSO. Publication of unsolicited manuscripts in JAAVSO requires a page charge of US $100/page for the final printed manuscript. Page charge waivers may be provided under certain circumstances.

Publication in *JAAVSO*

With the exception of abstracts of papers presented at AAVSO meetings, papers submitted to JAAVSO are peer-reviewed by individuals knowledgeable about the topic being discussed. We cannot guarantee that all submissions to JAAVSO will be published, but we encourage authors of all experience levels and in all fields related to variable star astronomy and the AAVSO to submit manuscripts. We especially encourage students and other mentees of researchers affiliated with the AAVSO to submit results of their completed research.

Subscriptions

Institutions and Libraries may subscribe to JAAVSO as part of the Complete Publications Package or as an individual subscription. Individuals may purchase printed copies of recent JAAVSO issues via Createspace. Paper copies of JAAVSO issues prior to volume 36 are available in limited quantities directly from AAVSO Headquarters; please contact the AAVSO for available issues.

Instructions for Submissions

The *Journal of the AAVSO* welcomes papers from all persons concerned with the study of variable stars and topics specifically related to variability. All manuscripts should be written in a style designed to provide clear expositions of the topic. Contributors are encouraged to submit digitized text in MS WORD, LATEX+POSTSCRIPT, or plain-text format. Manuscripts should be submitted through the JAAVSO submission portal (https://www.aavso.org/apps/jaavso/submit/) or may be mailed electronically to journal@aavso.org or submitted by postal mail to JAAVSO, 49 Bay State Road, Cambridge, MA 02138, USA.

Manuscripts must be submitted according to the following guidelines, or they will be returned to the author for correction:

Manuscripts must be:
1) original, unpublished material;
2) written in English;
3) accompanied by an abstract of no more than 100 words.
4) not more than 2,500–3,000 words in length (10–12 pages double-spaced).

Figures for publication must:
1) be camera-ready or in a high-contrast, high-resolution, standard digitized image format;
2) have all coordinates labeled with division marks on all four sides;
3) be accompanied by a caption that clearly explains all symbols and significance, so that the reader can understand the figure without reference to the text.

Maximum published figure space is 4.5″ by 7″. When submitting original figures, be sure to allow for reduction in size by making all symbols, letters, and division marks sufficiently large.

Photographs and halftone images will be considered for publication if they directly illustrate the text.

Tables should be:
1) provided separate from the main body of the text;
2) numbered sequentially and referred to by Arabic number in the text, e.g., Table 1.

References:
1) References should relate directly to the text.
2) References should be keyed into the text with the author's last name and the year of publication, e.g., (Smith 1974; Jones 1974) or Smith (1974) and Jones (1974).
3) In the case of three or more joint authors, the text reference should be written as follows: (Smith et al. 1976).
4) All references must be listed at the end of the text in alphabetical order by the author's last name and the year of publication, according to the following format: Brown, J., and Green, E. B. 1974, *Astrophys. J.*, **200**, 765.
Thomas, K. 1982, *Phys. Rep.*, **33**, 96.
5) Abbreviations used in references should be based on recent issues of JAAVSO or the listing provided at the beginning of *Astronomy and Astrophysics Abstracts* (Springer-Verlag).

Miscellaneous:
1) Equations should be written on a separate line and given a sequential Arabic number in parentheses near the right-hand margin. Equations should be referred to in the text as, e.g., equation (1).
2) Magnitude will be assumed to be visual unless otherwise specified.
3) Manuscripts may be submitted to referees for review without obligation of publication.

Online Access

Articles published in JAAVSO, and information for authors and referees may be found online at: https://www.aavso.org/apps/jaavso/

© 2020 The American Association of Variable Star Observers. All rights reserved.

The Journal of the American Association of Variable Star Observers
Volume 48, Number 2, 2020

Editorial

Variable Star Research

Table of Contents continued on following pages

Table of Contents continued on following pages

Table of Contents continued on next page

Editorial

Editorial in Two Parts

Nancy D. Morrison
Editor-in-Chief, *Journal of the AAVSO*

Department of Physics and Astronomy and Ritter Observatory, MS 113, The University of Toledo, 2801 W. Bancroft Street, Toledo OH 43606; jaavso.editor@aavso.org

Received November 30, 2020

1. Dual-anonymous review, revisited

In my previous editorial (Morrison 2020), I discussed the advantages of *JAAVSO*'s policy of having the author's and the referee's identities unknown to each other, as far as possible. If the referee does not know the author's name, affiliation, and professional status, the referee is better able to concentrate on the scientific merits of the article and provide an unbiased review. The main goal is to reframe the referee's thinking about the article. This practice is known in scientific publishing as dual anonymization.

As that editorial described, NASA has amassed much experience with dual anonymization in its peer reviews of research proposals, and it is adopting the practice broadly. NASA's research shows that the more complete the anonymization of the proposal, the more eectively bias is reduced. Even if the reviewer can guess the proposer's identity, this knowledge causes as little distraction as possible.

In *JAAVSO*'s current submission policy, we request that authors' identifying information be removed from the title/head of the article. Almost all authors comply with this policy, but many retain identifying information in the rest of the paper. Here are some guidelines for better anonymizing your article. Some of them appeared in my previous editorial, but I am repeating them here for completeness. After the AAVSO website update is complete, we will post these guidelines in the journal's web pages.

- Remove observatory identifying information if applicable. However, give enough relevant information to enable the reviewer to judge the science, such as: observatory longitude and latitude, general environment—Urban? Desert? Mountain top? and light pollution levels.

- Rather than naming the observers, use pseudonyms, for example: "Author A," "Collaborator C," etc. Make sure your and your colleagues' names are also removed from figure captions and other locations, and use the same naming convention there.

- When citing your previous work, don't acknowledge ownership. Rather than, "in previous work, we found...," say, for example: "Author (year) established...," or, "previous studies (author, year) demonstrated...."

- In acknowledgements, the only change from standard procedure should be to remove information about the roles of people who helped you, such as professor or thesis advisor. In this way, information about your student status (if applicable) will be less obvious. As always, include standard acknowledgements such as to software and data sources. If you acknowledge grant funding, you may include the name of the funding agency, but please do not include the grant number. However, I do need to know who gave you advice or other help—I need to know not to ask your mentors to referee your article!

In final revision of the paper after acceptance, you will have to make a fair amount of effort to re-insert the identifying material you previously omitted or removed. However, a last careful pass through the article will have benefits: you may well see problems that you did not notice in previous revisions. Your last-minute improvements will always be welcome.

2. Open data: the FTP archive

For many years, the AAVSO has maintained an archive where the public can access data file via FTP (File Transfer Protocol). The open availability of data that support published results has many benefits to science. It enables replication of research results, and it enables continuation of research over a long time base as published data sets are augmented. The history of the AAVSO exemplifies the fruitfulness of preserving data over long time periods.

In order for these benefits to be realized, it is essential for the data to be preserved in perpetuity. Although you may think first of depositing your data in your own archive, the probability of long-term accessibility is higher in the well-backed-up archive of an established organization, which has the obligation to preserve information openly and securely for the indefinite future. Data that you might consider depositing in the AAVSO archive include:

- Data you took

- Data already in an AAVSO archive, if you performed extensive manipulations on the data

- Computer code, although you may alternatively want to

deposit it in a public repository such as GitHub and cite the GitHub page in your article.

When you provide data for the repository, please include the precise name of the file in your article. Place it in a footnote at the bottom of the manuscript page where the data are described and in a short note following the acknowledgements. Our editorial staff will provide the complete link to the file.

JAAVSO articles sometimes include lengthy tables of reduced but unanalyzed observational data. Our practice will be to include such tables, in machine-readable format, in the FTP archive, with a short sample version of the table in the published article. When data are in a directly readable file, in a format such as text or FITS (Hanisch *et al.* 2001), they are more accessible than they are if the user has to copy and paste them from a table in a PDF-formatted article. FITS files can be read and written by data analysis software such as found at IRAF (NOAO 2019), and by R (Harris 2019), and VSTAR (Benn 2013).

We also encourage authors to provide the numerical values that went into a figure, if they are different from the data already on line. Those data would be in a separate file in the FTP archive, linked to in the figure caption.

We are constantly looking for new ways for this journal to engage the reader. If you have an idea about how you would like to use a figure or a table to communicate numerical data interactively, please contact me (jaavso.editor@aavso.org) and we'll try to find a way to make it happen.

References

Benn, D. 2013, VSTAR data analysis software (http://www.aavso.org/vstar-overview).

Hanisch, R. J., Farris, A., Greisen, E. W., Pence, W. D., Schlesinger, B. M., Teuben, P. J., Thompson, R. W., and Warnock III, A. 2001, *Astron. Astrophys.*, **376**, 359.

Harris, R. 2019, FITSio: FITS (Flexible Image Transport System) Utilities (https://cran.r-project.org/web/packages/FITSio/index.html).

Morrison, N. D. 2020, *J. Amer. Assoc. Var. Star Obs.*, **48**, 1.

NOAO (National Optical Astronomy Observatory). 2019, Image Reduction and Analysis Facility (IRAF) data analysis software (http://ast.noao.edu/data/software).

Light Curve Analysis of 33 Pulsating Red Giant Stars

Kate M. Blackham
Swinburne University of Technology, John Street, Hawthorn, Victoria, Australia 3122; 100627441@student.swin.edu.au

Received March 2, 2020; revised September 10, 2020, accepted September 14, 2020

Abstract This project sought to use the AAVSO VSTAR software package to confirm the classification and periodicity of 33 pulsating red giant stars listed within the AAVSO International Database and look for changes in their periodicity over time. V826 Cas and V451 Cep were found to be semiregular with periods of 419 and 385.4 days, respectively. There was no evidence that GO Peg is semiregular; the data are consistent with its being an irregular star. BR CVn has a period of 860 days. V854 Cas, TU CVn, and μ Cep show variations to their periodicity that, while within the few percentage wanderings typical of these stars, may be the beginnings of longer-term changes and warrant further investigation.

1. Introduction

Stars that have exhausted the hydrogen in their cores evolve off the main sequence. Red giants burn the hydrogen found in a shell around their cores, and their outer layers cool and expand. Later, the star begins to burn helium, first in its core and later in shells around that core. The presence of a helium-burning shell within a star causes its surface to expand and cool again. Stars with helium-burning shells are found in a region asymptotic to the red giant branch of the Hertzsprung–Russell (H–R) diagram, known as the asymptotic giant branch (AGB).

Many pulsating stars are found in the 600–1100 K wide instability strip that includes the Cepheid and RR Lyrae variables, but stars at many other locations on the H–R diagram can also become variable. It was suggested at the beginning of the last century that Cepheid and RR Lyrae stars might behave as thermodynamic heat engines and this would drive pulsations within their atmospheres, leading to variability in the light observed on Earth (Shapley 1914; Eddington 1918, 1919). However, the reason for the variability in the pulsating red giant, AGB, and supergiant star populations that exist outside the instability strip is not fully understood and therefore worth further investigation. One possible theory is that oscillations in semiregular and OGLE small amplitude red giant (OSARG) variables are broadly similar to the oscillations of Sun-like stars, which display stochastic excitation due to convection near to their surfaces; red giants with their increased luminosity and convection strength would therefore have a much increased oscillation amplitude (Christensen-Dalsgaard *et al.* 2001; Takayama *et al.* 2013). A competing theory is that highly luminous red giants act like Miras: their convection and oscillations are coupled in a complex manner that causes the turbulence to act at one time as a damping effect and later as a cause of excitation (Xiong and Deng 2013; Xiong *et al.* 2018).

Following a convention used by Percy (2007) all pulsating red giant, AGB, and supergiant stars are referred to as pulsating red giants (PRG) when discussed as a group within this project, although PRG is not a classification that occurs in the *General Catalogue of Variable Stars* (GCVS; Samus *et al.* 2017). This is not without justification; the classification of stars into groups such as Mira, semiregular, and irregular is arbitrary and there is no discontinuity as you cross between groups of the physical properties of period, amplitude, and degree of periodicity. The distinction between semiregular stars and irregular is particularly ill-defined. Semiregular stars, by their nature, display less predictable periodicity than other pulsating variables and SRB stars in particular may enter periods of irregular pulsation. The irregular category is therefore a mixture of truly irregular stars with no discernible periodicity and other variable stars for which observations have not yet been made in the quantity and over sufficient time to detect their true category.

PRGs, like all stars, evolve and change over time. The evolution from one type to another is rarely obvious over the course of a human lifetime, but with records for some stars dating back over 100 years (Mattei 1997; Henden 2013; AAVSO 2018) it is possible to identify changes that take place over many decades. For example, one hundred years' worth of data on V725 Sagittarii was sufficient for Henrietta Swope to identify that it had evolved from a type II Cepheid to a semiregular PRG (Swope 1937; Percy 2010, 2020). However, sometimes radical changes are obvious within a lifespan; T UMi was considered to be a Mira until around 1970 when its period began to change (Templeton *et al.* 2005) and it now displays an interesting and complicated periodicity, with periods of about 201 days and 109 days that are probably its fundamental and first overtone modes, respectively (Molnár *et al.* 2019).

While changing between one variable star classification and another requires significant changes to the physical properties of a star, more subtle changes also occur. The periods of PRGs can "wander," that is, increase or decrease by several percent over the course of several decades (Eddington and Plakidis 1929). The physical processes that are involved in PRGs' periods and their variation are poorly understood and since their periods last months to years, to stand any chance of detecting long-term changes to a PRG's period, amplitude, or mean magnitude, it is important to analyze long-term data that have been collected over many decades.

2. Project aims

The project was undertaken as part of a master's degree in astronomy and sought to investigate the long-term data held in the AAVSO's International Database, the AID (AAVSO 2013), on a group of 33 PRGs. All 33 PRGs were included in North (2004) as being suitable for amateur observation.

An initial list of 15 stars was explicitly chosen because they are poorly observed stars and of questionable classification. Four were thought to be Miras (V2582 Oph, V409 Per, V418 Cas, and V854 Cas), five were thought to be semiregular (EV Aqr, W Boo, RY Dra, UX Dra, and V336 Vul), and six were thought to be irregular (V826 Cas, V451 Cep, T Cyg, RU Crt, NSV 12441, and NSV 24346). However, the paucity of data meant that these were far from certain and North (2004) suggested that observers adopt them into their observing plans.

The remaining 17 PRGs were all well observed with many decades of observations held in the AID. They were selected from North's lists of 134 Miras, 104 semiregulars, and 11 irregular stars, excluding those stars for which similar studies (e.g. Percy and Qiu 2019) had already investigated any possible long-term changes.

No doubt thanks in part to North's plea, there was a noticeable increase in observations for the 16 questionably classified stars post-2004. While there are often insufficient data on these stars to observe any long-term changes, these stars were more likely to have been misclassified in 2004 and a reassessment of the properties of their light curves was therefore important.

For each star, an attempt was made to ascertain each star's period of variability or, in the case of irregular stars, verify that they do indeed display no periodicity. It is common for newly discovered or poorly observed stars to be misidentified due to lack of evidence. Stars originally believed to be irregular may be semiregular and vice versa. Confirmation of the classification of each PRG from its light curve was also attempted.

3. Equipment

3.1. AID

The American Association of Variable Star Observers (AAVSO) holds more than 42,000,000 variable star observations from over 5,000 observers dating back, for some stars, more than one hundred years in its AAVSO International Database, the AID (AAVSO 2013). The AID includes observations not just from AAVSO members, but from other amateur variable star observation groups internationally, including the British Astronomical Association. Hence the AID is the best resource available for analysis of long-term data of variable stars (Kafka 2019).

3.2. SIMBAD

SIMBAD is an astronomical database for over 11 million objects outside of the solar system. It includes basic data (including equatorial and galactic coordinates, proper motions, redshift, parallax, and spectral type), cross-identifiers for each object, and over 375,000 bibliographic references. The SIMBAD database can be queried not only by an object's name or identifier but also by its coordinates. SIMBAD is also linked to a number of other powerful tools including VizieR's 20,035 astronomical catalogues (including the GCVS), the Aladin Sky Atlas, and the CDS xMatch service.

3.3. VSX

The International Variable Star Index (VSX; Watson *et al.* 2014) was originally created using the entire Combined GCVS 4.2 with additional data from the Northern Sky Variability Survey (NSVS), the third All Sky Automated Survey (ASAS), the *Information Bulletin on Variable Stars* (IBVS), and new variable stars discovered by the Optical Gravitational Lensing Experiment (OGLE-II) and the Robotic Optical Transient Search Experiment (ROTSE-I) (VSXweb). A team of moderators update the VSX with the latest peer reviewed information. The page for each variable star holds information on its position, aliases, variability type, spectral type, magnitude range, and period, as well as links to relevant academic references.

3.4. VSTAR

Analysis was performed using the AAVSO's VSTAR data visualisation and analysis tool (Benn 2012). VSTAR is a free, open source application that runs on any operating system that supports JAVA. VSTAR can be used for any time-series data, but its origin as an AAVSO Citizen Sky Project means that it is designed primarily for the analysis of variable stars. The application will accept a wide variety of files as input, including AID files, .csv, .dat, .tsv, and .txt file types, as well as the files released from satellite missions such as Hipparcos and Kepler. VSTAR allows the user to plot light curves and phase diagrams based on the main period specified in the AAVSO's own Variable Star Index (VSX) or a user-supplied value, and can also display the data in table form. Data can be filtered in a variety of ways including by observation band (i.e. visual, Johnson and Cousins filters, etc.) and observer.

Light curves produced in VSTAR can be analyzed using its Fourier transform routine, which produces a power spectrum and table of what are referred to as "top hits." The Fourier transform routine allows users to find the most probable period, but also helps to identify potential secondary periods. Many PRGs exhibit secondary periods, but their cause is not currently known (Wood 2000; Percy and Qiu 2019). If multiple periods are found, the CLEANest algorithm (Foster 1995) can be applied to help create a model.

VSTAR also provides time-frequency analysis of data via an integrated wavelet analysis routine, which allows users to detect any long-term changes in a light curve.

4. Experimental technique

The analysis in this project relies on several algorithms integrated into VSTAR. Although the AID holds records of observations of many types including charge-coupled devices (CCD), to ensure that long-term changes are detected for the most part only visual data are considered in this project.

4.1. DC DFT

Fourier analysis is used to find periodic behavior from data. Assuming the best fit to the data has a sinusoidal shape, you can determine the period by testing trial periods (represented mathematically by frequencies). Then for each trial frequency you can calculate its power, which measures the statistical significance of that fit to the data. The frequency can then be plotted against the power in a graph called a periodogram or power spectrum (Figure 1). The highest peaks are therefore statistically significant and provide clues as to the true period.

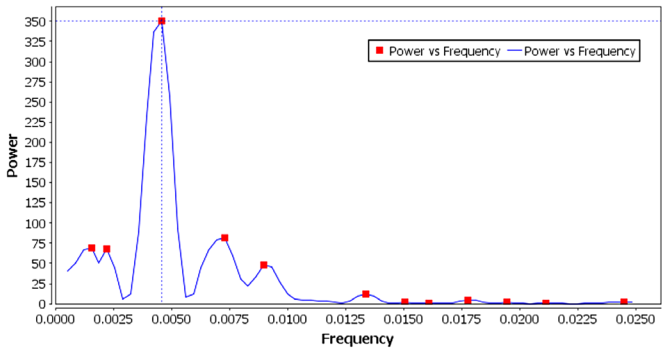

Figure 1. A periodogram for R Boo. Top hits are highlighted in VSTAR by red boxes. Note the statistically significant top hit at the center of the cross-hairs.

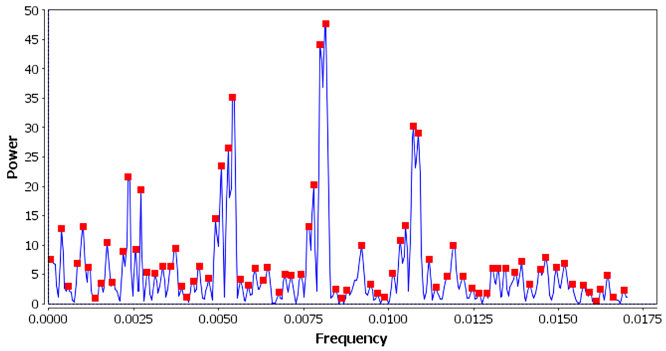

Figure 2. Power spectrum for the SRa star EV Aqr. Alias peaks are located at frequencies of approximately 0.0025, 0.0053, and 0.0107.

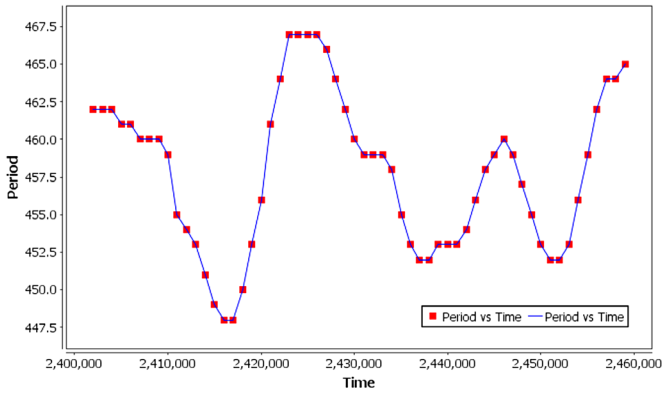

Figure 3. A plot of R Aur's period vs. time shows that its period has wandered within the expected several percent throughout the 154 years for which observations have been recorded.

Other peaks occur for a variety of reasons including the presence of noise. In Figure 1, the top hit represents a period of 219 days.

There are various algorithms that can be used to perform Fourier analysis on a data set, the most widely used being discrete Fourier transform (DFT) and fast Fourier transform (FFT). Both DFT and FFT rely on data being equally spaced with respect to time, an invalid assumption to make with astronomical data. Date-compensated discrete Fourier transform (DC DFT) was designed by Ferraz-Mello (1981) to be a more accurate Fourier transform method with data sets that have uneven spacing of observation dates.

4.2. CLEANest

False peaks can occur in power spectrums due to a star's location near the ecliptic, which causes recurrent seasonal gaps to appear in the star's light curve. This produces "alias" peaks in the power spectrum appear at frequencies governed by the equation:

$$\text{frequency} = \text{true frequency} \pm N/365.25 \qquad (1)$$

where N is an integer and the strongest alias peak is found where N = 1 (Percy and Qiu 2019).

These alias peaks (see Figure 2) arise because when the Sun is in the star's constellation, it is difficult, if not impossible, for astronomers to undertake an observation of it.

The CLEANest algorithm was developed to help remove false peaks from a power spectrum. It is also beneficial for detecting and describing light curves composed of more than one period (Foster 1995).

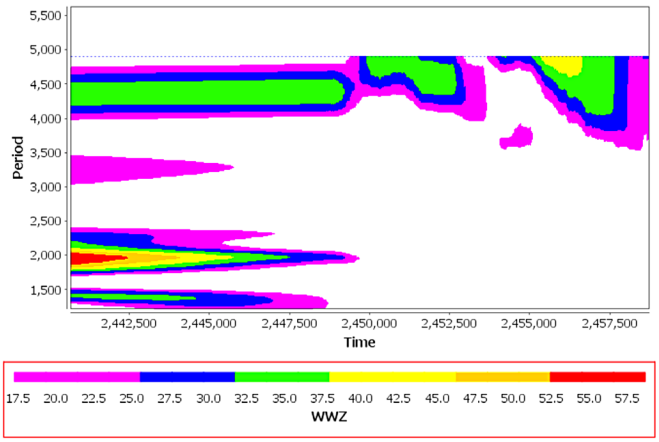

Figure 4a. A contour plot of period vs. time vs. the WWZ F-statistic for μ Cep from 13 Apr 1970 – 14 Aug 2019.

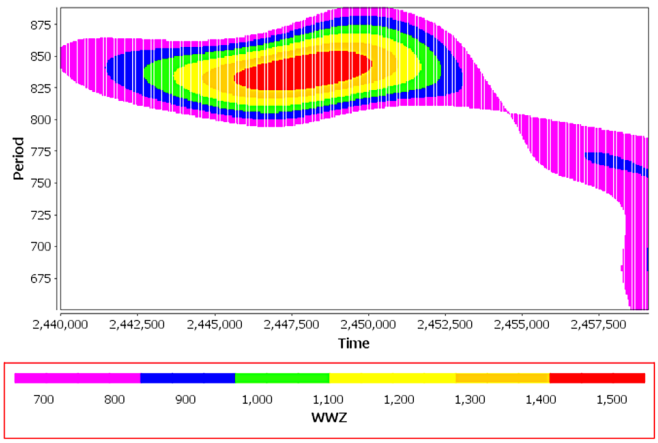

Figure 4b. A contour plot of period vs. time vs. the WWZ F-statistic for μ Cep from 6 Aug 1968 – 8 Sep 2020 showing clear variations in the light curve on time scales of hundreds of days.

4.3. WWZ

The AID holds data on in excess of 52,000 variable stars, with most of them added in recent decades (Schweitzer undated). While the majority of variable stars will probably not have enough observations to allow for the detection of long-term changes that accompany stellar evolution, as long as a variable

has been regularly observed for approximately 20 years its light curve may profit from undergoing time-frequency analysis.

The analysis technique for detecting evolution over time of parameters such as a light curve's period, amplitude, or phase is known as wavelet analysis. Exactly as the Fourier transform algorithm used in VSTAR allows for uneven spacing of observations over time, so must the wavelet analysis algorithm. Wavelet analysis of light curves is included in the VSTAR application via the weighted wavelet Z-transform (WWZ) algorithm (Foster 1996).

The WWZ algorithm creates plots for a variable star's period vs. time (see Figure 3), frequency vs. time, semi-amplitude vs. time, as well as the period vs. time vs. WWZ F-statistic as three-dimensional rotatable graph and as a contour plot (see Figure 4).

The contour plot uses regular x- and y-axes for time and period, respectively, with colors to represent the third dimension, the WWZ F-statistic, creating an image not unlike a topographic map. The WWZ F-statistic gives an indication as to the strength of the periodicity at that point in time (Foster 2010; AAVSO 2018).

5. Results

The overall results of my investigation of the 33 PRGs surveyed are summarized in Table 1, with the values shown ascertained from light curves, phase diagrams, power spectrums, and WWZ plots. For the sake of brevity, only the most distinctive or interesting figures are included in this paper, but other figures are available upon request.

Table 1. Summary of the 33 PRGs surveyed during this project.

Name	*GCVS Type*	*VSX Period (days)*	*Type*	*Period (days)*	*Range (mag)*
BZ And	LB	—	LB	—	1.3
W And	M	397.3	M	396.16	9
EV Aqr	SRA	124.2	SRA	122.55	2.8
R Ari	M	185.67	M	186.90	7.5
R Aur	M	457.51	M	457.52	7.5
X Aur	M	163.79	M	164.15	6
R Boo	M	223.4	M	223.58	7.5
W Boo	SRB	25.51	SRB	—	1.8
R Cam	M	270.22	M	269.99	7
V Cam	M	522.45	M	523.38	8.5
W Cas	M	405.57	M	406.03	5
V418 Cas	M	480	M	479.46	6.5
V826 Cas	LB	730	L	419	3
V854 Cas	M	332	M	329.72	5.5
μ Cep	SRC	835 (also 390)	SRC	825	2
V451 Cep	LB	—	SR	385.4 & 415.8	4
RU Crt	SRB	60.85	SRB	620	2.3
T Cyg	LB	—	LB	—	2.3
BR CVn	SRB	—	SRB	860	2
TU CVn	SRB	44.2	SRB	44.846	1.8
MV Del	SRB	25.099	SRB	—	1.2
RY Dra	SRB	300	SRB	276.7	2.2
UX Dra	SRB	175	SRB	177.34	1
R Lyr	SRB	46	SRB	46.54	1.2
V2582 Oph	M	262	M	261.82	5
V409 Per	M	355	M	344.64	2.5
GO Peg	SRB	79.3 (also 65)	L	—	1.9
KK Per	LC	—	LC	—	2
TV Psc	SR	49.1	SR	55.1	0.9
TV UMa	SRB	53.74	SRB	50–60, 170–200	2.5
V336 Vul	SRC	131.6 (also 113.8)	SRC	131.7 and 115.4	2.25
NSV 12441	LB	—	LB	—	0.5
NSV 24346	LB	583	LB	—	1.8

5.1. Notes on individual stars in Table 1

The magnitude of BZ And is tending to decrease. It also shows a very clear peak in its Fourier spectrum very close to P = 365 with an amplidude of 0.1. This might be a spurious result caused by some annual variation in observation.

There are insufficient data to confirm the periods of W Boo, RU Crt, MV Del, NSV 12441, and NSV 24346.

Using visual data from pre-2007 gives a period of 334 days for V854 Cas.

Harmonics can be detected for a number of the stars in this paper. R Cam has a harmonic of 134.99 days. V Cam has a harmonic of 261.69 days. W Cas has a harmonic of 203.02 days (and other periods of 135.34 and 101.51 days). BR CVn has a harmonic of 431 days. TU CVn has an overtone period of 22 days and WWZ suggests its period has tended towards lengthening after around Julian Day 2455000 (i.e. June 2009). R Lyr has a harmonic of 23.27 days. V2582 Oph has a harmonic of 130.91 days. V409 Per has a harmonic of 172.32 days. The first period of V336 Vul (131.7 days) has a harmonic of 65.8 days and a harmonic of 43.9 days.

RU Crt has a complicated variability pattern that appears to be the result of a pulsation period of approximately 60 days and a long secondary period of approximately 620 days.

GO Peg has reported periods of 79.3 and 65 days. However, neither period could be confirmed. GO Peg appears to be an irregular star according to the data held in the AID.

The data held in the AID confirm that TV Psc has a period of 55.1 days, but did not confirm that it also has a period of 49.1 days.

For TV UMa, WWZ suggests that possible periods are in the range 50–60 days and 170–200 days.

V826 Cas has a 3-magnitude slow variation.

5.2. V854 Cas

The data held in AID show that V854 Cas has a range of magnitude 11–16.5. Analysis via a DC DFT Standard Scan gives a top hit for a period of 333.77 days on the visual data and 329.72 on the more recent Johnson V data. V854 Cas is a poorly observed variable, however, no doubt due to its being a dimmer star and hence impossible to see with the naked eye. In 2007 there was a switch in the observations from being exclusively visual to exclusively Johnson V. Hence we can clearly see that V854 Cas's period has reduced in the more recent data (Figure 5); the slight difference in periods have caused the visual and Johnson V observations to be offset in time.

5.3. TU CVn

A DC DFT Standard Scan with CLEANest on the much more abundant visual data for TU CVn gives a period 44.846 days with a harmonic of 22 days. However, looking at the phase plot with the DC DFT values, it becomes immediately apparent that the Johnson V data mostly lie above the model. If the phase plot is repeated (Figure 6) but without the visual data this is

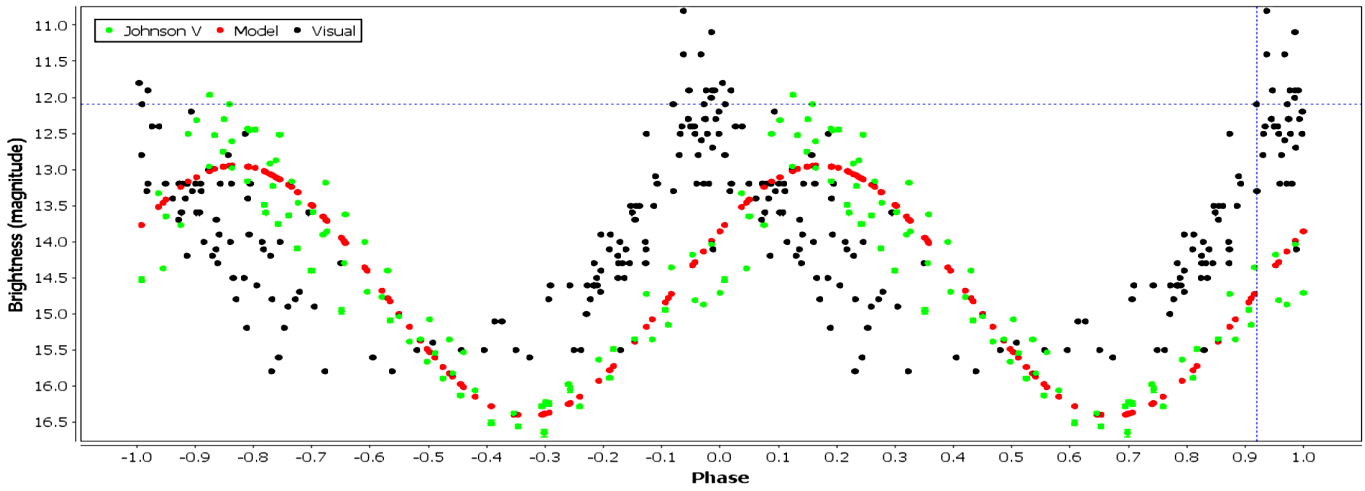

Figure 5. V854 Cas's wandering period is clear from its phase plot. The model is based on the Johnson V data.

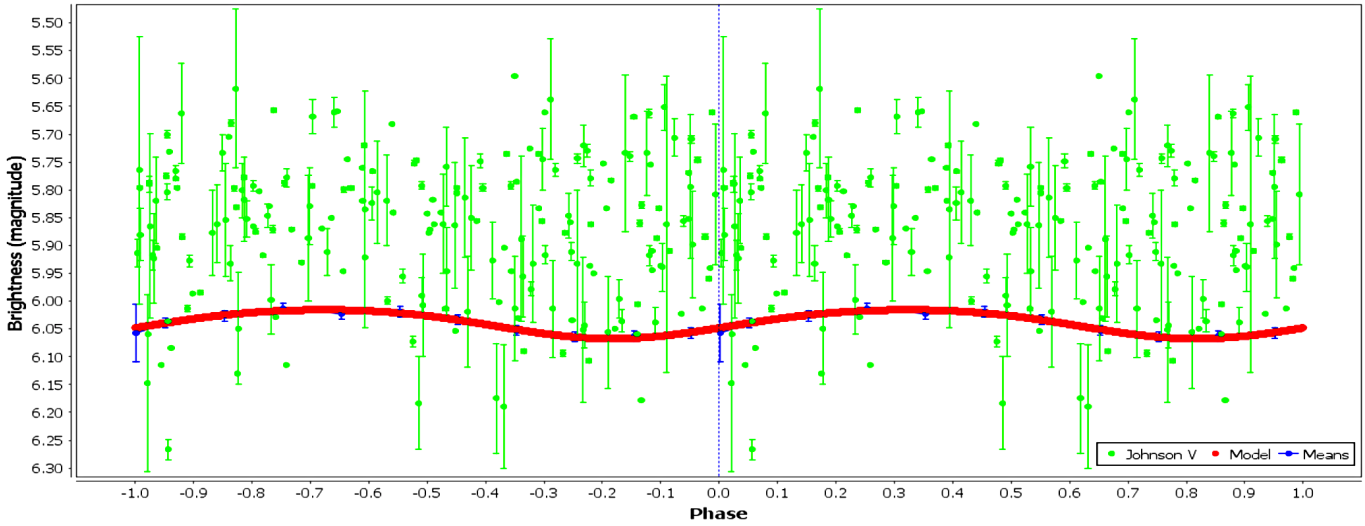

Figure 6. Phase plot of TU CVn with period of 44.846 and harmonic 22 days. The model is based on the visual data; note how the Johnson V observations are on average brighter.

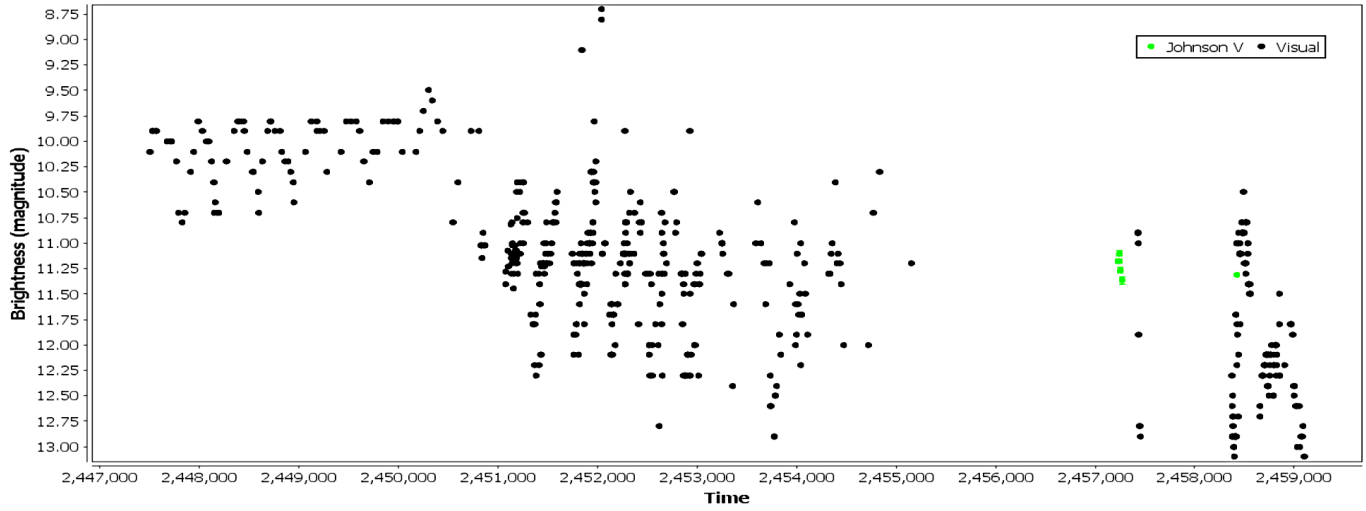

Figure 7. Light curve for V451 Cep between 5 Dec 1988 and 8 Sep 2020.

even more obvious (note that the model is a very good fit for the means of the visual data (the blue points)).

The Johnson V data held for TU CVn in AID span from June 1972 until August 2019. However, the oldest visual data were recorded in March 1955, with the most recent data recorded in October 2019. The differences between the position of the means in the visual and Johnson V datasets suggests that TU CVn has brightened. This is somewhat apparent in the raw data plot, where the mean brightness has increased from around magnitude 6.1 to magnitude 5.9. Note that the bandpasses of the Johnson V and visual are not identical so it is possible that the result shown here is due to a previous bias towards underestimating the brightness of TU CVn due to its spectrum (SIMBAD records TU Cvn as being a red star of spectral type M5). The difference in brightness between visual and V could well be the result of differences in the comparison stars used for visual versus for V; there is often an offset between visual and V in the AAVSO data, especially in the earlier years.

5.4. V451 Cep

The AID data suggest that V451 Cep has a period of 385.4 (and 415.8) days. Unfortunately the data only go back as far as 1988, but it appears that there was an abrupt change in the magnitude of V451 Cep during 1998. For the ten years preceeding 1998 its brightness only varied between magnitude 9.75–10.75, more recently it has been as bright as magnitude 10 and as dim as magnitude 13 (Figure 7). It is unclear whether this change in the magnitude range has an astronomical cause or not; it is possible that the sole early observer was using different comparison stars to later observers.

6. Discussion

As expected, many of the PRGs showed signs of having periods that wandered within a few percent, as can be seen from Table 1 and some of the WWZ plots such as Figure 3. Unfortunately, none of the selected stars displayed significant long-term changes to their periodicity. There are several instances where a model produced on the more recent Johnson V data has a different period and/or average magnitude from that produced by the generally older visual data, such as V854 Cas and TU CVn. Unfortunately, only time will tell whether these are at the beginning of a long-term change or if the differences are purely due to PRG wanderings. If these are the beginnings of long-term changes then it is thought that these are driven by a thermal pulse (Templeton *et al.* 2008).

7. Conclusion

This project aimed to confirm the classification and periodicity of a group of 33 PRGs and to look for any evidence of long-term changes in their periods.

Within the irregular stars group, I was able to detect a period of 385.4 (and 415.8) days for V451 Cep. I therefore tentatively suggest that it be updated to the SR classification instead. The relatively recent apparent abrupt change in magnitude range suggests that V451 Cep warrants close attention by amateur astronomers

Within the semiregular stars group, I was unable, despite a wealth of data, to confirm that GO Peg was an SRb star. In fact, all the evidence within the AID data points towards it being an irregular star instead.

Many of the semiregular and Mira stars had periods different from those published, but within the range expected due to PRGs' proclivity for their periods to wander by several percent.

The VSX lists BR CVn as an SRb with unknown period, however the AID data suggest a good fit for a period of 860 days with a harmonic of 431.4 days.

While I was unable to detect any long-term changes in the variability of the PRGs studied, three variables in particular warrant further investigation: V854 Cas, a Mira that appears to have decreased in period since 2007; TU CVn, an SRb for which WWZ analysis suggests a lengthening of its period around June 2009; and μ Cep, an SRc with a particularly complicated periodicity for which the contour plot (Figure 4a) suggests an event around JD 2450000 (9 October 1995) that has left its periodicity dominated largely by its 4,000-day period created by its non-spherical circumstellar nebula (De Wit *et al.* 2008), while is approximately 800-day pulsation period shows large variations (Figure 4b).

As is always the case with an observational science, more data would be beneficial, but this is especially the case with: NSV 12441, NSV 24346, W Boo, RU Crt, and MV Del. However, it is important not just that more data are collected, but the right type of data. W Boo, for example, has 10,607 observations stored in AID. Unfortunately, as a short-period PRG, W Boo would benefit greatly from observers prepared to adopt it in a regular observation program on a near-nightly basis.

8. Acknowledgements

I acknowledge with thanks the variable star observations from the AAVSO International Database contributed by observers worldwide and used in this research. I also wish to thank the AAVSO staff who archive these data and make them publicly accessible, and the developers of the VSTAR data analysis and visualization software package. This research has made use of the SIMBAD database, operated at CDS, Strasbourg, France. This research has also made use of the International Variable Star Index (VSX) database, operated at AAVSO, Cambridge, Massachusetts. I am extremely grateful to the anonymous reviewer whose helpful suggestions have much improved this paper. I also wish to thank JoDee Baker-Maloney, Blake Crosby, and the rest of the CHOICE team at the AAVSO for their invaluable training courses. Last, but by no means least, thanks go to my project supervisor Melissa Hulbert for much helpful feedback.

References

AAVSO. 2018, *Variable Star Classification and Light Curves Manual*, version 2.4, AAVSO, Cambridge, Mass.

Benn, D. 2012, *J. Amer. Assoc. Var. Star Obs.*, **40**, 852.

Christensen-Dalsgaard, J., Kjeldsen, H., and Mattei, J. A. 2001, *Astrophys. J.*, **562**, L141.

De Wit, W. J., *et al.* 2008, *Astrophys. J., Lett.*, **685**, 75.
Eddington, A. S. 1918, *Mon. Not. Roy. Astron. Soc.*, **79**, 1.
Eddington, A. S. 1919, *Mon. Not. Roy. Astron. Soc.*, **79**, 177.
Eddington, A. S., and Plakidis, S. 1929, *Mon. Not. Roy. Astron. Soc.*, **90**, 65.
Ferraz-Mello, S. 1981, Astron. J., 86, 619.
Foster, G. 1995, *Astron. J.*, **109**, 1889.
Foster, G. 1996, *Astron. J.*, **112**, 1709.
Foster, G. 2010, *Analyzing Light Curves: A Practical Guide* (http://www.lulu.com/shop/grant-foster/analyzing-light-curves-a-practical-guide/paperback/product-11037112.html).
Henden, A. A. 2013, observations from the AAVSO International Database (http://www.aavso.org).
Kafka, S. 2019, observations from the AAVSO International Database (https://www.aavso.org).
Mattei, J. A. 1997, *J. Amer. Assoc. Var. Star Obs.*, **25**, 57.
Molnár, L., Joyce, M., and Kiss, L. L. 2019, *Astrophys. J.*, **879**, 62.
North, G. R. 2004, *Observing Variable Stars, Novae and Supernovae*, Cambridge University Press, Cambridge.
Percy, J. R. 2007, *Understanding Variable Stars*, Cambridge University Press, Cambridge.
Percy, J. R. 2010, "Variable Star of the Season: V725 Sagittari" (https://www.aavso.org/vsots_v725sgr).
Percy, J. R. 2020, *J. Amer. Assoc. Var. Star Obs.*, **48** (https://www.aavso.org/apps/jaavso/article/3637/).
Percy, J. R., and Qiu, A. L. 2019, *J. Amer. Assoc. Var. Star Obs.*, **47**, 76.
Samus, N. N., Kazarovets, E. V., Durlevich, O. V., Kireeva, N. N., and Pastukhova, E. N., 2017, *Astron. Rep.*, **61**, 80, *General Catalogue of Variable Stars: Version GCVS 5.1* (http://www.sai.msu.su/gcvs/gcvs/index.htm).
Schweitzer, E. undated, "The Names and Catalogues of Variable Stars" (http://cdsarc.u-strasbg.fr/afoev/var/edenom.htx).
Shapley, H. 1914, *Astrophys. J.*, **40**, 448.
Swope, H. 1937, *Ann. Astron. Obs. Harvard Coll.*, **105**, 499.
Takayama, M., Saio, H., and Ita, Y. 2013, *Mon. Not. Roy. Astron. Soc.*, **431**, 3189.
Templeton, M. R., Mattei, J. A., and Wilson, L. A. 2005, *Astron. J.*, **130**, 776.
Templeton, M. R., Willson, L. A., and Foster, G. 2008, *J. Amer. Assoc. Var. Star Obs.*, **36**, 1.
Watson, C., Henden, A. A., and Price, C. A. 2014, AAVSO International Variable Star Index VSX (Watson+, 2006–2014; http://www.aavso.org/vsx).
Wood, P. R. 2000, *Publ. Astron. Soc. Australia*, **17**, 18.
Xiong, D.-R., and Deng, L.-C. 2013, *Res. Astron. Astrophys.*, **13**, 1269.
Xiong, D. R., Deng, L., and Zhang, C. 2018, *Mon. Not. Roy. Astron. Soc.*, **480**, 2698.

Spectroscopic Monitoring of the 2017–2019 Eclipse of VV Cephei

Ernst Pollmann
International Working Group ASPA, Emil-Nolde-Str. 12, 51375 Leverkusen, Germany; ernst-pollmann@t-online.de

Philip Bennett
Department of Physics and Atmospheric Science, 6310 Coburg Road, Dalhousie University, Halifax, NS B3H 4R2, Canada; Philip.Bennett@dal.ca

Received March 26, 2020; revised July 10, 2020; accepted September 10, 2020

Abstract VV Cephei is an M supergiant star that eclipses its B-type companion every 20.36 years. It is the eponymous member of the red supergiant + hot main-sequence binaries known as the VV Cephei stars. The red supergiant primary is surrounded by a circumstellar shell due to mass loss via a slow, stellar wind, and this circumstellar material interacts with the hot companion. Spectroscopic observations in the ultraviolet indicate the presence of material accreting onto the hot star from the wind of the M supergiant primary, and the probable presence of an accretion disk around the companion. The hot star and disk produce a local H II "bubble" that results in very prominent Hα emission originating from the vicinity of the companion. In this work, we report on a continuing campaign of spectroscopic observations of Hα emission from VV Cep over the period 2015–2020 by amateur observers of the ARAS spectroscopy group. We also present a newly discovered 42-day period variability in the equivalent width of this Hα emission.

1. Introduction

VV Cephei (M2 Iab + B0-2 V) is the best known, brightest, and eponymous member of the composite spectrum binaries with M supergiant primary stars and hot B-type main-sequence companions. The M supergiant primary is one of the largest known stars in size, with a radius of about 1000 $R_\odot$. Both the M supergiant and its companion are comparably massive, with masses near 20 $M_\odot$. The VV Cep binary system is observed nearly edge-on, and undergoes total eclipses every 20.36 years, which is one of the longest known periods of any eclipsing binary. This binary has been a system of particular interest for almost a century, following McLaughlin's (1936) discovery that the binary was eclipsing. It is one of the most massive, longest-period eclipsing binary systems known. McLaughlin (1934) first reported on the composite-spectrum binary, with its broad hydrogen emission lines and H and K lines of ionized calcium (Ca II). Subsequently, McLaughlin (1936) announced that the hot star in VV Cep had been eclipsed, establishing the system as an eclipsing binary. Goedicke (1939) carried out the first detailed spectroscopic analyses of this system. Wright (1970) presented an orbital solution for the M supergiant primary. Hutchings and Wright (1971) and Wright (1977) recognized that the Hα emission came from around the hot companion and used this prominent emission line to derive orbits of the secondary star.

The visible spectrum longward of 5000 Å, except for the very prominent emission line of Hα, is that of the luminous red supergiant primary. However, shortward of 4000 Å, the spectrum of the hot companion becomes increasingly dominant. This system has given its name to the class of similarly massive M supergiant binaries with hot companions: the VV Cephei stars (Cowley 1969). In VV Cep itself, the evolved M supergiant is surrounded by an extensive shell of circumstellar material due to mass lost from the red supergiant via a stellar wind, and this wind completely envelops the companion's orbit. Some of this material is captured by the hot companion, resulting in an accretion region around the B-type star, and emission from this accretion region mostly obscures the photospheric spectrum of the hot star in the ultraviolet. The companion is hot enough, at around spectral type B1 V, to ionize a local "bubble" of circumstellar gas, and it is recombination of ionized hydrogen in this H II region that produces the prominent Hα emission, as well as strong emission in the other hydrogen Balmer lines and in the Balmer continuum in the ultraviolet (see Figure 1). The ultraviolet spectrum is characterized by numerous emission lines of Fe II, which are probably pumped by strong emission in the Lyman-β line (Bauer and Bennett 2000) from the same H II region.

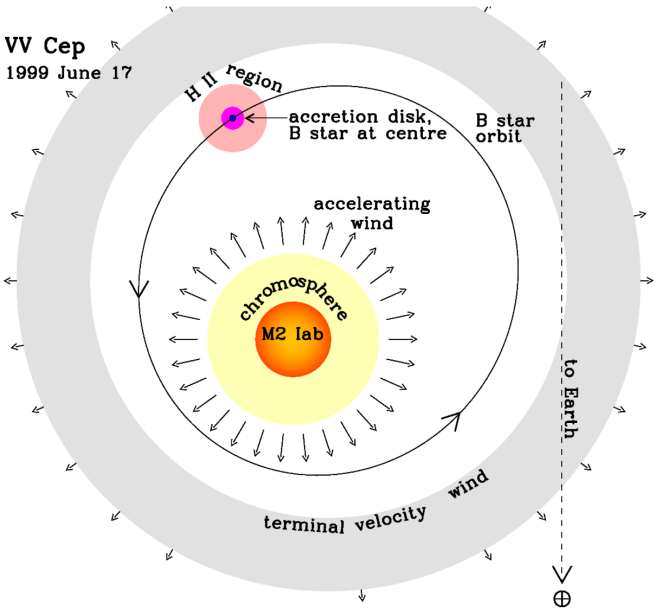

Figure 1. The orbit and structure in the orbital plane of the VV Cephei binary on 1999 June 17, drawn to scale (adapted from Bennett and Bauer 2015).

As noted, out of eclipse, the Hα spectral line at 6563 Å is particularly prominent in this star, with a peak emission flux several times that of the M star's continuum. The Hα line is one of the few features in the visible spectrum that arises from the hot companion, as established by a radial velocity behavior that runs counter to that of the red supergiant. Observations of the Hα emission line provide valuable information on the difficult-to-observe companion, and of a possible accretion disk around the hot companion (Wright 1977; Kawabata *et al.* 1981; Moellenhoff and Schaifers 1978, 1981). Despite the prominent wind accretion and interaction in this binary, direct mass transfer via Roche lobe overflow does not appear to be taking place. The spectroscopic orbit of the M supergiant is fairly well established, and the orbit is decidedly eccentric, with an eccentricity of e = 0.35 (Wright 1970). The two stars are reasonably well-separated, with a ratio of orbit semi-major axis to M star radius (a/R_1) of about 5, and a periastron separation to M star radius of ~3.3 (Bennett and Bauer 2015). Since mass transfer binaries undergoing Roche lobe overflow invariably have orbits circularized by tidal interactions, the eccentric nature of the VV Cep orbit suggests that VV Cep has never undergone significant episodes of Roche lobe mass transfer.

The ultraviolet spectrum appears to be largely of nonstellar origin, with strong inverse P Cygni line profiles of ionized metal lines (especially Fe II), and a continuum that varies by up to a factor of 3 outside of eclipse. Both the inverse P Cygni profiles—indicative of infalling circumstellar gas—and the variable Balmer emission continuum suggest an accretion source for the nonstellar UV spectrum (Bauer and Bennett 2000; Bennett and Bauer 2015). The spectroscopic orbit (Wright 1977) implies both stars are comparably massive, so the companion must be a luminous main-sequence star, but even so, the stellar source contributes only 30–50% of the UV luminosity. The rest of the luminosity must come from the accretion region, which is probably organized as an accretion disk around the hot star. The nonstellar component of the spectrum in the UV consists of Balmer continuum emission, and metal line emission (especially Fe II) powered by fluorescence with Lyman emission lines. The accretion disk is also hot, and appears to contribute to much of the ionization of neutral circumstellar hydrogen in a local, confined bubble around the hot star (Figure 1).

In this paper, we present an extensive set of high-cadence spectroscopic monitoring of the Hα emission line in VV Cep over the entire eclipse period of nearly three years. This continues the work previously presented by Pollmann, Bennett, and Hopkins (2016) and Pollmann *et al.* (2018). We also report on a newly discovered 42-day oscillation in the equivalent width (EW) and peak fluxes, and a 51-day radial velocity oscillation in the blue (V) component of the double-peaked Hα emission line. We attribute these periodic variations to the precession of the accretion disk around the hot B-type companion.

2. Observations and analysis

Long-term monitoring of the Hα region of the spectrum of VV Cep started in July 1996 (by EP) to observe the 1997–1999 eclipse, and has continued for 24 years to the present day. Since April 2010, observers of the *Astronomical Ring for Access to Spectroscopy (ARAS)* spectroscopy group have been involved in, and contributed substantially to, this long-term monitoring campaign. In 2015, a combined photometric and spectroscopic campaign was organized by J. Hopkins, P. Bennett, and E. Pollmann to monitor the recent 2017–2019 eclipse. This eclipse began (first contact) in continuum light, around the beginning of September 2017, and ended (fourth contact) at the start of April 2019. Over this period, medium-resolution spectroscopic observations were obtained in the red spectral region centered on Hα, using commercially available instrumentation such as the Shelyak Instruments LHires III spectrograph (R ~ 17000) and a CCD detector. We present a summary of the results of this observing program in this paper. In Figure 2, we show a typical LHires III spectrum of VV Cep observed in the red spectral region out of eclipse, with its central self-absorption feature dividing the observed Hα emission profile into characteristic blue and red components. For each spectrum, the total Hα equivalent width (EW), the EW and peak flux of the blue (V) and red (R) components, and radial velocity of the blue (V) emission component were measured. The total Hα EW variation over the entire 24-year observational period (see Figure 3) shows considerable variation outside of eclipse on both long and short timescales. Remarkably, weak, narrow Hα emission remains present even at mid-eclipse, as can be seen from Figure 4. This emission must be coming from spatially extended (and low velocity) regions far enough from the hot star so as to remain visible at mid-eclipse.

The slow Hα EW variation, occurring on decadal timescales (Figure 3, dashed curve), correlates with the orbital separation of the two stars, with the largest emission flux occurring near periastron. We report here on the discovery of a rapid 42-day variability that is also present in the EWs and peak fluxes of both the V and R components. A similar 51-day variability is present in the radial velocity of the V component. Surprisingly, this 42-day variability persists through total eclipse, as can be seen from Figure 5.

The continuous and high-cadence nature of these Hα observations allows the time-variation of the Hα red (R) and the blue (V) emission components to be analyzed in unprecedented detail. In principle, a detailed analysis of the Hα profile over the course of the eclipse should permit the geometry of the Hα emitting region to be determined. For this work, we simply present the results and an analysis of the period of the EW and the peak fluxes of the Hα V and R emission components and the radial velocity (RV) variation of the V emission component, and defer that complete analysis to a future work. Figure 6 shows the behavior of the EW and peak fluxes for the V and R components over the course of the eclipse. In particular, the asymmetric nature of the V / R eclipse curve, with its minimum occurring well prior to mid-eclipse, implies that the eclipse of the V component of the Hα emission during ingress proceeds much more quickly than that of the R component.

The AVE code of Barbera (1998) was used to carry out the PDM analysis. Results of this period analysis of the Hα emission line EW and of the peak flux of both V and R components of nearly 1000 spectra indicate a significant period of about 42 days. This 42-day period variation is shown in Figure 7 for the

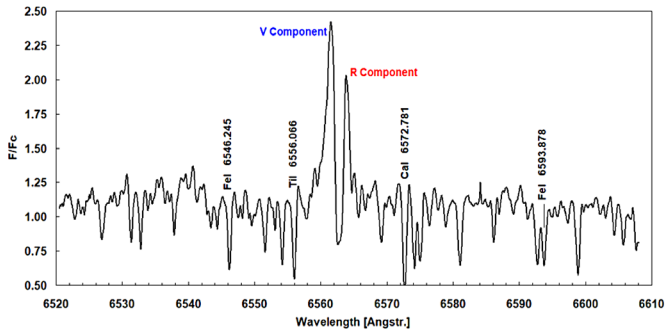

Figure 2. Typical out-of-eclipse spectrum of VV Cep showing double-peaked Hα emission.

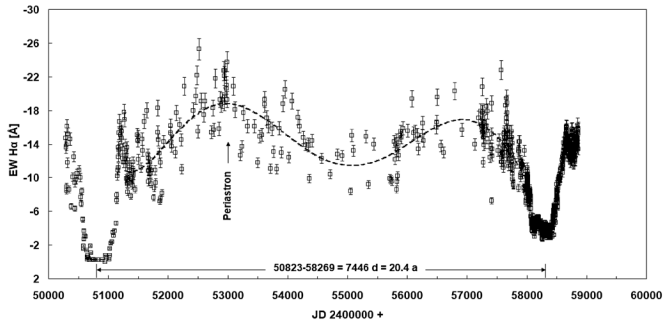

Figure 3. Hα equivalent width (EW) from 1996 to 2020.

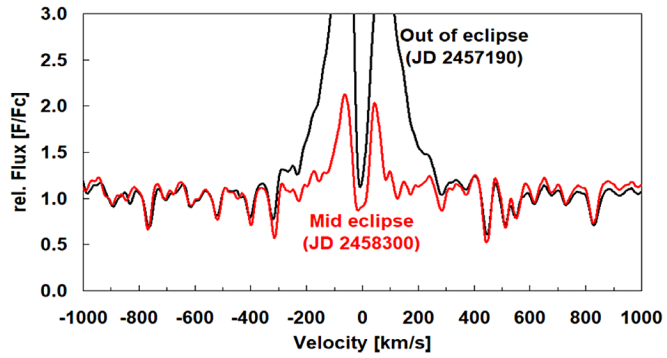

Figure 4. The narrow Hα profile during totality implies the emission here comes from a low velocity region extending beyond the occulting M supergiant, compared to the much broader out-of-eclipse profiles from the accretion disk. Only about 25% of the total flux comes from this extended region.

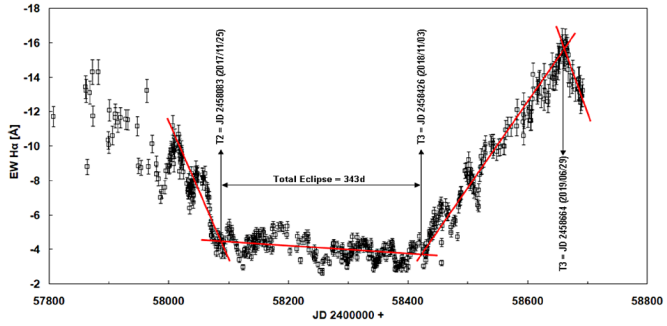

Figure 5. Hα emission EW for the 2017–2019 eclipse. The 42-day variability persists through totality.

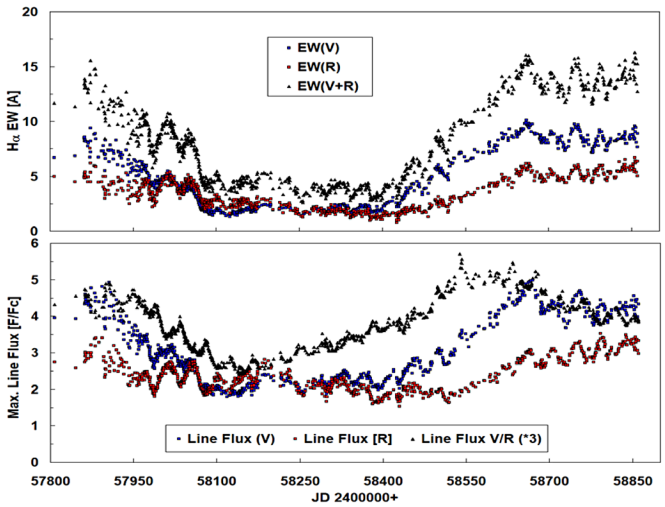

Figure 6. VV Cep Hα EWs and fluxes of blue (V) and red (R) emission peaks during the 2017–2019 eclipse.

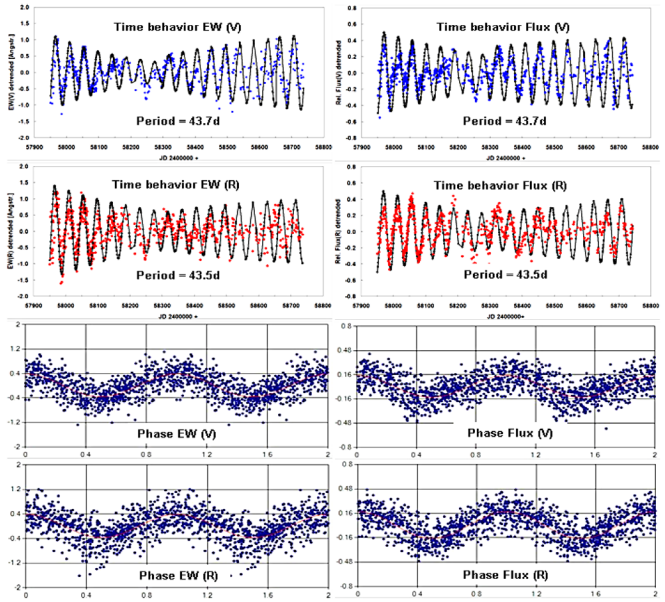

Figure 7. Periodic variability of EW (left) and peak line flux (right). Both periods are ~42 days

EW of the V and R components (left panels), as well as for the peak flux (right panels) of both emission components.

The 42-day variability is confirmed by a periodogram of the V/R ratio, shown in Figure 8. The source of the observed Hα variability is probably precession of the accretion disk. Although presumably oriented perpendicular to the hot star's rotation axis, this accretion disk need not lie exactly in the orbital plane of the binary. In this situation, the M supergiant would exert a torque on the accretion disk, accounting for the observed precession.

This variability resembles the 58-day semi-regular variability reported by Baldinelli *et al.* (1979), who obtained non-standard R-band photometry (using 103aE plates+RG1 filter) of VV Cep from 1976 to 1978. However, the Hα variability described here would seem to be an order of magnitude too small in amplitude to produce the ~0.1-magnitude variation in R flux seen by Baldinelli *et al* (1979).

A precessing accretion disk rotation axis with a period of 42 days should result in a similar radial velocity variability. Analysis of more than 400 medium-resolution spectra of VV Cep obtained from 2018 January to 2020 January confirms a similar short periodic variability in the radial velocity of the Hα V component. However, a period analysis (see Figure 9) of the velocity residuals (after subtraction of a smooth trend) gives a period of 51 days instead, but with relatively little power in this period, which only accounts for about one-third of the amplitude of the total short period variability.

Note that the radial velocity measurements were carried out with respect to the M supergiant reference frame. Variation in the width of the central absorption near eclipse might also alias the derived V component radial velocities. In any case, the radial velocity time series analysed here is relatively short. We will revisit the radial velocity analysis after more data have been obtained, and after carrying out a proper subtraction of the orbital solution first.

3. A proposed model

As summarized in the introduction, recombination of ionized hydrogen (H^+) in an H II region around the hot star and the accretion disk in VV Cep produces the observed Hα emission peak. The Hα emission profile is broadened by the high velocities present in the infalling gas, as well as from gas in the accretion disk rapidly orbiting the hot star. The low velocity wind enveloping the entire binary star system results in absorption at velocities near the center of the Hα line profile, resulting in a characteristic double-peaked emission profile with separate blue (V) and red (R) emission components.

The spectroscopic orbit implies the hot companion is also a massive star, and that must be (from its mass, and position on the main sequence) an early B star, probably of spectral class B0-2 V. It is difficult to be more precise because the UV spectrum is non-stellar. Moreover, the hot companion is not a compact object in the usual sense. Therefore, it is unlikely that gravitational accretion is the source of the energy powering the non-stellar UV source. The nature of the nonstellar luminosity (hydrogen Balmer and Lyman line emission, and Balmer continuum emission) is that of a recombination spectrum. This suggests the non-stellar emission is being powered by the local ionization of circumstellar hydrogen by the extreme ultraviolet (EUV) radiation field (i.e., at wavelengths shortward of 912 Å) of the hot companion star, with some contribution from the hot gas accreting around the companion star. In this scenario, the EUV continuum of the hot star and accretion region is being reprocessed into hydrogen recombination emission. This process, which depends on the local circumstellar hydrogen density and accretion disk orientation, is what we propose to cause the variable nature of the UV spectrum of VV Cep.

The size of the B star and its accretion disk, which together produce the UV continuum, are small compared to the M supergiant. We know this because the UV light curve drops quickly to zero during total eclipse, implying that the UV continuum flux comes from a small emitting volume, consistent with a hot star surrounded by a compact accretion disk source. But about 20–25% of the Hα flux remains present even at

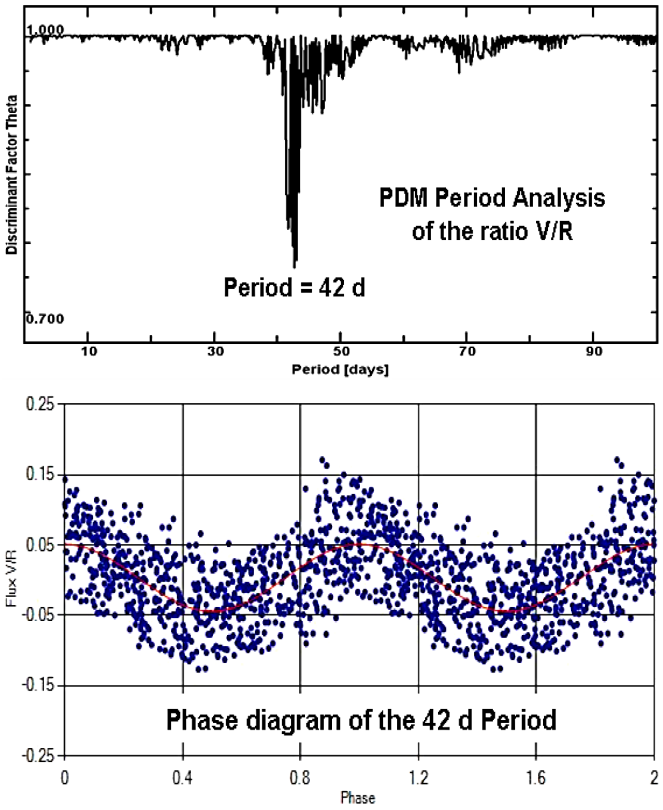

Figure 8. V/R period analysis. Top: PDM periodogram. Bottom: V/R values phased to 42-day period.

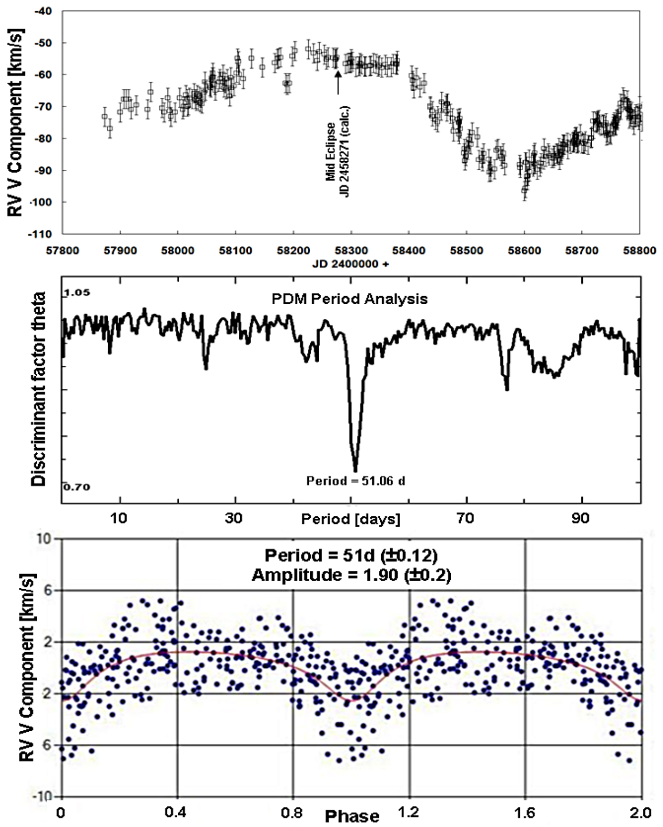

Figure 9. Radial velocity analysis of the V component of the Hα emission. Top: radial velocity of the Hα V component. Middle: Period analysis of the detrended data. Bottom: Phase plot of the radial velocity time series for the derived 51-day period.

mid-eclipse, so that some of this emission must come from an extended region on the sky that is larger than the projected disk of the M supergiant. A more detailed analysis of the evolution of the Hα profile during the eclipse now underway should provide valuable constraints on the size and structure of the emitting volume.

The observed 42-day period of Hα variability is typical of Be star disk precession periods (Schaefer *et al.* 2010) and it is tempting to suspect that mechanism (precession of the accretion disk) also causes the Hα variability in VV Cep, with its accretion disk. But the situation is more complicated than this because the accretion region in VV Cep is totally eclipsed for 19 months during totality. This behavior imposes a severe constraint on the process responsible for the variability. The rapidity of the 42-day variability implies this occurs on small physical scales. This is because a region undergoing a coherent variation cannot be larger than the distance over which the physical disturbance responsible for the variability propagates during the period of the variation. But for the variability to remain present during total eclipse, when the hot star and its accretion disk are totally eclipsed, requires that the precessing disk be communicating that information to a region outside the eclipsed volume. Since typical wind velocities in VV Cep, away from the immediate vicinity of the hot star, are ~20 km s^{-1}, wind travel times to cross an M star diameter (~1000 $R_\odot$) are about a year, or much longer than 42 days. The orbital velocities of both stars are of comparable speeds: ~20 km s^{-1}. There is no evidence of higher velocity flows on large scales in VV Cep. Therefore, the source of the variation cannot be gas flows or winds originating with the accretion disk—the velocities are just too slow.

This leaves radiation as the only obvious mechanism fast enough to propagate the 42-day variability over a region larger than that of the M supergiant's radius. The light travel time to cross the M supergiant radius (~1000 $R_\odot$) is less than an hour. The propagating radiation cannot be Hα directly because n = 2 level populations of H I are insufficient to scatter Hα light in the relatively cool circumstellar gas around VV Cep. Instead, we propose that extreme UV (EUV) radiation emitted by the accretion disk and hot star ionizes neutral hydrogen gas in two lobes directed above and below the plane of the accretion disk (Figure 10). Observations of VV Cep in the ultraviolet with the Hubble Space Telescope (Bauer, Gull, and Bennett 2008) demonstrated the existence of spatially extended emission in strong lines of Fe II. These prominent ultraviolet emission lines are excited by Lyman-β emission from the same recombination process into the hydrogen n = 3 level that produces the observed Hα emission.

In this model, it is the geometry of the H II region emission lobes, varying with the precession of the accretion disk, that gives rise to the 42-day Hα variability. As the disk precesses, these cones of ionization sweep through the neutral circumstellar wind in VV Cep much like a searchlight beam. Inside each H II lobe, circumstellar neutral hydrogen is ionized to H^+ by the disk's EUV radiation, and then recombines to produce Hα and higher Balmer line emission. The precession of the disk results in a modulation of the strength, and radial velocity, of the resulting Hα emission, which depends on the geometry of the bipolar emission cones relative to the stellar wind and the

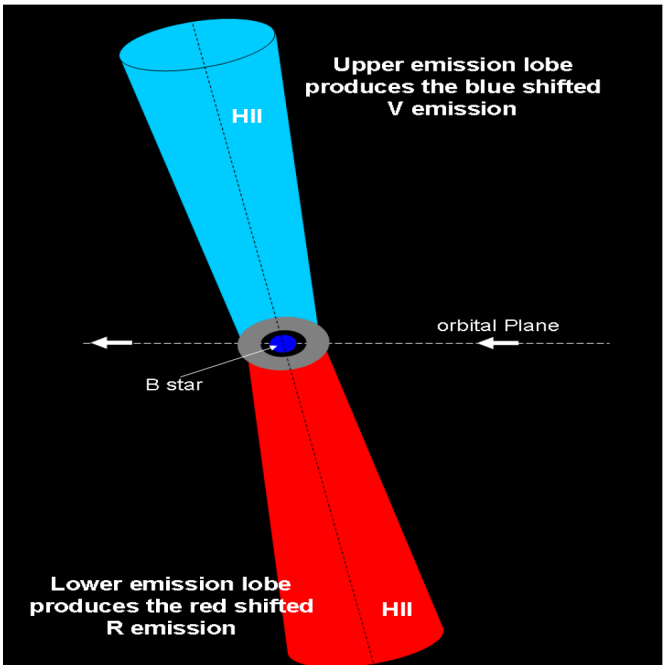

Figure 10. Model of two Hα emission lobes extending above and below the orbital plane from the precessing accretion disk.

position of the eclipsing supergiant. Out of eclipse, Hα emission from the H II region near the precessing accretion source is also observed directly. This model accounts for the continued presence of the 42-day Hα emission flux variability during total eclipse.

The Hα emission lobes are not exactly perpendicular to, but are obliquely inclined, to our line of sight due to the i ≈ 80° inclination of the orbital plane of VV Cep. The blue-shifted (V) emission comes from the lobe which opens towards the observer, while the red-shifted (R) emission comes from the lobe opening away from the observer. In addition, the blue V lobe must be more occulted by the red supergiant than the R lobe at the start of the eclipse, because the V lobe fluxes decline more steeply at eclipse ingress. We require this geometry to explain the asymmetric nature of the V and R curves. Further, the significantly narrower profile shape of the Hα emission during total eclipse (seen as red curve in Figure 4) implies a lower velocity source far from the accretion disc, confirming that not all the Hα emission comes from the immediate vicinity of the accretion disc.

4. Conclusions

We present medium-resolution (R ~ 17000), high cadence observations of the Hα emission line in VV Cep, observed by members of the *ARAS* group from 2010 to the present, and report the discovery of a rapid 42-day variability that is present in the EWs and peak fluxes of both the V and R components. A similar 51-day variability is present in the radial velocity of the V component. Surprisingly, this variability persists through total eclipse, when the hot companion star and surrounding accretion region are totally eclipsed.

To explain the continuation of the 42-day variability through total eclipse, we propose a model in which lobes of neutral

hydrogen gas are ionized by extreme ultraviolet radiation from a precessing accretion disk around the hot companion star in this massive binary system. Recombination from the resulting H II region produces the observed Balmer continuum and line emission, including the prominent Hα emission. As the accretion disk precesses with its 42-day period, the H II ionization lobes directed away from the disk sweep through the circumstellar gas around the M supergiant, producing the observed periodic variability in Hα fluxes and radial velocity, even when the accretion region itself is eclipsed.

5. Acknowledgements

We thank all observers of this campaign, without whose great cooperation such an extensive investigation would not have been possible: E. Bertrand, J. J. Boussat, E. Bryssinck, Ch. Buil, Ch. Revol, St. Charbonnel, Dong Li, P. Fosanelli, J. Foster, O. Garde, Th. Griga, J. Guarro, H. Kalbermatten, M. Keiser, K. Prast, F. Neußer, J. N. Terry, Ch. Kreider, B. Koch, Th. Lemoult, J. Martin, C. Sawicki, O. Thizy, F. Teyssier, T. Lester, J. Schirmer, M. Schwarz, P. Somogyi, Th. Garrel, M. Trypsteen, St. Ubaud, V. Desnoux, U. Zurmühl, A. Stiewing, S. Hold, and D. Hyde.

References

Barbera, R. 1998, AVE code, version 2.51 (http://www.gea.cesca.es).

Bardinelli, L., Ghedini, S., and Marmi, S. 1979, *Inf. Bull. Var. Stars*, No. 1675, 1.

Bauer, W. H., and Bennett, P. D. 2000, *Publ. Astron. Soc. Pacific*, **112**, 31.

Bauer, W. H., Gull, T. R., and Bennett, P. D. 2008, *Astron. J.*, **136**, 1312.

Bennett, P. D., and Bauer, W. H. 2015, in *Giants of Eclipse: The ζ Aur Stars and Other Binary Systems*, eds. T. Ake, E. Griffin, Astrophys. Space Sci. Libr. 408, Springer International Publishing, Cham, Switzerland, 85.

Cowley, A. P. 1969, *Publ. Astron. Soc. Pacific*, **81**, 297.

Goedicke, V. 1939, *Publ. Obs. Univ. Michigan*, **8**, 1.

Hutchings, J. B., and Wright, K. O. 1971, *Mon. Not. Roy. Astron. Soc.*, **155**, 203.

Kawabata, S., Saijo, K., Sato, H., and Saito, M. 1981, *Publ. Astron. Soc. Japan*, **33**, 177.

McLaughlin, D. B. 1934, *Astrophys. J.*, **79**, 380.

McLaughlin, D. B. 1936, *Harvard Coll. Obs. Announcement Card*, No. 397.

Moellenhoff, C., and Schaifers, K. 1978, *Astron. Astrophys.*, **64**, 253.

Moellenhoff, C., and Schaifers, K. 1981, *Astron. Astrophys.*, **94**, 333.

Pollmann, E., Bennett, P. D., and Hopkins, J. L. 2016, *Inf. Bull. Var. Stars*, No. 6156, 1.

Pollmann, E., Bennett, P. D., Vollmann, W., and Somogyi, P. 2018, *Inf. Bull. Var. Stars*, No. 6249, 1.

Schaefer, G., *et al.* 2010, *Astron. J.*, **140**, 1838.

Wright, K. O. 1970, *Vistas Astron.*, **12**, 147.

Wright, K. O. 1977, *J. Roy. Astron. Soc. Canada*, **71**, 152.

TYC 9291-1051-1: The First Precision Photometry and Analyses of the Active, Totally Eclipsing, Solar-type Binary

Ronald G. Samec
Faculty Research Associate, Pisgah Astronomical Research Institute, 1 PARI Drive, Rosman, NC 28772; ronaldsamec@gmail.comInstitute

Heather Chamberlain
Pisgah Astronomical Research Institute, 1 PARI Drive, Rosman, NC 28772; 4hcham@gmail.com

Walter Van Hamme
Department of Physics, Florida International University, Miami, FL 33199; vanhamme@fiu.edu

Received March 31, 2020; revised May 15, 2020; accepted July 22, 2020

Abstract CCD Bessell BVRI light curves of TYC 9291-1051-1 were taken on 9, 20, and 28 August 2019 in remote mode at Cerro Tololo InterAmerican Observatory with the 0.6-m SARA South reflector by R. Samec and W. Van Hamme. The variability of TYC 9291-1051-1 (UNSW V-633) was discovered by the University of New South Wales Extrasolar Planet Search (Christiansen *et al.* 2008), which classified it as an EW variable with a magnitude of V = 10.90 and a period of 0.42713 d. Five times of minimum light were determined from our present observations, which include two primary eclipses and three secondary eclipses. Linear and quadratic ephemerides were determined from all available times of minimum light. A ~13.3-year period study (~11,400 orbits) reveals that the period is increasing. This could be due to mass transfer making the mass ratio more extreme. Wilson-Devinney analyses reveals that the system is a A-type W UMa binary (P-shift = 0.5) with a mass ratio that is somewhat extreme, $M_2/M_1 = 0.260 \pm 0.004$ (star 1 is the more massive component, $M_1/M_2 = 3.8$). The total eclipse makes this a good determination (Terrell and Wilson 2005). Its Roche lobe fill-out is ~32%. The solution has two major spot regions, a mid-latitude cool spot of radius 19 ± 5 degrees and an equatorial weak hot spot (T-factor = 1.06) of 21 ± 6 degrees. We note that the hot spot is on the on the gainer which covers the Lagrangian, L1, point. This probably has to do with the mass transfer. The spot regions were variable during the 19-day interval of observation. The temperature difference of the components is about ~270 K, with the more massive component as the hotter one, so it is an A-type W UMa binary. The inclination is 83.25 ± 0.50°. The primary (with P-shift 0.5) minimum has a time of constant light with an eclipse duration of 13.3 minutes.

1. Active solar-type contact binaries

W UMa binaries are believed to be undergoing steady but slow angular momentum losses due to magnetic braking as stellar winds blow radially away on stiff bipolar field lines. The secondary component is decreasing in mass as it is absorbed by the primary component. They are usually highly evolved A-type W UMa binary stars (primary component is hotter) and are believed to be among the most ancient stars. These binaries eventually coalesce into blue straggler type, single, fast rotating A-spectral type stars (Guinan and Bradstreet 1988). Most are spotted and magnetically active as would be expected for short period solar-type binaries. See Figure 1. Twenty-five highly evolved extreme mass ratio binaries in this rare group are summarized in Samec *et al.* (2011). We explore another solar-type binary, TYC 9291-1051 in this paper.

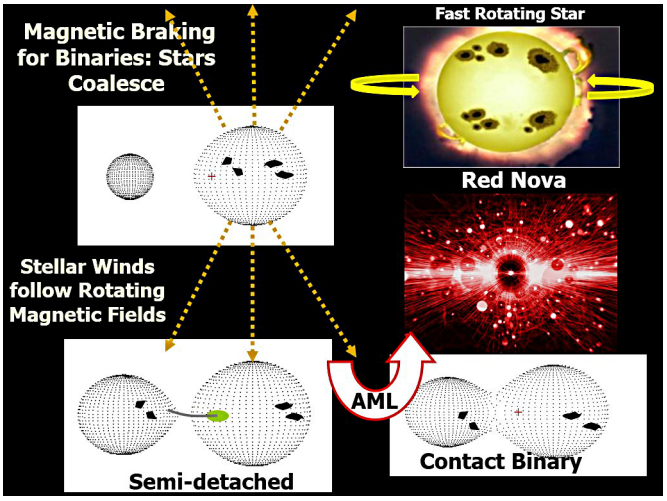

Figure 1. Depiction of a binary star made up of two solar-type stars undergoing magnetic braking which results in angular momentum loss (AML). Plasmas leave along North and South magnetic field lines, causing the magnetically active binary (detached spotted binary in the upper left-hand corner) to lose angular momentum and steadily fill its Roche lobe and move to a semidetached and then a contact binary configuration. The binary becomes unstable and a Red Novae event (Tylenda and Kamiński 2016) erupts finally resulting in a fast-rotating single star.

2. History, photometric targets, and observations

The variability of TYC 9291-1051-1 (UNSW V-633) was discovered by the University of New South Wales (UNSW) Extrasolar Planet Search (Christiansen *et al.* 2008), which classified it as an EW variable with a magnitude of V = 10.90 and an ephemeris of

$$HJD = 2453866.2150\,d + 0.42713\,d \times E \qquad (1)$$

A plot of UNS V-633 is given in Figure 2.

SIMBAD gives J = 10.44 ± 0.23, K = 10.015 ± 0.22 so J–K = 0.425 ± 0.045. GAIA DR2 gives parallax = 2.779 ± 0.036, Distance = 360 ± 5 pc. Observations of the system are continuously being undertaken by the All-Sky Automated Survey for Super Nova Search Program of Ohio State (ASAS-SN; Shappee *et al.* 2014; Kochanek *et al.* 2017). See Figure 2. The information included V = 12.07, amplitude = 0.54 mag, var. type EW, and an ephemeris:

$$\text{HJD} = 2456817.68537\,\text{d} + 0.4271315\,\text{d} \times \text{E} \qquad (2)$$

The ASAS-SN light curves are given in Figure 3. The preliminary results of this study were reported at the 235th meeting of the American Astronomical Society (Chamberlain *et al.* 2020).

Characteristics of the variable, comparison, and check star are listed in Table 1. The finding chart of the photometric targets is given in Figure 4. These are in the constellation Pavo. B, V light curves and B–V color curves from 9 and 20 August 2019 are shown in Figures 5 and 6.

Our 2019 BVRI light curves were taken on 9, 20, and 28 August 2019 at Cerro Tololo InterAmerican Observatory with the 0.6-m SARA South reflector by R. Samec and W. Van Hamme with a thermoelectrically cooled (–50° C) 2KX2K ANDOR camera with Bessell BVRI filters. Individual observations included 411 in B, 410 in V, 412 in R, and 415 in I. The observations are given in Table 2. The probable error of a single observation was 13 mmag in B and V, 17 mmag in R, and 20 mmag in I. This was evidently due to the strong magnetic activity. The nightly C–K values stayed constant throughout the observing run with a precision of about 1%. Exposure times varied: 75–100s in B, 40–75s in V, and 22–45s in R and I, depending on the time needed to obtain 1% photometry.

3. Period study

Five times of minimum light were determined from our present observations, which include two primary eclipses and three secondary eclipses:

HJD I = 2458705.61464 ± 0.00005, 2458716.71967 ± 0.0005 d

HJD II = 2458705.82757 ± 0.0012, 2458716.50625 ± 0.0037, and 2458724.62166 ± 0.0008 d.

Minima were calculated using a least squares minimization method (Mikulášek *et al.* 2014) to determine the minima for each curve, in B, V, R_c, and I_c. Standard errors were determined from these values. From the ASAS-SN curve, the data were phased with Equation 2. The minima were fit and 5 times of low light were determined. The ephemeris (Equation 2) was also input. A time of minimum light from MNRAS (Christiansen *et al.* 2008) was also used. From all of these, the following linear and quadratic ephemerides were determined:

$$\begin{aligned}\text{JD Hel Min I} = {} & 2458705.6129 \pm 0.00016\,\text{d} \\ & + 0.42712987 \pm 0.00000030 \times \text{E}\end{aligned} \qquad (3)$$

$$\begin{aligned}\text{JD Hel Min I} = {} & 2458705.6151 \pm 0.0009\,\text{d} \\ & + 0.4271345 \pm 0.0000006 \times \text{E} \\ & + 0.00000000033 \pm 0.00000000004 \times \text{E}^2\end{aligned} \qquad (4)$$

The quadratic and linear residuals are given in Table 3. The plot of the quadratic term overlying the linear residuals of Equation 4 is given in Figure 7.

Using Equation 3, the B, V, R, I magnitudes and B–V, R–I indices were phased and plotted into light curves and color curves for the observing run. They are given in Figures 8 and 9.

The quadratic ephemeris term yields an increasing orbital period of $\dot{\text{P}} = 5.47 \times 10^{-7}$ d / yr. If the period change is due to mass transfer to the primary component, the rate is (in a conservative scenario)

$$\frac{\text{dM}}{\text{dt}} = \frac{\dot{\text{P}}\,\text{M}_1\,\text{M}_2}{3\text{P}\,(\text{M}_1 - \text{M}_2)} = \frac{-1.45\times10^{-7}\,\text{M}_\odot}{\text{d}}. \qquad (5)$$

4. Light curve characteristics

The B, V, R, I light curves were phased and averaged at each quarter cycle, phases 0.0, 0.25, 0.50, and 0.75, and important differences were tabulated. These are given in Table 4. The night-to-night curves were of good photometric precision, averaging about 1%. The amplitude of the light curve varies from 0.59 to 0.32 mag in B to I. The O'Connell (the difference of maxima) effect, sometimes an indicator of spot activity, averages several times the noise level, 0.027 mag. The differences in minima are small, 0.032–0.058 mag, indicating contact light curves. The B–V color curves fall so very slightly at phase 0.0, and at phase 0.5, which is characteristic of contact binaries. This probably indicates that It is a W UMa contact binary.

5. Temperature

The 2MASS, J–K = 0.425 ± 0.045 for the binary. This corresponds to a G7.5 ± 3.5V eclipsing binary which yields a temperature of 5500 ± 250 K. Binary stars of this type are noted for having convective atmospheres, so spots are expected. In this case, the magnetic activity is especially high.

6. Light curve solution

The B, V, R, and I curves were pre-modeled with BINARY MAKER 3.0 (Bradstreet and Steelman 2002) and fits were determined in all filter bands. The result of the best fit was that of a A-type contact binary with a high fill-out of about 32% with two spots, one cooler and one slightly hotter than the photosphere. The parameters were then averaged and input into a four-color simultaneous light curve calculation using the 2016 Wilson-Devinney (WD) program (Wilson and Devinney 1971; Wilson 1979, 1990, 1994, 2008, 2012; Van Hamme 1998; Van Hamme and Wilson 2007; Wilson *et al.* 2010; Wilson and Van Hamme 2014). The solution was computed in Mode 3 (contact), started with the initial spot parameters and converged to in the solution. Convective parameters g = 0.32, A = 0.5 were used.

Table 1. Information on the stars used in this study.

Star	*Name*	*R.A. (2000)* h m s	*Dec. (2000)*[1] ° ′ ″	*V*	*J–K*
V (Variable)	TYC 9291-1051-1 GSC 9291 1051 2MASS J05194709+7736136 2MASS J18252748-6734471[2] ASAS 182528-6734.8	18 25 26.15064689	–67 34 39.785303135	12.200[3]	0.425 ± 0.045[3]
C (Comparison)	GSC 9291 958 3UC 045-269292	18 26 01.8201	–67 33 19.410	12.66[3]	0.38[3]
K (Check)	GSC 9291 0987	18 25 55.9738	–67 32 25.343	12.47[3]	0.26 ± 0.041[3]

[1] ICRS (IAU 2013). [2] Gaia Collaboration (2006). [3] SIMBAD (CDS 2007).

Table 2. Sample of first ten TYC 9291-1051-1 B, V, R, I observations.

Δ*B*	*HJD 2458700+*	Δ*V*	*HJD 2458700+*	Δ*R*	*HJD 2458700+*	Δ*I*	*HJD 2458700+*
–0.640	5.4525	–0.638	5.4531	–0.727	5.4515	–0.770	5.4485
–0.684	5.4547	–0.760	5.4555	–0.712	5.4536	–0.818	5.4519
–0.626	5.4571	–0.720	5.4579	–0.734	5.4560	–0.795	5.4540
–0.687	5.4594	–0.740	5.4602	–0.790	5.4583	–0.798	5.4564
–0.668	5.4626	–0.779	5.4634	–0.808	5.4614	–0.783	5.4587
–0.673	5.4650	–0.769	5.4659	–0.834	5.4639	–0.842	5.4618
–0.725	5.4675	–0.772	5.4683	–0.825	5.4664	–0.809	5.4643
–0.722	5.4700	–0.779	5.4708	–0.807	5.4689	–0.813	5.4668
–0.738	5.4725	–0.788	5.4733	–0.827	5.4713	–0.849	5.4692
–0.730	5.4749	–0.810	5.4758	–0.865	5.4738	–0.851	5.4717

Note: First ten data points of TYC 9291-1051-1 B, V, R, I observations.
The full table is available through the AAVSO ftp site at ftp://ftp.aavso.org/public/datasets/samec482-tyc9291.txt (if necessary, copy and paste link into the address bar of a web browser).

Table 3. TYC 9291-1051-1 period study quadratic and linear residuals.

	Epoch HJD 2400000+	*Cycle*	*HJD Linear Residual*	*HJD Quadratic Residual*	*WT*	*HJD Error*	*Reference*
1	51870.9100	–16001.5	0.0157	0.0038	0.05	—	Watson *et al.* 2014 (VSX)
2	53866.2150	–11330.0	–0.0165	–0.0082	0.05	—	Christiansen, *et al.* (2008)
3	56817.6854	–4420.0	–0.0135	–0.0017	0.05	—	Shappee *et al.* 2014; Kochanek *et al.* 2017 (ASAS-SN EPOCH)
4	57154.7031	–3631.0	–0.0012	0.0090	0.02	—	Shappee *et al.* 2014; Kochanek *et al.* 2017 (ASAS-SN)
5	57236.4974	–3439.5	–0.0023	0.0075	0.02	—	Shappee *et al.* 2014; Kochanek *et al.* 2017 (ASAS-SN)
6	57573.7158	–2650.0	–0.0029	0.0048	0.02	—	Shappee *et al.* 2014; Kochanek *et al.* 2017 (ASAS-SN)
7	57867.7999	–1961.5	0.0022	0.0078	0.02	—	Shappee *et al.* 2014; Kochanek *et al.* 2017 (ASAS-SN)
8	58024.5577	–1594.5	0.0034	0.0077	0.02	—	Shappee *et al.* 2014; Kochanek *et al.* 2017 (ASAS-SN)
9	58705.6146	0.0	0.0018	–0.0005	1.00	0.0003	Present observations
10	58705.8276	0.5	0.0011	–0.0011	1.00	0.0021	Present observations
11	58716.5063	25.5	0.0016	–0.0008	1.00	0.0003	Present observations
12	58716.7197	26.0	0.0014	–0.0010	1.00	0.0018	Present observations
13	58724.6217	44.5	0.0015	–0.0010	1.00	0.0001	Present observations

The parameters with errors were allowed to iterate during the light curve modeling. The mass ratio was found to be 0.26. The two spots did converge with some changes as expected, with T-factor of 0.87 and a mid-latitude position and an equatorial spot, very near L1) with T-factor = 1.06. The eclipses are total, so there was a time of constant light in the first eclipse (see Figure 8). A P-shift = 0.5 was inserted so that the WD contact mode would run more smoothly. This means that the primary eclipse is actually the secondary eclipse. But since the eclipses are so close in amplitude, this makes little difference in the interpretation. The parameters carrying an error were the ones that were iterated as the program ran; the others remained fixed in the code.

The light curve solution follows as Table 5. The fill-out was 31.5%. The inclination is 83.25 ± 0.50°. The difference of component temperatures was about 220 K, confirming that the components are in good thermal contact. The total eclipse duration is 13.3 minutes. The modeled period was 0.42710 d. The B, V, R, and I solution curves overlaying the data are given as Figure 10. The geometrical surface representations of TYC9291-1051-1 are shown with spots by orbital phases, 0.0, 0.25, 0.5, and 0.75 in Figure 11 a–d.

7. Discussion

TYC 9291-1051-1 is a A-type contact W UMa binary star. The period increase is probably due to the mass ratio becoming more extreme, so there is a continuous mass exchange with the primary component being the gainer. The hot spot in the neck of the binary may indicate such a mass exchange. The spectral type is that of a solar type with a surface temperature of 5500 K for the less massive component. The higher mass component has a temperature of ~5770 K (G2V). The mass ratio is 0.26, with an amplitude of 0.59–0.52 mag in B to I, respectively. The inclination is 83.25°, which results in a total eclipse at phase 0.0. The A-type W UMa is thought to be near the end of the contact binary phase. This is because the fill-out is unusually high. Very few A-types are in shallow contact (~0–10%). High fill-out means the stars are nearer reaching the maximum fill-out where mass can leave the binary system via the L2 point (see Figure 12).

The Roche lobe surface outlines for TYC 9291-1051-1 are displayed in Figure 13. Note the degree of fill-out.

8. Conclusion

Our period study of this contact W UMa binary has a 13.3-year time duration. The period is found to be strongly increasing at about the five-sigma level. This is due to mass is transferring to the more massive component. AML is also in progress. If this scenario continues, the system will reach an instability and a red novae coalescence event will take place. The system will become a rather normal, fast rotating, single ~F8V type field star (Tylenda and Kamiński 2016).

Table 4. Light curve characteristics for TYC 9291-1051-1.

Filter	*Phase 0.0*	*Mag ± σ* Max I*	*Phase 0.25*	*Mag ± σ* Max II*
B		–0.213 ± 0.005		–0.801 ± 0.010
V		–0.296 ± 0.006		–0.857 ± 0.008
R		–0.327 ± 0.008		–0.901 ± 0.010
I		–0.393 ± 0.007		–0.908 ± 0.028
Filter	*Phase 0.5*	*Mag ± σ* Min II*	*Phase 0.75*	*Mag ± σ* Min I*
B		–0.245 ± 0.006		–0.799 ± 0.006
V		–0.329 ± 0.010		–0.830 ± 0.035
R		–0.368 ± 0.006		–0.828 ± 0.014
I		–0.451 ± 0.010		–0.915 ± 0.008

Filter	*Min I – Max I ± σ*	*Max I – Max II ± σ*	*Min I – Min II ± σ*
B	0.588 ± 0.015	–0.002 ± 0.016	0.032 ± 0.011
V	0.562 ± 0.014	–0.027 ± 0.043	0.033 ± 0.016
R	0.574 ± 0.018	–0.073 ± 0.024	0.040 ± 0.014
I	0.515 ± 0.035	0.007 ± 0.036	0.058 ± 0.017

Filter	*Max II – Max I ± σ*	*Filter*	*Min II – Max I ± σ*
B	0.002 ± 0.016	B	0.556 ± 0.016
V	0.027 ± 0.043	V	0.529 ± 0.018
R	0.073 ± 0.024	R	0.534 ± 0.016
I	–0.007 ± 0.036	I	0.457 ± 0.038

**Magnitude is the variable star – comparison star magnitude.*

Table 5. B, V, R_c, I_c Wilson-Devinney program solution parameters for TYC 9291-1051-1.

Parameters	*Values*		
λB, λV, λR, λI (nm)	440, 550, 640, 790		
$g_1 = g_2$	0.32		
$A_1 = A_2$	0.5		
Inclination (°)	83.25 ± 0.50		
T_1, T_2 (K)	5500, 5770 ± 14		
Ω	2.325 ± 0.005		
$q(m_2/m_1)$	0.260±0.004		
Fill-outs: $F_1 = F_2$ (%)	31.5±0.015		
$L1/(L1+L2+L3)_I$	0.737 ± 0.001		
$L1/(L1+L2+L3)_R$	0.732 ± 0.001		
$L1/(L1+L2+L3)_V$	0.725 ± 0.001		
$L1/(L1+L2+L3)_B$	0.709 ± 0.001		
JD_o (days)	2458705.6144 ± 0.0004		
Period (days)	0.42710 ± 0.00005		
P-shift	0.5		
r_1/a, r_2/a (pole)	0.4785 ± 0.0007, 0.2633 ± 0.0015		
r_1/a, r_2/a (side)	0.5199 ± 0.0011, 0.2759 ± 0.0019		
r_1/a, r_2/a (back)	0.5480 ± 0.0014, 0.3201 ± 0.0041		
Spot I, Star 1		*Spot II, Star 1*	
Colatitude (°)	126 ± 10	Colatitude (°)	85 ± 4
Longitude (°)	288 ± 11	Longitude (°)	356 ± 6
Radius (°)	19 ± 5	Radius (°)	21 ± 6
T-factor	0.87 ± 2	T-factor	1.06 ± 0.04

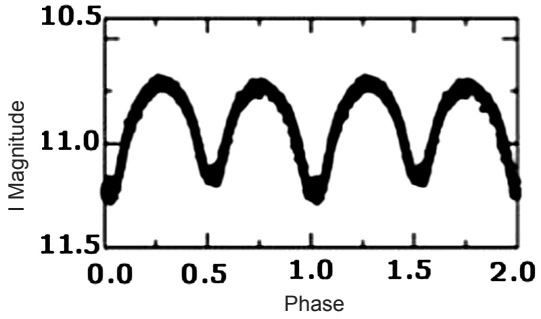

Figure 2. Plot of UNSW V-633, period = 0.42713 d (Christiansen *et al.* 2008). The magnitude is Johnson I.

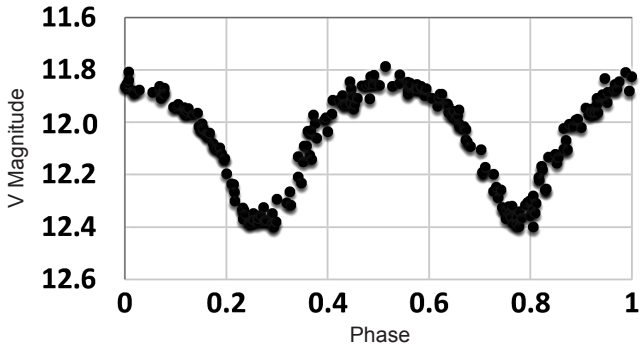

Figure 3. Curves from The ASASSN Site of ASAS J182528-6734.8 (TYC 9291-1051-1; Shappee *et al.* 2014; Kochanek *et al.* 2017).

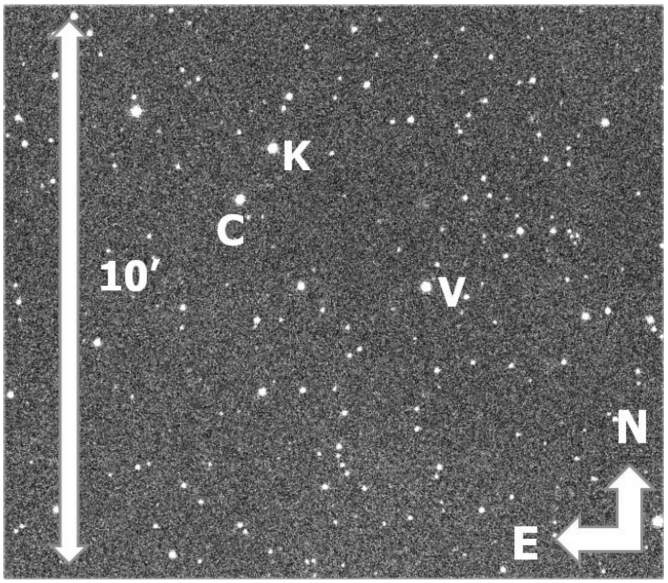

Figure 4. Finding chart of field of TYC 9291-1051-1 using actual image. V, variable, C, comparison star, and K, check star.

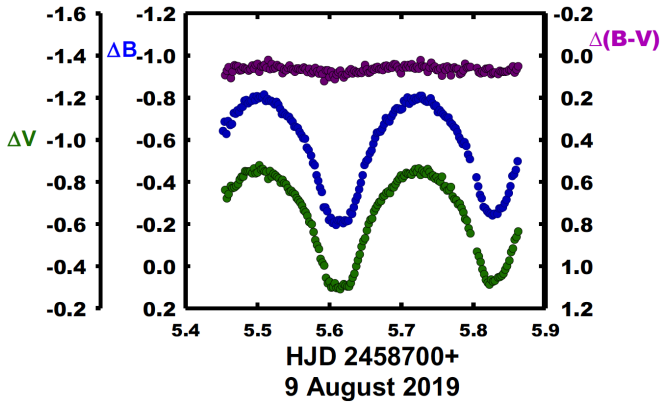

Figure 5. B, V, and B–V color curves of TYC 9291-1051-1 on 9 August 2019.

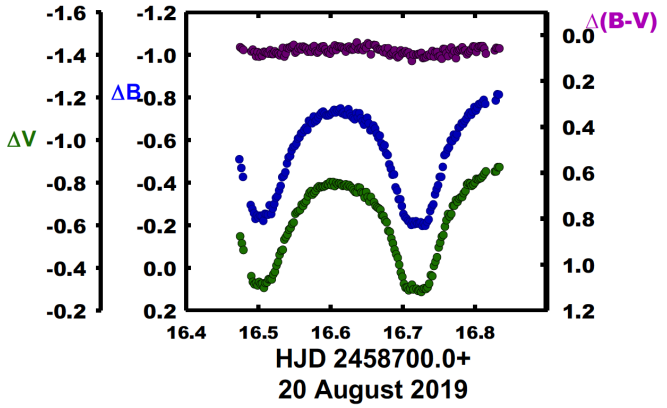

Figure 6. B, V, and B–V color curves of TYC 9291-1051-1 on 20 August 2019.

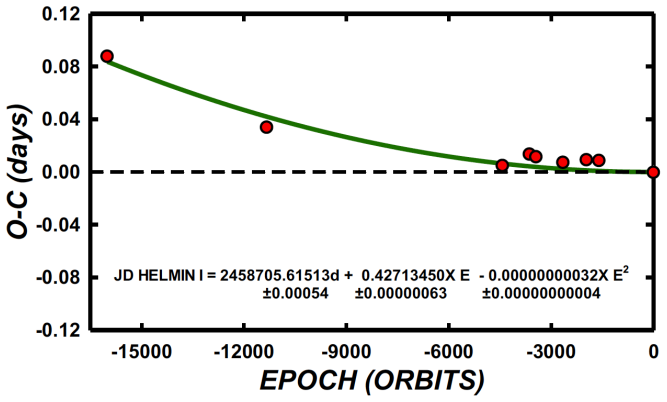

Figure 7. A plot of the quadratic term overlying the linear residuals of Equation 4.

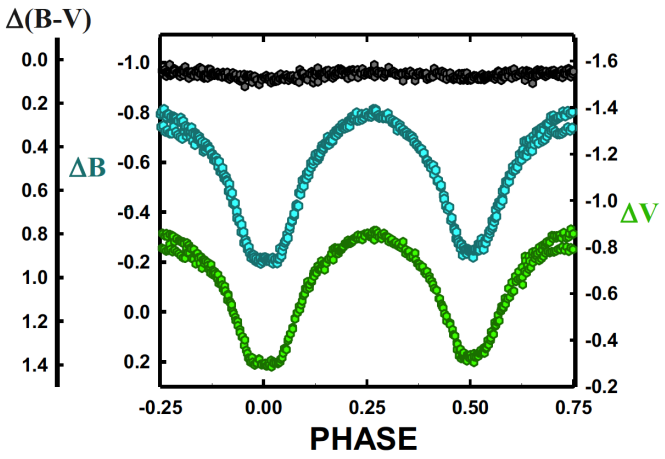

Figure 8. Phased B, V magnitude light curves and color curves (Equation 3). Note the effect of the spots (see phase 0.75) acting over a brief period of 19 days. The change is ~0.08 mag in B and V.

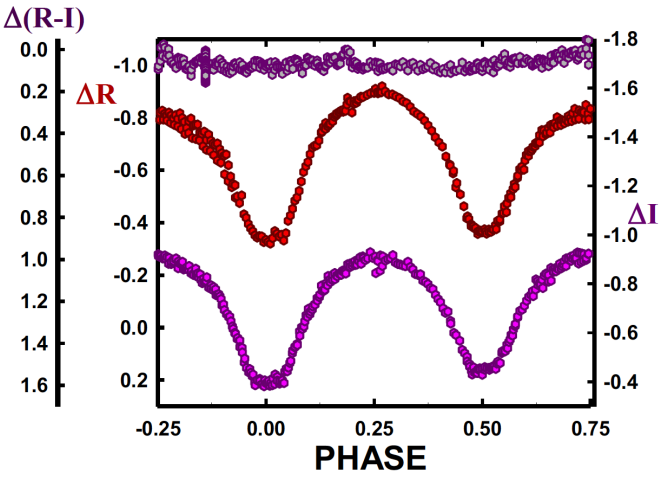

Figure 9. Phased R, I magnitude light curves and color curves (Equation 3). Note the effect of the spots acting over a brief period of 19 days. The shift is ~0.05 mag in R.

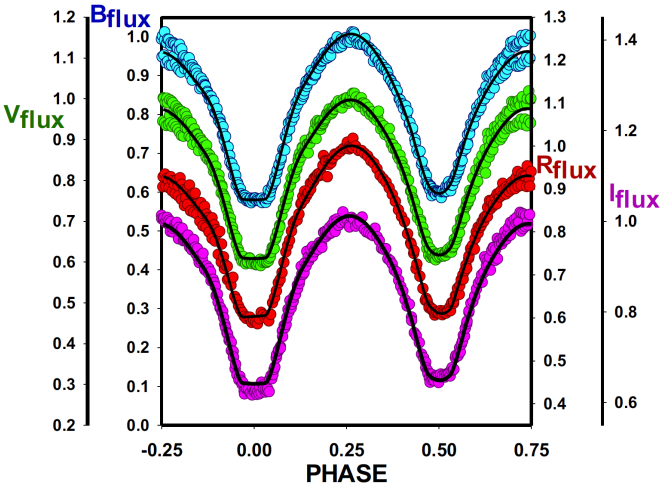

Figure 10. The B, V, R_c, I_c solution curves overlaying the normalized flux data.

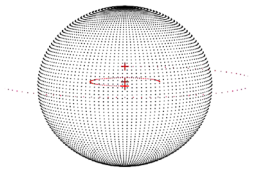

Figure 11a. Geometrical surface representation of TYC9291-1051-1 at phase 0.00.

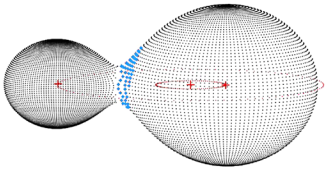

Figure 11b. Geometrical surface representation of TYC9291-1051-1 at phase 0.25. The blue spot is a hot spot.

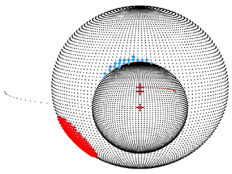

Figure 11c. Geometrical surface representation of TYC9291-1051-1 at phase 0.50. The red spot (on left) is a cool sunspot, the blue spot is a hot spot.

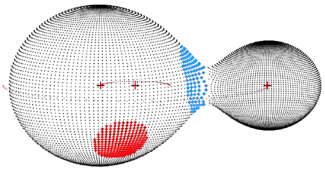

Figure 11d. Geometrical surface representation of TYC9291-1051-1 at phase 0.75. The red spot (on left) is a cool sunspot, the blue spot is a hot spot.

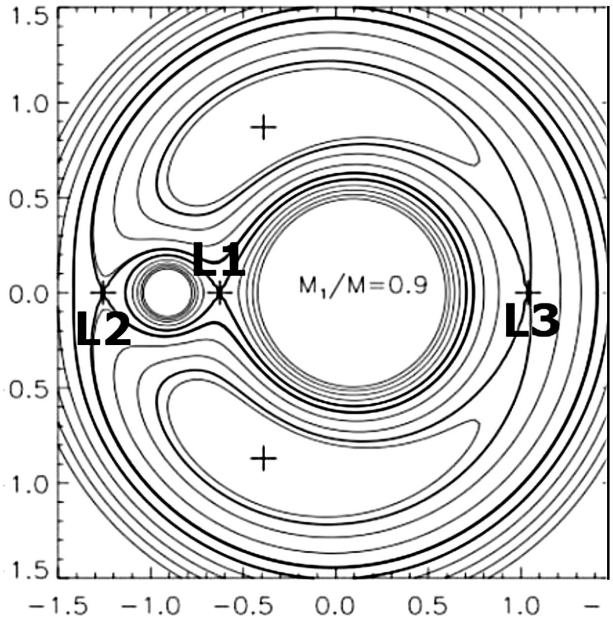

Figure 12. Roche lobe surfaces. Contact binaries have surfaces lying between L1 (fill-out = 0%) and L2 (fill-out = 100%), from http://vitaly.neustroev.net/teaching/2017b/astrophysics_of_interacting_binary_stars_02.pdf (Neustroev 2017). L points added by authors. The unit of the plot of Roche lobe surfaces are $a = a_1 + a_2 = 1$, the normalized semi-major axis.

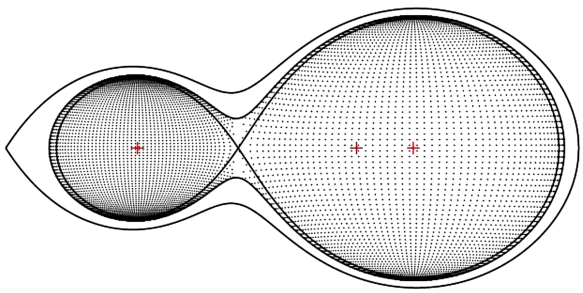

Figure 13. The Roche lobe surface of our solution.

9. Future work

Radial velocity curves are needed to obtain absolute (not relative) system parameters.

10. Acknowledgements

I would like to thank the American Association of Variable Star Observers for their support and for the services they supply to both amateurs and professionals alike.

References

Bradstreet, D. H., and Steelman, D. P. 2002, *Bull. Amer. Astron. Soc.*, **34**, 1224.

Centre de Donnees astronomiques de Strasbourg. 2007, SIMBAD Astronomical Database (http://simbad.u-strasbg.fr/simbad/).

Chamberlain, H., Samec, R., Caton, D., and Faulkner, D. 2020, *Bull. Amer. Astron. Soc.*, **52**, 114.02.

Christiansen, J. L., *et al.* 2008, *Mon. Not. Roy. Astron. Soc.*, **385**, 1749.

Guinan E. F., and Bradstreet D. H. 1988, in *Formation and Evolution of Low Mass Stars*, eds. A. K. Dupree, M. T. V. T. Lago, NATO Adv. Study Inst. Ser. C 241, Kluwer, Dordrecht, 345.

International Astronomical Union. 2013, International Earth Rotation and Reference Systems Service, International Celestial Reference System (ICRS; https://www.iers.org/IERS/EN/Science/ICRS/ICRS.html).

Kochanek, C. S., *et al.* 2017, *Publ. Astron. Soc. Pacific*, **129**, 104502.

Mikulášek, Z., Chrastina, M., Liška, J., Zejda, M., Janík, J., Zhu, L.-Y., and Qian, S.-B. 2014, *Contrib. Astron. Obs. Skalnaté Pleso*, **43**, 382.

Neustroev, V. 2017, "Astrophysics of Interacting Binary Stars" (http://vitaly.neustroev.net/teaching/2017b/astrophysics_of_interacting_binary_stars_02.pdf).

Samec, R. G., Labadorf, C. M., Hawkins, N. C., Faulkner, D. R., and Van Hamme, W. 2011, *Astron. J.*, **142**, 117.

Shappee, B. J., *et al.* 2014, *Astrophys. J.*, **788**, 48.

Terrell, D., and Wilson R. E. 2005, *Astrophys. Space Sci.*, **296**, 221.

Tylenda, R., and Kamiński, T. 2016, *Astron. Astrophys.*, **592A**, 134.

Van Hamme, W. V., and Wilson, R. E. 1998, *Bull. Amer. Astron. Soc.*, **30**, 1402.

Van Hamme, W., and Wilson, R. E. 2007, *Astrophys. J.*, **661**, 1129.

Watson, C., Henden, A. A., and Price, C. A. 2014, AAVSO International Variable Star Index VSX (Watson+, 2006–2014; http://www.aavso.org/vsx).

Wilson, R. E. 1979, *Astrophys. J.*, **234**, 1054.

Wilson, R. E. 1990, *Astrophys. J.*, **356**, 613.

Wilson, R. E. 1994, *Publ. Astron. Soc. Pacific*, **106**, 921.

Wilson, R. E. 2008, *Astrophys. J.*, **672**, 575.

Wilson, R. E. 2012, *Astron. J.*, **144**, 73.

Wilson, R. E., and Devinney, E. J. 1971, *Astrophys. J.*, **166**, 605.

Wilson, R. E., and Van Hamme, W. 2014, *Astrophys. J.*, **780**, 151.

Wilson, R. E., Van Hamme, W., and Terrell D. 2010, *Astrophys. J.*, **723**, 1469.

The V Photometric Light Curve of Supernova 2012aw from the Archive Data of Porziano Amateur Observatory

Corrado Spogli
Paolo Fagotti
Dario Vergari
Gianni Rocchi
Porziano Astronomical Observatory, Via Santa Chiara 2, 06081 Assisi, PG, Italy; corradospogli@yahoo.it, paolofagotti01@gmail.com, giannirocchi@gmali.com

Stefano Ciprini
Space Science Data Center, Agenzia Spaziale Italiana (SSDC-ASI), I-00133, Roma, Italy, and Istituto Nazionale di Fisica Nucleare (INFN), Sezione di Roma Tor Vergata, I-00133, Roma, Italy

Received April 13, 2020; revised July 29, 2020; accepted July 30, 2020

Abstract In this brief paper we present photometric observations and the V photometric light curve of the type-IIP SN 2012aw. We observed this source at Porziano Astronomical Amateur Observatory (Umbria, Italy) from 2012 March 16 to 2012 June 2 for a total of 26 nights. We hope that our work can provide useful data for further studies and research.

1. Introduction

SN 2012aw in M95 was discovered by Paolo Fagotti (Assisi, Italy) in CCD images taken on 2012 March 16.86 UT with a 0.5-m reflector (Fagotti *et al.* 2012).

It was classified as a type-IIP supernova from spectra obtained on 2012 March 19.5 UT by Itoh *et al.* (2012) and confirmed to be a very young type-II Supernova from Asiago spectra gathered on 2012 March 17.77 and 19.85 UT by Siviero *et al.* (2012). It resembles the type-IIP Supernova 1999gi about 4 to 5 days after the core collapse.

2. Photometric observations and light curve

The photometric system of Porziano Observatory consists of a 0.35-m Schmidt-Cassegrain telescope, equipped with HiSIS 23 CCD camera (Kodak KAF-0401E with 768 × 512 pixels) and B, V, R_c, I_c Johnson-Cousins broad band filters.

The frames were first corrected for bias and flat-field and then processed using a PC-based aperture photometry package developed by one of the authors using DAOPHOT routines (Stetson 1987). Further observations were provided through Paolo Fagotti's 0.5-m reflector (Fagotti *et al.* 2012).

All photometric measurements were closely related to the BVR_cI_c photometric sequence around SN2012aw, optimized by CCD observations and color corrections reported by Henden *et al.* (2012).

However, to estimate the magnitudes in the V band, we did not use all the stars observed by Henden *et al.* (2012) but only a subset of them; in particular, to carry out the differential photometry, we considered the comparison stars indicated with the letters b, c, d, l, and f, while the errors were calculated as standard deviations from the average.

All V-band data are given in Table 1. The corresponding light curve is shown in Figure 1.

B, V, R_c, I_c data reported in Table 2 were obtained using differential aperture photometry with a sample of comparison stars (n, e, f, i, k, l) from Henden *et al.* (2012) having color indices similar to our target to reduce color effects.

Magnitude errors were evaluated as standard deviations of the mean.

Our photometry shows a long flat maximum in V, distinctive of type-IIP supernovae, which lasted for about 70 days. The maximum in the V band, V = 13.24, was reached on 2012 March 27 UT (JD 2456014.397).

B, V, R_c, I_c observations of SN 2012aw for 10 nights are given in Table 2. A decrease in brightness in B and V magnitude was seen, as was an increase in brightness in R_c and I_c.

Figure 2 shows the variation of the color indices (B–V) versus (V–I_c). We can see that in the first phase of the explosion of SN 2012aw (B–V) is negative (–0.2), a color index value typical for a blue star. There is then a shifting towards positive values, with (B–V) = 0.8 being a color index value for a red star.

3. Conclusions

In this brief paper we presented our photometric observations of SN2012aw obtained at Porziano Amateur Observatory (Umbria, Italy) and a sample of B, V, R_c, I_c photometric data in order to expand knowledge of the phenomenology of these peculiar stars.

The results presented here are part of a project devoted to obtaining multiband light curves of a sample of supernovae. Our aim is to extend the historical database and information on this class of cataclysmic variables to help construct theoretical models.

4. Acknowledgement

A special thanks to the Astrofili Group of Mount Subasio and to the Confraternity of the Blessed Sacrament of Assisi.

Table 1. V data for SN 2020aw.

Date	*JD 2450000+*	*V Magnitude*	*Error*
12/03/16	6003.35	15.84	0.04
12/03/17	6004.44	13.87	0.01
12/03/17	6004.46	13.79	0.04
12/03/17	6004.48	13.77	0.05
12/03/17	6004.52	13.54	0.05
12/03/20	6007.4	13.38	0.03
12/03/20	6007.41	13.37	0.04
12/03/21	6008.47	13.39	0.01
12/03/22	6009.55	13.33	0.01
12/03/24	6011.5	13.31	0.01
12/03/26	6013.39	13.31	0.01
12/03/27	6014.4	13.24	0.05
12/03/27	6014.4	13.26	0.04
12/03/28	6015.41	13.24	0.05
12/03/29	6016.42	13.31	0.01
12/03/30	6017.53	13.31	0.01
12/04/01	6019.35	13.28	0.05
12/04/01	6019.35	13.25	0.03
12/04/08	6026.44	13.32	0.03
12/04/08	6026.46	13.33	0.04
12/04/08	6026.46	13.39	0.05
12/04/09	6027.32	13.37	0.04
12/04/09	6027.33	13.32	0.05
12/04/09	6027.33	13.29	0.05
12/04/20	6027.38	13.46	0.02
12/04/20	6038.38	13.45	0.03
12/04/21	6039.4	13.46	0.04
12/04/24	6042.37	13.53	0.05
12/04/24	6042.37	13.47	0.02
12/04/24	6042.37	13.68	0.04
12/04/27	6045.37	13.52	0.03
12/04/27	6045.38	13.53	0.04
12/05/04	6052.41	13.51	0.05
12/05/04	6052.42	13.57	0.03
12/05/10	6058.39	13.5	0.04
12/05/11	6059.37	13.57	0.05
12/05/12	6060.35	13.5	0.05
12/05/12	6060.36	13.52	0.05
12/05/12	6060.36	13.51	0.05
12/05/17	6065.37	13.54	0.04
12/05/17	6065.38	13.55	0.05
12/05/17	6065.38	13.56	0.03
12/05/18	6066.42	13.51	0.05
12/05/18	6066.42	13.55	0.04
12/05/19	6067.38	13.56	0.05
12/05/26	6074.42	13.57	0.05
12/06/02	6081.39	14.03	0.05

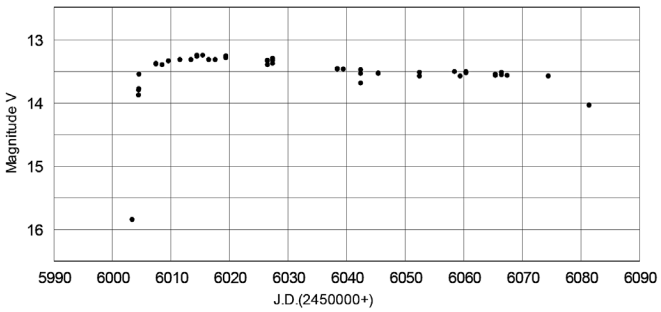

Figure 1. The V-band light curve of SN 2012aw from 2012 March 16 to 2012 June 2.

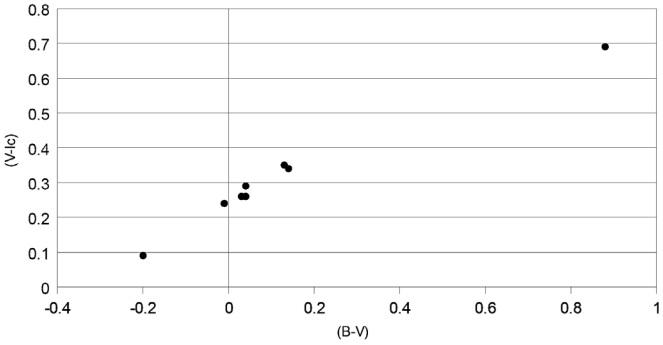

Figure 2. The color indices (B–V) versus (V–I_c) for SN 2012aw.

References

Fagotti, P., *et al.* 2012, *Cent. Bur. Astron. Telegrams*, No. 3054, 1.

Henden, A., Krajci, T., and Munari, A. 2012, *Inf. Bull. Var. Stars*, No. 6024, 1.

Itoh, R., Ui, T., and Yamanaka, M. 2012, *Cent. Bur. Astron. Telegrams*, No. 3054, 2.

Siviero, A., *et al.* 2012, *Cent. Bur. Astron. Telegrams*, No. 3054, 4.

Stetson, P. B. 1987, *Publ. Astron. Soc. Pacific*, **99**, 191.

Table 2. B, V, R_c, I_c observations of SN 2012aw for 10 nights.

Date	*JD 2450000.0+*	*B*	*Error*	*V*	*Error*	*Rc*	*Error*	*I_c*	*Error*
12/03/17	6004.44	13.67	0.01	13.87	0.01	13.87	0.01	13.78	0.01
12/03/21	6008.47	13.38	0.01	13.39	0.01	13.28	0.01	13.15	0.01
12/03/22	6009.55	13.37	0.01	13.33	0.01	13.18	0.01	13.07	0.01
12/03/24	6011.5	13.34	0.01	13.31	0.01	13.17	0.01	13.05	0.01
12/03/26	6013.39	13.35	0.01	13.31	0.01	13.15	0.01	13.02	0.01
12/03/29	6016.42	13.44	0.01	13.31	0.01	13.13	0.01	12.96	0.01
12/03/30	6017.53	13.45	0.01	13.31	0.01	13.13	0.01	12.97	0.01
12/04/27	6045.52	14.31	0.01	13.44	0.01	13.07	0.01	12.75	0.01
12/05/10	6058.39	—	—	13.49	0.01	13.05	0.01	12.73	0.01
12/05/17	6065.36	—	—	13.51	0.01	13.03	0.01	12.69	0.01

Photometry and Spectroscopy of P Cygni: Periodic Variation of the Intrinsic Hα-line Flux

Ernst Pollmann
Emil-Nolde-Str. 12, 51375 Leverkusen, Germany; ernst-pollmann@t-online.de

Received April 15, 2020; revised July 8, 31, 2020; accepted August 8, 2020

Abstract Simultaneous V-band photometry and high-resolution spectroscopy of P Cygni during the years 2005 to 2019 have been combined to yield a time series of the continuum-corrected line flux of Hα. For the first time, a clear dominant period, 318 ± 1.5 days, is derived.

1. Introduction

The international observation campaign "Photometry and Spectroscopy on P Cygni" started in November 2008 as a joint project among AAVSO, BAV, and the spectroscopy group ARAS. The aim of the campaign is, by the use of simultaneous photometric V brightness and Hα equivalent width (EW), to carry out a long-term monitoring of the intrinsic Hα-line flux, and thereby to extend the investigations by Markova *et al.* (2001a) and Markova *et al.* (2001b) on the anti-correlation between the Hα equivalent width and the photometric V brightness. To find out if and how the flux obtained from the spectral line profiles varies, the EW measurements are corrected for the effect of variation of the continuum flux. From these new data, there emerges a clear, dominant period of 318 days, to which future observations can be referred.

The current state of our campaign enables us, with all our collected data of the Hα equivalent width (shown in Figure 1) and the V-band measurements (shown in Figure 2), to try a period analysis of the intrinsic Hα-line flux, which is the primary aim of this campaign (http://astrospectroscopy.de/Projects). The intrinsic Hα-line flux (ordinate of Figure 3) was calculated by division of the Hα equivalent width EW by the flux derived from the simultaneous photometric V data of different observers.

2. Observations

The Hα spectra for the investigation presented here were obtained with 0.2-m to 0.5-m telescopes with a long-slit (in most cases) or an échelle spectrograph with resolutions of R ~ 10,000–20,000. All spectra included the 6400−6700 Å region, with S/N (at least) of ~100 for the continuum near 6605 Å, and exposure times ~1,200 sec. The spectra have been reduced with standard procedures (instrumental response, normalization, wavelength calibration) using the programs VisualSpec (Desnoux 2019) and the spectral classification software package xmk22 (Gray 2020). For V-band measurements the UBV photometric system UBV (Johnson-Morgan) was used. EW and V-band measurements have been obtained on the same night (time lag ~ 0.5–0.8 day at maximum).

From the definition of equivalent width,

$$EW_\lambda = \int_{\lambda 1}^{\lambda 2} \frac{F_c - F_\lambda}{F_c}\, d\lambda \qquad (1)$$

with F_λ the flux at wavelength λ and F_c the continuum flux, and from the relation between stellar magnitude and flux variations, $F_2 / F_1 = 10^{-0.4(m_2 - m_1)}$, it follows that the Hα-line flux is

$$F_{H\alpha} = C \times EW_{H\alpha(corr)} = C \times EW_{H\alpha(obs)} \times 10^{-0.4\,\Delta V}, \qquad (2)$$

where ΔV is the observed V magnitude minus a fiducial magnitude corresponding to a fiducial, wavelength-averaged, continuous flux that is included in the constant C.

The determination of the $EW_{H\alpha(obs)}$ has been performed as an integration over the wavelength range λ_1 = 6525 Å to λ_2 = 6605 Å in all spectra that had previously been cleared of telluric absorptions. The accuracy of the spectroscopic EW measurements are of the order ± 2–3% and the V measurements of the order ± 0.01–0.03 mag. The derived quantity is then not the line flux in physical units, but a quantity proportional to the physical line flux, corrected for continuum variations.

Use of the period search program ave (Astrogea 2020) in Figure 4 enables carrying out the main aim of the campaign, to determine periodicities of the continuum-corrected Hα EW.

3. Results

The continuum-corrected Hα EW data shown in Figure 3 enable the period analysis shown in Figure 4. The Lomb-Scargle-diagram shows a clear dominant period of 318.3 (± 1.5) days. The phase diagram of that period is shown in Figure 5. However, the dispersion of the continuum-corrected Hα EW in Figure 5 is too large to be explained by observational errors. Rather, it results mainly from real variations in line or continuum flux as the result of variations in the mass loss rate, stellar wind density, and changes of the ionization from JD 2453605 (2005 August 22) through JD 2458782 (2019 October 25) on a time scale different from the identified period.

Earlier results of the investigation period 2008 to 2013 (170 spectra and V-band measurements) published by Pollmann and Vollmann (2013) show in the Lomb-Scargle power spectrum periods of 242 days, 363 days, and 600 days, with a dominant period at 242 days. The current data set with 340 spectra and V-band data represents a more extended investigation period from 2005 to 2019 and gives, with the dominant period of 318.3 (± 1.5) days, with a much greater degree of confidence.

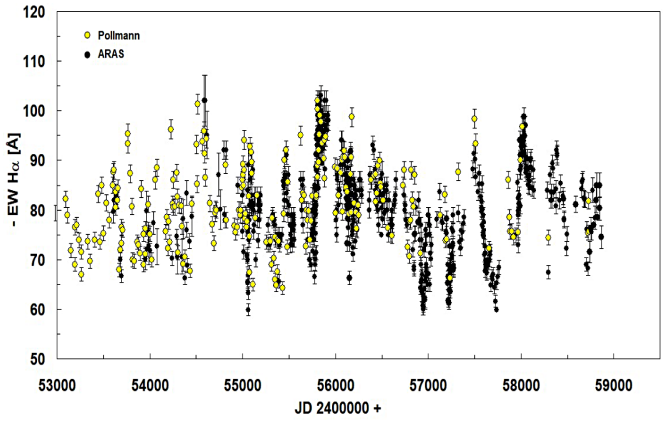

Figure 1. Long-term monitoring of the Hα equivalent width of P Cyg in collaboration with different observers of the ARAS group.

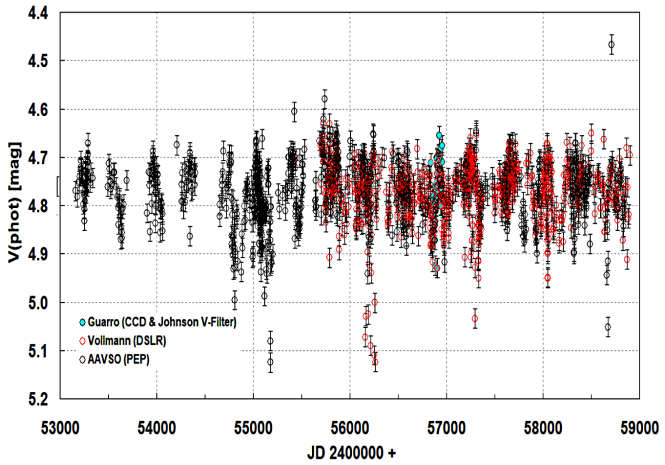

Figure 2. Long-term monitoring in V from the AAVSO International Database (photoelectric photometry (PEP) and DSLR) (Kafka 2019), and from J. Guarro (ARAS, CCD, and Johnson filter) (Balan *et al.* 2010).

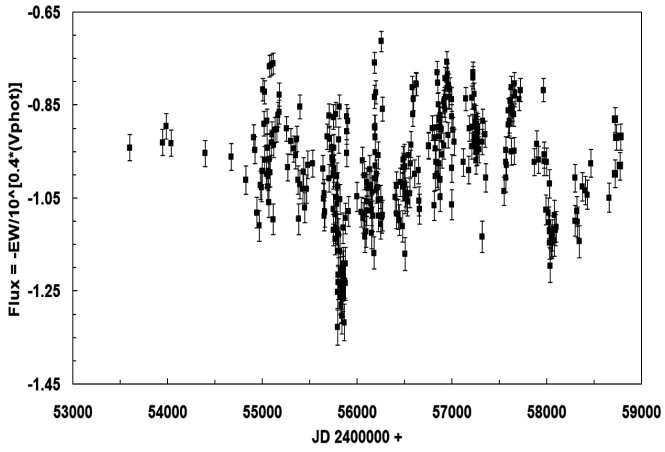

Figure 3. Long-term monitoring of the Hα EW, corrected for the variation in the underlying continuum.

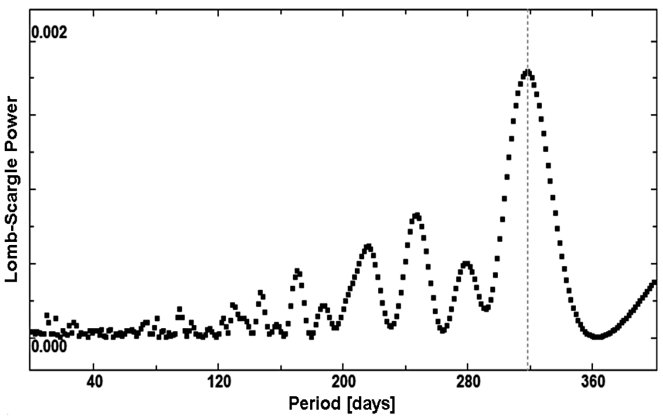

Figure 4. The Lomb-Scargle period analysis (period = 318.3 d (± 1.5)) of the Hα-line flux data in Figure 3, performed with the program AVE (Astrogea 2020).

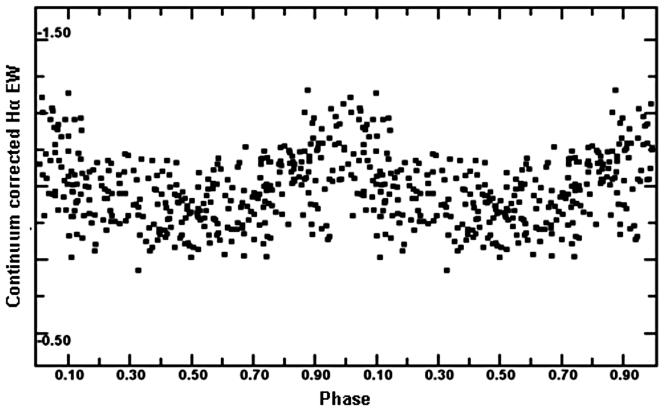

Figure 5. Phase diagram of the 318.3-day (± 1.5) period of Figure 4.

4. Conclusion

For the first time, through our data we have reliable evidence of the periodic character of the intrinsic flux of the Hα emission (see intermediate report 2014: http://www.astrospectroscopy.de/Projects). It will be of high interest to see how the found period can be improved with further data over the next years. It is planned to make the spectra used in Figure 3 for calculating the intrinsic Hα-line flux available on the author's website (Pollmann 2020).

5. Acknowledgements

I am grateful to the observers of the AAVSO (https://www.aavso.org), the BAV (http://www.bav-astro.eu/joomla/index.php/beobachtungspraxis/spektroskopie/kampagnen), and the ARAS group (http://www.astrosurf.com/aras)

References

Astrogea. 2020, AVE variable star analysis software, version 2.51 (http://www.astrogea.org/soft/ave/introave.htm).

Balan, A., Tycner, C., Zavala, R. T., Benson, J. A., Hutter, D. J., and Templeton, M. 2010, *Astron. J.*, **139**, 2269.

Desnoux, V. 2019, VisualSpec spectrography data processing software, version 4.4.7 (http://astrosurf.com/vdesnoux/).

Gray, R. O. 2020, XMK22 spectral classification software (http://www.appstate.edu/~grayro/MK/xmk22.htm)

Kafka, S. 2019, Optical variable star observations from the AAVSO International Database (https://www.aavso.org).

Markova, N., Morrison, N., Kolka, I., and Markov, H. 2001a, *Astron. Astrophys.*, **376**, 898.

Markova, N., Scuderi, S., de Groot, M., Markov, H., and Panagia, N. 2001b, *Astron. Astrophys.*, **366**, 935.

Pollmann, E. 2020, projects and publications (https://www.astrospectroscopy.de/Projects).

Pollmann, E., and Vollmann, W. 2013, *J. Amer. Assoc. Var. Star Obs.*, **41**, 24.

Optical Photometry of the Dwarf Nova QZ Serpentis in Outburst

Frank A. Kahle
Hilden, Germany; fakahle@web.de

Received April 21, 2020; revised September 8, 2020; accepted September 9, 2020

Abstract We present white-light and two-colour photometry of the dwarf nova QZ Serpentis during the 2020 March outburst and performed differential photometry in the filters Clear (white-light), Johnson–Cousins V and Johnson–Cousins R with respect to the comparison star USNOB1.0 1112-0250654. All observations were obtained in Hilden (Germany). A radial velocity study by Thorstensen *et al.* (2017) shows this system has an orbital period of 119.75 minutes. After removing linear trends in our data we estimate a superhump period of P_{sh} = 0.0855537 ± 0.0000421 days and a mass ratio of q = 0.133 ± 0.012.

1. Introduction

QZ Serpentis belongs to the class of dwarf novae, close binaries with a late-type main sequence secondary star filling its Roche lobe, transferring material through the inner Langrangian point L1 to the primary star. This transfer of material forms an accretion disk around the white dwarf primary star. These objects exhibit interesting effects due to the presence of an accretion disk, and various theories exist to explain these effects observed in dwarf novae. Theories such as change in mass-transfer rate (Bath 1973) and disk instability (Osaki 1974) offer explanations for effects observed when studying dwarf novae. These binary systems are known to have periods of quiescence, outbursts, and superoutbursts (Warner 1995).

The dwarf nova QZ Ser was discovered in 1998 by Katsumi Haseda. QZ Ser is located at J2000 R. A. 15^h 56^m 54.47^s, Dec. +21° 07' 19.0". Thorstensen *et al.* (2017) report the ephemeris T_0 = 52438.8144 and P = 0.08316078 day for the orbital period. From Thorstensen *et al.* (2002) we find the magnitude of the secondary star as V = 17.9 ± 0.4. For a finder chart see Figure 1.

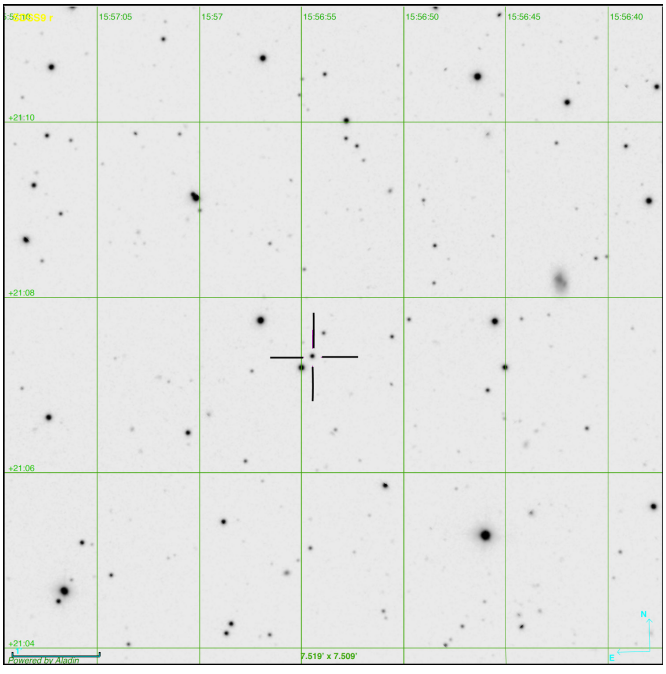

Figure 1. Finder chart for QZ Ser from "Aladin Sky Atlas." Note the V = 16.019 mag star app. 6" SE of QZ Ser.

In this paper, we present optical photometry of QZ Ser in the filters Clear (white-light), Johnson V, and Cousins R. The majority of the data were collected using the Clear filter.

2. Observations

From Schmeer (2020) we found QZ Ser to be in outburst on 2020 March 20. Our observations began two days later on 2020 March 21/22 in Hilden, Germany, using a 23.5-cm f/10 Celestron Schmidt-Cassegrain type telescope equipped with a f/6.3 focal reducer and a Moravian G2-1600 CCD camera (KAF-1603ME) operated in 2 × 2-binning. The scale of the camera was 2.44"/pixel, providing a 31.3' × 20.86' field of view.

We followed the outburst for roughly three weeks and collected data on fourteen nights. The complete list of observations is shown in Table 1. A typical image sequence consists of sets of 5 × C, R, V, R, 5 × C images and in total we collected 1,880 C (Clear) frames, 277 V frames, and 376 R frames. The Clear-band (white-light) exposure times have been set to 60 secs except for JD 2458951, where the Clear-band exposure times have been set to 70 seconds.

On each night we observed at least one full orbital period of QZ Ser. All Julian Dates reported in this paper have been heliocentrically corrected (HJD). The QZ Ser observations from HJD 2458947 and HJD 2458949 were acquired during full moon with approximately 47° and 38° separation, respectively, between QZ Ser and the moon.

3. Data reduction

The images were calibrated using standard IRAF and PYRAF software (IRAF (Tody 1986) is distributed by the National Optical Astronomy Observatories, which are operated by the Association of Universities for Research in Astronomy, Inc., under cooperative agreement with the National Science Foundation; PYRAF is a product of the Space Telescope Science Institute, which is operated by AURA for NASA). Bias frames, darks frames, and flat fields were median combined to create master frames using IRAF. Images were bias subtracted, dark subtracted, and flat divided. The CCD was kept at –10° C for all exposures. Each image was plate-solved with the Astrometry.net software package (Lang *et al.* 2010).

Table 1. Observation log.

UT date (yyyy-mm-dd)	*Epoch (JD hel.) 2450000+*	*Seeing (arcsec)*	*Filter*	*#*	*Remark*
2020-03-21/22	8930	1.90 ± 0.22	Clear (60s), V, R	140, C, 16, V, 28, R	
2020-03-22/23	8931	2.20 ± 0.67	V	87, V	
2020-03-23/24	8932	2.01 ± 0.25	Clear (60s), V, R	80, C, 8, V, 16, R	
2020-03-24/25	8933	1.68 ± 0.22	Clear (60s), V, R	90, C, 9, V, 18, R	
2020-03-25/26	8934	1.94 ± 0.29	Clear (60s), V, R	90, C, 9, V, 18, R	
2020-03-26/27	8935	1.54 ± 0.19	Clear (60s), V, R	90, C, 9, V, 18, R	
2020-03-27/28	8936	1.73 ± 0.20	Clear (60s), V, R	100, C, 10, V, 20, R	
2020-03-29/30	8938	2.26 ± 0.31	Clear (60s), V, R	140, C, 14, V, 28, R	
2020-03-31/01	8940	1.88 ± 0.37	Clear (60s), V, R	200, C, 20, V, 40, R	
2020-04-04/05	8944	1.98 ± 0.26	Clear (60s), V, R	200, C, 20, V, 40, R	
2020-04-05/06	8945	1.57 ± 0.19	Clear (60s), V, R	190, C, 19, V, 38, R	
2020-04-07/08	8947	1.66 ± 0.17	Clear (60s), V, R	190, C, 19, V, 38, R	full moon
2020-04-09/10	8949	1.60 ± 0.22	Clear (60s), V, R	200, C, 20, V, 40, R	full moon
2020-04-11/12	8951	1.66 ± 0.17	Clear (70s), V, R	170, C, 17, V, 34, R	Clouds

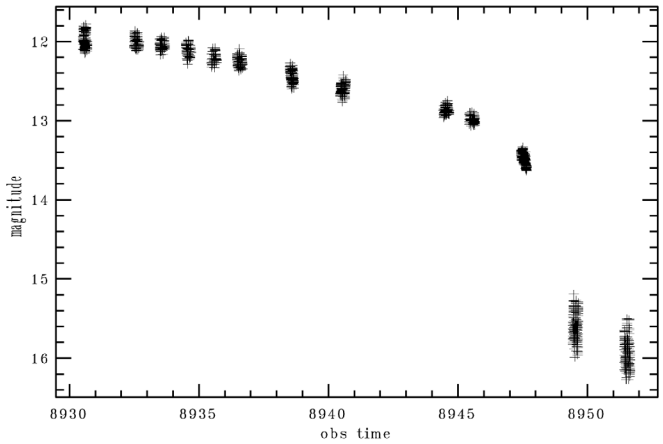

Figure 2. Clear-band light curve of QZ Ser from point-spread-function photometry during March 2020 superoutburst. The magnitude zero point for Clear and V-band are both set to 13.154 for the comparison star USNOB1.0 1111-0250033.

QZ Ser and several other stars were measured on each frame using the aperture photometry task phot from the IRAF implementation of DAOphot, with aperture radius set to 15". We note that our aperture photometry of QZ Ser is contaminated by the close neighbor USNOB1.0 1111-0250033. This star is approximately 6" SE of QZ Ser and has magnitude V = 16.019 (Zacharias *et al.* 2015). Because of the large magnitude difference this close neighbor does not affect our aperture photometry during outburst but it provides a significant flux contribution to our aperture photometry after QZ Ser has entered the dip phase. Therefore we switched to point spread function photometry whenever the close neighbor provided a significant flux contribution to our aperture photometry of QZ Ser.

We chose USNOB1.0 1112-0250654 (J2000 R.A. 15^h 57^m 10.1^s, Dec. +21° 13' 29.86"), alias 000-BBW-766 from AAVSO Chart X25228XE, as the comparison star to perform differential photometry. From AAVSO Chart X25228XE we find the comparison star V magnitude 13.253 ± 0.021. Lacking a comparison star R magnitude we estimated the comparison star's R magnitude using the transformations between SDSS and Johnson-Cousins Photometry from Jordi *et al.* (2006).

From APASS (Henden 2019) we find the magnitudes Johnson V = 13.154 ± 0.084, Sloan g = 13.461 ± 0.137, Sloan r = 13.046 ± 0.026, and Sloan i = 12.935 ± 0.037 for the comparison star. From the transformation g–r = (1.646 ± 0.008) (V–R) – (0.139 ± 0.004) we estimate R = 12.817 mag.

Since we calculated the comparison star R magnitude from APASS Sloan magnitudes we will make use of the comparison star APASS V magnitude instead of the V magnitude from AAVSO Chart X25228XE. Hereinafter 13.154 and 12.817 will be used as the comparison star V and R magnitudes.

Finally we note that no color correction has been applied to our V and R measurements.

4. Discussion

Figure 2 shows the overall light curve of QZ Ser by our CCD photometry during the 2020 March superoutburst. Since QZ Ser was reported to be in outburst on March 20 (Schmeer 2020) we may conclude that the outburst lasted at least 20 days and from Kato (2020a) we remark that superhumps were clearly present on March 21. Our light curve obtained on March 22/23 (Figure 4a) shows superhumps with an amplitude of 0.275 mag. Observational evidence for the onset of the dip after the plateau phase is clearly visible at approximately JD 2458947 from Figure 2.

From IRAF task polyfit we estimate that QZ Ser was fading in white light at a rate of 0.07(4) mag per day during the plateau phase (see Table 2 for fading rates in all three filters C, V, and R). To search for periodic signals in the light curve we used IRAF task pdm, and the generalized Lomb-Scargle (LS) and Analysis of Variance (AoV) period search implementations in the software package VARTOOLS (Hartman and Bakos 2016). After removing the linear trend of decline in our data obtained during the plateau phase we find the period candidate $P_{pdm} = 0.0855735764$ day with IRAF task pdm, whereas from the vartools search methods the candidates $P_{LS} = 0.08558217$ day and $P_{AoV} = 0.08550537$ day were found for the superhump period. Our first two nights of observations have been excluded from this calculation to avoid the inclusion of stage A superhumps. Combining these results we estimate a superhump period P_{sh} 0.0855537 ± 0.0000421 day.

Table 2. Fading rates.

Filter	*Fading mag/day*	*Remark*
Clear	0.07(4)	2458932 ≤ JD < 2458946 (1,120 obs.)
V	0.07(2)	2458932 ≤ JD < 2458946 (110 obs.)
R	0.07(0)	2458932 ≤ JD < 2458946 (216 obs.)

Table 3. Times of maximum light of QZ Ser.

Max JD hel. 2450000+	*Error*	*Filter*	*E[a] #*	*O–C[a] (days)*
8930.56438	0.0014	Clear	–23	–0.01488
8930.64994	0.0014	Clear	–22	–0.01491
8931.59103	0.0014	V	–11	–0.00382
8932.53212	0.0014	Clear	0	0
8932.61767	0.0014	Clear	1	0.00343
8933.55875	0.0014	Clear	12	0.01279
8934.49986	0.0028	Clear	23	0.01997
8934.58541	0.0028	Clear	24	0.00973
8935.61205	0.0014	Clear	36	0.01793
8936.46759	0.0014	Clear	46	0.02311
8936.55314	0.0014	Clear	47	0.02323
8936.63870	0.0014	Clear	48	0.02289
8938.52088	0.0014	Clear	70	0.01590
8938.60643	0.0014	Clear	71	0.00907
8940.48861	0.0014	Clear	93	0.01669
8940.57417	0.0014	Clear	94	0.01514
8940.65972	0.0014	Clear	95	0.00956
8944.50964	0.0014	Clear	140	0.01341
8944.59519	0.0014	Clear	141	0.00510
8945.45073	0.0014	Clear	151	0.01065
8945.53628	0.0014	Clear	152	0.01303
8945.62184	0.0014	Clear	153	0.01298
8947.50402	0.0014	Clear	175	0.00816
8949.47175	0.0014	Clear	198	0.01087
8949.55731	0.0014	Clear	199	0.01033
8951.43949	0.0014	Clear	221	0.01142
8951.52504	0.0014	Clear	222	0.00821
8951.61060	0.0014	Clear	223	0.00974

[a] *Against max = 2458932.53212 + 0.0855537 E.*

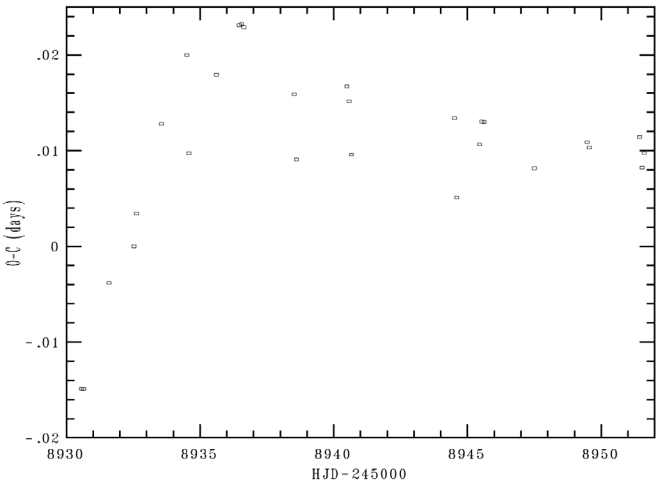

Figure 3. O–C diagram of superhump maxima of QZ Ser during the superoutburst. An ephemeris of HJD = 2458932.53212 + 0.0855537 E was used to draw this figure.

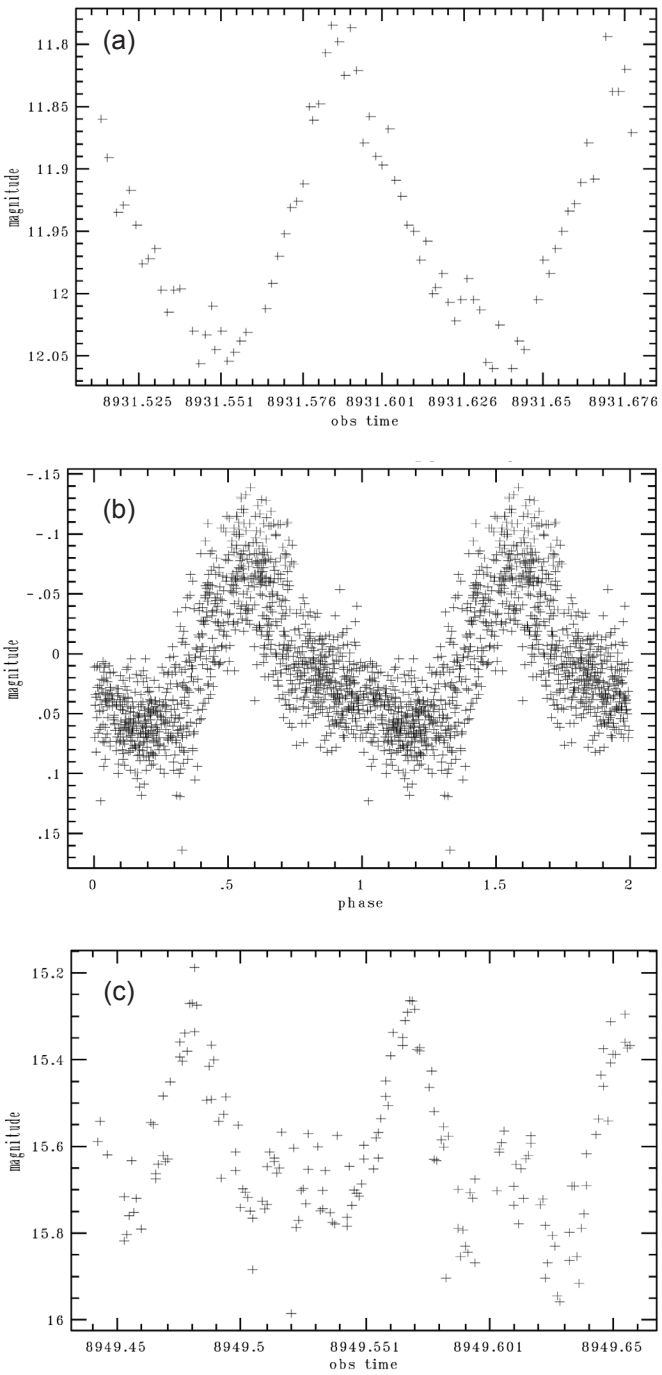

Figure 4. (a) V-band light curve for JD 2458931. (b) Detrended and phased Clear-band light curve during plateau phase. (c) Clear-band light curve for JD 2458949 from psf photometry.

The times of superhump maxima and the coresponding O–C diagram are shown in Table 3 and Figure 3. The times of maximum light have been derived from a cubic fit around each maximum. From Figure 3 we expect the transition from Stage A to Stage B superhumps approximately at HJD 2458934 / 35.

5. Acknowledgements

This research made use of the NASA Astrophysics Data System.

We are grateful to numerous collaborators of VSNET (Kato *et al.* 2004), including participants of CVNET and BAA,VSS alert, for the large contribution and to outburst detection and announcement by a number of variable star observers worldwide. We gratefully acknowledge the VSNET email notification service and the useful comments from an anonymous referee. We thank all contributors to the IRAF Community Distribution made available on github (https://iraf-community.github.io.) after NOAO dropped support for IRAF.

This research has made use of "Aladin sky atlas" (Bonnarel *et al.* 2000) developed at CDS, Strasbourg Observatory, France.

References

Bath, G. T. 1973, *Nat. Phys. Sci.*, **246**, 84.

Bonnarel, F., *et al.* 2000, *Astron. Astrophys., Suppl. Ser.*, **143**, 33.

Hartman, J. D., and Bakos, G. Á. 2016, *Astron. Comput.*, **17**, 1.

Henden, A. A. 2019, *J. Amer. Assoc. Var. Star Obs.*, **47**, 130.

Jordi, K., Grebel, E. K., and Ammon, K. 2006, *Astron. Astrophys.*, **460**, 339.

Kato, T. 2020a, vsnet-outburst 24846 (http://ooruri.kusastro.kyoto-u.ac.jp/mailarchive/vsnet-outburst/24846).

Kato, T. 2020b, vsnet-campaign-dn 9426 (http://ooruri.kusastro.kyoto-u.ac.jp/mailarchive/vsnet-campaign-dn/9426).

Kato, T., Uemura, M., Ishioka, R., Nogami, D., Kunjaya, C., Baba, H., and Yamaoka, H. 2004, *Publ. Astron. Soc. Japan*, 56, S1.

Lang, D., Hogg, D. W., Mierle, K., Blanton, M., and Roweis, S. 2010, *Astron. J.*, **139**, 1782.

Osaki, Y. 1974, *Publ. Astron. Soc. Japan*, **26**, 429.

Patterson, J. 2001, *Publ. Astron. Soc. Pacific*, **113**, 736.

Schmeer, P. 2020, vsnet-alert 24084 (http://ooruri.kusastro.kyoto-u.ac.jp/mailarchive/vsnet-alert/24084).

Thorstensen, J. R., Fenton, W. H., Patterson, J., Kemp, J., Halpern, J., and Baraffe, I. 2002, *Publ. Astron. Soc. Pacific*, **114**, 1117.

Thorstensen, J. R., Ringwald, F. A., Taylor, C. J., Sheets, H. A., Peters, C. S., Skinner, J. N., Alper, E. H., and Weil, K. E. 2017, *Res. Notes Amer. Astron. Soc.*, **1**, 29.

Tody, D. 1986, in *Instrumentation in Astronomy*, Society of Photo-Optical Instrumentation Engineers, Bellingham, Wash., 733.

Warner, B. 1995, *Cataclysmic Variable Stars*, Cambridge Univ. P., Cambridge.

Zacharias, N., *et al.* 2015, *Astron. J.*, **150**, 101.

Systematic Effects in the Visual Estimation of the Brightness of Red Variable Stars

Robert R. Cadmus, Jr.
Department of Physics, Grinnell College, Grinnell, IA 50112; cadmus@grinnell.edu

Received May 5, 2020; revised November 17, December 3, 2020; accepted December 4, 2020

Abstract Visual brightness estimates for red variable stars are complicated by a number of effects. These phenomena have been investigated by comparing visual estimates with V-band photometric measurements. The differences between these quantities for individual stars often vary with the V magnitude at the time of the measurement in a way that is different from the collective trend for many stars and corresponds to an underestimate of the full amplitude of variation by visual observers. This may result from biases introduced in the estimation process, specifically in the choice of comparison stars and in the interpolation of the brightness of the variable between them. These results may shed some light on the factors affecting the transformation between visual estimates and photometric V values for red stars and provide some guidance in the use of that transformation. They also provide insight into the visual estimation process itself.

1. Introduction

The extensive long-term monitoring of variable stars by thousands of visual observers coordinated by the American Association of Variable Star Observers (AAVSO) has produced a database that is a valuable resource for professional astronomers. While these estimates are generally reliable, there has been a persistent question regarding the relationship between visual estimates (m_v) and photometric magnitudes (V) for red stars (Percy *et al.* 1993). This relationship, in the form of the difference $m_v - V$, has been quantified at various times and in various ways. The work described here evolved from such an effort (Cadmus 2021). A general discussion of the procedure followed in that work as well as a discussion of the history of such determinations is included there. The result was the determination of the dependence of $m_v - V$ on V alone, on the B–V color alone, and on V and B–V together. The purpose of this paper is to explore specific issues associated with the visual estimating process that arose in that project. The focus here is on this group of red stars; although some of the insight may have more general applicability, that has not been confirmed.

2. Observations

The determination of the transformation between visual brightness estimates and photometric magnitudes reported by Cadmus (2021) involved the comparison of visual estimates for 38 mostly semiregular variable stars from the AAVSO International Database (Henden 2014; Kafka 2015–2020) with photometric observations made with the 0.61-m telescope at Grinnell College's Grant O. Gale Observatory. The measurements were made in the V and B bands using a photoelectric photometer incorporating an uncooled 1P21 photomultiplier and processed using conventional methods (see Cadmus 2015 and Cadmus 2021). They cover almost three decades from roughly May 1984 to December 2013 (JD 2445849 to 2456657), depending on the star. These stars are pulsating red giants and some are carbon stars, which are very red. They were selected on the basis of their likelihood to experience episodes of very reduced amplitude (see Cadmus 2015). The V data have been fit with a spline curve to facilitate matching the dates to those of the visual data, which are averages in 20-day bins. The shapes of the V light curves span the range from nearly sinusoidal to highly erratic. There is relatively little variation in B–V for most of the stars but for the carbon stars the B–V variation is very similar to the V variation, with large B–V associated with large V.

For reasons to be discussed in section 5.2, one would expect the $m_v - V$ transformation to be color-dependent. On the other hand, because the estimates are made by observers using a variety of instruments providing images with a range of brightness for the same star at the same time, one would be surprised to find that the transformation depends in a significant way on stellar brightness. The transformation does, in fact, behave as expected. The overall transformation for the entire collection of stars is nearly flat when plotted vs. V and sloped when plotted vs. B–V. These plots are shown in Figure 1 (adapted from Cadmus 2021).

As one can see from Figure 1, the distributions of data points are not as tidy as one might hope. The use of 38 stars gives coverage over a wide range of V and B–V, with each star contributing its part to the distributions. One might expect that the data for each star would simply be a chunk of the complete coherent distribution but this is not the case, leading to the clumpy appearance of the distributions in Figure 1. The vertical lines in panel b are for those stars that have so little variation in B–V that spline fits to those photometric data were not helpful or for S Aur, which is faint and very red, resulting in poor quality B data. The trends are clear and can be fit separately with straight lines as shown in Figure 1 or collectively with a function of both V and B–V to get equations that transform the m_v estimates to V values (Cadmus 2021). The fit to $m_v - V$ as a function of both V and B-V is:

$$m_v - V = 0.13 - 0.02\ V + 0.18\ (B–V). \quad (1)$$

The uncertainties in the coefficients in this transformation are primarily determined not by the uncertainties in the data or in the fitting process, but by the substantial differences in the behavior of the data for different stars that give widely

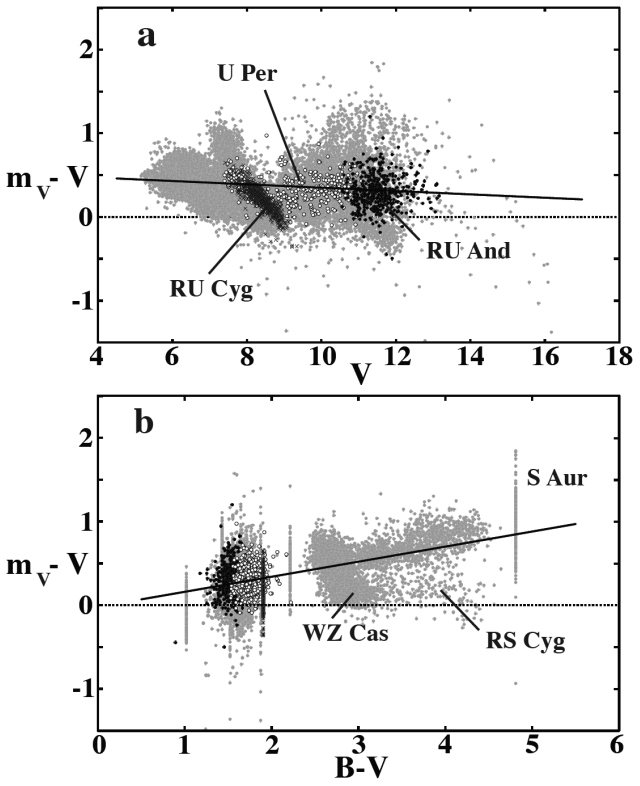

Figure 1. The visual / photometric difference m_v – V plotted vs. both V (panel a) and B–V (panel b). Each point corresponds to a single value in the binned visual light curve. The RU And data are represented by solid black points, the RU Cyg data by crosses, and the U Per data by open points. The data for all other stars are represented by gray points. The U Per distribution is partially obscured by the RU Cyg points but the data for these three stars also appear in Figure 2. The data for a few of the carbon stars are identified in panel b. The solid lines are linear fits to the m_v – V data vs. either V or B–V. A color version of this plot in which all the stars are differentiated is shown in Cadmus (2021). Figure adapted from Cadmus (2021), © 2021. The American Astronomical Society. All rights reserved.

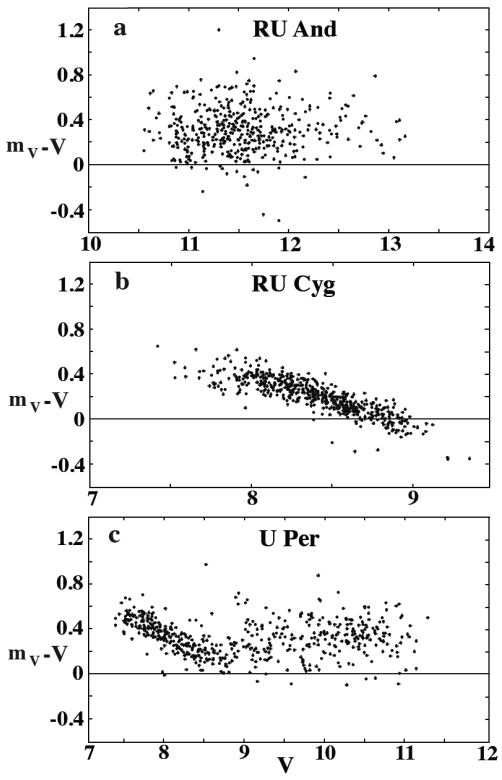

Figure 2. The visual/photometric difference m_v – V plotted vs. V for RU And (panel a), RU Cyg (panel b), and U Per (panel c). Figure adapted from Cadmus (2021), © 2021. The American Astronomical Society. All rights reserved.

varying transformations when the data for the stars are fit individually (Cadmus 2021). The primary source of uncertainty is therefore the choice of stars to include in the collective fit. To estimate the size of this effect the overall transformation was calculated by fitting 11 randomly-constructed groups of stars. The standard deviations in the resulting coefficients suggested that the constant is uncertain by roughly 0.2, the V coefficient by roughly 0.02, and the B–V coefficient by roughly 0.05, so the V slope is consistent with zero but the B–V slope is not. The more important point, however, is that this overall transformation is only a very rough representation of the general trend of a diverse set of data.

Figure 2 (adapted from Cadmus 2021) shows the contribution of three individual stars to these transformation distributions. The motivation for the present work lies in understanding these details.

The RU And distribution in panel a of Figure 2 is a case that looks like a part of the overall distribution. The data for RU Cyg in panel b illustrate the behavior of the distribution for a star with a strong V-dependence. The U Per distribution in panel c is an example of a more complex case with two regions of different character that will be discussed in more detail later.

As shown in Figure 1b the situation is neater for the B–V distribution except for the existence of a lower branch populated by two carbon stars. The emphasis here is on the variation of m_v – V with V for individual stars but this lower branch deserves a few comments. It is populated primarily by RS Cyg, with some contribution at the left end by WZ Cas. This might suggest that visual observers provide estimates for RS Cyg that are less affected by the overall color dependence than are the estimates for other very red stars, but this seems unlikely. Another possibility is that there is some other process that tends to cancel the color dependence for WZ Cas and RS Cyg. These two stars do not differ substantially from the stars in the upper branch in V, B–V, period, or difference in color relative to the comparison stars on the AAVSO charts. The presence of other stars close to these two variables might suggest the existence of very easy-to-use comparison stars, but the information available in this study does not indicate that they were heavily used and they are probably far enough from the variables to be resolved by most observers. In addition, a limited and crude laboratory experiment did not reveal any dramatic tendency for estimates to be affected by the presence of a nearby star. RS Cyg does have a larger amplitude and simpler light curve than the other carbon stars in this sample. Further investigation of this phenomenon is planned.

The distribution of the measurements of m_v – V vs. V for each star forms a clump that is often inclined relative to the nearly-flat overall trend. The tilt of these individual distributions is almost always with greater values of m_v – V at smaller values of V. This means that as the star gets brighter visual observers tend to underestimate the brightness to a greater extent so they report an amplitude of variation that is too small: an

amplitude deficit. The possibility of an amplitude deficit was previously noted for EU Del by Percy *et al.* (1993) and may be present in the data of Lebzelter and Kiss (2001). As a further check on the reality of this phenomenon binned AAVSO visual data were compared with AAVSO photometric V data. Several other investigations reported in Cadmus (2021) demonstrated that this effect is real and originates in the visual rather than in the photometric data. It is different for different stars but similar for different observers. The purpose of this paper is to investigate the nature of this unexpected dependence of $m_v - V$ on V and the resultant amplitude deficit. The amplitude deficits presented here were calculated as the negative of the slopes of the corresponding $m_v - V$ vs. V distributions, not from the amplitudes themselves, but that corresponds to a definition of the amplitude deficit as:

$$\text{Deficit} = \frac{(\text{photometric amplitude} - \text{visual amplitude})}{\text{photometric amplitude}} \quad (2)$$

The deficits for all the stars, in order of increasing deficit, are given in Table 1, which also includes mean V and B–V values, approximate typical V amplitudes, spectral types, and variability types. The photometric data were estimated from the Grinnell light curves; the spectral types and variability types were obtained from www.aavso.org/vsx. These are semiregular stars whose light varies on multiple time scales so the amplitude estimates are very approximate.

The deficit effect is more pronounced for stars with smaller amplitudes (Figure 3). The amplitudes reported here are estimates of the typical full amplitudes—the total ranges of variation in brightness—and do not reflect the most extreme variations.

The potential causes for the deficits, and for the shapes of the individual $m_v - V$ vs. V distributions in general, can be grouped into those that seem not to be involved (section 4), those that apparently affect the nature of the distributions but are not their underlying cause (section 5), and those that might cause these phenomena in general (section 6). A viable explanation for the deficit effect must account for the fact that the $m_v - V$ vs. V distributions are very different for different stars but each is well defined because different observers generate similar observations for each star. It is therefore helpful to look at sets of data that have been restricted in particular ways.

3. Insight from restricted sets of data

The multiplicity of possible causes for the strange behavior of the $m_v - V$ vs. V distributions can be simplified by considering only sets of data that eliminate some variables. For example, if the deficit persists when the $m_v - V$ vs. V distribution for an individual star is calculated using estimates associated with a single known observer, a single known chart, and a single known pair of comparison stars (an "OCC" set), variations in those factors can be eliminated as possible causes of the effect. This was tested in 99 OCC cases and the deficits usually persisted. The distributions for individual stars generated from the data for different OCC sets are generally a bit different, but

Table 1. Amplitude deficits and stellar characteristics, ordered by size of amplitude deficit.

Star	*Mean V*	*Mean B–V*	*Typical V Amplitude*	*Deficit*	*Spectral Type*	*Variability Type*
V778 Cyg	10.2	3.4	0.4	–0.244	C4,5J	SRA
S Aql	10.2	1.6	2.0	–0.157	M3e-M5.5 e	SRA
RZ UMa	9.3	1.6	0.7	–0.052	M5-M6	SRB
S Per	10.2	2.7	3.2	–0.047	M3Iae-M7	SRC
S Aur	10.8	4.8	2.3	–0.041	C4-5,4-5(N3)	SR
RU And	11.5	1.5	2.0	–0.012	M5e-M6e	SRA
Z UMa	7.5	1.6	1.6	–0.012	M5IIIe	SRB
R UMi	9.4	1.7	1.5	0.001	M7IIIe	SRB
U Boo	11.1	1.6	1.6	0.015	M4e	SRB
U Per	9.0	1.8	3.5	0.018	M5e-M7 e	Mira
RS Cyg	7.8	3.3	1.8	0.033	C8,2e(N0pe)	SRA
W Tau	10.1	2.2	1.3	0.039	M4-M6.5	SRB
RX Boo	7.6	1.8	0.6	0.071	M6.5e-M8IIIe	SRB
RY Dra	6.5	3.3	0.5	0.080	C4,5J(N4p)	SRB
RS Aqr*	11.7	1.6	3.0	0.081	M2e	Mira
X Her	6.2	1.5	0.6	0.097	M6e	SRB
W Cyg	5.9	1.6	1.0	0.106	M4e-M6eIII	SRB
V Boo	8.4	1.6	1.1	0.108	M6e	SRA
U LMi	11.2	1.4	1.4	0.127	M6e	SRA
RS Cnc	5.9	1.7	0.6	0.153	M6S	SRB
RV And	9.9	1.8	1.8	0.154	M4e	SRA
V CVn	7.3	1.6	1.3	0.158	M4e-M6eIIIa:	SRA
SW Vir	7.2	1.7	1.1	0.159	M7III	SRB
X Mon	8.0	1.5	1.5	0.171	M1eIII-M6ep	SRA
RS Lac	11.2	1.0	1.7	0.171	K0	SRD
RV Peg*	11.7	1.9	5.0	0.177	M6e	Mira
SX Her	8.3	1.6	0.9	0.202	G3ep-K0(M3)	SRD
U Del	6.7	1.7	1.0	0.209	M5II-III	SRB
U Cam	7.5	4.0	0.9	0.217	C3,9-C6,4e(N5)	SRB
X Lib*	11.7	1.7	3.0	0.259	M4e	Mira
UX Dra	6.2	2.8	0.5	0.267	C7,3(N0)	SRB
ST UMa	6.6	1.7	0.6	0.295	M4-M7III	SRB
WZ Cas	7.1	2.9	0.6	0.302	C9,2Jli(N1p)	SRB
TT Cyg	7.5	2.6	0.4	0.317	C5,4e(N3e)	SRB
RW Boo	7.9	1.5	0.6	0.348	M5-M7III	SRB
RT Hya*	8.2	1.6	1.3	0.363	M6e-M8e	SRB
RU Cyg	8.4	1.9	1.0	0.407	M6e-M8e	SRA
RW Sgr*	9.7	1.9	1.0	0.506	M4II/IIIe-M6III:e	SRA

** Only limited data are available for these stars.*
Note: The amplitude values are very approximate and represent the typical range of variation.

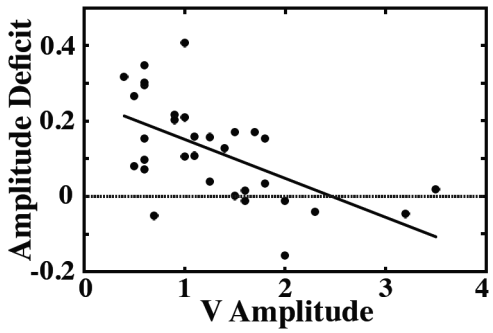

Figure 3. The relationship between the amplitude deficit and the approximate full amplitude of variation in V. The solid line is a linear fit to the data.

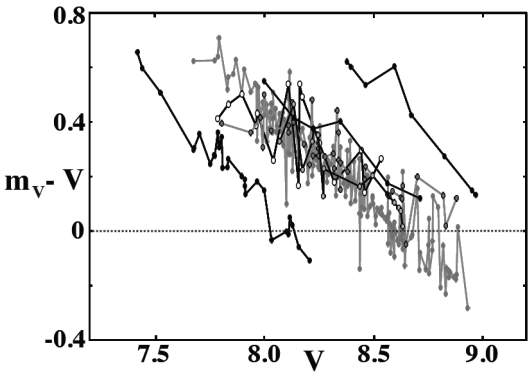

Figure 4. The variation of m_v – V with V for several OCC restricted data sets for RU Cyg. The points in each set are connected by lines to make the groups more apparent.

each shows the deficit effect. An example of this behavior is shown in Figure 4.

Figure 4 shows a sample of the OCC data sets that contribute to the complete m_v – V vs. V distribution for RU Cyg shown in Figure 2. RU Cyg was chosen as an example because the effects described here are so clear in that case, but they occur for most of the other stars in our program as well. If the visual/photometric differences had no dependence on V, each of these OCC patterns would be horizontal. However, in each case the distribution for each OCC set has a slope that arises from systematic effects in the observation process.

The nature of the m_v – V vs. V distributions involves a hierarchy of processes. At the most fundamental level, if an observer were always to report the same brightness, resulting in a severe underestimate of the range of variation, the distribution would have a slope of –1. The predominantly negative slopes of the real distributions are diluted versions of this extreme case. The chart and comparison star information is not available for most of the estimates in the AAVSO database so these restricted OCC sets of estimates are small and may be subject to systematic effects associated with particular observers. Nevertheless, the m_v – V vs. V distributions for the OCC sets are usually approximately linear with consistent negative slopes for each variable star.

The overall m_v – V vs. V distribution for a particular star is then the aggregate of all of its OCC sets of estimates. For a single variable star the primary difference in the OCC sets is the choice of comparison stars, which changes with the variable star's brightness, so the various OCC sets are offset from one another in V as shown in Figure 4. The effects of the observer and chart are usually less dramatic. If the range of the variable is small then the OCC sets substantially overlap and the resulting m_v – V vs. V distribution has a pronounced slope. If the amplitude of the variable is large, however, the individual diagonal OCC distributions are spread out over a substantial range of V and the overall distributions for such variables have a much smaller slopes, resulting in smaller deficits at larger amplitudes as seen in Figure 3. This sensitivity to the amplitude of variation at least partially explains why the m_v – V vs. V distributions for different stars look different. Unfortunately, it is not possible to reconstruct the entire observed distributions from the individual OCC distributions because essential information is not available for most estimates. While the numerous and varied OCC data sets discussed here provide useful information, it is important to remember that these cases are only a sample and may not be representative of all possible situations.

The examination of the OCC data sets strongly suggests that the deficits do not arise from differences in observers, charts, or comparison stars. With that background the following sections explore a variety of potential effects that may or may not be responsible for the deficit effect.

4. Possible factors that probably do not influence the shapes of the m_v – V vs. V distributions

The investigation of the cause of the star-dependent amplitude deficits is complicated by the large number of factors that can influence visual magnitude estimates. The effects described in this section were examined but found not to be primary causes of this phenomenon, but this information narrows the possible remaining options and has some relevance to understanding the visual estimating process generally.

4.1. The photometric data

The reliability of the photometric V data is discussed in detail in Cadmus (2021).

4.2. Stellar characteristics

No significant correlation was found between the size of the deficit for a given star and its values of mean B–V, period, declination, galactic latitude (which might be related to the number of comparison stars near a variable), or any other obvious stellar characteristic except V. The effect is apparently not caused in any direct way by any of these factors.

4.3. Angular orientation of the variable and the comparison stars

The angular positions of the comparison stars relative to the variables on the sky (the position angle effect) is known to affect observers' brightness estimates (Roberts 1897; Isles 1970; Williams 1987). However, a casual survey of AAVSO charts indicates that the comparison stars are reasonably well distributed around the variables and not likely to be the cause of major systematic effects in the present case. In addition, the orientation of the stars in the field is dependent on the optics used and the circumstances of the observations so any position angle effect should average out over the large number of observers and observations considered here.

4.4. Length of time spent viewing the stars

The color response of the human eye can vary on time scales ranging from hours to years (Sterken and Manfroid 1992) and Whiting (2012) has reported that red stars are perceived to be brighter if they are observed for a longer period of time. Both of these effects are difficult to investigate and are unlikely to operate in a manner that is systematic enough to produce deficits for many stars and many observers.

4.5. Observing conditions

In some cases there are effects associated with adverse observing conditions and small numbers of visual observers

at the ends of the observing seasons but these effects are not generally correlated with V.

4.6. Time dependence

There are detectable variations in the distributions over time, but these are not large enough or systematic enough to be responsible for the deficit effect in general.

5. Possible factors that may have some effect on the shapes of the m_v – V vs. V distributions but are probably not the underlying cause of the deficits

5.1. Binning of the visual data

Tests with various binning intervals showed that binning of the visual data may cause a small reduction in amplitude, especially if the period is short, but that it is not the cause of the differences of interest here.

5.2. Color differences between the variables and the comparison stars

The origin of the overall transformation between visual estimates and photometric V measurements may be related to a systematic, and generally unavoidable, difference of about 1.4 magnitude between the colors of the variable stars in this project and the less-red colors of the comparison stars on AAVSO charts (Cadmus 2021). The wavelength response of human vision is different for different observers and different situations, but generally lies a bit to the blue of the V passband (Hallett 1998) so a visual observer will perceive a red variable star as slightly dimmer relative to its comparison stars than would be measured photometrically. This is roughly consistent with the overall amount of offset between the photometric and the visual data but the m_v – V vs. V distributions for individual stars depend on factors that are unique to each star making detailed comparisons difficult. This is further complicated by the Purkinje effect (Thackeray 1935; Grouiller 1936; Percy 2007), which describes the dependence of the human wavelength response on light level. While the color difference between variable and comparison stars probably explains the overall offset for each star, most of the stars considered here have very little color change around their cycles so there is little phase-dependence in the color difference that would result in a variation of m_v – V with V.

5.3. Angular separation between the variable star and the comparison stars

For 72% of the program stars there is a clear correlation between increasing angular separation between the variable star and a comparison star and increasing brightness of the comparison star. With the color difference between variables and comparison stars that exists for these red stars it is possible that observations made with brighter, more distant comparison stars might be systematically different from those made with fainter comparison stars, leading to a variation of m_v – V with V. However this would not affect the OCC data sets, which involve only a single pair of comparison stars but still show the deficit effect, suggesting that angular separation is not a primary cause of the deficits.

5.4. Human observers

Although there is enough agreement among different observers to produce clear patterns, individual observers do generate different results, primarily in the overall offsets of the brightness estimates, which were found to be at least 0.6 magnitude in some cases that were investigated. The effect of these differences does not always average out but the fact that the deficit effect is present in individual OCC data sets shows that variation among observers is not a primary cause.

There is still the issue of phenomena that affect the estimates of a single observer. This will be addressed further in section 6, but one possibility that falls in the present "possible but unlikely" category is "anchoring": the well-established tendency for peoples' previous experience to inappropriately skew their judgments. This specific mechanism seems unlikely because the deviations between visual estimates and photometry generally scale gradually with V and are not enhanced near the extrema.

5.5. The comparison star charts

The comparison star charts themselves are, of course, attractive suspects for the cause of the deficits because they have the property of being different for different stars but similar, if not identical, for different observers. Previous investigators (Stanton 1978, Stanton 1981, and Zissell 2003, for example) have investigated the accuracy of the charts' comparison star sequences. This was also thoroughly explored in the present project and while the charts probably play a role, several investigations suggest that the nature of the charts, as opposed to the way that they are used, is not the primary culprit.

A number of the stars in the comparison star sequences for U Per and RU Cyg, which are particularly problematic cases, were measured at Grinnell and no systematic differences with the current AAVSO charts were found. In addition, distributions generated using OCC data sets that include only estimates that were known to have been made with specific charts usually show the deficit effect so it does not arise from chart-to-chart differences. There are some chart-dependent effects but no clear evidence that there is anything seriously wrong with any specific charts. This conclusion is blurred a bit by the tendency for the charts that were used to be correlated with observers and by the use of some non-AAVSO charts.

Inspection of the photometry tables associated with the AAVSO charts for the stars in this project revealed that, to a greater or lesser extent depending on the star, different catalogs or sources were used for comparison stars of different brightness, as one would expect, but no obvious widespread problems were found and the AAVSO comparison star values for the large-deficit star RU Cyg came almost entirely from one catalog, ruling out this process as a primary cause in this significant case.

U Per and S Per are interesting in this context because their m_v – V vs. V distributions have two components (see Figure 2c for U Per). When U Per is fainter than about V = 8.8 the distribution looks flat, although with a great deal of scatter, but when the star is brighter than this the distribution has a well-defined slope with much less scatter. The comparison star magnitudes that are associated with the bright, sloped regime are

from the Tycho-2 catalog and these were confirmed at Grinnell as discussed earlier. The slope does not appear to originate in a comparison star problem; a more likely explanation is offered in section 6. The sloped part of the S Per distribution apparently arises because this star was brighter earlier in this project when there was a systematic error in the comparison star chart, explaining the deficit in this specific situation. All this suggests that V-dependent effects in the charts resulting from the use of different source catalogs are involved in some cases, but that it not the underlying cause of the widespread deficits.

The overall offset between visual estimates and photometric measurements apparently occurs because the comparison stars are almost always less red than the variables of interest here, but a possible complication that might affect the shape of an individual star's m_v – V vs. V distribution is a variation of B–V with V within the comparison star sequence on a chart. This would cause the observer's estimate for a particular star to shift relative to the photometric value by an amount that depends on the star's brightness and produce the deficit effect. To investigate this possibility the comparison star V and B–V values were extracted from the AAVSO web site for the C-scale charts for each of the stars, except in a few cases for which that scale yielded only a few values. Linear fits to plots of B–V vs. V for the comparison stars revealed that there is a significant variation of B–V with V for the comparison stars on many of the charts, but not in a consistent direction and not correlated with the deficits for each of the stars, suggesting that whatever tendencies there might be for the colors of the comparison stars to depend systematically on V might affect the deficits of individual stars but are not the origin of the (primarily positive) deficits overall.

For chart problems to produce the kinds of m_v – V vs. V distributions that are reported here those problems would have to have a systematic variation with V, and that seems unlikely. Several of the processes discussed above might lead to systematic effects for individual variable stars but none provides a comprehensive explanation for the deficits generally.

5.6. Wavelength dependence of the light curve amplitude

The amplitudes of Miras, and presumably those of semiregular variables as well, are much greater in the visible than in the infrared (Reid and Goldston 2002). The typical visual response is more blue-sensitive than is the V passband (Hallett 1998) so on this basis one might expect a larger amplitude for the visual estimates than for V measurements, which is the opposite of what is reported here. This systematic variation in amplitude is undoubtedly in play but is apparently not a primary cause of the deficits.

5.7. Spectral variations over the star's cycle

The spectra of these stars change over their cycles and it is conceivable that those changes could affect the m_v – V vs. V distributions if they interacted with the difference in the visual and photometric wavelength responses. This is a difficult hypothesis to test because it requires a detailed comparison of phase-dependent spectra with both the V passband and the less-well-defined visual passband. That process is beyond the scope of this investigation but some general observations are possible.

The influence of spectral variations could take two forms (or a combination of both): the effect of the overall shape of the spectrum and the nature of specific spectral features. There is no evidence of a correlation between the deficits and either the mean B–V values or the spectral types of the stars. An ongoing project at Grinnell has provided a large collection of spectra of these stars but those data are not yet in a form that is appropriate for detailed analysis. However, a casual look at preliminary versions of the spectra revealed that their overall shapes fall into several categories. There is some systematic variation in the mean deficits among the categories but the variations of the deficit values within each category are much larger. The lack of a clear association of deficit with overall spectral shape suggests that the shape, and therefore its variation with phase, is probably not a primary cause of the deficits.

Exploring the possible role of most individual spectral features is beyond the scope of this investigation but the information is available to pursue one case. The behavior of the very strong Na D absorption feature in the spectrum of RS Cyg has been investigated as part of a separate project. Although the strength of this feature varies with phase, RS Cyg has a relatively small deficit, suggesting that variation of the Na absorption is not, by itself, sufficient to cause a deficit.

While these results on the possible effect of spectral variations are tentative and incomplete, they do not show clear signs that they might be important and do not offer any explanation for the shapes of the distributions shown in Figure 2. This question will be easier to address when fully processed spectra become available.

6. Possible explanations for the amplitude deficits

The final category of possible causes for the deficits—those that might be responsible for the existence of these effects as opposed to altering their details—is the most difficult to address in spite of the conspicuous, consistent, and widespread nature of the phenomenon. If the deficits do not appear to be caused by stellar characteristics or the identities of the observers, charts or comparison stars, then the cause probably lies in the observing process.

One possible cause of the slopes in the m_v – V vs. V distributions and the resulting amplitude deficits involves the relationship between scatter in the visual estimates and the use of comparison stars. If an observer's m_v estimates always scatter symmetrically around the photometric V value then as V changes the m_v – V vs. V distribution will be flat and there will be no deficit. However, if the observer's estimate options are constrained to lie between the magnitudes of the comparison stars, as is the case for a single OCC set, at some point as the star brightens the estimates that would be the brighter than V by the greatest amount exceed the limit of the brighter comparison star and are no longer available, possibly eroding the scatter of the estimates corresponding to negative m_v – V values. The same sort of process occurs at the faint end, so the m_v – V values might be systematically high when the star is bright and low when the star is dim and the m_v – V vs. V distribution would no longer be flat but have an overall negative slope. This corresponds to a deficit for the OCC set and ultimately for the star overall.

The scatter is a natural characteristic of the measurement process, but the use of discrete pairs of comparison stars might be involved in the amplitude deficit phenomenon.

Another particularly interesting possibility is revealed by plotting histograms of individual estimates for single OCC sets as shown in Figure 5. The nine examples in that figure are representative of the behavior of the entire set of 97 histograms (the data were too sparse in two cases) but are not always the best examples of each category. These were chosen to represent nine different observers and eight different stars, and because the numbers of estimates were large enough to make the patterns clear.

These examples show that for a given OCC case there is often a tendency for the estimates to fall near the center of the comparison star interval and for observers to avoid estimating the variable star's brightness to be the same as that of either comparison star: "central clustering." Roughly speaking, of the full set of OCC cases about 38% showed a very clear clustering of the estimates near the center of the comparison star interval, about 46% showed some tendency to cluster, and about 15% did not show any obvious clustering. Although these categories are only approximate the tendency to cluster was seen in roughly 84% of the OCC sets. Figure 6 illustrates this effect for the entire sample of OCC restricted data sets.

For each OCC set the central clustering fraction shown in Figure 6 was calculated as the fraction of all estimates falling within an interval of one third of the magnitude difference between the two comparison stars after adjusting the visual estimates to remove overall offsets relative to the V data. To better capture peaks this interval was centered on the mean of all estimates, which is not always ideal. Centering the interval at the midpoint of the two comparison stars significantly changed the results in individual cases but the overall distribution shown in Figure 6b was essentially unchanged. The deficits shown in Figure 6b were calculated using binned visual data but using the raw estimates does not change the overall appearance of the plot. In a few cases these results are confused by observers reporting estimates that fall outside the comparison star range and the usual "quantization" of the estimates to 0.1 magnitude occasionally compromises individual results, but the character of the overall result is not altered by these anomalies.

The distribution of central clustering fractions shown in Figure 6a demonstrates the strong tendency of the estimates to be more concentrated within the comparison star interval than would be expected for a uniform distribution. This tendency to report "middle" estimates produces the sort of underestimate of the range of the variable star that is the amplitude deficit for individual OCC sets. Figure 6b shows that there is a tendency for more concentrated OCC distributions to be associated with larger amplitude deficits, although the large amount of scatter suggests that some additional process (discussed below) is also involved.

This effect is not surprising. Observers are often instructed to estimate where the variable lies in brightness between the two comparison stars (AAVSO 2013), but it is difficult to make brightness comparisons between stars at the 0.1 magnitude level. Some experienced and skillful observers may well achieve this precision, but in practice many observers might decide among "like the fainter comparison star," "like the brighter comparison star," or "between the two stars," but with the "between" option the most common. Another way to say this is that they might not so much estimate where the variable falls in brightness between the two comparison stars as choose two comparison stars for which the variable falls in the middle. This tendency to concentrate estimates toward the center of the comparison star interval enhances the truncation effect described above and acts to increase the deficits.

If the variation of amplitude deficit with clustering fraction shown in Figure 6b demonstrates that the deficits arise from the tendency of observers to pick middle values, one might wonder why the amount of scatter is so large. There are several reasons for this. First, the estimating process involves human perception and judgment so scatter is inevitable. Second, the origin of much of the scatter is revealed by plotting deficit vs. clustering fraction for individual observers as in Figure 6b, which includes distinct symbols to identify the OCC data sets associated with two specific observers and shows that the trends for individual observers are often much better defined than is the case for the entire data set, supporting the idea that clustering of estimates is a primary cause of the deficits. However, although the ranges of clustering fractions are approximately the same for these two observers the deficits are systematically different, and the deficits for two other observers are similar in spite of substantially different degrees of clustering. This suggests that there is another process at work beyond central clustering.

A third reason for the scatter in Figure 6b is that the simple interpretation of these central clustering calculations is based on the assumption that the star's actual brightness variation is not concentrated in the middle of the interval. This is certainly not true in general. To explore the effect of the star's behavior on these estimate histograms the corresponding V histograms were constructed for each OCC data set after shifting the V data to remove the offset relative to the visual data. The shifts required varied dramatically for different OCC sets. A comparison of the distributions of estimates and V values over the range between the comparison star magnitudes showed that in approximately half of the cases the star's behavior did not resemble the central clustering of the visual estimates. In roughly 20% of the cases there was a clear correspondence, and in the remaining cases the situation was less clear. The visual estimates are observations of the star's behavior so some relationship between these two distributions is expected, but these results show that the central clustering of the estimates is not usually a simple reflection of the star's variations.

This tendency to pick middle values almost certainly contributes to the strange shapes, V-dependence, and amplitude deficits that are observed, but does not appear to be sufficient to explain the strength of the phenomenon. However, observers' choices of comparison stars can further amplify the impact of the central clustering effect. If the star's amplitude is large and the brightness of the comparison stars change to follow those variations the resulting estimates, even in the presence of some central clustering, will reasonably represent the actual behavior of V and there will be no significant deficit. However, if the star's amplitude is small and the choices of comparison star pairs are similar to each other, then estimates that are subject to the central clustering effect will tend to be concentrated near the center of the star's variation, resulting in a deficit. The effect is

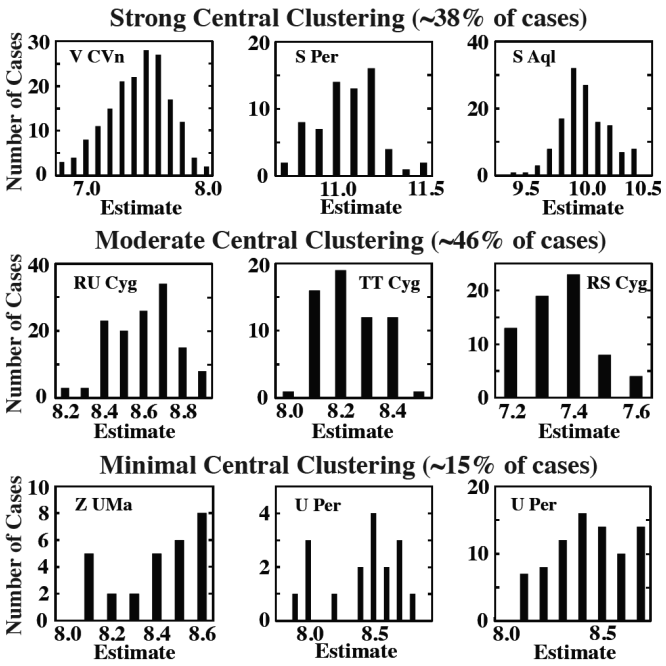

Figure 5. Examples of histograms of visual estimates for individual OCC sets of observations showing the general characteristics of those with different degrees of central clustering. In each case the limits of the "Estimate" axis are at or very close to the two comparison star magnitudes. The two U Per examples show estimates from different observers.

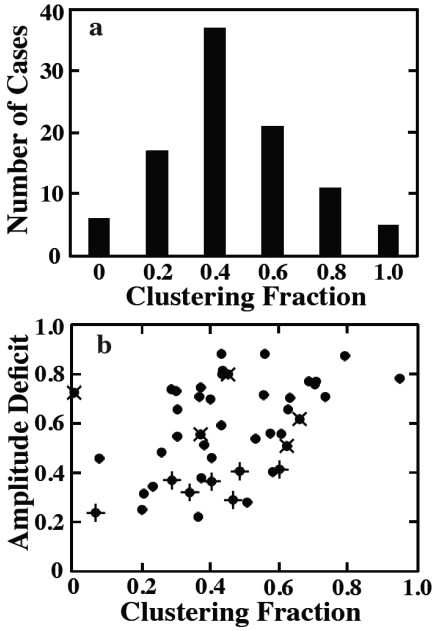

Figure 6. (a) The distribution of central clustering fractions for all 97 OCC data sets. (b) The dependence of the amplitude deficit on the central clustering fraction for OCC data sets with at least 30 estimates. The symbols that include an "x" or a "+" are for two selected observers.

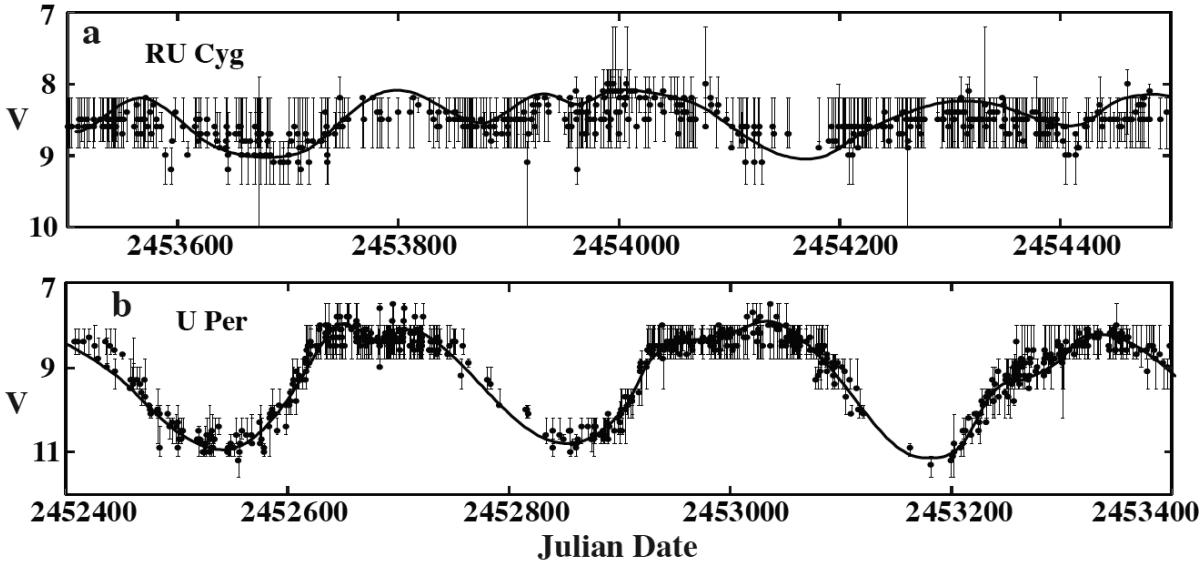

Figure 7. The effect of the choice of comparison stars on the size of the amplitude deficit. The curves are the V data, offset to match the visual data, the points are the individual m_v estimates, and the ends of the "error bars" represent the brightness of the two comparison stars used for each estimate. (a) Light curve data for RU Cyg illustrating how a near-constant set of comparison star choices can lead to a substantial amplitude deficit. (b) Data for U Per showing how agile comparison star choices can minimize the impact of central clustering and lead to a small deficit for the light curve overall.

enhanced if the comparison star pairs do not completely cover the actual range of variation. The effect of comparison star choices is illustrated in Figure 7.

The data shown in Figure 7 represent the bulk of the AAVSO visual estimates for these stars over the selected JD interval and for which comparison star information is available. Only a limited JD range is shown for clarity, but it is representative. RU Cyg is particularly interesting in this context because it has very little variation in B–V, eliminating color effects as a confounding factor. The variation in B–V for U Per is larger, but still small. The comparison star choices for several other stars that were analyzed in this way were more erratic so the deficits, or lack of them, were less visually obvious. In Figure 7a one can see that most of the estimates were made with nearly the same set of comparison stars, which do not always span the variation in V. This is not unexpected for a star with a small amplitude. It is also apparent that most of the estimates are near the middle of the comparison star ranges, as was shown in Figure 5. The result is a substantial underestimate of the amplitude of variation of RU Cyg and a relatively large deficit of 0.41. Much of the data in this case came from two observers. The data for U Per in Figure 7b illustrate the opposite situation: the V amplitude is large, the comparison star pairs follow that variation, and there is little underestimation of the amplitude of the light curve overall in spite of some central clustering. This case is discussed in more detail below.

The identification of minimal adjustment of the comparison star pairs for stars with smaller amplitudes as a contributing factor to the deficits reinforces the conclusion in section 2 that deficits generally decrease with increasing V amplitude as shown in Figure 3.

7. Discussion

Visual estimates of the brightness of red variable stars could be affected by many factors, but the surprising nature of the m_v – V vs. V distributions and their associated amplitude deficits does not appear to be caused by most of them. In particular, the persistence of this phenomenon in the OCC data sets eliminates many possibilities involving charts, comparison stars, and observers. The primary causes seem to be normal observational scatter, effects associated with the limitations of fixed comparison star intervals, and a tendency for observers to report estimates that are in the middle of the range between the comparison stars. These effects can operate in conjunction with a set of comparison star choices that are relatively restricted to amplify the deficits. None of this suggests any misbehavior on the part of the observers. If the amplitude of the star's variation is small then the useful comparison star options are limited; estimates near the middle of a pair of comparison stars, or at least not near the ends, may arise both because it is not easy to interpolate between them and because the pair may have been chosen to straddle the brightness of the variable.

This conclusion requires some qualification. This project involved a large amount of data (one spreadsheet had 1.5 million cells) and the possible involvement of numerous processes, so there is always the chance that something of significance slipped by unnoticed. The details of the variable star estimating process involve the ways in which the observers think and perceive, and that is both complicated and idiosyncratic. It is therefore possible, or likely, that the explanation for the deficits and other effects is different in different situations. There is also the possibility of selection effects. The analysis presented here was done with estimates that were accompanied by the identification of both the comparison stars and the chart that was used. These are limited subsets of the vast AAVSO database and in some cases are dominated by a small number of observers. However, the persistence of the deficit effect over a wide range of stars, observers, and other parameters suggests the likelihood of a dominant process. The fact that central clustering is pervasive and the role of a restricted set of comparison stars is clearly involved in some cases suggests that the combination of these two effects is that dominant process.

With this insight the origins of the strange two-part m_v – V vs. V distribution for U Per shown in Figure 2 becomes more clear. As described in Section 6 the relatively large amplitude of U Per results in a small deficit for the light curve as a whole, but there is a clear V-dependence in the sloped section at the bright end of the distribution. This can be understood by noticing that the corresponding regions around the maxima in the U Per light curve in Figure 7b are roughly flat and therefore similar to the RU Cyg data shown in Figure 7a. Most of the U Per OCC sets that were analyzed showed substantial central clustering (although the two shown in Figure 5 are not among them) so the amount of variation near the maxima is underestimated by the visual observers for the same reasons that were given for RU Cyg in section 6, leading to the slope in the bright section of the m_v – V vs. V distribution. This process is not applicable for the fainter section for which the distribution is flat. Another way to see the difference in the two sections is to realize that there are many more observations when the star is bright, as can be seen in Figure 7b, which means that there are many OCC sets whose m_v – V vs. V distributions are roughly aligned in the way that is illustrated in Figure 4, resulting in a strong, well-defined slope. The distributions of the OCC sets associated with the faint part of the light curve are spread out in V because of the star's more pronounced variation when faint, leading to a broad swath of OCC distributions that are flat overall.

This work was motivated by the need to discover whether the odd star-dependent behavior of the m_v – V vs. V relationship for red stars is a symptom of some underlying problem. It appears that it is not, but only reflects natural processes involved in making the estimates that do not compromise the overall calibration of the relationship between m_v – V and V. In addition, a number of other possible effects have been explored and eliminated as explanations.

8. Conclusions

The accurate visual estimation of the brightness of variable stars—especially red ones—is a tricky business that the members of AAVSO and similar organizations have executed admirably well. Given the difficulty of the task and the complexity of human vision, it is not surprising that some systematic effects occur. The most significant is the overall tendency of visual observers to increasingly underestimate the brightness of stars

as they become redder. The analysis presented here addresses the more limited question of why visual observers often underestimate the amplitudes of the variations as well. The primary mechanism appears to involve a pervasive tendency to report estimates that are clumped toward the center of the range between the comparison star magnitudes as well as the observer's choice of comparison stars. When the amplitude of the variable is small there will be little variation in the choice of comparison stars and central clumping of the estimates will have a greater effect than if the star's amplitude is greater. This leads to the observed decrease in amplitude deficit with increasing variable star amplitude. Unlike the overall color-induced error the deficits appear not to be a direct consequence of the stars' red colors. At the most basic level the phenomena discussed here arise because the photometric V measurement process is "seamless" while the visual observing process is fragmented by the use of discrete pairs of comparison stars. This result is based on the investigation of a limited set of stars, the range of possible relevant phenomena is large, and the influence of individual observers may be significant, so the explanations offered here may not be universal and should be treated with appropriate caution, but they do appear to be plausible.

The behavior of the variable leaves the observer with little discretion in the choice of comparison stars but perhaps greater awareness of the tendency to pick central values—sometimes appropriately and sometimes not—might lead to some mitigation of the effect of this phenomenon on visual light curves.

While this investigation considered only a particular group of red stars, further work may show whether the processes described here are relevant for other kinds of stars as well.

9. Acknowledgements

It is a pleasure to thank many Grinnell College undergraduate students for their assistance in this project and the thousands of visual observers who have provided the brightness estimates on which so much professional astronomy depends. The assistance of Lee Anne Willson is gratefully acknowledged, as are helpful comments by a reviewer. This research made use of the SIMBAD database, operated at CDS, Strasbourg, France. Financial support was provided by the National Science Foundation, Research Corporation, the American Astronomical Society, Sigma Xi, and Grinnell College.

Figures 1 and 2 adapted from Cadmus (2021), © 2021. The American Astronomical Society. All rights reserved.

ORCID ID. Robert R. Cadmus, Jr. https://orcid.org/0000-0003-1921-7421

References

AAVSO. 2013, *AAVSO Manual for Visual Observing of Variable Stars* (https://www.aavso.org/visual-star-observing-manual).

Cadmus, Jr., R. R. 2015, *J. Amer. Assoc. Var. Star. Obs.*, **43**, 3.

Cadmus, Jr., R. R. 2021, *Astron. J.*, in press.

Grouiller, H. 1936, *Observatory*, **59**, 86.

Hallett, P. E. 1998, *J. Amer. Assoc. Var. Star. Obs.*, **26**, 139.

Henden, A. A. 2014, variable star observations from the AAVSO International Database (https://www.aavso.org/aavso-international-database-aid).

Isles, J. 1970, *Astronomer*, **7**, 157.

Kafka, S. 2015–2020, variable star observations from the AAVSO International Database (https://www.aavso.org/aavso-international-database-aid).

Lebzelter, T., and Kiss, L. L. 2001, *Astron. Astrophys.*, **380**, 388.

Percy, J. R. 2007, *Understanding Variable Stars*, Cambridge Univ. P., Cambridge, 50.

Percy, J. R., Ralli, J. A., and Sen, L. V. 1993, *Publ. Astron. Soc. Pacific*, **105**, 287.

Reid, M. J., and Goldston, J. E. 2002, *Astrophys. J.*, **568**, 931.

Roberts, A. W. 1897, *Mon. Not. Roy. Astron. Soc.*, **57**, 483.

Stanton, R. H. 1978, *J. Amer. Assoc. Var. Star. Obs.*, **7**, 14.

Stanton, R. H. 1981, *J. Amer. Assoc. Var. Star. Obs.*, **10**, 1.

Sterken, C., and Manfroid, J. 1992, in *Variable Star Research: An International Perspective*, eds. J. R. Percy, J. A. Mattei, and C. Sterken, Cambridge Univ. P., Cambridge, 75.

Thackeray, A. D. 1935, *Observatory*, **58**, 285.

Whiting, A. B. 2012, *Observatory*, **132**, 148.

Williams, D. B. 1987, *J. Amer. Assoc. Var. Star. Obs.*, **16**, 118.

Zissell, R. E. 2003, *J. Amer. Assoc. Var. Star. Obs.*, **31**, 128.

BVR_cI_c CCD Observations and Analyses of the 0.9-day Period, Totally Eclipsing, Solar Type Binary, NS Camelopardalis

Ronald G. Samec
Faculty Research Associate, Pisgah Astronomical Research Institute, 1 PARI Drive, Rosman, NC 28772; ronaldsamec@gmail.com

Heather Chamberlain
Pisgah Astronomical Research Institute, 1 PARI Drive, Rosman, NC 28772; 4hcham@gmail.com

Daniel Caton
Davis Gentry
Riley Waddell
Dark Sky Observatory, Physics and Astronomy Department, Appalachian State University, 525 Rivers Street, Boone, NC 28608-2106; catondb@appstate.edu

Danny Faulkner
Johnson Observatory, 1414 Bur Oak Court, Hebron, KY 41048; dfaulkner@answersingenesis.org

Received May 15, 2020; revised June 6, July 21, 2020; Accepted July 30, 2020

Abstract CCD, BVR_cI_c light curves of NS Cam were taken on 2020 January 01, 20, 21, 22, 23, February 04, 22, 23, March 01, and April 07 at the Dark Sky Observatory, North Carolina, with the 0.81-m reflector of Appalachian State University by Daniel Caton, Danny Faulkner, and Ronald Samec. Five times of minimum light were determined from our present observations, which include three primary eclipse and two secondary eclipses. We selected four times of low light from parabola fits of ASAS-SN observations. The results include a newly determined quadratic ephemeris. Thus, from our 20.3-year study, the period is found to be decreasing. Since the estimated temperatures are ~6250 ± 500 K for the primary component and ~5690 K for the secondary component, this is probably due to magnetic braking. A Wilson-Devinney analysis reveals that the system is a W UMa shallow contact binary. The component temperature difference is ~560 K. The mass ratio is also somewhat extreme, $M_2/M_1 = 0.2130 \pm 0.0001$. The total eclipses make this a firm determination. Its Roche Lobe fill-out is 17%. The cool spot was at midlatitude (co-latititude = 45°), but overlaps the pole with a large radius of ~60° and a T-factor of ~0.68. The binary inclination is high, 85.0, resulting in total eclipses. As a result, the primary minimum has a time of constant light with an eclipse duration of 104 minutes.

1. History and observations

The initial study (light curves, classification, ephemeris, etc.) of NS Cam (NSV 3771, GSC 4373- 0708) was given by Khruslov (2006) of the SKYdot team. They classified it as an EB system with a maximum V magnitude of 12.9 and minima of 13.5 and 13.2 for the primary and secondary eclipses, respectively. The period was 0.90733 d. A number of publications have times of minimum light: Hübscher *et al.* (2012); Hübscher (2011); Hübscher and Monninger (2011). NS Cam appeared in "The 79th Name-List of Variable Stars" (Kazarovets *et al.* 2008). The system was observed by the All Sky Automated Survey as ASASSN-V J075539.65+741511.3 (Pojmański 2002), AAVSO Photometric All Sky Survey (APASS) DR9 (Henden *et al.*, 2015). ASASSN give a $V_{mean} = 12.78$, an amplitude of 0.51, and EW designation, J–K = 0.289, B–V = 0.4, E(B–V) = 0.032. Figure 1 shows the ASAS light curves.

The ASASSN ephemeris is:

$$\text{HJD (MinI)} = 2458026.13575 + 0.907311\ \text{d} \times \text{E} \qquad (1)$$

From the ASAS-SN curves we were able to phase the data with Equation 1 and do parabola fits to the primary and secondary minima to locate two times of "low light" within 0.001 phase of each. This system was observed as a part of our professional collaborative studies of interacting binaries at Pisgah Astronomical Research Institute from data taken from DSO observations. The observations were taken by D. Caton, R. Samec, and D. Faulkner.. Reduction and analyses were done by R. Samec. CCD, Johnson-Cousins B, V, R_c, I_c light curves of NS Cam were taken on 2020 January 01, 20, 21, 22, 23; 2020 February 04, 22, 23; 2020 March 01; and 2020 April 07 at the

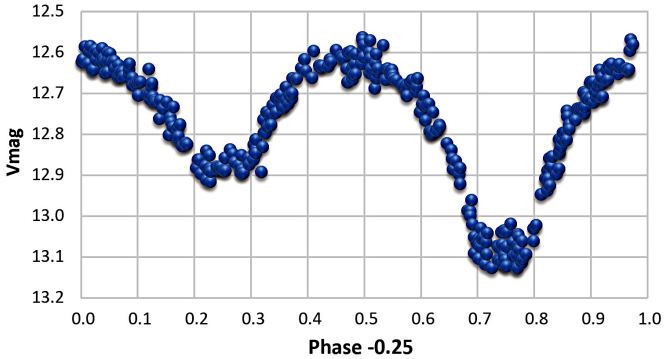

Figure 1. ASASSN-V J075539.65+741511.3 light curves (Kochanek *et al.* 2008; Shapee *et al.* 2014). Note the secondary eclipse shows a possible time of constant light (eg., a total eclipse) (Kohanek 2017).

Table 1. Sample of first ten NS Cam B, V, R_c, I_c observations.

ΔB	HJD 2458800+	ΔV	HJD 2458800+	ΔR	HJD 2458800+	ΔI	HJD 2458800+
–1.552	69.4809	–1.085	69.4814	–0.829	71.4788	–0.540	71.4791
–1.509	69.4825	–1.059	69.4830	–0.817	71.4804	–0.518	71.4807
–1.479	69.4841	–1.054	69.4846	–0.801	71.4820	–0.505	71.4823
–1.479	69.4857	–1.033	69.4862	–0.757	71.4876	–0.453	71.4879
–1.434	69.4889	–1.024	69.4893	–0.743	71.4892	–0.441	71.4895
–1.446	69.4905	–0.988	69.4910	–0.719	71.4908	–0.426	71.4911
–1.412	69.4921	–0.960	69.4926	–0.687	71.4952	–0.396	71.4955
–1.398	69.4937	–0.967	69.4942	–0.689	71.4968	–0.396	71.4971
–1.370	69.4986	–0.942	69.4990	–0.688	71.4984	-0.391	71.4987
–1.386	69.5002	–0.936	69.5007	–0.687	71.5020	-0.403	71.5023

Note: First ten data points of NS Cam B, V, R_c, I_c observations.
The full table is available through the AAVSO ftp site at ftp://ftp.aavso.org/public/datasets/samec482-nscam.txt (if necessary, copy and paste link into the address bar of a web browser).

Table 2. Photometric targets.

Star	Name	R.A. (2000) h m s	Dec. (2000)[1] ° ′ ″	V	J–K
V (Variable)	NS Cam GSC 4373-0708 NSV 3771 NSVS 685415 NSVS 767639 NSVS 685415 NSVS 738923 AN 213.1937 2MASS J05185809+3658060 HV 74374	07 55 39.62	+74 15 11.31	11.73	0.289±0.038
C (Comparison)	GSC 4373-0859 3UC329-031308	07 54 38.87	+74 14 20.81	12.99	0.28
K (Check)	GSC 4373-0770 3UC329-031303	07 54 33.18	+74 14 49.41	13.08	0.72

[1] *UCAC3 is the USNO CCD Astrograph Catalog (Zacharias* et al. *2010)*

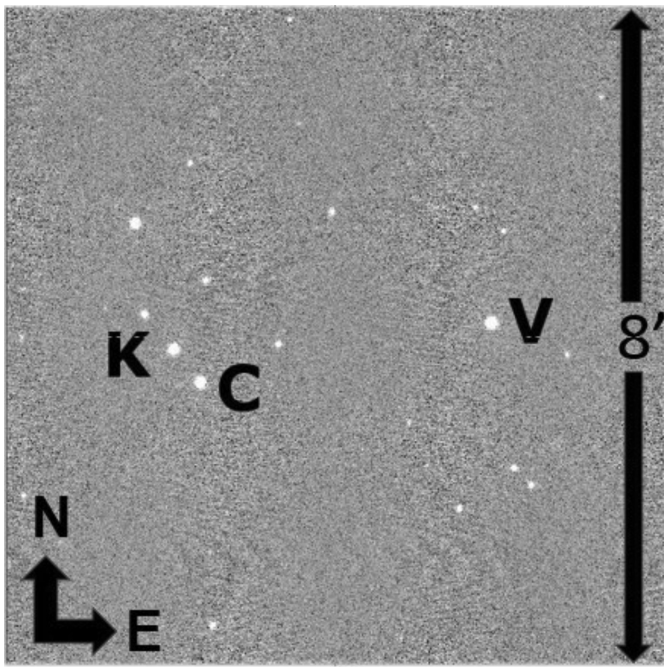

Figure 2. Finder chart, NS Cam (V), Comparison star (C), and check (K).

Dark Sky Observatory, North Carolina, with the 0.81-m reflector of Appalachian State University.

Individual observations included 923 in B, 922 in V, 917 in R_c, and 861 in I_c. The standard error of a single observation was 1.3% in B and V and 1.5% in R_c, and I_c. The nightly C–K values stayed fairly constant throughout the observing run with a precision of about 2%. Exposure times varied, from 50 s in B, 30 s in V, and 20 s in R_c and I_c. To produce these images, nightly images were calibrated with 25 bias frames, at least five flat frames in each filter, and ten 300-second dark frames. The observations are given in Table 1. Our photometric targets are designated V (variable), C (comparison), and check (K) and are given in Table 2. The variable's distance is 1,325 (56) pc (Gaia DR2 1135341864164077568). A finding chart of the field is given as Figure 2. B, V, and B–V nightly light curves of 2020 February 04 and 2020 January 01 are given in Figures 3 and 4, respectively.

2. Period determination

Five mean times (from B, V, R_c, I_c data) of minimum light were calculated from our present observations, three primary and two secondary eclipses:

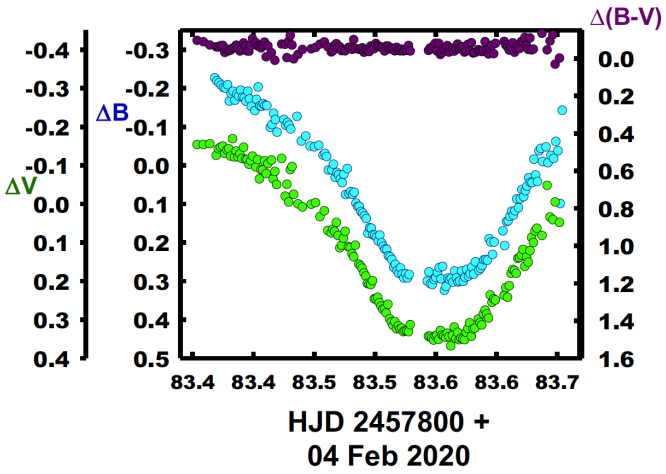

Figure 3. B, V light curves, B–V color curves from 2020 February 04.

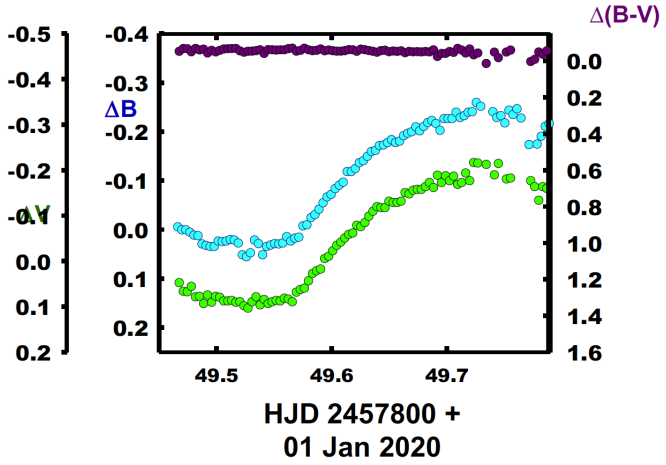

Figure 4. B, V light curves, B–V color curves from 2020 January 01.

$$\begin{aligned}\text{HJD (MinI)} &= 2458870.84278 \pm 0.00160,\\ &\quad 2458883.54736 \pm 0.00068,\\ &\quad 2458909.8621 \pm 0.0019\end{aligned}$$

(The second of the timings above was used as the initial epoch in the calculation for displayed in Table 3. The initial period was 0.907311d (ASASSN value).)

$$\begin{aligned}\text{HJD (MinII)} &= 2458849.5230 \pm 0.0011,\\ &\quad 2458946.6110 \pm 0.0006\end{aligned}$$

These minima were weighted as 1.0 in the period study. In addition, four times of low light were calculated from the ASAS-SN data and were weighted 0.1. From AAVSO's Bob Nelson's Binary O–C files (Nelson 2014) we obtained two minima from the BAVM 225. From these timings, ephemerides have been calculated, a linear and a quadratic one:

$$\begin{aligned}\text{HJD (MinI)} &= 2457883.6854 \pm 0.0005\\ &\quad + 0.90731683 \pm 0.00000017 \times E \qquad (2)\end{aligned}$$

$$\begin{aligned}\text{HJD (MinI)} &= 2458883.54853 \pm 0.00052\\ &\quad + 0.90731541 \pm 0.00000000040\\ &\quad - 0.00000000020 \pm 0.00000000005 \times E^2 \qquad (3)\end{aligned}$$

The results of the quadratic period study are displayed in Figure 5. The linear and quadratic residuals are shown in Table 3. We note here that our period study with only eleven times of minimum light (less the ASAS-SN times of low light) still gives a very similar quadratic term result –0.00000000019 ± 0.00000000006.

The quadratic ephemeris yields (although tentative) a $\dot{P} = -2.25 \times 10^{-7}$ d / yr or a mass exchange rate of

$$\frac{dM}{dt} = \frac{\dot{P} M_1 M_2}{3P (M_1 - M_2)} = \frac{-2.72 \times 10^{-8} M_\odot}{d}. \qquad (4)$$

in a conservative scenario (the primary component is the gainer). The phased B, V, R_c, and I_c light curves and B–V and R_c–I_c color curves are displayed in Figures 6 and 7, respectively, with Equation 2 used to phase the data.

3. Light curve characteristics

The curves are of good accuracy, averaging better than 1% photometric precision. Averages of the light curves at phase quadratures are given and important differences follow in Table 4. The primary amplitude of the light curve varies from 0.49 to 0.56 mag, I_c to B. The secondary amplitude was 0.28–0.29 mag. The O'Connell effect (Max I – Max II), a possible indicator of spot activity, averages about 0.015 mag. The differences in the two minima are 0.2–0.28 mag, I_c to B. A time of constant light occurs at our secondary minima and lasts some 104 minutes.

4. Temperature

The 2MASS J–K = 0.289 ± 0.038 for the binary star. This value corresponds to ~F8V ± 2, which yields a temperature of 6250 ± 500 K (Pecaut and Mamajek 2013). Fast rotating binary stars of this type are noted for having strong magnetic activity, so the binary is of solar-type with a convective atmosphere.

5. Light curve solution

The B, V, R_c, and I_c curves were pre-modeled with BINARY MAKER 3.0 (Bradstreet and Steelman 2002). Fits were determined in all filter bands, which were very stable. The solution was that of a shallow contact eclipsing binary. The parameters were then averaged (q = 0.215, fill-out = 0.08, i = 78.25, T_2 = 5650, with one cool spot) and input into a 4-color simultaneous light curve calculation using the Wilson-Devinney Program (Wilson and Devinney 1971; Wilson 1990, 1994, 2008, 2012; Van Hamme and Wilson 2007, 1998; Wilson *et al.* 2010; Wilson and Van Hamme 2014). Convective parameters g = 0.32, A = 0.5 were used. The computation was done in Mode 3 and converged to a solution. The spot turned out to be the major obstacle in computing the solution. (I first tried Mode 2 solution to determine the configuration, with the spot on the primary component. But the resulting configuration was nonphysical: The system was detached with a large spot tending to near zero or negative temperature (K). Also, the system had much the same mass ratio as our contact model.

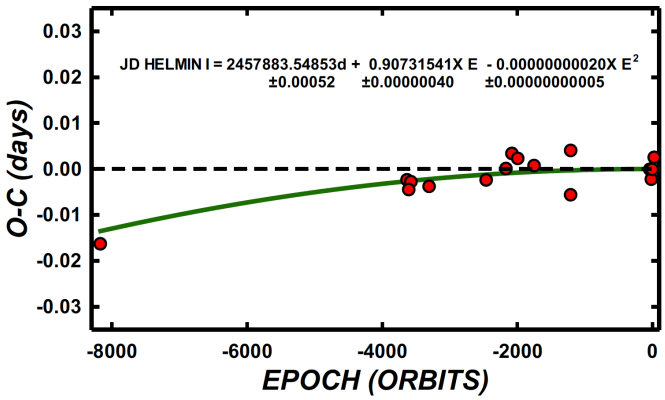

Figure 5. The linear residuals from quadratic equation (Equation 2) overlaying a plot of the quadratic term versus the orbital epoch in the period study of NS Cam.

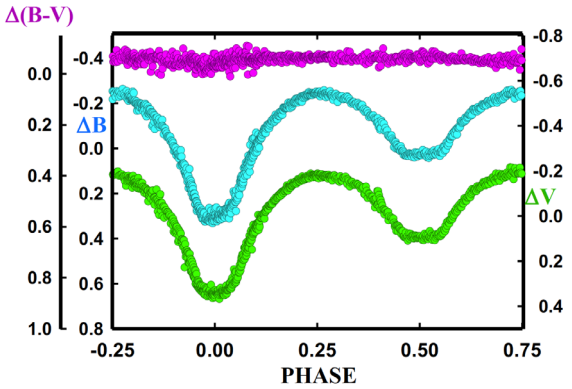

Figure 6. The phased B and V light curves and B–V color curve for NS Cam.

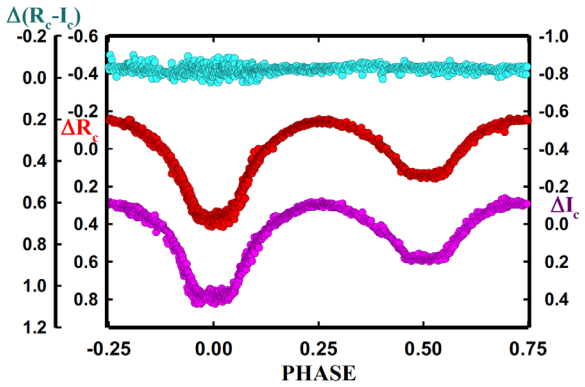

Figure 7. The phased R_c and I_c light curves and R_c–I_c color curve for NS Cam.

The separate components, if single and main sequence, would have a component temperature difference of about 3000 K. But the modeled component temperature difference was only 535 K. This would be very improbable. By switching the spot to the secondary component, the system converged to a contact solution with a reasonable spot temperature. This is very possible for a poor thermal contact system.) The spot was eventually found to be on the smaller component facing away from the primary component. We tried third light but that did not solve any fitting issues. The solution follows in Table 4. B, V, R_c, I_c normalized fluxes and B–V and R_c–I_c color curves overlaid by our solution curves of NS Cam are given in Figures 8 and 9. The geometrical representations are shown at quadratures in Figure 10a–d. The residuals of the light curves are shown in Figure 11. The fill-out of the binary is

$$f = \frac{\Omega_1 - \Omega_{ph}}{\Omega_1 - \Omega_2} = \frac{2.264754 - 2.2418}{2.264754 - 2.129279} = 0.17 \qquad (5)$$

where Ω_1 is the inner potential and Ω_2 is the outer potential.

6. Discussion

NS Cam is an eclipsing binary star with solar type components and a 0.9-day period. Since the eclipses were total, the mass ratio, q, is well determined (Terrell and Wilson 2005) with a fill-out of 17 ± 1%. The system has a fairly extreme mass ratio of ~0.21, and a component temperature difference of 560 K, which is consistent with a system in shallow contact. One major spot was needed in the final modeling. The cool spot (t-fact = 0.68) (The temperature of (Solar) sunspots have an umbral t-fact of 3800 K / 5800 K = 0.66 so our T-Fact is not strange, especially for fast rotating binary stars.) was facing away from the primary component with a colatitude of 45° and a large radius of 60°. The spot does include the pole of the secondary component. Spots of this size are better described as a spotted region, that is, it is probably made up of many spots in that region. The inclination of ~85° resulted in a time of constant light in the secondary eclipse. Its photometric spectral type indicates a primary surface temperature of ~6250 K and a secondary component temperature of ~5684 K, making it a solar type binary. Using Kepler's Law, mass ratio, M_1 = 1.18 $M_\odot$, and the orbital period, we obtain a semimajor axis, $a = a_1 + a_2 = 4.446\ R_\odot$. In terms of the solar radii, the dimensions of the system are given in Table 5.

7. Conclusion

A single 6250 K main-sequence single star would have a mass of 1.21 $M_\odot$. The mass ratio of 0.213 would mean the secondary component mass of 0.26 $M_\odot$. Such a main sequence star would have a temperature of 3250 K (M3.5V), which gives a component temperature difference of 3000 K! However, the actual value is only ~560 K. Thus, the secondary temperature is heavily influenced by the primary component, which makes the contact mode the only physical possibility. In the 23-year period study, the weak but steady decrease in the O–C curve may be due to the continuous magnetic braking. The longer, 0.9-day period (as compared to many W UMa binaries) results in a subdued but prevailing magnetic braking. Thus, the system will likely eventually coalesce into a single, fast rotating ~F4V star after a cataclysmic Red Novae event (Tylenda and Kamiński 2016).

8. Future work

Radial velocities would be highly desirable to obtain absolute (not relative) system parameters. Further light curves and eclipse timings will go toward affirming or disaffirming period scenario given here.

Table 3. Quadratic and linear residuals from NS Cam period study.

	Epoch 2400000+	*Cycle*	*Initial Residual*	*Linear Residual*	*Quadratic Residual*	*Weight*	*Error*	*Reference*
1	51473.4900	–8167.0	–0.0484	–0.0027	0.0000	1.0	—	Khruslov (2006)
2	55591.3528	–3628.5	–0.0166	0.0026	0.0009	1.0	0.0063	Hübscher (2011)
3	55644.4303	–3570.0	–0.0168	0.0021	0.0004	1.0	0.0076	Hübscher *et al.* (2012)
4	55614.4872	–3603.0	–0.0186	0.0005	–0.0013	0.5	vis	Hübscher and Lehman (2012)
5	55887.5897	–3302.0	–0.0167	0.0006	–0.0011	0.5	vis	Hübscher and Lehman (2012)
6	56654.2722	–2457.0	–0.0120	0.0004	–0.0011	0.5	0.0101	Hübscher (2014)
7	56920.1180	–2164.0	–0.0084	0.0023	0.0010	0.1	—	ASAS–SN (Shappee *et al.* 2014; Kochanek *et al.* 2017)
8	56999.9650	–2076.0	–0.0047	0.0055	0.0041	0.1	—	ASAS–SN (Shappee *et al.* 2014; Kochanek *et al.* 2017)
9	57787.9590	–1207.5	–0.0103	–0.0052	–0.0059	0.1	—	ASAS–SN (Shappee *et al.* 2014; Kochanek *et al.* 2017)
10	57788.8760	–1206.5	–0.0006	0.0045	0.0038	0.1	—	ASAS–SN (Shappee *et al.* 2014; Kochanek *et al.* 2017)
11	57077.9930	–1990.0	–0.0055	0.0042	0.0029	0.1	—	ASAS–SN (Shappee *et al.* 2014; Kochanek *et al.* 2017)
12	57297.1080	–1748.5	–0.0061	0.0022	0.0011	0.1	—	ASAS–SN (Shappee *et al.* 2014; Kochanek *et al.* 2017)
13	58849.5230	–37.5	–0.0002	–0.0019	–0.0012	1.0	0.0011	This paper
14	58870.8428	–14.0	–0.0022	–0.0041	–0.0033	1.0	0.0016	This paper
15	58883.5474	0.0	0.0000	–0.0019	–0.0012	1.0	0.0007	This paper
16	58909.8621	29.0	0.0027	0.0006	0.0014	1.0	0.0019	This paper
17	58946.6110	69.5	0.0055	0.0032	0.0041	1.0	0.0006	This paper
		r.m.s.	0.00315	0.00267				

Table 4. Light curve characteristics of NS Cam.

Filter	*Phase 0.00*	*Magnitude ± σ Min. I*	*Phase 0.25*	*Magnitude ± σ Max. I*
B		0.301 ± 0.018		–0.243 ± 0.006
V		0.345 ± 0.010		–0.179 ± 0.006
R		0.375 ± 0.020		–0.144 ± 0.006
I		0.370 ± 0.120		–0.103 ± 0.008
Filter	*Phase 0.50*	*Magnitude ± σ Min. I*	*Phase 0.75*	*Magnitude ± σ Max. I*
B		0.024 ± 0.004		–0.259 ± 0.014
V		0.092 ± 0.092		–0.198 ± 0.022
R		0.136 ± 0.007		–0.153 ± 0.005
I		0.174 ± 0.009		–0.118 ± 0.019

Filter	*Min. I – Max. II ± σ*	*Max. I – Max. II ± σ*	*Min. I – Min. II ± σ*
B	0.560 ± 0.032	0.016 ± 0.018	0.277 ± 0.021
V	0.543 ± 0.032	0.019 ± 0.042	0.253 ± 0.102
R	0.528 ± 0.025	0.009 ± 0.008	0.239 ± 0.026
I	0.487 ± 0.139	0.015 ± 0.002	0.196 ± 0.129

Filter	*Min. II – Max. II ± σ*	*Min. II – Max. I ± σ*
B	0.283 ± 0.018	0.268 ± 0.010
V	0.290 ± 0.114	0.271 ± 0.098
R	0.289 ± 0.012	0.280 ± 0.013
I	0.292 ± 0.028	0.277 ± 0.017

Table 5. B, V, Rc, Ic Wilson-Devinney program solution parameters for NS Cam.

Parameters	*Values of Contact Solution*
λB, λV, λR, λI (nm)	440, 550, 640, 790
$g_1 = g_2$	0.32
$A_1 = A_2$	0.5
Inclination (°)	85.0 ± 0.1
T_1, T_2 (K)	6250, 5689 ± 3
Ω	2.2418 ± 0.0005
$q(m_2/m_1)$	0.2130 ± 0.0002
Fill-outs: $F_1 = F_2$ (%)	17 ± 1
$L_1/(L_1+L_2)_I$	0.8422 ± 0.0005
$L_1/(L_1+L_2)_R$	0.8494 ± 0.0004
$L_1/(L_1+L_2)_V$	0.8577 ± 0.0004
$L_1/(L_1+L_2)_B$	0.8750 ± 0.0004
JDo (days)	2458883.5476 ± 0.0001
Period (days)	0.907393 ± 0.000004
R_1/a, R_2/a (pole)	0.4877 ± 0.0008, 0.2430 ± 0.0013
R_1/a, R_2/a (side)	0.5312 ± 0.0006, 0.2536 ± 0.0015
R_1/a, R_2/a (back)	0.5559 ± 0.0009, 0.2914 ± 0.0031
Spot I, Star 2	
Colatitude (°)	44.6 ± 0.2
Longitude (°)	177.4 ± 0.3
Radius (°)	59.7 ± 0.3
T-Factor (Tspot/Tsurface)	0.679 ± 0.03

Table 6. NS Cam system dimensions.

R1, R2 (pole, $R_\odot$)	2.1683 ± 0.0036	1.0804 ± 0.0089
R1, R2 (side, $R_\odot$)	2.4591 ± 0.0044	1.1271 ± 0.0107
R1, R2 (back, $R_\odot$)	2.4782 ± 0.0058	1.2951 ± 0.0213

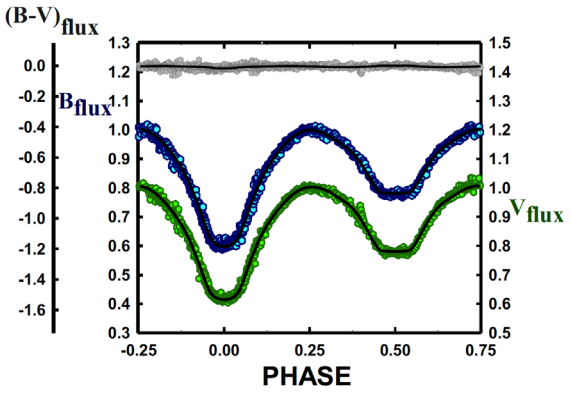

Figure 8. B and V normalized fluxes and B–V color curve overlaid by our solution curves of NS Cam.

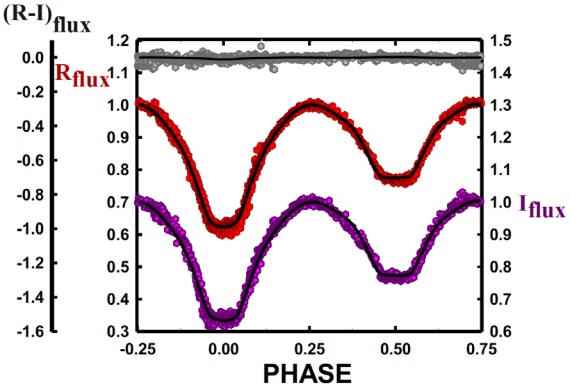

Figure 9. R_c and I_c normalized fluxes and R–I color curve overlaid by our solution curves of NS Cam.

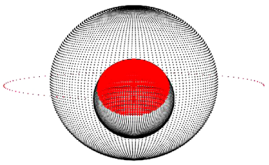

Figure 10a. NS Cam, geometrical representation at phase 0.0, with spot.

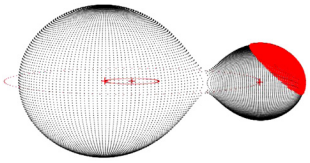

Figure 10b. NS Cam, geometrical representation at phase 0.25, with spot.

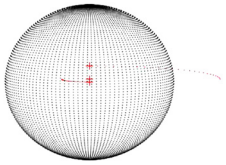

Figure 10c. NS Cam, geometrical representation at phase 0.50, with spot.

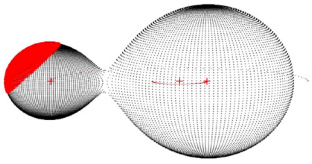

Figure 10d. NS Cam, geometrical representation at phase 0.75, with spot.

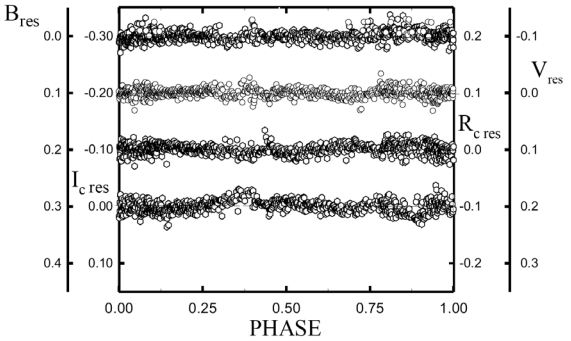

Figure 11. Residuals of the B, V, R_c, and I_c light curve solutionss.

References

Bradstreet, D. H., and Steelman, D. P. 2002, *Bull. Amer. Astron. Soc.*, **34**, 1224.

Henden, A. A., Levine, S., Terrell, D., and Welch, D. L. 2015, Amer. Astron. Soc., AAS Meeting #225, id.336.16.

Hübscher, J. 2011, *Inf. Bull. Var. Stars*, No. 5984, 1.

Hübscher, J. 2014, *Inf. Bull. Var. Stars*, No. 6118, 1.

Hübscher, J., and Lehmann, P. B. 2012, *Inf. Bull. Var. Stars*, No. 6026, 1.

Hübscher, J., Lehmann, P. B., and Walter, F. 2012, *Inf. Bull. Var. Stars*, No. 6010, 1.

Hübscher, J., and Monninger, G. 2011, *Inf. Bull. Var. Stars*, No. 5959, 1.

Kazarovets, E. V., Samus, N. N., Durlevich, O. V., Kireeva, N. N., and Pastukhova, E. N. 2008, *Inf. Bull. Var. Stars*, No. 5863, 1.

Kochanek, C. S., *et al.*, G. 2017, *Publ. Astron. Soc. Pacific*, **129**, 104502.

Khruslov, A.V. 2006, *Inf. Bull. Var. Stars*, No. 5699, 9.

Nelson, R. 2014, AAVSO O–C database (http://www.aavso.org/bob-nelsons-o-c-files).

Pecaut, M. J., and Mamajek, E. E. 2013, *Astrophys. J., Suppl. Ser.*, **208**, 9 (https://www.pas.rochester.edu/~emamajek/EEM_dwarf_UBVIJHK_colors_Teff.txt).

Pojmański, G. 2002, *Acta Astron.*, **52**, 397.

Shappee, B. J., *et al.* 2014, *Astrophys. J.*, **788**, 48.

Terrell, D., and Wilson, R. E. 2005, *Astrophys. Space Sci.*, **296**, 221.

Tylenda, R., and Kamiński, T. 2016, *Astron. Astrophys.*, **592A**, 134.

Van Hamme, W., and Wilson, R. E. 2007, *Astrophys J.*, **661**, 1129.

Van Hamme, W. V., and Wilson, R. E. 1998, *Bull. Amer. Astron. Soc.*, **30**, 1402.

Wilson, R. E. 1990, *Astrophys. J.*, **356**, 613.

Wilson, R. E. 1994, *Publ. Astron. Soc. Pacific*, **106**, 921.

Wilson, R. E. 2008, *Astrophys. J.*, **672**, 575.

Wilson, R. E. 2012, *Astron. J.*, **144**, 73.

Wilson, R. E., and Devinney, E. J. 1971, *Astrophys. J.*, **166**, 605.

Wilson, R. E., and Van Hamme, W. 2014, *Astrophys. J.*, **780**, 151.

Wilson, R. E., Van Hamme, W., and Terrell, D. 2010, *Astrophys. J.*, **723**, 1469.

Zacharias, N., *et al.* 2010, *Astron. J.*, **139**, 2184.

SZ Sculptoris: Light Curve Analyses and Period Study of the Totally Eclipsing, Galactic South Pole, Solar-Type Binary

Ronald G. Samec
Faculty Research Associate, Pisgah Astronomical Research Institute, 1 PARI Drive, Rosman, NC 28772, ronaldsamec@gmail.com

Walter Van Hamme
Florida International University, Department of Physics, 11200 SW 8th Street, CP 204 Miami, FL 33199; vanhamme@fiu.edu

Robert Hill
Department of Chemistry and Physics, Bob Jones University 1700 Wade Hampton Boulevard, Greenville, SC 29614; roberthill@yahoo.com

Received May 21, 2020; revised July 8, July 20, July 21, 2020; accepted July 21, 2020

Abstract We report here on the first precision *BVRI* observations, analysis and period study of SZ Sculptoris (GSC 6990-0597), a solar type (T ~ 5040 K), shallow contact, eclipsing binary. It was observed on 2019 October 05 and 2019 November 05 and 07 in remote mode with the Cerro Tololo InterAmerican Observatory 0.6-m SARA South reflector by R. Samec and R. Hill. The amplitude of the light curves was 0.74, 0.67, 0.65, and 0.61 mag in *B, V, R, I,* respectively. Six times of minimum light were calculated from three primary eclipses and three secondary eclipses with our present observations. Eight times of low light were also taken from ASAS-SN observations. Two additional timings were taken from the *BBSAG Bulletin* No. 39 and from APASS observations. From this 41-year interval orbital period study, it was found that the period is decreasing. This may be due to angular momentum loss (AML) resulting from rotating ion streams leaving along stiff magnetic bipolar field lines from the system. A linear ephemeris was also calculated. A *BVRI* Bessel filtered Wilson-Devinney Program (WD) solution gives a mass ratio, $m_2/m_1 = 0.3680 \pm 0.0007$, a small component temperature difference of 160 K, and a contact fill-out of only 7%. Thus, the system is in good thermal contact with a low fill-out. A mid-latitude spot (colatitude of 70°), radius of 18°, and T-factor of 0.66 ± 0.01 was calculated. The system is a W-type W UMa binary. An eclipse duration of ~ 21 minutes was determined for the primary eclipse and the light curve solution.

1. Introduction

In this paper, we continue our study of precision light curves of neglected, short period solar-type Southern eclipsing binaries (PY Aqr, Samec *et al.* 2019; CW Scl, Samec *et al.* 2017; DD Ind, Samec *et al.* 2016; ZZ Eri, Samec *et al.* 2015; etc.). This particular binary is of solar type. It is near the Southern galactic pole, and appears to have a time of constant light from the plot of the All-Sky Automated Survey for Supernovae (ASAS; Pojmański 2002) curves.

2. History and observations

SZ Scl is given in the *General Catalogue of Variable Stars* (GCVS; Samus *et al.* 2017) as an EW/KW eclipsing binary with a maximum of V = 12.98 and a minimum of 13.68 magitudes. Its ephemeris is given as

$$\text{HJD} = 2444406.8677\text{d} + 0.32082757\,\text{d} \times \text{E} \qquad (1)$$

SIMBAD gives J = 10.283 ± 0.024, K = 9.761 ± 0.020, so J–K = 0.522 ± 0.044, and lists the variable as a W UMa binary. Observations of the system are continuously being undertaken by the ASAS-SN program of Ohio State (Shappee *et al.* 2014; Kochanek *et al.* 2017). See the plot in Figure 1. The information included V = 11.88, amplitude = 0.59 mag, variable type EW, and an ephemeris:

$$\text{HJD} = 2457547.83478\,\text{d} + 0.320818\,\text{d} \times \text{E} \qquad (2)$$

Our 2019 *BVRI* light curves were taken on 2020 October 05 and 2019 November 05 and 07 at Cerro Tololo InterAmerican Observatory with the 0.6-m SARA South reflector by R. Samec and R. Hill with a thermoelectrically cooled (–50° C) 2KX2K ANDOR Camera with Bessell *BVRI* filters. These were taken in remote mode. Individual observations (differential photometry, V–C) included 598 in *B*, 601 in *V*, 589 in *R*, and 553 in *I*. The standard error of a single observation is 13 mmag in *B* and *V*, 14 mmag in *R*, and 16 mmag in *I*. The nightly C–K values stayed constant throughout the observing run with a precision of about 1%. Exposure times varied from 50s in *B* to 30s in *V* and 20s in *R* and *I*. The *BVRI* observations are given in Table 1. The identity of the photometric targets, V (variable, SZ Scl), C (comparison star), and K (check star) are given in Table 2. A finding chart for the field is given in Figure 2. The UCAC3

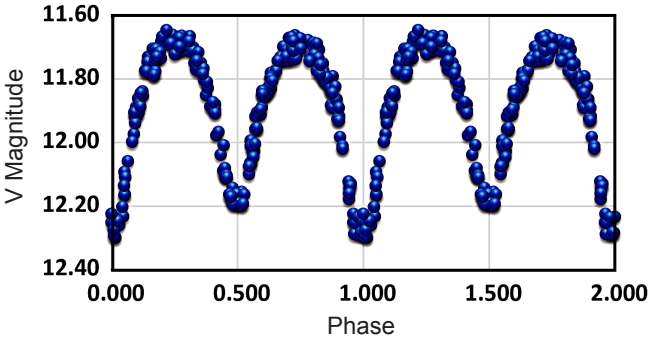

Figure 1. Light curve of ASASSN-V J001546.63-310545.4 (SZ Scl) (Shappee *et al.* 2014; Kochanek *et al.* 2017).

Table 1. Sample of first ten SZ SCL *B, V, R, I* observations.

ΔB	HJD 2458770+	ΔV	HJD 2458770+	ΔR	HJD 2458770+	ΔI	HJD 2458770+
1.108	1.5566	0.887	1.5518	0.779	1.5548	0.667	1.5554
1.127	1.5607	0.922	1.5580	0.788	1.5589	0.677	1.5595
1.142	1.5648	0.941	1.5622	0.829	1.5631	0.709	1.5636
1.191	1.5690	0.972	1.5663	0.861	1.5672	0.712	1.5678
1.237	1.5731	1.016	1.5705	0.899	1.5713	0.771	1.5719
1.312	1.5774	1.069	1.5746	0.957	1.5756	0.832	1.5762
1.444	1.5816	1.152	1.5789	1.015	1.5798	0.904	1.5804
1.550	1.6042	1.250	1.5830	1.191	1.5922	1.045	1.5928
1.467	1.6097	1.273	1.6061	1.191	1.5964	1.037	1.5971
1.410	1.6152	1.218	1.6117	1.175	1.6018	1.053	1.6026

Note: First ten data points of SZ Scl B, V, R, I observations.
The full table is available through the AAVSO ftp site at ftp://ftp.aavso.org/public/datasets/samec482-szscl.txt
(if necessary, copy and paste link into the address bar of a web browser).

Table 2. Photometric targets.

Star	Name	R. A. (2000) h m s	Dec. (2000) ° ‘ “	V[1]	J–K[2]
V (Variable)	SZ Scl GSC 6990 597 2MASS J00154668-3105449 ASAS 182528-6734.8 Gaia DR2 2319938821297094912	00 15 46.6730013523	–31 05 45.037874181[3]	11.831	0.522 ± 0.044
C (Comparison)	GSC 4515 626 3UC 336-015704	00 15 38.2369562975	–31 08 32. 536651500[3]	10.901	0.312 ± 0.052
K (Check)	GSC 6990 613 3UC118-000630	00 15 49.86144	–31 07 35.8824[2]	12.411 ± 0.017	0.36

[1] *APASS (Henden et al. 2009).* [2] *UCAC3 (Zacharias et al. 2010).* [3] *Gaia DR2 (Gaia Collab. 2016, 2018).*

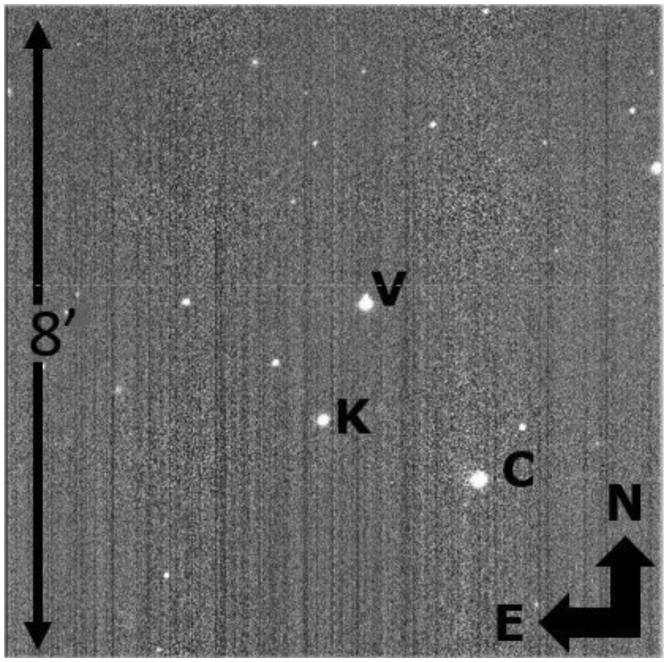

Figure 2. Finding chart of the SZ Scl field; variable star, SZ Scl (V), comparison star (C), check star (K).

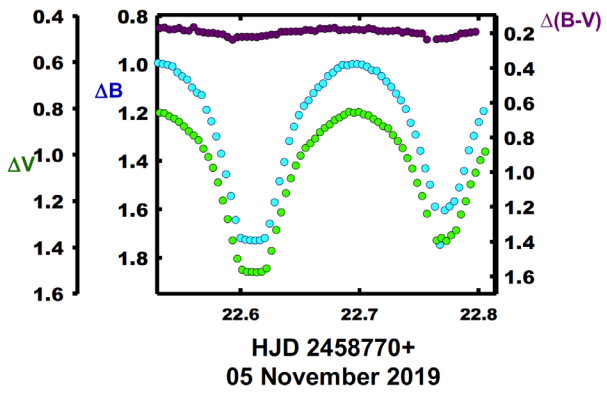

Figure 3. *B, V* light curves and *B–V* color curve from 2019 November 05.

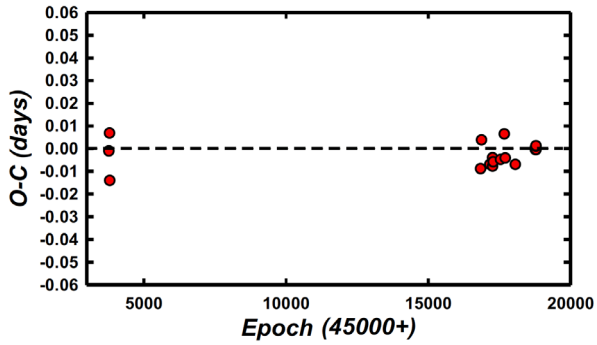

Figure 4. A plot of the quadratic residuals. Note there is a gap in the observations from 3,900 to –16.500 orbits.

is the USNO CCD Astrograph Catalog (Zacharias *et al.* 2010). Sample *B, V* light curves of 2019 November 05 are given in Figure 3.

3. Period study

Six times of minimum light were determined from our present *BVRI* observations, which included three primary eclipses and three secondary eclipses:

$$\begin{aligned} \text{HJD I} = {} & 2458771.75786 \pm 0.00029, \\ & 2458792.61086 \pm 0.00010, \\ & 2458794.53585 \pm 0.00021\,\text{d}, \end{aligned}$$

$$\begin{aligned} \text{HJD II} = {} & 2458771.59807 \pm 0.00094, \\ & 2458792.77217 \pm 0.00084, \\ & 2458794.69767 \pm 0.00079\,\text{d}. \end{aligned}$$

Minima were calculated using a least squares minimization method (Mikulášek *et al.* 2014) and was used to determine the minima for each curve, in *B, V, R,* and *I*. These were averaged and the standard error was computed.

Eight times of low light were also taken from data taken from ASAS SN observations. (The ASAS observations included ~250 data points spread over a little more than the last four years. Not enough points (maybe only one) were taken on each night to do normal times of minimum light. Minima were obtained from a plot of all the SN ASAS data phased with their period. Next, the data were fit with least square parabolas at the primary and secondary minima. The HJDs of low values of data nearest the times of minima were called times of "low light" (within 0.001 phase unit of the minima). These are not standard times of "minimum light", but they work well when the period study has gaps. Note their low weights.) Three additional timings of minima were taken from *BBSAG Bulletin* No. 39 (Locher 1978). Two minima were calculated from APASS data (Henden *et al.* 2009) on SZ Scl. Over this 41-year interval, the orbital period appears to be decreasing (at about the 45 sigma level; the errors shown here are standard errors). However, a large gap from HJD 43000 to 57000 is noted. This means the system should be patrolled for minima timings over the next decades to discern the true nature of the orbital period variations. The existence of the early BBSAG minima add an interesting but unsatisfying mystery to the present understanding of this binary.

$$\begin{aligned} \text{JD Hel Min I} = {} & 2458792.61142(77)\,\text{d} + 0.3208167(4) \\ & \times \text{E} - 0.000000000177(8) \times \text{E}^2 \end{aligned} \quad (3)$$

A decreasing period may be due to angular momentum loss (AML) resulting from rotating plasma streams leaving along stiff magnetic bipolar field lines from the system which are expected in such a binary.

A linear ephemeris was also calculated:

$$\text{JD Hel Min I} = 2458792.6187(26)\,\text{d} + 0.32082509(15) \times \text{E}. \quad (4)$$

The quadratic residuals are shown in Figure 4. Table 3 gives the quadratic and linear residuals of the period study. The *B, V* and *R, I* light curves and *B–V* and *R–I* color curves phased with Equation 3 are given in Figures 5, 6, and 7. In Figure 6, an expanded *B–V* color curve only is given to emphasize the variation in temperature of the system over the month due to spot activity.

The quadratic ephemeris yields a $\dot{\text{P}} = 1.09 \times 10^{-7}\,\text{d/yr}$ or a mass exchange rate of

$$\frac{\text{dM}}{\text{dt}} = \frac{\dot{\text{P}}\,\text{M}_1\,\text{M}_2}{3\text{P}\,(\text{M}_1 - \text{M}_2)} = \frac{5.289 \times 10^{-7}\,\text{M}_\odot}{\text{d}}. \quad (5)$$

in a conservative scenario.

4. Light curve characteristics

The curves are of good photometric precision, averaging about 1%. *BVRI* curve averages at quarter phased cycles and key differences are given in Table 4. The amplitude of the light curve varies from 0.74 to 0.61 mag in *B* to *I*. The O'Connell effect, a possible indicator of spot activity, is less than the noise level. The differences in minima is ~0.12 mag, indicating contact light curves. All color curves fall so very slightly at phase 0.0 and phase 0.5, which we have noticed is characteristic of contact binaries. This probably indicates that It is a W UMa contact binary.

5. Temperature

The 2MASS J–K = 0.522 ± 0.044 (SIMBAD) for the binary. This corresponds to a K2 ± 2V eclipsing binary, which yields a temperature of 5040 ± 250 K. Thus the binary is a dwarf, low temperature system. Binary stars of this type are noted for having convective atmospheres, so solar type spots and other magnetic activity are expected. In the case of fast spinning binaries, magnetic activity is especially high.

6. Light curve solution

The *B, V, R,* and *I* curves were pre-modeled with BINARY MAKER 3.0 (Bradstreet and Steelman 2002) and fits were determined in all filter bands. The averaged result of the best fitted residuals was that of a W-type contact binary with a low fill-out of about 11% with one major cool spot, about 0.9 times the temperature of the photosphere and a mass ratio range of 0.34 to 0.39. BINARY MAKER uses black body atmospheres so the first iterations with the Wilson program were the lights with full Kurucz atmospheres (1993). The averaged parameters were input into a 4-color simultaneous light curve calculation using the Wilson-Devinney Program (Wilson and Devinney 1971; Wilson 1990, 1994, 2008, 2012; Van Hamme and Wilson 1998; Van Hamme and Wilson 2007; Wilson *et al.* 2010; Wilson and Van Hamme 2014). The solution was computed in Mode 3 (contact) and converged with similar physical parameters as the binary maker fit. Convective parameters g = 0.32, A = 0.5 were used. The third light parameter yielded solid results which may be due to a an unseen field star which is only 5.7% the brightness of SZ Scl at phase 0.25 in V. The mass ratio was found to be

Table 3. Period Study of SZ Scl.

	Epoch HJD 2400000+	*Cycle*	*Linear Residual*	*Quadratic Residual*	*Weight*	*Error*	*Reference*
1	43812.3150	–46693.0	–0.0180	–0.0141	0.2	—	BBSAG Bull 39 (Locher 1978)
2	43783.4530	–46783.0	–0.0057	–0.0011	0.5	—	BBSAG Bull 39 (Locher 1978)
3	43805.4380	–46714.5	0.0028	0.0068	0.5	—	BBSAG Bull 39 (Locher 1978)
4	56847.8050	–6062.0	0.0279	–0.0089	0.1	—	ASAS (Pojmański 2002)
5	56882.3057	–5954.5	0.0399	0.0038	0.5	0.0064	APASS (Henden *et al.* 2009)
6	57175.8440	–5039.5	0.0233	–0.0070	0.1	—	ASAS (Pojmański 2002)
7	57267.6010	–4753.5	0.0243	–0.0041	0.1	—	ASAS (Pojmański 2002)
8	57269.8430	–4746.5	0.0205	–0.0078	0.1	—	ASAS (Pojmański 2002)
9	57291.8210	–4678.0	0.0220	–0.0059	0.1	—	ASAS (Pojmański 2002)
10	57547.8350	–3880.0	0.0176	–0.0049	0.1	—	ASAS (Pojmański 2002)
11	57680.0233	–3468.0	0.0259	0.0064	0.5	—	APASS (Henden *et al.* 2009)
12	57714.6610	–3360.0	0.0145	–0.0042	0.1	—	ASAS (Pojmański 2002)
13	58069.6430	–2253.5	0.0036	–0.0070	0.1	—	ASAS (Pojmański 2002)
14	58771.5981	–65.5	–0.0067	0.0001	1.0	0.0009	Present observation
15	58771.7579	–65.0	–0.0073	–0.0005	1.0	0.0003	Present observation
16	58792.6109	0.0	–0.0079	–0.0006	1.0	0.0001	Present observation
17	58792.7722	0.5	–0.0070	0.0003	1.0	0.0008	Present observation
18	58794.5359	6.0	–0.0079	–0.0005	1.0	0.0002	Present observation
19	58794.6977	6.5	–0.0065	0.0009	1.0	0.0008	Present observation

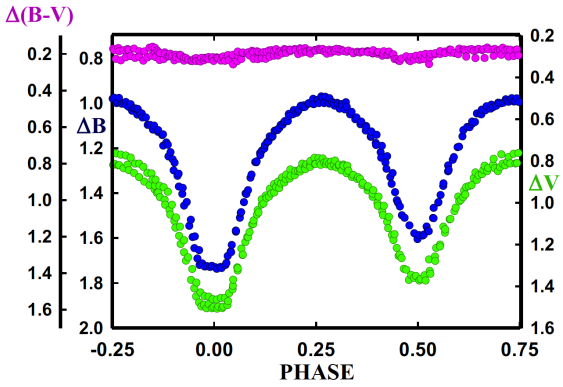

Figure 5. Phased *B, V* light curves and *B–V* color curves. Note the effect of the spots acting over a month's time. The maximum change was ~0.06 mags in *V*.

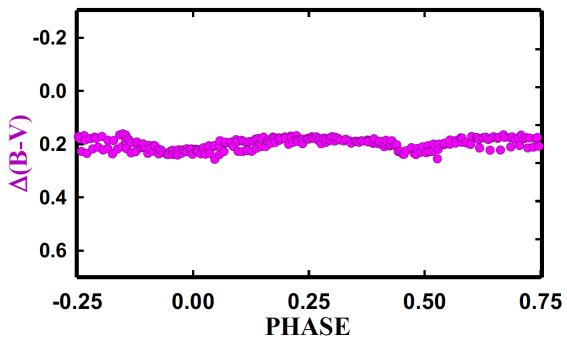

Figure 6. *B–V* color index curve only, to emphasize the variation in temperature of the system over the month due to spot activity.

0.37 with a fill-out of only 7%. The cool spot did converge with some changes as expected with t-factor of 0.66 and mid-latitude position (colatitude 70°). The secondary eclipse showed an interval of constant light, an eclipse of 21 minutes' duration. The inclination was 88.2 ± 0.5°. The difference of component temperatures was low, about 160 K, showing that the system is in good thermal contact despite its shallow contact. The modeled

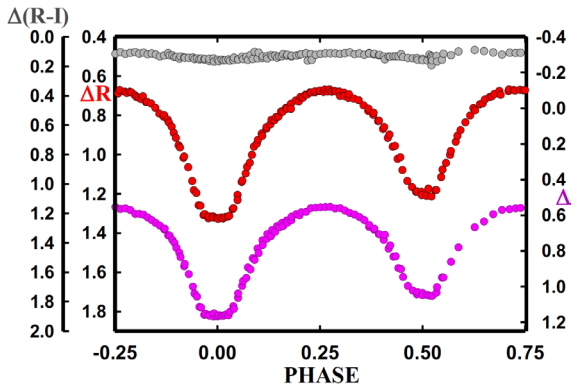

Figure 7. Phased *R, I* light curves and *R–I* color curve.

period was 0.3208185 d. The solution is given in Table 5. The plots of the light curve solutions are shown in Figures 8 and 9. The geometrical surfaces of the binary at phases 0.0, 0.25, 0.5, and 0.75 are displayed in Figure 10a–d.

7. Discussion

SZ Scl is a W-type (the more massive component is cooler) shallow contact W UMa binary. The period decrease is probably due to magnetic braking which causes the binary to lose angular momentum as plasmas leave the system on stiff rotating bipolar magnetic field lines. The cool spot is a firm indication of the magnetic nature of the binary. Both components of this binary are of solar type with a surface temperature of ~5203 K (G9V) and ~5040 K (K2V) for the components. The mass ratio is 0.37 (M_2/M_1), with an amplitude of 0.74–0.61 mag in *B* to *I*, respectively. The inclination is 88.2°, which results in a total eclipse at phase 0.0.

Table 4. Light curve characteristics of SZ Scl.

Filter	*Phase 0.000*	*Magnitude ± σ Min. I*	*Phase 0.25*	*Magnitude ± σ Max I*
B		1.731 ± 0.005		0.992 ± 0.010
V		1.485 ± 0.023		0.812 ± 0.015
R		1.327 ± 0.003		0.675 ± 0.007
I		1.166 ± 0.004		0.556 ± 0.001
Filter	*Phase 0.500*	*Magnitude ± σ Min. II*	*Phase 0.75*	*Magnitude ± σ Max II*
B		1.591 ± 0.013		0.988 ± 0.008
V		1.363 ± 0.009		0.802 ± 0.026
R		1.204 ± 0.011		0.673 ± 0.002
I		1.047 ± 0.007		0.562 ± 0.001

Filter	*Min. I – Max. I ± σ*	*Max. I – Max. II ± σ*	*Min. I – Min. II ± σ*
B	0.739 ± 0.015	0.005 ± 0.018	0.140 ± 0.019
V	0.674 ± 0.038	0.010 ± 0.042	0.122 ± 0.032
R	0.652 ± 0.010	0.003 ± 0.008	0.123 ± 0.014
I	0.610 ± 0.005	–0.006 ± 0.002	0.119 ± 0.011

Filter	*Min. II – Max. II ± σ*	*Min. II – Max. I ± σ*
B	0.604 ± 0.022	0.599 ± 0.023
V	0.561 ± 0.035	0.552 ± 0.025
R	0.531 ± 0.013	0.529 ± 0.018
I	0.485 ± 0.008	0.491 ± 0.008

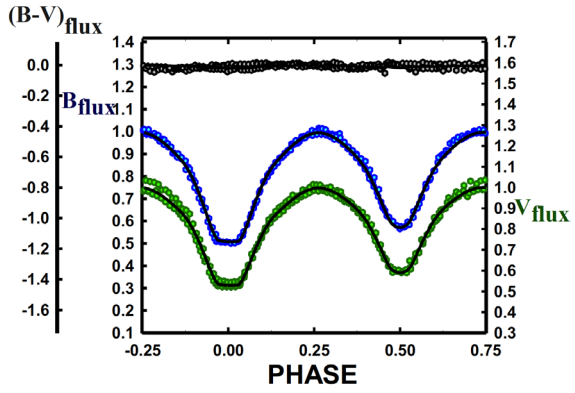

Figure 8. *B,V* and *B–V* normalized flux overlaid by the third light WD solution.

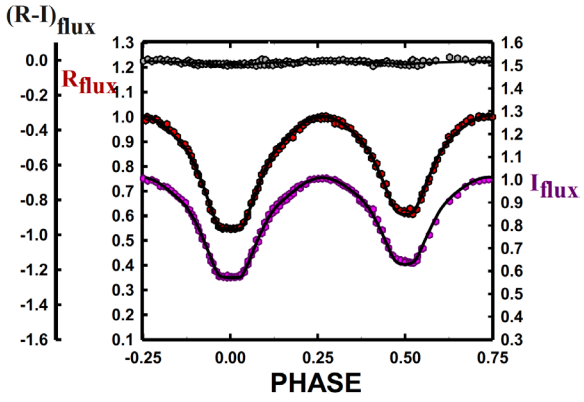

Figure 9. *R,I* and *R–I* normalized flux overlaid by the third light WD solution.

Table 5. *B, V, R, I* synthetic light curve solution for SZ Scl.

Parameters	*Values*
λB, λV, λR, λI (nm)	440, 550, 640, 790
$g_1 = g_2$	0.32
$A_1 = A_2$	0.5
Inclination (°)	88.2 ± 0.5
T_1, T_2 (K)	5040, 5203 ± 2
Ω	2.5968 ± 0.0017
$q(m_2/m_1)$	0.3680 ± 0.0007
Fill-outs: $F_1 = F_2$ (%)	0.07 ± 0.01
$L_1/(L_1+L_2)_I$	0.6836 ± 0.0073
$L_1/(L_1+L_2)_R$	0.6804 ± 0.0072
$L_1/(L_1+L_2)_V$	0.6734 ± 0.0015
$L_1/(L_1+L_2)_B$	0.6624 ± 0.0086
JDo (days)	2458792.6113 ± 0.0001
Period (days)	0. 3208185 ± 0.0000002
L_{3I} at phase 0.25[1]	0.0736 ± 0.0007
L_{3R} at phase 0.25	0.0551 ± 0.0005
L_{3V} at phase 0.25	0.0568 ± 0.0012
L_{3B} at phase 0.25	0.0618 ± 0.0007
r_1/a, r_2/a (pole)	0.4424 ± 0.0009, 0.2792 ± 0.0015
r_1/a, r_2/a (side)	0.4737 ± 0.0013, 0.2915 ± 0.0018
r_1/a, r_2/a (back)	0.5012 ± 0.0017, 0.3264 ± 0.0032
Spot I, Primary Component	
Colatitude (°)	69.9 ± 0.3
Longitude (°)	174.1 ± 0.3
Radius (°)	18.06 ± 0.07
T-Factor	0.66 ± 0.01

[1] *Third Light at phase 0.25*

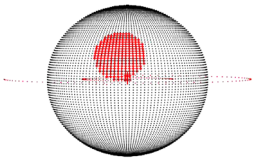

Figurea 10a. SZ Scl, Geometrical representation at phase 0.0.

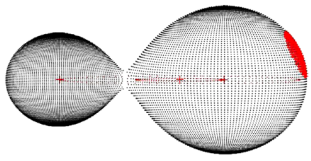

Figure 10b. SZ Scl, Geometrical representation at phase 0.25.

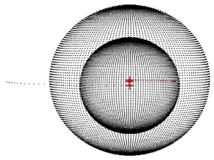

Figure 10c. SZ Scl, Geometrical representation at phase 0.50.

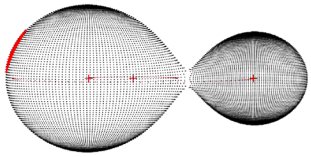

Figure 10d. SZ Scl, Geometrical representation at phase 0.75.

8. Conclusion

The period study of this contact W UMa binary has a 41-year duration. The period was found to be strongly decreasing at about the 45σ level. Albeit, there was a large gap in the observations which begs further study. If this result holds up under more study, the system may merge over time, first resulting in a Red Novae event (Tylenda and Kamiński 2016) and the coalescence of the system into a fast-rotating FK Comae Berenices variable (Sikora *et al.* 2020).

9. Future work

Radial velocity curves are needed to obtain absolute system parameters.

10. Acknowledgements

Dr. Samec would like to thank the American Astronomical Society (AAS) and the American Association of Variable Star Observers for providing venues for the presentation of his research results over the years and for the recent creative approach to the AAS 236 virtual meeting where the preliminary study of SZ Scl is presented (https://aas236-aas.ipostersessions.com/default.aspx?s=78-C1-FC-C6-88-20-B0-54-8A-AD-00-EF-65-A4-BB-6A).

This research has made use of the APASS database, located at the AAVSO web site. Funding for APASS has been provided by the Robert Martin Ayers Sciences Fund.

References

Bradstreet, D. H., and Steelman, D. P. 2002, *Bull. Amer. Astron. Soc.*, **34**, 1224.

Gaia Collaboration, *et al.* 2016, *Astron. Astrophys.*, **595A**, 1.

Gaia Collaboration, *et al.* 2018, *Astron. Astrophys.*, **616A**, 1.

Henden, A. A., Welch, D. L, Terrell, D., and Levine, S. E. 2009, Amer. Astron. Soc. Meeting 214, id.407.02.

Kochanek, C. S., *et al.*, G. 2017, *Publ. Astron. Soc. Pacific*, **129**, 104502.

Kurucz, R. L. 1993, in *Light Curve Modeling of Eclipsing Binary Stars*, ed. E. F. Milone Springer Verlag, N. Y., 93.

Locher, K. 1978, *BBSAG Bull.*, No. 39, 5.

Mikulášek, Z., Chrastina, M., Liška, J., Zejda, M., Janík, J., Zhu, L.-Y., and Qian, S.-B. 2014, *Contrib. Astron. Obs. Skalnaté Pleso*, **43**, 382.

Pojmański, G. 2002, *Acta Astron.*, **52**, 397.

Samec, R. G., Chamberlain, H. A., and Van Hamme, W. 2019, *J. Amer. Assoc. Var. Star Obs.*, **47**, 29.

Samec, R. G., Clark, J. D., Van Hamme, W., and Faulkner, D. R. 2015, *Astron. J.*, **149**, 48.

Samec, R. G., Norris, C. L., Hill, B. L., Van Hamme, W., and Faulkner, D. R. 2017, *J. Amer. Assoc. Var. Star Obs.*, **45**, 3.

Samec, R. G., Norris, C. L., Van Hamme, W., Faulkner, D. R., and Hill, R. L. 2016, *Astron. J.*, **152**, 219.

Samus N. N., Kazarovets E. V., Durlevich O. V., Kireeva N. N., and Pastukhova E. N., 2017, *Astron. Rep.*, **61**, 80, *General Catalogue of Variable Stars*: Version GCVS 5.1 (http://www.sai.msu.su/gcvs/gcvs/index.htm).

Shappee, B. J., *et al.* 2014, *Astrophys. J.*, **788**, 48.

Sikora, J., Rowe, J., Howell, S. B., Mason, E., and Wade, G. A. 2020, *Mon. Not. Roy. Astron. Soc.*, **496**, 295.

Tylenda, R., and Kamiński, T. 2016, *Astron. Astrophys.*, **592A**, 134.

Van Hamme, W. V., and Wilson, R. E. 1998, *Bull. Amer. Astron. Soc.*, 30, 1402.

Van Hamme, W., and Wilson, R. E. 2007, *Astrophys. J.*, **661**, 1129.

Wilson, R. E. 1990, *Astrophys. J.*, **356**, 613.

Wilson, R. E. 1994, *Publ. Astron. Soc. Pacific*, **106**, 921.

Wilson, R. E. 2008, *Astrophys. J.*, **672**, 575.

Wilson, R. E. 2012, *Astron. J.*, **144**, 73.

Wilson, R. E., and Devinney, E. J. 1971, *Astrophys J.*, **166**, 605.

Wilson, R. E., and Van Hamme, W. 2014, *Astrophys. J.*, **780**, 151.

Wilson, R. E., Van Hamme, W., and Terrell, D. 2010, *Astrophys. J.*, **723**, 1469.

Zacharias, N., *et al.* 2010, *Astron. J.*, **139**, 2184.

V725 Sagittarii: Unique, Important, Neglected

John R. Percy
Department of Astronomy and Astrophysics, and Dunlap Institute for Astronomy and Astrophysics, University of Toronto, 50 St. George Street, Toronto, ON M5S 3H4, Canada; john.percy@utoronto.ca

Received June 15, 2020; revised June 30, 2020; accepted July 24, 2020

Abstract During the last century, V725 Sgr gradually changed from a 12-day Cepheid to an 85-day yellow semiregular giant. This paper presents wavelet analysis of AAVSO visual observations from 1982 to 2020, and Fourier analysis of ASAS-SN observations from 2016 to 2018. The results confirm that the previously-identified pulsation period has increased from about 50–60 days to 80–90 days since 1982. In the ASAS-SN data, there appear to be both a 82.6-day period and a possible 160.0-day period, though the latter is not prominent after pre-whitening. If it is real, however, the two periods could be interpreted as a first overtone period and a fundamental period, respectively. Evidence for two (or more) periods can also be seen in the ASAS-SN light curve, and in the visual data. The total V range is 1.1 magnitude. Since recent results in the literature indicate that V725 Sgr is a K4 yellow giant, it should be classified as a SRd variable. In view of its continuing changes, it needs and deserves to be monitored more systematically.

1. Introduction

Since 1926, V725 Sgr gradually changed from a 12-day Cepheid to a 85-day cool semiregular variable. Prior to 1926, it may have varied on a time scale of a few days. Between 1926 and 1935, its period increased smoothly from 12 to 21 days. In 1968–1969, its time scale was 45–50 days and, in 1973, it was about 50 days. Between 1985 and 2000, the period increased from 60 ± 2 days to 85 ± 3 days, the variability being semiregular. It is still listed as a Classical Cepheid in SIMBAD (Wenger *et al.* 2000). See Percy *et al.* (2006)—hereafter Paper 1—for a detailed account of its changing period, amplitude, and mean magnitude, and for additional references to the star.

Paper I pointed out that the behavior of V725 Sgr was consistent with a thermal flash and blue loop from the asymptotic giant branch (AGB) in the H-R diagram. It also noted that, since the behavior of the star might continue to change, and be semiregular, the star should be monitored regularly.

Unfortunately, that appears not to be the case. SIMBAD (simbad.u-strasbg.fr) records only one specific study of the star since 2006. AAVSO visual observations are sparse, and AAVSO CCD observations are apparently non-existent.

Battinelli and Demers (2010), however, obtained 32 VRIJHK observations of the star in 2008–2009. These indicate a semiregular variability with a time scale of about 70 days, and an amplitude of about one magnitude. Their multicolor photometry indicated that V725 Sgr had the colors of a K4 giant, so it should be classified as an SRd star, not as a pulsating red giant as Paper 1 did on the basis of limited spectroscopic information.

V725 Sgr was also observed in three surveys. It was observed by ASAS, the All-Sky Automated Survey (Pojmański 1997), between HJD 2451948 and 2455137 (2001–2009), a mean period of 78.06 days was derived. The phase diagram shows considerable scatter. It was also observed by Gaia, Data Release 2, from 2014 to 2016 (Gaia Collab. *et al.* 2018). The anonymous referee kindly determined a period of near 82 days from the Gaia data.

The star was also observed for 900 days from 2016 to 2018 by the All-Sky Automated Survey for Supernovae (ASAS-SN, Jayasinghe *et al.* 2018, 2019). The present paper presents an analysis of the ASAS-SN observations, and of the sparse visual observations in the AAVSO International Database (Kafka 2020) since JD 2445000 (1982).

2. Data and analysis

The ASAS-SN data and the AAVSO visual observations since JD 2445000 were analyzed using the Fourier and wavelet analysis routines in the AAVSO time-series analysis package VSTAR (Benn 2013).

3. Results

Figure 1 shows the ASAS-SN light curve of V725 Sgr. It is clearly not monoperiodic. It appears to be a superposition of at least two signals. The changes in amplitude from cycle to cycle suggest that the two periods are not close, but may differ by a factor of more like 1.5 to 3.

Figure 2 shows the Fourier spectrum of the ASAS-SN data. There are peaks at periods of 82.6 and 160.0 days, with comparable amplitudes of 0.23 and 0.22 mag, respectively. The amplitudes, as defined here, are the coefficients of the sine curves with the stated periods.

However, the anonymous referee has pointed out that, if the ASAS-SN data are pre-whitened for the 82.6-day period, the next significant period in the Fourier spectrum is 104 days, which is not prominent in Figure 2. The Fourier spectrum of the sparse AAVSO visual data, covering the same time interval as the ASAS-SN data, shows the 82.6-day period, but neither the 160.0-day period nor the 104-day period is prominent. So the situation is not clear. This is not surprising, given the limitations of the data, and the semiregularity of the star.

The Fourier spectrum of all the AAVSO visual measurements, since JD 2445000, shows a very weak peak at a period of 69.6 days, with an amplitude of 0.09 mag. There is also a peak at a period close to one year, which may be spurious. The data are rather sparse, they have limited accuracy, and any period present is likely to be changing. Therefore, it seemed more appropriate to carry out wavelet analysis, even in view of the limitations of the data.

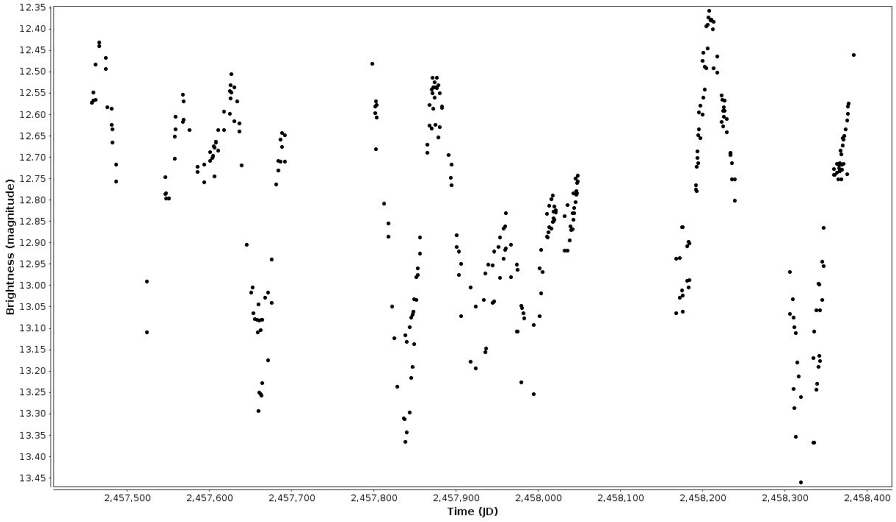

Figure 1. The ASAS-SN V light curve of V725 Sgr from 2016 to 2018.

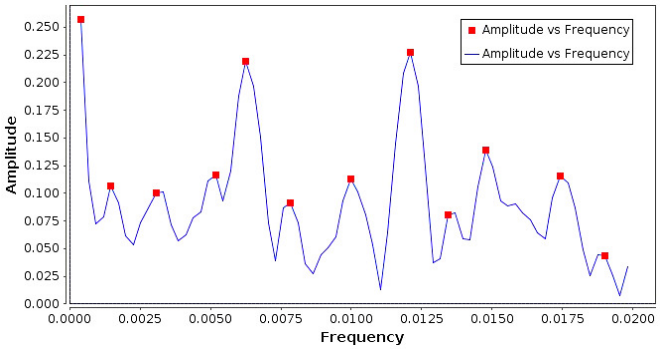

Figure 2. The Fourier spectrum of the ASAS-SN observations of V725 Sgr shown in Figure 1. It shows periods of 82.6 and 160.0 days.

Figure 3 shows the result. There appears to be a period, at the bottom of the graph, which increases from about 50 days at the beginning of the data to about 80 days at the end. This is the period that was identified in Paper 1. It is also consistent with the various periods already mentioned. There are also random signals at periods between 100 and 200 days. Given the sparseness of the data, it is not clear whether these additional signals are significant.

In particular, however, in the interval of the ASAS-SN data (JD 2457400–24584000), there are periods in Figure 3 which are consistent with those suggested in Figure 1, and shown in Figure 2, namely 82.6 and 160.0 days. It is therefore possible that the star was pulsating with those two different periods at that time.

4. Discussion

The primary period of V725 Sgr has persisted, and now has a value of about 85 days. It is not clear whether the period has stabilized.

The two periods in Figure 2 are in a ratio close to 1:2. The shorter period is not a harmonic; *if it is real*, then it is almost certainly an overtone. The ratio of the first overtone period to the fundamental period is close to 0.5 in pulsating red giants (Xiong and Deng 2007, Percy 2020), and in pulsating yellow giants (e.g. Fokin 1994). Indeed, such a ratio is one possible explanation for the alternating deep and shallow minima in RV Tauri stars, and the semi-regularity in SRd stars. If the longer period is actually 104 days, the interpretation is less clear, because the 82.6/104 ratio does not correspond to any obvious ratio of overtone periods.

Many red giants pulsate in the first overtone and the fundamental e.g. Mattei *et al.* (1997), Percy (2020). For pulsating yellow giants such as RV Tauri and SRd variables, double-mode pulsation also appears to be the case (Fokin 1994). The light curve in Figure 1 is typical of SRd variables.

The amplitude of the dominant pulsation period has varied as a function of time. This is normal; the pulsational amplitudes of pulsating red giants vary by factors of up to ten, on time scales of tens of pulsation periods (Percy and Abachi 2013). The same is true of yellow giants—RV Tauri and SRd variables (Percy 2015). Figure 3 clearly illustrates the complexity of the behavior of this star.

Paper 1 outlined the possible changes in the mean magnitude of the star but, given the miscellaneous sources of the data, and the complex variability, the reality of these changes are still uncertain. No changes are apparent in the AAVSO visual light curve since JD 2445000. Data before that are very scattered, but also very sparse.

Although the variability of V725 Sgr is now like that of a pulsating red giant, its (J–K) color, +0.869 according to SIMBAD, is not as cool as a typical red SR variable, namely +1.2. The (J–K) color quoted by SIMBAD is based on 2MASS data, and is consistent with the average values quoted by Battinelli and Demers (2010). These authors make a strong case that, at the time of their observations, V725 Sgr was a K4 giant. It should therefore be classified as an SRd variable. Its future is unclear. Which modes will be excited? Has the period stabilized, or will it continue to change? Will the star become cooler, and rejoin the AGB?

In view of the interesting and complex behavior of this star in the last few years, and the uniqueness of a star which is

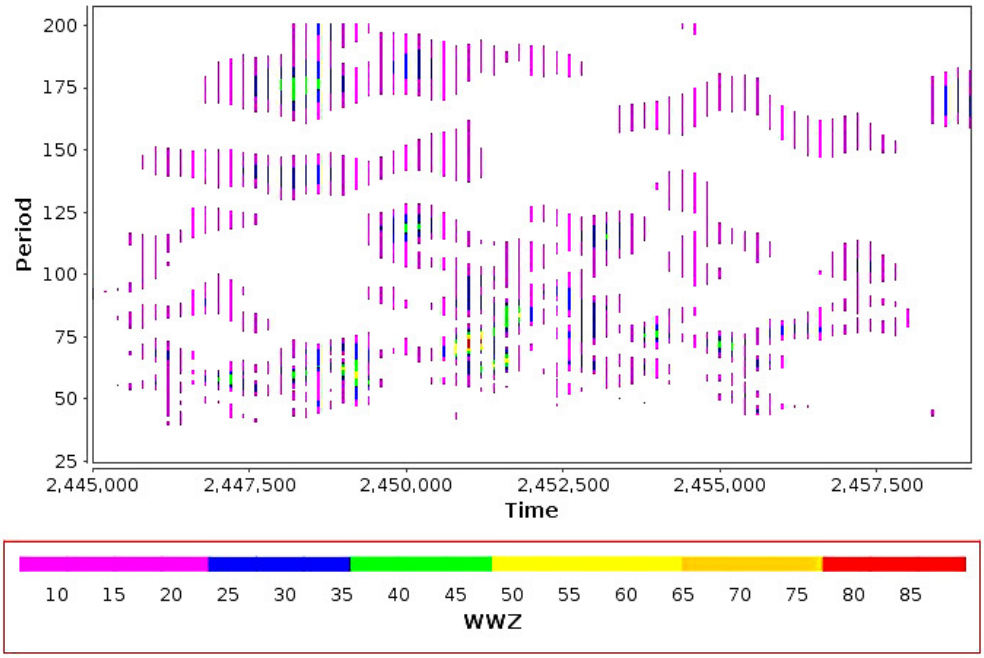

Figure 3. The wavelet diagram for the AAVSO visual observations of V725 Sgr. There is a period which slowly increases, with variable amplitude, from about 50 to 90 days. There are various longer-period signals, which may or may not be statistically significant. One strong signal is consistent with the 160-day period found by ASAS-SN between 2016 and 2018.

changing before our eyes, we again urge observers to monitor this star regularly, with CCD techniques and multicolor filters if possible. It needs and deserves such systematic monitoring.

5. Conclusions

A century ago, V725 Sgr was a Cepheid with a period of a few days. It is now a pulsating yellow giant with a period of about 85 days, and at least one longer period. These may represent two different pulsation modes. This star continues to change its physical and pulsation properties, rapidly and significantly, and needs and deserves to be monitored regularly—as regularly as more famous stars such as SS Cyg and R CrB.

6. Acknowledgements

We thank the ASAS-SN team for making their data and results publicly available. We also thank the AAVSO observers and staff for making and archiving the AAVSO data. We also thank the anonymous referee for suggesting significant improvements to this paper.

This project made use of the SIMBAD database, maintained in Strasbourg, France. The Dunlap Institute is funded through an endowment established by the David Dunlap family, and the University of Toronto.

References

Battinelli, P., and Demers, S. 2010, *Publ. Astron. Soc. Pacific*, **122**, 144.

Benn, D. 2013, VStar data analysis software (https://www.aavso.org/vstar-overview).

Fokin, A. B. 1994, *Astron. Astrophys.*, **292**, 133.

Gaia Collaboration, *et al.* 2018, *Astron. Astrophys.*, **616A**, 1.

Jayasinghe, T., *et al.* 2018, *Mon. Not. Roy. Astron. Soc.*, **477**, 3145.

Jayasinghe, T., *et al.* 2019, *Mon. Not. Roy. Astron. Soc.*, **486**, 1907.

Kafka, S. 2020, variable star observations from the AAVSO International Database (https://www.aavso.org/aavso-international-database-aid).

Mattei, J. A., Foster, G., Hurwitz, L. A., Malatesta, K. H., Willson, L. A., and Mennessier, M. O. 1997, in *Proceedings of the ESA Symposium "Hipparcos–Venice '97"*, ESA-SP 402, European Space Agency, Noordwijk, The Netherlands, 269.

Percy, J. R. 2015, *J. Amer. Assoc. Var. Star Obs.*, **43**, 176.

Percy, J. R. 2020, *J. Amer. Assoc. Var. Star Obs.*, **48**, 10.

Percy, J. R., and Abachi, R. 2013, *J. Amer. Assoc. Var. Star Obs.*, **41**, 193.

Percy, J. R., Molak, A., Lund, H., Overbeek, D., Wehlau, A. F., and Williams, P. F. 2006, *Publ. Astron. Soc. Pacific*, **118**, 805.

Pojmański, G. 1997, *Acta Astron.*, **47**, 467.

Wenger, M., *et al.* 2000, *Astron. Astrophys., Suppl. Ser.*, **143**, 9.

Xiong, D. R., and Deng, L. 2007, *Mon. Not. Roy. Astron. Soc.*, **378**, 1270.

Analysis of ASAS-SN Observations of Short-Period Mira Stars

John R. Percy
Patricia Golaszewska
Department of Astronomy and Astrophysics, and Dunlap Institute of Astronomy and Astrophysics, University of Toronto, Toronto ON M5S 3H4, Canada; john.percy@utoronto.ca

Received June 15, 2020; revised June 30, 2020; accepted July 6, 2020

Abstract We have analyzed observations of a uniform sample of 36 stars in the ASAS-SN variable star catalog, with mean magnitudes between 10 and 12, classified as Mira by the catalog, and with periods of 150 days or less. They presumably represent a transition from Mira type to semiregular type. The stars show a wide variety of light curve shapes, and of deviation from periodicity. The amplitude increases with increasing period, as is well known, but no other properties, including the degree of periodicity, seem to depend on period.

1. Introduction

The All-Sky Automated Survey for Supernovae—ASAS-SN (Jayasinghe *et al.* 2018, 2019)—uses a network of up to 24 telescopes around the world to survey the entire visible sky every night down to about 18th magnitude, and has been doing so for up to 2,000 days. ASAS-SN has identified over 50,000 new variable stars, determined periods and ranges for those that are periodic, classified them using machine learning, and made the information and data publicly available online (asas-sn.osu.edu/variables). It has also used machine learning to uniformly classify 412,000 known variables—many of them also observed by the AAVSO.

We have been using ASAS-SN data to study the complex variability of pulsating red giants (PRGs). Percy and Fenaux (2019) examined the analysis and classification of about 50 red semiregular stars, and identified problems with the ASAS-SN analysis and classification of these. Percy (2020a) used ASAS-SN data to study bimodal PRGs; Percy and Wallace (2020) used them to study PRGs which also had a long secondary period; and Percy (2020b) used them to study several dozen poorly-studied stars previously classified as "irregular" (most of them were non-variable, or microvariable at best). In this paper, we use ASAS-SN data to study 36 stars, classified as Mira stars, having periods less than 150 days, i.e. shorter than the periods of "traditional" Mira stars.

Mira stars, by definition, have visual ranges of 2.5 magnitudes or more. Most have periods of several hundred days; Mira itself has a period of about 330 days. PRGs with smaller ranges would be classified as semiregular (SR) or irregular (L). Note that, in general, the term *range* refers to the difference between the maximum and minimum magnitude; ASAS-SN uses a slightly different definition, as explained below. We wondered: would the short-period Miras be relatively periodic with visual ranges of 2.5 magnitudes or more, or would they be semiregular, with periodic components with full range less than 2.5 magnitudes, or would they represent some sort of smooth transition from typical Mira stars (Willson and Marengo 2012) to typical SR variables (Kiss and Percy 2012)?

2. Data and analysis

We analyzed a uniform sample of 36 stars from the ASAS-SN variable star catalog, with mean magnitudes between 10 and 12, classified by ASAS-SN as Mira stars (visual range greater than 2.5 magnitudes), with periods less than 150 days. The shortest period of the stars in our sample was 87.7 days. The declinations of the stars were +79 to –70 degrees. The datasets were uniform in the sense that they are typically 1,500–2,000 days long—about 15–20 pulsation periods for a typical star in our sample.

The ASAS-SN data were downloaded, the light curves were inspected, and the data were analyzed using the Fourier-analysis routine in the AAVSO VSTAR time-series package (Benn 2013). Our intention was not just to determine a single period and amplitude, as ASAS-SN does, but also to look for evidence, in the light and phase curves and Fourier spectrum, of more complex behavior such as harmonics, overtones, and long secondary periods (LSPs)—a poorly-understood phenomenon which occurs in about a third of SR variables. Note: in this paper, *overtones* are higher modes of pulsation, the lowest mode being the fundamental. *Harmonics* are non-physical periods which occur in the Fourier spectrum if the phase curve is non-sinusoidal. In that case, the phase curve can be synthesized by the sum of sine curves with the harmonic periods.

Specifically, harmonics have periods which are integral fractions of the pulsation period; the first is exactly half of the actual physical period. The first overtone is most commonly *about* half of the pulsation period, if the dominant pulsation periods are those of the fundamental mode and the first-overtone mode (Xiong and Deng 2007; Percy 2020a). Therefore, overtones can be mistaken for harmonics, and vice versa. The presence of overtones is also evident in the light curve as adjacent pulsation cycles with noticeably different amplitudes. LSPs might show up as slow variations in the light curve, or as low-frequency peaks in the Fourier spectrum. Given that the amplitudes of LSPs are generally 0.5 mag. or less (Percy and Wallace 2020), and that the lengths of our datasets are limited, and that our stars are to some degree non-periodic, and that the total ranges of these stars are greater than 2.5 magnitudes by definition, LSPs might be difficult to detect in these stars, if

they are present. There is a similar limitation on our ability to detect overtones and harmonics in the Fourier spectra.

3. Results

The results of our analyses are given in Table 1. As well as the names of the stars, Table 1 gives the period PA and range RA from the ASAS-SN catalog, the period P and amplitude A from our analyses, a quantity F, and notes. Our amplitude A is the coefficient of the sine curve with period P. We would expect it to be half the ASAS-SN value, but RA is up to 30 percent greater than 2A, because of the ASAS-SN definition of range—it is the difference between the 5th and 95th percentile of the magnitude distribution (Jayasinghe *et al.* 2019).

We define the quantity F as (R–2A)/R, where R is here defined as the *total* maximum-to-minimum range of the data, i.e. it differs from the ASAS-SN range R, which is defined as indicated above. In the absence of errors, F would be 0 if the star was perfectly periodic, and 1 if the star had no periodicity, and was completely irregular. So F is a measure of the deviation from perfect periodicity. It quantifies the difference between the extreme values of the brightness variation, and the typical values based on the mean period and its amplitude. We hypothesized that F might be closer to 0 for longer-period, larger-amplitude stars.

In the "Notes" column, an asterisk * indicates that there were AAVSO visual data; (*) indicates that the visual data were sparse. We analyzed the visual data in case they could provide additional insight on the star's behavior. Usually they didn't.

Figure 1 shows the relationship between amplitude A and pulsation period P. The average amplitude increases with period—on average from about 0.9 mag. at P = 90 days, to about 1.5 mag. at P = 150 days—as many other studies have shown. The relationship in Figure 1 shows considerable scatter, which is not surprising, given the complexity of the individual stars' variability and the limited time span of the data.

Figure 2 shows the relationship between our parameter F = (R–2A)/R and pulsation period. We hypothesized that the longer-period stars would be more regular (F = 0) and the shorter-period stars would be less regular (F > 0). A very weak trend is seen in Figure 2 (but with much scatter) in the sense that shorter-period stars are very slightly less regular.

Figures 3 and 4 show representative phase or light curves. Figure 3, SS Cas, is almost periodic, and has a sawtooth light and phase curve. Figure 4, RX Lyn, is much more irregular.

Table 1. Analysis of ASAS-SN observations of short-period Mira stars.

Name: ASAS-SN-V	*V* Name*	*PA(d)*	*P(d)*	*RA*	*A*	*F*	*Notes*
J000936.51+513400.7	SS Cas	141.28	141.06	3.31	1.58	0.10	*
J044542.23+750604.9	X Cam	143.29	142.96	5.06	2.31	0.13	*
J053220.76-103721.4	FP Ori	144.99	145.29	2.14	0.91	0.33	
J075403.04-192017.6	ES Pup	138.55	138.03	1.91	0.86	0.31	
J082807.98+382022.8	RX Lyn	145.30	143.91	2.48	1.05	0.42	(*)
J083225.15-570212.9	IZ Car	104.59	104.70	3.42	1.48	0.30	(*)
J083652.88-464344.0	—	108.52	109.48	2.81	1.25	0.26	
J105340.86-531127.8	RU Vel	123.35	123.21	2.35	1.12	0.10	*
J110101.35-542441.4	CI Vel	137.84	138.20	3.44	1.34	0.33	
J111711.74-301051.3	BD Hya	118.46	118.30	3.04	1.29	0.50	
J124401.06-304214.7	V0455 Cen	104.01	103.23	2.98	1.31	0.27	
J150847.62-415948.9	OV Lup	95.15	97.49	2.51	1.15	0.38	*
J153709.22-422104.1	HH Lup	125.08	118.26	2.66	1.28	0.17	
J162313.17+440828.4	AY Her	130.99	129.02	2.38	1.02	0.32	(*)
J163255.65+065129.7	SS Her	108.01	107.81	3.33	1.49	0.40	*
J163302.23-673519.2	KM TrA	126.93	127.34	1.83	0.57	0.61	
J165447.09-651208.0	Z TrA	149.83	149.97	3.52	1.69	0.28	(*)
J170129.45+222838.1	SY Her	116.01	115.66	3.83	1.97	0.16	*
J170457.11-121205.8	UX Oph	115.59	116.29	3.32	1.52	0.24	*
J173705.97+181304.6	FR Her	136.05	134.66	2.79	1.12	0.32	(*)
J180428.19-290814.7	V0795 Sgr	87.70	87.06	2.63	1.13	0.32	
J182117.96-302543.1	V1599 Sgr	137.20	137.82	2.13	0.83	0.34	
J182144.18+040912.3	V0915 Oph	112.24	111.67	3.68	1.62	0.19	(*)
J190008.26-181510.5	V0733 Sgr	102.32	102.26	2.52	1.14	0.26	
J191743.80-172845.0	AL Sgr	92.05	90.02	2.37	0.78	0.61	*
J192008.66+414058.8	HO Lyr	99.75	100.28	3.03	1.36	0.22	*
J193131.25+344217.5	DD Cyg	146.69	146.24	2.50	1.22	0.24	*
J194154.61+544034.2	V0369 Cyg	104.79	104.54	4.05	1.79	0.19	(*)
J195245.97+562050.4	V0392 Cyg	96.47	96.37	1.86	0.66	0.51	*
J200011.10-695254.3	BQ Pav	111.11	109.99	2.79	1.24	0.31	*
J201511.08-060903.8	Z Aql	132.66	128.30	3.97	1.71	0.32	*
J204002.88-284732.6	R Mic	137.62	137.76	4.23	1.93	0.26	*
J210422.53+234918.2	R Vul	136.86	136.59	4.49	2.29	0.26	*
J212305.76+005015.6	RW Aqr	143.53	140.19	3.83	1.84	0.29	*
J215829.19-691236.5	RW Ind	144.86	144.99	4.39	1.96	0.29	
J232114.21+785732.6	RY Cep	149.83	149.63	3.28	1.39	0.22	*

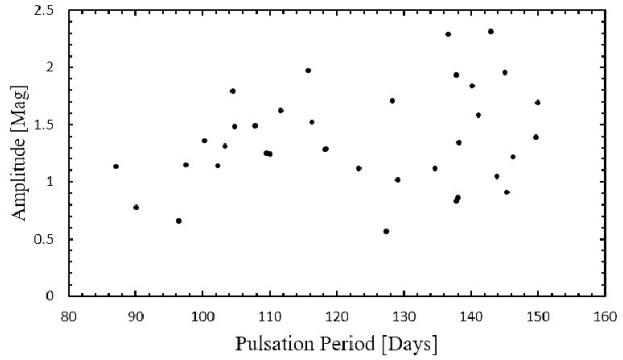

Figure 1. The relationship between V amplitude and period in days. On average, the amplitude increases with increasing period—a well-known result.

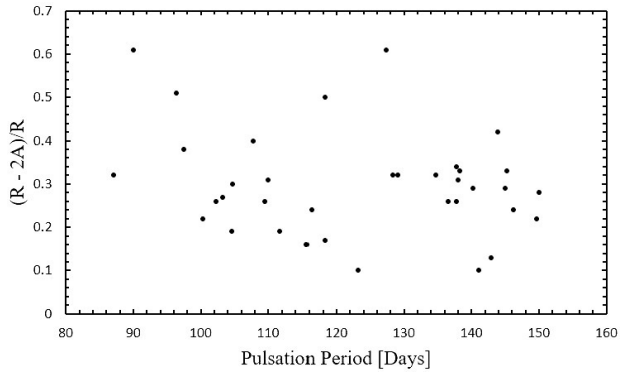

Figure 2. The relationship between the quantity F (see text) and the period in days. F is a measure of deviation from perfect periodicity. There is a very slight downward trend between F and period, with much scatter.

Fourteen of the 36 stars have 2A less than 2.5 magnitudes, so they would not be classified as Mira if they were perfectly periodic; the larger ASAS-SN range and the Mira classification is presumably a result of deviations from perfect periodicity. Nine of the stars have an ASAS-SN range RA which is less than 2.5 magnitudes.

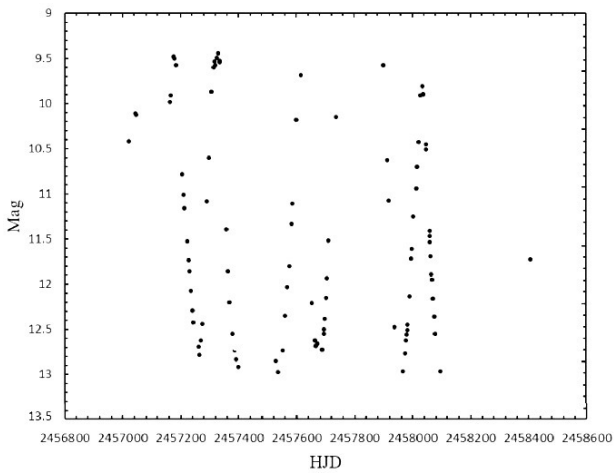

Figure 3. The light curve for SS Cas, from ASAS-SN data. The variability is close to periodic, but the phase curve is saw-toothed.

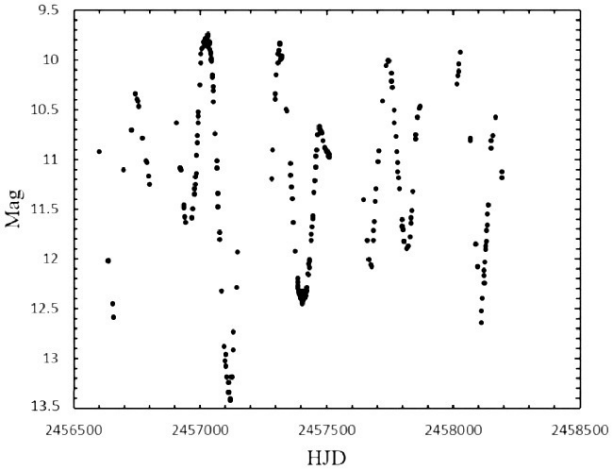

Figure 4. The light curve of RX Lyn, from ASAS-SN data. Note the large deviations from monoperiodicity.

4. Discussion

The periods that we derive are slightly different from the ASAS-SN periods, presumably because the latter were derived from a shorter dataset, and the periods of PRGs are known to be slightly unstable, and the variability complex. As mentioned above, the ASAS-SN ranges RA are up to 30 percent greater than 2A, presumably due to the ASAS-SN definition of range.

Hence our quantity F. In the absence of errors, F = 0 if the variability was perfectly periodic, and F = 1 if it was perfectly non-periodic. As it is, F ranges from 0.10 to 0.61. There is a very weak tendency for the longer-period stars to be more periodic and less irregular, but the tendency is not strong enough to call a correlation. There is certainly not a smooth transition from the longer-period Mira stars to the shorter-period ones.

The most interesting result of this study is the wide range of behavior in this sample of stars. Some stars (e.g. SS Cas (Figure 3), HO Lyr, DD Cyg, V915 Oph, and R Vul) are nearly periodic; others (e.g. RX Lyn (Figure 4), Z Aql, and KM TrA) are noticeably irregular. Most have reasonably sinusoidal light and phase curves, but V369 Cyg, SS Cas, FP Ori, and UX Oph have sawtooth phase curves; RY Cep has rounded maxima and sharp minima; FP Ori has a faster rise to maximum and a slower decrease; V733 Sgr has the opposite; RU Vel has a sharp maximum. Several of these stars show harmonics in their spectra, confirming that the light curve is non-sinusoidal. V794 Sgr, AL Sgr, IZ Car, and Z TrA have slow variations in pulsation *amplitudes*, which are found in many PRGs (Percy and Abachi 2013). BD Hya has a sudden transition from shallow minima to deep ones. Most of the stars have small cycle-to-cycle fluctuations in amplitude which could be due to overtones, but only SY Her, V1599 Sgr, and RW Ind seem to show possible overtones in the Fourier spectrum. KM TrA, R Mic, and V1599 Sgr show possible evidence of an LSP in the light curve; others may have LSPs, but these probably have amplitudes of 0.5 or less, and may not show up in the light curve or Fourier spectrum. The data for X Cam, RW Aqr, HH Lup, and CI Vel are somewhat sparse. Light curves of all of these variables are freely available on the ASAS-SN website: https://asas-sn.osu.edu/variables.

This project was carried out by an undergraduate student majoring in astronomy and physics. Projects such as this are

an excellent way for students to develop and integrate their science, math, and computer skills, and to be introduced to the research process—motivated by knowing that they are doing real science, with real data.

5. Conclusions

We have shown that our uniform sample of 36 Mira stars with periods less than 150 days shows a wide range of light and phase curve shapes, and degrees of periodicity. Other than a positive correlation between amplitude and period, this variety of behavior does not seem to correlate with period, though there is a very weak tendency for the longer-period stars to be slightly more periodic.

6. Acknowledgements

This paper made use of ASAS-SN photometric data. We thank the ASAS-SN project team for their remarkable contribution to stellar astronomy, and for making the data freely available on-line. We thank the AAVSO observers and staff for making the visual observations, and making them publicly available, and also for creating the VSTAR time-series analysis package. We acknowledge and thank the University of Toronto Work-Study Program for financial support. The Dunlap Institute is funded through an endowment established by the David Dunlap Family and the University of Toronto.

References

Benn, D. 2013, VSTAR data analysis software (https://www.aavso.org/vstar-overview).

Jayasinghe, T., *et al.* 2018, *Mon. Not. Roy. Astron. Soc.*, **477**, 3145.

Jayasinghe, T., *et al.* 2019, *Mon. Not. Roy. Astron. Soc.*, **486**, 1907.

Kiss, L. L., and Percy, J. R. 2012, *J. Amer. Assoc. Var. Star Obs.*, **40**, 528.

Percy, J. R. 2020a, *J. Amer. Assoc. Var. Star Obs.*, **48**, 10.

Percy, J. R. 2020b, *J. Amer. Assoc. Var. Star Obs.*, **48**, 50.

Percy, J. R., and Abachi, R. 2013, *J. Amer. Assoc. Var. Star Obs.*, **41**, 193.

Percy, J. R., and Fenaux, L. 2019, *J. Amer. Assoc. Var. Star Obs.*, **47**, 202.

Percy, J. R., and Wallace, A. M., 2020, *J. Amer. Assoc. Var. Star Obs.*, **48**, 31.

Willson, L. A., and Marengo, M. 2012, *J. Amer. Assoc. Var. Star Obs.*, **40**, 516.

Xiong, D. R., and Deng, L. 2007, *Mon. Not. Roy. Astron. Soc.*, **378**, 1270.

CCD Minima for Selected Eclipsing Binaries in 2019

Robert H. Nelson
Mountain Ash Observatory, 1393 Garvin Street, Prince George, BC V2M 3Z1, Canada; bob.nelson@shaw.ca

Received June 26, 2020; revised July 27, 2020; accepted July 27, 2020

Abstract 204 CCD-based times of minima of eclipsing binary stars are presented.

1. Introduction

This is a continuation of a series of 21 papers published in the (sadly) now-defunct *Information Bulletin on Variable Stars* (IBVS), the latest being Nelson (2019a).

Eclipse timings are very important in tracking changes in the period of eclipsing binaries. The eclipse timing difference (O–C) plot is, as is well known, an important tool in detecting small changes in orbital periods and outlining their long-term trends. There are many reasons as to why the period of a given eclipsing binary might change. One of the most commonly made assumptions—in the case of overcontact binaries (and others)—is that the period change is due to the transfer of mass (most often, but not always) from the star of lesser mass to its companion. In the latter case there will be a steady period increase, detectable as data fitting an upward-facing parabola in the O–C plot. Unfortunately, there have been many papers in the literature where authors blithely assume that any steady period change must be due to mass transfer. The equations work even if the use of them might be invalid.

This is one of the reasons why my colleagues and I undertook a series of papers reviewing the period-change literature with a view to establishing a reliable case for mass exchange in selected overcontact binaries (Nelson *et al.* 2014, 2015, 2016, 2020). In them we sorted out some of the unfortunate mistakes in period change papers, as well as period change conclusions no longer supported by subsequent timing data. One of the most glaring lapses in period change analyses is the neglect of the light time effect (LiTE) due to a seen or unseen companion to the eclipsing pair. This defect was highlighted in a paper by Hill *et al.* (1989) in a study of 44 Boo in which the authors pointed out that all previous analyses had neglected the effect of the known (brighter) star A in the A-BC configuration (where BC is the eclipsing pair) and were therefore invalid. The fact that at least 42 ± 5% of overcontact binaries brighter than $V_{max} = 10$ have a gravitationally bound companion was established by Pribulla and Ruciński (2006), thus stressing the need for taking LiTE into account. The light time effect (LiTE) can be dealt with by equations due to Irwin (1952, 1959), and numerous authors have employed these routines in their analyses of period change as has the present author.

Other causes of period variation are magnetic cycles due to the Applegate effect (Applegate 1989, 1992), mass loss through the Lagrangian L_2 point, and angular momentum loss through a stellar wind (Kallrath and Milone, 1999; Linial and Sari 2017).

Thus, the acquisition of eclipse timings is important. However, not all systems are equally meriting of attention. There are some systems for which the period is closely constant; they therefore require timings only every three to five years or longer; in that case yearly timings would be a waste of precious clear-sky time. On the other hand, there are systems for which there have been no timings for many years, as well as those whose periods are changing rapidly and unpredictably, therefore requiring close attention. Observers are encouraged to visit the database containing EXCEL files for over 5,000 eclipsing binaries at Nelson (2019b, 2020) in order to make good choices of observing targets that will be of maximum benefit to the astronomical community. In addition, some of the files, (for example AB And), contain formulas using the LiTE equations; readers are encouraged to explore the capabilities of the analysis.

The eclipse timings reported below were all selected with these principles in mind.

2. The equipment

a) Mountain Ash Observatory (MAO)
Location: 53° 54' 41.7" N, 122° 47' 22.8" W, Prince George, BC, Canada
Mount: Paramount ME (German Equatorial)
OTA: 33 cm f/4 Newtonian
Detector: SBIG-10 XME (2184 x 1472 pixels, each 6.8 microns)
Filters: B, V, Rc, Ic, clear
Flats: Light box
Software: THESKY6 + CCDSOFT5

b) Desert Blooms Observatory (DBO)
Location: 30° 24' 54.7" N, 110° 15' 27" W, Benson, Arizona
Mount: Paramount Taurus 400 (Fork)
OTA: 40 cm f/6.8 Meade LX-200
Detector: OSI 683 (1663 × 1252 pixels, each 10.8 microns)
Filters: B, V, R_c, I_c, clear, r'
Flats: Illuminated screen
Software: THESKYX + IMAGER

3. Data reduction

All data were reduced in the usual way (bias, darks, flats), followed by aperture photometry using MIRA UE (Mirametrics 2020), usually using one comparison (C) and one check (K) star. When the C–K plot was found to be not flat, a second (or sometimes third) check star was employed to sort out the situation. Occasionally, new variable stars have been discovered.

Table 1. Sample of first ten times of minima for 204 eclipsing binaries.

Star Name	*Time of Min. HJD–2400000*	*Error (days)*	*Type*	*Filter*	*O–C (days)*	*Observatory*
AB And	58774.6124	0.0008	II	BVI	0.0008	DBO
AB And	58774.7781	0.0006	I	BVI	0.0006	DBO
AB And	58801.6610	0.0004	I	BVI	0.0004	DBO
AB And	58819.5830	0.0003	I	BVI	0.0003	DBO
AB And	58837.6715	0.0008	II	BVI	0.0008	DBO
QX And	58786.6839	–0.0001	II	c	–0.0001	MAO
V0363 And	58788.7220	–0.0015	II	c	–0.0015	MAO
V0404 And	58781.6826	–0.0056	II	BRVI	–0.0056	DBO
V0404 And	58847.5982	–0.0033	I	BVRI	–0.0033	DBO
V0527 And	58725.7539	0.0019	I	c	0.0019	MAO

Remarks: To save space, in Table 1 GSC star names have been shortened to a leading "G" only but with the constellation in the filename. Times of minimum are heliocentric Julian dates with the leading 24 removed. O–C values were computed using elements computed from the O–C database listed in the references (Nelson, 2019b, 2020). The remote observatory, Desert Blooms (DBO), in Benson, Arizona, is described in Nelson (2002). Readers wishing original data are welcome to write to the author. The full table is available through the AAVSO ftp site at ftp://ftp.aavso.org/public/datasets/nelson482-ccdminima.txt (if necessary, copy and paste link into the address bar of a web browser).

Minimum time determinations were performed using MINIMA v27 (Nelson 2013). In it, six methods for minimum determination are available: Parabolic fit, Digital tracing paper, Bisector of chords, Kwee and van Woerden (Kwee and van Woerden 1956), Five-term Fourier fit, and Sliding Integrations (Ghedini 1982). Generally speaking, the two most reliable methods are Kwee and van Worden and Fourier fitting (roughly equivalent), but the other methods are useful as well. With very good data, precisions approaching ±0.0001 day (as determined from the sample standard deviation of the output values) are possible; however, with poor quality data, standard errors of up to ±0.001 day or worse have been encountered. A rule of thumb, employed by this observer, is to take the sample standard error and double it. The reason for this is that unseen systematic factors can distort the measured times (sky transparency gradients for example); experience with many O–C files has supported this practice. Whenever possible, all observing runs were long enough to cover both points of inflection (maximum slope) of the light curve; however, problems with the weather and other factors occasionally prevented this from happening. In each of those cases, the estimated error was increased correspondingly.

4. The data

For each star, Table 1 gives time of minimum, error, type (primary or secondary), O–C value, and the observatory at which the data were obtained.

5. Acknowledgements

Thanks are due to Environment Canada for the website satellite views (Meteorol. Serv. Canada 2020) that were essential in predicting clear times for observing runs in this cloudy locale. Thanks are also due to Attilla Danko for his Clear Sky Charts (Danko 2020).

This research has made use of the SIMBAD database, operated at CDS, Strasbourg, France.

References

Applegate, J. H. 1989, *Astrophys. J.*, **337**, 865.
Applegate, J. H. 1992, *Astrophys. J.*, **385**, 621.
Danko, A. 2020, Clear Sky Chart (https://www.cleardarksky.com).
Ghedini, S. 1982, *Software for Photometric Astronomy*, Willmann-Bell, Richmond, Va.
Hill, G., Fisher, W. A., and Holmgren, D. 1989, *Astron. Astrophys.*, **211**, 81.
Irwin, J. B. 1952, *Astrophys. J.*, **116**, 211.
Irwin, J. B. 1959, *Astron. J.*, **64**, 149.
Kallrath, J., and Milone, E. F. 1999, *Eclipsing Binary Stars: Modeling and Analysis*, Springer, New York.
Kwee, K. K., and van Woerden, H. 1956, *Bull. Astron. Inst. Netherlands*, 12, 327.
Linial, I., and Sari, R. 2017, *Mon. Not. Roy. Astron. Soc.*, **469**, 2441 (arXive:1705.01435).
Mirametrics. 2020, Image Processing, Visualization, Data Analysis (https://www.mirametrics.com).
Meteorological Service of Canada. 2020, Satellite Images for North America (http://weather.gc.ca/).
Nelson, R. H. 2013, Software by Bob Nelson, (https://www.variablestarssouth.org/bob-nelson/).
Nelson, R. H. 2017, *Inf. Bull. Var. Stars*, No. 6195, 1.
Nelson, R. H. 2019a, *Inf. Bull. Var. Stars*, No. 6262, 1.
Nelson, R. H. 2019b, Bob Nelson's O–C Files, (http://www.aavso.org/bob-nelsons-o-c-files).
Nelson, R. H. 2020, Bob Nelson's O–C Files, (http://binaries.boulder.swri.edu/binaries).
Nelson, R. H., Milone, E. F., and Terrell, D. 2020, *New Astron. Rev.*, in preparation.
Nelson, R. H., Terrell, D., and Milone, E. F. 2014, *New Astron. Rev.*, **59**, 1.
Nelson, R. H., Terrell, D., and Milone, E. F. 2015, *New Astron. Rev.*, **69**, 1.
Nelson, R. H., Terrell, D., and Milone, E. F. 2016, *New Astron. Rev.*, **70**, 1.
Pribulla, T., and Ruciński, S. M. 2006, *Astron. J.*, **131**, 2986.

Photometry of TIC 230386284, a Recently Found Bright Eclipsing Star in Draco

Maksym Pyatnytskyy
Dzhona Makkeina 37, apt. 6, Kyiv, 01042, Ukraine; mpyat2@gmail.com

Received July 8, 2020; revised November 15, 2020; accepted November 17, 2020

Abstract The results of photometry are presented for the star TIC 230386284, of EA+UV type, recently found by the author while mining TESS data. The depth of primary eclipses in the Johnson V band derived from the author's measurements was found to be significantly smaller (0.024 mag) compared to the TESS bandpass (0.11 mag). This was interpreted as a result of light contamination by an extremely close optical companion having a very different color. Estimation of the upper brightness limit of the variable out of eclipses and flares in the Johnson V band and brightness of the contaminating star was done; the contaminating star appeared to be brighter in V than the variable by at least 1.3 mag.

1. Introduction

The TESS spacecraft (Ricker *et al.* 2014), designed to search for new extrasolar planets, generates plenty of data. This huge array is a rich source for mining new variables. A goal of the current work is a refinement of some parameters of the star TIC 230386284 (J2000: 19 03 17.46, +63 59 35.9) found by the author while mining the TESS data. TESS data with two-minute cadence with Presearch Data Conditioning (PDC) correction (Jenkins *et al.* 2016), available through the MAST portal (https://mast.stsci.edu/portal/Mashup/Clients/Mast/Portal.html), were used for the analysis. The star was registered in the AAVSO VSX database (Watson *et al.* 2014) as PMAK V41 (https://aavso.org/vsx/index.php?view=detail.top&oid=1540365). TIC 230386284 is an eclipsing binary system with the primary and the secondary minima of similar depth (depth of the primary minima is 0.11 mag in TESS filter). The star also demonstrates flares, so, taking into account its spectral type (M3.5V), it was classified as EA+UV variable. The flares reach an amplitude of 0.14 mag in the TESS bandpass. The total number of flares was manually counted for TESS data for sectors from 14 to 18, 20, 21, and from 23 to 26 (274 observational days in total), see Table 1.

There were also many low-amplitude flares (< 0.015 mag in the TESS bandpass). They were not counted in this work, since they sometimes look like noise sparks.

A part of the TESS light curve is shown in Figure 1.

Interestingly, SuperWASP (Butters *et al.* 2010) data (unfiltered photometry) show very shallow minima (the primary minimum depth is about 0.03 mag). The minima in ASAS-SN (Kochanek *et al.* 2017) V data were barely visible because the data were too noisy. Combining TESS (sectors from 14 to 18 were available at the time of mining), SuperWASP, and ASAS-SN data, the following parameters of the eclipsing variability were determined: a period of 0.341493 d and epoch of the primary eclipse HJD 2458748.7177. These parameters were published in VSX.

Table 1. Crude estimation of the flare rate for TIC 230386284.

	Total number of flares for 274 days	*Mean number of days between flares*
Flares > 0.1 mag (TESS)	3	91
Flares > 0.03 mag (TESS)	16	17
Flares > 0.015 mag (TESS)	60	5

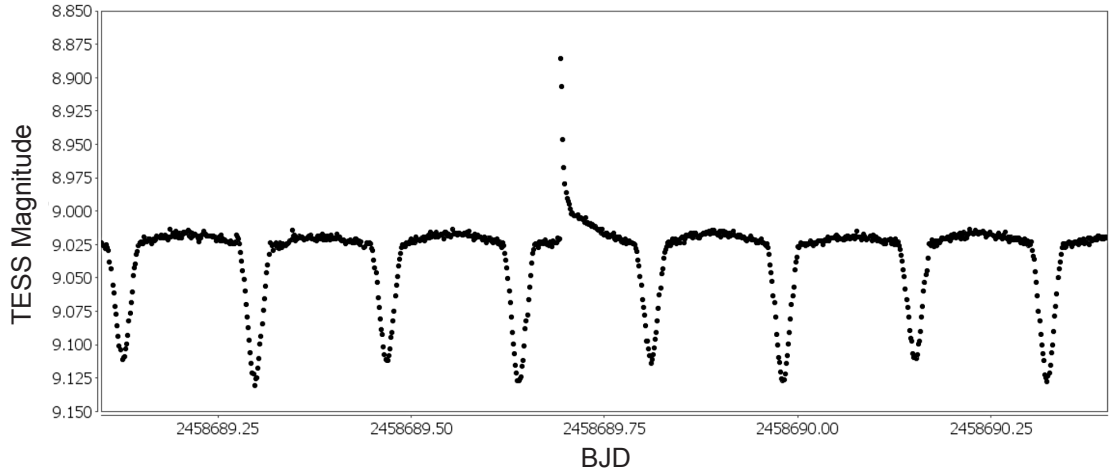

Figure 1. A part of the TESS light curve for TIC 230386284. Eclipsing minima and a sporadic flare are clearly seen. TESS magnitudes were derived from TESS fluxes. The zero level was adjusted to make the median magnitude value equal to the TESS magnitude for TIC 230386284 (9.02 mag) from the *TESS Input Catalog v8* (Stassun *et al.* 2019).

The question remained about a variability range in the Johnson V band: the ASAS-SN data were not reliable to estimate it (however, even from those noisy data, it was obvious that the variability range in the V band is significantly less than in the TESS one; the reason for this was unclear). This was a motivation to make additional observations of the system.

A side goal was an estimation of the applicability of a simple uncooled 12-bit monochrome CMOS camera with a 0.33-inch sensor for variable star research.

2. Methods

The author used a 6-inch f/5 Newtonian on an equatorial tracking mount. A monochrome uncooled CMOS camera ZWO ASI120MM-S placed in the primary focus of the telescope was equipped with a photometric V filter. The observational place location was in a relatively highly polluted urban area. Scientific frames were collected during seven nights from April to June of 2020.

To extend the effective dynamic range of the 12-bit CMOS camera and improve the signal-to-noise ratio, calibrated scientific frames were separated by groups of four or five images (depending on exposure used for the session), aligned, and stacked. The total exposure of stacked images was 60 s. The author used IRIS astronomical software (Buil 1999–2018) to calibrate and align images plus a set of utilities (Pyatnytskyy 2018) to create master calibration frames and to stack images by small groups.

The ASTROIMAGEJ software (Collins *et al.* 2017) was used to perform differential aperture photometry. One comparison star and a check star from a standard AAVSO sequence were used (Table 2). One-band transformation was applied to the data using the Tv_b-v transformation coefficient obtained from the photometry of the AAVSO Standard Field for M67. The value of Tv_b-v appeared to be rather small (0.0086(0.0042)) so the transformation introduced a minor correction to the data. The value of the (B–V) index for the target variable (1.35) was taken from APASS DR10 (Henden *et al.* 2018). Each point in the resulting light curve is a binned average of three observations; uncertainty is the standard deviation (Figure 2, upper pane). There are 339 binned observations in total.

Further analysis and visualization of the data were done mainly with VSTAR (Benn 2013).

3. Results and discussion

Figure 2 shows the phase plots for TIC 230386284 in different filters. The curve in the Johnson V filter represents the author's observations. The flat region of the curve out of eclipsing minima corresponds to Johnson V magnitude 10.47.

The depth of the primary minima in the TESS filter is 0.11 mag while in the Johnson V filter it is only 0.024 mag.

A search in the Vizier catalog service gave the following result: according to *The Washington Visual Double Star Catalog* (WDS; Mason *et al.* 2019) the star is a component of an optical triple system: there are two very close components (AB) separated by 0.2 arcsec (magnitude 10.60 mag according to the WDS) and a third faint component with a magnitude 14.00 mag, with a separation of 3.6 arcsec. This third component is visible in the author's frames; its location is in a good agreement with the WDS data (see Figure 3). The variable is assumed to be one of the stars of the AB close pair.

The optical binarity of AB component was established by Jódar *et al.* (2013). They used the Lucky Imaging technique to resolve very close optical components. Unfortunately, no information about the components but angular separation and positional angle are given in the article.

We can assume that the second non-variable component of the AB pair has a very different color (more "bluish" than the variable of type M3.5V) so its flux in the TESS filter is substantially smaller than the flux of the eclipsing variable (the TESS filter covers a range of wavelengths from approximately 600 to 1000 nm (Ricker 2014)). Then we can adjust the V magnitude of the contaminating star so that the depths of the minima of the "de-blended" light curve will be the same as for the TESS light curve. This gives us the upper limit of the brightness of the variable and the lower limit of the brightness of the contaminating star (in the V filter).

Such a fitting gives a total V magnitude of 10.745 for the contaminating stars (component C plus the non-variable component of the AB pair). The magnitude of the C component from the WDS is 14.00, which gives the estimated upper limit of the magnitude of the contaminating component of AB pair as 10.80 V. The magnitude out of eclipses (and flares) of the variable in the V filter appears to be greater than 12.09, which is about three magnitudes more than the TESS magnitude from the *TESS Input Catalog v8* (Stassun *et al.* 2019). Note that under this approach the contaminating component is brighter in V than the variable by at least 1.3 mag. The "de-blended" folded light curve along with the TESS data is shown in Figure 4. It is seen that the author's data are in excellent agreement with the period and the epoch previously determined using TESS, SuperWASP, and ASAS-SN V data.

4. Conclusions

Photometric measurements with a simple uncooled 0.33-inch monochrome CMOS camera and a small 6-inch f/5 Newtonian show that the eclipsing range of the EA+BY variable TIC 230386284 (found by the author while mining the TESS

Table 2. Comparison and check stars.

AAVSO UID	*Type*	*R. A. (2000)* *h m s*	*Dec. (2000)* *° ′ ″*	*B*	*V*	*B–V*
000-BNM-079	Comparison	19 02 54.86	+63 56 56.0	10.693	10.168	0.525
000-BNM-081	Check	19 03 42.04	+64 11 15.0	11.773	10.795	0.978

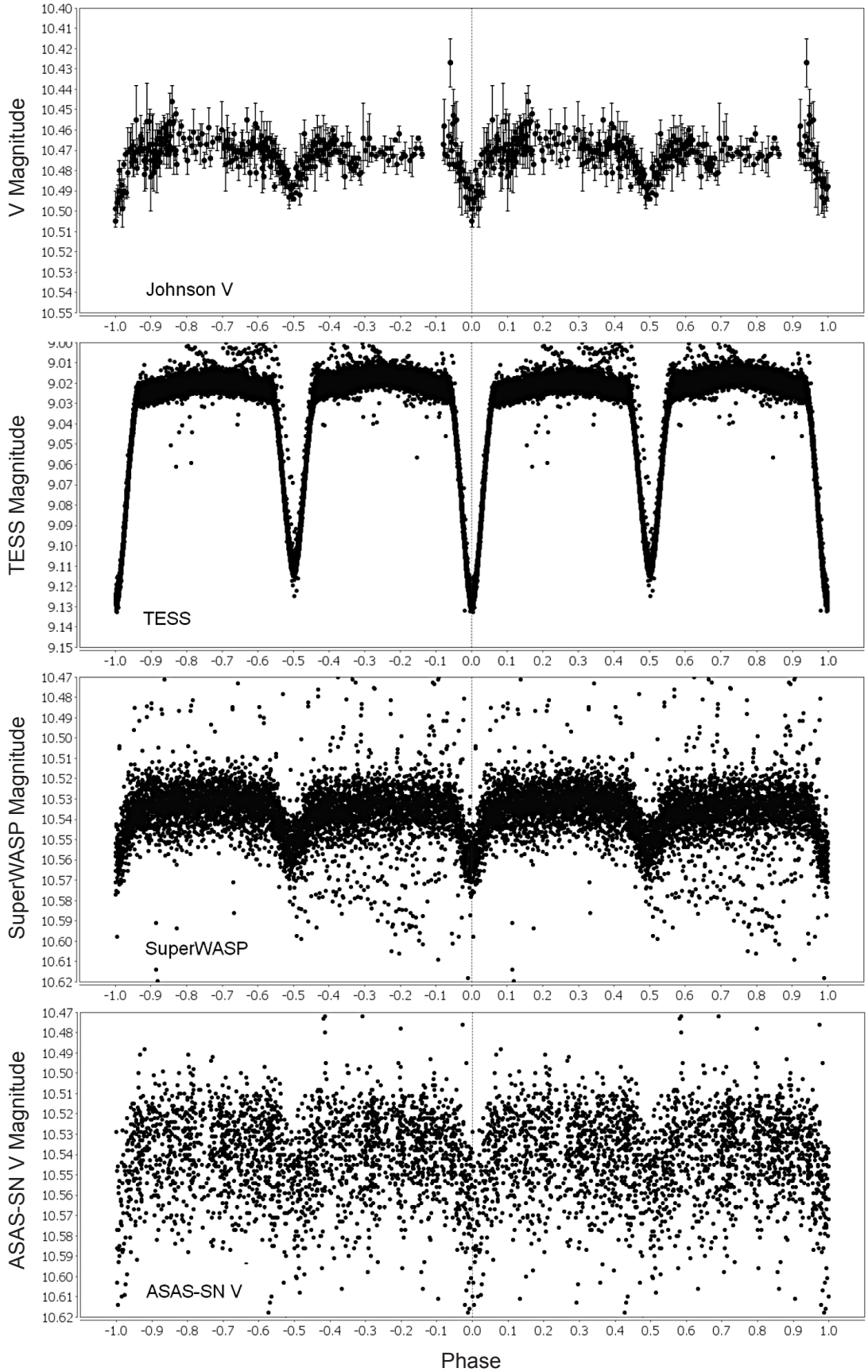

Figure 2. Phase plots for TIC 230386284 (period 0.341493, epoch 2458748.7177) in different filters. Data in the Johnson V filter (top panel) are the author's observations. TESS data are for sectors from 14 to 18.

data archive) in the Johnson V filter is significantly smaller (more than four times smaller in terms of magnitude) compared to the TESS filter. This was interpreted as a result of light contamination by a nearby (in the sense of angular distance) star having a very different color. The upper limit of the brightness of the target variable in the V band was estimated to be 12.09 mag, while the observed magnitude of the triple optical star that includes the variable was measured as 10.47 mag in the Johnson V band (out of eclipses and flares of the variable).

The previously determined period and epoch of the eclipsing variability of TIC 230386284 were confirmed by the author's data.

The nature of the contaminating object is not clear yet. It appears to be very blue. What it can be—a white dwarf, O- or B- star as a part of the multiple star system, or a background source—remains unknown. Additional spectroscopy and multi-color photometry research could shed light on this question.

It was also demonstrated that a simple uncooled CMOS camera (ZWO ASI120MM-S) can be used as a precise instrument for differential aperture photometry of bright stars.

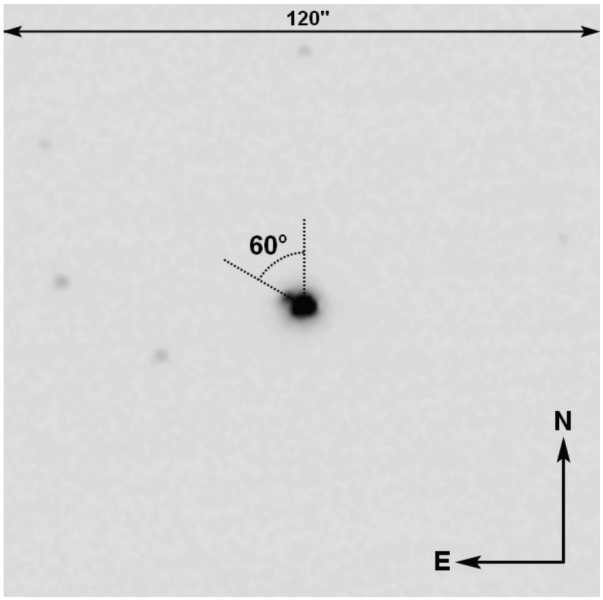

Figure 3. The image of TIC 230386284. A faint "C" component is clearly visible, the estimated positional angle is shown. A positional angle from WDS is 67° for the year 2006 and 65° for 2015.

5. Acknowledgements

This paper includes data collected with the TESS mission, obtained from the MAST data archive at the Space Telescope Science Institute (STScI). Funding for the TESS mission is provided by the NASA Explorer Program. STScI is operated by the Association of Universities for Research in Astronomy, Inc., under NASA contract NAS 5–26555.

Also, this research has made use of the VizieR catalogue access tool, CDS, Strasbourg, France (DOI: 10.26093/cds/vizier). The original description of the VizieR service was published in *Astron. Astrophys., Suppl. Ser.*, **143**, 23.

This research was made possible through the use of the AAVSO Photometric All-Sky Survey (APASS), funded by the Robert Martin Ayers Sciences Fund and NSF AST-1412587.

This research has made use of the International Variable Star Index (VSX) database, operated at AAVSO, Cambridge, Massachusetts, USA.

References

Benn, D. 2013, VSTAR data analysis software (https://www.aavso.org/vstar-overview).

Buil, C. 1999–2018, IRIS astronomical images processing software (http://www.astrosurf.com/buil/iris-software.html).

Butters, O. W., *et al.* 2010, *Astron. Astrophys.*, **520**, L10.

Collins, K. A., Kielkopf, J. F., Stassun, K. G., and Hessman, F. V. 2017, *Astron. J.*, **153**, 77.

Jenkins, J. M., *et al.* 2016, *Proc. SPIE*, **9913**, 99133E.

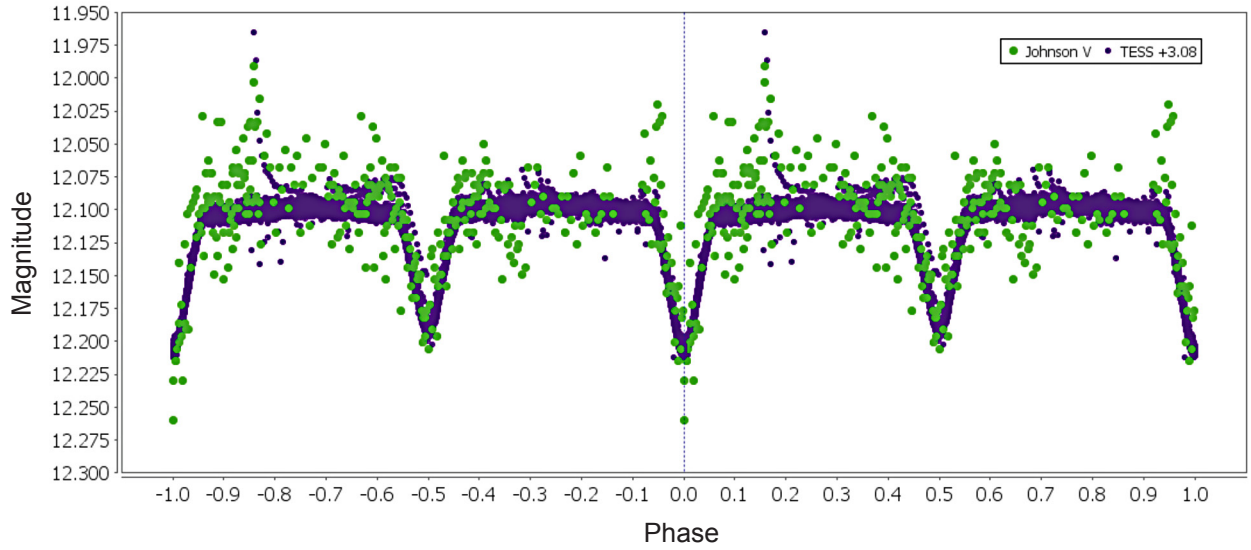

Figure 4. Phase plot for TIC 230386284 (period 0.341493, epoch 2458748.7177). The "de-blended" Johnson V light curve and the TESS light curve (baseline is shifted by 3.08 mag).

Jódar, E., Pérez-Garrido, A., Díaz-Sánchez, A., Villó, I., Rebolo, R., and Pérez-Prieto, J. A. 2013, *Mon. Not. Roy. Astron. Soc.*, **429**, 859.

Henden, A. A., Levine, S., Terrell, D., Welch, D. L., Munari, U., and Kloppenborg, B. K. 2018, AAS Meeting #232, id. 223.06.

Kochanek, C. S., *et al.* 2017, *Publ. Astron. Soc. Pacific*, **129**, 104502.

Mason, B. D., Wycoff, G. L., Hartkopf, W. I., Douglass, G. G., and Worley, C. E. 2019, VizieR Online Data Catalog: *The Washington Visual Double Star Catalog*.

Pyatnytskyy, M. Yu. 2018, FITS Command-line Utilities (http://fits-command-line-utilities.sourceforge.net).

Ricker, G. R., *et al.* 2014, *Proc. SPIE*, **9143**, 914320.

Stassun, K. G., *et al.* 2019, *Astron. J.*, **158**, 138.

Watson, C., Henden, A. A., and Price, C. A. 2014, AAVSO International Variable Star Index (VSX, Watson+, 2005–2020, https://www.aavso.org/vsx).

CCD Photometry, Light Curve Modeling, and Period Study of Four Overcontact Binary Systems: EI CMi, NSVS 3092802, V1309 Her, and V958 Mon

Kevin B. Alton
UnderOak Observatory, 70 Summit Avenue, Cedar Knolls, NJ 07927; kbalton@optonline.net

Received July 20, 2020; revised October 2, 2020; accepted October 14, 2020

Abstract Precise time-series multi-color light curve data were acquired at Desert Blooms Observatory (DBO) from EI CMi (2018–2019), NSVS 3092802 (2018–2019), V958 Mon (2018), and V1309 Her (2018). Except for V958 Mon, only monochromatic CCD photometric data are available from automated surveys which employ sparse sampling strategies. Each target produced new times of minimum from data acquired at DBO which along with other eclipse timings from the literature and those extrapolated from various sources were used to generate new ephemerides. Secular analyses (eclipse timing differences vs. epoch) revealed changes in the orbital period of each system; related evidence suggests that V1309 Her may be a ternary system. Simultaneous modeling of multicolor light curve data from each target was accomplished using the Wilson-Devinney code. Each system exhibits a total eclipse, therefore a unique photometrically derived value for the mass ratio (q_{ptm}) could be determined which subsequently provided initial estimates for the physical and geometric elements of each variable system.

1. Introduction

Overcontact binaries (OCBs), also known as EW or W UMa-type variables, share a common atmosphere with varying degrees of physical contact. Light curves (LCs) typically exhibit eclipse minima with near equal depth that reveal little color change, thereby suggesting they have similar surface temperatures. Assuming that one defines the most massive as the primary star, as is the case herein, the majority of OCBs have mass ratios ($q = m_2 / m_1$) that range from unity to as low as 0.065–0.08 (Sriram *et al.* 2016; Mochnacki and Doughty 1972; Paczyński *et al.* 2007; Arbutina 2009). For the most part, their evolutionary lifetimes are spent in physical contact (Stępień 2006; Gazeas and Stępień 2008; Stępień and Kiraga 2015). Furthermore, depending on many factors, including rate of angular momentum loss, mass ratio, total mass, orbital period, and metallicity, OCBs are destined to coalesce into fast rotating stars or to alternatively produce exotic objects such as blue stragglers (Qian *et al.* 2006; Stępień and Kiraga 2015), double degenerate binaries, supernovae, or even double black holes (Almeida *et al.* 2015).

The latest estimates appearing on the NASA Chandra website (https://chandra.harvard.edu/xray_sources/binary_stars.html) suggest that over 80% of all stars are in some arrangement of two or more gravitationally bound partners. Advances in detector technology and algorithms to reliably classify variable stars from large data sets have not only led to significantly increased density of eclipsing binaries (EBs) detected in a given survey field but an improvement in the statistical estimates for the prevalence of OCBs. Early estimates (van't Veer 1975) suggested that 1/500 stars in the study sample (GCVS; Kukarkin *et al.* 1970) was a contact binary (CB), while later on Ruciński (1994) projected that the incidence of CBs found amongst F-K type main sequence stars located in older clusters was somewhat greater 1/250–300. The microlensing technique advanced by the OGLE Survey (Udalski *et al.* 1992) produced a rich source of low amplitude EBs that would have otherwise gone undetected. Nearly two-thirds of the 931 eclipsing binaries detected during this study were classified as contact binaries (Ruciński 1997a, 1997b). Classification of 11,099 EBs detected in the ASAS study (Paczyński *et al.* 2006) revealed that 48.6% were OCBs, while Christiansen *et al.* (2008) found a slightly larger proportion (56.9%) amongst all detected EBs in a University of New South Wales Survey. Prša *et al.* (2011) reported a 1.5-fold increase in the occurrence rate of EB stars found in the Kepler field (1.2%) as opposed to the earlier Hipparcos survey (0.8%). In the Kepler field-of-view (FOV), 25.4% of the manually classified EBs were determined to be OCBs, which translates into 1 OCB per 328 target stars. Differences in the demographic breakdown of OCBs as a fraction of total eclipsing binaries clearly depends on the survey catalog, selection criteria, galactic latitude, or cluster age. Nonetheless, far from being a rare type of eclipsing variable, OCBs in some cases have been shown to represent over 50% of the total population of EBs found in a study sample.

Aside from a comprehensive (V, g', i', and r') study of V958 Mon published by Michaels (2016), no other multi-color light curves with Roche modeling have been reported for any of the other binary systems described herein. As a result, this investigation also provides the first published photometric mass ratio (q_{ptm}) estimates along with preliminary physical and geometric characteristics for NSVS 3092802, V1309 Her, and EI CMi.

2. Observations and data reduction

Time-series images were acquired at Desert Blooms Observatory (DBO, USA, 31.941 N, 110.257 W) with an SBIG STT-1603ME CCD camera mounted at the Cassegrain focus of a 0.4-m Schmidt-Cassegrain telescope. This focal-reduced (f/6.8) instrument produces an image scale of 1.36 arcsec/pixel (bin = 2 × 2) and a field-of-view (FOV) of 17.2 × 11.5 arcmin. Image acquisition was performed using TheSkyX professional edition 10.5.0 (Software Bisque 2019). Computer time was

updated immediately prior to each session and exposure time for all images adjusted to 75 s. The CCD camera is equipped with B, V, R_c, and I_c filters manufactured to match the Johnson-Cousins Bessell specification. Dark subtraction, flat correction, and registration of all images collected at DBO were performed with AIP4WIN v2.4.0 (Berry and Burnell 2005). Instrumental readings from V1309 Her and V958 Mon were reduced to catalog-based magnitudes using APASS DR9 values (Henden *et al.* 2009, 2010, 2011; Smith *et al.* 2011), whereas the MPOSC3 star fields (Warner 2007) built into MPO CANOPUS v 10.7.1.3 (Minor Planet Observer 2010) were used for EI CMi and NSVS 3092802.

3. Results and discussion

Light curves were generated using an ensemble of at least four non-varying comparison stars. The identity, J2000 coordinates, and color indices (*B–V*) for these stars are provided in Table 1. Only data from images taken above 30° altitude (airmass < 2.0) were included; considering the proximity of all program stars, differential atmospheric extinction was ignored. Uncertainty in comparison star measurements made in the same FOV typically stayed within ± 0.007 mag for V-, I_c-, and R_c-, and ± 0.010 mag for B-passbands. CCD images annotated with the location of target and comparison stars are shown for EI CMi (Figure 1), NSVS 3092802 (Figure 2), V958 Mon (Figure 3), and V1309 Her (Figure 4). All photometric data can be retrieved from the AAVSO International Database via the International Variable Star Index (Watson *et al.* 2014; https://www.aavso.org/data-download).

3.1. Photometry and ephemerides

Times-of-minimum (ToM) and associated errors were calculated using the method of Kwee and van Woerden (1956) as implemented in PERANSO v2.5 (Paunzen and Vanmunster 2016). Curve fitting all eclipse timing differences (ETD) was accomplished using scaled Levenberg-Marquardt algorithms (QTIPLOT 0.9.9-rc9; IONDEV SRL 2020). The acquisition dates and number of data points for each bandpass used for the determination of ToM values and/or Roche modeling are summarized in Table 2. The results from these analyses are separately discussed for each binary system in the subsections below.

3.1.1 EI CMi

EI CMi was initially detected in the calibration fields for the Sloan Digital Sky Survey (Henden and Stone 1998) and confirmed to be an EW binary by Greaves and Wils (2003). Later on (2001–2009) EI CMi was also captured by the All Sky Automated Survey (ASAS, Pojmański *et al.* 2005). When period folded by ANOVA (Paunzen and Vanmunster 2016), LC data from ASAS yielded an orbital period of 0.362536 ± 0.000006 d.

Fifteen new ToM measurements (5 / bandpass) were extracted from photometric data acquired at DBO. These along with seven other eclipse timings found in the literature (Table 3) were used to calculate a new linear ephemeris (Equation 1) based on near term data produced between 2014 and 2020:

$$\text{Min.I (HJD)} = 2458899.4685\,(3) + 0.36253496\,(13)\,\text{E}. \quad (1)$$

Table 1. Astrometric coordinates (J2000), V-magnitudes and color indices (B–V) for EI CMi (Figure 1), NSVS 3092802 (Figure 2), V958 Mon (Figure 3), and V1309 Her (Figure 4) with their corresponding comparison stars used in this photometric study.

Star Identification	*R.A. (J2000)* h m s	*Dec. (J2000)* ° ′ ″	*V mag.*	*(B–V)*
(T) EI CMi[a]	07 57 06.278	+01 17 19.91	13.239	0.645
(1) GSC 00180-1688	07 50 09.835	+00 45 52.16	12.250	0.508
(2) GSC 00180-1188	07 47 48.722	+00 12 53.28	11.931	0.716
(3) GSC 00180-1176	07 45 08.287	+00 34 16.39	13.077	0.430
(4) GSC 00180-2269	07 51 52.498	+00 39 38.05	12.854	0.521
(5) GSC 00180-2280	07 51 24.298	+00 05 05.82	12.664	0.491
(T) NSVS 3092802[a]	19 47 22.495	+53 52 34.32	13.075	0.830
(1) GSC 03935-0749	19 47 33.233	+53 55 40.76	11.735	0.708
(2) GSC 03935-0605	19 47 25.318	+53 54 42.77	12.992	0.751
(3) GSC 03935-0365	19 46 49.236	+53 52 21.11	12.043	0.641
(4) GSC 03935-0885	19 46 44.561	+53 50 37.97	12.623	0.751
(5) GSC 03935-1077	19 46 58.442	+53 45 45.18	11.760	0.614
(T) V958 Mon[b]	06 22 06.393	+04 28 16.47	11.976	0.844
(1) GSC 00140-1092	06 21 28.259	+04 22 59.44	12.750	0.534
(2) GSC 00140-0803	06 21 55.665	+04 26 50.65	13.305	0.553
(3) GSC 00140-1189	06 21 56.880	+04 27 05.92	12.794	0.602
(4) GSC 00140-0335	06 21 28.259	+04 22 59.44	13.434	0.600
(5) GSC 00140-1059	06 22 06.121	+04 29 51.18	12.549	1.372
(T) V1309 Her[b]	17 55 35.842	+43 48 20.15	12.123	0.560
(2) GSC 03101-1293	17 55 23.098	+43 54 29.38	11.329	0.677
(3) GSC 03101-1051	17 54 45.406	+43 51 10.62	13.237	0.785
(4) GSC 03101-1288	17 54 47.784	+43 50 36.64	13.023	0.760
(5) GSC 03101-1624	17 55 27.878	+43 49 06.49	13.394	0.718

[a] V-mag and (B–V) for comparison stars derived from MPOSC3 database described by Warner (2007). [b] V-mag and (B–V) for comparison stars derived from APASS DR9 database described by Henden et al. *(2009, 2010, 2011) and Smith* et al. *(2011).*

When all ToM data were included (2002–2019), plotting (Figure 5) the difference between observed eclipse times and those predicted by the linear ephemeris against epoch (cycle number) reveals what appears to be a quadratic relationship (Equation 2) where:

$$\text{ETD} = -4.658 \pm 5.07 \cdot 10^{-4} - 5.715 \pm 2.503 \cdot 10^{-7}\,\text{E} - 1.054 \pm 0.147 \cdot 10^{-10}\,\text{E}^2. \quad (2)$$

In this case the ETD residuals vs. epoch can be described by a second order polynomial with a negative quadratic coefficient ($-1.054 \cdot 10^{-10}$), suggesting that the orbital period has been slowly decreasing over time at the rate of 0.0184 (26) $s \cdot y^{-1}$. A secular period change associated with an ETD diagram described by a parabola is often attributed to mass transfer or by angular momentum loss (AML) due to magnetic stellar wind. Ideally, when AML dominates, the net effect is a decreasing orbital period. If conservative mass transfer from the primary to a secondary star prevails, then the orbital period can also speed up. The separation increases when conservative mass transfer from the less massive to a more massive component takes place or spherically symmetric mass loss from either body (e.g. a wind but not magnetized) occurs. In mixed situations (e.g. mass transfer from less massive star, together with AML) the orbit evolution depends on which process prevails. It should

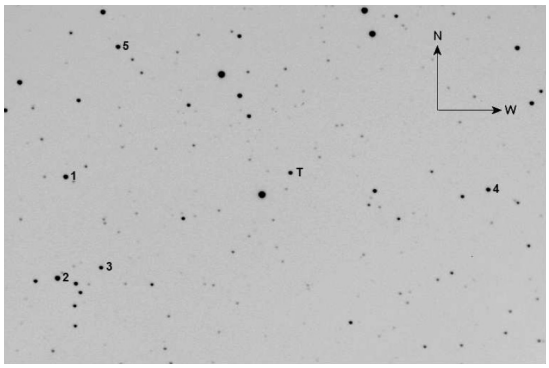

Figure 1. CCD image (V-mag) of EI CMi (T) showing the location of comparison stars (1–5) used to generate MPOSC3-derived magnitude estimates. The FOV for all OCBs reported herein is 17.2 × 11.5 arcmin.

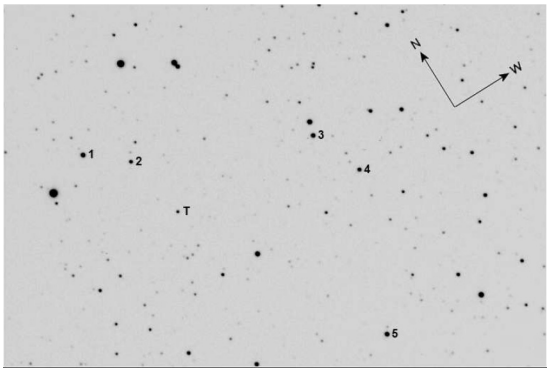

Figure 2. CCD image (V-mag) of NSVS 3092802 (T) showing the location of comparison stars (1–5) used to generate MPOSC3-derived magnitude estimates.

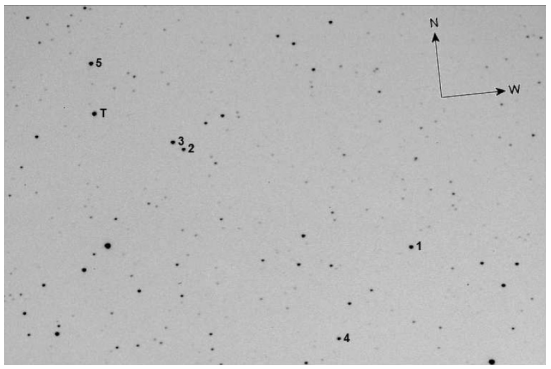

Figure 3. CCD image (V-mag) of V958 Mon (T) showing the location of comparison stars (1–5) used to generate APASS-derived magnitude estimates.

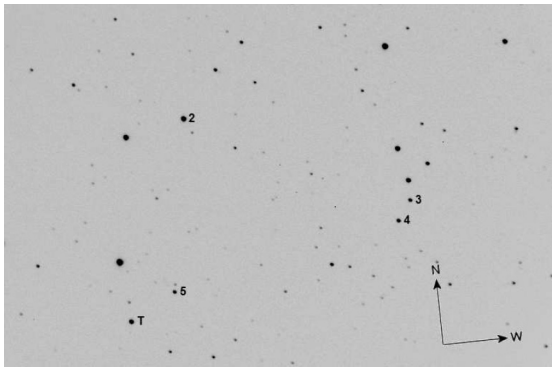

Figure 4. CCD image (V-mag) of V1309 Her (T) showing the location of comparison stars (2–5) used to generate APASS-derived magnitude estimates.

Table 2. Chronicle of image acquisition dates and number of data points in each bandpass (BVI_cR_c) used for the determination of ToM values and/or Roche modeling.

Target Identification	*B*	*V*	I_c	R_c	*Dates*
EI CMi	425	428	438	—	December 21, 2018–February 7, 2019
NVSV 3092802	612	634	619	—	September 22, 2018–June 3, 2019
V958 Mon[a]	289	304	297	—	January 31, 2018–February 4, 2018
V958 Mon	271	295	277	295	November 27, 2018–December 12, 2018
V1309 Her	413	381	424	—	June 21, 2018–June 25, 2018

[a] *LCs incomplete only used for determination of ToM values.*

Table 3. EI CMi times-of-minimum (April 25, 2002–February 7, 2019), cycle number and residuals (ETD) between observed and predicted times derived from the updated linear ephemeris (Equation 1).

HJD 2400000+	*HJD Error*	*Cycle No.*	*ETD*[a]	*Reference*
52390.49000	nr	–17954	–0.02582	1
53478.47100	nr	–14953	–0.01224	2
55564.86480	0.00030	–9198	–0.00714	2
56726.43420	0.00170	–5994	0.00024	3
56968.60670	0.00020	–5326	–0.00061	4
57013.56200	0.00200	–5202	0.00036	5
58473.85137	0.00023	–1174	–0.00110	6
58473.85231	0.00017	–1174	–0.00015	6
58473.85325	0.00020	–1174	0.00078	6
58475.84528	0.00033	–1168.5	–0.00113	6
58475.84560	0.00025	–1168.5	–0.00081	6
58475.84777	0.00037	–1168.5	0.00136	6
58479.83289	0.00030	–1157.5	–0.00141	6
58479.83393	0.00011	–1157.5	–0.00036	6
58479.83490	0.00027	–1157.5	0.00060	6
58487.80863	0.00033	–1135.5	–0.00143	6
58487.81033	0.00016	–1135.5	0.00027	6
58487.81096	0.00025	–1135.5	0.00089	6
58521.70709	0.00010	–1042	0.00001	6
58521.70799	0.00024	–1042	0.00091	6
58521.70890	0.00030	–1042	0.00182	6
58899.46830	0.00010	0	–0.00021	7

[a] *ETD = Eclipse Time Difference.* [b] *nr = Not reported.*
References: 1. Greaves and Wils (2003); 2. Diethelm (2011); 3. Hübscher and Lehmann (2015); 4. Juryšek et al. *(2017); 5. Paschke (2015); 6. This study at DBO; 7. Paschke (2020).*

be noted that only six eclipse timings for EI CMi are available before 2018. Nonetheless, the apparent quadratic fit of the ETD residuals (Figure 5), would suggest a secular change in the orbital period similar to many other contact systems reported in the literature (Giménez *et al.* 2006). Given the paucity of data, no other underlying variations in the orbital period stand out such as those that might be caused by magnetic cycles (Applegate 1992) or the presence of an additional gravitationally bound stellar-sized body. At a minimum, another decade of precise times of minimum will still be needed to confirm whether the orbital period of this system is truly changing in a predictable fashion.

3.1.2. NSVS 3092802

Broad band (450–1000 nm) monochromatic CCD-derived photometric data for this system were first obtained from the ROTSE-I survey between 1999 and 2000 (Akerlof *et al.* 2000;

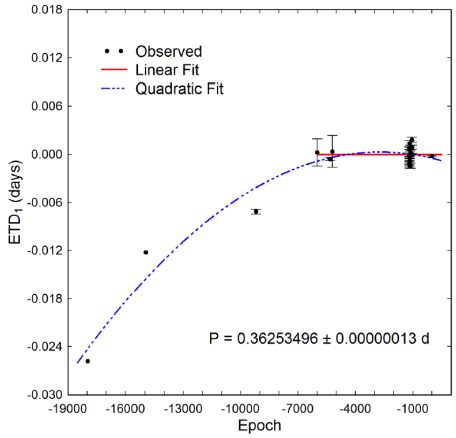

Figure 5. Eclipse timing differences (ETD) vs. epoch for EI CMi calculated using the updated linear ephemeris (Equation 1). When available, measurement uncertainty is denoted by the hatched vertical lines. The dashed blue line represents the quadratic fit while the solid red line within the figure insert indicates the linear fit.

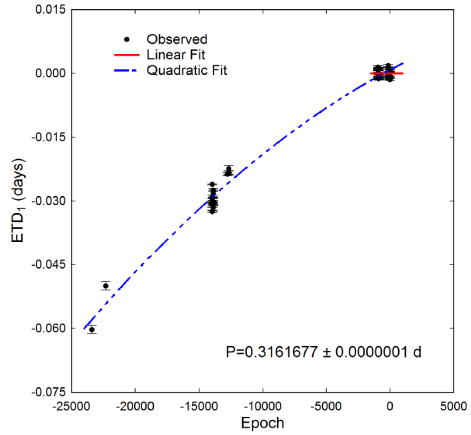

Figure 6. Eclipse timing differences (ETD) vs. epoch for NSVS 3092802 calculated using the updated linear ephemeris (Equation 3). Measurement uncertainty is denoted by the hatched vertical lines. The solid red line within the figure illustrates the linear fit while the blue dashed line represents the quadratic fit (Equation 4) from all data.

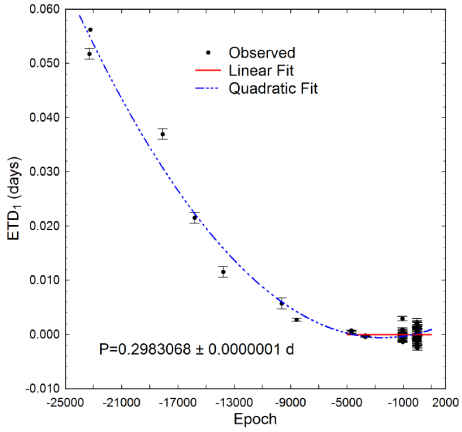

Figure 7. Eclipse timing differences (ETD) vs. epoch for V958 Mon calculated using the updated linear ephemeris (Equation 5). Measurement uncertainty is denoted by the hatched vertical lines. The solid red line within the figure indicates the linear fit while the blue dashed line represents the quadratic fit (Equation 6) from all data.

Table 4. NSVS 3092802 times-of-minimum (April 20, 1999–July 20, 2019), cycle number and residuals (ETD) between observed and predicted times derived from the updated linear ephemeris (Equation 3).

HJD 2400000+	*HJD Error*	*Cycle No.*	*ETD*[a]	*Ref.*
51288.83150	0.0010	–23392	–0.06025	1
51630.77720	0.0010	–22310.5	–0.04997	1
54261.62850	0.0002	–13989.5	–0.03050	2
54265.58132	0.0004	–13977	–0.02977	2
54266.53348	0.0001	–13974	–0.02612	2
54267.63531	0.0006	–13970.5	–0.03088	2
54270.63727	0.0003	–13961	–0.03250	2
54277.59640	0.0004	–13939	–0.02907	2
54279.65005	0.0006	–13932.5	–0.03051	2
54288.50580	0.0004	–13904.5	–0.02745	2
54290.55753	0.0003	–13898	–0.03081	2
54291.50600	0.0003	–13895	–0.03085	2
54291.66478	0.0009	–13894.5	–0.03015	2
54292.61189	0.0008	–13891.5	–0.03155	2
54293.56367	0.0008	–13888.5	–0.02827	2
54295.61650	0.0003	–13882	–0.03053	2
54645.62100	0.0004	–12775	–0.02373	2
54663.48481	0.0004	–12718.5	–0.02339	2
54670.59962	0.0006	–12696	–0.02236	2
54684.50996	0.0005	–12652	–0.02340	2
58383.69494	0.0003	–952	–0.00107	3
58383.69685	0.0002	–952	0.00084	3
58383.69744	0.0003	–952	0.00143	3
58389.70235	0.0002	–933	–0.00085	3
58389.70339	0.0001	–933	0.00020	3
58389.70431	0.0002	–933	0.00111	3
58396.65790	0.0003	–911	–0.00099	3
58396.65904	0.0000	–911	0.00015	3
58396.65993	0.0002	–911	0.00104	3
58398.71274	0.0004	–904.5	–0.00124	3
58398.71286	0.0004	–904.5	–0.00112	3
58398.71521	0.0006	–904.5	0.00123	3
58401.71667	0.0003	–895	–0.00091	3
58401.71757	0.0000	–895	0	3
58401.71864	0.0003	–895	0.00107	3
58411.67596	0.0003	–863.5	–0.00089	3
58411.67635	0.0002	–863.5	–0.00051	3
58411.67671	0.0002	–863.5	–0.00014	3
58632.83577	0.0006	–164	–0.00043	3
58632.83591	0.0007	–164	–0.00028	3
58634.89022	0.0004	–157.5	–0.00106	3
58634.89239	0.0002	–157.5	0.00111	3
58634.89302	0.0004	–157.5	0.00173	3
58637.89387	0.0005	–148	–0.00101	3
58637.89603	0.0002	–148	0.00115	3
58637.89667	0.0003	–148	0.00179	3
58663.66249	0.0001	–66.5	–0.00006	4
58663.82083	0.0002	–66	0.0002	4
58680.73610	0.0002	–12.5	0.00049	4
58681.84148	0.0000	–9	–0.00072	4
58682.79091	0.0003	–6	0.00021	4
58683.73774	0.0002	–3	–0.00147	4
58683.89634	0.0001	–2.5	–0.00095	4
58684.68702	0.0001	0	–0.00068	4
58684.84642	0.0002	0.5	0.00063	4

[a] *ETD = Eclipse Time Difference. References: 1. NSVS; 2. SuperWASP; 3. This study at DBO; 4. The International Variable Star Index.*
This table is available through the AAVSO ftp site at

ftp://ftp.aavso.org/public/datasets/Alton-eicmi-tab4.txt

(if necessary, copy and paste link into the address bar of a web browser).

Table 5. V958 Mon times-of-minimum (December 3, 1999–December 12, 2018), cycle number and residuals (ETD) between observed and predicted times derived from the updated linear ephemeris (Equation 5).

HJD 2400000+	HJD Error	Cycle No.	ETD[a]	Ref.	HJD 2400000+	HJD Error	Cycle No.	ETD[a]	Ref.
51515.9100	0.0010	–23294.5	0.05175	1	58451.7891	0.0005	–43.5	–0.00105	7
51525.8910[b]	nr[c]	–23261	0.03948	2	58451.7901	0.0002	–43.5	–0.00008	7
51535.9010	0.0010	–23227.5	0.05620	1	58451.7906	0.0005	–43.5	0.00043	7
53068.5822	0.0010	–18089.5	0.03694	3	58451.7912	0.0003	–43.5	0.00096	7
53744.6792	0.0010	–15823	0.02152	3	58451.7921	0.0007	–43.5	0.00188	7
54355.8999	0.0010	–13774	0.01154	3	58451.9376	0.0006	–43	–0.00172	7
55588.6470	0.0003	–9641.5	0.00570	4	58451.9392	0.0015	–43	–0.00015	7
55907.8323	0.0003	–8571.5	0.00270	5	58451.9393	0.0009	–43	–0.00007	7
57065.7080	0.0001	–4690	0.00046	6	58451.9396	0.0002	–43	0.00026	7
57066.6032	0.0001	–4687	0.00074	6	58451.9407	0.0005	–43	0.00133	7
57071.6742	0.0001	–4670	0.00053	6	58455.8150	0.0010	–30	–0.00231	7
57359.8379	0.0001	–3704	–0.00017	6	58455.8160	0.0006	–30	–0.00129	7
57360.7327	0.0002	–3701	–0.00029	6	58455.8163	0.0010	–30	–0.00104	7
57361.7766	0.0002	–3697.5	–0.00046	6	58455.8169	0.0017	–30	–0.00043	7
57362.8209	0.0002	–3694	–0.00023	6	58455.8172	0.0001	–30	–0.00014	7
57363.7158	0.0002	–3691	–0.00025	6	58455.9664	0.0014	–29.5	–0.00004	7
58149.6041	0.0004	–1056.5	–0.00132	7	58455.9675	0.0010	–29.5	0.00102	7
58149.6051	0.0001	–1056.5	–0.00027	7	58455.9677	0.0008	–29.5	0.00120	7
58149.6083	0.0007	–1056.5	0.00292	7	58455.9684	0.0008	–29.5	0.00190	7
58149.7535	0.0003	–1056	–0.00105	7	58456.8606	0.0006	–26.5	–0.00085	7
58149.7540	0.0001	–1056	–0.00053	7	58456.8616	0.0001	–26.5	0.00018	7
58149.7545	0.0002	–1056	–0.00002	7	58456.8621	0.0007	–26.5	0.00067	7
58150.6482	0.0003	–1053	–0.00126	7	58456.8626	0.0004	–26.5	0.00117	7
58150.6490	0.0001	–1053	–0.00041	7	58456.8636	0.0011	–26.5	0.00218	7
58150.6500	0.0003	–1053	0.00054	7	58461.7809	0.0011	–10	–0.00252	7
58150.7974	0.0003	–1052.5	–0.00116	7	58461.7821	0.0008	–10	–0.00136	7
58150.7986	0.0001	–1052.5	–0.00003	7	58461.7832	0.0008	–10	–0.00030	7
58150.7996	0.0004	–1052.5	0.00095	7	58461.7843	0.0003	–10	0.00087	7
58151.6922	0.0003	–1049.5	–0.00138	7	58461.7853	0.0008	–10	0.00179	7
58151.6932	0.0001	–1049.5	–0.00034	7	58464.7643	0.0009	0	–0.00224	7
58151.6942	0.0003	–1049.5	0.00069	7	58464.7656	0.0004	0	–0.00098	7
58153.7810	0.0001	–1042.5	–0.00071	7	58464.7661	0.0006	0	–0.00048	7
58153.7815	0.0001	–1042.5	–0.00020	7	58464.7667	0.0002	0	0.00014	7
58153.7822	0.0002	–1042.5	0.00051	7	58464.7677	0.0006	0	0.00115	7
58161.6866	0.0001	–1016	–0.00017	8	58464.9160	0.0013	0.5	0.00030	7
58449.9996	0.0004	–49.5	–0.00077	7	58464.9162	0.0002	0.5	0.00051	7
58450.0002	0.0010	–49.5	–0.00015	7	58464.9165	0.0009	0.5	0.00082	7
58450.0004	0.0012	–49.5	0.00005	7	58464.9173	0.0007	0.5	0.00166	7
58450.0006	0.0012	–49.5	0.00026	7					

[a] *ETD = Eclipse Time Difference.* [b] *Outlier.* [c] *Not reported. References: 1. NSVS; 2. Otero* et al. *(2004); 3. ASAS; 4. Diethelm (2011); 5. Nelson (2012); 6. Michaels (2016); 7. This study at DBO; 8. The International Variable Star Index.*
This table is available through the AAVSO ftp site at ftp://ftp.aavso.org/public/datasets/Alton-eicmi-tab5.txt (if necessary, copy and paste link into the address bar of a web browser).

Gettel *et al.* 2006) and thereafter classified as a WUMa-type variable according to Hoffman *et al.* 2009. These data are maintained in the Northern Sky Variability Survey (NSVS; Woźniak *et al.* 2004) archives (https://skydot.lanl.gov/nsvs/nsvs.php). NSVS 3092802 was also imaged during the SuperWASP survey (Butters *et al.* 2010) which provided a rich source of photometric data taken (30-s exposures) at modest cadence that repeats every 9 to 12 min. In some cases (18) SuperWASP measurements taken between 2007 and 2008 were amenable to further analysis using the method of Kwee and van Woerden (1956) to estimate ToM values. Light curve data (BVI_c) acquired at DBO produced 26 new ToM values. These results along with other eclipse timings (Table 4) derived from the NSVS archives, SuperWASP, and the International Variable Star Index were used to calculate a new linear ephemeris (Equation 3) based on near-term data (2018–2019):

$$\text{Min.I (HJD)} = 2458684.6877\,(3) + 0.3161677\,(4)\,\text{E}. \quad (3)$$

When all ToM data were included (1999–2019), a quadratic relationship (Equation 4) was established after plotting (Figure 6) the difference between the observed eclipse times and those predicted by the linear ephemeris against epoch whereby:

$$\text{ETD} = 8.01 \pm 3.06 \cdot 10^{-4} + 1.59 \pm 0.12 \cdot 10^{-6}\,\text{E} - 3.93 \pm 0.66 \cdot 10^{-11}\,\text{E}^2. \quad (4)$$

In this case the ETD residuals vs. epoch suggest that the orbital period has been very slowly decreasing ($-0.008\,(1)\,\text{s} \cdot \text{y}^{-1}$), based on the negative quadratic coefficient ($-3.93\,(66) \cdot 10^{-11}$).

3.1.3. V958 Mon

Monochromatic photometric data for V958 Mon were first obtained from the ROTSE-I survey between 1999 and 2000 (Akerlof *et al.* 2000; Woźniak *et al.* 2004; Gettel *et al.* 2006) and classified later as a W UMa-type variable (Hoffman *et al.* 2009).

Table 6. V1309 Her times-of-minimum (June 29, 1999–June 25, 2018), cycle number and residuals (ETD) between observed and predicted times derived from the updated linear ephemeris (Equation 7).

HJD 2400000+	*HJD Error*	*Cycle No.*	*ETD*[a]	*Ref.*	*HJD 2400000+*	*HJD Error*	*Cycle No.*	*ETD*[a]	*Ref.*
51358.6965	0.0008	–18752	0.03764	1	54628.6353	0.0002	–9911.5	0.01117	2
51364.7978	0.0009	–18735.5	0.03585	1	54639.5444	0.0005	–9882	0.00868	2
53121.5467	0.0005	–13986	0.01760	1	54643.4312	0.0004	–9871.5	0.01166	2
53143.3703	0.0019	–13927	0.01800	1	54650.4557	0.0002	–9852.5	0.00842	2
53150.3981	0.0006	–13908	0.01800	1	54651.5686	0.0003	–9849.5	0.01162	2
53150.5821	0.0015	–13907.5	0.01705	1	54652.4907	0.0003	–9847	0.00908	2
53152.6185	0.0003	–13902	0.01904	2	54656.5613	0.0002	–9836	0.01091	2
53154.4662	0.0005	–13897	0.01736	1	54670.4290	0.0003	–9798.5	0.00792	2
53154.6557	0.0004	–13896.5	0.02190	2	54674.5005	0.0003	–9787.5	0.01065	2
53162.6047	0.0003	–13875	0.01840	2	54675.4226	0.0004	–9785	0.00804	2
53163.5308	0.0006	–13872.5	0.01983	2	54681.5281	0.0004	–9768.5	0.01049	2
53169.6355	0.0002	–13856	0.02139	2	54682.4520	0.0002	–9766	0.00964	2
53171.6701	0.0002	–13850.5	0.02166	2	54684.4864	0.0005	–9760.5	0.00975	2
53172.5934	0.0003	–13848	0.02024	2	54919.9164	0.0003	–9124	0.00808	6
53173.5150	0.0003	–13845.5	0.01710	1	55067.4980	0.0008	–8725	0.00575	7
53177.5864	0.0007	–13834.5	0.01978	2	55309.9582	0.0002	–8069.5	0.00656	8
53179.6159	0.0009	–13829	0.01490	2	56540.3713	0.0050	–4743	–0.00163	9
53198.4841	0.0004	–13778	0.01902	2	56799.4766	0.0067	–4042.5	–0.00052	10
53203.4748	0.0005	–13764.5	0.01625	1	57132.5591	0.0020	–3142	0.00085	11
53204.5877	0.0005	–13761.5	0.01947	2	57516.5008	0.0060	–2104	0.00228	11
53208.4701	0.0006	–13751	0.01814	2	58288.8163	0.0004	–16	–0.00139	12
53223.4501	0.0003	–13710.5	0.01779	2	58288.8172	0.0002	–16	–0.00045	12
53227.5205	0.0003	–13699.5	0.01940	2	58290.8506	0.0002	–10.5	–0.00142	12
53229.3671	0.0025	–13694.5	0.01662	1	58290.8517	0.0003	–10.5	–0.00029	12
53229.5522	nr[b]	–13694	0.01678	1	58290.8525	0.0003	–10.5	0.00046	12
53230.4812	0.0004	–13691.5	0.02106	2	58292.7001	0.0002	–5.5	–0.00133	12
53242.4995	0.0006	–13659	0.01812	2	58292.7011	0.0001	–5.5	–0.00036	12
53250.4519	0.0008	–13637.5	0.01800	1	58292.7021	0.0004	–5.5	0.00069	12
53258.4049	0.0004	–13616	0.01848	2	58292.8844	0.0003	–5	–0.00196	12
53617.3741	0.0011	–12645.5	0.01462	3	58292.8854	0.0002	–5	–0.00099	12
53941.3920	0.0010	–11769.5	0.01357	4	58292.8864	0.0002	–5	–0.00002	12
54316.4573	0.0002	–10755.5	0.01580	2	58294.7343	0.0003	0	–0.00155	12
54328.4762	0.0003	–10723	0.01351	2	58294.7363	0.00027	0	0.00048	12
54331.4360	0.0002	–10715	0.01422	2	58294.7369	0.00027	0	0.00102	12
54333.4700	0.0001	–10709.5	0.01382	2	58294.9196	0.0002	0.5	–0.00118	12
54364.3497	0.0050	–10626	0.00817	5	58294.9206	0.0001	0.5	–0.00021	12
54623.6415	0.0002	–9925	0.01088	2	58294.9216	0.0003	0.5	0.00084	12
54626.5978	0.0006	–9917	0.00807	2					

[a] *ETD = Eclipse Time Difference.* [b] *Not reported. References: 1. Blättler and Diethelm (2004); 2. SuperWASP; 3. Diethelm (2006); 4. Diethelm (2007); 5. Diethelm (2008); 6. Nelson (2010); 7. Diethelm (2010); 8. Nelson (2011); 9. Hübscher (2014); 10. Hübscher and Lehmann (2015); 11. Hübscher (2017); 12. This study at DBO. This table is available through the AAVSO ftp site at ftp://ftp.aavso.org/public/datasets/Alton-eicmi-tab6.txt (if necessary, copy and paste link into the address bar of a web browser).*

Included with the ToM data summarized in Table 5 are 51 new values (BVI_cR_c) acquired at DBO, 19 times which were gathered from the literature, and five others that were extracted from period-folded LCs from the NSVS (0.298301 ± 0.000012 d) and ASAS (0.298302 ± 0.000006 d) surveys. Accordingly a new linear ephemeris (Equation 5) was calculated from near-term eclipse timings (2015–2018):

$$\text{Min.I (HJD)} = 2458464.7666\,(2) + 0.2983068\,(1)\,\text{E}. \quad (5)$$

When all data were included (1999–2018) a quadratic relationship (Equation 6) was established after plotting (Figure 7) the difference between the observed eclipse times and those predicted by the linear ephemeris against epoch such that:

$$\text{ETD} = 1.681 \pm 1.95 \cdot 10^{-4} + 6.335 \pm 1.125 \cdot 10^{-7}\,\text{E} + 1.283 \pm 0.055 \cdot 10^{-10}\,\text{E}^2. \quad (6)$$

Since the quadratic coefficient is positive ($+1.283 \cdot 10^{-10}$), in this case the ETD residuals vs. epoch suggests that the orbital period has been increasing ($0.027\,(1)\,\text{s} \cdot \text{y}^{-1}$).

3.1.4. V1309 Her

Photometric data for V1309 Her were initially obtained from the ROTSE-I survey between 1999 and 2000 (Akerlof *et al.* 2000; Woźniak *et al.* 2004; Gettel *et al.* 2006) and thereafter classified as a WUMa-type variable, according to Hoffman *et al.* (2009). Between 2005 and 2013 the Catalina Sky Survey (Drake *et al.* 2014) also included photometric data from V1309 Her. This system was also imaged during the SuperWASP (Butters *et al.* 2010) survey in 2004 and 2006–2008. As previously described for NSVS 3092802, in some cases the cadence and LC quality were sufficiently high to determine new ToM values. The light curve derived from photometric data collected at DBO included 17 new ToM measurements which are summarized in Table 6. These results along with other published eclipse timings (Table 6) were used

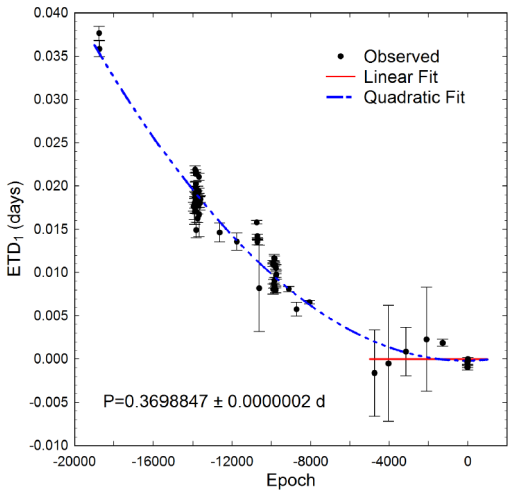

Figure 8. Eclipse timing differences (ETD) vs. epoch for V1309 Her calculated using the updated linear ephemeris (Equation 7). Measurement uncertainty is denoted by the hatched vertical lines. The solid red line within the figure indicates the linear fit while the blue dashed line represents the quadratic fit (Equation 8) from all data.

to calculate a new linear ephemeris (Equation 7) based on data acquired between 2015 and 2018:

$$\text{Min.I(HJD)} = 2458294.7356(5) + 0.3698846(2)\,E. \quad (7)$$

Secular analysis of potential period variations benefited significantly by the addition of eclipse timings captured by the SuperWASP survey (Butters *et al.* 2010). When all ToM data were included (1999–2018), plotting (Figure 8) the difference between the observed eclipse times and those predicted by the linear ephemeris against epoch reveals what appears to be a quadratic relationship (Equation 8) where:

$$\text{ETD} = -2.00 \pm 6.295 \cdot 10^{-4} + 2.211 \pm 1.511 \cdot 10^{-6}\,E + 1.023 \pm 0.090 \cdot 10^{-10}\,E^2. \quad (8)$$

In this case the ETD residuals vs. epoch can be described by an expression with a positive quadratic coefficient ($+1.023 \cdot 10^{-10}$), suggesting that the orbital period has been slowly increasing over time at the rate of $0.017(2)\,s \cdot y^{-1}$. This value, but not the sign for Q, would be refined as described below.

Another orbital period change was discovered which appears to be sinusoidal in nature and embedded within the residuals remaining after the initial quadratic fit (Equation 8). Cyclic changes of eclipse timings can result from the gravitational influence of unseen companion(s), the so-called light-time effect (LiTE). It is not unreasonable to propose that V1309 Her is a ternary system since a significant number (>50%) of contact binaries observed from the Northern Hemisphere exist as multiple systems (Pribulla and Ruciński 2006). To address this possibility LiTE analyses were performed using the simplex code for MATLAB® reported by Zasche (2009).

A quadratic relationship (Equation 9) between ETD and epoch takes the general form:

$$\text{ETD}_{\text{fitted}} = c + b \cdot E + Q \cdot E^2 + \tau. \quad (9)$$

When the orbital period change is monotonic, the last term ($\tau = 0$) can be ignored. However, in this case τ from Equation 9 is expanded as follows:

$$\tau = \frac{a_{12} \sin i}{c}\left[(1-e^2)\frac{\sin(\nu+\omega)}{1+c\cdot\cos\nu} + \sin\omega\right] \quad (10)$$

Accordingly, the associated parameters in the LITE equation (Irwin 1959) were derived, which include parameter values for P_3 (orbital period of star 3 and the 1–2 pair about their common barycenter), orbital eccentricity e, argument of periapsis ω, true anomaly ν, time of periastron passage T_0, and amplitude $A = a_{12} \sin i_3$. In this case a_{12} is the semi-major axis of the 1–2 pair's orbit about the three-star system center of mass, and i_3 is the orbital inclination of the putative third body in a three-star system.

Two viable solutions (Table 7) were produced using the Zasche *et al.* (2009) code for simplex optimization. The first (LITE-1; Figure 9) was derived with a circular orbit ($e = 0$) and the second where e was allowed to freely vary (LITE-2; Figure 10). Strictly based on the sum of squared residuals, the best fit was with an elliptical orbit (LITE-2) although the other parameter estimates where $e = 0$ may not be meaningfully different. The LITE-2 results are consistent with a putative third body orbiting elliptically ($e = 0.83 \pm 0.18$) every ~9.5 y at a distance no farther than 4.9 ± 1.1 A.U. from the common center of gravity. The minimum mass of a coplanar ($i_3 = 90°$) orbiting third body was calculated to be $\sim 0.126 \pm 0.001\,M_\odot$ based on the derived mass function ($f(M_3) = 0.0072 \pm 0.0001$). The corresponding added luminosity (L_3) of a third main sequence star was estimated to be ~0.03% according to Equation 11, where M_{min} is the estimated minimum mass ($i_3 = 90°$):

$$L_3(\%) = \frac{100 \cdot M_{min}^{3.5}}{L_1 + L_2 + M_{min}^{3.5}}. \quad (11)$$

This very small percent contribution of light would not be expected nor did it require adjustment by the WD2003 code third light parameter ($l_3 = 0$) in order to accurately simulate the LC model fits around minimum light (section 3.4).

Modulated changes in the orbital period can also result from magnetic activity cycles or apsidal motion of a binary pair. Since contact binary systems are tidally locked with circular orbits, apsidal motion can be immediately eliminated from consideration. Short-period binaries are magnetically very active due to the formation of photospheric starspots, chromospheric plages, and other high energy disturbances (Berdyugina 2005). The corresponding hydromagnetic dynamo can produce changes in the gravitational quadrupole moment of the active star via redistribution of the internal angular momentum with corresponding changes in the magnetic torque within the stellar convective zone. When the gravitational quadrupole moment of the active component increases, its companion experiences a stronger gravitational force which then moves closer to the system barycenter. The orbital period will decrease according to this scenario. By contrast, when the

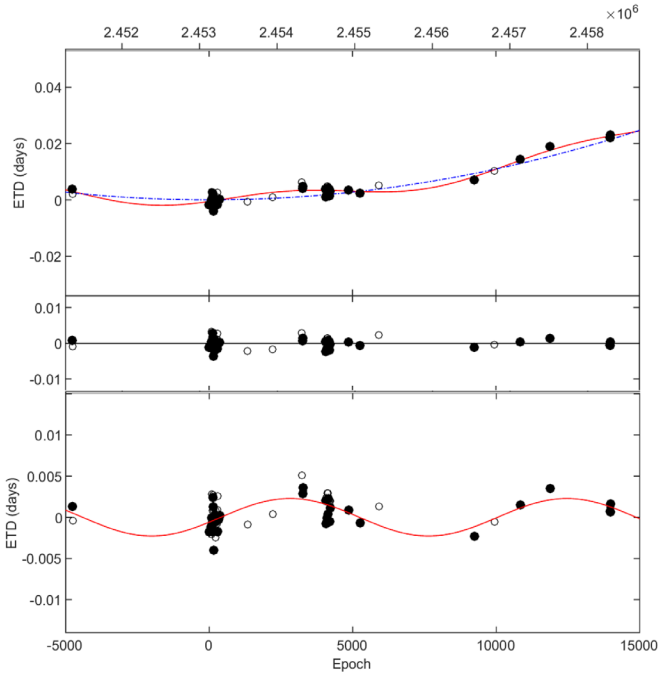

Figure 9. LITE-1 fit (Table 7) using eclipse timing differences (ETD) determined for V1309 Her between 1999 and 2018. The solid red line in the top panel describes the fit for circular (e=0) orbit (P_3=9.78 y) of a putative third body while the dashed blue line defines the quadratic fit from the eclipse timing residuals. Solid circles (●) represent times at Min I whereas open circles (○) indicate times at Min II. The middle panel illustrates the total residuals remaining after LITE analysis, and the bottom panel depicts the modeled fit after subtracting out the quadratic component.

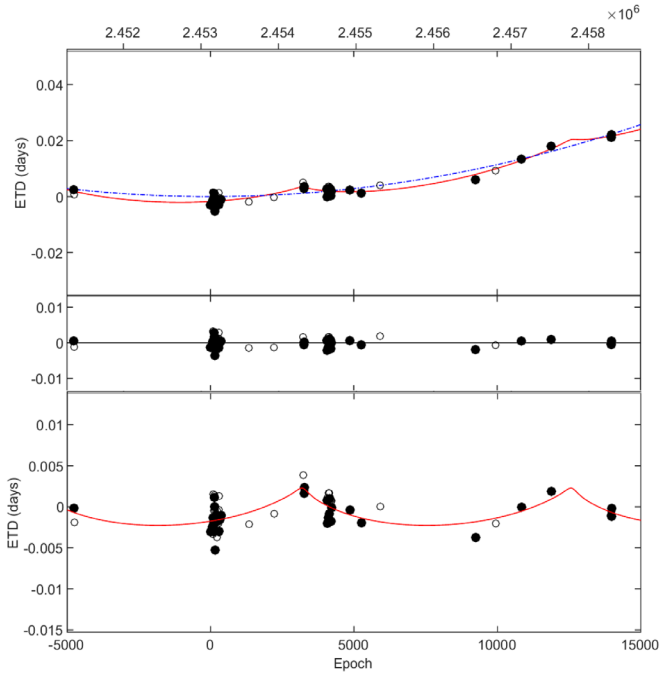

Figure 10. LITE-2 fit (Table 7) using eclipse timing differences (ETD) determined for V1309 Her between 1999 and 2018. The solid red line in the top panel describes the fit for an elliptical (e = 0.83) orbit (P_3=9.5 y) of a putative third body while the dashed blue line defines the quadratic fit from the eclipse timing residuals. Solid circles (●) represent times at Min I whereas open circles (○) indicate times at Min II. The middle panel illustrates the total residuals remaining after LiTE analysis, and the bottom panel depicts the modeled fit after subtracting out the quadratic component.

gravitational quadrupole moment of the active star weakens, the orbital period increases. A detailed examination of the energetics ($\Delta E/E_{sec}$) required to produce this effect attributed to Applegate (1992) was performed according to Völschow *et al.* (2016) and the accompanying "Eclipse Time Variation Calculator" webmodule (http://theory-starformation-group.cl/applegate/index.php). $\Delta E/E_{sec}$ is defined as the energy required to drive the Applegate mechanism divided by the available energy produced in the magnetically active star. This value determines whether the Applegate mechanism is energetically feasible. Solutions are provided from the two-zone model and the constant density model by Völschow *et al.* (2016), along with a solution based on the thin-shell model by Tian *et al.* (2009). Tian *et al.* (2009) derived a relationship between the energetics necessary to drive the Applegate mechanism and the observed variability in eclipse timings:

$$\frac{\Delta E}{E_{sec}} = 0.233 \cdot \left(\frac{M_{sec}}{M_\odot}\right)^{3} \cdot \left(\frac{R_{sec}}{R_\odot}\right)^{-10} \cdot \left(\frac{T_{sec}}{6000\ K}\right)^{-4} \cdot \left(\frac{a_{bin}}{R_\odot}\right)^{4} \cdot \left(\frac{\Delta P}{s}\right)^{2} \cdot \left(\frac{P_{mod}}{y}\right)^{-1}. \quad (12)$$

The measureables in this case include the secondary mass (M_{sec}), radius (R_{sec}), temperature (T_{sec}), semi-major axis of the binary pair (a_{bin}), the modulation period of the binary pair (P_{mod}), and ΔP where:

$$\frac{\Delta P}{P_{bin}} = 2\pi \left(\frac{O-C}{P_{mod}}\right). \quad (13)$$

Since the $\Delta E/E_{sec}$ value (0.0228) was below one, then this would energetically favor orbital period modulations that arise from the Applegate mechanism.

The two-zone model provides two solutions, one requiring more energy and one requiring less energy. Therein the finite shell two-zone model accounts for all essential physics involved with the Applegate effect from main-sequence low mass companions (0.1–0.6 $M_\odot$). Accordingly the latter energy solution is:

$$\frac{\Delta E^{-}}{E_{sec}} = k_1 \cdot \frac{M_{sec} R_{sec}^2}{P_{bin}^2 P_{mod} L_{sec}} \cdot \left(1 \pm \sqrt{(1 - k_2 G) \frac{a_{bin}^2 M_{sec} P_{bin}^2}{R_{sec}^5}} \frac{\Delta P}{P_{bin}}\right)^2, \quad (14)$$

wherein k_1 is assigned a value of 0.133 and k_2 is 3.42. Since the calculated value for $\Delta E^{-} / E_{sec}$ is less than unity (0.422), this model also indicates that V1309 Her is a potential candidate for orbital period modulation by magnetic cycles.

The apparent sinusoidal-like behavior is supported by data collected over the past 19 years, which is only equal to two cycles of orbital period variation. Therefore, some caution should be exercised such that these findings are considered preliminary and not a definitive solution. Moreover, at this time

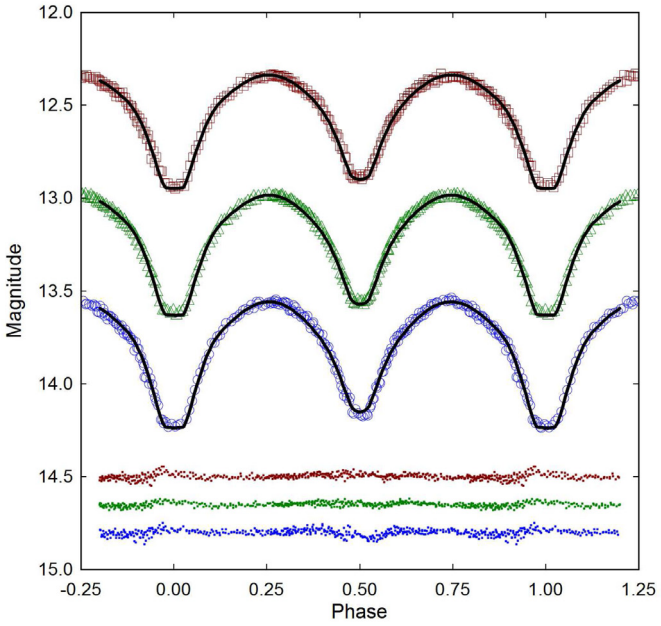

Figure 11. Period-folded (0.3625350 ± 0.0000001 d) CCD light curves for EI CMi produced from photometric data collected at DBO between December 21, 2018, and February 7, 2019. The top (I_c), middle (V) and bottom curve (B) shown above were reduced to MPOSC3-based catalog magnitudes using MPO CANOPUS. In this case, the Roche model assumed an W-subtype overcontact binary with no spots; residuals from the model fits are offset at the bottom of the plot to keep the values on scale.

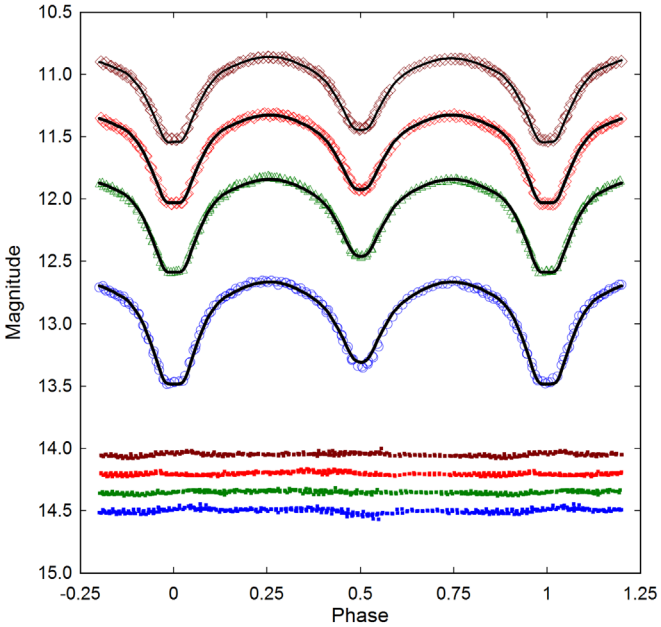

Figure 13. Period-folded (0.2983068 ± 0.0000001 d) CCD light curves for V958 Mon produced from photometric data obtained at DBO between November 27, 2018, and December 12, 2018. Starting from top to bottom the I_c, R_c, V, and B light curves were reduced to APASS DR9 catalog magnitudes using MPO CANOPUS. In this case, the Roche model assumed a W-type overcontact binary; residuals from the model fits are offset at the bottom of the plot to keep the values on scale.

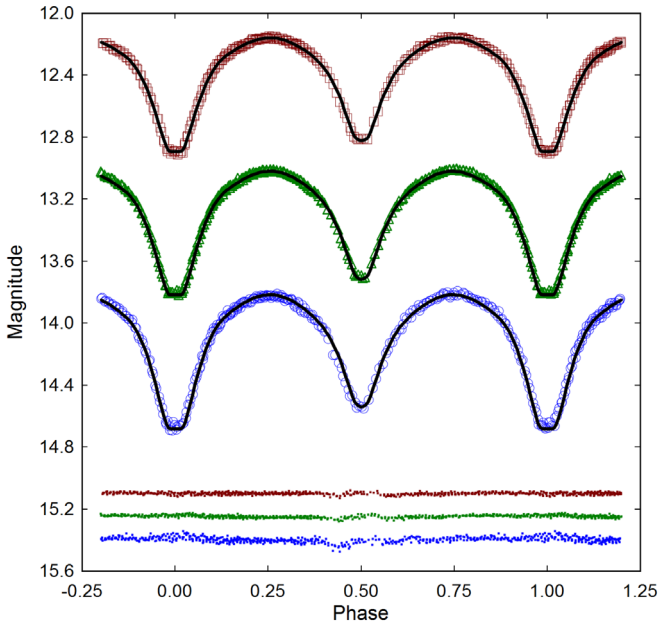

Figure 12. Period-folded (0.3161697 ± 0.0000001 d) CCD light curves acquired from NSVS 3092802 at DBO between September 22, 2018, and June 03, 2019. The top (I_c), middle (V) and bottom curve (B) shown above were reduced to MPOSC3-based catalog magnitudes using MPO CANOPUS. In this case, the Roche model assumed an W-subtype overcontact binary with no spots; residuals from the model fits are offset at the bottom of the plot to keep the values on scale.

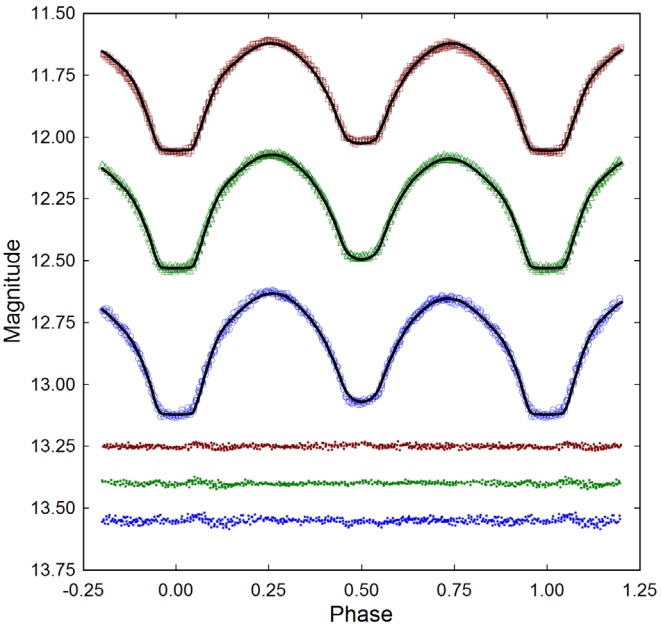

Figure 14. Period-folded (0.3698847 ± 0.0000002 d) CCD light curves for V1309 Her obtained at DBO between June 21, 2018, and June 25, 2018. The top (I_c), middle (V), and bottom curves (B) were reduced to APASS DR9 catalog magnitudes using MPO CANOPUS. The Roche model assumed a W-type overcontact binary with one cool spot on each star; residuals from the model fits are offset at the bottom of the plot to keep the values on scale.

Table 7. Orbital period modulation (P_3) and putative third-body solution to the light-time effect (LiTE) observed from changes in V1309 Her eclipse timings.

Parameter	*Units*	*LiTE-1*[a]	*LiTE-2*[b]
HJD0–2400000		53121.5485 ± 0.0003	53121.5498 ± 0.0003
P_3	(y)	9.78 ± 0.37	9.50 ± 0.39
ω		0.000651 ± 0.000025	0.000670 ± 0.000027
A (semi-ampl.)	(d)	0.0023 ± 0.0008	0.0023 ± 0.0005
ω	(°)	—	103.6 ± 22.3
e_3		0 ± 0.136	0.83 ± 0.18
a'_{12} sin i'	(a.u.)	0.3949 ± 0.1374	0.4013 ± 0.0859
$f(M_3)$(mass func.)	($M_\odot$)	0.00064 ± 0.00012	0.00072 ± 0.00001
M_3 (i=90°)	($M_\odot$)	0.121 ± 0.008	0.126 ± 0.001
M_3 (i=60°)	($M_\odot$)	0.141 ± 0.008	0.146 ± 0.001
M_3 (i=30°)	($M_\odot$)	0.255 ± 0.016	0.265 ± 0.001
Q (quad. coeff.)	(10^{-10})	1.0964 ± 0.0001	1.141 ± 0.0001
Sum of squared residuals		0.00134781	0.00120855

[a] *Zasche* et al. *(2009)—simplex optimization with third body circular orbit.* [b] *Zasche* et al. *(2009)—simplex optimization with third body elliptical orbit.*

it is not possible to firmly establish whether the gravitational effect of a third body or variations in the quadrupole moment is responsible for cyclic changes in the orbital period of V1309 Her. Unfortunately, without other supporting evidence such as might be derived from space-based spectro-interferometry and/or direct imaging, secular analyses still leaves us with two equally plausible but distinctly different phenomenological origins for cyclic modulation of the dominant orbital period.

3.2. Effective temperature estimation

The effective temperature (T_{eff1}) of the more massive, and therefore most luminous component (defined as the primary star herein) was derived from a composite of astrometric (USNO-A2.0, USNO-B1.0, and UCAC4) and photometric (2MASS, SDSS-DR8, and APASS) survey measurements that were as necessary transformed to (B–V) (http://www.aerith.net/astro/color_conversion.html; http://brucegary.net/dummies/method0.html). Interstellar extinction (A_V) and reddening ($E(B–V) = A_V / 3.1$) were estimated for targets within the Milky Way Galaxy according to the procedure described by Amôres and Lepine (2005). This model, which is simulated in a Linux-based companion program (ALEXTIN; http://www.galextin.org/explain.html), requires the Galactic coordinates (*l, b*) and the distance in kpc (Bailer-Jones 2015). After subtracting out reddening to arrive at a value for intrinsic color, $(B–V)_0$, T_{eff1} estimates were interpolated for each system using the values reported for main sequence dwarf stars by Pecaut and Mamajek (2013). Additional sources used to establish a median value for each T_{eff1} included low resolution spectra obtained from LAMOST-DR5 (Zhao *et al.* 2012; Rui *et al.* 2019), the Gaia DR2 release of stellar parameters (Andrae *et al.* 2018), and an empirical relationship (Houdashelt *et al.* 2000) based on intrinsic color where $0.32 \leq (B–V)_0 \leq 1.35$. The median results, summarized in Table 8, were adopted for Roche modeling of LCs from each binary system.

3.3. Roche modeling approach

Roche modeling of LC data from all four OCBs was initially performed with PHOEBE 0.31a (Prša and Zwitter 2005) and then refined using WDWINT56A (Nelson 2009). Both programs feature a MS Windows-compatible GUI interface to the Wilson-Devinney WD2003 code (Wilson and Devinney 1971; Wilson 1979, 1990). WDWINT56A incorporates Kurucz's atmosphere models (Kurucz 2002) that are integrated over BVR_cI_c passbands. In all cases, the selected model was Mode 3 for an overcontact binary. Other modes (detached and semi-detached) were attempted but never approached the model fit (χ^2 value reported for each bandpass in PHOEBE 0.31a) achieved with Mode 3. With each of these variable systems, the internal energy transfer to the surface is driven by convective (7500 K) rather than radiative processes; therefore, the value for bolometric albedo ($A_{1,2} = 0.5$) was assigned according to Ruciński (1969) while the gravity darkening coefficient ($g_{1,2} = 0.32$) was adopted from Lucy (1967). Logarithmic limb darkening coefficients (x_1, x_2, y_1, y_2) were interpolated (van Hamme 1993) following any change in the effective temperature (T_{eff2}) of the secondary star during model fit optimization using differential corrections (DC). All but the temperature of the more massive star (T_{eff1}), $A_{1,2}$ and $g_{1,2}$ were allowed to vary during DC iterations. In general, the best fits for T_{eff2}, i, q, and Roche potentials ($\omega_1 = \omega_2$) were collectively refined (method of multiple subsets) by DC using the multicolor LC data until a simultaneous solution was found. Not uncommon for OCB systems, LCs from V1309 Her exhibit varying degrees of asymmetry during quadrature (Max I > Max II) which is often called the O'Connell effect (O'Connell 1951). Surface inhomogeneity often attributed to star spots was addressed in V1309 Her by the addition of two cool spots to obtain the best fit LC simulations. Only EI CMi required third light correction ($l_3 > 0$) to improve Roche model fits. Since each system clearly undergoes a total eclipse, Roche model convergence to a unique value for q is expected according to Terrell and Wilson (2005), thereby obviating the need for any formal "q-search" exercise. These general findings are described in more detail within the subsections for each variable that follow.

3.4. Roche modeling results

Without radial velocity (RV) data it is generally not possible to unambiguously determine the mass ratio, subtype (A or W), or total mass of an eclipsing binary system. Nonetheless since

Table 8. Estimation of effective temperature (T_{eff1}) of the primary star in EI CMi, NSVS 3092802, V958 Mon, and V1309 Her.

	EI CMi	*NSVS 3092802*	*V958 Mon*	*V1309 Her*
DBO $(B–V)_0$	0.461 ± 0.019	0.741 ± 0.015	0.797 ± 0.025	0.532 ± 0.013
Median combined $(B–V)_0$[a]	0.534 ± 0.052	0.759 ± 0.036	0.846 ± 0.020	0.505 ± 0.004
Galactic reddening (E(B–V))	0.110 ± 0.007	0.054 ± 0.001	0.031 ± 0.001	0.031 ±0.002
Survey T_{eff1}[b] (K)	6130 ± 209	5410 ± 100	5250 ± 65	6160 ± 11
Gaia T_{eff1}[c] (K)	5757^{+441}_{-195}	5789^{+380}_{-68}	5005^{+133}_{-98}	6592^{+609}_{-525}
Houdasheldt T_{eff1}[d] (K)	6102 ± 276	5405 ± 308	5174 ± 330	6121 ± 212
LAMOST DR5 T_{eff1}[e] (K)	5866 ± 215	—	5201 ± 20	6233 ± 19
Median T_{eff1} (K)	5980 ± 246	5410 ± 224	5190 ± 90	6196 ± 115
Spectral Class	F6V[f]	G8V-G9V[g]	G8V[f]	F4V[f]

[a] Surveys and DBO intrinsic $(B–V)_0$ determined using reddening values (E(B–V)) from each star. [b] T_{eff1} interpolated from median combined $(B–V)_0$ using Table 4 in Pecaut and Mamajek (2013). [c] Values from Gaia DR2 (http://vizier.u-strasbg.fr/viz-bin/VizieR?-source=I/345/gaia2). [d] Values calculated with Houdasheldt (2000) empirical relationship. [e] Values from LAMOST DR5 (http://dr5.lamost.org/search). [f] Spectral class from LAMOST DR5. [g] Spectral class interpolated from median combined $(B–V)_0$: Pecaut and Mamajeck (2013).

a total eclipse is observed in the LCs from all four systems, a unique mass ratio value for each system could be found (Terrell and Wilson 2005). Standard errors reported in Tables 9–12 are computed from the DC covariance matrix and only reflect the model fit to the observations which assume exact values for any fixed parameter. These errors are generally regarded as unrealistically small, considering the estimated uncertainties associated with the mean adopted T_{eff1} values along with basic assumptions about $A_{1,2}$, $g_{1,2}$ and the influence of spots added to the Roche model. Normally, the value for T_{eff1} is fixed with no error during modeling with the WD code despite measurement uncertainty which can arguably approach 10% relative standard deviation (R.S.D.) without supporting spectral data. The effect that such uncertainty in T_{eff1} would have on modeling estimates for q, i, $\omega_{1,2}$, and T_{eff2} has been investigated with other overcontact binaries including A- (Alton 2019; Alton *et al.* 2020) and W-subtypes (Alton and Nelson 2018). As might be expected any change in the fixed value for T_{eff1} results in a corresponding change in the T_{eff2}. These findings are consistent whereby the uncertainty in the model fit for T_{eff2} would be essentially the same as that established for T_{eff1}. Furthermore, varying T_{eff1} by as much as 10% did not appreciably affect the uncertainty estimates (R.S.D. < 2.2%) for i, q or $\omega_{1,2}$ (Alton 2019; Alton and Nelson 2018; Alton *et al.* 2020). Assuming that the actual T_{eff1} values for each of the four OCBs investigated herein fall within 10% of the adopted values used for Roche modeling (a reasonable expectation based on T_{eff1} data provided in Table 8), then uncertainty estimates for i, q or $\omega_{1,2}$ along with spot size, temperature, and location would likely not exceed 2.2% R.S.D.

The fill-out parameter (f) which corresponds to the outer surface shared by each star was calculated according to Equation 15 (Kallrath and Milone 1999; Bradstreet 2005) where:

$$f = (\omega_{inner} - \omega_{1,2}) / (\omega_{inner} - \omega_{outer}) , \quad (15)$$

wherein ω_{outer} is the outer critical Roche equipotential, ω_{inner} is the value for the inner critical Roche equipotential, and $\omega = \omega_{1,2}$ denotes the common envelope surface potential for the binary system. In all cases the systems are considered overcontact since $0 < f < 1$.

3.4.1. EI CMi

LC parameters, geometric elements, and their corresponding uncertainties are summarized in Table 9. According to Binnendijk (1970) the deepest minimum (Min I) of a W-type overcontact system occurs when a cooler more massive constituent occludes its hotter but less massive binary partner. The flattened-bottom dip in brightness that is sustained for 0.43 h at Min I (Figure 11) indicates a total eclipse of the secondary star; WD modeling proceeded under the assumption that EI CMi is a W-subtype. Since according to the convention used herein whereby the primary star is the most massive ($m_2 / m_1 \leq 1$), a phase shift (0.5) was introduced to properly align the LC for subsequent Roche modeling. These assumptions proved to be similarly true for NSVS 3092802, V958 Mon, and V1309 Her and will not be repeated in their respective subsections. It should also be noted that larger model fit residuals around minimum light are observed where photometric values are expected to be most variable.

It quickly became obvious that model-simulated LCs at Min I and Min II were consistently deeper than the observed values in all three bandpasses. This was rectified by allowing the third light parameter (l_3) to freely vary during DC optimization. These findings (Table 9) suggest the presence of a blue-rich ($l_3(B) > l_3(V) > l_3(I_c)$) field star in the distant background that has contaminated light arriving from EI CMi. Potential secular changes in the orbital period that might arise from the influence of a third gravitational body cannot be evaluated at this time due to the limited availability of precise eclipse timing data. Despite the lack of supporting evidence for a stellar body in close proximity, the presence of a hot main sequence star in the same neighborhood as EI CMi would likely overwhelm any photometric measurement, thereby discounting this possibility. Nonetheless, it is still possible that a nearby faint blue object such as a cool (T_{eff} < 8000 K) white dwarf could satisfactorily explain the blue-rich third light.

A three-dimensional rendering (Figure 15) using BINARY MAKER 3 (BM3; Bradstreet and Steelman 2004) with the final WDWINT56A modeling results illustrates the secondary star transit across the primary face during Min II ($\Phi = 0.5$), thereby confirming that the secondary star is totally eclipsed at Min I.

Table 9. Lightcurve parameters evaluated by Roche modeling and the geometric elements derived for EI CMi assuming it is a W-subtype W UMa-type eclipsing variable with no spots.

Parameter[a]	*Observed*
T_{eff1} (K)[b]	5980
T_{eff2} (K)	6314 (4)
q (m_2 /m_1)	0.436 (1)
A[b]	0.50
g[b]	0.32
$\omega_1 = \omega_2$	2.671 (4)
i°	89 (1)
L_1 / (L_1 + L_2)B[c]	0.6034 (4)
L_1 / (L_1 + L_2)V	0.6226 (2)
L_1 / (L_1 + L_2)I_c	0.6388 (2)
l_3 (B)[d]	1.166 (5)
l_3 (V)	0.890 (4)
l_3 (c)	0.733 (4)
r_1 (pole)	0.4401 (5)
r_1 (side)	0.4724 (6)
r_1 (back)	0.5056 (7)
r_2 (pole)	0.3043 (12)
r_2 (side)	0.3198 (15)
r_2 (back)	0.3643 (29)
Fill-out factor (%)	30.0
RMS (B)[e]	0.01280
RMS (V)	0.00834
RMS (I_c)	0.00978

[a] All uncertainty estimates for T_{eff2}, q, $\omega_{1,2}$, i, $r_{1,2}$, and L_1 from WDWINT56A (Nelson 2009). [b] Fixed with no error during DC. [c] L_1 and L_2 refer to scaled luminosities of the primary and secondary stars, respectively. [d] fractional percent luminosity of third light parameter (l_3) at $\Phi = 0.25$. [e] Monochromatic residual mean square error from observed values.

Table 10. Lightcurve parameters evaluated by Roche modeling and the geometric elements derived for NSVS 3092802 assuming it is a W-subtype W UMa-type eclipsing variable with no spots.

Parameter[a]	*Observed*
T_{eff1} (K)[b]	5410
T_{eff2} (K)	5693 (2.2)
q (m_2 / m_1)	0.521 (1)
A[b]	0.50
g[b]	0.32
$\omega_1 = \omega_2$	2.88 (2)
i°	88.4 (3)
L_1 / (L_1 + L_2)B[c]	0.5678 (3)
L_1 / (L_1 + L_2)V	0.5875 (1)
L_1 / (L_1 + L_2)I_c	0.6034 (1)
r_1 (pole)	0.4163 (2)
r_1 (side)	0.4430 (3)
r_1 (back)	0.4734 (4)
r_2 (pole)	0.3087 (6)
r_2 (side)	0.3232 (8)
r_2 (back)	0.3593 (13)
Fill-out factor (%)	10.7
RMS (B)[d]	0.00849
RMS (V)	0.00479
RMS (I_c)	0.00412

[a] All uncertainty estimates for T_{eff2}, q, $\omega_{1,2}$, i, $r_{1,2}$, and L_1 from WDWINT56A (Nelson 2009). [b] Fixed with no error during DC. [c] L_1 and L_2 refer to scaled luminosities of the primary and secondary stars, respectively. [d] Monochromatic residual mean square error from observed values.

Table 11. Lightcurve parameters evaluated by Roche modeling and the geometric elements derived for V958 Mon assuming it is a W-type W UMa variable.

Parameter[a]	*DBO No spot*	*Michaels*[b] *2016*
T_{eff1} (K)[c]	5150	5465 (3)
T_{eff2} (K)	5510 (3)	5111
q (m_2 / m_1)	0.434 (1)	2.25 (2)
A[c]	0.50	0.5
g[c]	0.32	0.32
$\omega_1 = \omega_2$	2.734 (2)	5.489 (26)
i°	85.2 (3)	86.4 (4)
$A_P = T_S / T_{star}$[d]	—	1.17 (4)
θ_P (spot co-latitude)[d]	—	113 (2)
Φ_P (spot longitude)[d]	—	356 (1)
r_p (angular radius)[d]	—	12 (2)
L_1 / (L_1 + L_2)B[e]	0.5854 (5)	—
L_1 / (L_1 + L_2)V	0.6092 (2)	0.4101 (4)
L_1 / (L_1 + L_2)R_c	0.6222 (5)	—
L_1 / (L_1 + L_2)I_c	0.6308 (3)	—
l_3(V)	—	0.0121 (42)
r_1 (pole)	0.4283 (3)	—
r_1 (side)	0.4568 (4)	0.3103 (7)
r_1 (back)	0.4849 (5)	—
r_2 (pole)	0.2913 (3)	—
r_2 (side)	0.3042 (3)	0.4884 (39)
r_2 (back)	0.3384 (5)	—
Fill-out factor (%)	5.1	19
RMS (B)[f]	0.01048	—
RMS (V)	0.00826	—
RMS (R_c)	0.01024	—
RMS (I_c)	0.00803	—

[a] All DBO uncertainty estimates for T_{eff2}, q, $\omega_{1,2}$, i, $r_{1,2}$, and L_1 from WDWINT56A (Nelson 2009). [b] Spotted solution only presented; primary defined as hotter, not more massive star (q > 1). [c] Fixed with no error during DC. [d] Secondary star spot parameters in degrees (θ_p, Φ_p, and r_p) or A_p in fractional degrees (K). [e] L_1 and L_2 refer to scaled luminosities of the primary and secondary stars, respectively. [f] Monochromatic residual mean square error from observed values.

3.4.2. NSVS 3092802

LC parameters and geometric elements with their associated uncertainty for this W-subtype W UMa-type binary can be found in Table 10. During this epoch, model fits at minimum and maximum (Max I ~ Max II) light did not require the addition of spots. As expected for a system exhibiting a total eclipse at Min I, a three-dimensional rendering produced using BM3 (Figure 16) shows a transit of the hotter secondary across the face of the primary star during Min II ($\Phi = 0.5$).

3.4.3. V958 Mon

Unlike the other three OCB systems reported herein, multi-color (V, g', r', and i') LCs for V958 Mon have been published (Michaels 2016). It should be noted therein, the primary star is defined as the hotter binary partner and not the more massive entity. The corresponding LC parameters and geometric elements derived from Roche modeling with the WD code are summarized in Table 11 along with new results from this investigation. Michaels (2016) adopted a slightly lower T_{eff} for the more luminous star, however, this was not expected to produce any meaningful difference (Alton *et al.* 2020) where comparisons could be made. In general these findings compare favorably with regard to mass ratio (1 / q = 0.444 vs. 0.434) and orbital inclination (86.4 vs. 85.3°). Model fits for the LC data

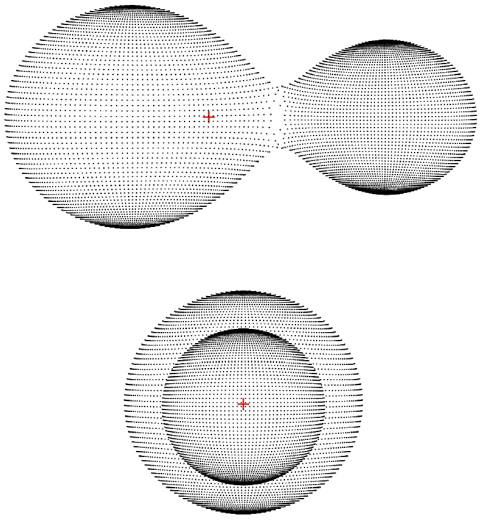

Figure 15. Three-dimensional spatial model of EI CMi illustrating (top) the mutually shared (f = 0.3) atmosphere of the binary system and (bottom) the secondary star transit across the primary star face at Min II (Φ = 0.5).

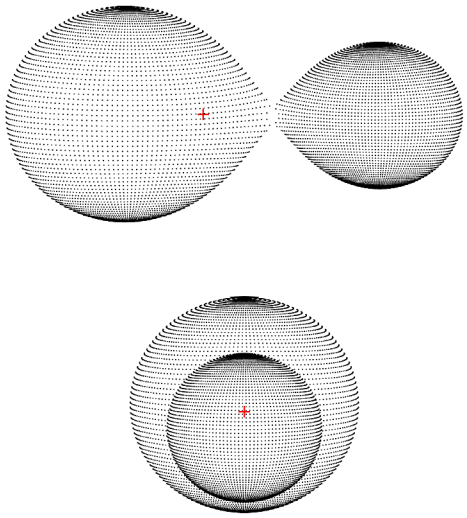

Figure 17. Three-dimensional spatial model of V958 Mon during 2018–2019 illustrating (top) the shallow contact (f = 0.05) between both stars and the secondary star transit across the primary star face at Min II (Φ = 0.5).

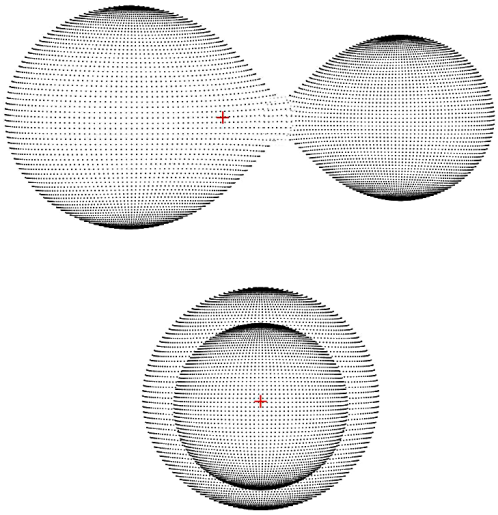

Figure 16. Three-dimensional spatial model of NSVS 3092802 illustrating (top) the mutually shared (f = 0.107) atmosphere of the binary system and (bottom) the secondary star transit across the primary star face at Min II (Φ = 0.5).

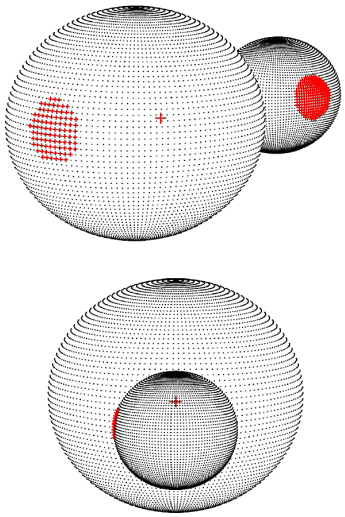

Figure 18. Three-dimensional spatial model of V1309 Her during 2018 illustrating (top) the location of each cool spot and (bottom) the secondary star transit across the primary star face at Min II (Φ = 0.5).

acquired at DBO did not show any meaningfully significant improvement by the addition of a spot. LCs produced by Michaels (2016) were best fit by the addition of a hot spot on the more massive star, a difference that is not uncommon given these photometric data were collected three years earlier. A three-dimensional rendering of the DBO modeled data produced using BM3 (Figure 17) shows a transit of the hotter secondary across the primary star face during Min II (Φ = 0.5), an observation consistent with a total eclipse at Min I. The most significant difference is that Michaels (2016) invoked third light (l_3) presumably to improve the simulated fits at Min I and Min II, whereas the DBO-derived data did not require this additional parameter ($l_3 = 0$). There are an insufficient number of eclipse timings to propose the presence of a dim third body (section 3.1.3.). Nonetheless, it is not obvious why LCs from the same target collected during another epoch would exhibit this behavior. In addition, the fill-out factors varied widely (~4% vs. 19%), most likely due to differences in spot location and/or adding third light ($l_3 \neq 0$) to the Roche model.

3.4.4. V1309 Her

LC parameters and geometric elements with their associated uncertainty derived from Roche modeling of this W-subtype W UMa-type binary are summarized in Table 12. During 2018, LCs exhibited significant asymmetry such that model simulations during quadrature (phase = 0.75) and at Min I were poorly fit. It is not unreasonable to assume that OCBs as a class are magnetically active and can harbor starspots. V1309 Her has been poorly studied so it is no surprise that there are no Doppler Imaging data to support the presence of spots. This can be said for the vast majority of published papers which include star spots to improve the light curve fit during Roche modeling. X-ray luminosity is commonly used as an indicator of stellar magnetic activity (Wright *et al.* 2011) and has been investigated

Table 12. Lightcurve parameters evaluated by Roche modeling and the geometric elements derived for V1309 Her assuming it is a W-type W UMa variable.

Parameter[a]	*No spot*	*Cool spot*
T_{eff1} (K)[b]	6196	6196
T_{eff2} (K)	6586 (4)	6330 (2)
q (m_2 / m_1)	0.182 (1)	0.213 (1)
A[b]	0.50	0.5
g[b]	0.32	0.3
$\omega_1 = \omega_2$	2.141 (1)	2.232 (2)
i°	86.2 (3)	82.3 (2)
$A_P = T_S / T_{star}$[c]	—	0.83 (1)
θ_P (spot co-latitude)[c]	—	87 (1)
Φ_P (spot longitude)[c]	—	177 (1)
r_P (angular radius)[c]	—	14.0 (1)
$A_S = T_S / T_{star}$[d]	—	0.87 (1)
Φ_S (spot co-latitude)[d]	—	86 (3)
Φ_S (spot longitude)[d]	—	75.5 (2.1)
r_S (angular radius)[d]	—	21.30 (24)
$L_1 / (L_1 + L_2)B$[e]	0.7591 (3)	0.7780 (2)
$L_1 / (L_1 + L_2)V$	0.7745 (1)	0.7835 (1)
$L_1 / (L_1 + L_2)I_c$	0.7884 (1)	0.7884 (1)
r_1 (pole)	0.5052 (2)	0.4899 (3)
r_1 (side)	0.5555 (4)	0.5343 (5)
r_1 (back)	0.5808 (4)	0.5596 (5)
r_2 (pole)	0.2390 (3)	0.2452 (9)
r_2 (side)	0.2504 (3)	0.2562 (11)
r_2 (back)	0.2964 (7)	0.2963 (22)
Fill-out factor (%)	39.3	23.4
RMS (B)[f]	0.01219	0.00808
RMS (V)	0.00862	0.00518
RMS (I_c)	0.01075	0.00732

[a] All uncertainty estimates for T_{eff2}, q, $\omega_{1,2}$, i, $r_{1,2}$, and L_1 from WDWINT56A (Nelson 2009). [b] Fixed with no error during DC. [c] Primary star spot parameters in degrees (θ_P, Φ_P, and r_P) or A_P in fractional degrees (K). [d] Secondary star spot parameters in degrees (θ_S, Φ_S, and r_S) or A_S in fractional degrees (K). [e] L_1 and L_2 refer to scaled luminosities of the primary and secondary stars, respectively. [f] Monochromatic residual mean square error from observed values.

in eclipsing contact binary stars (Szczygiel *et al.* 2008; Stępień *et al.* 2001). Unlike the other three systems described herein, two of which are much closer, there is circumstantial evidence that V1309 Her is magnetically active based on data acquired from the ROSAT all-sky survey (Voges *et al.* 1999). In this case an X-ray source (hardness ratio = 0.13) was detected within 2 arcsec of its optical counterpart. Aside from arriving at a mathematically convenient solution, there is physical justification for the presence of starspot(s) in order to address the light curve asymmetry exhibited by V1309 Her. In this case, a single cool spot was positioned on the primary star to deepen Min I while another cool spot was placed on the secondary star to improve the LC simulation around phase = 0.75 (Figure 18). In addition, this spatial rendering produced using BM3 shows the hotter secondary transiting across the primary star face during Min II ($\Phi = 0.5$), reaffirming that a total eclipse occurred during Min I.

According to LITE analysis (section 3.1.4), a putative third body would be too dim to detect by CCD photometry. As expected, there was no need to invoke a third light correction ($l_3 = 0$) to achieve an acceptable model fit at minimum light.

3.5. Stellar parameters

Fundamental stellar parameters were estimated for each binary system using results from the best fit LC simulations. Previous experience (Alton 2019; Alton *et al.* 2020; Alton and Nelson 2018) with other OCBs would suggest that uncertainty (R.S.D.) for each of these estimates is at least 2.2%. However, without the benefit of RV data which define the orbital motion, mass ratio, and total mass of the binary pair, these results should be considered "relative" rather than "absolute" parameters and regarded as preliminary.

Starting with EI CMi, a calculation template is described below for estimating the solar mass and size, semi-major

Table 13. Fundamental stellar parameters for EI CMi using the photometric mass ratio ($q_{ptm} = m_2 / m_1$) from Roche model fits of LC data (2018–2019) and the estimated mass based on empirically derived M-PRs for overcontact binary systems.

Parameter	*Primary*	*Secondary*
Mass ($M_\odot$)	1.17 ± 0.05	0.51 ± 0.02
Radius ($R_\odot$)	1.15 ± 0.01	0.79 ± 0.01
a ($R_\odot$)	2.54 ± 0.03	2.54 ± 0.03
Luminosity ($L_\odot$)	1.52 ± 0.25	0.89 ± 0.02
M_{bol}	4.30 ± 0.18	4.88 ± 0.02
Log (g)	4.38 ± 0.02	4.35 ± 0.02

Table 14. Fundamental stellar parameters for NSVS~3092802 using the mean photometric mass ratio ($q_{ptm} = m_2 / m_1$) from the Roche model fits of LC data (2018–2019) and the estimated mass based on empirically derived M-PRs for W UMa type variable stars}

Parameter	*Primary*	*Secondary*
Mass ($M_\odot$)	1.06 ± 0.04	0.55 ± 0.02
Radius ($R_\odot$)	1.00 ± 0.01	0.74 ± 0.01
a ($R_\odot$)	2.29 ± 0.02	2.29 ± 0.02
Luminosity ($L_\odot$)	0.77 ± 0.01	0.52 ± 0.01
M_{bol}	5.04 ± 0.02	5.46 ± 0.02
Log (g)	4.46 ± 0.02	4.44 ± 0.02

Table 15. Fundamental stellar parameters for V958 Mon using the mean photometric mass ratio ($q_{ptm} = m_2 / m_1$) from the Roche model fits of LC data (2018) and the estimated mass based on empirically derived M-PRs for W UMa type variable stars.

Parameter	*Primary*	*Secondary*
Mass ($M_\odot$)	1.030 ± 0.02	0.45 ± 0.01
Radius ($R_\odot$)	0.97 ± 0.01	0.66 ± 0.01
a ($R_\odot$)	2.14 ± 0.01	2.14 ± 0.01
Luminosity ($L_\odot$)	0.64 ± 0.01	0.36 ± 0.01
M_{bol}	5.23 ± 0.01	5.85 ± 0.01
Log (g)	4.48 ± 0.01	4.45 ± 0.01

Table 16. Fundamental stellar parameters for V1309 Her using the mean photometric mass ratio ($q_{ptm} = m_2 / m_1$) from the Roche model fits of LC data (2018) and the estimated mass based on empirically derived M-PRs for W UMa type variable stars.

Parameter	*Primary*	*Secondary*
Mass ($M_\odot$)	1.27 ± 0.04	0.27 ± 0.01
Radius ($R_\odot$)	1.29 ± 0.01	0.64 ± 0.01
a ($R_\odot$)	2.50 ± 0.02	2.50 ± 0.02
Luminosity ($L_\odot$)	2.21 ± 0.17	0.59 ± 0.01
M_{bol}	3.89 ± 0.02	5.32 ± 0.02
Log (g)	4.32 ± 0.02	4.26 ± 0.02

axis, solar luminosity, bolometric V-mag, and surface gravity of each component. Three empirically derived mass-period relationships (M-PR) for W UMa binaries have been published. The first M-PR was reported by Qian (2003) while two others followed from Gazeas and Stępień (2008) and then Gazeas (2009). According to Qian (2003) when the primary star is less than 1.35 $M_\odot$ or the system is W-type its mass can be determined from Equation 16:

$$\log(M_1) = 0.391\ (59) \cdot \log(P) + 1.96\ (17), \qquad (16)$$

where P is the orbital period in days and leads to $M_1 = 1.10 \pm 0.09\ M_\odot$ for the primary. The M-PR (Equation 17) derived by Gazeas and Stępień (2008):

$$\log(M_1) = 0.755\ (59) \cdot \log(P) + 0.416\ (24), \qquad (17)$$

corresponds to an OCB system where $M_1 = 1.21 \pm 0.10\ M_\odot$. Gazeas (2009) reported another empirical relationship (Equation 18) for the more massive (M_1) star of a contact binary such that:

$$\log(M_1) = 0.725\,(59) \cdot \log(P) - 0.076\,(32) \cdot \log(q) + 0.365\,(32). \qquad (18)$$

from which $M_1 = 1.18 \pm 0.08\ M_\odot$. The mean of three values ($M_1 = 1.17 \pm 0.05\ M_\odot$) estimated from Equations 16–18 was used for subsequent determinations of M_2, semi-major axis a, volume-radii r_L, and bolometric magnitudes (M_{bol}) using the formal errors calculated by WDWINT56A (Nelson 2009). The secondary mass = $0.51 \pm 0.02\ M_\odot$ and total mass ($1.67 \pm 0.06\ M_\odot$) were determined using the photometric mass ratio ($q_{ptm} = 0.436 \pm 0.001$) from Roche modeling. In general, the size, mass, luminosity, and surface gravity of the more massive binary component of an OCB closely match values obtained from solitary dwarf main-sequence (MS) stars. By comparison, a single MS dwarf star with a mass similar to the secondary (late K-type) would be considerably smaller ($R_\odot \sim 0.57$), cooler ($T_{eff} \sim 4000$ K) and far less luminous ($L_\odot \sim 0.075$). This is consistent with the general finding that a secondary star in an OCB is over-sized and over-luminous for its mass (Webbink 2003) particularly with W-subtype OCBs where extreme mass ratios ($q \ll 1$) can be observed.

The semi-major axis, $a(R_\odot) = 2.54 \pm 0.03$, was calculated from Newton's version (Equation 19) of Kepler's third law where:

$$a^3 = (G \cdot P^2\ (M_1 + M_2)) / (4\pi^2). \qquad (19)$$

The effective radius of each Roche lobe (r_L) can be calculated over the entire range of mass ratios ($0 < q < \infty$) according to an expression (Equation 20) derived by Eggleton (1983):

$$r_L = (0.49q^{2/3}) / (0.6q^{2/3} + \ln(1 + q^{1/3})), \qquad (20)$$

from which values for r_1 (0.4522 ± 0.0003) and r_2 (0.3098 ± 0.0002) were determined for the primary and secondary stars, respectively. Since the semi-major axis and the volume radii are known, the radii in solar units for both binary components can be calculated where $R_1 = a \cdot r_1 = 1.15 \pm 0.01\ R_\odot$ and $R_2 = a \cdot r_2 = 0.79 \pm 0.01\ R_\odot$.

Luminosity in solar units ($L_\odot$) for the primary (L_1) and secondary stars (L_2) was calculated from the well-known relationship derived from the Stefan-Boltzmann law (Equation 21) where:

$$L_{1,2} = (R_{1,2}/R_\odot)^2\ (T_{1,2}/T_\odot)^4. \qquad (21)$$

Assuming that $T_{eff1} = 5980$ K, $T_{eff2} = 6314$ K, and $T_\odot = 5772$ K, then the solar luminosities ($L_\odot$) for the primary and secondary are $L_1 = 1.52 \pm 0.25$ and $L_2 = 0.89 \pm 0.02$, respectively.

The same approach described for EI CMi was used to determine the preliminary stellar attributes for NSVS 3092802 (Table 14), V958 Mon (Table 15), and V1309 Her (Table 16). Similar results for only V958 Mon have been previously published (Michaels 2016) wherein they agreed favorably (±5%) with those derived from this investigation (Table 15).

4. Conclusions

New times of minimum for EI CMi (n=15), NSVS 3092802 (n=26), V958 Mon (n=60), and V1309 Her (n=17) based on multicolor CCD data were determined from LCs acquired at DBO. Additional values extracted from the SuperWASP, NSVS, and ASAS surveys as well as from the AAVSO International Database via the InternationalVariable Star Index are reported herein. These along with other published values led to new linear ephemerides. In each case all eclipse timings produced what appears to be a quadratic relationship suggesting that their respective orbital periods are changing at different but constant rates. The ETD-diagram for V1309 Her proved to be the most complex with underlying sinusoidal-like variations in the eclipse timing residuals. Two equally probable causes for orbital period modulation include a third gravitationally bound low-mass stellar object or the so-called Applegate effect.

The adopted effective temperatures (T_{eff1}) were based on a composite of sources that included values from an assortment of photometric and astrometric surveys, the Gaia DR2 release of stellar characteristics (Andrae *et al.* 2018), and estimates from LAMOST DR5 spectral data (Zhao *et al.* 2012; Rui *et al.* 2019). Each OCB clearly experiences a total eclipse which is evident as a flattened bottom during Min I, a characteristic of W-subtype variables. It follows that photometric mass ratios determined by Roche modeling should prove to be reliable substitutes for mass ratios derived from RV data. Nonetheless, spectroscopic studies (RV and high resolution classification spectra) will be required to unequivocally determine a total mass and spectral class for each system. Consequently, all parameter values and corresponding uncertainties reported herein should be considered preliminary.

5. Acknowledgements

This research has made use of the SIMBAD database operated at Centre de Données astronomiques de Strasbourg, France. In addition, the Northern Sky Variability Survey hosted by the Los Alamos National Laboratory (https://skydot.lanl.

gov/nsvs/nsvs.php), the All Sky Automated Survey Catalogue of Variable Stars (http://www.astrouw.edu.pl/asas/?page=acvs) and the International Variable Star Index (AAVSO) were mined for essential information. This work also presents results from the European Space Agency (ESA) space mission Gaia. Gaia data are being processed by the Gaia Data Processing and Analysis Consortium (DPAC). Funding for the DPAC is provided by national institutions, in particular the institutions participating in the Gaia MultiLateral Agreement (MLA). The Gaia mission website is https://www.cosmos.esa.int/gaia. The Gaia archive website is https://archives.esac.esa.int/gaia. This paper makes use of data from the first public release of the WASP data as provided by the WASP consortium and services at the NASA Exoplanet Archive, which is operated by the California Institute of Technology, under contract with the National Aeronautics and Space Administration under the Exoplanet Exploration Program. The use of public data from LAMOST is also acknowledged. Guoshoujing Telescope (the Large Sky Area Multi-Object Fiber Spectroscopic Telescope LAMOST) is a National Major Scientific Project built by the Chinese Academy of Sciences. Funding for the project has been provided by the National Development and Reform Commission. LAMOST is operated and managed by the National Astronomical Observatories, Chinese Academy of Sciences. Many thanks to the anonymous referee whose valuable commentary led to significant improvement of this paper.

References

Akerlof, C., *et al.* 2000, *Astron. J.*, **119**, 1901.
Almeida, L. A., *et al.* 2015, *Astrophys. J.*, **812**, 102.
Alton, K. B. 2019, *J. Amer. Assoc. Var. Star Obs.*, **47**, 7.
Alton, K. B., and Nelson, R. H. 2018, *Mon. Not. Roy. Astron. Soc.*, **479**, 3197.
Alton, K. B., Nelson, R. H. and Stępień, K. 2020, *J. Astrophys. Astron.*, **41**, 26.
Amôres, E. B., and Lépine. 2005, *Astron. J.*, **130**, 659.
Andrae, R., *et al.* 2018, *Astron. Astrophys.*, **616A**, 8.
Applegate, J. H. 1992, *Astrophys. J.*, **385**, 621.
Arbutina, B. 2009, *Mon. Not. Roy. Astron. Soc.*, **394**, 501.
Bailer-Jones, C. A. L. 2015, *Publ. Astron. Soc. Pacifc*, **127**, 994.
Berdyugina, S. V. 2005, *Living Rev. Solar Phys.*, **2**, 8.
Berry, R., and Burnell, J. 2005, *The Handbook of Astronomical Image Processing*, 2nd ed., Willmann-Bell, Richmond VA.
Binnendijk, L. 1970, *Vistas Astron.*, **12**, 217.
Bradstreet, D. H. 2005, in *The Society for Astronomical Sciences 24th Annual Symposium on Telescope Science*, The Society for Astronomical Sciences, Rancho Cucamonga, CA, 23.
Bradstreet, D. H., and Steelman, D. P. 2004, BINARY MAKER 3, Contact Software (http://www.binarymaker.com).
Butters, O. W., *et al.* 2010, *Astron. Astrophys.*, **520**, L10.
Christiansen, J. L., *et al.* 2008, *Mon. Not. R. Astron. Soc.*, **385**, 1749.
Diethelm, R. 2006, *Inf. Bull. Var. Stars*, No. 5713, 1.
Diethelm, R. 2007, *Inf. Bull. Var. Stars*, No. 5781, 1.
Diethelm, R. 2008, *Inf. Bull. Var. Stars*, No. 5837, 1.
Diethelm, R. 2010, *Inf. Bull. Var. Stars*, No. 5920, 1.
Diethelm, R. 2011, *Inf. Bull. Var. Stars*, No. 5992, 1.
Drake, A. J., *et al.* 2014, *Astrophys. J., Suppl. Ser.*, **213**, 9.
Eggleton, P. P. 1983, *Astrophys. J.*, **268**, 368.
Gazeas, K. D. 2009, *Commun. Asteroseismology*, **159**, 129.
Gazeas, K., and Stępień, K. 2008, *Mon. Not. Roy. Astron. Soc.*, **390**, 1577.
Gettel, S. J., Geske, M. T., and McKay, T. A. 2006, *Astron. J.*, **131**, 621.
Giménez, A., Guinan, E., Niarchos, P., and Rucinski, S., eds. 2006, *Close Binaries in the 21st Century: New Opportunities and Challenges*, Springer, Dordrecht.
Greaves, J., and Wils, P. 2003, *Inf. Bull. Var. Stars*, No. 5458, 1.
Henden, A. A., Levine, S. E., Terrell, D., Smith, T. C., and Welch, D. L. 2011, *Bull. Amer. Astron. Soc.*, **43**.
Henden, A. A., and Stone, R. C. 1998, *Astron. J.*, **115**, 296.
Henden, A. A., Terrell, D., Welch, D., and Smith, T. C. 2010, *Bull. Amer. Astron. Soc.*, **42**, 515.
Henden, A. A., Welch, D. L., Terrell, D., and Levine, S. E. 2009, *Bull. Amer. Astron. Soc*., **41**, 669.
Hoffman, D. I., Harrison, T. E., and McNamara, B. J. 2009, *Astron. J.*, **138**, 466.
Houdashelt, M. L., Bell, R. A., and Sweigart, A. V. 2000, *Astron. J.*, **119**, 1448.
Hübscher, J. 2014, *Inf. Bull. Var. Stars*, No. 6118, 1.
Hübscher, J. 2017, *Inf. Bull. Var. Stars*, No. 6196, 1.
Hübscher, J., and Lehmann, P. B. 2015, *Inf. Bull. Var. Stars*, No. 6149, 1.
IonDev SRL. 2020, QTIPLOT 0.9.9-rc9 (https://www.qtiplot.com).
Irwin, J. B. 1959, *Astron. J.*, **64**, 149.
Juryšek, J., *et al.* 2017, *Open Eur. J. Var. Stars*, **179**, 1.
Kallrath, J., and Milone, E. F. 1999, *Eclipsing Binary Stars: Modeling and Analysis*, Springer, New York.
Kukarkin, B. V., *et al.* 1970, *General Catalogue of Variable Stars. Volume II*, 3rd. ed., Moscow.
Kurucz, R. L. 2002, *Baltic Astron.*, **11**, 101.
Kwee, K. K., and van Woerden, H. 1956, *Bull. Astron. Inst. Netherlands*, **12**, 327.
Lucy, L. B. 1967, *Z. Astrophys.*, **65**, 89.
Michaels, E. J. 2016, *J. Amer. Assoc. Var. Star Obs.*, **44**, 53.
Minor Planet Observer. 2010, MPO Software Suite (http://www.minorplanetobserver.com), BDW Publishing, Colorado Springs.
Mochnacki, S .W., and Doughty, N. A. 1972, *Mon. Not. Royal Astron. Soc.*, **156**, 51.
Nelson, R. H. 2009, WDWINT56A: Astronomy Software by Bob Nelson (https://www.variablestarssouth.org/bob-nelson).
Nelson, R. H. 2010, *Inf. Bull. Var. Stars*, No. 5929, 1.
Nelson, R. H. 2011, *Inf. Bull. Var. Stars*, No. 5966, 1.
Nelson, R. H. 2012, *Inf. Bull. Var. Stars*, No. 6018, 1.
O'Connell, D. J. K. 1951, *Publ. Riverview Coll. Obs.*, **2**, 85.
Otero, S., Wils, P., and Dubovsky, P. A. 2004, *Inf. Bull. Var. Stars*, No. 5570, 1.
Paczyński, B., Sienkiewicz, R., and Szczygieł, D. M. 2007, *Mon. Not. Roy. Astron. Soc.*, **378**, 961.
Paczyński, B., Szczygieł, D. M., Pilecki, B., and Pojmański, G. 2006, *Mon. Not. Royal Astron. Soc.*, **368**, 1311.
Paschke, A. 2015, *Open Eur. J. Var. Stars*, **172**, 1.
Paschke, A. 2020, *BAV Rundbrief*, **69**, 101.

Paunzen, E., and Vanmunster, T. 2016, *Astron. Nachr.*, **337**, 239.
Pecaut, M., and Mamajek, E. E. 2013, *Astrophys. J., Suppl. Ser.*, **208**, 9.
Pojmański, G., Pilecki, B., and Szczygieł, D. 2005, *Acta Astron.*, **55**, 275.
Pribulla, T., and Ruciński, S. M. 2006, *Astron. J.*, **131**, 2986.
Prša, A., and Zwitter, T. 2005, *Astrophys. J.*, **628**, 426.
Prša, A., *et al.* 2011, *Astron. J.*, 141, 83
Qian, S-B. 2003, *Mon. Not. Roy. Astron. Soc.*, **342**, 1260.
Qian, S., Yang, Y., Zhu, L., H., He, J., and Yuan, J. 2006, *Astrophys. Space Sci.*, **304**, 25.
Ruciński, S. M. 1969, *Acta Astron.*, **19**, 245.
Ruciński, S. M. 1994, *Publ. Astron. Soc. Pacific*, **106**, 462.
Ruciński, S. M. 1997a, *Astron. J.*, **113**, 407.
Ruciński, S. M. 1997b, *Astron. J.*, **113**, 1112.
Rui, W., *et al.* 2019, *Pub. Astron. Soc. Pacifc*, **131**, 024505.
Smith, T. C., Henden, A. A., and Starkey, D. R. 2011, in *The Society for Astronomical Sciences 30th Annual Symposium on Telescope Science*, The Society for Astronomical Sciences, Rancho Cucamonga, CA, 121.
Software Bisque. 2019, TheSkyX professional edition 10.5.0 (http://www.bisque.com).
Sriram, K., Malu, S., Choi, C. S., and Rao, P. 2016, *Astron. J.*, **151**, 69
Stępień, K. 2006, *Acta Astron.*, **56**, 199.
Stępień, K., and Kiraga, M. 2015, *Astron. Astrophys.*, **577A**, 117.
Stępień, K., Schmitt, J. H. M. M., and Voges, W. 2001, *Astron. Astrophys.*, **370**, 157.
Szczygieł, D. M., Socrates, A., Paczyński, B., Pojmański, G., and Pilecki, B. 2008, *Acta Astron.*, **58**, 405.
Terrell, D., and Wilson, R. E. 2005, *Astrophys. Space Sci.*, **296**, 221.
Tian, Y. P., Xiang, F. Y., and Tao, X. 2009, *Astrophys. Space Science*, **319**, 119.
Udalski, A., Szymanski, M., Kaluzny, J., Kubiak, M., and Mateo, M. 1992, *Acta Astron.*, **42**, 253.
van Hamme, W. 1993, *Astron. J.*, **106**, 2096.
van't Veer, F., 1975, *Astron. Astrophys.*, **40**, 167.
Voges, W., *et al.* 1999, *Astron. Astrophys.*, **349**, 389.
Völschow, M., Schleicher, D. R. G., Perdelwitz, V., and Banerjee, R. 2016, *Astron. Astrophys.*, **587**, 34.
Warner, B. D. 2007, *Minor Planet Bull.*, **34**, 113.
Watson, C., Henden, A. A., and Price, C. A. 2014, AAVSO International Variable Star Index VSX (Watson+, 2006–2014; http://www.aavso.org/vsx).
Webbink, R. F. 2003, in *3D Stellar Evolution*, ASP Conf. Proc. 293, 76.
Wilson, R. E. 1979, *Astrophys. J.*, **234**, 1054.
Wilson, R. E. 1990, *Astrophys. J.*, **356**, 613.
Wilson, R. E., and Devinney, E. J. 1971, *Astrophys. J.*, **166**, 605.
Woźniak, P. R., *et al.* 2004, *Astrophys. J.*, **127**, 2436.
Wright, N. J., Drake, J. J., Mamajek, E. E., and Henry, G. W. 2011, *Astrophys. J.*, **743**, 48.
Zasche, P., Liakos, A., Niarchos, P., Wolf, M., Manimanis, V., and Gazeas, K. 2009, *New Astron.*, **14**, 121.
Zhao, G., Zhao, Y.-H., Chu, Y.-Q., Jing, Y.-P., and Deng, L.-C. 2012, *Res. Astron. Astrophys.*, **12**, 723.

A Photometric Study of the Contact Binary GR Piscium

Edward J. Michaels
Stephen F. Austin State University, Department of Physics, Engineering, and Astronomy, P. O. Box 13044, Nacogdoches, TX 75962; emichaels@sfasu.edu

Received July 27, 2020; revised August 16, 2020; accepted August 18, 2020

Abstract High-quality CCD photometric light curves of the eclipsing binary GR Psc are presented. The new multicolor light curves display total eclipses which were analyzed using the Wilson-Devinney program. The light curve solution describes the system as a contact configuration with a mass ratio of $M_2/M_1 = 0.431$, a fill-out of f=47%, and a small temperature difference between the component stars of $\Delta T = 51$K. A period study revealed this A-type contact binary has a decreasing orbital period. A small asymmetry was found in the light curves, indicating an elevated temperature in the contact region of the primary star. This hot region is likely the consequence of mass and energy exchange through the connecting neck of the common envelope.

1. Introduction

GR Psc (GSC 01747-00967) was first identified as an eclipsing binary from the All-Sky Automated Survey (ASAS) observations (Pojmański *et al.* 2002). An orbital period of 0.494320 d and a maximum visual magnitude of 11.09 were determined from the ASAS data. The variability of this star was also identified in the Northern Sky Variability Survey (NSVS, Woźniak *et al.* 2004; Nicholson and Varley 2006). Gettel *et al.*'s (2006) catalogue of bright contact binary stars gives an orbital period of 0.494339 d, a visual magnitude of 11.263, and an eclipse amplitude of 0.669 magnitude. Terrell *et al.* (2012) found a color index of (B–V) = 0.404. Gaia DR2 data give a distance of 524 pc and an effective temperature of 6910K (Bailer-Jones *et al.* 2018; Gaia Collaboration 2018).

In this paper, the first photometric study of GR Psc is presented. The photometric observations and data reduction methods are presented in section 2. New times of minima and period analysis are presented in section 3. Analysis of the light curves using the Wilson-Devinney (WD) model is presented in section 4. Discussion of the results and conclusions are presented in section 5.

Table 1. Observation log.

Filter	*Dates*	*No. Nights*	*No. Images*
B	2019 Oct 21, 22, 23 Nov 17, 18, 19	6	940
V	2019 Oct 21, 22, 23 Nov 17, 18, 19	6	951
Sloan g'	2019 Oct 21, 22, 23 Nov 17, 18, 19	6	962
Sloan r'	2019 Oct 21, 22, 23 Nov 17, 18, 19	6	957

2. Photometric observations

Multi-band photometric observations of GR Psc were acquired in October and November 2019 with the 0.36-m Ritchey-Chrétien robotic telescope located at the Waffelow Creek Observatory (https://obs.ejmj.net). A SBIG-STXL camera equipped with a cooled KAF-6303E CCD (–30° C, 9 µm pixels) was used for imaging. Observations were obtained in four passbands each night, Johnson B and V and Sloan g' and r'. The observation dates and number of images acquired are given in the Table 1 observation log. Nightly bias, dark, and flat frames were acquired for image calibration. MIRA software (Mirametrics 2015) was used for image calibration and the ensemble differential aperture photometry of the light images. The locations of the comparison and check stars are shown in the Figure 1 finder chart. Table 2 lists the comparison and check star coordinates and their standard magnitudes taken from the AAVSO Photometric All-Sky Survey data base (APASS; Henden *et al.* 2015). The GR Psc instrumental magnitudes for each star were converted to standard magnitudes using the APASS comparison star magnitudes. The Heliocentric Julian Date (HJD) of each observation was converted to orbital phase (φ) using the following epoch and orbital period: $T_0 = 2458807.4790$ and $P = 0.49431813$. The folded light curves for the Johnson B and V passbands are shown in Figure 2 and the Sloan g' and r' in Figure 3. All light curves in this paper were plotted from orbital phase –0.6 to 0.6, with negative phase defined as (φ – 1). Error bars were omitted from the plotted points for clarity. The check star magnitudes were plotted and inspected each night, but no significant variability was found (bottom panels of Figures 2 and 3). The standard deviations for all check star observations are in Table 2.

Table 2. APASS comparison and check star magnitudes.

System	*R.A. (2000) h*	*Dec. (2000) °*	*B*	*V*	*g′*	*r′*
GR Psc	1.158867	+22.65541				
GSC 01747-00427 (C1)	1.163354	+22.69605	11.343	10.271	10.817	10.003
GSC 01747-00315 (C2)	1.154917	+22.68626	11.128	10.512	10.827	10.414
GSC 01747-00927 (C3)	1.155674	+22.77302	10.823	10.212	10.579	10.081
GSC 01747-00409 (K)	1.166047	+22.73883	11.948	10.948	11.428	10.725
Standard deviation of observed K-star magnitudes			± 0.011	± 0.007	± 0.008	± 0.006

Table 3. Average light curve properties.

	Min I Mag.	*Min II Mag.*	*Δ Mag. Min II – Min I*	*Max I Mag.*	*Max II Mag.*	*Δ Mag. Max II – Max I*	*Mag. Range Max II – Min I*
B	12.244 ±0.003	12.155 ±0.002	-0.089 ±0.003	11.514 ±0.002	11.500 ±0.002	-0.015 ±0.003	0.744 ±0.003
V	11.786 ±0.002	11.708 ±0.002	-0.077 ±0.003	11.089 ±0.002	11.078 ±0.002	-0.012 ±0.002	0.708 ±0.002
g'	12.046 ±0.004	11.970 ±0.004	-0.076 ±0.006	11.342 ±0.004	11.326 ±0.004	-0.016 ±0.006	0.720 ±0.006
r'	11.736 ±0.004	11.672 ±0.004	-0.064 ±0.005	11.057 ±0.004	11.050 ±0.004	-0.007 ±0.005	0.686 ±0.005

Secondary Total Eclipse Duration: 21.3 ± 0.2 minutes.

The standard error of a single observation ranged from 5 to 10 mmag. Each light curve shows a flat secondary minimum, indicating a total eclipse. The light curve properties for each passband are given in Table 3 (Min I, Min II, Max I, Max II, Δm, and total eclipse duration). The observations can be accessed from the AAVSO International Database (Kafka 2017).

3. Period study and ephemerides

From the observations, seven new minima timings were determined using the Kwee and van Woerden (1956) method. Four minima timings were available for each eclipse, one from each of the four passbands observed (B, V, g', r'). No significant offsets were found between the timings in each set. The minimum for each eclipse was computed by averaging the four timings. The new times of minima are collected in Table 4, along with additional eclipse timings found in the literature.

The initial ephemeris used to calculate the O–C residuals in Table 4 was taken from the International Variable Star Index (VSX; Watson *et al.* 2006):

$$\text{HJD Min I} = 2452856.8533 + 0.494320\ E. \quad (1)$$

The O–C residuals of Equation 1 are shown in the top panel of Figure 4. The general trend of the residuals indicates the orbital period of GR Psc is continuously decreasing. A least-squares solution to the residuals of Equation 1 gives the following quadratic ephemeris:

$$\text{HJD Min I} = 2458807.4790(4) + 0.4943181(2)\,E - 1.67(8)\times10^{-10}\,E^2. \quad (2)$$

The rate of period change for this solution is $dP/dt = -2.5(1)\times10^{-7}$ d yr^{-1}, about 2.1 seconds per century. The best-fit quadratic line from Equation 2 is the solid line in the middle panel of Figure 4, with the residuals shown in the bottom panel.

An updated linear ephemeris was computed by least-squares using the residuals of Equation 1 is given by:

$$\text{HJD Min I} = 2458807.479(2) + 0.4943188(1)\ E. \quad (3)$$

Due to the changing period of this star, only the most recent minima times (2016–2019) were used in this solution. The best-fit linear line from Equation 3 is the solid line segment shown in the top panel of Figure 4. This new linear ephemeris should be useful for predicting future primary eclipse times but will need to be updated frequently.

Table 4. Times of minima and O–C residuals.

Epoch HJD 2400000+	*Error*	*Cycle*	*O–C*	*References*
51467.80630	—	–2810.0	0.00780	Nicholson and Varley (2006)
52856.85330	—	0.0	0.00000	GCVS (Samus *et al.* 2017), VSX (Watson *et al.* 2014)
55528.66030	0.00010	5405.0	0.00740	Diethelm (2011)
55577.35080	—	5503.5	0.00738	Nagai (2012)
55585.25800	—	5519.5	0.00546	Nagai (2012)
55805.48000	0.00030	5965.0	0.00790	Hübscher and Lehman (2013)
55818.57890	0.00100	5991.5	0.00732	Banfi *et al.* (2012)
55859.36060	0.00010	6074.0	0.00762	Hübscher and Lehman (2013)
55894.70210	0.00040	6145.5	0.00524	Diethelm (2012)
56558.82180	0.00020	7489.0	0.00602	Samolyk (2015)
56578.10010	—	7528.0	0.00584	Nagai (2014)
56952.79470	0.00020	8286.0	0.00588	Samolyk (2015)
57703.66490	0.00010	9805.0	0.00400	Samolyk (2017)
58050.67770	0.00010	10507.0	0.00416	Samolyk (2018)
58369.51249	0.00005	11152.0	0.00255	Ozavci *et al.* (2019)
58778.80858	0.00019	11980.0	0.00168	present paper
58779.79751	0.00019	11982.0	0.00197	present paper
58780.78610	0.00020	11984.0	0.00192	present paper
58803.77171	0.00008	12030.5	0.00165	present paper
58805.74886	0.00024	12034.5	0.00152	present paper
58806.73795	0.00023	12036.5	0.00197	present paper
58807.72602	0.00018	12038.5	0.00140	present paper

4. Analysis

4.1. Color, temperature, spectral type, absolute magnitude, luminosity

To determine the observed color of this system, the large number of observations (over 900 in each passband) were binned in both phase and magnitude with a phase width of 0.01. The phases and magnitudes in each bin were averaged. Figure 5 shows the resulting binned V light curve and the (B–V) color curve (bottom panel). The average observed color over the entire phase range is (B–V) = 0.438 ± 0.009. The color excess for this system, E(B–V) = 0.035 ± 0.018, was determined from

dust maps based on Pan-STARRS 1 and 2MASS photometry and Gaia parallaxes (Green *et al.* 2018). A small color excess for this system is not unexpected, given its low galactic latitude (b = –41°) and proximity to Earth. The distance, $d = 524^{25}_{23}$ pc, was determined from the Gaia DR2 parallax (Bailer-Jones *et al.* 2018; Gaia 2016, 2018). Subtracting the color excess from the average observed color gives an intrinsic color of $(B–V)_o = 0.40 \pm 0.02$.

A spectroscopically determined temperature is not available for this star. A machine-learning regression analysis using Gaia DR2 data, combined with data from four spectroscopic surveys, gives a temperature of $T_{eff} = 6811 \pm 145$ K, and a spectral type of F2 (Bay *et al.* 2019; Pecaut and Mamajek 2013). This temperature will be assigned to the primary star for light curve modeling in section 4.2.

4.2. Light curve modeling

Light curve solutions were obtained using the 2015 version of the Wilson-Devinney (WD) program where computations were done simultaneously in all four passbands (Wilson and Devinney 1971; Van Hamme and Wilson 1998). For input data, the observed standard magnitudes were binned in both phase and magnitude (see section 4.1). For each color, 100 normal points were formed from the observations. For WD modeling, these magnitude normal points were converted to normalized flux, with each point assigned a weight equal to the number of observations forming that point.

The light curves are smoothly varying and have similar minima depths, which suggests the stars are in a contact configuration with a common convective envelope. The WD program was therefore configured for overcontact binaries (Mode 3). The Kurucz stellar atmosphere model was applied (Kurucz 2002). The primary star's effective temperature was fixed at $T_1 = 6811$ K (see section 4.1). The subscripts 1 and 2 refer to the hotter and cooler components, respectively. With the effective temperature below 7200 K, standard convective parameters were used: gravity brightening, $g_1 = g_2 = 0.32$ (Lucy 1968) and bolometric albedo value $A_1 = A_2 = 0.5$ (Ruciński 1969). Logarithmic limb darkening coefficients were calculated by the program from tabulated values using the method of Van Hamme (1993). The adjustable parameters include the inclination (i), mass ratio ($q = M_2/M_1$), potential ($\Omega_1 = \Omega_2$), temperature of the secondary star (T_2), the band-specific luminosity for each wavelength (L), third light (l), and phase shift. Since no spectroscopic mass ratio is currently available for the system, a search for the solution was made using several fixed values of mass ratio. The results of this q-search gave a clear residual minimum at about q = 0.430 (see Figure 6). This value was used as the starting mass ratio for the final solution iterations where the mass ratio was an adjustable parameter. The final best-fit solution parameters are shown in column 2 of Table 5. The filling-factor was computed using the method of Lucy and Wilson (1979) given by:

$$f = \frac{\Omega_{inner} - \Omega}{\Omega_{inner} - \Omega_{outer}}, \quad (4)$$

where Ω_{inner} and Ω_{outer} are the inner and outer critical equipotential surfaces and Ω is the equipotential that describes the stellar surface. When third light was included in the adjustable parameters, only negligibly small or negative values resulted. This indicates there is no detectable third light contribution to the system light. The solution also did not find a phase-shift necessary to fit the observations; they had been accurately phased by the ephemeris. Figure 7 shows the normalized light curves for each passband overlaid by the synthetic solution curves (solid lines), and with the residuals shown in the bottom panel.

Table 5. Results derived from light curve modeling.

Parameter	*No Spot*	*Spot*
f (filling factor)	48%	47%
i (°)	83.8 ± 0.4	83.9 ± 0.3
T_1 (K)	[1]6811	[1]6811
T_2 (K)	6762 ± 5	6760 ± 4
$\Omega_1 = \Omega_2$	2.619 ± 0.010	2.619 ± 0.009
q (M2/M1)	0.433 ± 0.008	0.431 ± 0.006
$L_1/(L_1+L_2)$ (B)	0.680 ± 0.012	0.682 ± 0.010
$L_1/(L_1+L_2)$ (V)	0.678 ± 0.012	0.680 ± 0.010
$L_1/(L_1+L_2)$ (g')	0.679 ± 0.012	0.681 ± 0.010
$L_1/(L_1+L_2)$ (r')	0.677 ± 0.011	0.679 ± 0.010
r_1 side	0.4832 ± 0.0008	0.4814 ± 0.0008
r_2 side	0.3409 ± 0.0074	0.3452 ± 0.0061
Spot		*Star$_1$*
colatitude (°)	—	98 ± 5
longitude (°)	—	4 ± 2
spot radius (°)	—	19 ± 2
temp. factor	—	1.06 ± 0.02

[1] *Assumed.*

The subscripts 1 and 2 refer to the star being eclipsed at primary and secondary minimum, respectively.

Note: The errors in the stellar parameters result from the least-squares fit to the model. The actual uncertainties are considerably larger.

4.3. Spot model

The light curves of GR Psc are not perfectly symmetric, as evidenced by the small O'Connell effect. In each light curve, the peak magnitude following secondary minimum (Max II, φ = 0.75) is slightly brighter than the maximum following the primary eclipse (Max I, φ = 0.25). The small differences in the peak magnitudes for each color (Δm) are given in Table 3. The O'Connell effect is generally attributed to hot or cool spots on one or both stars. Light curve asymmetries are often difficult to detect by visual inspection. To better characterize the asymmetries in the GR Psc light curves, an analysis was performed on the normalized flux points using a truncated twelve-term Fourier fit given by:

$$I(\varphi) = a_0 + \sum_{(n=1)}^{12} (a_n \cos(2\pi n\varphi) + b_n \sin(2\pi n\varphi)), \quad (5)$$

where I(φ) is the flux at phase φ and a_0, a_n, and b_n are the Fourier coefficients (Wilsey and Beaky 2009; Akiba *et al.* 2019). Figure 8 shows the Fourier fits to the normalized flux points for each color. In Figure 9 the two halves of the B light curve are superimposed to reveal the asymmetries. The bottom panel shows the difference in normalized flux, ΔI(φ), for each color.

The asymmetry is color dependent, with the B and g′ light curves showing the most deviation and the r′ curve the least. Assuming the asymmetries are caused by star spots, these flux differences indicate a possible hot spot on the primary star, near to but not centered at the contact region of the two stars. The excess light seen in the light curve solution near orbital phase φ = 0.80 also supports a hot spot near this location (see Figure 7).

The program BINARY MAKER 3.0 (BM3) was used to model a hot spot near the neck region of the primary star (Bradstreet and Steelman 2002). The initial orbital and stellar parameters were taken from the WD spotless model with the addition of the spot parameters: colatitude, longitude, spot radius, and temperature factor (T_s / T_{eff}). The spot values were adjusted until a good fit resulted between the synthetic and observed light curves. A new WD solution was then obtained using the spot parameters from the BM3 fit. The best-fit WD spotted solution parameters are shown in column 3 of Table 5. Figure 10 shows the final spotted model fits (solid lines) to the observed light curves with the residuals shown in the bottom panel. The fit improved considerably for this solution with the residuals 28% lower than the spotless model. BM3 generated a graphical representation of the spot model shown in Figure 11.

5. Discussion and conclusions

The secondary total eclipse of GR Psc provided the necessary constraints for a well determined mass ratio (Wilson 1978; Terrell and Wilson 2005). The WD solution mass ratio, combined with an estimate for the primary star's mass, were used to calculate provisional absolute stellar parameters for this system. The primary mass was calculated using the Gazeas and Stępień (2008) period-mass relation for contact binaries,

$$\log M_1 = (0.755 \pm 0.059) \log P + (0.416 \pm 0.024), \qquad (6)$$

where P is the orbital period. Equation 8 gives a primary star mass of $M_1 = 1.5 \pm 0.1\, M_\odot$. The secondary star's mass, $M_2 = 0.66 \pm 0.05\, M_\odot$, was determined using the mass ratio. The primary star of a contact binary is typically on the main sequence, providing a second method for estimating its mass. Using the primary's effective temperature, the mass was interpolated from the tables of Pecaut and Mamajek (2013), giving a value of $1.44\, M_\odot$. The two values are in good agreement, differing by only 4%. The separation between the mass centers of the stars was calculated using Kepler's Third Law. Using the spotted solution parameters, the WD light curve program (LC) computed the mean radius and bolometric magnitude (M_{bol}) of each star. The stellar luminosities were calculated using the following equation:

$$M_{bol} = 4.74 - 2.5 \log (L / L_\odot) . \qquad (7)$$

The calculated stellar masses, radii, luminosities, and the semi-major axis are collected in Table 6.

The nonlinear O–C variations in the orbital periods of eclipsing binaries are caused by mass loss from the system, third bodies, or mass transfer between the component stars.

Table 6. Provisional absolute parameters.

Parameter	*Symbol*	*Value*
Stellar masses	M_1 ($M_\odot$)	1.5 ± 0.1
	M_2 ($M_\odot$)	0.66 ± 0.05
Semi-major axis	a ($R_\odot$)	3.42 ± 0.08
Mean stellar radii	R_1 ($R_\odot$)	1.66 ± 0.03
	R_2 ($R_\odot$)	1.17 ± 0.03
Bolometric magnitude	$M_{bol,1}$	2.93 ± 0.09
	$M_{bol,2}$	3.72 ± 0.12
Stellar luminosity	L_1 ($L_\odot$)	5.4 ± 0.4
	L_2 ($L_\odot$)	2.6 ± 0.3

The calculated values in this table are provisional. Radial velocity observations are necessary for direct determination of M1, M2, and a.

The decreasing orbital period of GR Psc may be the result of magnetic braking, but the apparent lack of dark spots on the stars indicates little magnetic activity at the current time. Light-time effects could also cause apparent orbital period change due to the binary pair orbiting a third body. In this case the observed period change may be a small part of a sinusoidally varying ephemeris. No appreciable third light was found in the WD light curve solutions, but this does not preclude a third, very low luminosity star in the system. Additional minima timings over many years will be necessary to determine if GR Psc is a trinary system. Given this system's contact configuration, the decreasing orbital period could also be caused by conservative mass exchange from the primary star to the less massive secondary. Using the rate of period change computed in section 2 and the estimated stellar masses gives a mass transfer rate of $-5.3\,(2) \times 10^{-10}\, M_\odot$ / day. The matter and energy exchange through the neck of the common envelope would explain the higher local temperature found in this region (Van Hamme and Wilson 1985). Additional supporting evidence for the location of this hot region can be seen in the Figure 5 color plot. The system light is slightly bluer at the orbital phases that provide the best direct line-of-sight to the hot spot, at approximately φ = 0.2 and φ = 0.8 (see Figure 11). The light is reddened a small amount at primary eclipse as the secondary star transits the slightly hotter primary star and blocks from view the hot spot in the neck region.

GR Psc is an A-type W UMa contact binary where the primary eclipse is a transit of the larger star by the smaller and slightly cooler secondary component (Binnendijk 1970). The best-fit WD spotted solution gives a temperature difference between the component stars of only 51 K, a mass ratio of $M_2 / M_1 = 0.431$, and a moderate degree of contact with a filling factor of 47%. A period analysis indicates a decreasing orbital period likely caused by mass exchange. The hot spot modeled in the neck region of the primary star is not unexpected, given the energy exchange that must occur between the stars. To confirm the provisional absolute stellar parameters presented here, a future spectroscopic study of this system would be invaluable.

6. Acknowledgements

This research was made possible through the use of the AAVSO Photometric All-Sky Survey (APASS), funded by the Robert Martin Ayers Sciences Fund. This research has made

use of the SIMBAD database and the VizieR catalogue access tool, operated at CDS, Strasbourg, France. This work has made use of data from the European Space Agency (ESA) mission Gaia (https://www.cosmos.esa.int/gaia), processed by the Gaia Data Processing and Analysis Consortium (DPAC, https://www.cosmos.esa.int/web/gaia/dpac/consortium). Funding for the DPAC has been provided by national institutions, in particular the institutions participating in the Gaia Multilateral Agreement. I would like to offer my sincere thanks to the editorial staff at JAAVSO for their support, and to acknowledge the anonymous referee who provided a careful review and valuable recommendations for this paper.

References

Akiba, T., Neugarten, A., Ortmann, C., and Gokhale, V. 2019, *J. Amer. Assoc. Var. Star Obs.*, **47**, 186.

Bailer-Jones, C., Rybizki, J., Fouesneau, M., Mantelet, G., and Andrae, R. 2018, *Astron. J.*, **156**, 58.

Banfi, M., *et al.* 2012, *Inf. Bull. Var. Stars*, No. 6033, 1.

Bay, Y., Liu, J.-F.g, Bai, Z.-R., Wang, S., and Fan, D.-W. 2019, *Astron. J.*, **158**, 93.

Binnendijk, L. 1970, *Vistas Astron.*, **12**, 217.

Bradstreet, D. H., and Steelman, D. P. 2002, *Bull. Amer. Astron. Soc.*, **34**, 1224.

Diethelm, R. 2011, *Inf. Bull. Var. Stars*, No. 5960, 1.

Diethelm, R. 2012, *Inf. Bull. Var. Stars*, No. 6011, 1.

Gaia Collaboration, *et al.* 2016, *Astron. Astrophys.*, **595A**, 1.

Gaia Collaboration, *et al.* 2018, *Astron. Astrophys.*, **616A**, 1.

Gazeas, K., and Stępień, K., 2008, *Mon. Not. Roy. Astron. Soc.*, **390**, 1577.

Gettel, S. J., Geske, M. T., and McKay, T. A. 2006, *Astron. J.*, **131**, 621.

Green, G. M., *et al.* 2018, *Mon. Not. Roy. Astron. Soc.*, **478**, 651.

Henden, A. A., *et al.* 2015, AAVSO Photometric All-Sky Survey, data release 9, (https://www.aavso.org/apass).

Hübscher, J., and Lehmann, P. B. 2013, *Inf. Bull. Var. Stars*, No. 6070, 1.

Kafka, S. 2017, variable star observations from the AAVSO International Database (https://www.aavso.org/aavso-international-database).

Kurucz, R. L. 2002, *Baltic Astron.*, **11**, 101.

Kwee, K. K., and van Woerden, H. 1956, *Bull. Astron. Inst. Netherlands*, **12**, 327.

Lucy, L. B., 1968, *Astrophys. J.*, **151**, 1123.

Lucy, L. B., and Wilson, R. E. 1979, *Astrophys. J.*, **231**, 502.

Mirametrics. 2015, Image Processing, Visualization, Data Analysis, (https://www.mirametrics.com).

Nagai, K. 2012, *Bull. Var. Star Obs. League Japan*, No. 53, 1.

Nagai, K. 2014, *Bull. Var. Star Obs. League Japan*, No. 56, 1.

Nicholson, M. and Varley, H. 2006, *Inf. Bull. Var. Stars*, No. 5700, 16.

Ozavci, I., *et al.* 2019, *Open Eur. J. Var. Stars*, **203**, 1.

Pecaut, M. J., and Mamajek, E. E. 2013, *Astrophys. J., Suppl. Ser.*, **208**, 9 (http://www.pas.rochester.edu/~emamajek/EEM_dwarf_UBVIJHK_colors_Teff.txt).

Pojmański, G. *et al.* 2002, *Acta Astron.*, **52**, 397.

Ruciński, S. M. 1969, *Acta Astron.*, **19**, 245.

Samolyk, G. 2015, *J. Amer. Assoc. Var. Star Obs.*, **43**, 77.

Samolyk, G. 2017, *J. Amer. Assoc. Var. Star Obs.*, **45**, 121.

Samolyk, G. 2018, *J. Amer. Assoc. Var. Star Obs.*, **46**, 184.

Samus N. N., Kazarovets E. V., Durlevich O. V., Kireeva N. N., and Pastukhova E. N. 2017, *Astron. Rep.*, **61**, 80 (*General Catalogue of Variable Stars: Version GCVS 5.1*, http://www.sai.msu.su/groups/cluster/gcvs/gcvs).

Terrell, D., Gross, J., and Cooney, W. R. 2012, *Astron. J.*, **143**, 99.

Terrell, D., and Wilson, R. E. 2005, *Astrophys. Space Sci.*, **296**, 221.

van Hamme, W. 1993, *Astron. J.*, **106**, 2096.

van Hamme, W., and Wilson, R. E. 1985, *Astron. Astrophys.*, **152**, 25.

van Hamme, W., and Wilson, R. E. 1998, *Bull. Amer. Astron. Soc.*, **30**, 1402.

Watson, C., Henden, A. A., and Price, C. A. 2014, AAVSO International Variable Star Index VSX (Watson+, 2006–2014; http://www.aavso.org/vsx).

Wilsey N. J., and Beaky M. M. 2009, in *The Society for Astronomical Sciences 28th Annual Symposium on Telescope Science*, The Society for Astronomical Sciences, Rancho Cucamonga, Calif, 107.

Wilson, R. E. 1978, *Astrophys. J.*, **224**, 885.

Wilson, R. E., and Devinney, E. J., 1971, *Astrophys. J.*, **166**, 605.

Woźniak, P. R., *et al.* 2004, *Astron. J.*, **127**, 2436.

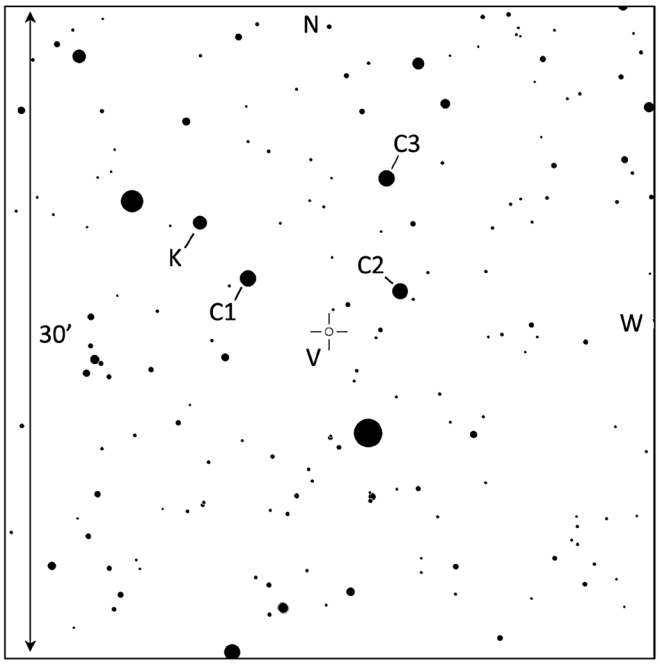

Figure 1. Finder chart for GR Psc (V), comparison (C1–C3), and check (K) stars.

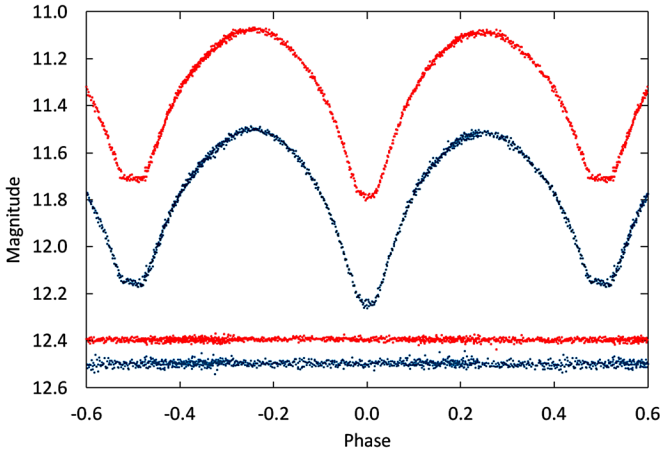

Figure 2. The observed Johnson B and V light curves in standard magnitudes. The bottom curves are the Johnson B and V check star magnitudes offset +0.52 and +1.42 magnitudes, respectively. For both sets of curves, the top curve is Johnson V and the bottom curve is Johnson B.

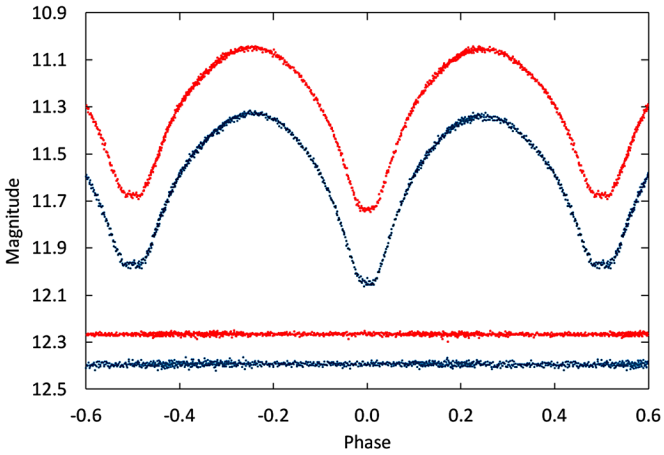

Figure 3. The observed Sloan g' and r' light curves in standard magnitudes. The bottom set of curves are the Sloan g' and r' check star magnitudes offset by +0.90 and 1.60, respectively. For both sets of curves, the top curve is Sloan r' and the bottom curve is Sloan g'.

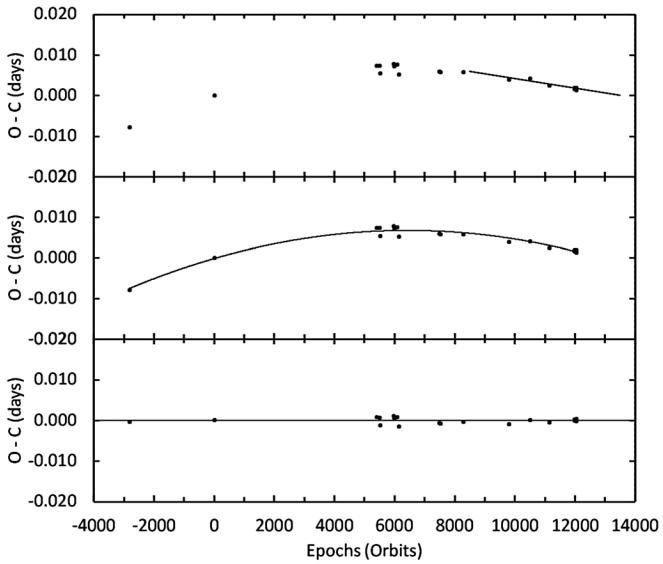

Figure 4. The top panel shows the residuals (dots) calculated from the linear ephemeris of Equation 1. The solid line segment is the best-fit linear line from Equation 3 using minima times from 2016 to 2019. The middle panel shows the O–C residuals from Equation 1 with the solid line the quadratic ephemeris fit from Equation 2. The bottom panel shows the residuals after removing the downward parabolic change.

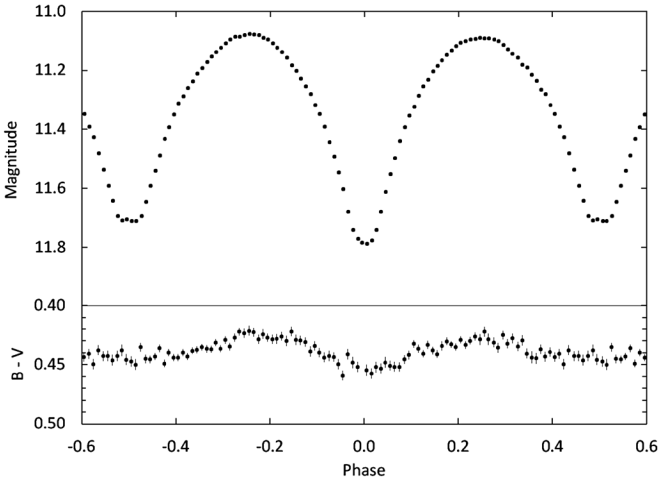

Figure 5. Light curve of all V band observations in standard magnitudes (top panel). The observations were binned with a phase width of 0.01. The errors for each binned point are about the size of the plotted points. The B–V colors were calculated by subtracting the linearly interpolated binned B and V magnitudes.

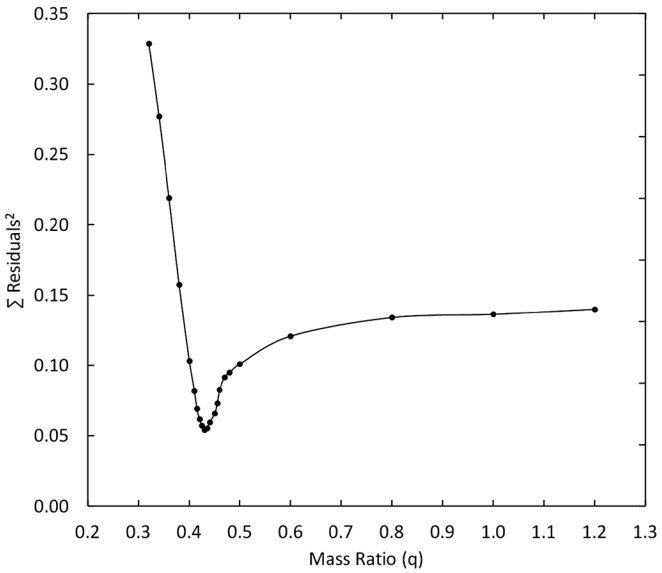

Figure 6. Results of the q-search showing the relation between the sum of the residuals squared and the mass ratio (q).

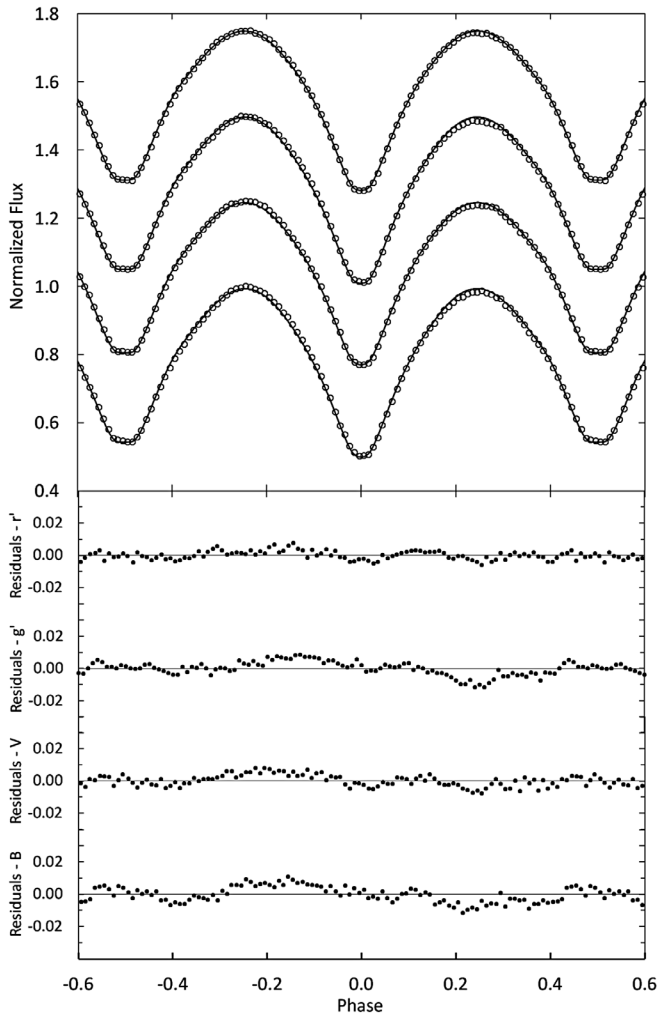

Figure 7. Comparison between the WD spotless best-fit model (solid curve) and the observed normalized flux curve. From top to bottom the filters are r' g' V B. Each light curve is offset by 0.25 for this combined plot. The residuals are shown in the bottom panel. Error bars are omitted from the points for clarity.

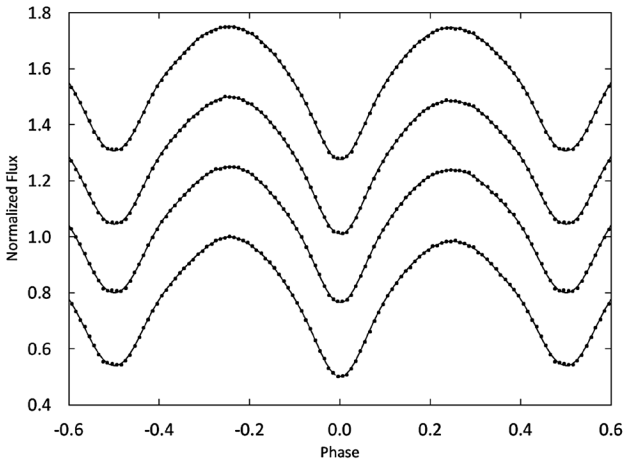

Figure 8. The normalized flux for GR Psc. From top to bottom the plotted points correspond to the r' g' V B filters. The Fourier fits are the solid lines. Each curve is offset by 0.25 for this combined plot. Error bars are omitted from the points for clarity.

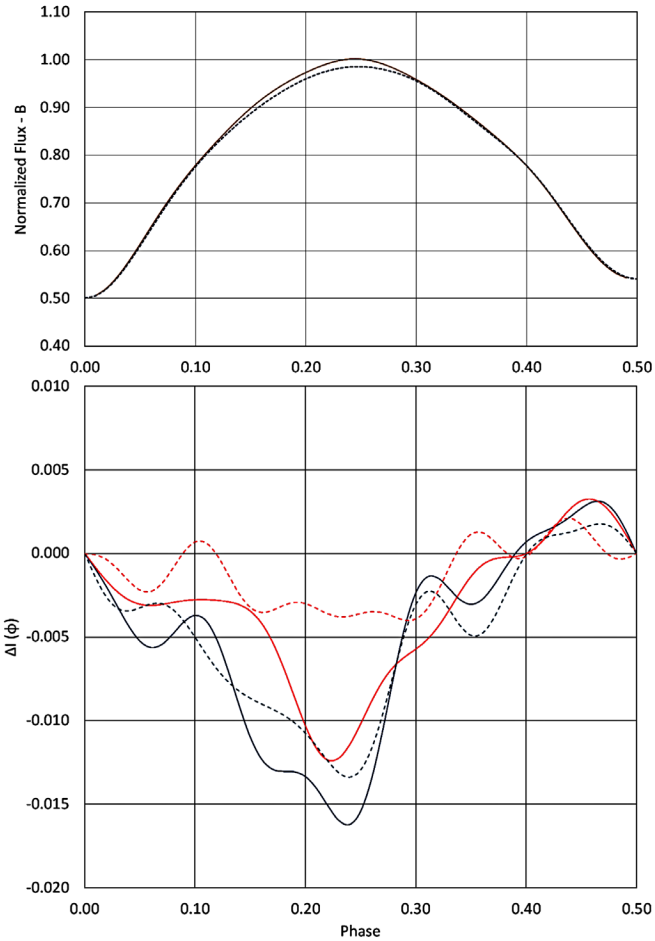

Figure 9. The top panel superimposes the two halves of the B light curve to reveal the light curve asymmetries. The dashed line is orbital phase (φ) 0.0 to 0.5, and the solid line 0.5–1.0. The bottom panel shows the differences between the two halves of the light curve for each color. The solid blue line is the B filter, the solid red line the V, the dashed blue line the g', and the dashed red line the r'.

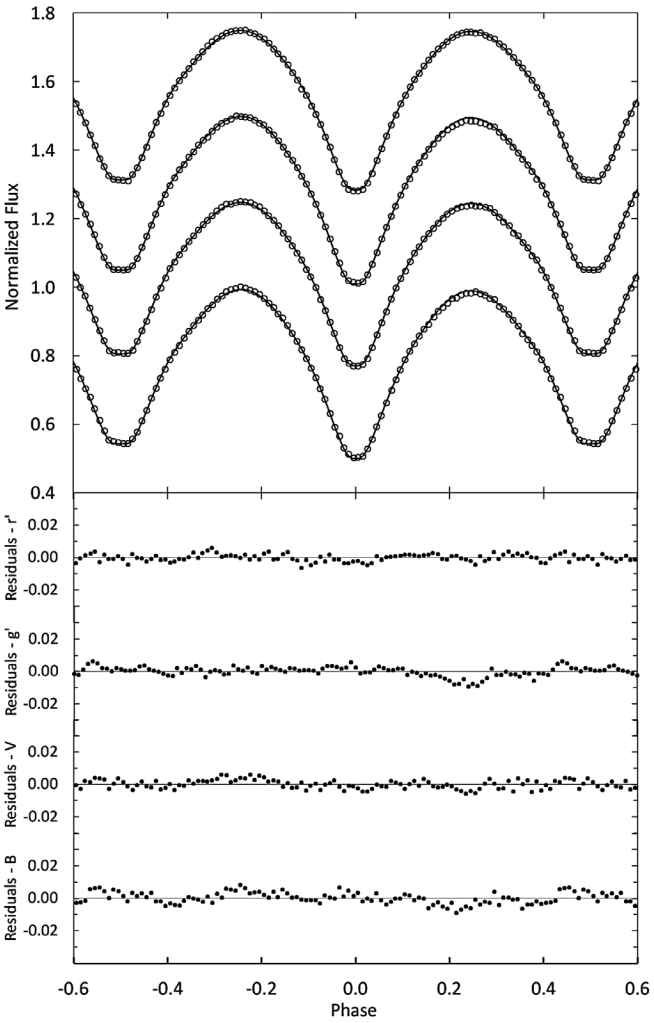

Figure 10. Comparison between the WD spotted best-fit model (solid curve) and the observed normalized flux curve. From top to bottom the filters are r' g' V B. Each light curve is offset by 0.25 for this combined plot. The residuals are shown in the bottom panel. Error bars are omitted from the points for clarity.

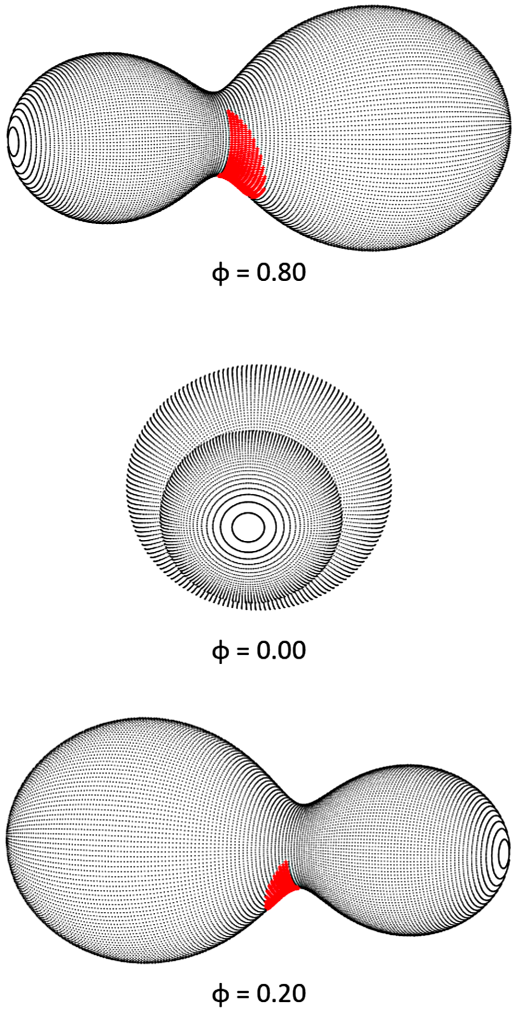

Figure 11. Roche Lobe surfaces of the best-fit WD spot model showing spot locations. The orbital phase is shown below each diagram.

Maintaining the Ephemeris of 20 CoRoT Planets: Transit Minimum Times and Potential Transit Timing Variations

Hans J. Deeg
Instituto de Astrofisica de Canarias, C. Vía Láctea S/N, E-38205 La Laguna, Tenerife, Spain, and Universidad de La Laguna, Dept. de Astrofísica, E-38206 La Laguna, Tenerife, Spain; address correspondence to hdeeg@iac.es

Peter Klagyivik
Instituto de Astrofisica de Canarias, C. Vía Láctea S/N, E-38205 La Laguna, Tenerife, Spain, Universidad de La Laguna, Dept. de Astrofísica, E-38206 La Laguna, Tenerife, Spain, and Institute of Planetary Research, German Aerospace Center, Rutherfordstrasse 2, D-12489 Berlin, Germany

James D. Armstrong
University of Hawai'i Institute for Astronomy, 34 Ohia Ku Street, Pukalani, HI 96768

David Nespral
Instituto de Astrofisica de Canarias, C. Vía Láctea S/N, E-38205 La Laguna, Tenerife, Spain, and Universidad de La Laguna, Dept. de Astrofisica, E-38206 La Laguna, Tenerife, Spain

Lev Tal-Or
Department of Physics, Ariel University, Ariel 40700, Israel

Roi Alonso
Instituto de Astrofisica de Canarias, C. Vía Láctea S/N, E-38205 La Laguna, Tenerife, Spain, and Universidad de La Laguna, Dept. de Astrofisica, E-38206 La Laguna, Tenerife, Spain

Richelle Cabatic
Dartmouth College, Thayer School of Engineering, 14 Engineering Drive, Hanover, NH 03755

Cameron Chaffey
Department of Physics, University of California, Davis, CA 95616

Bartek Gauza
Centre for Astrophysics Research, School of Physics, Astronomy and Mathematics, University of Hertfordshire, College Lane, Hatfield AL10 9AB, United Kingdom

Sergio Hoyer
Aix Marseille Université, CNRS, CNES, LAM, Marseille, France

Christopher J. Lindsay
Yale University Department of Astronomy, 52 Hillhouse Avenue, New Haven, CT 06511

Paulo Miles-Páez
European Southern Observatory, Garching, Germany

Patricio Rojo
Department of Astronomy, Universidad de Chile

Brandon Tingley
Bøggildsvej 14, 8530 Hjortshøj, Denmark

Received May 31, 2020; revised September 21, 2020; accepted September 27, 2020

Abstract We present 33 transit minimum times of 20 transiting planets discovered by the CoRoT space mission. These have been obtained from ground-based observations since the mission's end in 2012, with the objective to maintain the ephemeris of these planets and to identify potential transit time variations. Twelve of the observed planets are in the CoRoT fields near the galactic center and the remaining eight planets are in the fields near the anticenter. We detect indications for significant transit timing variations in the cases of CoRoT 3b, 11b, 13b, 27b. For two more planets (CoRoT 18b and 20b) we conclude that timing offsets in early follow-up observations led to ephemerides in discovery publications that are inconsistent with timings from follow-up observations in later epochs. In the case of CoRoT-20b, this might be due to the influence from a further non-transiting planet. We also note that a significant majority (23 of 33) of our reported minimum times have negative O–C values, albeit most of them are within the expected uncertainty of the ephemeris. All acquired light curves are available at the Strasbourg Astronomical Data Center (CDS).

1. Introduction

CoRoT was the first satellite mission with a principal dedication to extrasolar planets (Baglin *et al.* 2006; Auvergne *et al.* 2009), having led to the discovery of 37 transiting planets to date (Deleuil *et al.* 2018, with Moutou *et al.* 2013 for a more detailed overview of the first 23 planets). The mission was active in the years 2008–2012 and pointed to 24 different fields which were all within two circular zones with a radius of about 7 degrees, called the "CoRoT Eyes." One of them was near the galactic center (centered at 18^h 50^m, 0° in equatorial coordinates) and the other one near the anticenter (at 6^h 50^m, 0°). The 24 pointings acquired during the lifetime of CoRoT had durations of varying lengths, of 24 to 153 days, and the precision of the ephemeris predicting the times of future transit events is limited accordingly. In particular, planets detected during the short pointings or planets with transits of low signal-to-noise might become "lost" within a few years, due to uncertainties in the timing of transits that are exceeding 3 hours (Deeg *et al.* 2015; see also Dragomir *et al.* 2020 for a similar concerns regarding the current TESS and the previous Kepler/K2 missions). This error was considered the maximum permissible in order to observe a transit reliably during a night with a predicted transit. Given this danger of future transits of the CoRoT planets becoming unobservable in practice, but with the objective to revise the CoRoT planets for the presence of eventual transit timing variations (TTVs), two projects to re-observe their transits from the ground were initiated. The results from the first one were recently published by Raetz *et al.* (2019, hereafter R+19), covering CoRoT-5b, 8b, 12b, 18b, 20b, and 27b. In this contribution we provide further transit timings of all of them (except CoRoT-5b) and of another 16 CoRoT planets, and indicate potential TTVs. We note that that the TESS mission (Ricker *et al.* 2015) will provide further transit timings which can then be contrasted against the presented ephemeris. CoRoT anticenter planets were observed in TESS sectors 6 and 7 in winter 2018/2019 and will be observed again in sectors 33 and 34 scheduled for winter 2020/2021, while TESS pointings to the CoRoT center fields are still to be scheduled and will happen at earliest in spring 2022. In particular, we expect that the transit timings presented here—between the CoRoT and eventual TESS observations—will be useful to check if linear ephemerides describe well the transit times or if changing planet orbital periods fit better to the observations. A joint analysis of the ground-based timings presented here and elsewhere, together with those from CoRoT and TESS, is the subject of a forthcoming paper (Klagyivik *et al.*, in prep).

2. Observations and analysis

The light curves that have been used for the transit times reported here were acquired with a variety of telescopes, as listed in Table 1. Unless indicated otherwise, CCD imaging in R filters was used, with temporal resolutions that were appropriate to the given target, ranging from 10 seconds to 3 minutes, and the light curves were obtained using the observers' particular photometry software. The extraction of the transit's mid-time, T_c, from the light curves was however performed consistently by an experienced member of our team (HJD), employing the following considerations:

Usually, ground-based transit timings are being derived from light curves that include both transit ingress and egress. For example, nearly all light curves which are collected in the Exoplanet Transit Database (ETD; Poddany *et al.* 2010) are from full transits. However, for about half of the cases reported in this communication, the timings are based on partial transits that include only ingress or egress. This difference arose from a combination of limited observing windows and the uncertainty in the predicted transit times. In the cases of incomplete transits, the moments of first (T_1) or last contact (T_4) were derived by visual inspection of the light curves, given that these contacts are the features in a transit light curve that can most reliably be recognized. The trustworthiness of each determination of T_1 or T_4 was evaluated from a comparison of our ground-based light curves against those from CoRoT, considering the following factors:

– The overall noise of the light curve and clearness of recognizing an in- or egress.

– The slope of the in- or egress in comparison to the CoRoT light curves.

– The time-difference between the observed and the predicted moment of T_1 or T_4, considering the expected prediction error.

– In cases where a complete in- or egress was observed, the duration of the in/egress and the amplitude of the transit were also evaluated against CoRoT curves.

Only detections considered as secure are included in this communication. For partial transits, their center-times, T_c, were then derived as :

$$T_c = T_1 + T_{14}/2 \text{ or } T_c = T_4 - T_{14}/2, \quad (1)$$

where T_{14} is the duration of an entire transit, for which the values that were reported in the planets' discovery publications were used (see Table 2 for references). If our ground-observations included both T_1 and T_4, the times T_c were derived from averaging T_1 and T_4. In cases with well recognizable in- and egress slopes or for full transits, T_c was derived using the bisected chord method, unless noted otherwise in Table 1.

Error estimates of T_c are based on visual estimations of an acceptable range for T_1 or T_4 values, combined with the errors of $T_{14}/2$ that have been reported in the literature, or—for the full transits—considering the range of acceptable results from the bisected chord method.

It was attempted to write and use a specific pipeline to recognize the moments of T_1 or T_4 and to determine their values and errors. Due to the large variety of light curves in terms of S/N, transit coverage, and temporal resolution, this effort did not however provide results of sufficiently consistent reliability. Since most results reported here are based only on in- or egress observations, the use of more sophisticated methods for the determination of T_c for the cases of fully observed transits was then also discarded.

3. Results and discussion of individual systems

Table 1 lists the transit times, T_c, that have been observed in this project, together with their error, σ_{T_c}, and the type of transit that was observed: I = ingress (T_1) , E = egress (T_4), B = both an in- and egress was observed at least partially, F = full transit observed. Times are indicated in barycenter-corrected universal time. Furthermore, we indicate cycle numbers and O–C residuals against the ephemerides that are compiled in Table 2. The next column, S/N_{O-C}, is an indicator for the relevance of an O–C residual, in terms of the number of "sigmas." The noise N corresponds to the expected uncertainty of the transit time T_c, based on the period and epoch error of a given ephemeris. N is then obtained by the error-sum of the timing measurement error and the uncertainty of the ephemeris:

$$S/N_{O-C} = (O-C)/\sqrt{(\sigma_{T_c}{}^2 + \sigma_{eph}{}^2)} \qquad (2)$$

where

$$\sigma_{eph}{}^2 = \sigma_E{}^2 + (E\,\sigma_P)^2 \,,$$

with σ_E and σ_P being the ephemeris' epoch and period errors from Table 2, and E being the cycle number. The next column indicates the telescopes used and the rightmost one provides references to further T_c values that we are aware of. For entries from ETD, in some cases (indicated in Table 1) we list only the number of timings with ETD's quality indicator of DQ ≤ 3, meaning good to excellent curves.

Large values of S/N_{O-C} should only be considered as first indicators for potential TTVs; these are discussed in the notes to the individual systems that follow below. S/N_{O-C} is not a reliable indicator for TTVs because the errors of the ephemeris in the literature did not only depend on quantifiable parameters which are relevant for an ephemeris' precision (transit depth, in/egress duration, photometric noise, length of coverage; Deeg 2015; Deeg and Tingley 2017), but they were also derived using a variety of different methods. This led to significant inconsistencies among their reported errors, as was pointed out by Deeg and Tingley (2017).

Below we provide comments on all systems observed, in the order of their listing in Table 1. Plots of light curves for all timing measurements of Table 1 (except for previously published curve by the Euler 1.2 m of CoRoT-18b, which was not obtained by our team) are shown in the Appendices, whereas the corresponding tabulated light curves are available at the VizieR service of the Strasbourg Astronomical Data Center (CDS) via anonymous ftp to cdsarc.u-strasbg.fr (130.79.128.5) or via http://cdsarc.u-strasbg.fr/viz-bin/qcat?J/other/JAVSO.

3.1. Discussion of individual systems

CoRoT-2b For this system, ETD currently lists timings from over 90 follow-up observations, with more than half of them being considered of good to excellent data quality, using ETD's data quality (DQ) indicator of 3 or lower as reference. All of these timings line up very well and are within an O–C of ±0.01 d against the ephemeris of Alonso *et al.* (2008), of which our measurement is no exception. CoRoT-2b counts also with a few which pre-discovery timings obtained about 2 years before the CoRoT observations (Rauer *et al.* 2010). Our light curve taken with the IAC80 (Figure 1) has been analyzed many times in a university course using the TAP (Gazak *et al.* 2012) transit analyzer with a multi-parametric MCMC chain, from which the T_c value in Table 1 has been derived.

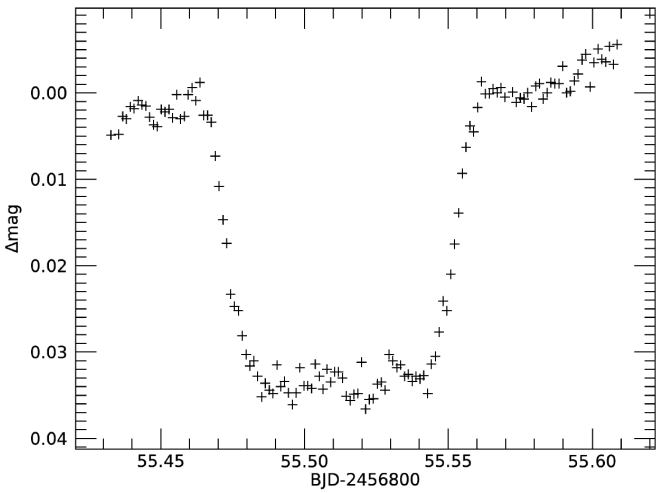

Figure 1. Light curve of a transit of CoRoT-2b acquired with the IAC80 on 2014 Jul 16. The vertical axis is in uncalibrated relative magnitudes. This plot is similar to those shown in the Appendices for all transits observed for this work.

CoroT-3b In data acquired with the 10.4-m Gran Telescopio Canarias (GTC) on 2017 Aug 20, the transit appears 2.25 hours earlier than predicted from the ephemeris of Deleuil *et al.* (2008). An alternative ephemeris derived from the same original CoRoT data by Triaud *et al.* (2009) leads to a similar offset, with the GTC transit being 2.11 h too early. In either case, the deviation in the transit time is much larger than the uncertainty of CoRoT-3b's ephemeris, which was ±6 resp. ±4 minutes in Aug 2017. The ETD database provides three timing values taken in 2009, 2010, and 2017, which do not indicate any deviation in periodicity. A revision of the underlying light curves in ETD however led us to the conclusion that these are of too low quality for the provision of meaningful estimates of the transit times, as they lack any well recognizable partial or full transits. This target does therefore exhibit likely transit timing variations and should be re-observed with priority, with results from TESS being awaited.

CoRoT-8b A first analysis of our transit times showed a significant deviation from the ephemeris published in CoRoT-8b's discovery paper (Bordé *et al.* 2010), which incidentally claimed the potential presence of transit timing variations. An error in the ephemeris by Bordé *et al.* was then found, with its T_0 being ~85 minutes earlier than the first transit in the CoRoT data. Also, R+19 published a revised ephemeris based on their own follow-up observations (Table 1) plus the full set of CoRoT transits. Against these revised ephemeris, our transit-timing acquired with the IAC80 is within the expected uncertainties.

CoRoT-9b After discovery of this planet (Deeg *et al.* 2010), a further transit was observed by CoRoT itself in a dedicated pointing on 2011 Jul 4, which was observed simultaneously by the Spitzer mission in the 4.5μm band (Bonomo *et al.* 2017). The mid-transit times, T_c, differ between the CoRoT and the Spitzer observation by only 104 seconds, which implies that

Table 1. Observed transit center times. They are indicated in barycenter corrected universal time.

CoRoT Planet	*T_c (BJD_{UTC}−2400000)*	*σ_{T_c} (d)*	*Type*	*Cycle (E)*	*O–C (d)*	*S/N_{O-C}*	*Telescope, Reference[1]*	*Reference to Further T_c values*
				Center Field				
2b	56855.51267	0.00036	F	1502	–0.0035	–1.4	IAC80	>90 T_c in ETD
3b	57986.46160[2]	0.00130	B	870	–0.0938	–20.6	GTC	
8b	56885.53000	0.00300	B	426	–0.0047	–1.1	IAC80	2 T_c in R+19; 2 T_c in ETD (DQ≤3)
9b	56889.89534	0.00330	E	16[3]	0.0056	1.6	LCO 2M–FTN; LCO 1M–SSO	
10b	56868.43692	0.00700	E	196	–0.0643	–1.6	IAC80	
11b	56828.41800	0.00500	E	745	–0.0368	–3.8	WISE 0.46m	3 T_c in ETD
16b	56834.63000	0.00800	F	357	–0.0442	–0.6	IAC80	
16b	56861.38200	0.00800	F	362	–0.0535	–0.7	LCO 1M–SAAO	
17b	56852.49700	0.01000	F	512	–0.0795	–0.5	LT	
27b	56810.47029	0.00500	E	297	–0.0837	–4.5	IAC80	
27b	56853.37729	0.00500	E	309	–0.0806	–4.2	STELLA	
29b	56075.23000	0.00700	F	113	0.0006	0.1	LCO 2M–FTN	2 T_c in Pallé *et al.* (2016)
29b	56853.43500	0.00500	B	386	0.0000	0.0	IAC80 (Cabrera *et al.* 2015)	2 T_c in Pallé *et al.* (2016)
30b	56861.48000	0.00500	F	132	0.0388	1.2	IAC80 (Bordé *et al.* 2020)	
36b	55814.17090	0.00400	E	28	0.0032	0.8	WISE 1m	
36b	56864.45890	0.00500	E	215	0.0000	0.0	IAC80	
				Anticenter Field				
4b	57021.48092	0.00700	E	313	–0.1249	–1.1	IAC80	
12b	56997.60750	0.00500	E	919	0.0098	0.8	IAC80	3 T_c in R+19; 6 T_c in ETD
12b	57099.41510	0.00110	F	955	0.0079	0.6	LT	3 T_c in R+19; 6 T_c in ETD
13b	57046.42800	0.00300	F	559	–0.0523	–3.1	IAC80	
14b	57019.54396	0.01000	F	1476	–0.0441	–0.2	IAC80	
14b	57084.57000	0.00300	F	1519	–0.0401	–0.2	Danish 1.54m	
14b	57087.59500	0.00400	F	1521	–0.0393	–0.2	Danish 1.54m	
15b	57061.06708	0.01000	I	754	–0.0052	–0.2	LCO 1M–SSO	
15b	57789.42240[2]	0.00090	F	992	–0.0155	–0.5	GTC	
18b	55589.63389[4]	0.00000	F	141	–0.0044	–17.8	Euler 1.2m (Hebrard *et al.* 2011)	4 T_c in R+19; 3 T_c in ETD (DQ≤3)
18b	57056.50700	0.00300	F	946	–0.0008	–0.3	IAC80	4 T_c in R+19; 3 T_c in ETD (DQ≤3)
20b	55515.55635	0.00200	I	27	–0.0111	–4.9	WISE 1m (Deleuil *et al.* 2012)	2 T_c in R+19; 3 T_c in ETD
20b	56633.99030	0.00200	F	148	–0.0019	–0.7	LCO 2M–FTN	
37b	55913.57646	0.01030	I	3	–0.0048	–0.5	WISE 0.46m	
37b	55953.67150	0.00390	I	5	0.0006	0.2	IAC80	
37b	56334.52250	0.00320	I	24	0.0000	0.0	IAC80	

[1] The full names of the telescopes are provided in the acknowledgements. A reference is only given if the observation has been reported previously.

[2] Light curve obtained from white–light fluxes of a time–series of spectra taken with the GTC's OSIRIS instrument using the R1000R grism. T_c and its error was derived from a multi–parameteric fit of the transit (Nespral 2019).

[3] Cycle number in the ephemeris by Bonomo et al. *(2017), which is based on a reobservation by Spitzer on 2010 Jun 18. The cycle number would be 24 in the original ephemeris by Deeg* et al. *(2010), which counts from the first CoRoT transit. See also discussion of CoRoT–9b.*

[4] Reconstructed T_c value, based on the ephemeris by Hébrard et al. *(2011) and a light curve from the Euler 1.2m provided in the same paper, see text to CoRoT-18b.*

transit mid-times have little dependence on the wavelength. These observations covered a baseline between the first and last transit of 3.1 years and permitted Bonomo *et al.* the derivation of an ephemeris of improved precision. This ephemeris however has an epoch (T_0) that was reset to another transit that they observed with Spitzer on 2010 Jun 18.

Due to the long orbital period, the transits of CoRoT-9b last 8.1 hours with in/egresses of about 1 hour, implying that transit features are difficult to detect due to the slowly varying flux-levels. The light curve of a transit on 2014 Aug 20 was acquired first with the 2-m LCO telescope on Mt. Haleakala, Hawaii, followed by the 1-m LCO telescope at Siding Springs, Australia, using in both cases a PanSTARRS i-band filter. While the 2-m telescope generated a featureless flat light curve—having fallen completely into the central part of the transit—the curve from the 1-m telescope showed an egress, which was modeled in detail using the UFIT/UTM transit modeler (Deeg 2014). This software employs a Monte-Carlo Markov Chain (MCMC) algorithm, in which we kept the transit model fixed to the values given in the CoRoT-9b discovery paper (Deeg *et al.* 2010) while leaving only three parameters free. These were the mid-time of the transit and the offset and slope of the off-transit flux-level as a function of time. The best shows an excellent agreement between the model and the data (Figure 2), and indicates a T_c that is only 8 minutes later than predicted by the ephemeris of Bonomo *et al.* (2017).

CoRoT-10b Our T_c value listed in Table 1 is the first successful reobservation of CoRoT-10b (discounting an unreliable entry in ETD) and shows a moderate 1.6-sigma deviation from the original ephemeris by Bonomo *et al.* (2010). 10b was one of the CoRoT planets which was in danger of getting "lost" (Deeg *et al.* 2015) and our reobservation permits a dramatic increase in the precision of its ephemeris. A new derivation of the period has therefore been included in Table 2.

Table 2. Ephemeris of planets mentioned in this work.

CoRoT Planet	T_0 *(BJD−2400000)*	σ_{T_0} *(d)*	P *(d)*	σ_P *(d)*	*Source*
			Center field		
2b	54237.53562	0.00014	1.7429964	1.7E-06	Alonso *et al.* 2008
3b*	54283.13940	0.00030	4.2568000	5.0E-06	Deleuil *et al.* 2008
3b	54283.13388	0.00025	4.2567994	3.5E-06	Triaud *et al.* 2009
8b	54239.03317	0.00049	6.2124450	7.0E-06	R+19
9b	54603.34470	0.00010	95.2738000	1.4E-03	Deeg *et al.* 2010
9b*	55365.52723	0.00037	95.2726560	6.8E-05	Bonomo et al. 2017
10b*	54273.34360	0.00120	13.2406000	2.0E-04	Bonomo et al. 2010
10b	54273.34360	0.00120	13.2402720	3.6E-05	T_0: Bonomo *et al.* 2010; P: this work
11b	54597.67900	0.00030	2.9943300	1.1E-05	Gandolfi *et al.* 2010
16b	54923.91380	0.00210	5.3522700	2.0E-04	Ollivier *et al.* 2012
17b	54923.30930	0.00360	3.7681000	3.0E-04	Csizmadia *et al.* 2011
27b	55748.68400	0.00100	3.5753200	6.0E-05	Parviainen *et al.* 2014
29b*	55753.11500	0.00100	2.8505700	6.0E-06	Cabrera *et al.* 2015
29b	55753.11500	0.00100	2.8505616	7.2E-06	T_0: Cabrera *et al.* 2015; P: Pallé *et al.* 2016
30b	55665.51460	0.00120	9.0600500	2.4E-04	Bordé *et al.* 2020
36b	55656.90480	0.00049	5.6165307	2.3E-05	T_0: S. Grziwa (priv.com.); P: this work
			Anticenter Field		
4b	54141.36416	0.000890	9.20205000	3.7E-4	Aigrain *et al.* 2008
7b	54398.07756	0.000600	0.85359159	6.0E-7	Barros *et al.* 2014
12b*	54398.62707	0.000360	2.82804200	1.3E-5	Gillon *et al.* 2010
12b	54398.62771	0.000240	2.82805268	6.5E-7	R+19
13b	54790.80910	0.000600	4.03519000	3.0E-5	Cabrera *et al.* 2010
14b	54787.66940	0.005300	1.51214000	1.3E-4	Tingley *et al.* 2011
15b	54753.56080	0.001100	3.06036000	3.0E-5	Bouchy *et al.* 2011
18b	55321.72412	0.000180	1.90006930	2.8E-6	Hébrard 2011
18b*	55321.72565	0.000240	1.90009000	5.0E-7	R+19
20b	55266.00010	0.001400	9.24285000	3.0E-4	Deleuil *et al.* 2012
20b*	55266.00160	0.001000	9.24318000	9.0E-6	R+19
24b	54789.61100	0.006000	5.11340000	6.0E-4	Alonso *et al.* 2014
24c	54795.38030	0.026500	11.75900000	6.3E-3	Alonso *et al.* 2014
37b	55853.44678	0.000330	20.04482300	1.3E-4	T_0: D. Gandolfi (priv. comm.); P: this work

* *If more than one ephemeris is given, the starred one is used for the O–C residuals of Table 1.*

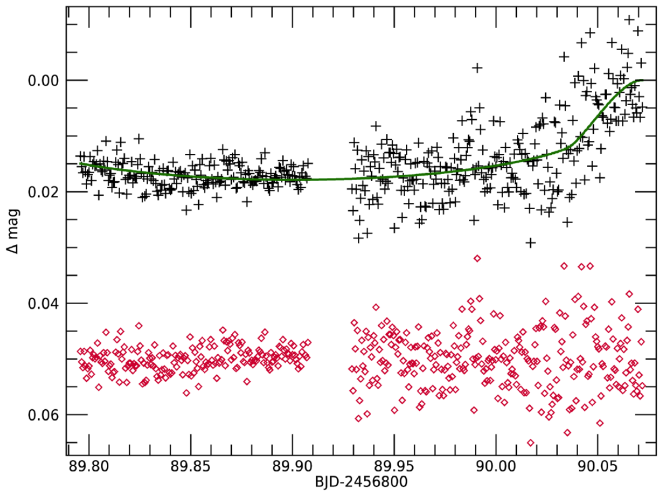

Figure 2. Light curve of a partial transit of CoRoT-9b observed on 2014 Aug 20 with the 2-m LCO telescope at Haleakala Observatory, Hawaii and the 1-m LCO telescope at Siding Springs, Australia (crosses; left section from the 2-m and right one from the 1-m), with the best fit of a transit-model (solid line) to the 1-m data. A slight slope in the LCO 1-m data that was originally present has been removed from both data and model fit. The 2-m LCO observations were not used in the fit but were shifted in Δ mag for an optimal agreement with the transit model. The square symbols (red in electronic version) are the residuals, which are offset downwards by 0.05mag for better visibility.

CoRoT-11b Relative to the ephemeris in the discovery paper by Gandolfi *et al.* (2010), our timing from 2014 June 19 taken with the 0.46-m telescope of WISE observatory, Israel, is early by 53 minutes, which is 3.8 times larger than the uncertainty implied by that ephemeris.

The ETD and TRESCA databases contain three further transits of good quality taken in 2011 and 2012, which corroborate transit times that are about 4 sigma earlier than implied by the Gandolfi *et al.* ephemeris. A revision of that ephemeris, which was entirely based on CoRoT transits acquired between 2008 Apr 15 and Sep 7, does not reveal any source for this discrepancy. CoRoT-11b might therefore be a case of a real transit timing variation.

CoRoT-16b The light curves underlying our two timing measurements in Table 1, if taken individually, would not have been of sufficient quality for inclusion in that table, given their noisiness which is due to the target's faintness (R mag = 15.5). An overlay of both light curves (Figure 3) indicates however a good agreement between the two, showing a correct transit duration of 0.1 d and depth of 1%, therefore warranting their inclusion. We note that the transits occur about 0.05 d or 70 min before the predicted transit times, using the ephemeris of the CoRoT-16b discovery paper (Ollivier

et al. 2012). This deviation is however smaller than the ephemeris' 1-sigma uncertainty of ± 103 minutes at the epoch of our observations.

CoRoT-17b The transits of this planet are difficult to observe, due to their shallowness of ~0.4% and the target's faintness (Rmag=15.3). CoRoT-17b was observed 3 times within a few weeks at the Liverpool 2-m telescope, on 2014 Jun 9, Jul 13, and Jul 28. Similar to CoRoT-16b, the individual transits where not of sufficient quality, but a combination of them (Figure 4) shows a feature that is reasonably close to the expected transit duration (4.7 h = 0.195 d) and depth (0.4%) to be considered a very likely detection. The value of Tc given in Table 1 was derived from the combined light curve (black line in Figure 4) and was assigned to 2014 Jul 13, which was the best of the three data sets. This T_c is 1.9 h earlier than indicated by the ephemeris from CoRoT data (Csizmadia *et al.* 2011), but is well within the ephemeris' uncertainty of ± 3.7 h at the epoch of our observations.

CoRoT-27 Both our light curves (Figure 5), acquired on 2014 Jun 1 and 2014 Jul 14, show a likely detection of an egress that is about 2.0 h earlier than predicted by the discovery paper's ephemeris (Parviainen *et al.* 2014), corresponding to a 4.5-sigma deviation against the ephemeris' uncertainty of ± 25 min at that epoch. R+19 report two later observing attempts from June 2016, which did not detect the transit at all. From this non-detection they conclude that "the transit must have happened at least 3.9 h earlier or 4.5 h later" (relative to Parviainen's ephemeris). If we extrapolate our deviation of 2.0 h to the epoch of R+19's observations, they should have detected the transits at 3.3 h earlier, well within their observing window. We therefore expect that CoRoT 27b has a notable transit timing variation with an increasingly non-linear offset relative to Parviainen's ephemeris.

CoRoT-29b This planet was among the targets to be observed for the project reported here, but its follow-up concluded in time for inclusion into the CoRoT-29b discovery publication (Cabrera *et al.* 2015). The T_c from the IAC80 observations on 2014 Jul 14 (E = 386) was therefore used in the derivation of the ephemeris by Cabrera *et al.* A light curve of the observation from the LCO's 2-m FTN telescope at E = 113 is also shown in that paper, but without quoting any T_c, which has therefore been included in Table 1. Two further transit timings, acquired with the GTC on 2014 Jul 31 and 2015 Aug 7 for a spectrophotometric study, have been published by Pallé *et al.* (2016). From these, they provide an updated orbital period (included in Table 2), which is also in good agreement with our T_c measures.

CoRoT-30b Transit observations of this planet were acquired within the project reported here, but similar to CoRoT-29b, they arrived in time to have been reported in the planet's recent discovery publication (Bordé *et al.* 2020). However, Bordé *et al.*'s principal ephemeris (their Table 6) is only based on model fits to CoRoT data and does not take the IAC80 observation from 2014 Jul 22 (E = 132) into account. They note however that the inclusion of the T_c from that observation increases the precision of the planet's period, arriving at 9.060347(39) days.

CoRoT-36b (CoRoT-ID 652345526, UCAC2 34324554, at R.A. $18^h\ 31^m\ 00.26^s$ Dec. +07° 11' 00.3" J2000) is a Jupiter-sized planet with a period of 5.6 days that has been included among the 37 CoRoT planets that are quoted in the overview paper by Deleuil *et al.* (2018), although a detailed publication is still pending (Grziwa *et al.* in prep). The ephemeris given in Table 2 has been determined from a T_0 based on CoRoT data (Grziwa 2020) and from the IAC80 timing on 2014 Jul 25 (E = 215).

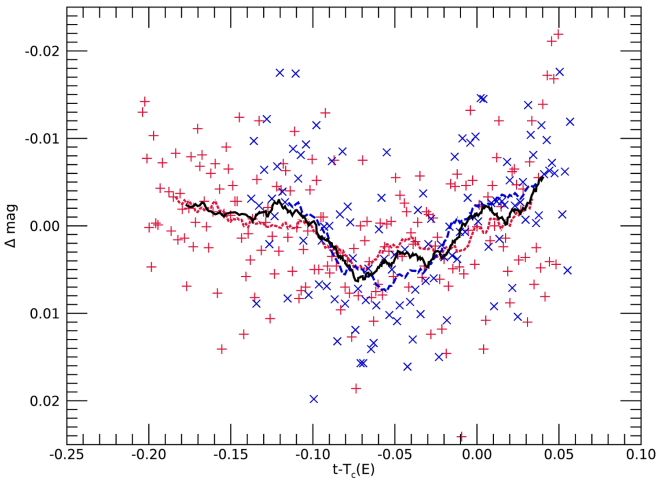

Figure 3. Superposition of light curves of CoRoT-16b transits observed on 2014 Jun 26 (crosses, red in electronic version) with the IAC80 and on 2014 Jul 22 (×-symbols, blue) with the LCO 1m at SAAO, in this case using a PanSTARRS i-band filter. The dotted red and the dashed blue lines are boxcar smoothings over 25 points of the individual light curves, while the solid black line is a smoothing of the combination of both curves. The horizontal axis indicates the time in days, relative to the predicted transit time T_c(E) from the ephemeris of Ollivier *et al.* (2012), with E = 357 and 362.

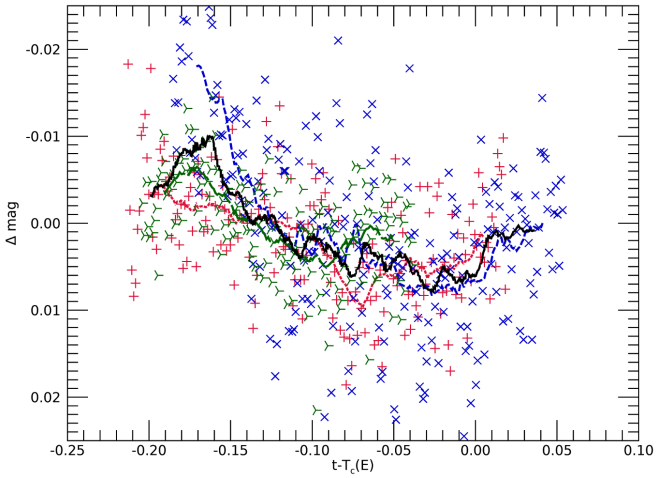

Figure 4. Similar to Figure 3, showing transits of CoRoT-17b observed on 2014 Jun 9 (crosses, red), 2014 Jul 13 (×-symbols, blue) and 2014 Jul 28 (tri-star symbols, green). The corresponding smoothed light curves are dotted, short dashed and long-dashed, respectively, while the solid black line is the combined smoothed light curve. In all three nights, the airmass was increasing during the observation, which is the likely source for the general slope that is common to all three data sets.

CoRoT-4b Our T_c value obtained from an egress is the first published reobservation of CoRoT-4b (Aigrain *et al.* 2008, with a more detailed description in Moutou *et al.* 2008) and is within the expected timing error of the original ephemeris.

CoRoT-12b For this planet numerous ground-based follow-up observations exist, as its 1.9% deep transits are relatively easy to observe. Considering our Tc, those from R+19, and the

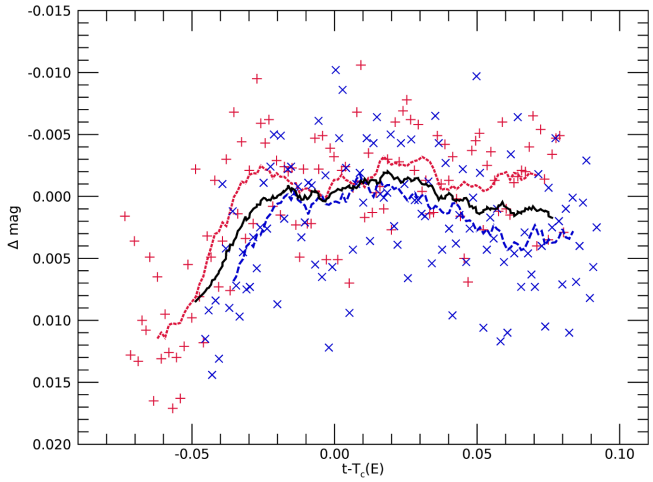

Figure 5. Similar to Figure 3, but for CoRoT-27b observed with the IAC80 on 2014 June 1 (crosses, red) and the STELLA 1m telescope on 2014 July 14 (×-symbols, blue), with the combined smoothed light curve being in solid black. Both transits are significantly earlier than predicted from the ephemeris of Parviainen *et al.* (2014), causing coverage of the egress only. The smoothing of the curves has been over 15 points.

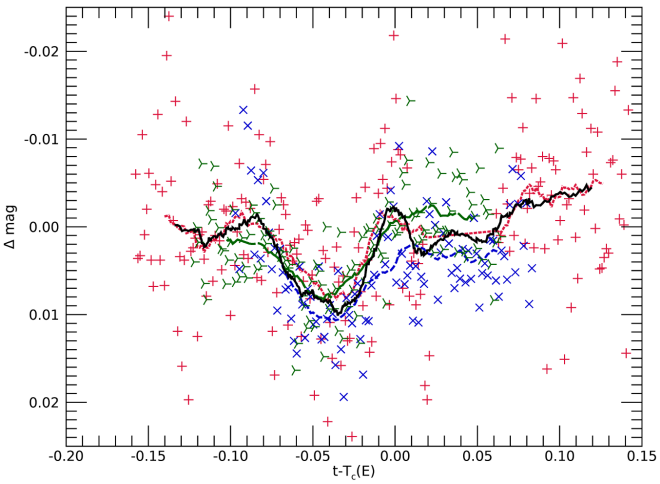

Figure 6. Similar to Figure 3, showing transits of CoRoT-14b observed with the IAC80 on 2014 Dec 27 (red crosses, with dotted smoothed curve) and the Danish 1.54m telescope on 2015 Mar 2 (blue ×-symbols, smoothed short-dashed line) and on 2015 Mar 5 (green tri-stars, smoothed long-dashed line), with the combined smoothed curve in solid black.

good-quality ones from ETD (DQ of 3 or better), they are all well described by the original ephemeris of Gillon *et al.* (2010) or by the revised one of R+19. We note that Gillon *et al.* hinted at potential TTVs with an amplitude of ~1 minute and a period of ~68 days. Unfortunately, the precision of the ground-based follow up is not sufficient to corroborate the further presence of this feature.

CoRoT-13b The T_c value obtained from the light curve (Figure 5) is 76 minutes early versus the ephemeris of the discovery paper (Cabrera *et al.* 2010), which corresponds to 3.1 times its uncertainty at the observation's epoch, indicating potential TTVs.

CoRoT-14b Three transits of good quality were observed with the IAC80 and the Danish 1.54-m telescope (Figure 6). They were about 1 h earlier than predicted by the discovery ephemeris of Tingley *et al.* (2011), but are well within the

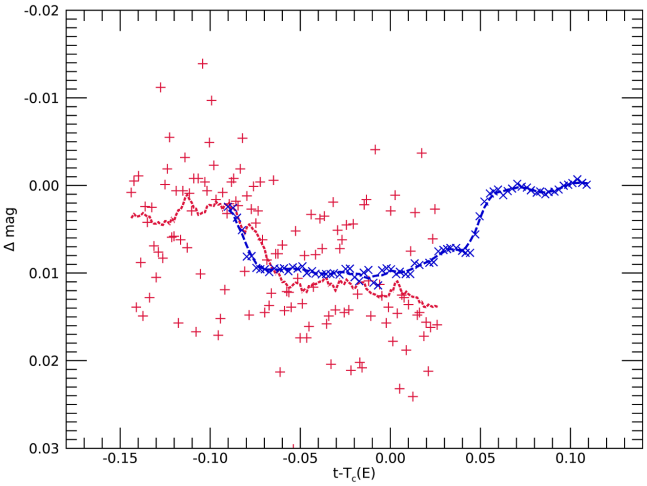

Figure 7. Similar to Figure 3, showing transits of CoRoT-15b acquired with the 1-m LCO telescope (crosses, red) and the 10.4-m GTC (×-symbols, blue). For the GTC data, the smoothed line (dashed) was generated with a boxcar smoothing over only 5 points. Due to the very different noise-characteristics, we refrain from showing the combined curve.

ephemeris' uncertainty of 4.6 to 4.7 h at the observations' epochs.

CoRoT-15b The light curve of an ingress was acquired on 2015 Feb 7 with the 1-m LCO telescope at SSO and a nearly complete transit was acquired on 2017 Feb 4 with the 10.4-m GTC. The GTC light curve was derived from the white-light summation of spectra that were taken with the R1000R filter for a study of transit spectroscopy (Nespral 2019). Both transits (Figure 7) agree well with the ephemeris of Bochy *et al.* (2011).

CoRoT-18b Our transit observed on 2015 Feb 2 (E = 946) with the IAC80 is 28 minutes behind the ephemeris in the discovery paper (Hébrard *et al.* 2011). The very small uncertainty in their quoted period, given the short CoRoT pointing from 2010 Mar 5 to 29, is explained by them from follow-up observations made with the Euler 1.2-m telescope about eight months later (on 2011 Jan 28 at E = 141), which were used to refine their ephemeris. We note that for unspecified reasons, Hébrard's ephemeris has a zero-epoch on 2010 May 5, well past the coverage by CoRoT, while the first transit observed by CoRoT corresponds to E = –32.

With the small period-uncertainty by Hebrard *et al.*, the lateness of our IAC80 timing of 28 minutes translates into an error of 7.6 sigma against their ephemeris. However, good-quality entries in ETD (of DQ ≤ 3) as well as the four timings acquired by R+19 all show a similar trend of being late by 7 to 8 sigma against Hebrard's ephemeris. These offsets, both in terms of their absolute sizes and in terms of their significance, diminish greatly however if the revised ephemeris of R+19 is employed, against which our IAC80 timing is early by only 1 minute. We note that Hebrard *et al.* do not indicate the T_c of their Euler observations at E = 141, but using their ephemeris (see also their Figure 3) we can reconstruct its value (see entry in Table 1). This T_c is now 6 minutes or 17.8 sigma early against the ephemeris by R+19. However, given that all further published timings, over the range of E = 714 to 1865 , agree well with the R+19 ephemeris, the Euler 1.2-m timing seems to be an outlier and the presence of significant timing variations is unlikely.

CoRoT-20b Our timing obtained with the LCO 2-m telescope is within 3 minutes of the refined ephemeris of R+19, who had two later timing measurements at their disposal. Three further timings from low-quality light curves are also available in ETD. We note that the original ephemeris of Deleuil *et al.* (2012) was already based on a ground-based timing taken with the 1-m WISE telescope, whose Tc value has been included in Table 1. However, this timing has a significant offset against the ephemeris by R+19. Rey *et al.* (2018) provide evidence from radial velocity follow-up for a further non-transiting planet c with an orbital period of 1,675 days on an eccentric orbit. They also imply that planet *c* should induce TTVs on planet *b* whose amplitude of a few minutes would vary with the period of planet *c* (see their Figure 7). Such variations are at the limit of the precision of the current ground-timings, albeit the poor fit of the WISE timing (with an offset by 16 minutes) against the later timings might be related to planet *c*. A more thorough analysis of all available timings together with those from TESS should be the subject of further work.

CoRoT-37b (CoRoT-ID 617963863, TYC 4792-1886-1) is a planet transiting an F4 star in the young cluster NGC 2232, with an orbital period of 20 days (Gandolfi *et al.*, in prep). It was announced as CoRoT-32b in several conferences in 2013 and 2014. Under that denominator it was also mentioned in refereed papers by Guenther *et al.* (2013) and Hatzes (2014), while a dedicated publication is still pending. In the overview of CoRoT detections by Deleuil *et al.* (2018) however it is mentioned as CoRoT-37b. The reason for the change in numbering was a publication by Boufleur *et al.* (2018), which assigned the name CoRoT-32 to an unrelated system (CoRoT 223977153, UCAC2 34993171). The ephemeris given in Table 2 has been derived from a linear fit using a T_0 derived from CoRoT data (Gandolfi 2020) and from the T_c of the follow-up observations given in Table 1.

In the following, we comment on several more CoRoT planets that are not included in Table 1:

CoRoT-7b Ground observations of the very shallow (0.032% deep, Legér *et al.* 2009) transits of this Super-Earth are extremely challenging. They were intended on 2010 Jan 15 and 2013 Jan 15, both times with the 10.4-m GTC and the OSIRIS imager, using a strongly defocused point-spread function, without obtaining reliable transit detections. After the initial discovery in mission data acquired between October 2007 and March 2008, CoRoT observed this planet in a further pointing from January to March 2012. An ephemeris from this reobservation was published by Barros *et al.* (2014), with greatly improved precision over the original one by Legér *et al.* (2009).

CoRoT-24b and c This multiplanet system was never attempted to be reobserved by us, given the unlikely recovery of reliable transits due to their shallowness, 0.15% for *b* and 0.26% for *c* (Alonso *et al.*, 2014), and the very large timing uncertainties, which in 2014 were already ± 5.5 h and ± 24 h for the two planets.

CoRoT-19b, 22b, 23b, 26b, 31b Transits of these planets were also observed, but the resulting light curves remained inconclusive, mostly due to being too noisy for the expected transit depth, showing features that are incompatible with a transit, or being too short to be of discriminatory value. The remaining CoRoT-planets had failed observations due to weather or technical issues or our inability to schedule their observation.

4. Conclusions

Table 1 provides 33 ground-based timing measurements from 20 exoplanet systems. Of them, six systems have timings with $S/N_{O-C} > 3$, that is, the observed deviation from the ephemeris was more than 3 times the expected uncertainty. We consider four of these systems (CoRoT-3b, 11b, 27b, 13b) to display indications for potential TTVs. For these systems, further timing measurements over longer epochs will be needed to corroborate such a diagnostic. In the other two cases, CoRoT 18b and 20b, the planets' original ephemeris (Hébrard *et al.* 2011 and Deleuil *et al.* 2012, respectively) were based not only on the CoRoT data but also on early ground follow-up timings that are included in Table 1. In both cases, our follow-up at later epochs (and for 18b, also further timings from ETD) provide timings that are consistent with the linear ephemeris which R+19 had derived from their own follow-up timings. In these revised ephemerides, the notable outlier is the early ground-based observation that had influenced the discovery ephemeris. In the case of CoRoT-20b, this discrepancy might have arisen from TTVs with amplitudes that vary on time-scales of years and which are induced by a long-periodic non-transiting planet. A more thorough analysis of these case is required however in order to ascertain that the early timing outliers could have been caused by the presence of further planets.

Of further note is that a large majority, 23 out of the 33 entries in Table 1, has timings that are earlier than expected, with negative O–C values. This would correspond to periods that are (or are becoming) shorter than the ephemeris periods. However, no corresponding systematics in timings from Kepler planets without identified TTVs (see Rowe and Thompson 2015, Holczer *et al.* 2016, Kane *et al.* 2019 for planets identified with TTVs) have been reported, while such a trend, if real, should have been found in the Kepler mission data, given Kepler's much longer temporal coverage and higher photometric precision. We surmise therefore that our mostly negative O–C values could be the result of some unrecognized systematics that affected many of the original ephemeris derivations from the CoRoT data.

In all cases, we are awaiting a recovery of transits of most of the CoRoT planets in data from TESS and from future ground and space missions, which will maintain the legacy of the planets that were discovered by the first space mission dedicated to exoplanets.

5. Acknowledgements

This work is based on observations of the following telescopes (also provided are the acronyms used in Table 1): IAC80: 80-cm telescope of the Instituto de Astrofísica de Canarias at Teide Observatory, Tenerife, Spain. We thank the night operators at Teide Observatory for the acquisition of several of the listed observations. LCO: 1-m telescopes of

the Las Cumbres Observatory, at Siding Springs Observatory, Australia (SSO), and at the South African Astronomical Observatory (SAAO), and the 2-m Faulkes Telescope North (FTN) at Haleakala Observatory, Hawaii. WISE: Tel-Aviv University 0.46-m and 1-m telescopes at WISE Observatory, Israel. LT: 2-m Liverpool Telescope of the Liverpool John Moores University, at the Roque Muchachos Observatory, La Palma, Spain. Danish 1.54-m telescope at ESO's La Silla Observatory. GTC: 10.4-m GTC telescope at Roque Muchachos Observatory, La Palma, Spain. We thank the staff of GTC for their support during queue observations. STELLA: 1.2-m STELLA-WiFSIP telescope of the Leibniz-Institut für Astrophysik Potsdam, at the Teide Observatory, Tenerife, Spain. Both Teide Observatory and Roque Muchachos Observatory are observatories of the Instituto de Astrofísica de Canarias.

The CoRoT space mission, launched on 27 December 2006, was developed and operated by CNES, with the contribution of Austria, Belgium, Brazil, ESA, Germany, and Spain. We acknowledge the use of the IAS CoRoT Public Archive (http://idoc-corot.ias.u-psud.fr/) and the COROT Archive at CAB (https://sdc.cab.inta-csic.es/corotfa). We acknowledge the use and the usefulness of the ETD (http://var2.astro.cz/ETD) and TRESCA (http://var2.astro.cz/EN/tresca) databases of the Czech Astronomical Society. We thank Ankit Rohatgi for making freely available to the community the superb WebPlotDigitizer tool (https://automeris.io/WebPlotDigitizer/), which permitted an efficient recovery of several older time-series that had only been preserved in graphical form.

HD, PK, DN acknowledge support by grants ESP2015-65712-C5-4-R and ESP2017-87676-C5-4-R of the Spanish Secretary of State for R&D&i (MINECO). SH acknowledges CNES funding through grant 837319.

References

Aigrain, S., *et al.* 2008, *Astron. Astrophys.*, **488**, L43.
Alonso, R., *et al.* 2008, *Astron. Astrophys.*, **482**, L21.
Alonso, R., *et al.* 2014, *Astron. Astrophys.*, **567**, A112.
Auvergne, M., *et al.* 2009, *Astron. Astrophys.*, **506**, 411.
Baglin, A., Auvergne M., Barge, P., Deleuil, M., Catala, C., Michel, E., Weiss, W., and COROT Team. 2006, in *Proceedings of "The CoRoT Mission Pre-Launch Status—Stellar Seismology and Planet Finding,"* ESA SP-1306, eds. M. Fridlund, A. Baglin, J. Lochard, L. Conroy, ESA Publications Division, Noordwijk, The Netherlands, 33.
Barros, S. C. C., *et al.* 2014, *Astron. Astrophys.*, **569**, A74.
Bonomo, A. S., *et al.* 2017, *Astron. Astrophys.*, **603**, A43.
Bonomo, A. S., *et al.* 2010, *Astron. Astrophys.*, **520**, A65.
Bordé, P., *et al.* 2010, *Astron. Astrophys.*, **520**, A66.
Bordé, P., *et al.* 2020, *Astron. Astrophys.*, **635**, A122.
Bouchy, F., *et al.* 2011, *Astron. Astrophys.*, **525**, A68.
Boufleur, R. C., Marcelo, E., Janot-Pacheco, E., Andrade, L., Ferraz-Mello, S., do Nascimento, Jr., J.-D., de La Reza, R. 2018, *Mon. Not. Roy. Astron. Soc.*, **473**, 710.
Cabrera, J., *et al.* 2010, *Astron. Astrophys.*, **522**, A110.
Cabrera, J., *et al.* 2015, *Astron. Astrophys.*, **579**, A36.
Csizmadia, Sz., *et al.* 2011, *Astron. Astrophys.*, **531**, A41.
Deeg, H. J. 2014, Astrophysics Source Code Library, record ascl:1412.003.
Deeg, H. J. 2015, *Astron. Astrophys.*, **578**, A17.
Deeg, H. J., Klagyivik, P., Alonso, R., and Hoyer, S. 2015, in *The Space Photometry Revolution—CoRoT Symposium 3, Kepler KASC-7 Joint Meeting, Toulouse, France*, ed. R. A. García, J. Ballot, EPJ Web of Conferences, 101, id.06020, EDP Sciences, Les Ulis Cedex, France.
Deeg, H. J., et al, 2010, Nature **464**, 384.
Deeg, H. J., and Tingley, B. 2017, *Astron. Astrophys.*, **599**, A93.
Deleuil, M., *et al.* 2018, *Astron. Astrophys.*, **619**, A97.
Deleuil, M., *et al.* 2012, *Astron. Astrophys.*, **538**, A145.
Deleuil, M., *et al.* 2008, *Astron. Astrophys.* **491**, 889.
Dragomir, D., *et al.* 2020, Astron. J., **159**, 219.
Gandolfi, D. 2020, private communication.
Gandolfi, D., *et al.* 2010, *Astron. Astrophys.*, **524**, A55.
Gandolfi, D., *et al.* in preparation.
Gazak, J. Z., Johnson, J. A., Tonry J., Dragomir, D., Eastman, J., Mann, A. W., and Agol, E. 2012, *Adv. Astron.*, ID 697967.
Gillon, M., *et al.* 2010, *Astron. Astrophys.*, **520**, A97.
Grziwa, S. 2020, private communication.
Grziwa, S., *et al.* in preparation.
Guenther, E. W., *et al.* 2013, *Astron. Astrophys.*, **556**, A75.
Hatzes, A. P. 2014, *Nature*, **513**, 353.
Hébrard, G., *et al.* 2011, *Astron. Astrophys.*, **533**, A130.
Holczer, T., *et al.* 2016, *Astrophys. J., Suppl. Ser.*, **225**, 9.
Kane, M., Ragozzine, D., Flowers, X., Holczer, T., Mazeh, T., and Relles, H. M. 2019, *Astron. J.*, **157**, 171.
Klagyivik, P., Deeg, H. J., Csizmadia, Sz., and Cabrera, J. in preparation.
Léger, A., *et al.* 2009, *Astron. Astrophys.*, **506**, L287.
Moutou, C., *et al.* 2008, *Astron. Astrophys.*, **488**, L47.
Moutou, C., *et al.* 2013, *Icarus*, **226**, 1625.
Nespral, D. 2019, Ph. D. thesis, Universidad de La Laguna (https://dialnet.unirioja.es/servlet/tesis?codigo=263977).
Ollivier, M., *et al.* 2012, *Astron. Astrophys.*, **541**, A149.
Pallé, E., *et al.* 2016, *Astron. Astrophys.*, **589**, A62.
Parviainen, H., *et al.* 2014, *Astron. Astrophys.*, **562**, A140.
Poddaný, S., Brát, L., and Pejcha, O., 2010, *New Astron.*, **15**, 297.
Raetz, St., Heras, A. M., Fernández, M., Casanova V., and Marka C. 2019, *Mon. Not. Roy. Astron. Soc.*, **483**, 824.
Rauer, H., *et al.* 2010, *Astron. J.*, **139**, 53.
Rey, J., *et al.* 2018, *Astron. Astrophys.*, **619**, A115 .
Ricker, G. R., *et al.* 2015, *J. Astron. Telesc. Instrum. Syst.*, **1**, id. 014003.
Rowe, J. F., and Thompson, S. E. 2015, Uniform Modeling of KOIs, NASA document KSCI-19084-001, eprint arXiv:1504.00707.
Tingley B., *et al.* 2011, *Astron. Astrophys.*, **528**, A97.
Triaud, A. H. M. J., *et al.* 2009, *Astron. Astrophys.*, **506**, 377.

Appendix A: Transit light curves of CoRoT planets in the galactic center field.

The light curves are ordered first by planet number and then by the BJD. The telescope used is also indicated.

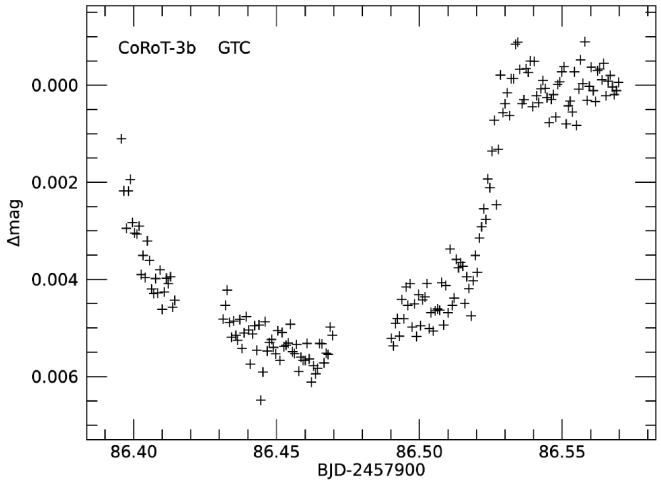

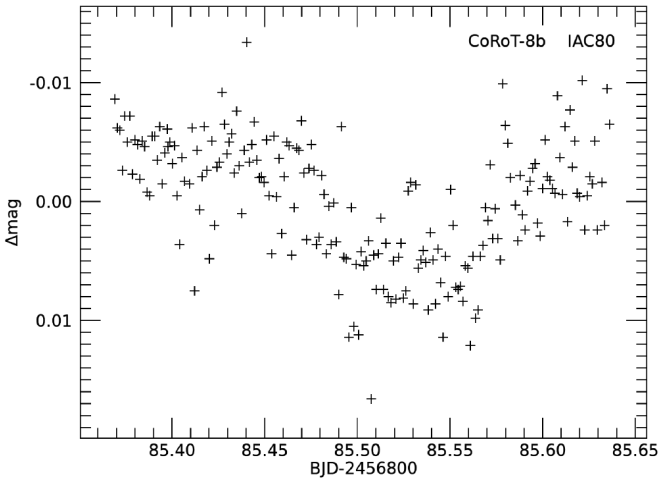

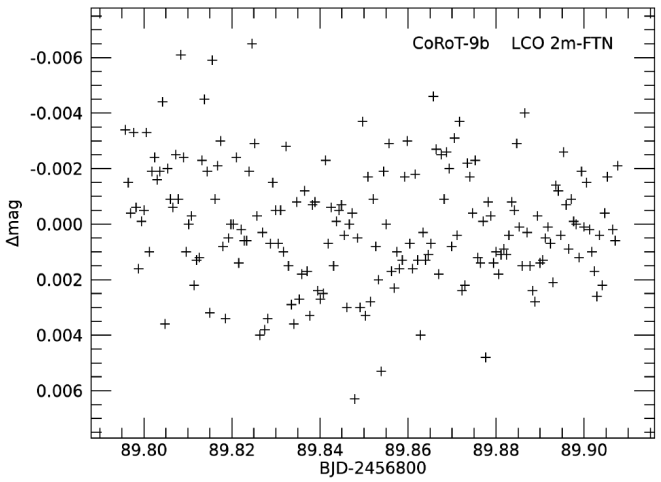

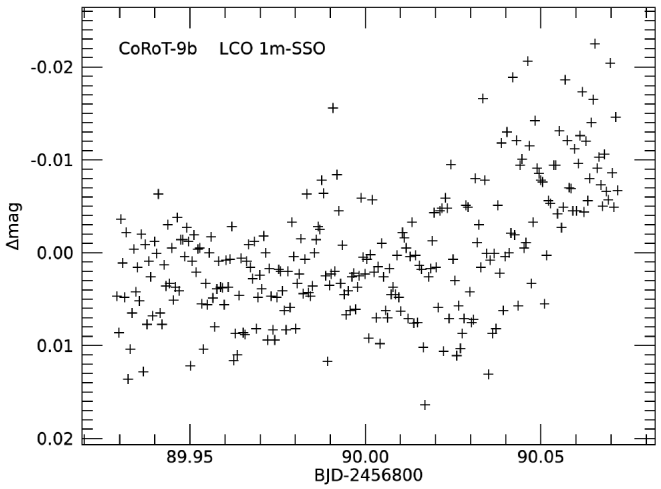

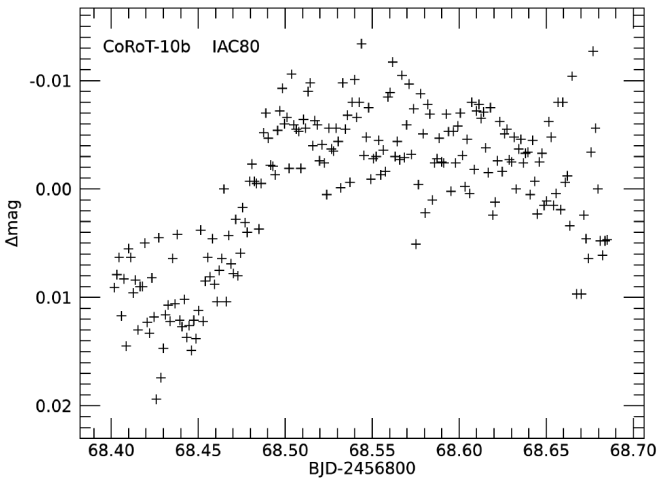

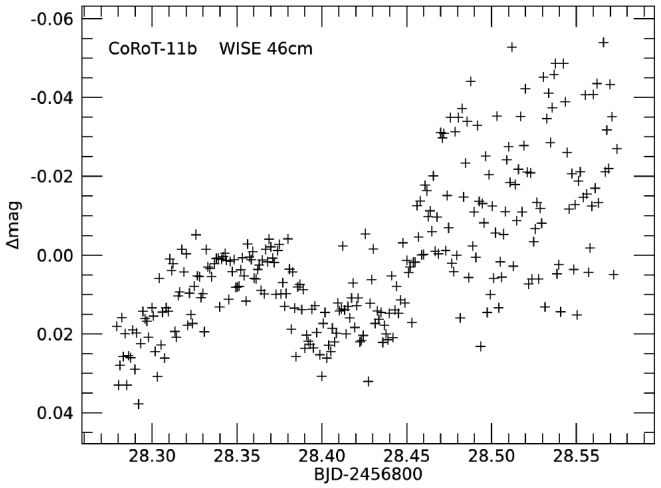

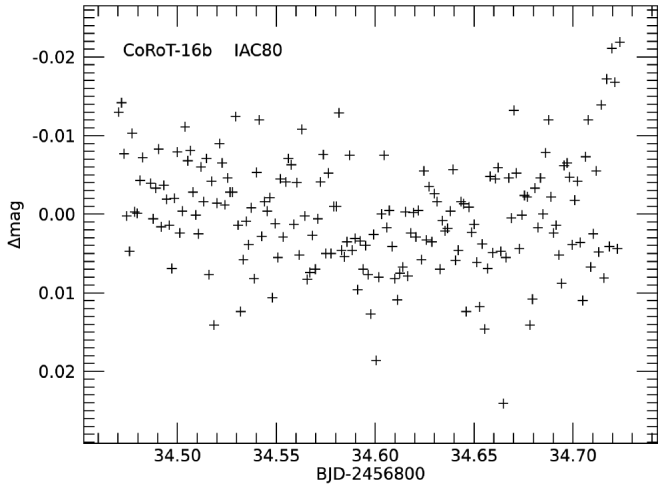
CoRoT-16b IAC80
Δmag
BJD-2456800

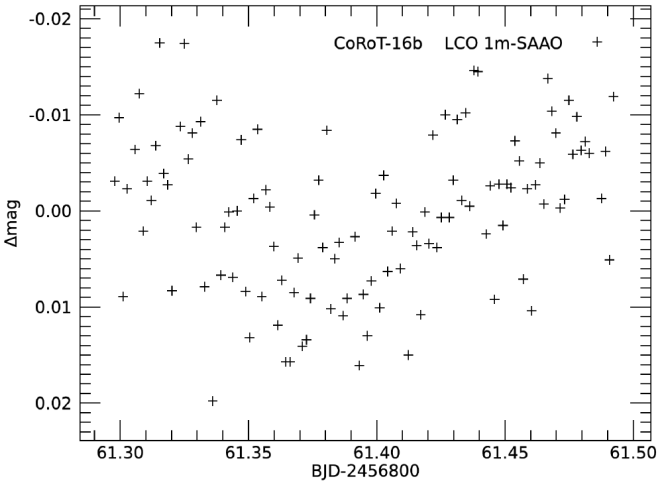
CoRoT-16b LCO 1m-SAAO
Δmag
BJD-2456800

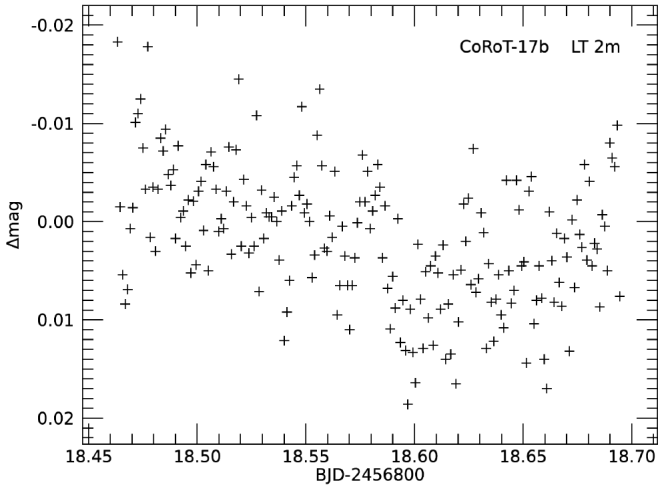
CoRoT-17b LT 2m
Δmag
BJD-2456800

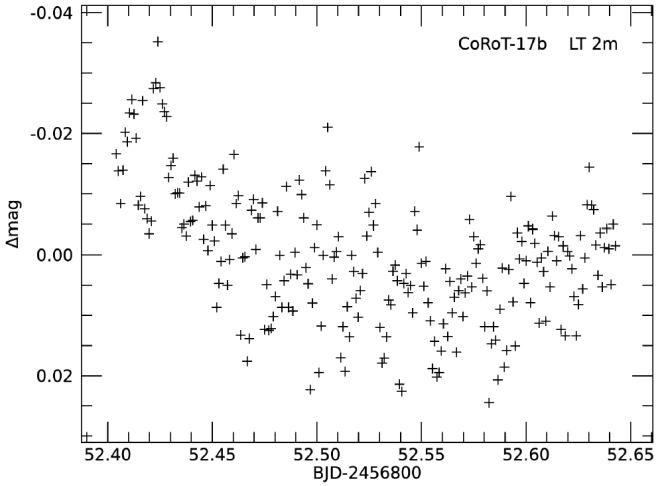
CoRoT-17b LT 2m
Δmag
BJD-2456800

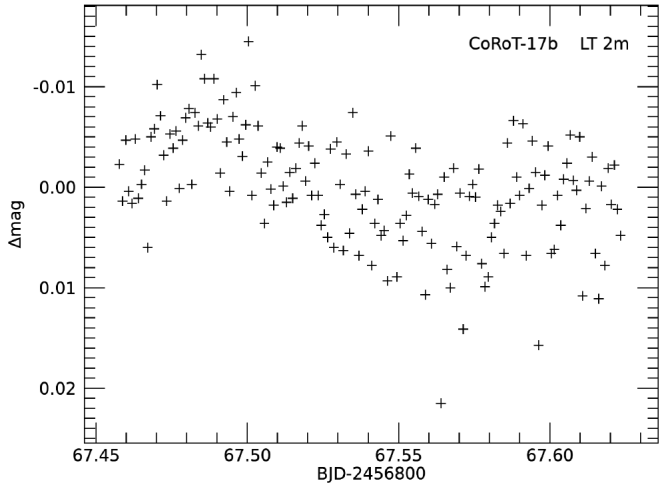
CoRoT-17b LT 2m
Δmag
BJD-2456800

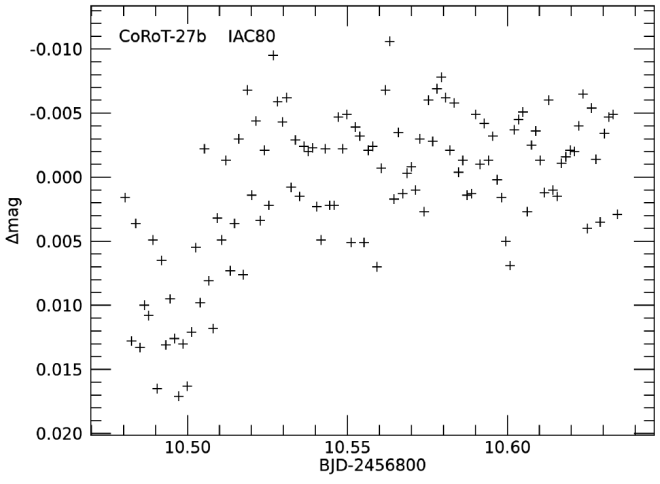
CoRoT-27b IAC80
Δmag
BJD-2456800

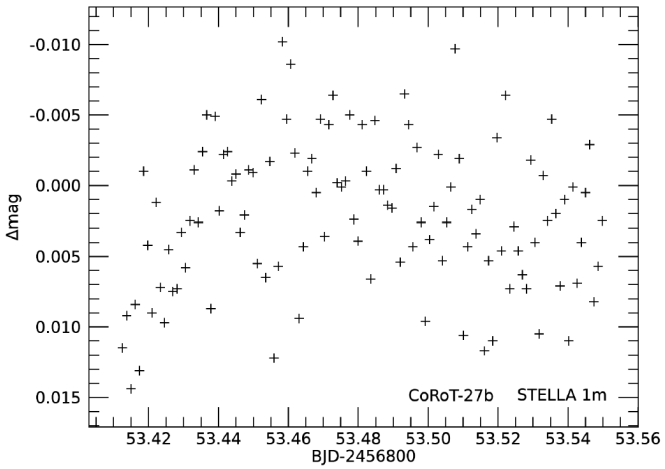
CoRoT-27b STELLA 1m
Δmag
BJD-2456800

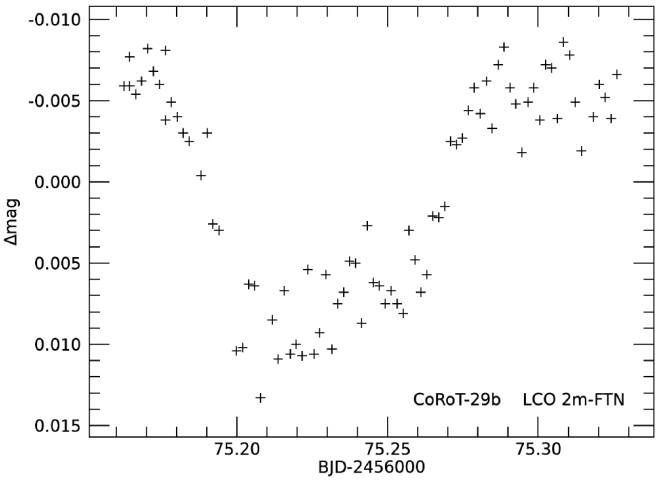
CoRoT-29b LCO 2m-FTN
Δmag
BJD-2456000

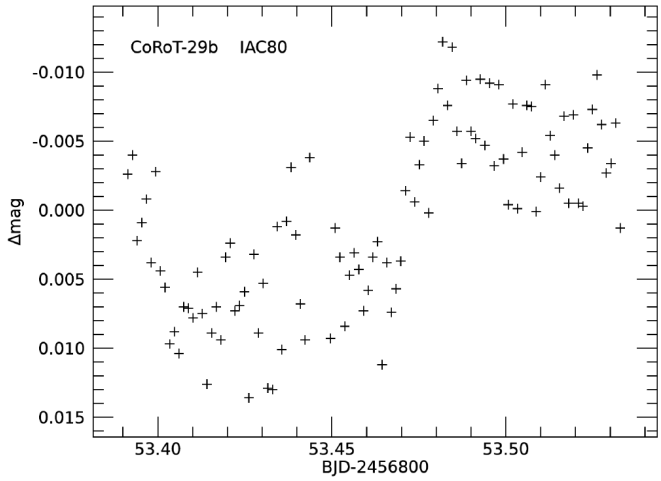
CoRoT-29b IAC80
Δmag
BJD-2456800

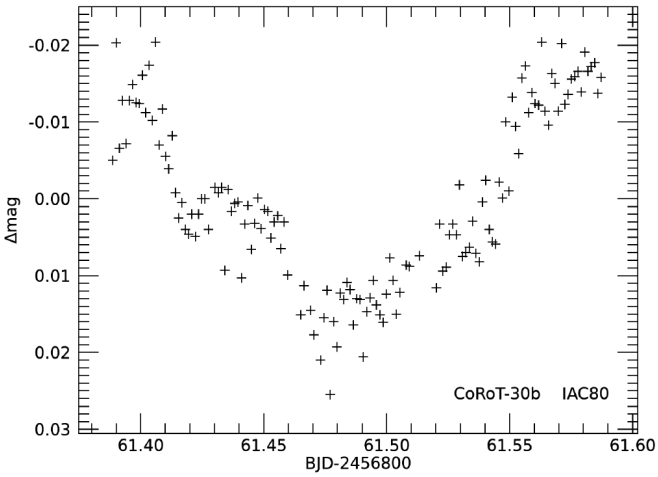
CoRoT-30b IAC80
Δmag
BJD-2456800

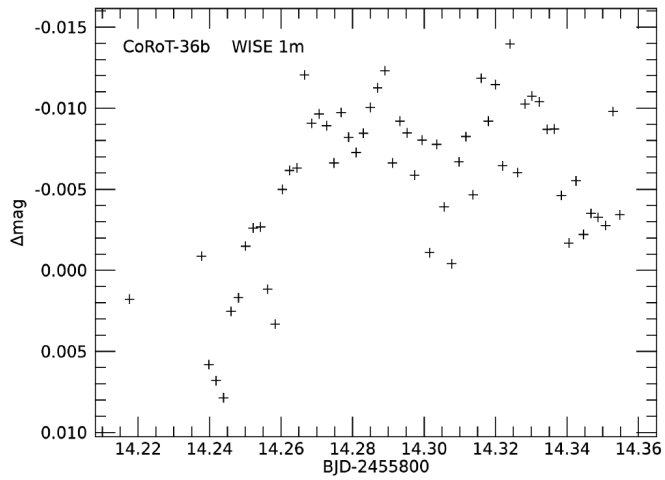
CoRoT-36b WISE 1m
Δmag
BJD-2455800

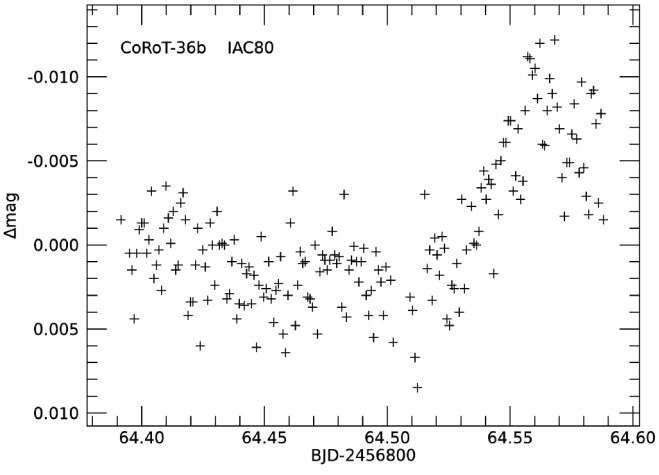
CoRoT-36b IAC80
Δmag
BJD-2456800

Appendix B: Transit light curves of CoRoT planets in the galactic anticenter field.

The light curves are ordered first by planet number and then by the BJD. The telescope used is also indicated.

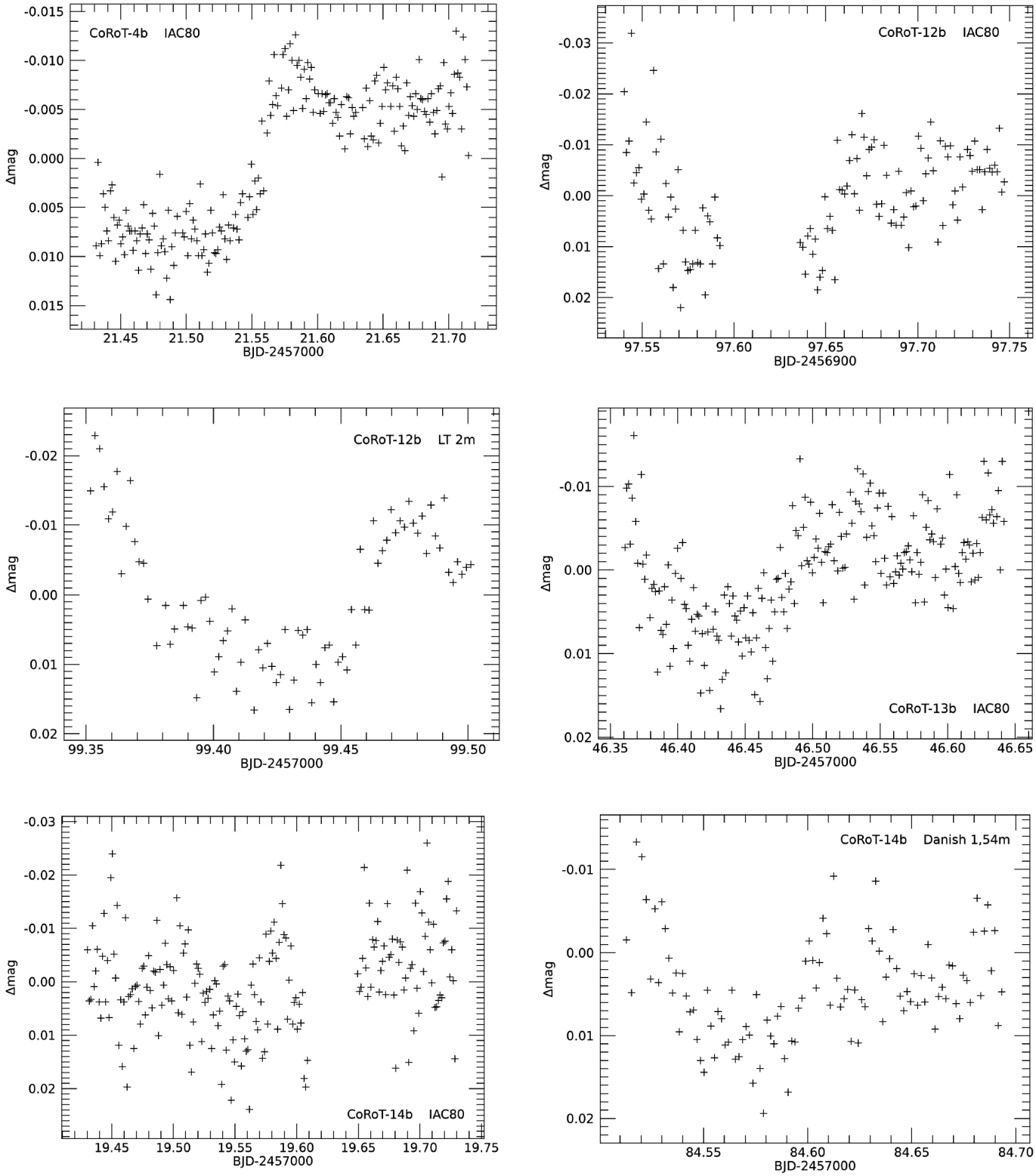

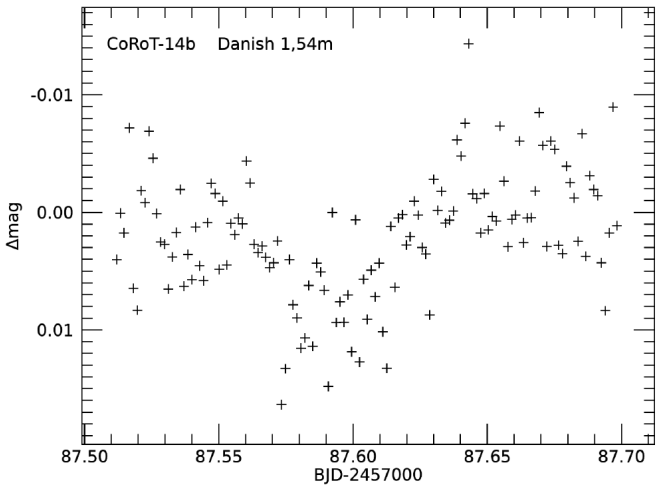
CoRoT-14b Danish 1,54m
Δmag
BJD-2457000

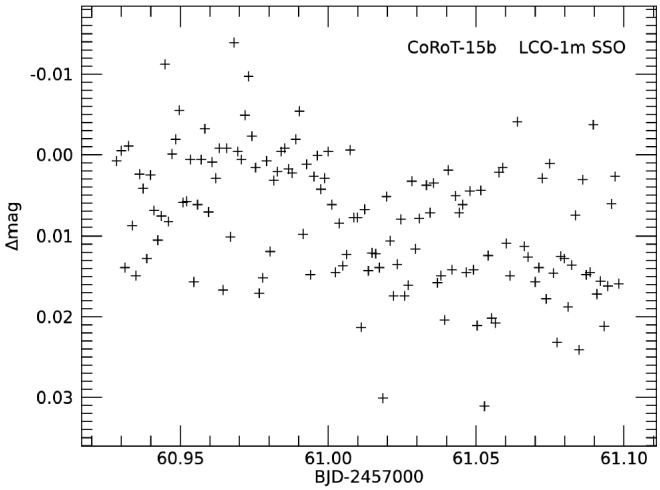
CoRoT-15b LCO-1m SSO
Δmag
BJD-2457000

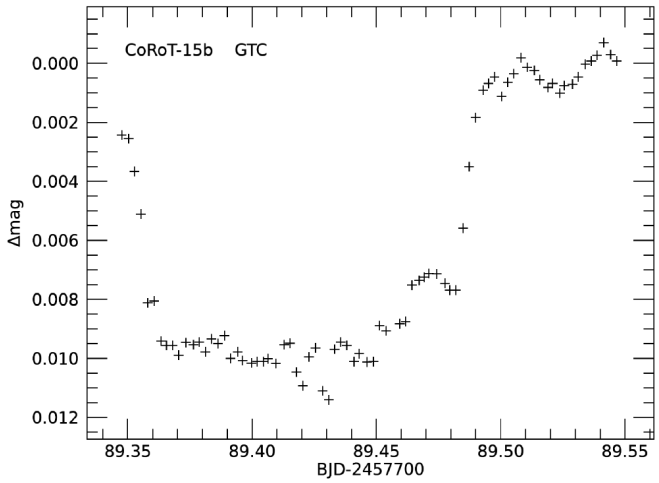
CoRoT-15b GTC
Δmag
BJD-2457700

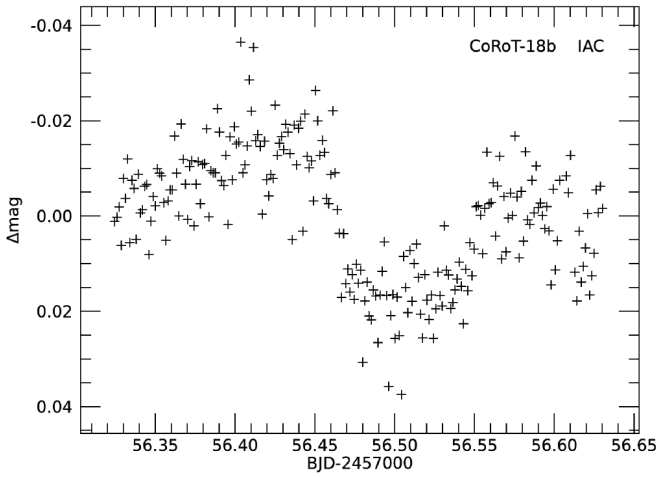
CoRoT-18b IAC
Δmag
BJD-2457000

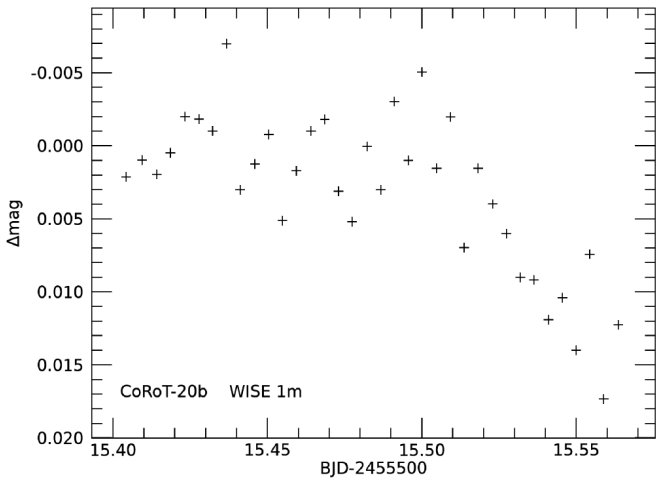
CoRoT-20b WISE 1m
Δmag
BJD-2455500

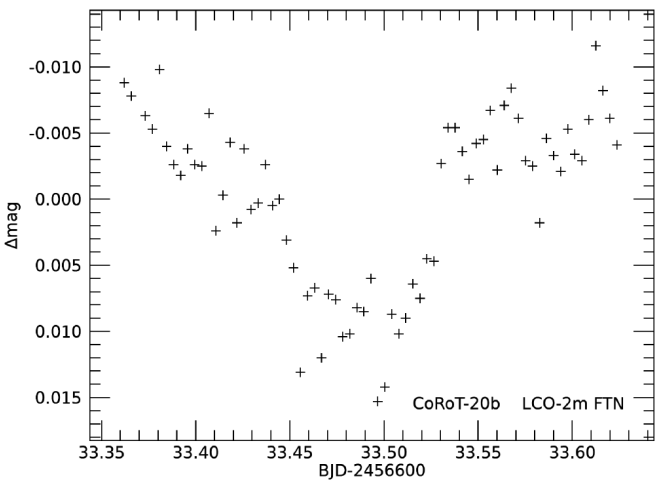
CoRoT-20b LCO-2m FTN
Δmag
BJD-2456600

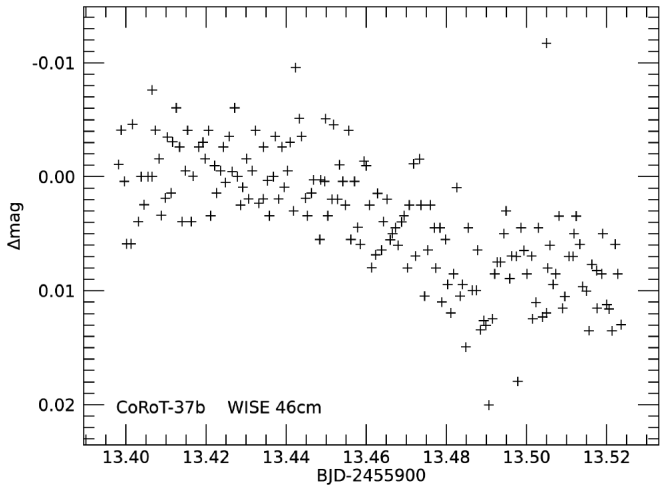
CoRoT-37b WISE 46cm
Δmag
BJD-2455900

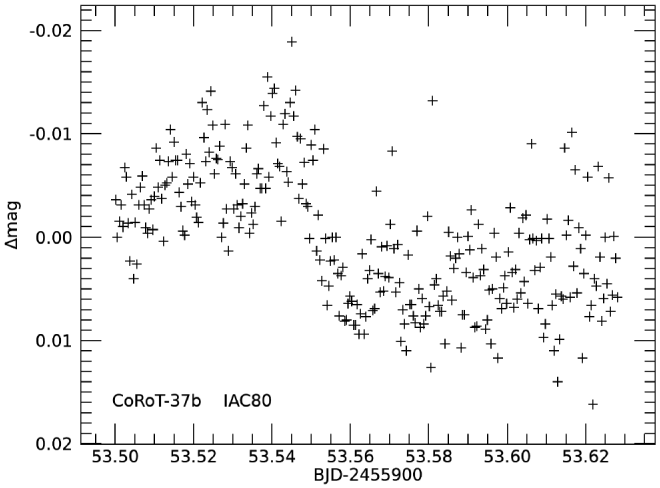
CoRoT-37b IAC80
Δmag
BJD-2455900

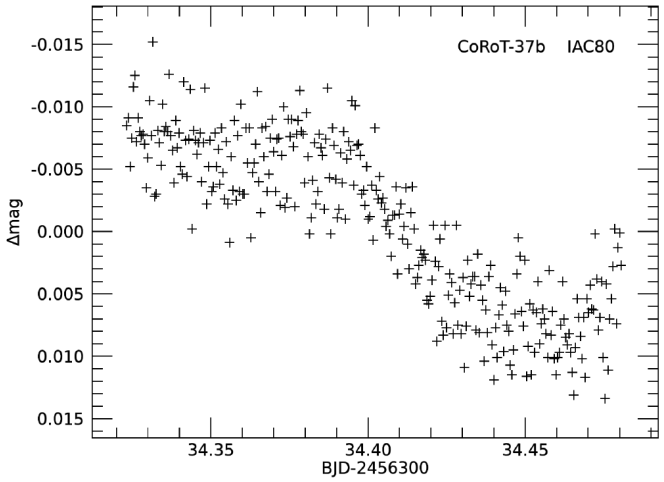
CoRoT-37b IAC80
Δmag
BJD-2456300

The Discovery of a New EA-Type Variable, TIC 160164029

Gabriel C. Neagu
Diana M. Manole
Calin Popovici Astroclub, Regiment 11 Siret, Galati, Romania; gabrielneagu874@gmail.com, manolediana771@gmail.com

Received July 30, 2020; revised October 13, 2020; accepted October 19, 2020

Abstract This paper presents the discovery of an EA variable star, TIC 160164029, previously unknown in VSX, Simbad, and VizieR. The variability was discovered using the software LCSIGNALFINDER and LCVIEWER for the analysis of TESS photometry products (PDC_SAP curve). The data were mathematically analyzed using VSTAR.

1. Introduction

Algol-type eclipsing variables (EA) are binaries with spherical or slightly ellipsoidal components. It is possible to specify the moments or beginning and end of the eclipses. Between eclipses the light remains almost constant or varies insignificantly because of reflection effects, slight ellipsoidality of the components, or physical variations (Samus *et al.* 2017).

Amateur astronomers analyzing online available time series photometry occasionally discover EA variables. This paper reports such a discovery.

2. Methodology

The flux time series photometry data were downloaded from MAST (Space Tel. Sci. Inst. 2020) and analyzed for periodicity using LcSignalFinder (Schmitt *et al.* 2019) using the settings presented in Figure 1.

After discovering a periodically variable signal coming from the star TIC 160164029 suggesting an eclipsing binary of EA type, we checked Simbad, VizieR, and VSX (Watson *et al.* 2014) to see if it was a known variable star, but confirmed that it was not. Although LCSIGNALFINDER presented a period, the available data from Zwicky Transient Facility (Masci *et al.* 2019) and TESS (Ricker *et al.* 2014) were used to determine the period of this variable star using DCDFT (Ferraz-Mello 1981) algorithm, available in VSTAR (Benn 2013). For the analysis of the range, the TESS data were shifted to ZTF g-band zero point. Also, the ZTF r-band observations were shifted to ZTF g-band zero point.

To calculate the range, a polynomial fit was applied to the maxima and minima to help identify the extrema and calculate the errors of measurement. The mean magnitude was taken as a baseline, and from that was extracted the arithmetic median of five random points around the extrema.

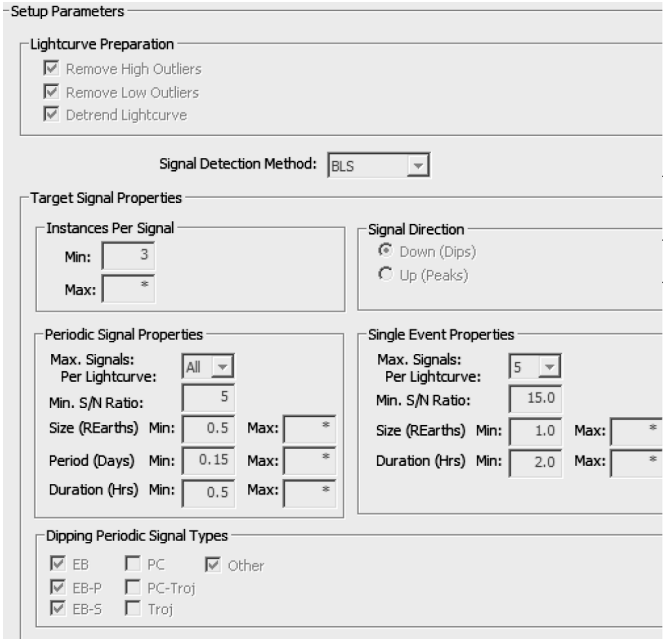

Figure 1. Representative image showing the settings used for the detection of the periodic variable signals in TESS data.

3. Results

Using this technique we obtained the results shown in Table 1. Figures 2 and 3 are the phase plot of TIC 160164029 and the power spectrum of the DCDFT, respectively.

4. Discussion

The purpose of this paper is to report an example of an EA variable which has been not recognized previously. The basis of this statement is that position searches (i.e., R.A. and Dec.) in SIMBAD, and position searches in the *General Catalogue of Variable Stars* (Samus *et al.* 2017) and through the SAO/NASA ADS Astronomy Query Form (http://adsabs.harvard.edu/abstract_service.html) failed to find any reference to the target star TIC 160164029.

The fact that the star shows variability with the presented period suggests that the variability is of EA type. The power spectrum of the DCDFT transform shows half of the real period. The period resulting from here had to be multiplied by 2.

Table 1. Table showing the variable star data results for TIC 160164029.

Period (d)	*Min. Mag. (g)*	*Max. Mag. (g)*	*Prime Eclipse Time (JD)*
0.83955 ± 0.000006	14.434 ± 0.004	13.808 ± 0.015	2459003.728

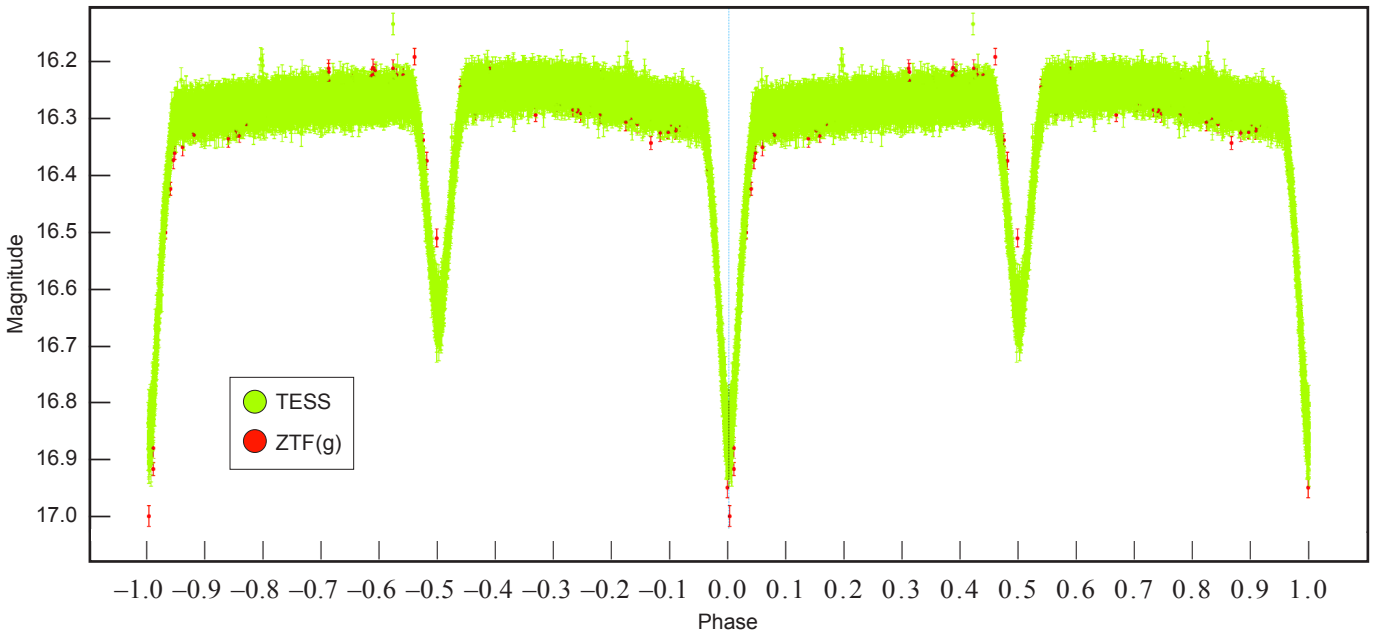

Figure 2. Phase plot in two cycles of TIC 160164029 using TESS and ZTF data. Period: 0.83955. Epoc: 2459003.728.

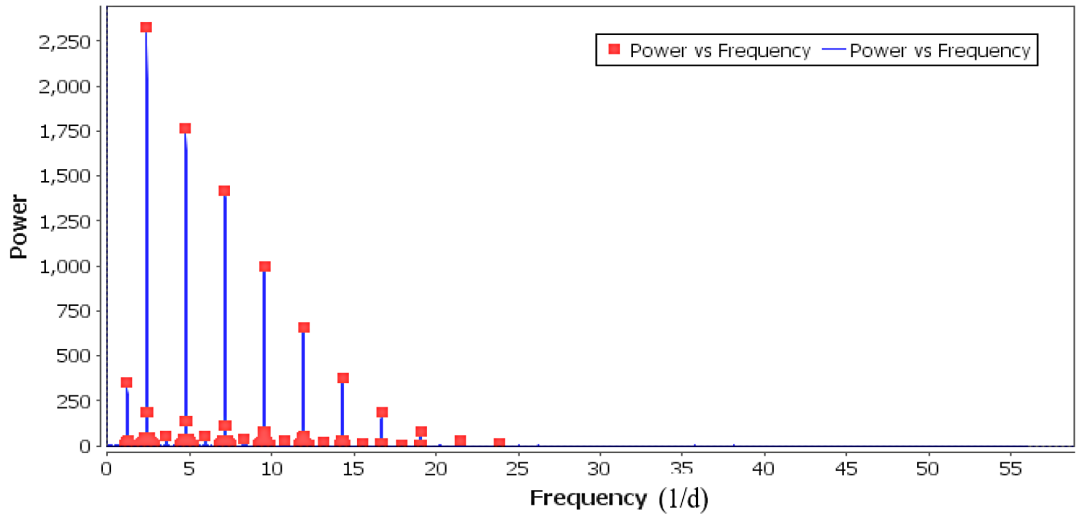

Figure 3. The power spectrum of the DCDFT transform from VSTAR. The biggest frequency is accompanied by aliases.

5. Conclusion

The star TIC 160164029 is proposed as a new EA candidate with a period of 0.83955 d. The discovery was made analyzing the TESS database in sectors 25 and 26.

6. Acknowledgements

This research used the SIMBAD database and the AAVSO International Variable Star Index (VSX) variable star type designations.

References

Benn, D. 2013, VSTAR data analysis software (http://www. aavso.org/vstar-overview).

Ferraz-Mello, S. 1981, *Astron. J.*, **86**, 619.

Masci, F. J., *et al.* 2018, *Publ. Astron. Soc. Pacific*, **131**, 018003.

Ricker, G. R., *et al.* 2014, *Proc. SPIE*, **9143**, 914320.

Samus, N. N., Kazarovets, E. V., Durlevich, O. V., Kireeva, N. N., and Pastukhova, E. N. 2017, *Astron. Rep.*, **61**, 80 (*General Catalogue of Variable Stars: Version GCVS 5.1*, http://www.sai.msu.su/groups/cluster/gcvs/gcvs).

Schmitt, A. R., Hartman, J. D., and Kipping, D. M. 2019, arXiv191008034S.

Space Telescope Science Institute. 2020, Transiting Exoplanet Survey Satellite (TESS), Missions and Data (https://archive.stsci.edu/missions-and-data/transiting-exoplanet-survey-satellite-tess).

Watson, C., Henden, A. A., and Price, C. A. 2014, AAVSO International Variable Star Index VSX (Watson+, 2006–2014; http://www.aavso.org/vsx).

Kepler Observations of Three SRS: Stars—V616 Lyrae, V607 Lyrae, and V621 Lyrae

Jennifer Cash
Don Walter
Wesley Red
Gabrielle Jones
South Carolina State University, 300 College Street, Orangeburg, SC 29117; jcash@scsu.edu, dwalter@scsu.edu, wesleyared@gmail.com, jonesgabrielle0189@gmail.com

Received August 3, 2020; revised August 5, 2020; accepted September 28, 2020

Abstract Kepler data for three SRS: stars, V616 Lyrae, V607 Lyrae, and V621 Lyrae, were analyzed to study their period structure. Two of the stars had confirmed SRS light curve characteristics. V616 Lyr shows two strong periods at 16.91 days and 8.18 days. V607 Lyr shows one strong period at 13.55 days. V616 Lyr and V607 Lyr also display amplitude changes common to the SR stars. Variability was not detected for V621 Lyr. Evidence for solar-like oscillations in V616 Lyr is presented.

1. Introduction

Semiregular, or SR, stars are a class of pulsating variable for giant and supergiant stars with intermediate to late spectral types and periods of tens to thousands of days. The *General Catalogue of Variable Stars* (GCVS) variability type descriptions explain the "semiregular" nature of these stars by referring to "noticeable periodicity in their light changes, accompanied or sometimes interrupted by various irregularities" (Samus *et al.* 2017). Traditionally the classification was divided into four subgroups (SRa, SRb, SRc, and SRd) depending on the level of periodicity, amplitudes, and/or spectral types.

The "76th Name-List of Variable Stars" introduced a new subgroup of the SR variability type—SRS stars—which are "Semiregular pulsating red giants with short periods (several days to a month), probably high-overtone pulsators." and AU Ari was named as the prototype for this category (Kazarovets *et al.* 2001). As of May 2018, the AAVSO International Variable Star Index (VSX) listed 375 stars classified as SRS stars and another 19 uncertain SRS: designations (Watson *et al.* 2017). The era of large surveys has dramatically increased the number of stars in the VSX database with 73,917 SRS stars and another 36,510 SRS: candidates as of July 2020, with most of the new ones detected by OGLE and ASASSN-V missions.

Studies of the SR stars are complicated by both the multiperiodic structure common to many SR stars (Kiss *et al.* 1999; Fuentes-Morales and Vogt 2014) and amplitude changes common in pulsating red giants (Percy and Laing 2017). As pointed out by Koen *et al.* (2002), these complications mean that "long, uninterrupted time series of observations are required to make reliable deductions." Cadmus (2015) summarized efforts in the long term monitoring of SR stars and called for additional observations and analysis of this stellar type. The Kepler Mission provided an opportunity to study variable stars with high precision and long temporal baselines. The recent review paper by Molnár *et al.* (2016) details some successes in variable star research using Kepler data. Hartig *et al.* (2014) presented results for long-period SR stars in the Kepler field and was able to study the multiperiodic nature common to many SR stars. While the entire category of SR stars shows a range of behaviors, the SRS stars form the short-period, small-amplitude extreme end. As such the careful analysis of members of this class can eventually provide additional insight into the underlying physical processes at work.

Several SRS: stars are included in the field of view of the original Kepler mission. These are stars which have not been well observed prior to Kepler; see section 2.2 for additional details. The high precision, closely spaced, and long baseline observations by Kepler have the potential to provide a much clearer view of the variable nature of these stars. While they were included as "test cases" for the analysis in the Hartig *et al.* (2014) work, the authors pointed out that additional analysis would be needed to carefully determine the period structure for these three stars. This paper presents that analysis.

2. Observations

2.1. Target stars

The three SRS: stars presented in this study are in the region of the open cluster NGC 6791 and were originally identified as variables by Bruntt *et al.* (2003). Table 1 lists the three stars along with their cross identification numbers and current period values from the GCVS.

Table 1. Target stars.

Kepler Ident.	*GCVS Name*	*NGC 6791 Ident.*	*Max.*	*GCVS Period (days)*
2437359	V616 Lyr	V73	14.84	20.9
2569737	V607 Lyr	V97	16.49	9.563
2570059	V621 Lyr	V99	17.54	10:

2.2. Previous ground-based photometric observations

After being identified as variables by Bruntt *et al.* (2003), additional ground based observations have been quite limited. V616 Lyr had subsequent observations by Mochejska *et al.* (2003) which indicated an irregular variability with an estimated period of 34 days. Mochejska *et al.* (2005) determined a period

of 13.6206 days for V607 Lyr, but did not list any period for V621 Lyr. One additional study of V621 Lyr (de Marchi *et al.* 2007) was also not able to confirm any variability for this star.

There are minimal observations in the AAVSO database for these stars with a total of 32 observations for V616 Lyr, 4 observations for V607 Lyr, and 5 observations for V621 Lyr. In all three cases the observations are spaced far enough apart that they are insufficient to perform any period analysis.

2.3. Spectroscopic observations

Our earlier work (Hartig *et al.* 2014) included spectroscopic classification of all three stars. We classified V616 Lyr as G9 III based on our spectra taken in 2011 May with the four-meter Mayall telescope at Kitt Peak National Observatory. This agrees favorably with the classification of K0 III-IV from Kinman (1965) based on photographic plates. V607 Lyr and V621 Lyr were too faint on the dates of our observations to acquire spectra. Instead, Hartig *et al.* (2014) used V–K colors from the Naval Observatory Merged Astrometric Dataset (NOMAD) and found V607 Lyr to be a K0 and V621 Lyr a G8. They also stated that these three stars are likely on the red giant branch (RGB).

A search of a number of databases turned up no useful additional spectral data for these stars. We searched ASAS, ASAS-SN, APOGEE, LAMOST, and articles in the literature. The Kepler Index Catalog (KIC) does give T_{eff} for our stars based on SDSS colors and model atmospheres (Brown *et al.* 2011) and they generally agree with our results in Table 2 within the margin of error noted in Brown *et al.*

With the classifications given in Hartig *et al.* (2014), including their likely location on the RGB, along with the calibration of MK spectral types from Drilling and Landolt (2000), we determined the T_{eff} and calculated log $(L/L_{\odot})$ as shown in Table 2. The values in Table 2 will be used later in the Conclusions section.

2.4. Kepler observations

The Kepler Space Telescope collected long cadence data for these stars for various quarters over the lifetime of the original mission. V616 Lyr is the brightest of the three stars and was observed as a target object during all 17 quarters of the original Kepler mission. V607 Lyr was observed as a target object for quarters 2–10 and 13–17, while V621 Lyr, the faintest of our stars, was observed as a target object only for quarters 6–9 and 14–17. Both target pixel files and processed light curve files for these observations can be downloaded from the on-line MAST archive.

While the missing quarters for these stars would normally be unrecoverable, our stars lie within an open cluster which was an area of interest for the Kepler mission and observed as a series of 20×100 pixel custom apertures covering the region during the entire mission. This allows the possibility of extracting the target stars during quarters where the individual target was not observed or where the default aperture was too small to capture the entire flux. In the analysis sections for each star we indicate the specific KID numbers for the custom aperture used to extract or re-extract data we used. Figure 1 shows the locations of the three target stars in the cluster on one section of a Kepler Full Frame Image (FFI).

Table 2. Spectroscopic quantities.

GCVS Name	*Spectral Type*[a]	*T_{eff} (K) (This study)*	*log $(L/L_{\odot})$ (This study)*
V616 Lyr	G9 III	4730	1.78
V607 Lyr	K0	4660	1.82
V621 Lyr	G8	4800	1.74

[a] *From Hartig* et al. *2014.*

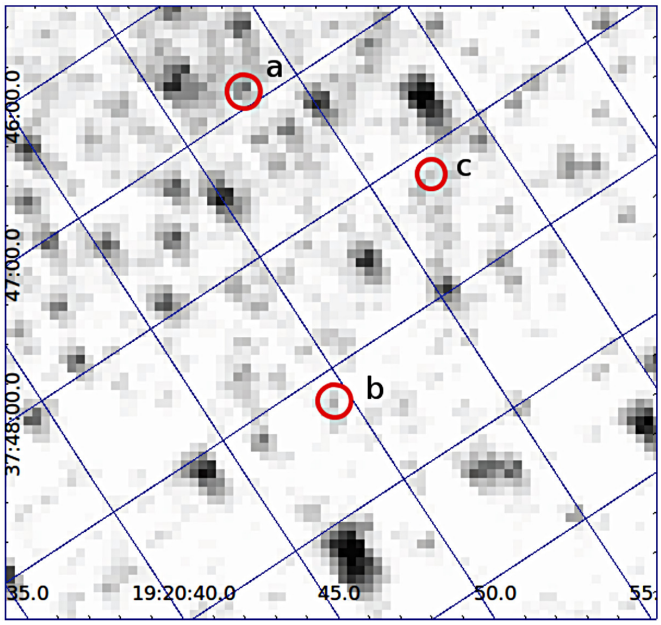

Figure 1. A section of the Kepler FFI for the region of the open cluster NGC 6791 including our three target stars, a) V616 Lyr, b) V607 Lyr, c) V621 Lyr.

3. Analysis and results

3.1. General Kepler analysis

Each target for the Kepler mission defines a default aperture to be used for the standard aperture photometry (SAP) surrounded by a larger target aperture of data which is saved in a target pixel file. For each of our stars, we examined the light curves produced by the default aperture as well as slightly larger or smaller apertures selected from the target pixel file. In particular, we looked for indications that the default aperture might not include enough of the variable star's flux at maximum or that too much scattered flux from a neighboring star might be included for a particular star. The details of this analysis are given for each star in the sections below.

The Kepler mission observations also include several instrumental effects that must be properly dealt with in the data analysis stage. Some of these effects are described in more detail in papers by Hartig *et al.* (2014) and Molnar *et al.* (2016) as well as the *Kepler Data Processing Handbook* (Smith *et al.* 2017). For quarters in which we extracted the light curves from the target pixel files, these instrumental effects needed to be removed via co-trending, using the PyKE software function kepcotrend (Still and Barclay 2012). To maintain consistency in the analysis between quarters, the co-trending was performed

on the standard aperture photometry (SAP) light curves for all quarters regardless of whether they came from the default target apertures or were re-extracted from target pixel files.

Following co-trending, the light curve sections for each quarter were cleaned to remove null values and problematic quality-flagged data points. The individual quarters were then shifted to a common mean flux level to form a long-baseline light curve. These full light curves were examined visually, and period analysis was done using a Lomb-Scargle algorithm. The dominant periods found by the Lomb-Scargle analysis were further tested using both phase folding and curve fitting.

3.2. V616 Lyr

The Kepler mission included V616 Lyr as a target for quarters Q01 though Q17, meaning that target pixel files and light curve files were available from the archive for the entire mission. We examined the target pixel files to determine if the default aperture sufficiently captures the flux from the star. Of our three stars, V616 Lyr is the brightest without very close neighboring stars, and examination of alternate aperture choices did not show any problems with the default aperture. Once this was determined, the instrumental effects were removed using the steps outlined in section 3.1 above.

The light curve for V616 Lyr shows the typical SR "noticeable periodicity" with the changing curve shape typical of multiperiodic signals. Figure 2 shows a section of the light curve where these changes are particularly evident.

The Lomb-Scargle periodogram for V616 Lyr indicates two dominant periods in the light curve as shown in Figure 3. The dominant period peak is found at 16.91 days with an additional strong peak at a period of 8.18 days. The dominant peak at 16.91 days is surrounded by other side peaks and the structure as seen in Figure 3b may indicate the presence of an additional weaker signal at a period in the range between 15 and 16 days.

The splitting of the periodogram in the regions of the two dominant periods is often seen in stochastically excited oscillators (Bedding *et al.* 2005). Following the method of Bedding, we have fit the periodogram in the regions near these dominant frequencies with Lorentzian profiles. The resulting fits are shown in Figure 4. For the strongest peak, Figure 4a, the Lorentzian gives a central frequency of 0.0598 d^{-1} and a full width half max of 0.0039 d^{-1}, which translate to a period of 16.7 days and a mode lifetime of 82 days. It is noted that the asymmetry in the structure of the periodogram results in a Lorentzian peak that is offset slightly toward lower periods compared to the peak period. For the secondary peak, Figure 4b, the Lorentzian profile gives a central frequency of 0.122 d^{-1} and a full width half max of 0.0031 d^{-1}, which translate to a period of 8.2 days and a mode lifetime of 103 days.

Curve fitting shows that many of the features in the light curve for V616 Lyr are reproduced with a two-period fit using the two dominant periods of 16.91 days and 8.18 days. Figure 5 shows two sections of the light curve where the fit to the light curve is more and less successful in matching the data. In general, the maxima and minima of the light curve are sharper than a pure sinusoidal curve of the fitting model, which caused the curve fit to have a lower amplitude than the data, but we also see that there are amplitude changes in the light curve which are not matched well with the two-period fit. After trying three period fits with the dominant periods of 16.91 and 8.18 along with a third period in the range of 14.5 to 16.5 days, we find that a period of 15.3 days shows some improvement, but not enough to justify confidence that the third period has any astrophysical significance. As such, we use the two dominant periods in our conclusions.

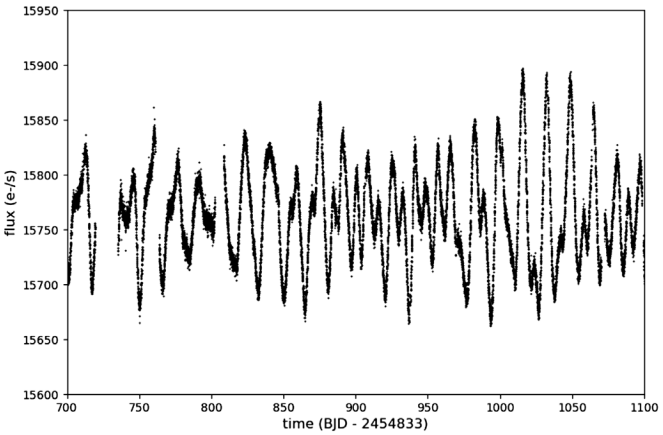

Figure 2. A section of the composite Kepler light curve for V616 Lyr showing the typical SR star "noticeable periodicity" but also indications of mutli-periodicity as the curve shape changes over the span.

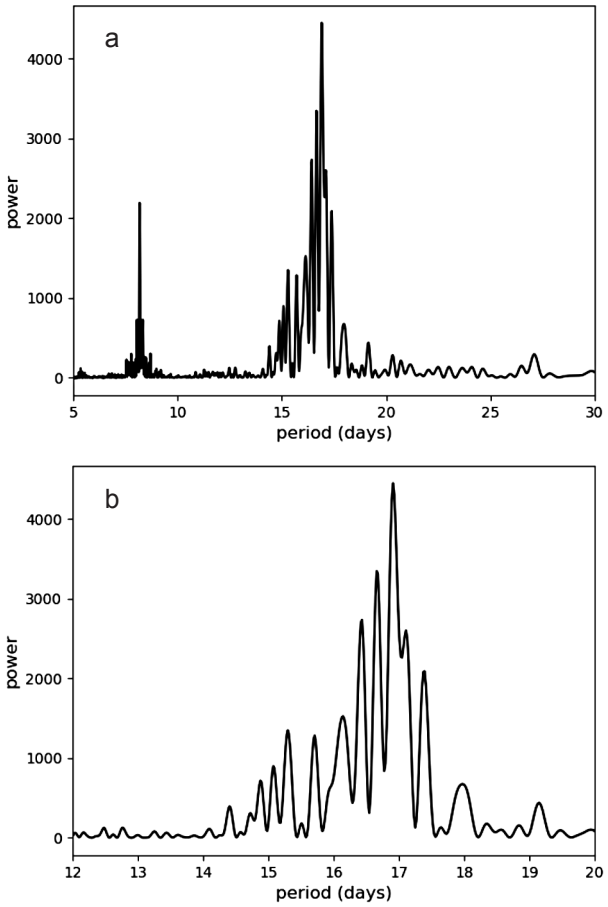

Figure 3. The Lomb-Scargle periodogram for V616 Lyr: a) the range from 5 days to 30 days showing the two dominant periods found in the light curve, b) a close up of the region from 12 days to 20 days showing the structure surrounding the dominant period.

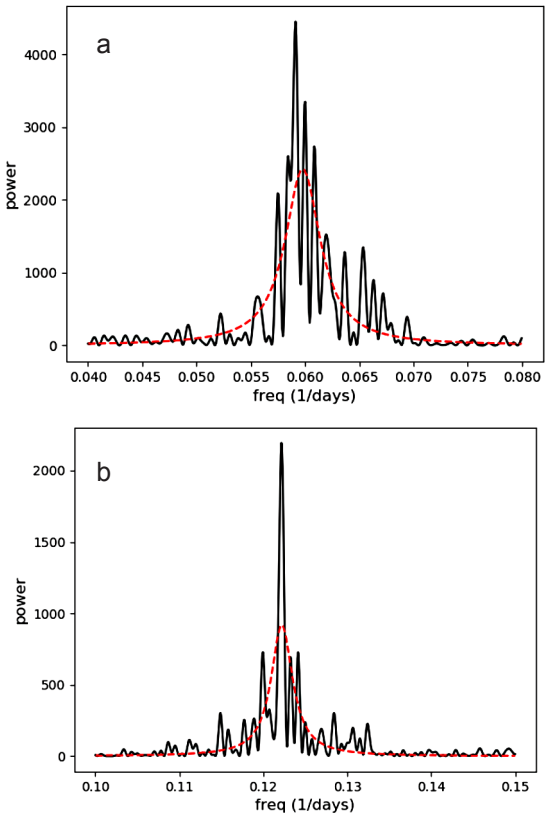

Figure 4. The Lomb-Scargle periodogram in units of frequency for V616 Lyr, with the Lorentzian fits to the two main peaks: a) the dominant peak at a period of 16.7 days and b) the secondary peak at a period of 8.2 days.

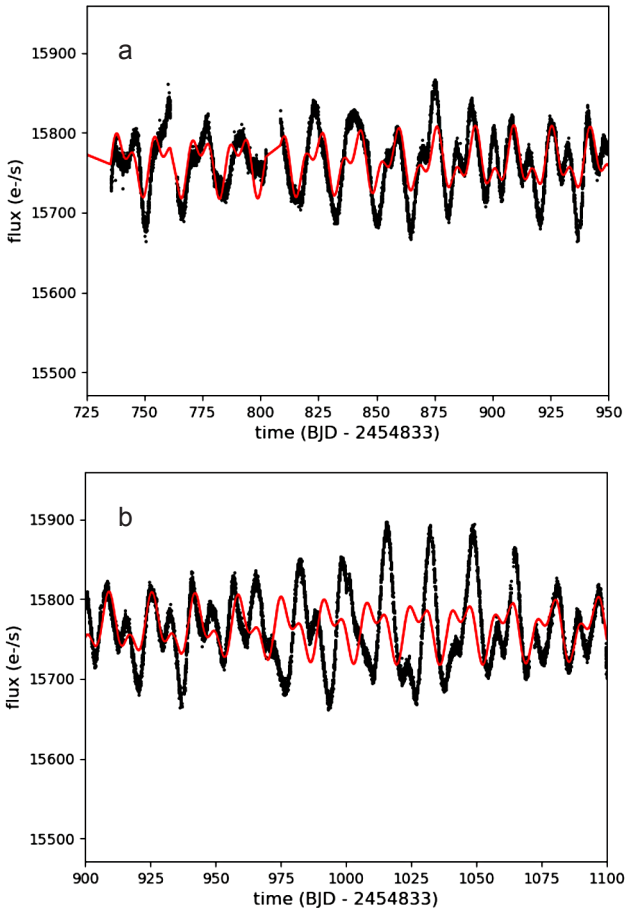

Figure 5. Sections of the V616 Lyr light curve with the data points shown as black dots and a model fit using 16.91 days and 8.18 days as a red line. a) shows a section where the model fit is good, while b) shows a section where the model fit is significantly weaker.

3.3. V607 Lyr

For V607 Lyr, the Kepler mission observed the star for 14 of the 17 quarters. To get a full light curve spanning the entire mission, we needed to extract data for quarters 1, 11, and 12 from the open cluster custom apertures. The star fell on Kepler ID 100000929 for quarter 1, and KID 100000928 was used for quarters 11 and 12.

Since V607 Lyr is a fainter star, the default aperture used by the Kepler pipeline was smaller than that used for V616 Lyr. In some quarters, the default aperture used was only two pixels. By examining these default apertures and comparing the light curves created from larger apertures, we determined that the default aperture missed flux at the maxima of the star's oscillation. We constructed new apertures that better captured the variability. The extracted light curves using these new apertures were co-trended and shifted as described in the general analysis section 3.1 above.

Visual inspection of the full light curve shows the strong periodicity with some variation to the curve shape and amplitude as seen in Figure 6. The oscillations are much more regular for V607 Lyr compared to those for V616 Lyr.

Period analysis for V607 Lyr, as shown in the periodogram in Figure 7, indicates several periods. There is a strong peak at a period of 13.55 days which dominates the light curve, but there is also a pair of lower power peaks at periods of 14.48 and 14.68 days. Curve fitting with a single period of 13.55 days provides a reasonable fit for the timing of the light curve as shown in Figure 8 but not the amplitudes, due to the fact

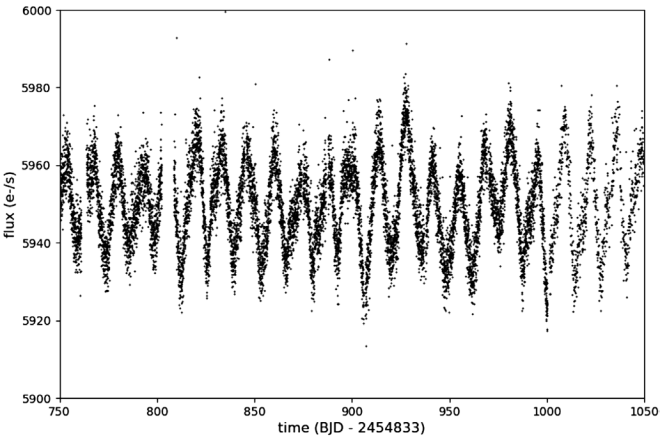

Figure 6. Section of the V607 Lyr light curve showing strong periodicity accompanied by some variation in curve shape and height.

that the maxima and minima are steeper than a pure sinusoidal variation as well as to the variable amplitudes over the full span. Adding in one or two additional periods in the range of 14.48–14.68 days creates beat periods in the curve fitting which better approximate the changing amplitudes, but these periods may not represent pulsation periods but some other mechanism of amplitude change. Since this periodogram is significantly

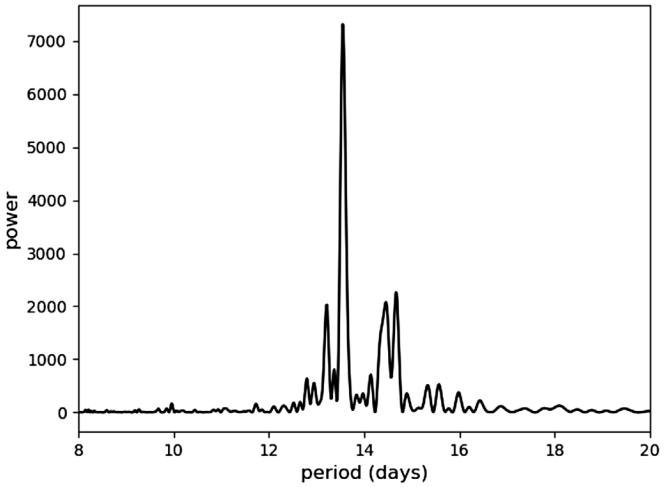

Figure 7. The Lomb-Scargle periodogram for V607 Lyr showing the dominant periods found in the light curve.

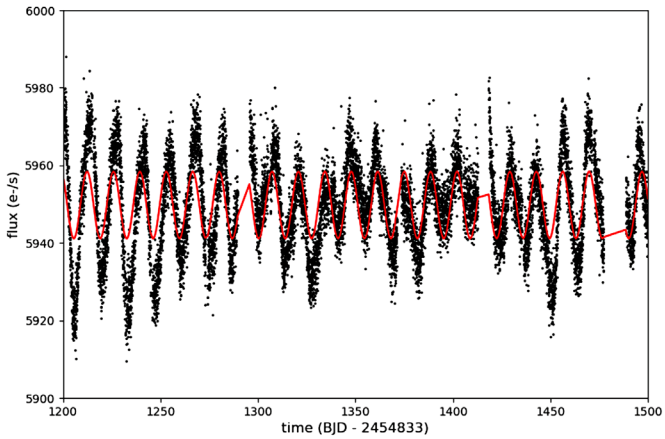

Figure 8. The V607 Lyr light curve data shown as black dots with a solid red line showing the curve fit using the 13.55-day period.

narrower without the characteristic splitting seen for V616 Lyr, we did not fit this peak with a Lorentzian profile.

3.4. V621 Lyr

The original Kepler mission included V621 Lyr as a specific target for only eight quarters. V621 Lyr is found on the KID 100000930 custom aperture for the missing quarters. The default apertures for this star are not consistent between the different quarters and vary from six pixels down to a single pixel. Complicating the analysis is the fact that V621 Lyr is faint, with a nearby brighter star identified only as TGM2014 15004 in Simbad.

Figure 9a shows the region of our star from a Kepler Full Frame Image (FFI) in the middle of quarter 6. Figure 9b shows the region of these stars from the DSS image (rotated to align with the Kepler FFI) with V621 Lyr marked with cross-hairs using the Aladin viewer. From these images it is clear that Kepler is barely resolving V621 Lyr and any aperture for the star will contain flux from the nearby brighter star TGM2014 15004 located below and to the left of V621 Lyr.

After trying several possible apertures, we selected a two-pixel aperture that included the pixel with the target coordinates

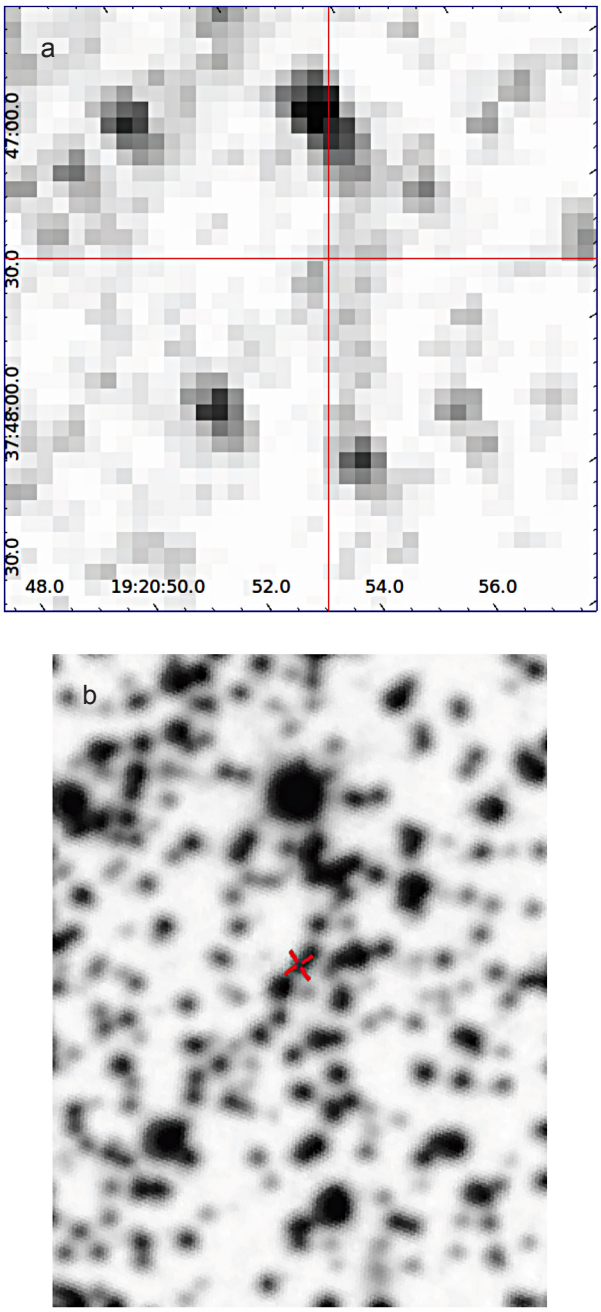

Figure 9. a) Kepler FFI image for the region around V621 Lyr which is marked with a red cross-hair; b) DSS image for the region around V621 Lyr which is marked with a red cross-hair.

for V621 Lyr as well as a second pixel geometrically closest to the target coordinates. For comparison, we also extracted a light curve for the neighboring brighter star using a similar procedure. To remove the instrumental effects, we co-trended using the first five co-trending basis vectors. For quarters 2 and 12, significant instrumental artifacts remained in the light curves for both our target star and the neighboring bright star and these quarters were excluded from our full light curve.

Visual examination of the light curve for V621 Lyr as shown in Figure 10 indicates that we do not have the kind of clear variation seen in V616 Lyr or V607 Lyr. The light curve is dominated by scatter on the order of 0.25% of the flux.

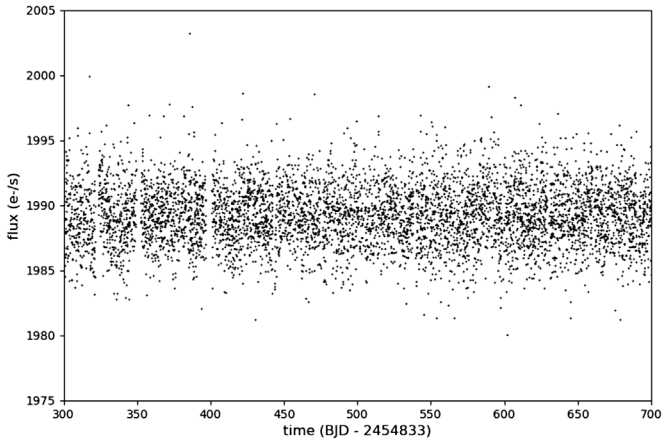

Figure 10. A section of the light curve for V621 Lyr showing little obvious variability.

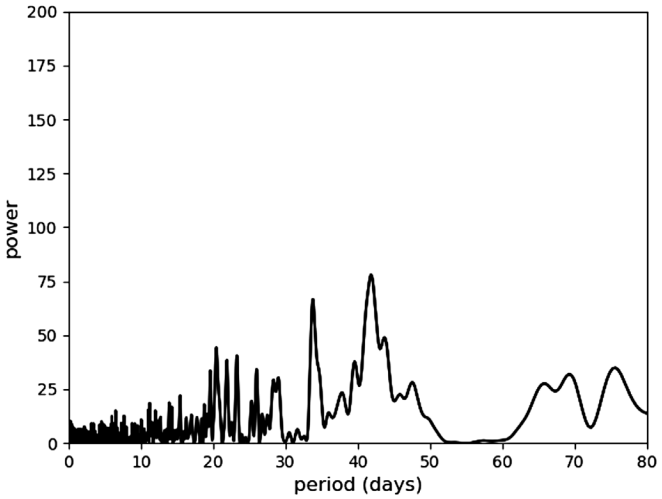

Figure 11. The Lomb-Scargle periodogram for V621 Lyr for the range of 2 days to 80 days.

Running period analysis on this light curve using a Lomb-Scargle periodogram, as seen in Figure 11, results in only low power signals. Analysis of the neighboring brighter star shows a similar pattern of low power signals in this period range indicating that the signals may be remaining instrumental effects and not indicative of astrophysical variability in our target star.

4. Conclusions

4.1. V616 Lyr

Our analysis of V616 Lyr supports its classification as an SRS type variable. It has a dominant period of less than 20 days with amplitude changes typical of the semiregular stars. V616 Lyr is clearly multiperiodic, showing two dominant periods. There may be additional weaker periods which may be related to the changing amplitudes, but we caution against a strict interpretation that these are true pulsation periods. Percy and Laing (2017) point out that these amplitude variations remain unexplained.

Using the interpretation of Bedding *et al.* (2005), V616 Lyr shows strong indications of stochastically excited oscillations with a mode lifetime of approximately 82 and 103 days for the dominant and secondary periods, respectively (corresponding to 5 and 12.6 pulsational cycles). The analysis on L2 Pup in Bedding *et al.* (2005) found a similar relationship of a mode lifetime of 12.5 pulsation cycles. Bedding *et al.* (2010) also concluded that red giants can have mode lifetimes greater than 10 days such as those we find for V616 Lyr.

Table 3. Periods detected in Kepler data.

Source	*V616 Lyr periods (days)*	*V607 Lyr periods (days)*
This work	16.91 and 8.18	13.55
Neilsen *et al.* (2013)	16.68	14.733
Reinhold *et al.* (2013)	17.45, 14.24	
McQuillan *et al.* (2014)	16.415	13.767
Hartig *et al.* (2014)	370.11, 189.10, 16.5	371.31, 189.10, 13.54

As V616 Lyr is a bimodal pulsating red giant, we can compare the two dominant periods similar to the work of Percy (2020). In the case of V616 Lyr, the dominant longer period (Pa) and shorter period (Pb) have a log (Pa) value of 1.23 and a value of 0.48 for the ratio of the periods (Pb / Pa). These values place V616 Lyr in the lower left grouping of stars in the Peterson diagram shown as Figure 1 of Percy 2020. These shorter period stars with period ratios around 0.5 were interpreted as ones oscillating in the first and third overtone modes or possibly the fundamental and first overtone modes.

As pointed out by Koen *et al.* (2002), the combination of these stars' multiperiodicity along with the semiregular nature of the SRS stars results in changing the curve shape over time, which can be difficult to analyze. This helps to explain how other observers could find very different periods when examining these stars for short time spans with ground-based data.

The Kepler observations for V616 Lyr were also analyzed by other research groups but with some important differences in analysis which have the potential to influence their results. The results from Neilsen *et al.* (2013) and McQuillan *et al.* (2014) used an automated analysis to determine "rotational" periods using the standard PDC light curves. In these papers, they looked only for a single period and did not look for the expected multiperiodicity often found in SRS stars. Reinhold *et al.* (2013) used only a single quarter of Kepler data. Hartig *et al.* (2014) used custom apertures but did not fully remove the instrumental effects from those light curves. Table 3 shows a comparison of the results of this work with these other sources for both V616 Lyr and V607 Lyr discussed in the next section.

4.2. V607 Lyr

Our analysis of V607 Lyr also supports its classification as an SRS type variable. It has a dominant period less than 20 days with amplitude changes typical of the semiregular stars. Again we have identified additional weaker periods which may be related to the changing amplitudes or stochastic nature of the oscillations.

Unlike V616 Lyr, V607 Lyr is dominated by only one oscillation period. While the bimodal pulsators are common in the red giants, single dominating periods are also found. Without the bimodal periods, it is harder to interpret which pulsation mode is active in V607 Lyr. The much narrower peak for V607 Lyr also indicates that whatever mode of oscillation

is in action, it is significantly more stable than the oscillations in V616 Lyr.

As discussed for V616 Lyr, there are variations between the analysis of the Kepler data on V607 Lyr done by different authors as seen in Table 3 in the previous section. In the case of V607 Lyr, the periods found have somewhat more consistency due to the more stable nature of the star. Again we argue that the more careful analysis done in this paper using custom apertures as opposed to the standard PDC light curves is more likely to yield a reliable period estimate.

4.3. V621 Lyr

Our analysis of V621 Lyr was not able to confirm variability in this faint star. Kepler observations have high frequency resolution but are not highly resolved spatially. The crowded field around V621 Lyr complicates the analysis enough that we cannot claim that V621 Lyr is not a variable, but we clearly do not detect any strong variability in the region including V621 Lyr and the neighboring stars during the four years of the Kepler mission.

4.4. Solar-like oscillations

The question of solar-like oscillations (stochastically excited and damped) in red giants has been the subject of discussion for some time with results supporting detections from the ground and space including Merline (1999), Stello *et al.* (2007), Hekker *et al.* (2010), and numerous others. Using the higher signal-to-noise data from Kepler, Bedding *et al.* (2010) found unambiguous evidence of solar-like oscillations in red giants. Bedding *et al.* (2005) found solar-like oscillations in the SR M star L2 Puppis while Mosser *et al.* (2013 and references therein) used ground-based and Kepler data to demonstrate that solar-like oscillations are found in SR variables over a wide range of spectral types.

Aerts *et al.* (2010) discuss the location of pulsating red giants on the HR Diagram, specifically those that have been shown to have solar-like oscillations. Their Figure 2.2 plots log $(L/L_{\odot})$ vs log T_{eff} using results from an earlier work by Carrier and Eggenberger (2006). The values from Table 2 of our paper place V616 Lyr and V 607 Lyr into Figure 2.2 from Aerts *et al.* at positions very close to the G9.5 IIIb star ε Oph, a pulsating red giant. This does not prove that the oscillations in V616 Lyr and V 607 Lyr are solar-like; however we note they do occupy a part of the pulsation HR diagram where similar G and K stars with confirmed solar-like oscillations are found. In particular as noted above for V616 Lyr, the evidence of solar-like oscillations is strongly supported by splitting of the periodogram in the regions of the two dominant periods. The spectroscopic results further support that in the case of V616 Lyr. No such splitting of the periodogram occurred for V607 Lyr so the evidence of solar-type oscillations is less convincing. We draw no conclusion about solar-like oscillations in V621 Lyr since were unable to detect any variation in its light curve.

5. Acknowledgements

This paper includes data collected by the Kepler mission. Funding for the Kepler mission is provided by the NASA Science Mission directorate. The data presented in this paper were obtained from the Mikulski Archive for Space Telescopes (MAST). STScI is operated by the Association of Universities for Research in Astronomy, Inc., under NASA contract NAS5-26555. We also acknowledge the support of the Kepler GO office staff and the PyKE software project.

Support for this work includes SC State's NSF PAARE award AST-1358913, NSF EiR award AST-1901296, and NASA Kepler awards NNX11AB82G and NNX13AC24G. Support for student work on this project was provided by the South Carolina NASA Space Grant Consortium.

This research has made use of the International Variable Star Index (VSX) database, operated at AAVSO, Cambridge, Massachusetts. Portions of the analysis were performed with the computer program TS, developed by the American Association of Variable Star Observers.

References

Aerts, C, Christensen-Dalsgaard, J., and Kurtz, D. W. 2010, *Asteroseismology*, Springer Science+Business Media B. V., Dordrecht, 43.

Bedding, T. R., Kiss, L. L, Kjeldsen, H., Brewer, B. J., Dind, Z. E., Kawaler, S. D., and Zijlstra, A. A. 2005, *Mon. Not. Roy. Astron. Soc.*, **361**, 1375.

Bedding, T. R, *et al.* 2010, *Astrophys. J., Lett.*, **713**, L176.

Brown, T. M., Latham, D. W., Everett, M. E., and Esquerdo, G. A. 2011, *Astron. J.*, **142**, 112.

Bruntt, H., Grundahl, F., Tingley, B., Frandsen, S., and Thomsen, B. 2003, *Astron. Astrophys.*, **410**, 323.

Cadmus, R. R. 2015, *J. Amer. Assoc. Var. Star Obs.*, **43**, 3.

Carrier, F., and Eggenberger, P. 2006, *Mem. Soc. Astron. Ital.*, **77**, 326.

de Marchi, F., *et al.* 2007, *Astron. Astrophys.*, **471**, 515.

Drilling, J. S., and Landolt A. U. 2000, in *Allen's Astrophysical Quantities*, 4th ed., ed. A. N. Cox, Springer-Verlag, New York, 381.

Fuentes-Morales, I., and Vogt, N. 2014, *Astron. Nachr.*, **335**, 1072.

Hartig, E., Cash, J., Hinkle, K. H., Lebzelter, T., Mighell, K. J., and Walter, D. K. 2014, *Astron. J.*, **148**, 123.

Hekker, S., Barban, C. Faudin, F. De Ridder, J., Kallinger, T., Morel, T., Chaplin, W.J., and Elsworth, Y. 2010, *Astron. Astrophys.*, **520A**, 60.

Kazarovets, E., Samus, N., and Durlevich, O. 2001, *Inf. Bull. Var Stars*, No. 5135, 1.

Kinman, T. D. 1965, *Astrophys. J.*, **142**, 655.

Kiss, L., Szatmáry, K., Cadmus, R. R., Jr., and Mattei, J. A. 1999, *Astron. Astrophys.*, **346**, 542.

Koen, C., Laney, D., and van Wyk, F. 2002, *Mon. Not. Roy. Astron. Soc.*, **335**, 223.

McQuillan, A., Mazeh, T., and Aigrain, S. 2014, *Astrophys. J., Suppl. Ser.*, **211**, 24.

Merline, W. J 1999, in *Precise Stellar Radial Velocities*, ed. J. B. Hearnshaw, C. D. Scarfe, ASP Conf. Ser 185, IAU Colloq. 170, Astronomical Society of the Pacific, San Francisco, 187.

Mochejska, B. J., Stanek, K. Z., and Kaluzny, J. 2003, *Astron. J.*, **125**, 3175.

Mochejska, B. J., *et al.* 2005, *Astron. J.*, **129**, 2856.
Molnár, L., Szabó, R., and Plachy, E. 2016, *J. Amer. Assoc. Var. Star Obs.*, **44**, 168.
Mosser, B., *et al.* 2013, *Astron. Astrophys.*, **559A**, 137.
Nielsen, M. B., Gizon, L., Schunker, H., and Karoff, C. 2013, *Astron. Astrophys.*, **557**, L10.
Percy, J. R., 2020, *J. Amer. Assoc. Var. Star Obs.*, **48**, 10.
Percy, J. R., and Laing, J. 2017, *J. Amer. Assoc. Var. Star Obs.*, **45**, 197.
Reinhold, T., Reiners, A., and Basri, G. 2013, *Astron. Astrophys.*, **560A**, 4.
Samus, N. N., Kazarovets, E. V., Durlevich, O. V., Kireeva, N. N., and Pastukhova, E. N., 2017, *Astron. Rep.*, **61**, 80, *General Catalogue of Variable Stars: Version GCVS 5.1* (http://www.sai.msu.su/gcvs/gcvs/index.htm).
Smith, J., *et al.* 2017, in *Kepler Data Processing Handbook* (KSCI-19081-002), ed. J. M. Jenkins, NASA Ames Research Center, Moffett Field, Calif., 159.
Stello, D., *et al.* 2007, *Mon. Not. Roy. Astron. Soc.*, **377**, 584
Still, M., and Barclay, T. 2012, "PyKE: Reduction and analysis of Kepler Simple Aperture Photometry data," Astrophysics Source Code Library, record ascl:1208.004 (http://adsabs.harvard.edu/abs/2012ascl.soft08004S).
Watson, C., Henden, A., and Price, C. 2017, AAVSO International Variable Star Index VSX (Watson+, 2006-2014; http://www.aavso.org/vsx).

The W-type W UMa Contact Binary MU Cancri

Andrew P. Odell *(deceased May 2019)*
Emeritus Associate Professor of Physics and Astronomy, Northern Arizona University, Flagstaff, AZ 86011

Joel A. Eaton
7050 Bakerville Road, Waverly, TN 37185; eatonjoel@yahoo.com

Received August 11, 2020; revised October 15, 2020; accepted October 20, 2020

Abstract We use three complete light curves for MU Cancri, a faint W-type W UMa contact binary, to investigate possible mechanisms for changes in such binaries' light curves. The standard Roche model, as implemented by the Wilson-Devinney code, does not fit the observations at their level of precision. Most of this discrepancy can be explained by placing one or two moderate starspots (r_{spot} ~ 10–12°) on the more massive component. However, this does not resolve the discrepancy, since the solutions for the three epochs have different mass ratios, implying unmodelled changes in eclipse depths. This, in turn, implies that more spots are changing the depths in unpredictable ways. Thus we are confronted with limits on just how precisely light curve solutions can define the physical properties of a contact binary. We use spectra to classify the star (G3–G7) and to measure a spectroscopic mass ratio (q = 2.63), significantly closer to 1.0 than the photometric mass ratios (3.0–3.3), but this difference is unlikely to be caused by third light. And we also extend the period study of Alton and Stępień.

1. Introduction

MU Cancri (GSC 01397-01030; TYC 1397-1030-1; NSVS 10133793; $V \approx 12.1$) is a faint contact binary discovered by Pepper *et al.* (2007). It came to our attention when Shanti Priya, Sriram, and Vivekananda Rao (2013) published a photometric study finding a mass ratio surprisingly large (close to unity) for such a star. Consequently, we have obtained complete light curves at three epochs in 2014 and 2016, another incomplete one in 2019, and spectra for measuring radial velocities in 2013. In the meantime Alton and Stępień (2018) have obtained a light curve, which they analyzed with the Wilson-Devinney model, and did a period analysis, finding periodic changes in the times of conjunction, presumably from an orbit with an unseen companion.

Contrary to Shanti Priya *et al.* (2013), we find that this star is a rather conventional W-type W UMa binary with some moderately small spots on its surface. We have analyzed the new light curves in three ways: 1) as a standard W UMa binary without spots, 2) with third light, and 3) with dark spots.

2. Observations

2.1. Photometry

We took new light curves of MU Cnc for three epochs, 2014 (16 Feb. and 17–18 March UT), 2016-February (17, 18, 24, and 28 February and 1 March UT), and 2016-November (14 and 15 Nov. UT), and a partial light curve for 24 April 2019. The first of these comes from Mt. Bigelow Observatory of the University of Arizona, the others from the robotic telescope ROBO at Lowell Observatory. Our photometry consists of differential magnitudes measured with the usual commercially available *BVRI* filters (Cousins *RI*); they are not transformed to the standard system via observations of standard stars. Since the variable and comparison stars were all on the same CCD images, we have not corrected them for differential extinction, either. The data are available from the AAVSO ftp archive as the ASCII file MUCnc-JAAVSO-482.txt at ftp://ftp.aavso.org/public/datasets/. Listed are the Reduced Julian Date (RJD = HJD–2400000) of observation, and differential magnitudes of the variable and check stars for the four passbands. The datasets are identified by a symbol at the end of each line, namely, 2014, 2016-feb, 2016-nov, and 2019. Entries with missing data are identified with magnitudes equal to 99.999. There are roughly 250, 300, 140, and 75 data in each color, respectively, for the four epochs.

The standard deviations of the check-star observations for the *V* band, which indicate the precision of the data, were 0.016, 0.004, 0.003, and 0.004, respectively, for our four epochs, 2014–2019. Averages of the check star ΔVs for the last three epochs agreed to within ± 0.001 mag.

Figure 1 shows the comparison stars we used at the two observatories. The comp star for 2014 was the average of the

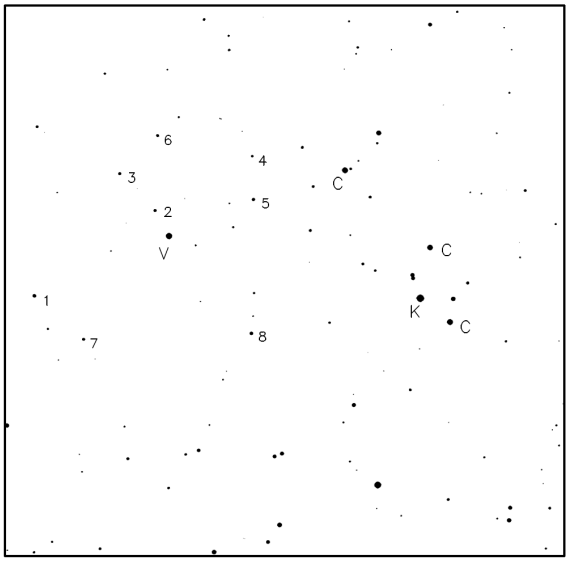

Figure 1. Comparison stars used. This is a 20 × 20 arcmin. field from the red Palomar Sky Survey. MU Cnc is marked with a V, the 8 comparisom stars used in 2014 with numbers, the 3 comparison and check stars for 2016 and 2019 with Cs and a K, respectively.

eight numbered stars. For the three later epochs, the comp was the average of the three stars labeled C, and K was the check star.

2.2. Spectroscopy

We also obtained 20 spectra for MU Cnc with the Meinel spectrograph at Steward Observatory in Dec. 2013 (Table 1), covering the wavelength range 4150–4900Å (0.71Å / pix, R ~ 3500). These provide a spectral classification of the star and measurements of the radial velocities of both binary components.

To determine a spectral type, we compared spectra for the two conjunctions with spectra of some single stars artificially broadened to $v_{rot} \sin i = 150$ km s^{-1} used in a paper about W Crv (Eaton, Odell, and Nitschelm 2020). These were HD 38722 (F8), HD 50692 (G0 V), HD 42807 (G2 V), HD 31501 (G8 V), and HD 103095 (K1 V). MU Cnc is definitely later than G2 but earlier than G8 and is marginally later (cooler) at primary eclipse than at secondary eclipse. Given the standards available, we can only say the type is in the range G3–G7.

Odell derived the radial velocities by using IRAF to fit double Gaussians to cross-correlation functions. These are the velocities given in Table 1, where, following the photometric convention, Star 1 is the component eclipsed at primary minimum and Star 2 is the one eclipsed at secondary minimum. We have fit sine curves to them to derive the orbital elements $K_1 = 254 \pm 14$ km s^{-1}, $K_2 = 102 \pm 4$ km s^{-1}, and $\gamma = 21 \pm 3$ km s^{-1}, for which the spectroscopic mass ratio is $q_{sp} = 2.50 \pm 0.46$. They are plotted with the data in Figure 2; you will notice that the lines representing the elements do not cross at phase zero. This is because γ is 13 km s^{-1} larger for the fainter star. This must result from a systematic error on one side of that star's orbit, likely near phase 0.25. That would mean K_1 should be increased by approximately this offset to give $K_1 \sim 267$ km s^{-1} and $q_{sp} \sim 2.63$. In any case, this spectroscopic mass ratio is significantly larger than the photometric mass ratio, which we will try to explain by invoking third light.

Table 1. Radial velocities for MU Cnc.

RJD	*Phase*	*RV$_1$*	*RV$_2$*
56636.8090	0.964	—	–21.7
56636.8234	0.014	—	33.4
56636.8308	0.039	—	44.9
56639.7396	0.035	—	32.0
56639.7526	0.079	–13.2	93.8
56639.7850	0.191	–245.2	123.9
56639.8291	0.342	–200.7	101.9
56639.8363	0.367	–128.0	80.8
56639.8781	0.510	—	10.1
56639.8851	0.534	—	7.8
56640.7633	0.552	—	–1.5
56640.7709	0.578	89.9	–44.0
56640.7831	0.620	185.6	–50.7
56640.7923	0.652	240.7	–70.0
56640.8049	0.695	280.2	–75.9
56640.8135	0.725	282.8	–80.7
56640.8462	0.837	273.8	–66.1
56640.8547	0.866	211.5	–49.1
56640.8715	0.924	—	–15.8
56640.8786	0.948	—	–2.1

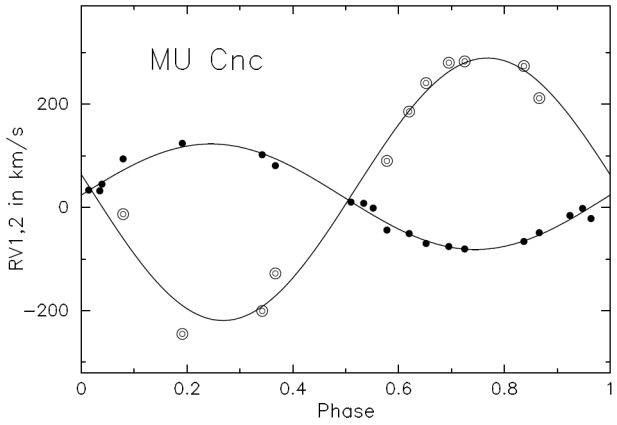

Figure 2. Velocity curves for MU Cnc. Circles are for the photometric primary star (eclipsed at phase 0.0), dots for the brighter photometric secondary. Lines are the fitted sine curves for which $K_1 = 254$ and $K_2 = 102$ km s^{-1}.

3. Ephemeris

Alton and Stępień (2018) analyzed the times of minimum, finding that they vary periodically, probably from the light-time effect in a triple system. To their seven newly determined times of minimum (ToMs), we have added 15 more from Mt. Bigelow and ROBO and have added 27 others we measured with published archival data, the latter coming from Harvard patrol plates, NSVS (Northern Sky Variability Survey; Wozniak *et al.* 2004), CSS (Catalina Sky Survey; Univ. Arizona 2006–2009), ASAS (All Sky Automated Survey; Pojmański 1997), and KELT (Kilodegree Extrememly Little Telescope; Pepper *et al.* 2007).

All these times of minimum are listed in Table 2. The sigmas in column 2 are estimated uncertainties, used for weighting (σ^{-2}) in the determination of light elements. The epochs listed in column 3 were carefully identified by Odell by extending the best apparent period at a given epoch backward in time. The (O–C)s in column 4 are with respect to the period found for recent data (Equation 2); the(O-C)s in column 5 come from fitting these residuals with a quadratic but with the data unweighted (Equation 3). Column 6 gives the data archive and the year from which the time of minimum was obtained.

To determine a time of minimum (ToM), Odell entered the data (ΔMag vs. HJD) in a spreadsheet, which he used to plot them against themselves reflected about a trial ToM, adjusting the trial ToM to make the reflected light curve coincide with the direct light curve on the plot. He estimated an uncertainty of 0.5–1 min. for continuous photometry. For the archival data, we estimate uncertainties of 0.01 d. for Harvard, 0.003 for ASAS, 0.005 for CSS, 0.003 for NSVS, and 0.0015 for KELT. For determinations taken from the literature, we have tried to use the published values but have set a minimum uncertainty of 0.0003 d., feeling that smaller values are unrealistic and wanting to avoid having such values bias our analysis of period changes.

Figure 3 shows the timings for a period determined for modern data, roughly RJD > 50,000. For earlier (Harvard) data the period seems to be much shorter, giving the following two piece-wise linear relationships:

$$\text{HJD (Obs)} = 4553526.379(8) + 0.2910074(1)\,\phi, \quad \text{for RJD} < 50{,}000, \qquad (1)$$

Table 2. Times of minimum light.

RJD	*σ (d)*	*Epoch*	*$(O–C)_1$*	*$(O–C)_2$*	*Source**
22082.475	0.01	–108052.0	0.6045	–0.0321	Harvard-1919
23516.863	0.01	–103123.0	0.5867	–0.0002	Harvard-1923
28603.6150	0.01	–85643.0	0.4219	–0.0051	Harvard-1937
29585.7900	0.01	–82268.0	0.4261	0.0271	Harvard-1939
32262.6150	0.01	–73069.5	0.3630	0.0354	Harvard-1947
43131.8740	0.01	–35719.0	0.1204	0.0110	Harvard-1976
44308.7200	0.01	–31675.0	0.1076	0.0149	Harvard-1980
46095.7950	0.01	–25534.0	0.0684	–0.0015	Harvard-1985
47200.9000	0.01	–21736.5	0.0494	–0.0080	Harvard-1988
51554.7130	0.0030	–6775.5	0.0087	–0.0109	NSVS-2000
52622.8630	0.0005	–3105.0	–0.0065	–0.0197	Pilecki and Stępień (2012)
52727.7750	0.0030	–2744.5	–0.0049	–0.0176	ASAS-2003
53036.8320	0.0030	–1682.5	–0.0043	–0.0153	ASAS-2004
53432.7584	0.0015	–322.0	–0.0018	–0.0109	KELT-2005
53432.9054	0.0015	–321.5	–0.0003	–0.0094	KELT-2005
53474.6641	0.0015	–178.0	–0.0021	–0.0110	KELT-2005
53475.6840	0.0015	–174.5	–0.0007	–0.0096	KELT-2005
53526.4680	0.0030	0.0	0.0014	–0.0072	NSVS-2000
53702.8257	0.0030	606.0	0.0049	–0.0029	NSVS-2000
53853.5680	0.0030	1124.0	0.0022	–0.0050	NSVS-2000
53874.6611	0.0050	1196.5	–0.0032	–0.0103	CSS-2006
54194.6394	0.0050	2296.0	0.0057	–0.0001	—
54066.8890	0.0050	1857.0	0.0102	0.0040	CSS-2007
54479.6860	0.0050	3275.5	0.0045	–0.0002	CSS-2008
54905.7275	0.0050	4739.5	0.0022	–0.0010	CSS-2009
55290.7349	0.0003	6062.5	–0.0013	–0.0034	Diethelm (2010)
55555.8430	0.0050	6973.5	–0.0066	–0.0079	CSS-2011
55572.8704	0.0003	7032.0	–0.0035	–0.0047	Diethelm (2011)
55667.7409	0.0003	7358.0	–0.0034	–0.0044	Diethelm (2011)
55668.3223	0.0020	7360.0	–0.0040	–0.0050	28SC+ST7XME
55669.3402	0.0020	7363.5	–0.0047	–0.0057	28SC+ST7XME
55932.8517	0.0003	8269.0	–0.0059	–0.0063	Diethelm (2012)
55932.9996	0.0004	8269.5	–0.0036	–0.0039	Diethelm (2012)
55984.3678	0.0010	8446.0	0.0008	0.0005	Rukmini and Shanti Priya (2016)
56704.7696	0.0005	10921.5	–0.0015	–0.0004	Bigelow-2014
56733.7267	0.0005	11021.0	–0.0002	0.0009	Bigelow-2014
56733.8732	0.0005	11021.5	0.0008	0.0019	Bigelow-2014
56734.5997	0.0005	11024.0	–0.0003	0.0009	Bigelow-2014
56734.7469	0.0005	11024.5	0.0014	0.0026	Bigelow-2014
56734.8925	0.0005	11025.0	0.0015	0.0027	Bigelow-2014
56792.6577	0.0005	11223.5	0.0005	0.0018	Bigelow-2014
57435.8048	0.0005	13433.5	0.0077	0.0096	ROBO-2016
57442.6434	0.0005	13457.0	0.0075	0.0094	ROBO-2016
57442.9344	0.0005	13458.0	0.0074	0.0094	ROBO-2016
57446.8636	0.0005	13471.5	0.0080	0.0099	ROBO-2016
57448.9006	0.0005	13478.5	0.0079	0.0098	ROBO-2016
57454.5746	0.0003	13498.0	0.0071	0.0091	Alton and Stępień (2018)
57455.5936	0.0003	13501.5	0.0076	0.0095	Alton and Stępień (2018)
57456.6118	0.0003	13505.0	0.0072	0.0092	Alton and Stępień (2018)
57469.5617	0.0003	13549.5	0.0070	0.0090	Alton and Stępień (2018)
57471.5995	0.0003	13556.5	0.0077	0.0097	Alton and Stępień (2018)
57484.5498	0.0003	13601.0	0.0079	0.0099	Alton and Stępień (2018)
57495.6085	0.0003	13639.0	0.0081	0.0101	Alton and Stępień (2018)
57706.8808	0.0005	14365.0	0.0046	0.0067	ROBO-2016
57707.8995	0.0005	14368.5	0.0047	0.0069	ROBO-2016
57788.2161	0.0005	14644.5	0.0016	0.0038	Nagai (2018)
57788.3610	0.0005	14645.0	0.0010	0.0032	Nagai (2018)
58159.1059	0.0005	15919.0	–0.0054	–0.0031	Nagai (2019)
58443.1321	0.0005	16895.0	–0.0084	–0.0061	Nagai (2019)
58597.8020	0.0005	17426.5	–0.0122	–0.0100	ROBO-2019

* *Source is the data archive and the year from which the time of minimum was obtained.*

Table 3. MU Cnc: light curve solutions.

Parameter	*No Spots or L3*	*L3, No Spots*	*Spots, 2014*	*Spots, 2016-Feb.*	*Spots, 2016-Nov.*	*Alton and Stępień (2018)*
i (°)	80.4(3)	80.40 (fixed)	79.6(3)	79.9(2)	79.1(3)	81.35
q (M_2 / M_1)	3.089(11)	2.63 (fixed)	3.026(26)	3.090(3)	3.295(13)	2.825
ω	6.651(18)	5.995(10)	6.542(36)	6.669(9)	6.945(17)	6.283
fillout	12.3 ± 1.7%	20.5 ± 1.5%	17.6%	10.7%	9.7%	16.4%
T_1 (K, fixed)	5600	5600	5600	5600	5600	5807
T_2 (K)	5451(70)	5422(110)	5493(17)	5550(27)	5508(27)	5620
$<\sigma_{fit}>$	0.0049	0.0056	0.0059	0.0026	0.0017	
				$\ell 3/(\ell_1 + \ell_2)$		
B	—	0.079	—	—	—	0.064
V	—	0.068	—	—	—	0.073
R_c	—	0.075	—	—	—	—
I_c	—	0.094	—	—	—	0.558
			Spots on the More Massive Component			
long (°)	none	none	49(10)	159(5) and 328(4)	146(3)	none
rspot (°)	—	—	10.8(8)	12.3(11) and 11.0(7)	14(1)	—

Note: Numbers in parentheses are the errors of the last digits. All spots are assumed to be on the equator and to have a temperature 80% of the underlying photosphere.

and

$$\mathrm{HJD\,(Obs)} = 4553526.4666(14) + 0.29101355(14)\,\phi, \quad \text{for RJD} > 50000, \quad (2)$$

numbers in parentheses being uncertainties of the last digits, ϕ being the phase. These fits are shown in the top panel of Figure 3.

We have also fit the linear residuals with a quadratic equation, weighting the data equally, to give the following quadratic elements:

$$\mathrm{HJD\,(Obs)} = 4553526.4752(4) + 0.2910122(1)\,\phi + 4.1(1)\times 10^{-11}\phi^2. \quad (3)$$

This quadratic fit is not very convincing, and a quadratic fit calculated with realistic weights simply failed to fit the data.

It's disturbing that we have found an abrupt period increase at just the break between the ToMs from Harvard patrol plates and modern measurements; obviously one should be skeptical of this result. Yet the light curves seem to be reasonable, and Odell's extension of the phases did not break on close inspection [JAE]. Also, there have been precipitate period changes in other contact binaries (e.g. Pribulla *et al.* 1997).

The residuals from Eqation 2 are clearly cyclic as discovered by Alton and Stępień. These are shown in the lower panel of Figure 3. The period seems to be in the range 2930 ± 100 d. Fitting a sine curve to these residuals (Equation 4), we derive a semiamplitude of 9.2 min, corresponding to an orbit with $a_{1,2}\sin i = 1.10$ au for a light-time effect.

$$\mathrm{(O–C)} = 0.0064(5)\sin(2\pi(\mathrm{RJD} - 50{,}712)/2930) \quad (4)$$

The variation expected in the γ velocity of the eclipsing system would then be ± 4 km s^{-1} over 8 years. There is obviously more here than motion in a wide orbit, since the last three points in the lower panel of Figure 3 depart considerably from the fitted curve.

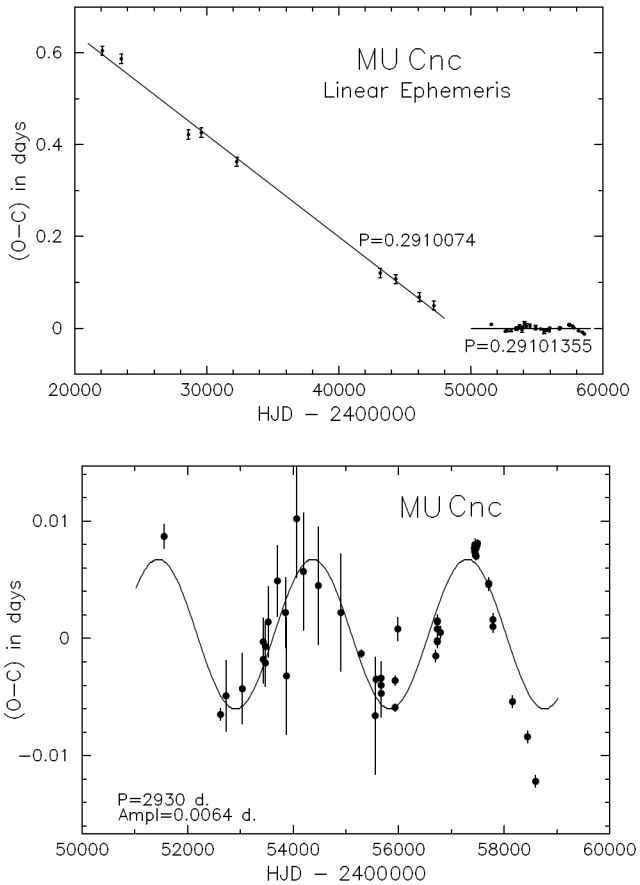

Figure 3. (O–C) diagrams for MU Cnc. Upper: Piece-wise linear ephemerides for residuals with respect to Equation 2. Lower: Periodic deviations from the linear fit for modern data (Equation 2). The sinusoid is the fit of Equation 4.

4. Light curve solutions

Our three complete light curves give us the opportunity to look at changes in the light curve and their possible causes.

Some elements cannot change materially over a period of a few years, so they have to be the same for all three of our epochs. These include the total mass M_1+M_2, the mass ratio, q, the inclination, i, third light, and—likely—the total luminosity of the system. Others might well change, such as spottedness from random variation in magnetism, and both the degree of fillout (Ω) and the temperature difference (T_1-T_2), should the energy-transfer mechanism change, perhaps through magnetic modulation.

We have solved our light curves with the Wilson-Devinney code (WD 2015 version; see Wilson and Devinney (1971); Wilson (1990, 1994); Wilson and van Hamme (2015)), finding the elements in Table 3. These are roughly consistent with Alton and Stępień's solution (see Table 3, column 7). In these calculations we adopted a temperature of the primary consistent with its spectral class, convective gravity darkening (Lucy 1967), convective reflection effect (Ruciński 1969), the Kurucz-atmospheres option in the WD code, and linear limb-darkening coefficients from van Hamme (1993) calculated by the WD code. The σ_{fit}s listed are the median weighted residuals calculated by the WD code. The quoted errors of the elements are the standard deviations of the three solutions for columns 2 and 3, and the standard errors from the WD code, multiplied by 3 per Popper (1984) for the others. Calculated fits are shown in Figures 4 through 8.

We also included both velocity curves in the solution for the cases having no spots but omitted the velocities of the less massive star for the analyses with spots.

4.1. No third light, no spots

This represents the traditional approach to contact binaries. We started by solving the three light curves separately to see just how much variation in the elements to expect. For the principal elements, the range was 0.005 in Ω (potential of the surface), 0.012 in q, 0.42° in i, and 189 K in T_2. We then picked roughly average values for those element not expected to vary and solved the light curves again to detect changes in the potentially more volatile elements. Results are given in column 2 of Table 3, a plot of the fit for 2016-feb, our most extensive data set, in Figure 4. With the mass ratio fixed, Ω increased by 0.037 from 2014 to 2016-nov, with fillout decreasing from 15% to 9%, and T2 falling by 144 K.

4.2. Third light?

The marked difference between the mass ratios determined photometrically and spectroscopically suggests that the putative third star giving the light-time effect seen in Figure 3 is also contributing a measurable amount of third light. To test this idea, we solved the light curves again with the mass ratio fixed at the spectroscopic value (2.63). Results are given in column 3 of Table 3 and plotted for 2016-feb in Figure 5. Although the mean residuals we found are slightly smaller than for the solution without third light, this result is not convincing physically. The third light derived varied by a factor of about 3–4 amongst our three light curves when we solved them individually, and the average value we give in Table 3 has a spectrum much too like the eclipsing pair (too early) to be light from a dwarf companion, as did the spectrum of ℓ_3 in the separate solutions.

4.3. Minimal spots

This system is a W-type contact binary with the cooler, more massive component eclipsing its companion at primary minimum. That is obvious from the velocity curves in Figure 2, but it also follows from the shapes of the eclipses. Such systems have long been suspected of being heavily spotted. In fact, a different level of uniform spottedness between the components has even been suggested as the cause of their apparent temperature difference (e.g. Eaton *et al.* 1980; Eaton 1986; Barnes *et al.* 2004; Stępień 2009). Barnes *et al.* found evidence in their wonderful Doppler images of AE Phe that both components of that star are highly spotted, finding convincing trails of some individual spots in their line profiles and arguing somewhat less convincingly for evidence of *many* more small spots. So we wonder what effect spots have on this system.

Even a cursory inspection of Figures 4 and 5 shows that the model does not really fit the data at the level of their precision. Such deviations are usually explained by invoking spots, often a rather surprising number of them (e. g. Samec *et al.* 2010) and in bizarre locations (e. g. Samec *et al.* 2011). We have looked at the question of just how few spots we would need to explain these deviations. And we have also decided to place the spots only on the larger, more massive star, if possible. Obviously there could be spots on both stars, as Barnes *et al.* (2004) found for AE Phe. Furthermore, from our experience with RS CVn binaries we do not think the WD model is good enough to measure spot latitudes, so we place the spots on the equator. Latitude can be quite difficult to determine, even with top-of-the-line Doppler images (see Barnes *et al.* 2004, section 4).

We'll start with a spot solution for 2016-nov. The light curve here lies below the calculations on the rising branch of primary minimum, and a single moderate spot improves the fit markedly (Table 3, column 6 and Figure 6).

The light curves for 2014 and 2016-feb are both more complicated, 2014 showing an approximate classical O'Connell effect, with phases near 0.25 noticeably depressed. At this epoch, we started with a single spot to remove this depression. (Table 3, column 4 and Figure 7), although not at the longitude we had expected. There are likely more spots for 2014, but the data are not precise enough to justify looking further.

The light curves for 2016-feb showed the rising branches of both eclipses depressed, requiring two spots. These we placed on the cooler component, although they could have been on either. However, there may be some distortion of secondary minimum by the eclipse of the spot at longitude 328° that settles the ambiguity for that spot (Figure 8).

We again set the stable parameters to average values for the three solutions (i = 79.51° and q = 3.180) and solved the light curves a second time. The mean residuals increased a meaningless 7–18%, the spots remained roughly the same, but the fillout dropped from ~18% from the first two epochs to 6% for 2016-nov.

The big question here is whether changes in spots can account for the apparent variation in such physical quantities as Ω and T_1-T_2. In our analysis of the three epochs, it did not. The variation of the derived inclination remains above the uncertainties of measurement, but the unexpected variation

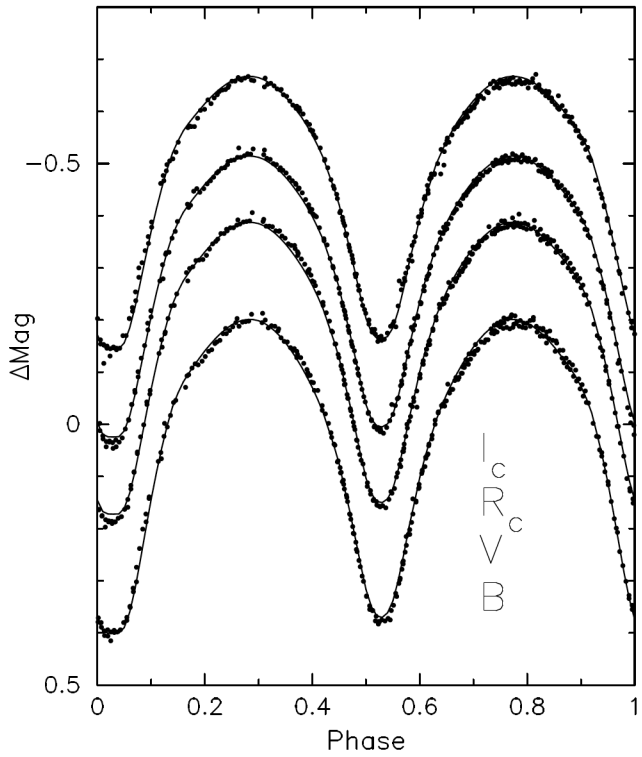

Figure 4. Light curve fit for February 2016 with no third light or spots. Notice how the fitted curve lies above the observations on both rising branches ($\phi \sim 0.2$ and 0.7) and below on the falling branch of secondary eclipse.

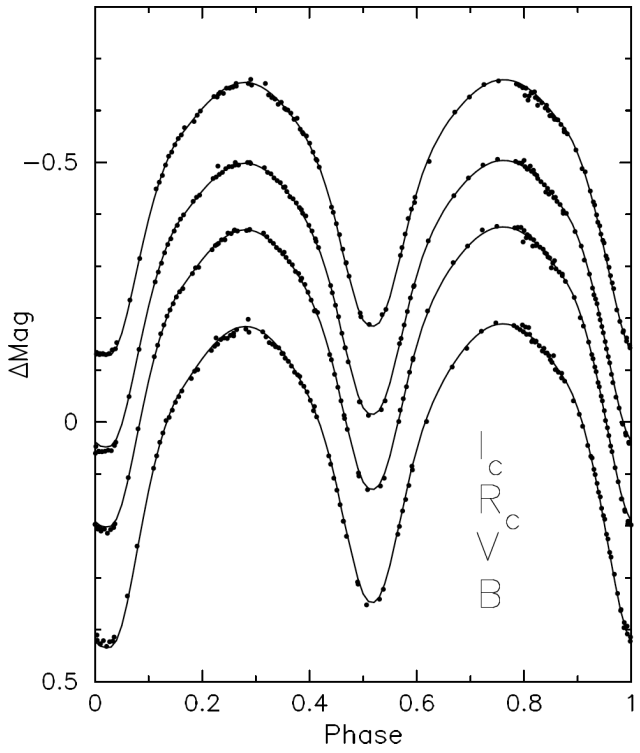

Figure 6. Light curve fit for 2016-nov with one dark starspot on the larger component.

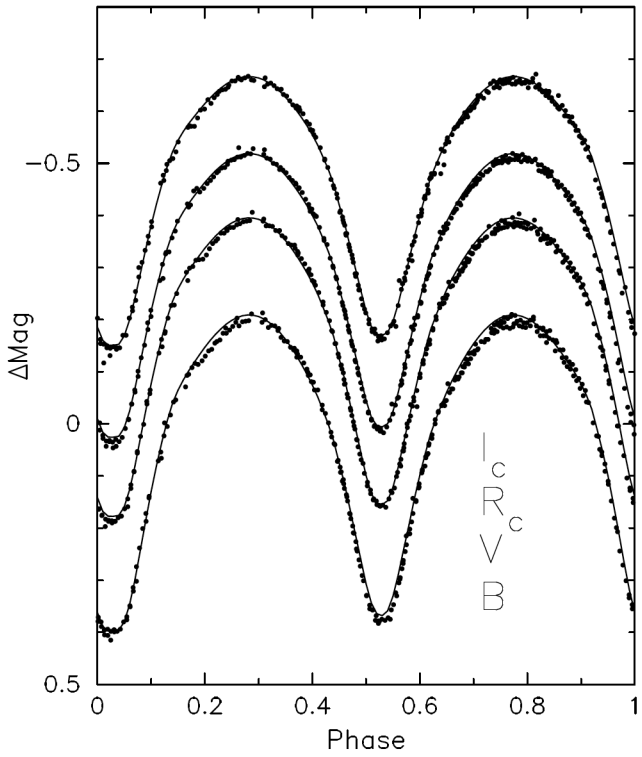

Figure 5. Light curve fit for February 2016 with third light. We fix the mass ratio at its spectroscopic value, fit the light curves, and derive the third light for the four passbands.

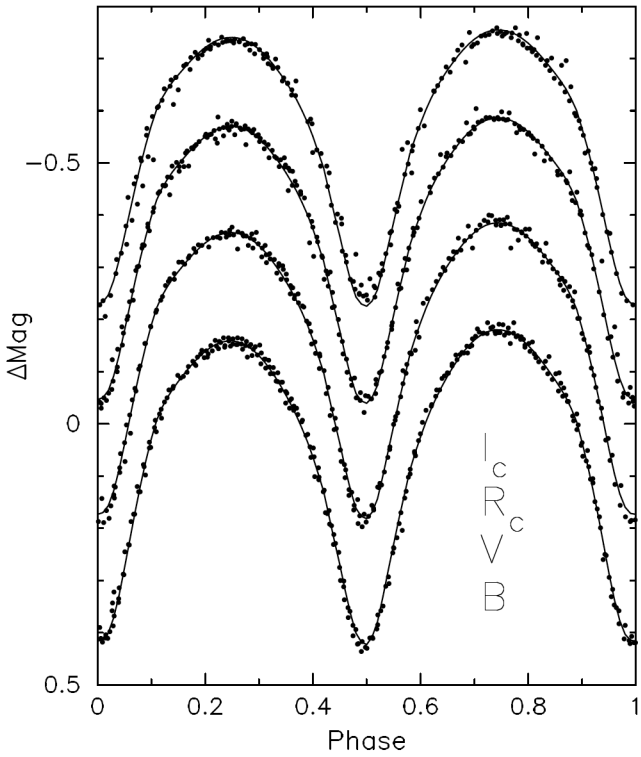

Figure 7. Light curve fit for 2014 with a dark starspot on the larger component.

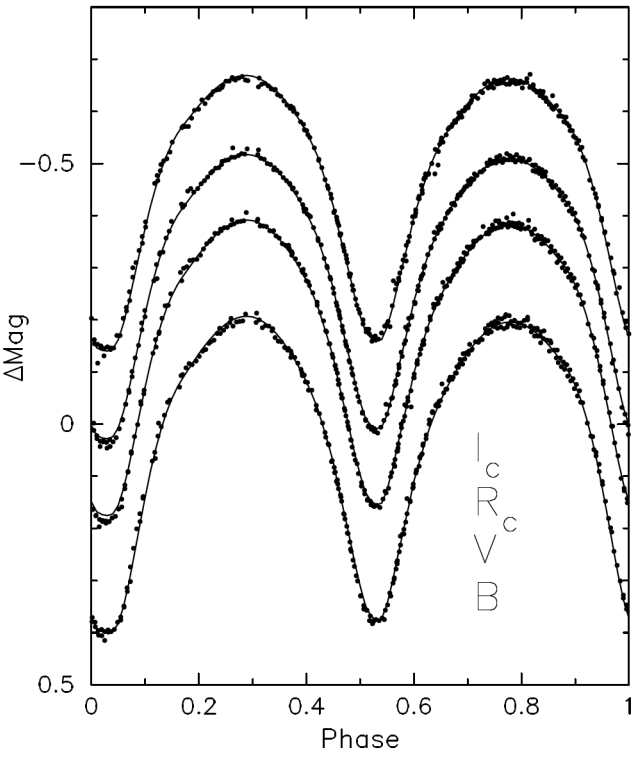

Figure 8. Light curve fit for 2016-feb with two dark starspots on the larger component.

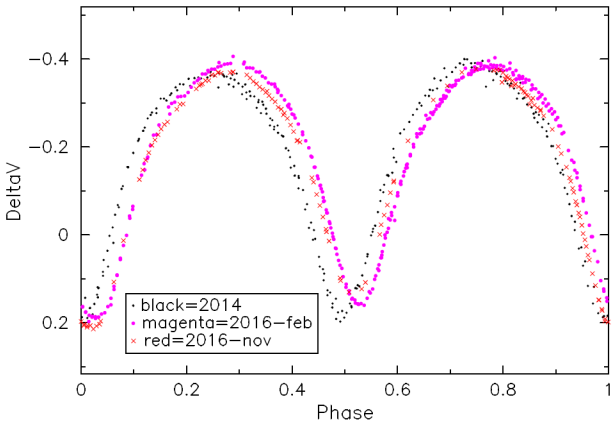

Figure 9. A comparison of the levels and shapes of the light curves at the three epochs. Symbols: small black dots = 2014, large magenta dots = 2016-feb, and red xs = 2016-nov.

of the mass ratio is completely perverse. Here, we are back to the question of whether spottedness is the cause of the W-type phenomenon. We will not address that possibility at this time, if merely to reflect Odell's extreme skepticism of light curve solutions featuring large numbers of apparently arbitrarily located spots. However, if a changing distribution of spots is not the cause of the changing depth of the eclipses, then some *unknown* mechanism must be responsible.

5. Discussion

We have complete light curves for three epochs, two of which were taken with the same instrument. The small magnitude differences between the comp and check stars for those two latter epochs show that the photometric system was quite stable and that the comparison stars did not vary. Thus we would expect any changes between these light curves to be caused by the star itself, not by changes in the photometric system. Furthermore, since this star has marginally total eclipses, the light curve solutions should be fairly reliable.

Including third light did not explain the discrepancy between photometric and spectroscopic mass ratios. Most likely that results from systematic errors in the velocities of fainter component. The main effects of third light on the solution are to give a larger mass ratio (closer to 1.0) and a thicker common envelope. Indeed, the solution from Alton and Stępień—itself with third light—shows both effects, giving a derived mass ratio and larger filling factor consistent with our values.

Dark starspots certainly can explain some of the more obvious deviations of the star from the Roche model. However, including only one or two such spots did not resolve the problem of changes of q, i, and Ω amongst the light curves. At this time, that would seem to imply a much more extensive distribution of dark spots, one that really does not change greatly with time. This would make the cool contact binaries different from the RS CVn binaries, which show much larger apparent concentrations of spots with putative magnetic cycles. We do not think these latter phenomena are seen in W UMa binaries, but the data that would reveal them are rather scanty (but see Ruciński and Paczynski (2002) for a cautionary tale). A further point in favor of much more extensive spottedness is a variation in the general levels of the light curves. Figure 9, a plot of the *V* light curve for the three epochs, shows that the level at both maxima changed, despite our expecting the star to have a constant brightness beyond the slight depressions modelled with a few discrete spots.

Envelope circulation in these contact binaries must have significant effects on their magnetism, at least in its distribution. The W UMa systems are fairly strong sources of chromospheric/transition-region emission with high levels of X-ray flux, roughly covered uniformly with active regions (Ruciński and Vilhu 1983; Ruciński *et al.* 1985; Stępień *et al.* 2001; Chen *et al.* 2006), which means they are almost certainly highly magnetic. The apparent lack of large concentrations of spots in contact systems may reflect the inability of spots to stick around long enough to develop large structures. Also, such concentrations are readily explained by a random distribution of such spots, but only if the spots are moderately large and not too numerous (Eaton *et al.* 1996). As the spots become smaller and more numerous, the effect of random clumping declines.

Spots, at least in the Sun, seem to be a superficial phenomenon not anchored deeply in the star—somewhat like Jupiter's Red Spot and analogous to weather (e.g., Zhao *et al.* 2001). This should be obvious by consideration of the difference between the effects of kG magnetic fields in solar-type and Ap stars. By way of speculation, we would hypothesize that the circulation sweeps the spots produced by any dynamo in the more massive star off its face onto its less massive companion where they are subducted by the flow and their magnetic field redistributed. This mechanism provides a possible source of the ephemeral dark spots often invoked to explain peculiarities of

W UMa-type light curves, as we have done here. The inevitable random variations in the distribution of spots being carried along by the circulation would still give measurable temporary concentrations of spots.

Perhaps the most important upshot here is that there are limits to just how precisely we can know the physical properties of a contact binary from light curve solutions. Our fits show that the mass ratio, for instance, seems to be uncertain by up to 9% (the range of values in columns 4–6 in Table 3). This is in contrast to the tenths of a percent derived as formal errors of a typical fit. It also echos Popper's (1984) reasoning in arguing that such formal errors are misleading, that they underestimate the true uncertainties by about a factor of three. This result is unfortunate, since it limits our ability to define changes in physical properties, most notably the fillout, that might be related to fluctuations of the energy-transfer mechanism.

6. Acknowledgements

Joel Eaton thanks Jonna Peterson, Gary Steffens, and Brian Skiff for their help in locating various data and analyses Odell had done before he died in May 2019. Andy Odell would acknowledge the graceous amounts of observing time allotted to his research programs over the years by the University of Arizona and Lowell Observatory.

References

Alton, K. B., and Stępień, K. 2018, *Acta. Astron.*, **68**, 449.
Barnes, J. R., Lister, T. A., Hilditch, R. W., and Collier Cameron, A. 2004, *Mon. Not. Roy. Astron. Soc.*, **348**, 1321.
Chen, W. P., Sanchawala, K., and Chiu, M. C. 2006, *Astron. J.*, **131**, 990.
Diethelm, R. 2010, *Inf. Bull. Var. Stars*, No. 5945, 1.
Diethelm, R. 2011, *Inf. Bull. Var. Stars*, No. 5992, 1.
Diethelm, R. 2012, *Inf. Bull. Var. Stars*, No. 6011, 1.
Eaton, J. A. 1986, *Acta. Astron.*, **36**, 79.
Eaton, J. A., Henry, G. W., and Fekel, F. C. 1996, *Astrophys. J.*, **462**, 888.
Eaton, J. A., Odell, A. P., and Nitschelm, C. 2020, *Mon. Not. Roy. Astron. Soc.*, in press.
Eaton, J. A., Wu, C.-C., and Ruciński, S. M. 1980, *Astrophys. J.*, **239**, 919.
Lucy, L. B. 1967, *Z. Astrophys.*, **65**, 89.
Lucy L. B. 1968, *Astrophys. J.*, **151**, 1123.
Nagai, K. 2018, *Bull. Var. Star Obs. League Japan*, No. 64, 1.
Nagai, K. 2019, *Bull. Var. Star Obs. League Japan*, No. 66, 1.
Pepper, J., *et al.* 2007, *Publ. Astron. Soc. Pacific*, **119**, 923.
Pilecki, B., and Stępień, K. 2012, *Inf. Bull. Var. Stars*, No. 6012, 1.
Pojmański, G. 1997, *Acta. Astron.*, **47**, 467.
Popper, D. M. 1984, *Astron. J.*, **89**, 132.
Pribulla T., Chochol, D., Rovithis, P., and Rovithis-Livanou, H. 1997, *Inf. Bull. Var. Stars*, No. 4435, 1.
Ruciński, S. M. 1969, *Acta Astron.*, **19**, 245.
Ruciński, S. M., and Paczynski, B. 2002, *Inf. Bull. Var. Stars*, No. 5321, 1.
Ruciński, S. M., and Vilhu, O. 1983, *Mon. Not. Roy. Astron. Soc.*, **202**, 1221.
Ruciński, S. M., Vilhu, O., and Whelan, J. A. J. 1985, *Astron. Astrophys.*, **143**, 153.
Rukmini, J., and Shanti Priya, D. 2016, *J. Chem. Biol. Phys. Sci.*, **6**, 926.
Samec, R. G., Labadorf, C. M., Hawkins, N. C., Faulkner, D. R., and Van Hamme, W. 2011, *Astron. J.*, **142**, 117.
Samec, R. G., Melton, R. A., Figg, E. R., Labadorf, C. M., Martin, K. P., Chamberlain, H. A., Faulkner, D. R., and van Hamme, W. 2010, *Astron. J.*, 140, 1150.
Shanti Priya, D. Sriram, K., and Vivekananda Rao, P. 2013, *Res. Astron. Astrophys.*, **13**, 465.
Stępień, K. 2009, *Mon. Not. Roy. Astron. Soc.*, **397**, 857.
Stępień, K., Schmitt, J. H. M. M., and Voges, W. 2001, *Astron. Astrophys.*, **370**, 157.
University of Arizona. 2006, 2007, 2008, 2009, Catalina Sky Survey (http://www.lpl.arizona.edu/css).
van Hamme, W. 1993, *Astron. J.*, **106**, 2096.
Wilson, R. E. 1990, *Astrophys. J.*, **356**, 613.
Wilson, R. E. 1994, *Publ. Astron. Soc. Pacific*, **106**, 921.
Wilson, R. E., and Devinney, E. J. 1971, *Astrophys. J.*, **166**, 605.
Wilson, R. E., and van Hamme, W. 2015, *Computing Binary Star Observables*, privately published manual, U. Florida web site.
Wozniak, P. R., *et al.* 2004, *Astron. J.*, **127**, 2436.
Zhao, J., Kosovichev, A. G., and Duvall, T. L., Jr. 2001, *Astrophys. J.*, **557**, 384.

U, B, V, R_c, I_c Photometric Observations of the Dwarf Nova DX Andromedae During the Years 2018–2019

Corrado Spogli
Via Palazzolo 21 Frazione, Spada 06020 Gubbio (PG), Italy; corradospogli@yahoo.it

Gianni Rocchi
Via Achille Grandi 14, 06038 Spello (PG), Italy; giannirocchi2@gmail.com

Dario Vergari
Via Cantalmaggi 24, 06024 Gubbio (PG), Italy

Stefano Ciprini
Space Science Data Center, Agenzia Spaziale Italiana (SSDC-ASI), I-00133, Roma, Italy, and Istituto Nazionale di Fisica Nucleare (INFN), Sezione di Roma Tor Vergata, I-00133, Roma, Italy; stefano.ciprini.asdc@gmail.com

Received August 26, 2020; revised September 16, 2020; accepted September 16, 2020

Abstract In this paper we present U, B,V, R_c, I_c photometric observations of the dwarf nova DX Andromedae made in the years 2018–2019 at the private Rocchi observatory located in Spello (Umbria). We observed the variable for 86 nights in B,V, R_c, I_c photometric filters. We detected an outburst of this dwarf nova. We summarize the significant variations in the color indices during the outburst cycle and in the minimum phase.

1. Introduction

Cataclysmic variables are binaries with a white dwarf accreting from a main sequence or subgiant companion. An important subclass is the dwarf novae. They are characterized by recurrent outbursts in the optical light curve, and typical amplitudes of the outbursts are in the range of 2 to 6 magnitudes. The outbursts occur at intervals typically ranging from a few days to months. These values are typical for the most pre-eminent members of the class, but the less well studied class of WZ Sge objects have longer recurrence times and may dominate the total population of CVs. DX Andromedae was discovered by Romano (1958) as a variable star and it was clear by the early 1960s that DX And could be classified as a dwarf nova of the U Gem type (Weber 1962). Data held by the AAVSO extending back to the early 1980s (Mattei 1980) show that the outburst occur at intervals of between eight months and a year. Bruch *et al.* (1987) observed DX And photographically over 10 nights between 1980 and 1983 and caught the star once in outburst. Echevarria (1984) observed the variable photometrically in UBVRI and listed colors for DX And, (B–V) = 0.3 and (U–B) = –0.55, that were obtained when the variable was at an intermediate level of brightness (mv = 13.5). In 1987 another outburst was observed by members of the AAVSO (Mattei *et al.* 1987). Spectroscopic observations were made by Bruch (1989), who reported that DX And exhibits a considerable contribution of the secondary star to the continuum energy distribution as well as the line spectrum. Drew *et al.* (1993) determined a binary period of 0.44167 day and a mass ratio of 0.96 through spectroscopic observations when DX And was at minimum.

Drew *et al.* (1993) reported that the distance to DX And is 630 pc and the star is 180 pc below the galactic plane. Recent measurements estimate the distance for this variable at 599 pc; this value can be found in the Gaia catalog (Gaia Collab. 2016, 2018). Hilditch (1995) found that the star shows light variations over the 10.6-h orbital period explained primarily by an ellipsoidal variation of amplitude 0.13 mag caused by synchronous rotation of the roche-lobe-filling companion star. Hilditch (1995) studied the color indices (R–I) and classified the secondary of DX And as a KO-1 V star. Now DX And is a well-known dwarf nova with a long outburst recurrence time (270–330 days (Šimon 2000)) and a long orbital period (P = 10.6 hours, Bruch *et al.* 1997). Spogli *et al.* (2006, 2007) reported UBVR_c I_c observations of two outbursts of this star and the relative light curves. Spogli *et al.* (2006), analyzing 40 photometric observations in the R_c filter at minimum, reported a phase-diagram of DX And in quiescence considering a hypothetical period of 10.645 days. This variation is superimposed on an ellipsoidal variation well defined by Hilditch (1995). The origin of the additional variability is unknown; probably there is a third body around the binary system, but with the small number of data points, random or red noise variability cannot be ruled out easily. In this paper we present the results of our observations made in the years 2018–2019 at Gianni Rocchi's amateur astronomical observatory.

2. Photometric observations and light curve

The star was monitored for 86 nights from 28 September 2018 to 7 March 2019.The outburst of this dwarf nova began on 8 December 2018 and it ended on 26 December 2018. We observed DX And during the outburst for 10 nights, all the nights it was possible. The rise phase lasted two days. The maximum of the outburst was reached on 10 December 2018. The star remained at maximum for another two days before starting a slow decline that lasted until 26 December. All the

observations were obtained with a 0.12-m f/7 apochromatic refractor telescope by Skywatcher Esprit trade-mark, equipped with an Orion G3 CCD camera (Sony Ic × 419all), R_c, I_c Schuler filters, and U, B, V Baader filters. The exposure time was 240 sec. Our photometric system has been carefully tested by observing the M67 sequence (Chevalier and Ilovaisky 1991). The CCD frames were first corrected for de-biasing and flat fielding, then processed for aperture photometry. All the B, V, R_c, I_c data were obtained in differential photometry using the photometric comparison stars C1, C2 reported by Spogli *et al.*(2007). The U magnitudes were measured only during the outburst and for a few days after the decline when the star was in minimum phase. We note that the outburst amplitude is larger at higher frequencies: that is, in the different bands we have $\Delta U = 5.4$, $\Delta B = 4.8$, $\Delta V = 3.7$, $\Delta R_c = 3.1$, $\Delta I_c = 3.0$. All photometric data are reported in Table 1. Data are not corrected for interstellar reddening.

In Table 2 we report the maximum and minimum values, and the mean values at minimum for DX And.

In Figure 1 we report the light curve of DX And during the years 2018–2019 in all the filters we used at Gianni Rocchi's private amateur observatory. We left out the error bars because they are smaller than the data points here.

If we consider only a single filter, the light curve is well represented by Figure 2 in which we can see clearly an outburst of type B (Drew *et al.* 1990).

In type B outbursts the instability occurs as a result of redistribution of the surface density in the inner parts of the disc and propagation inward and outward. Hence, the outburst begins almost simultaneously at all wavelengths and the emission is very strong in the U band. The instability of the B type outburst, starting in the inner parts of the disk and propagating outwards (inside-out outburst), produces a rather symmetric light curve with a relatively low mass transfer rate (Smak 1984).

The oscillations are between R_c magnitudes 14.4 and 14.7. The star oscillates between V magnitudes 15.0 and 15.3. In B band at minimum there is a wide scattering of values. The star oscillates between B magnitudes 15.8 and 16.3.

The mean value is around $I_c = 14.05$ magnitude, but there is a large scattering from 13.8 to 14.4 of I_c magnitude. We calculated the difference in magnitude between one comparison star and the other, and we found that the mean value of $I(c2) - I(c1) = 0.72 \pm 0.08$ magnitude and the data display on a straight line. Therefore, the sky around Spello is not affected by pollution, and the large scattering is a peculiar feature of the variable.

3. A study of color indices

During the minimum phase the color indices of DX And are fairly stable and they oscillate around mean values. In the outburst phase there is rapid variation in all color indices that is tending to assume negative values or close to zero. Data on color indices are reported in Table 3. Our data are in agreement with the color indices reported by Hildtch (1995) and Echevarria *et al.* (1984) for a secondary of KO-1 V.

In Figure 8 we can see that during the maximum of the outburst the color index (U–B) is included between –0.5 and –1 and during the decline between –0.5 and 0.0. At minimum (U–B) varies from 0 to 0.5.

In Figure 9 we can see that at minimum (B–V) is between 1.4 and 0.6, while in outburst it is between 0.2 and 0.0.

At minimum ($V-I_c$) is between 1.4 and 0.6, while in outburst it is between 0.2 and 0.4.

4. The time series in V and R_c bands

We performed time series observations on two nights for DX And, on 06 February 2019 and 08 February 2019, the first in R_c band, the second in V. The star was observed in R_c for almost 2.1 hours for a total of 32 photometric observations, while with the V filter 34 photometric observations were obtained over 2.3 hours. In Tables 4 and 5 we report all data. In Table 6 we report the data for a star in the field of DX And. We can see the stability of this star in respect to DX And, which confirms that our photometric system is stable and that the dwarf nova is affected by flickering caused by variations in the mass transfer rate from the secondary to the disc and to the primary. The oscillations in V are between magnitudes 14.95 and 15.20, while in R_c they are between 14.40 and 14.63.

5. Conclusions

We have presented our U, B, V, R_c, I_c observations of DX And, a dwarf nova characterized by a long interval between two consecutive outbursts. The star has been observed for 86 nights: 76 nights when the star was at minimum and 10 nights when the star was in outburst.

The profile of the outburst and the time-scales confirm the results obtained by Šimon (2000). Also, the color indices are in substantial agreement with our previous B, V, R_c, I_c observations (Spogli *et al.* 1998, 2006, 2007). These new data increase the historical database on this variable source and they can help to constrain theoretical models.

6. Acknowledgements

Thanks to the boys of the Cero di Sant'Antonio and to the St. Anthony Corporation bearers with whom Corrado Spogli has shared the honor of carrying on his shoulders the "Cero of St. Anthony" (a heavy candle-shaped wooden structure) up to Mount Ingino in Gubbio for almost fifty years every May 15th to celebrate the Patron Saint of the city that is Saint Ubaldo.

References

Bruch, A. 1989, *Astron. Astrophys., Suppl. Ser.*, **78**, 145.

Bruch, A., Fischer, F.-J., and Wilmsen, U. 1987, *Astron. Astrophys., Suppl. Ser.*, **70**, 481.

Bruch, A., Vrielmann S., Hessman F. V., Kochsiek, A., and Schimpke, T. 1997, *Astron. Astrophys.*, **327**, 1107.

Chevalier, C., and Ilovaisky, S. A. 1991, *Astron. Astrophys., Suppl. Ser.*, **90**, 225.

Drew, J. E., Hoare, M. G., and Woods, J. A. 1990, *Mon. Not. Roy. Astron. Soc.*, **250**, 144.

Drew, J. E., Jones, D. H. P., and Woods, J. A. 1993, *Mon. Not. Roy. Astron. Soc.*, **260**, 803.

Echevarria, J. 1984, *Rev. Mex. Astron. Astrofis.*, **9**, 99.
Gaia Collaboration, *et al.* 2016, *Astron. Astrophys.*, **595A**, 1.
Gaia Collaboration, *et al.* 2018, *Astron. Astrophys.*, **616A**, 1.
Hilditch, R. W. 1995, *Mon. Not. Roy. Astron. Soc.*, **273**, 675.
Mattei, J. A. 1980, private communication.
Mattei, J. A., Langhans, T., and Dyck, G. 1987, *IAU Circ.*, No. 4387, 1.
Romano, G. 1958, *Mem. Soc. Astron. Ital.*, **29**, 177.
Šimon V. 2000, *Astron. Astrophys.*, **364**, 694.
Smak J. 1984, *Acta Aastron.*, **34**, 161.
Spogli, C., Fiorucci, M., Capezzali, D., Rocchi, G., Mancinelli, V., Brunozzi, P., and Fagotti, P. 2006, *Inf. Bur. Var. Stars*, No. 5716, 1.
Spogli, C., Fiorucci, M., Rocchi G., and Capezzali, D. 2007, *Inf. Bur. Var. Stars*, No. 5792, 1.
Spogli, C., Fiorucci, M., and Tosti, G. 1998, *Astron. Astrophys, Suppl. Ser.*, **130**, 485.
Weber, R. 1962, *Mem. Soc. Astron. Ital.*, **33**, 39.

Table 1. U, B, V, R_c, I_c observed magnitude data for the dwarf nova DX And.

Date	*JD (2450000.0+)*	*U*	*Error*	*B*	*Error*	*V*	*Error*	R_c	*Error*	I_c	*Error*
09/23/18	8386.25	—	—	16.24	0.02	15.01	0.01	14.52	0.01	13.98	0.01
09/26/18	8388.30	—	—	0.68	0.02	15.14	0.01	14.47	0.01	14.06	0.02
09/27/18	8389.26	—	—	15.97	0.02	15.13	0.01	14.55	0.01	—	—
09/28/18	8390.26	—	—	16.19	0.02	15.18	0.01	14.58	0.01	—	—
09/29/18	8391.36	—	—	—	—	15.25	0.02	—	—	—	—
10/02/18	8394.33	—	—	16.08	0.04	15.06	0.02	14.53	0.01	14.09	0.02
10/03/18	8395.26	—	—	16.16	0.02	15.24	0.01	14.68	0.01	14.08	0.01
10/07/18	8399.30	—	—	16.41	0.02	15.22	0.01	14.66	0.04	14.39	0.01
10/08/18	8400.28	—	—	16.08	0.01	15.11	0.03	14.48	0.01	13.91	0.01
10/12/18	8404.27	—	—	16.09	0.02	15.06	0.02	14.47	0.01	13.97	0.01
10/13/18	8405.27	—	—	15.93	0.02	15.09	0.01	14.59	0.01	13.96	0.02
10/19/18	8411.25	—	—	15.99	0.05	15.16	0.01	14.55	0.01	13.94	0.04
10/20/18	8412.24	—	—	16.31	0.02	15.09	0.01	14.58	0.01	14.09	0.02
10/22/18	8414.25	—	—	16.18	0.05	15.21	0.03	14.54	0.01	14.21	0.03
10/23/18	8415.25	—	—	16.03	0.01	15.03	0.01	14.34	0.02	13.99	0.03
10/24/18	8416.26	—	—	16.04	0.02	15.21	0.01	14.61	0.01	13.97	0.01
10/25/18	8417.25	—	—	15.92	0.02	15.11	0.02	14.63	0.01	14.03	0.02
11/06/18	8429.25	—	—	16.21	0.01	15.12	0.03	14.63	0.01	14.33	0.01
11/08/18	8431.31	—	—	16.05	0.05	15.11	0.05	14.46	0.03	13.94	0.04
11/09/18	8432.34	—	—	16.01	0.01	15.21	0.01	14.55	0.02	14.33	0.01
11/10/18	8433.26	—	—	16.04	0.02	15.15	0.01	14.58	0.01	13.97	0.01
11/11/18	8434.24	—	—	16.06	0.02	15.12	0.02	14.49	0.01	13.95	0.02
11/12/18	8435.27	—	—	15.86	0.04	15.08	0.01	14.54	0.03	14.07	0.03
11/13/18	8436.26	—	—	16.11	0.01	15.13	0.03	14.43	0.02	13.89	0.04
11/15/18	8438.27	—	—	15.99	0.02	15.10	0.02	14.51	0.04	13.93	0.01
11/16/18	8439.25	—	—	16.07	0.01	15.11	0.01	14.49	0.01	13.94	0.03
11/17/18	8440.26	—	—	16.19	0.01	15.19	0.01	14.61	0.01	14.13	0.03
11/18/18	8441.21	—	—	16.02	0.01	15.16	0.02	14.52	0.01	13.95	0.02
11/28/18	8451.27	—	—	15.97	0.01	15.12	0.02	14.58	0.01	14.05	0.02
11/29/18	8452.28	—	—	15.89	0.05	15.02	0.04	14.51	0.01	13.96	0.05
11/01/18	8454.22	—	—	16.06	0.01	15.11	0.02	14.53	0.01	13.95	0.02
12/04/18	8457.33	—	—	16.03	0.05	15.08	0.04	14.66	0.01	13.99	0.05
12/05/18	8458.26	—	—	16.05	0.01	14.89	0.02	14.45	0.01	13.72	0.05
12/08/18	8461.21	—	—	12.41	0.02	12.38	0.01	12.22	0.01	12.17	0.03
12/08/18	8461.22	—	—	12.34	0.03	12.35	0.03	12.19	0.01	12.09	0.03
12/08/18	8461.23	—	—	12.39	0.05	12.36	0.02	12.18	0.05	12.11	0.02
12/08/18	8461.25	—	—	12.34	0.01	12.35	0.03	12.22	0.03	12.08	0.01
12/08/18	8461.26	—	—	12.35	0.01	12.37	0.05	12.19	0.01	12.12	0.03
12/08/18	8461.28	—	—	12.37	0.05	12.32	0.04	12.20	0.01	—	—
12/09/18	8462.30	11.61	0.11	11.83	0.01	11.81	0.03	11.68	0.02	11.59	0.02
12/10/18	8463.23	11.11	0.14	11.69	0.02	11.72	0.03	11.48	0.02	11.45	0.04
12/10/18	8463.25	11.03	0.05	11.68	0.02	11.69	0.02	11.57	0.02	11.42	0.04
12/10/18	8463.27	10.94	0.05	11.67	0.02	11.70	0.02	11.54	0.02	11.41	0.04
12/10/18	8463.37	11.15	0.02	11.72	0.02	11.71	0.02	11.51	0.02	11.45	0.02
12/11/18	8464.24	11.11	0.12	11.71	0.03	11.69	0.02	11.54	0.02	11.44	0.04
12/11/18	8464.26	11.27	0.01	11.76	0.01	11.73	0.02	11.56	0.02	11.41	0.05
12/11/18	8464.28	11.14	0.08	11.85	0.01	11.74	0.01	11.58	0.01	11.48	0.02
12/11/18	8464.29	11.28	0.04	11.79	0.02	11.76	0.02	11.57	0.02	11.44	0.01
12/11/18	8464.31	11.23	0.03	11.71	0.02	11.71	0.02	11.51	0.02	11.41	0.01
12/11/18	8464.34	11.16	0.04	11.77	0.02	11.68	0.02	11.52	0.02	11.47	0.01
12/11/18	8464.35	11.22	0.02	11.73	0.02	11.65	0.02	11.49	0.02	11.38	0.01
12/12/18	8465.22	11.08	0.15	11.73	0.01	11.71	0.01	11.52	0.01	11.44	0.05
12/15/18	8468.25	11.45	0.02	12.06	0.01	11.95	0.01	11.81	0.01	11.65	0.02

Table continued on next page

Table 1. U, B, V, R_c, I_c observed magnitude data for the dwarf nova DX And, cont.

Date	*JD (2450000.0+)*	*U*	*Error*	*B*	*Error*	*V*	*Error*	R_c	*Error*	I_c	*Error*
12/18/18	8471.27	11.78	0.21	12.43	0.01	12.28	0.02	12.08	0.02	11.92	0.03
12/23/18	8476.37	13.33	0.16	13.64	0.05	13.44	0.02	13.14	0.02	12.81	0.02
12/23/18	8476.39	13.36	0.04	—	—	—	—	—	—	—	—
12/23/18	8476.39	13.41	0.05	—	—	—	—	—	—	—	—
12/23/18	8476.40	13.32	0.07	—	—	—	—	—	—	—	—
12/25/18	8478.20	14.41	0.03	14.65	0.01	14.34	0.01	13.93	0.01	13.62	0.01
12/25/18	8478.21	14.35	0.02	—	—	—	—	—	—	—	—
12/25/18	8478.21	14.41	0.04	—	—	—	—	—	—	—	—
12/25/18	8478.21	14.29	0.03	—	—	—	—	—	—	—	—
12/25/18	8478.22	14.27	0.05	—	—	—	—	—	—	—	—
12/26/18	8479.19	15.01	0.14	15.29	0.02	14.71	0.01	14.17	0.01	13.70	0.02
12/26/18	8479.21	15.37	0.07	—	—	—	—	—	—	—	—
12/27/18	8480.26	15.74	0.04	15.72	0.02	14.94	0.01	14.39	0.01	13.93	0.01
12/27/18	8480.27	15.91	0.03	—	—	—	—	—	—	—	—
12/29/18	8482.20	—	—	15.92	0.02	15.06	0.01	14.41	0.02	13.91	0.02
12/30/18	8483.20	16.43	0.02	15.91	0.02	14.99	0.01	14.39	0.01	13.88	0.03
12/31/18	8484.20	—	—	15.84	0.01	15.11	0.02	14.51	0.02	13.94	0.02
01/01/19	8485.24	—	—	16.07	0.03	15.06	0.04	14.46	0.01	13.91	0.01
01/02/19	8486.20	—	—	15.91	0.02	15.12	0.02	14.48	0.01	14.04	0.02
01/03/19	8487.20	16.27	0.02	15.97	0.01	15.07	0.02	14.47	0.01	14.03	0.01
01/04/19	8488.20	15.51	0.03	16.02	0.02	15.02	0.04	14.51	0.05	14.24	0.05
01/06/19	8490.19	16.08	0.01	15.95	0.05	15.03	0.01	14.39	0.03	13.85	0.03
01/07/19	8491.26	16.15	0.05	15.89	0.05	15.11	0.03	14.55	0.02	13.84	0.01
01/09/19	8493.28	16.16	0.03	15.96	0.04	15.04	0.03	14.48	0.02	13.99	0.01
01/11/19	8495.27	16.04	0.01	15.92	0.02	15.07	0.03	14.51	0.01	13.88	0.01
01/12/19	8496.20	15.96	0.05	15.98	0.01	15.09	0.01	14.50	0.04	13.76	0.04
01/14/19	8498.27	16.25	0.02	16.21	0.01	15.14	0.01	14.57	0.01	13.87	0.02
01/15/19	8499.23	—	—	15.81	0.02	15.06	0.03	14.46	0.02	13.97	0.03
01/18/19	8502.28	—	—	16.11	0.02	15.17	0.03	14.53	0.02	14.02	0.02
01/26/19	8510.22	—	—	15.98	0.01	15.18	0.03	14.55	0.01	14.22	0.01
01/28/19	8512.35	—	—	15.91	0.01	15.12	0.02	14.62	0.02	13.98	0.01
02/04/19	8519.25	—	—	15.85	0.04	15.22	0.01	14.64	0.01	14.29	0.01
02/05/19	8520.23	—	—	15.97	0.05	15.03	0.01	14.51	0.01	13.86	0.01
02/06/19	8521.23	—	—	16.31	0.02	15.18	0.01	14.55	0.01	14.04	0.01
02/07/19	8522.23	—	—	15.83	0.01	15.11	0.05	14.56	0.02	13.76	0.01
02/08/19	8523.25	—	—	15.85	0.03	15.08	0.01	14.52	0.01	14.03	0.01
02/12/19	8527.23	—	—	15.89	0.03	15.02	0.01	14.47	0.01	13.91	0.01
02/13/19	8528.26	—	—	16.23	0.02	15.24	0.02	14.61	0.01	13.98	0.01
02/14/19	8529.23	—	—	16.13	0.05	15.09	0.01	14.49	0.03	13.88	0.01
02/15/19	8530.32	—	—	15.56	0.01	15.28	0.01	14.54	0.01	14.02	0.01
02/16/19	8531.24	—	—	16.02	0.04	15.05	0.03	14.44	0.01	14.01	0.01
02/17/19	8532.23	—	—	16.49	0.01	15.14	0.01	14.56	0.01	13.87	0.01
02/18/19	8533.24	—	—	15.81	0.04	15.13	0.03	14.47	0.04	13.75	0.02
02/18/19	8533.25	—	—	16.16	0.02	15.16	0.01	14.55	0.01	13.97	0.01
02/18/19	8533.27	—	—	15.79	0.05	15.01	0.01	14.48	0.01	14.01	0.02
02/18/19	8533.28	—	—	15.75	0.04	15.06	0.03	14.53	0.01	14.02	0.01
02/20/19	8535.26	—	—	15.79	0.02	15.09	0.02	14.61	0.02	14.01	0.02
02/21/19	8536.25	—	—	16.03	0.03	15.18	0.01	14.51	0.03	13.86	0.02
02/21/19	8536.26	—	—	—	—	15.21	0.00	—	—	—	—
02/21/19	8536.26	—	—	—	—	15.05	0.01	—	—	—	—
02/21/19	8536.26	—	—	—	—	15.15	0.03	—	—	—	—
02/21/19	8536.27	—	—	—	—	15.09	0.01	—	—	—	—
02/22/19	8537.25	—	—	16.10	0.02	15.15	0.02	14.49	0.02	13.84	0.01
02/23/19	8538.30	—	—	15.68	0.04	15.13	0.01	14.47	0.02	13.79	0.01
02/24/19	8539.25	—	—	15.57	0.02	15.33	0.02	14.76	0.01	—	—
02/25/19	8540.29	—	—	15.77	0.02	15.07	0.02	14.55	0.02	13.84	0.01
02/26/19	8541.25	—	—	—	—	—	—	14.56	0.04	13.79	0.01
02/27/19	8542.26	—	—	15.87	0.01	14.89	0.02	14.48	0.02	13.92	0.02
02/28/19	8543.26	—	—	15.84	0.02	15.23	0.02	14.46	0.02	13.88	0.02
02/28/19	8543.27	—	—	15.85	0.05	15.17	0.04	14.53	0.02	14.40	0.04
02/28/19	8543.29	—	—	—	—	15.09	0.02	14.54	0.02	14.24	0.01
03/03/19	8546.24	—	—	—	—	15.03	0.01	14.32	0.05	13.95	0.05
03/04/19	8547.25	—	—	—	—	15.21	0.01	14.47	0.01	14.01	0.04
03/05/19	8548.26	—	—	16.09	0.03	15.11	0.02	14.46	0.02	13.84	0.01
03/05/19	8548.27	—	—	15.71	0.04	15.17	0.03	14.72	0.02	13.79	0.01
03/07/19	8550.25	—	—	15.96	0.02	15.13	0.03	14.49	0.01	14.17	0.01

Table 2. The main characteristics of the photometric data.

	U	*Error*	*B*	*Error*	*V*	*Error*	R_c	*Error*	I_c	*Error*
Maximum Values	10.94	0.05	11.69	0.02	11.65	0.02	11.51	0.02	11.38	0.02
Minimum Values	16.43	0.02	16.49	0.02	15.33	0.02	14.76	0.02	14.40	0.04
Mean Values at Minimum	16.10	0.20	15.98	0.17	15.11	0.07	14.52	0.07	13.98	0.14
Mean Values at Maximum	11.17	0.16	11.74	0.05	11.71	0.04	11.54	0.05	11.44	0.05

Table 3. The mean values of color indices of DX And.

	(U–B)	*Error*	*(B–V)*	*Error*	$(V–R_c)$	*Error*	$(R_c–I_c)$	*Error*	$(V–I_c)$	*Error*
Mean Values Maximum	–0.56	0.13	0.03	0.04	0.17	0.03	0.09	0.04	0.27	0.03
Mean Values Minimum	0.23	0.19	0.87	0.17	0.59	0.07	0.53	0.14	1.12	0.13

Table 4. Time series observations in the V band.

Date	*JD (2458523.000+)*	*Magnitude V*	*Error*	*Date*	*JD (2458523.000+)*	*Magnitude V*	*Error*
08/02/19	258	15.13	0.02	08/02/19	305	15.14	0.01
08/02/19	260	15.09	0.01	08/02/19	308	14.95	0.01
08/02/19	263	15.01	0.01	08/02/19	311	15.11	0.01
08/02/19	266	15.09	0.02	08/02/19	314	15.08	0.01
08/02/19	269	15.01	0.02	08/02/19	316	15.13	0.01
08/02/19	272	15.14	0.01	08/02/19	319	15.13	0.01
08/02/19	274	15.01	0.01	08/02/19	322	15.06	0.01
08/02/19	277	15.08	0.02	08/02/19	325	15.09	0.00
08/02/19	281	15.01	0.01	08/02/19	328	15.02	0.05
08/02/19	283	15.11	0.02	08/02/19	331	15.06	0.03
08/02/19	286	15.05	0.01	08/02/19	334	15.02	0.01
08/02/19	288	15.11	0.02	08/02/19	336	15.16	0.03
08/02/19	292	14.98	0.01	08/02/19	339	15.04	0.04
08/02/19	294	15.08	0.02	08/02/19	342	15.05	0.04
08/02/19	297	15.08	0.01	08/02/19	344	15.22	0.02
08/02/19	301	15.02	0.01	08/02/19	347	15.17	0.02
08/02/19	303	15.08	0.01	08/02/19	351	15.11	0.01

Table 5. Time series observations in the R_c band.

Date	*JD (2458521.000+)*	*Magnitude R*	*Error*	*Date*	*JD (2458521.000+)*	*Magnitude R*	*Error*
06/02/19	239	14.55	0.01	06/02/19	287	14.49	0.01
06/02/19	242	14.58	0.01	06/02/19	290	14.51	0.01
06/02/19	245	14.54	0.01	06/02/19	292	14.41	0.04
06/02/19	248	14.56	0.01	06/02/19	295	14.63	0.01
06/02/19	253	14.48	0.01	06/02/19	298	14.55	0.01
06/02/19	256	14.53	0.01	06/02/19	301	14.48	0.02
06/02/19	259	14.48	0.02	06/02/19	304	14.59	0.01
06/02/19	262	14.51	0.02	06/02/19	306	14.60	0.03
06/02/19	265	14.49	0.01	06/02/19	309	14.50	0.02
06/02/19	267	14.59	0.01	06/02/19	312	14.49	0.01
06/02/19	270	14.54	0.01	06/02/19	315	14.46	0.01
06/02/19	273	14.49	0.01	06/02/19	321	14.47	0.01
06/02/19	276	14.53	0.01	06/02/19	323	14.48	0.01
06/02/19	278	14.54	0.02	06/02/19	326	14.49	0.01
06/02/19	281	14.51	0.02	06/02/19	329	14.60	0.04
06/02/19	284	14.56	0.01	06/02/19	332	14.48	0.01

Table 6. Time series observations of a stable star: the TYC 3242 352.

Date	*JD*	*Magnitude V*	*Error*	*Date*	*JD*	*Magnitude V*	*Error*
08/02/19	2458523.258	11.76	0.01	08/02/19	2458523.305	11.72	0.03
08/02/19	2458523.260	11.78	0.02	08/02/19	2458523.308	11.79	0.04
08/02/19	2458523.263	11.77	0.05	08/02/19	2458523.311	11.72	0.03
08/02/19	2458523.266	11.73	0.02	08/02/19	2458523.314	11.77	0.01
08/02/19	2458523.269	11.78	0.04	08/02/19	2458523.316	11.77	0.01
08/02/19	2458523.272	11.79	0.02	08/02/19	2458523.319	11.76	0.06
08/02/19	2458523.274	11.78	0.01	08/02/19	2458523.322	11.74	0.02
08/02/19	2458523.277	11.76	0.01	08/02/19	2458523.325	11.80	0.02
08/02/19	2458523.280	11.77	0.02	08/02/19	2458523.328	11.73	0.03
08/02/19	2458523.283	11.76	0.03	08/02/19	2458523.331	11.75	0.01
08/02/19	2458523.286	11.78	0.03	08/02/19	2458523.333	11.78	0.02
08/02/19	2458523.288	11.75	0.03	08/02/19	2458523.336	11.76	0.02
08/02/19	2458523.291	11.75	0.03	08/02/19	2458523.339	11.74	0.02
08/02/19	2458523.294	11.75	0.06	08/02/19	2458523.342	11.76	0.01
08/02/19	2458523.297	11.74	0.01	08/02/19	2458523.341	11.75	0.02
08/02/19	2458523.301	11.76	0.01	08/02/19	2458523.347	11.69	0.04
08/02/19	2458523.302	11.79	0.02	08/02/19	2458523.350	11.74	0.02

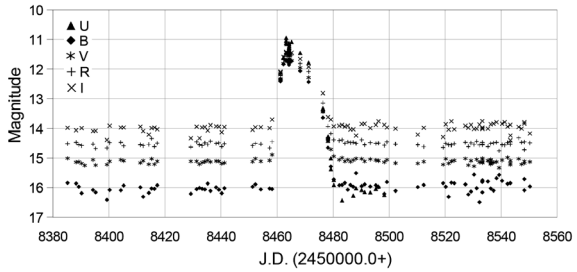

Figure 1. Light curve of DX And during the years 2018–2019 in UBVR$_c$I$_c$ filters.

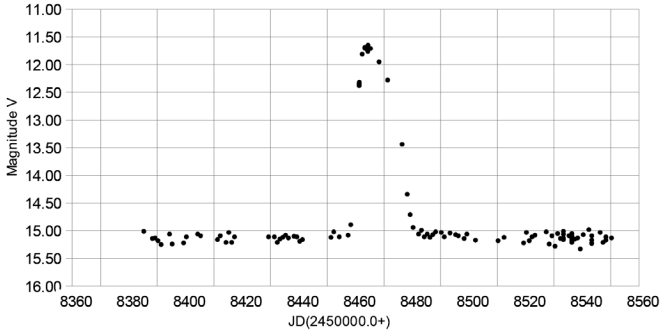

Figure 2. Light curve of DX And during the years 2018–2019 in V band.

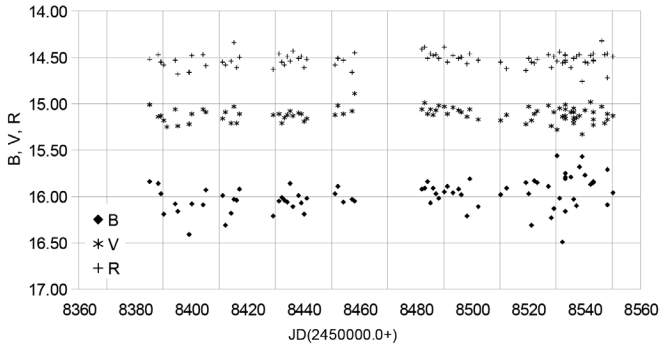

Figure 3. Light curves of DX And, phase at minimum, in the filter B, V, R$_c$ without the outburst.

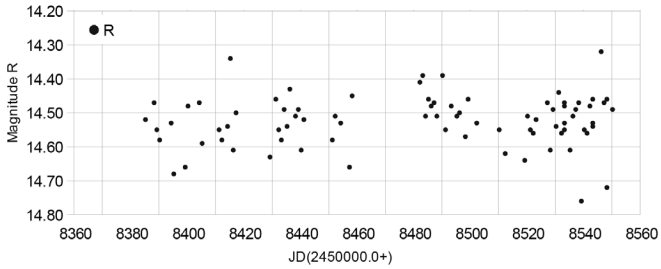

Figure 4. Light curve of DX And, phase at minimum, without the outburst in R$_c$ band.

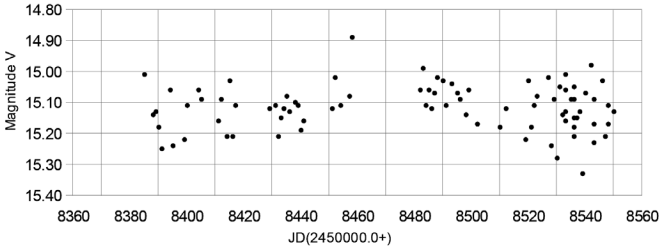

Figure 5. Light curve of DX And in V band at minimum.

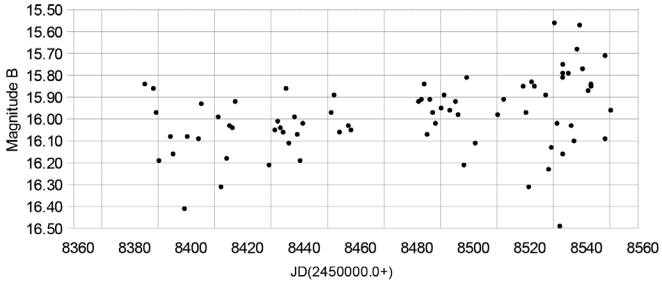

Figure 6. The light curve of DX And, phase at minimum, in B band.

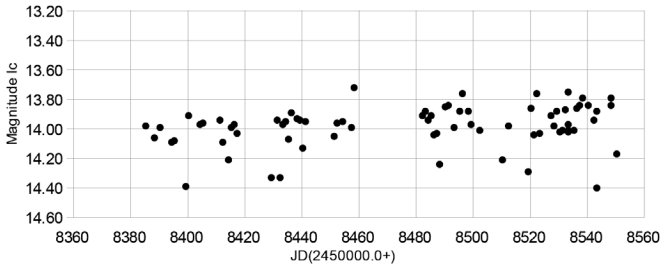

Figure 7. DX And. In I_c band at minimum there is a wide scattering of values.

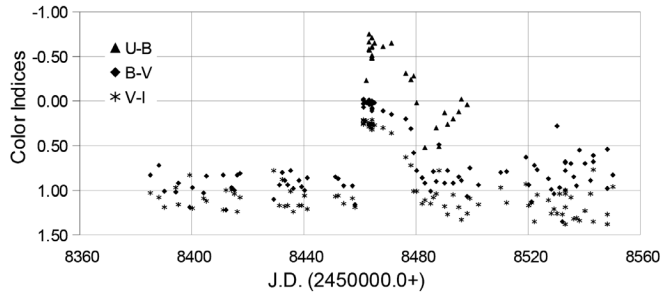

Figure 8. DX And, 2018–2019. The variations of color indices (U–B), (B–V), and (V–I) with time.

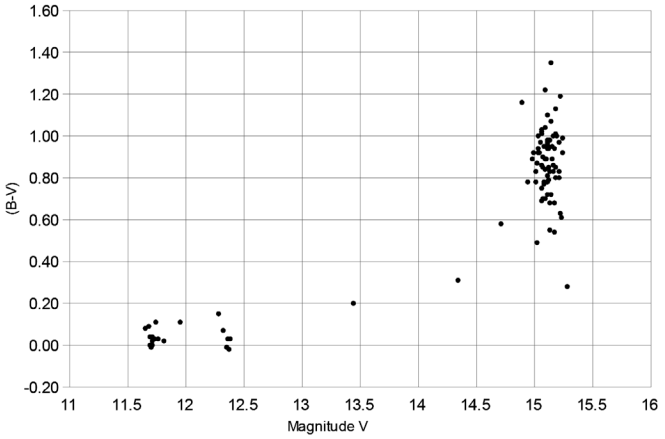

Figure 9. DX And. The color index (B–V) for V magnitude.

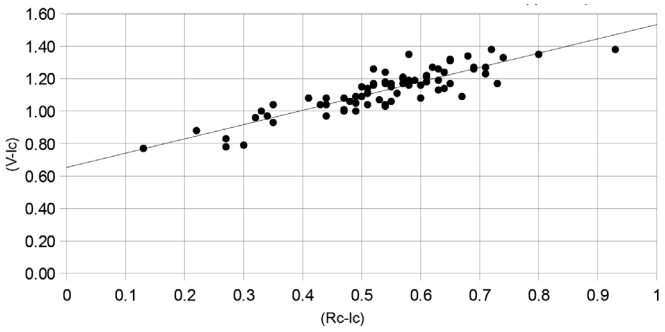

Figure 10. DX And. The color index (V–I_c) as a function of (R_c–I_c) at minimum.

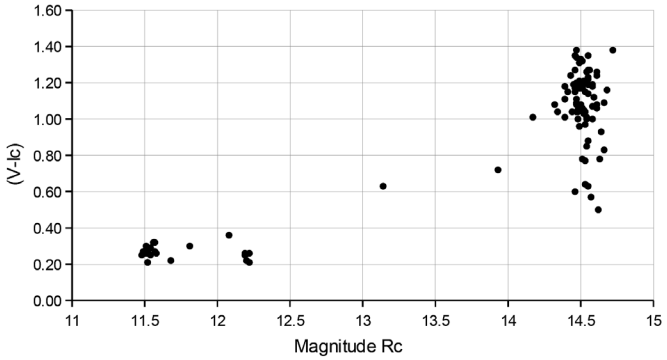

Figure 11. DX And. The color index (V–I_c) for magnitude R_c.

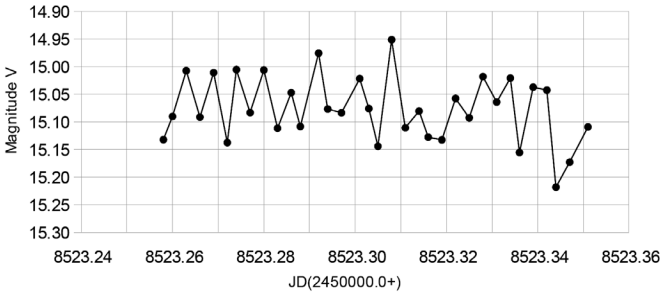

Figure 12. DX And. Time series observations in V band.

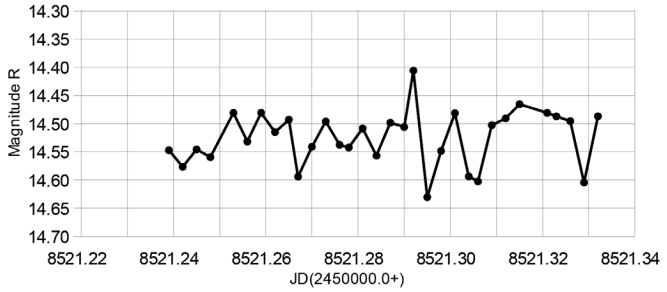

Figure 13. DX And. Time series observations in R_c band.

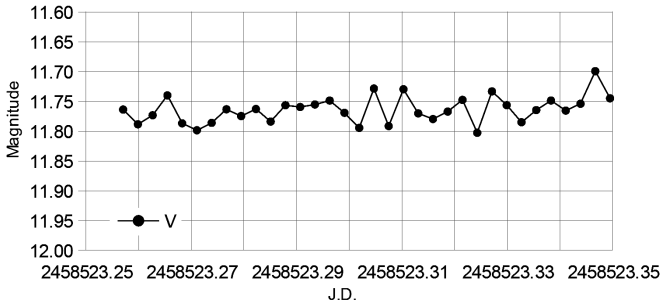

Figure 14. Time series observations of TYC 3242 352.

Expansion and Reinterpretation of the O–C Diagram of the High Amplitude δ Scuti Star RS Gruis

Roy A. Axelsen
P. O. Box 706, Kenmore, Queensland 4069, Australia; reaxelsen@gmail.com

Tim Napier-Munn
49 Limosa Street, Bellbowrie, Queensland 4070, Australia; tgnm@bigpond.cocm

Received October 14, 2020; revised November 4, 12, 2020; accepted November 12, 2020

Abstract Photometry obtained with a digital single lens reflex (DSLR) camera and a CMOS astronomical camera from 2016 to 2020 expands the O–C diagram of RS Gru to cover a span of nearly 68 years. Analysis of the data reveals that a previous report of a constant rate of increase of the period between October 2003 and July 2013 may not be correct. Instead, evidence is presented that there was a constant rate of increase of the period from October 2003 to October 2010 followed by a constant but slower rate of increase from July 2011 to July 2020, with the latter described by the expression $dP/dt = 2.99\ (0.96) \times 10^{-8}$ d yr^{-1} or $dP/Pdt = 2.04\ (0.65) \times 10^{-7}$ yr^{-1}. A new quadratic ephemeris derived from the 2011 to 2020 observations is TOM (HJD) = 2459045.1247 (0.0002) + 0.14701221 (0.00000004) E + 6.0X10^{-12} (1.9×10^{-12}) E2 for which zero time occurred on 14 July 2020 UTC.

1. Introduction

RS Gru (HD 206379) is a high amplitude δ Scuti star with a period of 0.147 d (3.53 h), and a magnitude range of 7.9 to 8.5 approximately in V. Its variability was first reported by Hoffmeister (1956). Rodriguez *et al.* (1995) reported times of maximum from observations taken by them and others between 1952 and 1988, and determined that the period was 0.147010864 d (0.000000022) at HJD 2447464.7095 (0.004). They fitted a quadratic function to the data and from this calculated that the period had decreased at a constant rate of $dP/dt = -1.56\ (0.12) \times 10^{-8}$ d yr^{-1}, or $dP/Pdt = -10.6\ (0.8) \times 10^{-8}$ yr^{-1}.

Garcia (2012) reported a dataset expanded by observations taken over the years 2003 to 2010 comprising personal observations and data from the AAVSO International Database. He fitted a cubic model to 37 times of maximum from 1952 to 2010, although examination of his Figure 5 shows a fit which is not optimal. He found a period of 0.14705874 d from Fourier analysis of observations in international databases.

Axelsen (2014) reported personal photoelectric and DSLR photometric observations, and analyzed the resulting enlarged dataset of 50 times of maximum to 2013. He reproduced Garcia's (2012) analysis, applied a cubic fit to the entire 1952 to 2013 dataset, and confirmed that it was not optimal. A quadratic fit was calculated for a subset of the data, comprising 28 times of maximum from 2003 to 2013, which was interpreted to indicate that the period was increasing at a constant rate of $dP/Pdt = 84.95\ (15.74) \times 10^{-8}$ yr^{-1}, considered by the author to be the highest rate of increase reported for a Population I high amplitude δ Scuti star with radial pulsation. However, inspection of Axelsen's (2014) Figure 3 suggests that a period jump occurred prior to the last three groups of observations followed by a new trend. This paper investigates the latter suggestion and reports the results of the analysis of that data and subsequent observations. A new ephemeris for RS Gru is calculated.

2. Methods

Images for photometry were taken for several hours each night through an 80-mm refractor at f/7.5 on an autoguided mount. The images were taken with a Canon EOS 500D camera in 2016, 2017, and 2018, and a ZWO ASI1600MM Pro CMOS astronomical camera with a Johnson V filter in 2019 and 2020. Images were calibrated with dark, flat, and bias frames (DSLR images) or dark and flat frames (ZWO images). Transformed V magnitudes, using standard stars from the E Regions (Menzies *et al.* 1989), were calculated from measurements of the DSLR images, and non-transformed V magnitudes were derived from the images taken with the ZWO camera. Table 1 lists the comparison and check stars.

RAW DSLR images were processed in AIP4WIN (Berry and Burnell 2011). Images captured in the FITS format by the ZWO camera were processed in ASTROIMAGEJ (Collins *et al.* 2017). Light curves were drawn and times of maximum determined for each peak using either PERANSO (Vanmunster 2013) or VSTAR (Benn 2012). The times of maximum were taken to be the times of the maximum values of polynomial expressions fitted to the peaks and the adjacent ascending and descending limbs of the light curves. Five times of maximum were obtained in July and August 2016, 5 in May 2018, 6 in August and September 2018, 4 in August 2019, and 7 in July 2020, making a total of 32. The fitting of linear and quadratic functions to O–C data was performed using regression analysis in Microsoft EXCEL and in MINITAB (https://www.minitab.com/en-us/).

Table 1. Comparison and check stars.

Star	*Star Name*	*V*	*B–V*
Comparison	HD 206442	8.485	0.490
Check star, DSLR camera	HD 206344	9.171	0.641
Check star, ZWO camera	HD 206584	8.451	0.950

3. Results

Figures 1 and 2 show the light curve of RS Gru and the check star obtained during one night with the DSLR and ZWO cameras, respectively. It is evident that the precision is better with the ZWO camera.

Table 2 presents all times of maximum, epochs, and O–C (observed minus computed) values for observations between November 1952 and July 2020, a time span of 67 years and 8 months. The calculations of the O–C values are based on zero epoch at HJD 2459045.12400, the time of maximum of the first light curve peak obtained by the author in July 2020, and a period of 0.147011369 d from the linear ephemeris calculated by Axelsen (2014). The O–C diagram drawn from values in this table is shown in Figure 3. The first part of the diagram, between epochs –168149 and –78718, is drawn from observations made between 1952 and 1988 which were published by Rodriguez *et al.* (1995), who interpreted the data to indicate that the period was decreasing at a constant rate.

Figure 4 shows a part of the O–C diagram of RS Gru drawn from observations published by Axelsen (2014), who fitted a quadratic model to the data, and interpreted the diagram to indicate that the period was increasing at a constant rate of $dP/Pdt = 84.95\,(15.74) \times 10^{-8}\,yr^{-1}$. However, careful inspection of this figure leads to the observation that the rate of change in the period between epochs –41664 and –24233 may be different from that between epochs –22305 and –17326. Furthermore, a period jump may have occurred between these two epoch ranges. There is one discrepant data point, O–C –0.02343 at epoch –24239.

Figure 5 shows the O–C diagram of RS Gru from October 2003 to October 2010, in which the dashed line represents a fitted quadratic model. The solitary discrepant data point shown as a filled square is not included in the model. From the times of maximum and the epochs, it is calculated that the period of RS Gru was increasing at a constant rate of $dP/dt = 7.8\,(3.1) \times 10^{-8}\,d\,yr^{-1}$ or $dP/Pdt = 2.3\,(2.1) \times 10^{-7}\,yr^{-1}$.

Figure 6 shows the O–C diagram of RS Gru from July 2011 to July 2020, between epochs –22305 and 35. Inspection suggests that a linear model may fit the data, but examination of the plots of residuals versus epochs from linear and quadratic models (Figures 7 and 8, top right panels) reveals that the latter yields a better fit. In addition, the quadratic model also reveals a better result for the normal probability plot (more data points on the line), and plots of the residuals versus fits, residuals versus order of observations and the histogram of the residuals (Figures 9 and 10). A quadratic ephemeris is therefore preferred, and is given by the following formula, derived from the times of maxima and the epochs:

$$\begin{aligned} \text{TOM (HJD)} = {} & 2459045.1247\,(0.0002) + 0.14701221 \\ & (0.00000004)\,E + 6.0 \times 10^{-12}\,(1.9 \times 10^{-12})\,E2\,. \end{aligned} \quad (1)$$

The period was thus 0.14701221 (0.00000004) d at zero time, very close to the time of the first peak of the light curve captured on 14 July 2020 UTC.

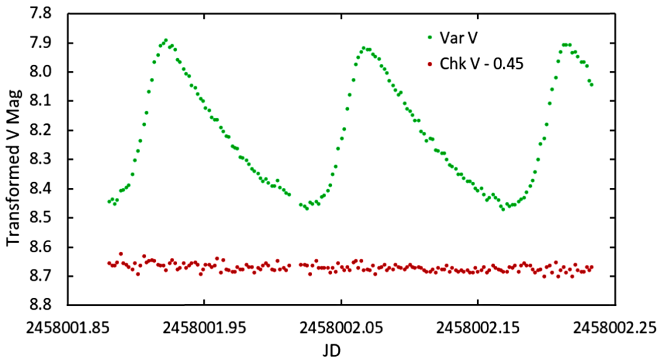

Figure 1. Light curve of RS Gru and check star from data taken during one night with the Canon EOS 500D DSLR camera. The check star data are shifted for optimal viewing.

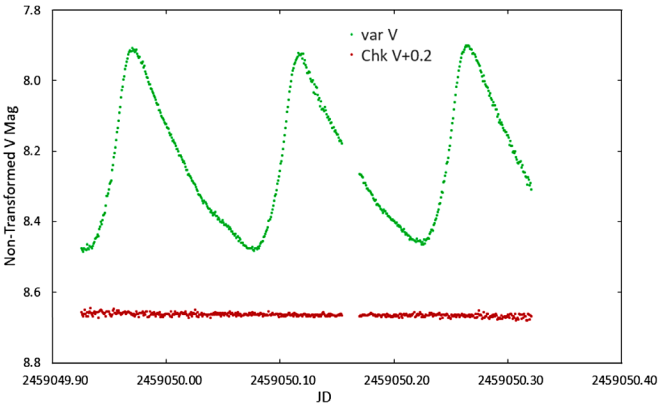

Figure 2. Light curve of RS Gru taken during one night with the ZWO ASI1600MM Pro camera. The check star data are shifted for optimal viewing.

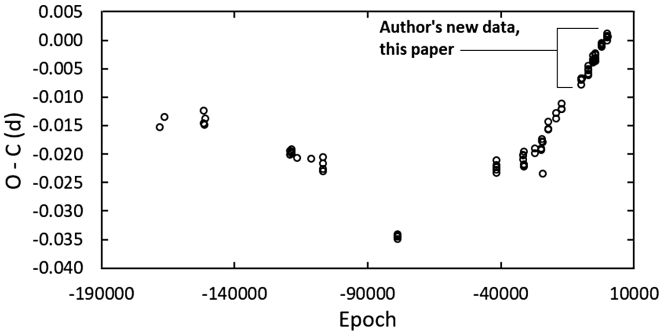

Figure 3. O–C (observed minus computed) diagram of RS Gru, November 1952–July 2020, drawn from the data in Table 2. The calculations of O–C values are based on zero epoch at HJD 2459045.12400, the time of maximum of the first light curve peak obtained in July 2020, and a period of 0.147011369 d, the linear ephemeris calculated by Axelsen (2014).

4. Discussion

Sterken (2005) discusses uncertainties in the interpretation of O–C diagrams. Specifically, he states "It is rather difficult to decide whether an O–C curve should be represented by a continuous curve (second degree polynomial) or by a sequence of short linear segments. The latter approach leads to the interpretation that the period of the star undergoes sudden changes." Even though one model may yield smaller residuals than another and would therefore be the preferred one, doubt may still exist as to the physical reality of the behavior of the star.

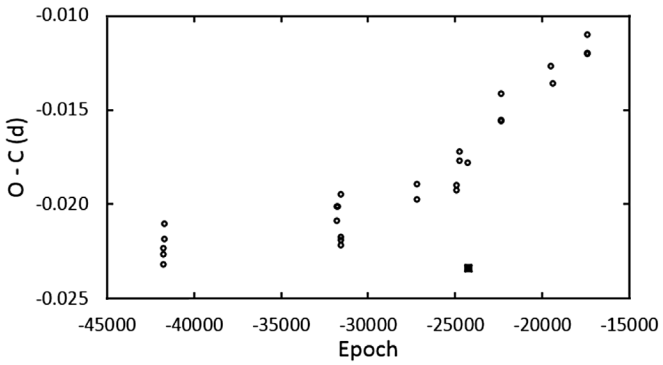

Figure 4. Part of the O–C diagram of RS Gru, Octiber 2003–July 2013 corresponding to Figure 3 of Axelsen (2014). The single discrepant data point is represented by a filled black square. Note that the scales of the two axes are different from those in the original paper because the original periods and epochs for calculating the O–C tables differ. The basis for the calculations of the O–C values is given in the legends for Table 2 and Figure 3.

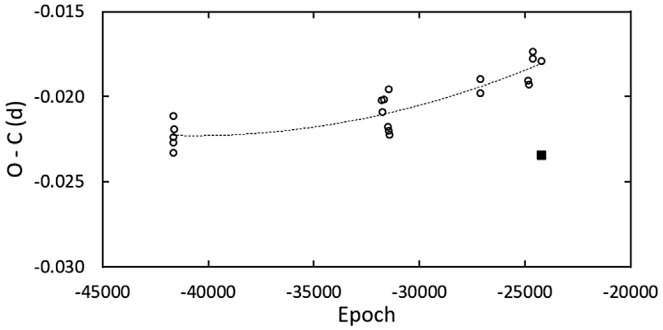

Figure 5. O–C diagram of RS Gru, October 2003–October 2010. A quadratic function is fitted to the data, after excluding the discrepant data point (the filled black square). The basis for the calculations of the O–C values is given in the legends for Table 2 and Figure 3.

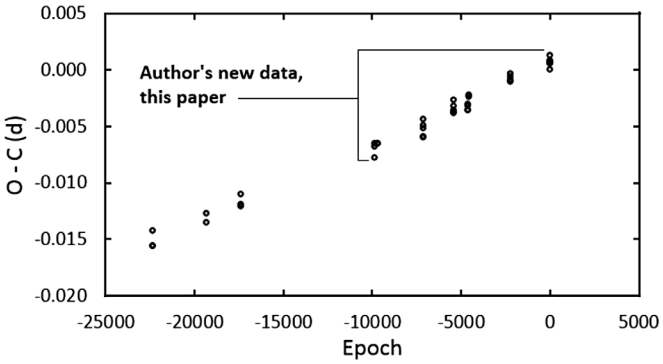

Figure 6. O–C diagram of RS Gru, July 2011–July 2020. The author's new observations, reported in this paper, are represented by the data between epochs –10000 and zero approximately, i. e., the last six groups of data in this figure. The basis for the calculations of the O–C values is given in the legends for Table 2 and Figure 3.

The other point Sterken (2005) makes is that "piecewise linear segments can only point out the occurrence of a period jump, but cannot reveal exactly when such events do occur—unless a series of contiguous cycles has been observed."

Rodriguez *et al.* (1995) interpreted the O–C diagram of RS Gru from data taken between 1952 and 1988 to be represented by a quadratic model, a smooth continuous curve which implied a decreasing period at a constant rate. On the other hand, Garcia's (2012) Figure 5 shows some of the groups of data points from the Rodriguez (1995) O–C diagram joined by straight lines, which on face value suggests that the author considered that there may have been times during which the period was constant, between which period jumps occurred. Despite these aspects of Garcia's Figure 5, he describes the fitting of a cubic function (a smooth curve) to all of the RS Gru data he reported.

There is, however, another piece of evidence supporting the occurrence of period jumps in RS Gru. Figure 3 of Laney *et al.* (2003), which is reproduced with permission as Figure 11 in the present paper, is an O–C diagram of this star which graphs the data of Rodriguez *et al.* (1995) from epoch -100,000 to zero epoch and additional data between zero epoch and epoch 40,000, but Laney *et al.* do not tabulate the numerical values underlying the additional data. Most of it would appear to fit into the gap in the O–C diagram in Figure 3 of the present paper, between epoch –78,718 and epoch –41,651. There are two period jumps in Figure 3 of Laney *et al.* (2003), one of them after zero epoch and the other after epoch 20,000.

Figure 4 of the present paper provides evidence of another period jump. The figure represents the data published initially by Axelsen (2014), who interpreted the plot to indicate that the period of RS Gru was increasing at a constant rate, since a quadratic model could be applied to the data. However, careful inspection of the figure suggests the alternative interpretation that the period was increasing at a constant rate between epochs –41664 and –24233, after which a period jump may have occurred. The remaining data in the plot, from epoch –22305 to epoch –17326, could conceivably represent the development of a new trend.

Support for the latter interpretation is provided by Figure 6, in which the O–C diagram between epochs –22305 and 35 shows what could be a linear trend. However, as demonstrated in Figures 7 and 8, a quadratic function provides a better fit, indicating that the period of RS Gru is slowly increasing at a constant rate during the time over which these observations were made.

What causes period changes in δ Scuti stars? Attempted answers to this question involve consideration of complex astrophysical processes, which are discussed by Breger and Pamyatnykh (1998). Their discussion is paraphrased selectively in what follows. It has been determined that the rates of observed period changes in δ Scuti variables are greater than rates predicted from theoretical evolutionary models by about a factor of 10. The causes of non-evolutionary period changes are not known. However, for δ Scuti stars with more than one mode of pulsation, it has been suggested that period changes, including period jumps, may be caused by non-linear mode interactions, but this could not apply to RS Gru, a radially pulsating Population I star. Stars such as RS Gru with known period changes are high amplitude stars that occur in the central part of the instability strip, near the theoretical Blue Edge of the fundamental radial mode in a $\log g - \log T_{eff}$ diagram (Figure 3 of Breger and Pamyatnykh 1998). These authors note that the clustering may, however, be accidental because this is the most populated part of the central instability strip. However, fundamental radial mode instability appears or disappears at this line,

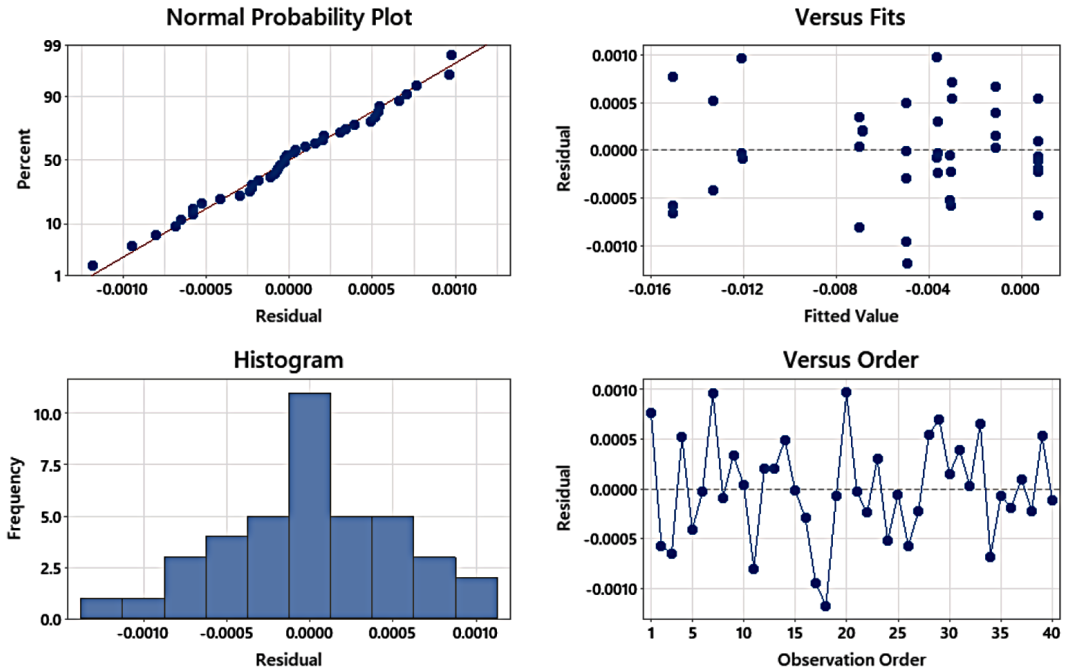

Figure 7. Analysis of the residuals from the quadratic fit to the O–C data. Compare each of the four panels in the above figure to the corresponding panel in Figure 8 below. For each panel, the behavior of the residuals is better in Figure 7, indicating that the second order model is preferred.

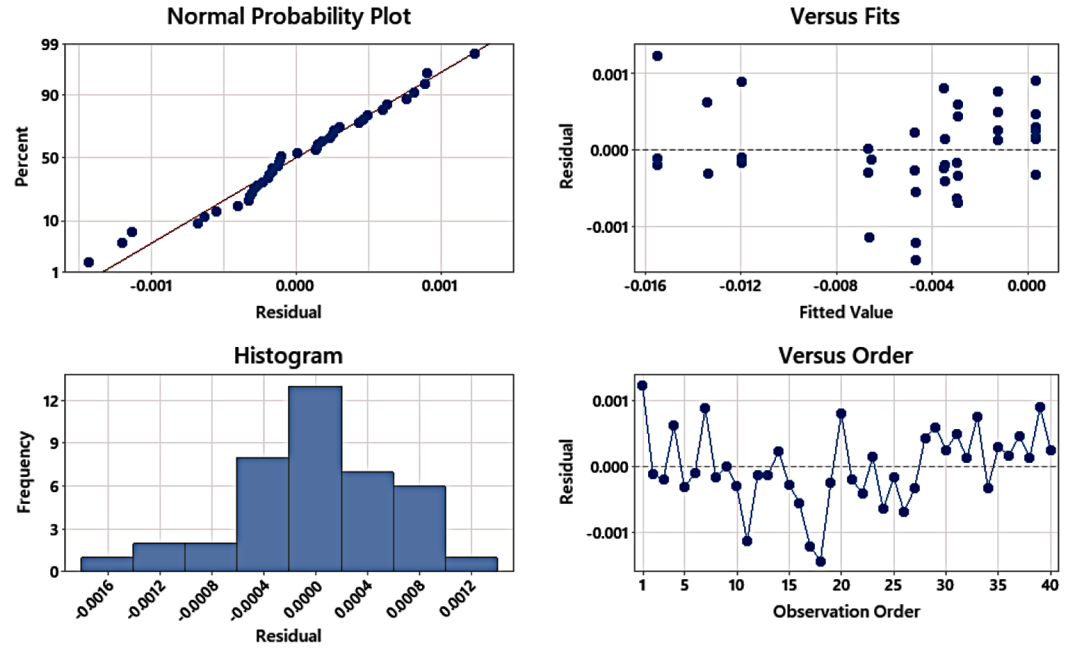

Figure 8. Analysis of the residuals from the linear fit to the O–C data. As indicated in the legend to Figure 7, the residuals from the linear model do not fit the data as well as the residuals from the second order model. In particular, the non-linear behavior of the residuals vs the fitted values indicates a model imperfection which is eliminated by moving to a quadratic model (Figure 7).

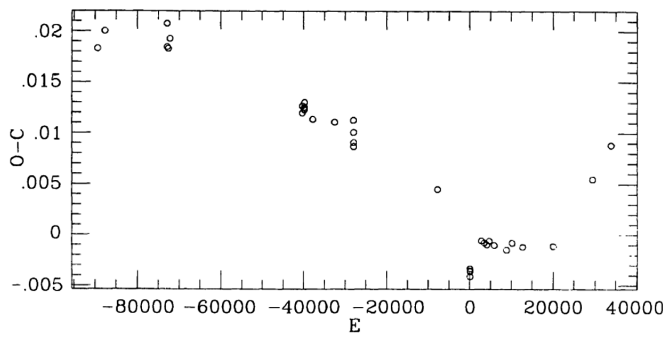

Figure 9. This is a reproduction (with permission) of Figure 3 of Laney *et al.* (2003). The O–C diagram implies period jumps after zero epoch and after epoch 20,000.

Table 2. O-C data for RS Gru.

Maximum	*TOM (HJD)*	*Epoch*	*O–C (d)*	*Primary Source*	*Maximum*	*TOM (HJD)*	*Epoch*	*O–C (d)*	*Primary Source*
1	2434325.2940	–168149	–0.01531	1	42	2455482.5796	–24233	–0.01790	11
2	2434573.4510	–166461	–0.01350	1	43	2455766.0212	–22305	–0.01426	9
3	2436756.5710	–151611	–0.01233	2	44	2455767.0489	–22298	–0.01560	9
4	2436760.5380	–151584	–0.01464	2	45	2455768.0779	–22291	–0.01567	9
5	2436801.5540	–151305	–0.01481	3	46	2456196.9130	–19374	–0.01279	9
6	2436853.3030	–150953	–0.01382	3	47	2456205.8798	–19313	–0.01368	9
7	2441538.4027	–119084	–0.01943	4	48	2456496.9639	–17333	–0.01207	9
8	2441538.5490	–119083	–0.02015	4	49	2456497.1119	–17332	–0.01108	9
9	2441610.4379	–118594	–0.01980	4	50	2456497.9929	–17326	–0.01213	9
10	2441611.3200	–118588	–0.01977	4	51	2457598.9665	–9837	–0.00664	12
11	2441611.4677	–118587	–0.01908	4	52	2457599.1132	–9836	–0.00694	12
12	2441612.3493	–118581	–0.01955	4	53	2457599.9945	–9830	–0.00778	12
13	2441915.4856	–116519	–0.02070	4	54	2457626.0166	–9653	–0.00665	12
14	2442687.5892	–111267	–0.02081	5	55	2457627.0457	–9646	–0.00664	12
15	2443355.4610	–106724	–0.02165	6	56	2458001.9269	–7096	–0.00448	13
16	2443355.6092	–106723	–0.02047	6	57	2458002.0734	–7095	–0.00498	13
17	2443360.4584	–106690	–0.02264	6	58	2458002.9552	–7089	–0.00526	13
18	2443360.6050	–106689	–0.02305	6	59	2458003.1015	–7088	–0.00591	13
19	2447464.7095	–78772	–0.03494	7	60	2458003.9834	–7082	–0.00613	13
20	2447468.5324	–78746	–0.03434	7	61	2458250.2298	–5407	–0.00375	14
21	2447468.6793	–78745	–0.03445	7	62	2458251.2599	–5400	–0.00270	14
22	2447472.6489	–78718	–0.03416	7	63	2458257.1394	–5360	–0.00367	14
23	2452920.0196	–41664	–0.02272	8	64	2458257.2862	–5359	–0.00388	14
24	2452921.9311	–41651	–0.02237	8	65	2458258.1688	–5353	–0.00333	14
25	2452922.0772	–41650	–0.02328	8	66	2458360.0474	–4660	–0.00362	15
26	2452923.9905	–41637	–0.02113	8	67	2458360.1949	–4659	–0.00315	15
27	2452925.0188	–41630	–0.02191	8	68	2458370.9263	–4586	–0.00361	15
28	2454373.9645	–31774	–0.02023	9	69	2458371.0736	–4585	–0.00326	15
29	2454374.9929	–31767	–0.02091	9	70	2458371.9565	–4579	–0.00249	15
30	2454387.9307	–31679	–0.02018	9	71	2458372.1036	–4578	–0.00233	15
31	2454417.0373	–31481	–0.02179	10	72	2458719.05179	–2218	–0.00099	16
32	2454417.9191	–31475	–0.02202	9	73	2458719.19904	–2217	–0.00075	16
33	2454417.9216	–31475	–0.01956	10	74	2458720.08075	–2211	–0.00111	16
34	2454423.9464	–31434	–0.02223	10	75	2458720.22839	–2210	–0.00048	16
35	2455059.0379	–27114	–0.01981	9	76	2459045.12400	0	0.00000	17
36	2455059.9208	–27108	–0.01898	9	77	2459045.27163	1	0.00062	17
37	2455391.7254	–24851	–0.01907	11	78	2459046.00657	6	0.00050	17
38	2455394.6654	–24831	–0.01930	11	79	2459046.30088	8	0.00079	17
39	2455422.0115	–24645	–0.01734	9	80	2459047.03562	13	0.00047	17
40	2455423.0401	–24638	–0.01775	9	81	2459049.97662	33	0.00124	17
41	2455481.6920	–24239	–0.02343	11	82	2459050.27000	35	0.00060	17

Note: Observations were made between November 1952 and July 2020. The calculations of O–C values are based on zero epoch at HJD 2459045.12400, the time of maximum of the first light curve peak obtained in July 2020, and a period of 0.147011369 d, the linear ephemeris calculated by Axelsen (2014).

Primary sources: 1. Hoffmeister (1956), November 1952 and July 1953 observations; 2. Oosterhoff and Walraven (1966), July 1959 observations; 3. Kinman (1961), August and October 1959 observations; 4. Dean et al. *(1977), August 1972 to August 1973 observations; 5. McNamara and Feltz (1976), October 1975 observations; 6. Balona and Martin (1978), July and August 1977 observations; 7. Rodriguez* et al. *(1995), October and November 1988 observations; 8. Derekas* et al. *(2009), October 2003 observations; 9. Axelsen (2014), including personal observations from September 2007 to July 2013; 10. Mattei (2013), observer DSI, November 2007 observations; 11. Garcia (2012), July and October 2010 observations; 12. This paper, author's data, August 2016 observations; 13. This paper, author's data, September 2017 observations; 14. This paper, author's data, May 2018 observations; 15. This paper,author's data, August and September 2018 observations; 16. This paper, author's data, August 2019 observations; 17. This paper, author's data, July 2020 observations.*

depending on the direction of stellar evolution, and the authors suggest that this may have a role in future period change interpretations. With respect to the direction of period change, it is seen that the expected theoretical prediction of increasing period with increasing evolutionary status is not borne out in practice, since the numbers of stars with increasing and decreasing periods are about equal.

5. Conclusion

RS Gru has long been known as a high amplitude δ Scuti star which exhibits period changes. At various times, the period has decreased at a constant rate, remained apparently constant between period jumps, and most recently, after yet another apparent period jump, has increased at a constant rate of $dP/dt = 7.8\,(3.1) \times 10^{-8}$ d yr^{-1} or $dP/Pdt = 2.3\,(2.1) \times 10^{-7}$ yr^{-1}. The period on 14 July 2020 UTC was 0.14701221 (0.00000004) d.

6. Acknowledgements

The first author gratefully acknowledges the support of a research grant from the Edward Corbould Research fund of the Astronomical Association of Queensland for the purchase of a photoelectric photometer which yielded some of the observations of RS Gru listed in Table 2.

We acknowledge with thanks the variable star observations from the AAVSO International Database (Henden 2013) contributed by observer DSI and used in this research.

References

Axelsen, R. A. 2014, *J. Amer. Assoc. Var. Star Obs.*, **42**, 44.

Balona, L. A., and Martin, W. L. 1978, *Mon. Not. Roy. Astron. Soc.*, **184**, 1.

Benn, D. 2012, *J. Amer. Assoc. Var. Star Obs.*, **40**, 852.

Berry, R., and Burnell, J. 2011, AIP4WIN v. 2.4.0, provided with *The Handbook of Astronomical Image Processin*g, Willmann-Bell, Richmond, VA.

Breger, M., and Pamyatnykh, A. A. 1998, *Astron. Astrophys.*, **332**, 958.

Collins, K. A., Kielkopf, J. F., Stassun, K. G., and Hessman, F. V. 2017, *Astron. J.*, **153**, 77.

Dean, J. F., Cousins, A. W. J., Bywater R. A., and Warren, P. R. 1977, *Mem. Roy. Astron. Soc.*, **83**, 69.

Derekas, A., *et al.* 2009, *Mon. Not. Roy. Astron. Soc.*, **394**, 995.

Garcia, J. R. 2012, *J. Amer. Assoc. Var. Star Obs.*, **40**, 272.

Henden, A. A. 2013, variable star observations from the AAVSO International Database (https://www.aavso.org/aavso-international-database-aid).

Hoffmeister, C. 1956, *Veröff. Sternw. Sonneberg*, **3**, 1.

Kinman, T. D. 1961, *Bull. Roy. Obs.*, Series E, No. 37, 151.

Laney, C. D., Joner, M., and Rodriguez, E. 2003, in *Interplay of Periodic, Cyclic and Stochastic Variability in Selected Areas of the H-R Diagram*, ed C. Sterken, Astron. Soc. Pac. Conf. Ser. 292, 203.

McNamara, D. H., and Feltz, K. A., Jr. 1976, *Publ. Astron. Soc. Pacific*, **88**, 510.

Menzies, J. W., Cousins, A. W. J., Banfield, R. M., and Laing, J. D. 1989. *S. Afr. Astron. Obs. Circ.*, **13**, 1.

Oosterhoff, P. T. and Walraven, T. 1966, *Bull. Astron. Inst. Netherlands*, **18**, 387.

Rodriguez, E., Rolland, A., Costa, V., and Martin, S. 1995, *Mon. Not. Roy. Astron. Soc.*, **277**, 965.

Sterken, C. 2005, in *The Light Time Effect in Astrophysics: Causes and cures of the O–C diagram*, ed. C. Sterken, Astron. Soc. Pac. Conf. Ser. 335, 3.

Vanmunster, T. 2013, Light curve and period analysis software, PERANSO v.2.50 (http://www.cbabelgium.com/peranso).

Exoplanets for Everyone

Todd Duncan
Erika Dunning
Justin Hurworth
Erin Mercer
Department of Physics, Pacific University, 2043 College Way, Forest Grove, OR 97116; tduncan@pacificu.edu

Received July 24, 2020; revised July 31, 2020; accepted August 4, 2020

Abstract We report the detection of transiting exoplanet HD 189733b by photoelectric photometry using a modest setup and procedure easily accessible to many amateur astronomers and college or high school students. Detecting an exoplanet transit first-hand can be an inspiring experience. By describing our approach, we hope to make it easier for others to share this experience, using equipment they may already have available.

1. Introduction

Exoplanets capture the popular imagination like few other scientific topics, offering an opportunity to inspire wonder and motivate engagement in the process of science. For this purpose, photoelectric photometry (PEP) has some advantages over CCD/CMOS imaging. The procedure is relatively simple and maintains a direct connection between the observer and the star (Rochford 2013). Participants can look through the telescope and see the target and comparison stars, then watch numbers displayed on the photometer that match qualitatively with relative brightness perceived by eye. It's easy to understand the photometer as an extension of their own senses. Even the data reduction process is relatively straightforward and can be done by hand or with a simple spreadsheet. Only a brief background explanation is required for anyone to follow the steps of the observation/data analysis process. This allows participants to directly connect their starwatching experience to the resulting light curve indicating the presence of an orbiting planet. In this way the transit can come to life as something real and immediate rather than being understood only abstractly and obscured behind layers of computer image analysis.

For these reasons, it seems valuable to develop education and outreach activities based on the live observation of exoplanet transits using PEP. The first step in developing such activities is of course to determine if it's even possible to clearly detect a transit with a standard portable telescope and photometer. This paper describes our successful observation of a transiting exoplanet using an SSP-3 photometer and 8-inch Schmidt-Cassegrain telescope. We provide enough detail to encourage others to replicate and expand these observations with similar equipment they may be able to find (as we did) collecting dust in a storeroom or cabinet at their local college or astronomy club.

2. Methods

We chose HD 189733b for our test observations because of its bright host star and large transit depth (V = 7.7 mag, depth = 2.4%). Its short orbital period (2.2 days), summer-autumn visibility at mid-northern latitudes, and proximity to the Dumbbell Nebula (M27) also make it well-suited for public outreach events. A nearby star of similar magnitude and color index (HD 345459, less than 10 arc minutes away) provides an ideal comparison star (Chéreau 2020). We used a Meade 8-inch f/10 Schmidt-Cassegrain telescope and an Optec SSP-3 Generation 1 solid state photometer, set to 10 × gain and 10-second integration time (Optec 2012).

Our telescope has an equatorial mount and clock drive but no go-to capability, so we star-hopped our way to HD 189733. We began on Altair and then moved north about 10 degrees to find the constellation Sagitta. We then centered on γ Sagittae (a magnitude 3.5 star) and moved north about 3 degrees to reach HD 189733. (Chéreau 2020). M27 is a helpful marker to confirm that the correct field of view has been located. Figure 1 shows the field of view, with comparison and variable stars labeled along with the region of sky in which the background was recorded for both stars.

Eric Jensen's Tapir web interface (Jensen 2013) makes it easy to predict observability of transits from any location. A suitable opportunity presented itself on July 3, 2020, with predicted transit midpoint at 8:15 UT (predicted ingress at 7:19 UT and predicted egress at 9:09 UT). We began observations at about 6:30 UT and ended prematurely due to clouds at about 8:30 UT.

We followed a standard differential photometry procedure (Calderwood 2020), modified slightly for the situation. To maximize signal to noise ratio, we used a clear filter rather than a standard photometric color filter. We also used the same background sky region for both stars, as indicated in Figure 1, and measurement sequence sky-comparison-variable-sky-comparison-variable…, etc. We linearly interpolated to estimate sky readings at the times of each star reading, and similarly to estimate comparison star readings at the time of each variable star reading.

3. Results

Our results are shown in Figures 2 and 3, indicating a clear detection of the transit at the predicted time, despite non-ideal conditions. M27 was barely visible in the eyepiece due to background light from the nearly full Moon and streetlights in a residential neighborhood. Clouds forced an early end to observations, so we were only able to see the first half of the

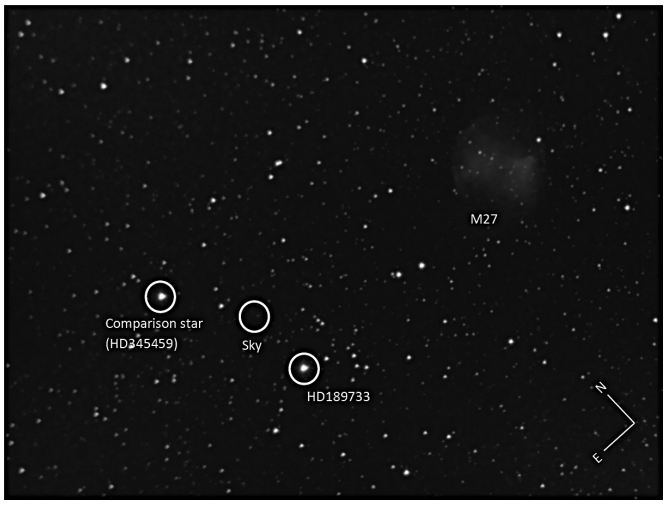

Figure 1. Field of view (about half a degree across) near HD 189733. The comparison star and region of sky for background readings are shown as well as the Dumbbell Nebula (M27) for reference. Photo by the authors.

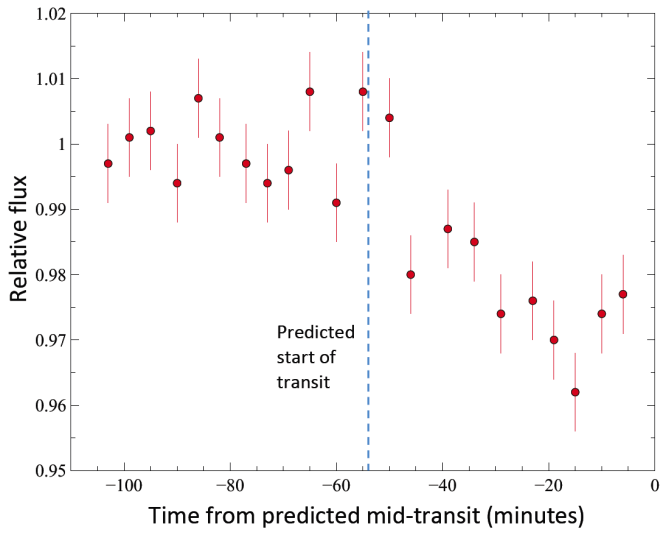

Figure 2. Individual HD 189733b data points obtained from 40-second integration on variable star, comparison star, and sky background. Relative flux is the ratio of net variable and comparison star readings, normalized to the mean ratio pre-transit.

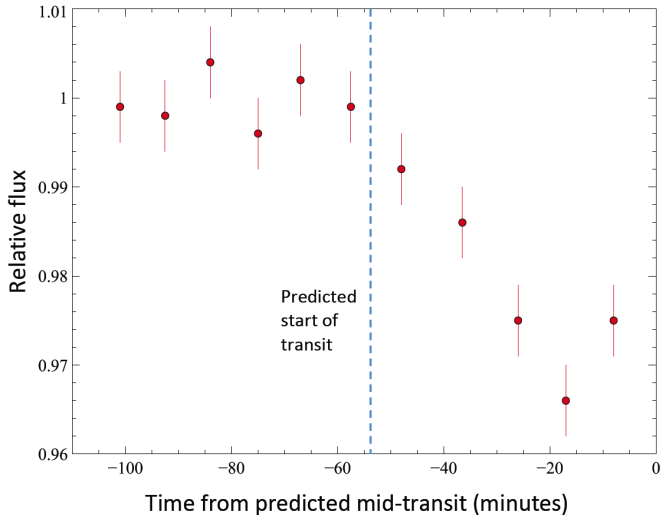

Figure 3. Data from Figure 2, binned in non-overlapping pairs.

transit. Our success under these conditions is encouraging for the possibility of incorporating "live" exoplanet transit viewing into astronomy education and outreach events in a wide variety of settings.

Importantly, the star was high in the sky from our location throughout the observation window (zenith distance ranged from about 30 to 40 degrees). Because of this and the close proximity and similar color indices of the two stars, no correction for atmospheric extinction was needed to reduce the data and generate the graphs shown in Figures 2 and 3.

4. Discussion and conclusions

One important objective in observing exoplanet transits is of course to gather data for the scientific community. In this regard, CCD/CMOS cameras have distinct advantages, and the bulk of scientific work on transits will be done with cameras. But there is also value in creating an experience of connection for participating observers. Here photoelectric photometry still has something to contribute with its simplicity and direct connection between the data and the observing experience. Our results suggest that live PEP exoplanet observations can be successfully incorporated into education and outreach events in easily accessible public spaces. This opens up many possibilities for going beyond just showing people the sky, but also engaging them in the process by which we discover the wonders they read or hear about in the news.

For example, the next step in our project is to incorporate exoplanet observations into some of the public "sidewalk star parties" we offer in our community. One telescope with attached photometer will be used to record data that will be entered directly into a spreadsheet and graphed in almost real-time, so that participants can see a display of the unfolding light curve as the transit happens. Another scope (with attached camera) will display the field of view on a screen for easy viewing of the transiting and comparison stars. Other volunteers will demonstrate models of how an exoplanet transit produces a decrease in brightness, and point out where in the sky the transiting star is located to help participants view it through binoculars. There are many variations on how such an event can be arranged to create an immersive experience for the participants that helps them really understand how we know there are planets around other stars.

Just as with PEP and DSLR imaging (Littlefield 2010), there are likely additional methods waiting to be discovered for detecting transits utilizing equipment that observers already have on hand or can easily access. Hopefully these examples will encourage others to explore possibilities for more people to directly experience transit observations. More generally, we hope the examples help inspire others to look for creative ways to do more than they thought was possible, more simply than they imagined it could be done.

5. Acknowledgements

The authors gratefully acknowledge support for this project from Pacific University and Portland Community College. Erika Dunning gratefully acknowledges scholarship support from

the National Science Foundation S-STEM Grant No. DUE-1565169.

References

Calderwood, T. 2020, *The Hitch-hiker's Guide to AAVSO Photoelectric Photometry (PEP)* (https://www.aavso.org/pep-observers-guide).

Chéreau, F. 2020, STELLARIUM planetarium software, version 0.20.2 (http://www.stellarium.org).

Jensen, E. L. N. 2013, TAPIR: A Web Interface for Transit/Eclipse Observability, Astrophysics Source Code Library ascl:1306.007 (https://astro.swarthmore.edu/transits).

Littlefield, C. 2010, *J. Amer. Assoc. Var. Star Obs.*, **38**, 212.

Optec, Inc. 2012, *Model SSP-3 Generation 2 Solid-State Stellar Photometer: Technical Manual for Theory of Operations and Operating Procedures*, Optec Inc., Lowell, Mich.

Rochford, P. 2013, "Contributing to Astronomy in 2013 Using Mid-Twentieth Century Technology" (https://www.cloudynights.com/item.php?item_id=2881).

Southern Eclipsing Binary Minima and Light Elements in 2019

Tom Richards
Pretty Hill Observatory, Kangaroo Ground, Vic., Australia; tomprettyhill@gmail.com

Mark Blackford
Congarinni Observatory, Congarinni, NSW, Australia; markgblackford@outlook.com

Neil Butterworth
Townsville Observatory, Mount Louisa, Qld., Australia; neilb2@bigpond.net.au

Robert Jenkins
Theta Observatory, Salisbury, SA, Australia; robynnabara@ozemail.com.au

Received July 13, 2020; accepted August 5, 2020

Abstract We present 156 times of minima of 68 southern hemisphere eclipsing binary stars acquired in 2019, plus two earlier (V676 Cen). These observations were acquired and analyzed by the authors who are members of the Southern Eclipsing Binary group of Variable Stars South (VSS) (http://www.variablestarssouth.org), using DSLR and CCD detectors. For seven of the systems we have derived updated light elements and present those as well as O–C values for the VSS minima. This paper is the fifth in a series; previous papers were published in the *Open European Journal on Variable Stars*.

1. Observations

Equipment and software used are set out in Table 1. Observer initials abbreviate the name of an author of this paper, surname last. Instrument refers to the telescope and objective diameter in cm, or to the DSLR camera used. Remaining columns refer to the software used for the purposes listed. See the References section of this paper for the software mentioned in this table.

All observers using PERANSO employed polynomial fitting for minima estimation. MINIMA25 takes the weighted mean and standard deviation of the means of six methods: parabolic fit, tracing paper, bisectors of chords, Kwee-van Woerden (Kwee and Van Woerden 1956), Fourier fit, and sliding integrations.

CCD or DSLR image sets were obtained in hours-long runs. Each observer analysed their own image sets as follows:

1. Calibrated them using bias frames, dark frames, and flat field frames.

2. Executed differential aperture photometric measurements on the calibrated sets.

3. Performed minima estimation on the photometric data.

This paper is the fifth in a series; previous papers were published in the *Open European Journal on Variable Stars* (Richards *et al.* 2016, 2017, 2018, 2019).

2. Results

Appendix A lists the minima estimates. Columns 1 and 2 list the GCVS designation and GCVS variability type of the target stars in lexical order of constellation abbreviation, as listed in (Samus *et al.* 2017). One entry refers to the ASAS-SN catalogue (Shappee *et al.* 2014). In some cases, more recent work may propose different variability types. Columns 3 and 4 record the heliocentric Julian dates of minima and the uncertainty (in days) as reported by the algorithm used in the photometry software. Column 5 lists the minimum type, primary (P) or secondary (S). We define the primary minimum as the deeper one in our observations where that can be determined, otherwise we assume the epoch recorded in the AAVSO Variable Star Index (Watson *et al.* 2006)—hereafter referred to as VSX—is of a primary minimum. Column 6 gives the filter used: B and V are Johnson *B* and *V*, or the transformed equivalent in the case of DSLR color sensors, R is Cousins *R*, and r' and i' are Sloan *r*' and *i*'. G is the green plane image from a tri-color DSLR camera. Column 7 gives the initials of the observer.

3. Analysis

Table 2 lists revised light elements for seven binaries in Appendix A. These are binaries for which we have derived four or more primary minima in 2019 and earlier years, spread over at least three observing seasons. (See Richards *et al.* 2016, 2017, 2018, 2019 for the earlier primary minima). Binaries with revised light elements reported in earlier papers in this series are excluded.

For these systems we derived new linear light elements by ordinary least squares regression. The regression used all the VSS primary minima times and the VSX epoch time as minima data. The VSX epoch and period were used to obtain an orbital cycle count for the minima data. By regressing the (HJD) minima times against cycles we obtained a best-fit period as the slope of the regression line, and a corrected zero epoch as the y-intercept at the earliest VSS minimum. The new zero epoch is the regressed value of the earliest VSS minimum.

Table 2 contains the resulting light elements for the systems we analysed. The first five columns list the system, the epoch

Table 1. Observers, equipment, and software.

Observer	*Instrument*	*Imaging*	*Calibration*	*Photometry*	*Minima*
TR	41 cm R-C + SBIG STXL-6303e	MAXIM	MUNIWIN	MUNIWIN	PERANSO
MB	8-cm refractor +Atik One 6.0	MAXIM	MAXIM	MAXIM	MAXIM
MB	35-cm R-C + SBIG STT-3200	THESKYX PROFESSIONAL	MAXIM	MAXIM	MAXIM
NB	Canon 650D	MAXIM	MAXIM	MAXIM	MINIMA25E
RJ	25 cm GSO RCA + QSI-583 CCD.	MAXIM	MAXIM	MAXIM	MINIMA25E

Notes: MAXIM DL (Diffraction Limited 2012); MINIMA25 (Nelson, R. H. 2019); MUNIWIN (Motl, D. 2011); PERANSO (Vanmunster 2013); THESKYX PROFESSIONAL (Software Bisque 2020).

Table 2. Revised linear light elements for systems with four or more VSS primary minima estimates, regressed from the VSX light elements.

Identifier	E_0	$E_{0_{err}}$	P	P_{err}	SD_{resid}	*No. Obs.*	*Interval*
YY Aps	2457505.114202	0.000659	0.85555536	2.69E-07	0.00145	4	1115
V0535 Ara	2456869.972074	0.000184	0.62930210	1.46E-08	0.00038	4	1818
BR Mus	2457439.073090	0.000910	0.79819773	1.45E-07	0.00232	6	1171
EZ Oct	2457504.118065	0.000270	0.28587823	3.66E-08	0.00065	5	1106
V0954 Sco	2457220.054859	0.004089	1.26858891	1.30E-06	0.00874	4	1464
RS Sgr	2455778.073564	0.000954	2.41568415	1.45E-07	0.00199	4	2911
FM Vel	2457446.001513	0.000865	0.38952718	2.90E-08	0.00196	5	1093

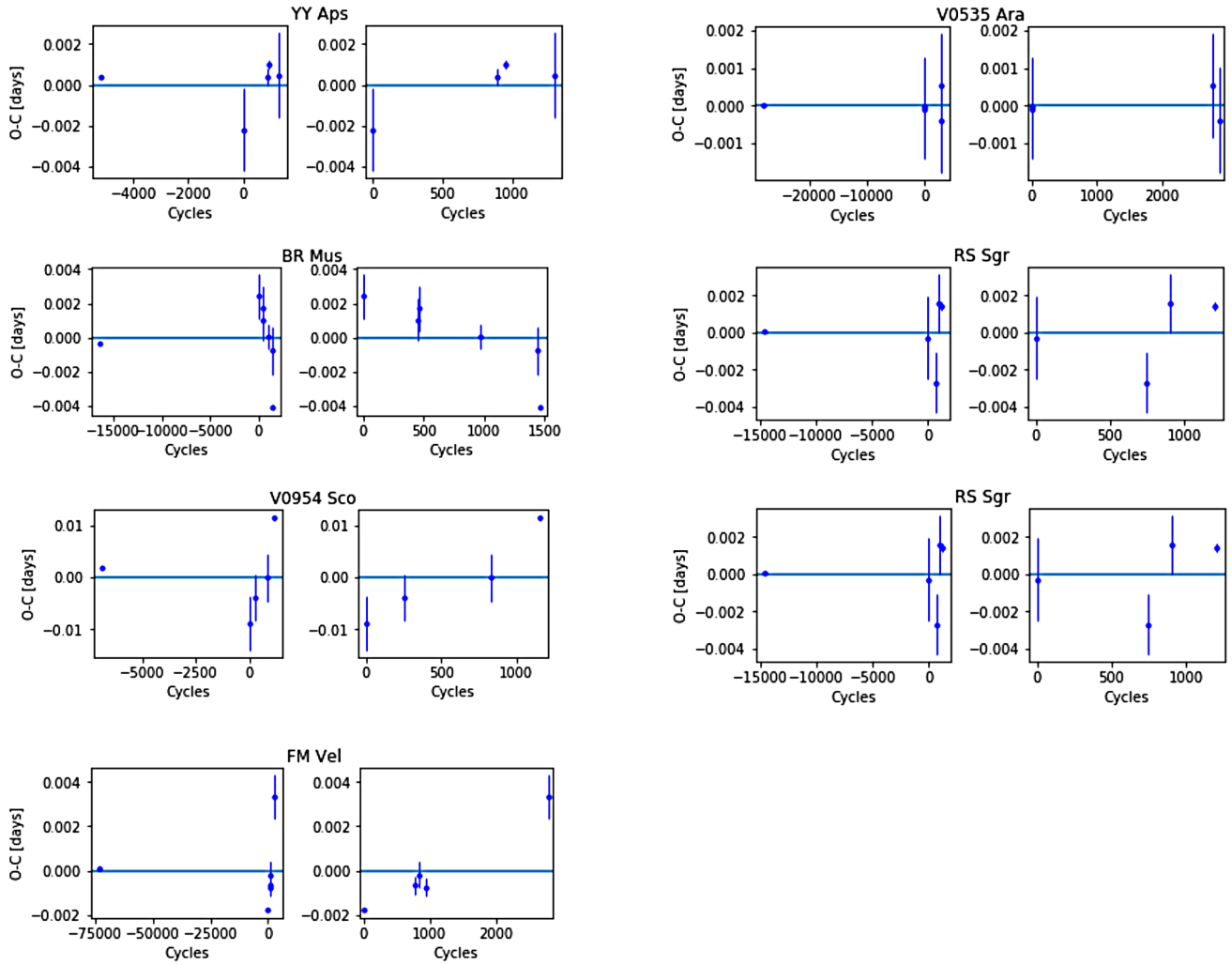

Figure 1. Residual (O–C) plots of the minima estimates against the light elements listed in Table 2. Left hand panels for each binary system show VSX and VSS minima, right hand panels the VSS minima only. Orbital cycle numbers count from zero at the first (regressed) VSS minimum, incrementing by the regressed period.

and standard error, and the period and standard error. The next column records the standard deviation of the residuals of the minima from the regression prediction. The smaller the number, the better are the minima data fitted to a linear fit (constant period). No. Obs is the number of VSS primary minima estimates used in the regression, and Interval is the time interval in days covered by them.

For each system in Appendix A, in Figure 1 we present plots of the residuals of the observed minima from the calculated regression (aka O–C values). The regression is the horizontal line at O–C = 0. The left-hand panel in each pair for a star shows (by the left edge) the VSX minimum, together with (near the right edge) the VSS minima. The latter are zoomed into in the right panel to exhibit any structure in the residuals which may indicate variation in the period. The error bars are those reported for the time of minimum by the software used for minima estimation.

The primary interest in the Table 2 light elements, and the Figure 1 residual plots, lies in indication of period change. The right-hand plots of BR Mus, V0954 Sco and FM Vel strongly indicate that a linear model is inadequate to represent the minima times. Those three systems also have the highest residual standard deviations. For the other systems the case for non-linear ephemerides is less clear. For them, however, it must be remarked that with the very large time gap between the original VSX epoch and those of the VSS, there could easily be non-linear models, e.g. sinusoidal or parabolic, that would fit the data shown. For a discussion on the problems of model fitting to minima data with large gaps, see the study of GZ Pup in Richards (2020).

The error bars in those plots are a poor indicator of the reliability of the individual minima estimates; since (as an informal study by TR has shown) different minima estimation algorithms can deliver error estimates differing by an order of magnitude on the same data. Implementations of the Kwee-Van Woerden algorithm (Kwee and van Woerden 1956) typically report a far smaller error than polynomial fits. For this reason and because VSX epoch data do not include errors, weighted linear regressions were not used in this study.

4. Conclusion

We have presented 158 minima estimates of 68 southern eclipsing binaries made by the authors in 2019, and a period analysis for seven of them where our data warrant it. In three cases there is a strong indication of period variability. It is outside the scope of this report to further investigate that, which requires mining the literature for earlier minima estimates and obtaining ongoing minima data acquisition in future years.

5. Acknowledgements

This research has made much use of the International Variable Star Index (VSX) database, operated at AAVSO, Cambridge, Massachusetts. (Watson *et al*. 2006).

References

Diffraction Limited. 2012, MaximDL image processing software (http://www.cyanogen.com).

Kwee, K. K., and van Woerden, H. 1956, *Bull. Astron. Inst. Netherlands*, **12**, 327.

Motl, D. 2011, C-Munipack (http://c-munipack.sourceforge.net).

Nelson, R. H. 2019, Software by Bob Nelson (https://www.variablestarssouth.org/software-by-bob-nelson/).

Richards, T. 2020, *VSS Newsletter*, 2020-2, 3-12 (https://www.variablestarssouth.org/vss-community/vss-newsletters/).

Richards, T., Blackford, M., Bohlsen, T., Butterworth, N., Lowther, S., Jenkins, R., and Powles, J. 2017, *Open Eur. J. Var. Stars*, No. 182, 1.

Richards, T., Blackford, M., Butterworth, N., Crawford, G., and Jenkins, R. 2018, *Open Eur. J. Var. Stars*, No. 189, 1.

Richards, T., Blackford, M., Butterworth, N., Crawford, G., and Jenkins, R. 2019, *Open Eur. J. Var. Stars*, No. 198, 1.

Richards, T., Blackford, M., Butterworth, N., Evans, P., and Jenkins, R. 2016, *Open Eur. J. Var. Stars*, No. 177, 1.

Samus N. N., Kazarovets E. V., Durlevich O. V., Kireeva N. N., and Pastukhova E. N. 2017, *Astron. Rep.*, **61**, 80 (*General Catalogue of Variable Stars: Version GCVS 5.1*, http://www.sai.msu.su/groups/cluster/gcvs/gcvs).

Shappee, B. J., *et al.* 2014, *Astrophys. J.*, **788**, 48.

Software Bisque. 2020, TheSkyX professional (http://www.bisque.com).

Vanmunster, T. 2013, light curve and period analysis software, peranso v.2.50 (http://www.cbabelgium.com/peranso).

Watson, C. L., Henden, A. A., and Price, A. 2006, in *The Society for Astronomical Sciences 25th Annual Symposium on Telescope Science*, The Society for Astronomical Sciences, Rancho Cucamonga, Calif., 47 (http://www.aavso.org/vsx).

Appendix A: Minima estimates

Identifier	*Type*	*HJD of min.*	*Error*	*Min.*	*Filter*	*Observer*
II Aps	EW/KE	2458670.92385	0.00226	S	V	TR
MR Aps	EB	2458620.13966	0.00106	P	i'	TR
MR Aps	EB	2458624.09879	0.00261	S	i'	TR
MR Aps	EB	2458710.13585	0.00004	S	V	RJ
YY Aps	EB	2458619.90331	0.00206	P	r'	TR
YY Aps	EB	2458622.04136	0.00600	S	V	TR
V0535 Ara	EW	2458611.25151	0.00138	P	V	MB
V0535 Ara	EW	2458688.02545	0.00138	P	V	MB
V0610 Ara	EW	2458648.97530	0.00360	P	G	NB
V0878 Ara	EW:	2458654.97200	0.00380	S	V	NB
V0878 Ara	EW:	2458659.98090	0.00130	P	V	NB
V0625 Car	EW	2458601.99662	0.00039	S	V	MB
V0625 Car	EW	2458609.88956	0.00044	P	V	MB
V0625 Car	EW	2458610.02782	0.00047	S	V	MB
BH Cen	EB/KE	2458611.98856	0.00073	P	B	MB
BH Cen	EB/KE	2458611.98888	0.00070	P	I	MB
BH Cen	EB/KE	2458611.98891	0.00073	P	V	MB
BH Cen	EB/KE	2458613.17604	0.00096	S	B	MB
BH Cen	EB/KE	2458613.17616	0.00093	S	I	MB
BH Cen	EB/KE	2458613.17619	0.00093	S	V	MB
BH Cen	EB/KE	2458615.15530	0.00097	P	I	MB
BH Cen	EB/KE	2458615.15537	0.00109	P	B	MB
BH Cen	EB/KE	2458615.15540	0.00085	P	V	MB
V0676 Cen	EW/KW	2458241.06161	0.00012	P	r'	TR
V0676 Cen	EW/KW	2458241.20884	0.00006	S	r'	TR
V0676 Cen	EW/KW	2458580.97149	0.00054	S	r'	TR
V0676 Cen	EW/KW	2458581.11803	0.00064	P	r'	TR
V0676 Cen	EW/KW	2458581.26396	0.00063	S	r'	TR
V0701 Cen	EB/KE	2458609.12690	0.00140	P	G	NB
V0757 Cen	EW/KW	2458599.07912	0.00125	S	V	MB
V0757 Cen	EW/KW	2458599.25175	0.00135	P	V	MB
V0757 Cen	EW/KW	2458610.06147	0.00087	S	V	MB
V0757 Cen	EW/KW	2458610.23385	0.00126	P	V	MB
V0757 Cen	EW/KW	2458615.03940	0.00170	P	V	NB
V0758 Cen	EW/KE	2458611.01730	0.00380	P	V	NB
V0759 Cen	EW/RS	2458586.09960	0.00390	P	G	NB
V0759 Cen	EW/RS	2458658.97780	0.00370	P	V	NB
V0901 Cen	EW/RS	2458537.02129	0.00140	S	r'	TR
V1362 Cen	EW	2458657.95880	0.00220	P	G	NB
DM Cir	EW	2458654.13409	0.00113	P	V	MB
DM Cir	EW	2458656.06781	0.00100	P	V	MB
DM Cir	EW	2458657.03629	0.00134	S	V	MB
FQ CMa	EA+DSCT	2458531.05914	0.00055	P	V	MB
FQ CMa	EA+DSCT	2458548.08865	0.00233	S	V	MB
FQ CMa	EA+DSCT	2458847.04749	0.00060	P	B	MB
V0711 CrA	EB	2458729.94262	0.00062	P	V	NB
V0734 CrA	EA	2458712.04957	0.00079	P	V	MB
V0734 CrA	EA	2458713.02792	0.00078	P	V	MB
YY Eri	EW/KW	2458846.02929	0.00013	P	R	MB
YY Eri	EW/KW	2458846.99383	0.00012	P	R	MB
YY Eri	EW/KW	2458847.15406	0.00017	S	R	MB
DY Gru	EW/KW	2458674.19998	0.00086	P	R	MB
DY Gru	EW/KW	2458675.20866	0.00084	P	R	MB
DY Gru	EW/KW	2458678.06431	0.00097	S	R	MB
DY Gru	EW/KW	2458678.23237	0.00073	P	R	MB
DY Gru	EW/KW	2458776.01642	0.00099	P	V	MB
DY Gru	EW/KW	2458776.18324	0.00138	S	V	MB
V Gru	EW/KW	2458678.20098	0.00031	P	G	NB
V Gru	EW/KW	2458727.99620	0.00110	P	G	NB
V Gru	EW/KW	2458730.17521	0.00052	S	G	NB
SZ Hor	EW/KW	2458823.06965	0.00006	P	V	RJ
SZ Hor	EW/EK	2458828.07006	0.00006	P	V	RJ
BO Ind	EW	2458680.04546	0.00236	S	V	MB
BO Ind	EW	2458681.25973	0.00237	S	V	MB
BO Ind	EW	2458682.07175	0.00219	S	V	MB
BO Ind	EW	2458682.27209	0.00239	P	V	MB

Table continued on following pages

Appendix A: Minima estimates (cont.).

Identifier	*Type*	*HJD of min.*	*Error*	*Min.*	*Filter*	*Observer*
CU Ind	EW	2458735.02180	0.00087	S	R	MB
CU Ind	EW	2458735.18860	0.00099	P	R	MB
DD Ind	EW	2458728.16121	0.00069	S	V	MB
DD Ind	EW	2458729.97456	0.00072	S	V	MB
DD Ind	EW	2458730.15635	0.00072	P	V	MB
DD Ind	EW	2458731.96997	0.00133	P	R	MB
DD Ind	EW	2458731.97036	0.00126	P	I	MB
ST Ind	EW/KW	2458715.08663	0.00081	P	V	MB
ST Ind	EW/KW	2458728.95241	0.00077	S	V	MB
ST Ind	EW/KW	2458729.15346	0.00087	P	V	MB
TV Ind	EB	2458719.06029	0.00110	P	V	MB
TV Ind	EB	2458731.16962	0.00114	P	V	MB
GG Lup	EA	2458592.03938	0.00122	P	I	MB
GG Lup	EA	2458600.19409	0.00154	S	I	MB
GG Lup	EA	2458676.02807	0.00228	S	V	MB
RR Men	EA/D	2458516.13901	0.00150	P	r'	TR
XY Men	EB/KE	2458507.03335	0.00190	P	r'	TR
DG Mic	EA	2458707.02077	0.00032	P	V	NB
DI Mic	EA	2458686.05352	0.00146	S	r'	TR
BR Mus	EW/KE	2458586.08245	0.00137	P	r'	TR
BR Mus	EW/KE	2458610.02510	0.00008	P	V	RJ
BS Mus	EB/KE	2458576.07301	0.00018	P	V	RJ
eta Mus	EA	2458602.21272	0.00457	P	I	MB
eta Mus	EA	2458678.89444	0.00437	P	I	MB
TU Mus	EB/KE	2458556.03646	0.00020	S	V	RJ
TU Mus	EB/KE	2458617.07656	0.00016	S	V	RJ
TU Mus	EB/KE	2458619.15787	0.00012	P	V	RJ
TV Mus	EW/KW	2458575.09753	0.00150	P	r'	TR
TV Mus	EW/KW	2458580.22234	0.00120	S	r'	TR
TW Mus	EW/KW	2458538.24476	0.00121	S	r'	TR
V0398 Nor	EA	2458656.91950	0.00310	P	V	NB
EZ Oct	EW/KW	2458592.02865	0.00008	P	V	RJ
EZ Oct	EW/KW	2458592.17046	0.00007	S	V	RJ
EZ Oct	EW/KW	2458618.04283	0.00006	S	V	RJ
EZ Oct	EW/KW	2458756.97994	0.00005	S	V	RJ
EZ Oct	EW/KW	2458757.12349	0.00006	P	V	RJ
VV Ori	EA/KE	2458510.04224	0.00532	P	V	MB
ASASSN-V J184530.00-593235.0 (Pav)	EA:	2458711.12866	0.00191		R	MB
BF Pav	EW	2458701.99496	0.00036	S	R	MB
BF Pav	EW	2458702.14641	0.00041	P	R	MB
BF Pav	EW	2458710.91366	0.00051	P	R	MB
BF Pav	EW	2458711.06455	0.00053	S	R	MB
BF Pav	EW	2458713.93679	0.00075	P	V	MB
BF Pav	EW	2458713.93689	0.00077	P	R	MB
BF Pav	EW	2458713.93704	0.00086	P	I	MB
BF Pav	EW	2458714.08754	0.00075	S	I	MB
BF Pav	EW	2458714.08756	0.00082	S	V	MB
BF Pav	EW	2458714.08782	0.00073	S	R	MB
BF Pav	EW	2458716.96002	0.00042	P	V	MB
BF Pav	EW	2458717.11078	0.00050	S	V	MB
V0401 Pav	EW	2458621.06321	0.00061	P	r'	TR
V0401 Pav	EW	2458621.22654	0.00064	S	r'	TR
AD Phe	EW/KW	2458785.03012	0.00008	P	V	RJ
AD Phe	EW/KW	2458815.04430	0.00008	P	V	RJ
AE Phe	EW/KW	2458775.05009	0.00123	S	V	MB
BQ Phe	EW	2458780.07172	0.00010	S	V	RJ
GY Pup	EW/KW	2458517.08537	0.00800	P	r'	TR
GZ Pup	EW/KW	2458487.02517	0.00160	P	V	TR
GZ Pup	EW/KW	2458487.18540	0.00090	S	V	TR
GZ Pup	EW/KW	2458513.12673	0.00110	S	V	TR
HI Pup	EW/KW	2458490.05477	0.00150	P	V	TR
NO Pup	EA/KE:	2458494.97609	0.00461	S	R	MB
NO Pup	EA/KE:	2458498.12561	0.00134	P	R	MB
V0410 Pup	EB	2458488.02543	0.00611	S	R	MB
V0410 Pup	EB	2458494.15991	0.00505	S	R	MB
V0410 Pup	EB	2458548.04227	0.00393	P	R	MB

Table continued on next page

Appendix A: Minima estimates (cont.).

Identifier	*Type*	*HJD of min.*	*Error*	*Min.*	*Filter*	*Observer*
V0653 Pup	EW	2458485.17682	0.00150	S	r'	TR
V0653 Pup	EW	2458486.14701	0.00150	P	r'	TR
CP Scl	EW	2458778.05987	0.00073	S	V	MB
CP Scl	EW	2458778.21715	0.00098	P	V	MB
CW Scl	EW	2458779.05251	0.00087	S	V	MB
UY Scl	EW	2458759.18866	0.00065	S	V	MB
UY Scl	EW	2458760.10020	0.00056	P	V	MB
UY Scl	EW	2458775.03874	0.00048	P	V	MB
UY Scl	EW	2458775.94910	0.00064	S	V	MB
UY Scl	EW	2458776.13181	0.00068	P	V	MB
V0760 Sco	EA/DM	2458714.98705	0.00022	P	V	NB
V0954 Sco	EB	2458684.01785	0.00038	P	V	NB
RS Sgr	EA/SD	2458688.97438	0.00024	P	V	NB
V2509 Sgr	EB/KE	2458610.17480	0.00630	S	G	NB
V2509 Sgr	EB/KE	2458683.02100	0.00220	S	V	NB
QW Tel	EW	2458681.02766	0.00051	P	V	NB
V0343 Tel	EB	2458705.97525	0.00055	P	V	NB
GN TrA	EA/KE	2458701.06456	0.00218	S	V	MB
GN TrA	EA/KE	2458714.89195	0.00087	P	V	MB
AQ Tuc	EW	2458739.02394	0.00020	S	V	RJ
BU Vel	EW	2458515.04053	0.00120	P	V	TR
FM Vel	EW/KW	2458506.10282	0.00110	S	r'	TR
FM Vel	EW/KW	2458538.04364	0.00100	S	r'	TR
FM Vel	EW/KW	2458539.01810	0.00100	P	r'	TR
FM Vel	EW/KW	2458539.21201	0.00090	S	r'	TR
V0362 Vel	EW	2458610.01938	0.00013	S	G	NB

Recent Minima of 244 Eclipsing Binary Stars

Gerard Samolyk
P.O. Box 20677, Greenfield, WI 53220; gsamolyk@wi.rr.com

Received September 8, 2020; accepted September 8, 2020

Abstract This paper continues the publication of times of minima for eclipsing binary stars. Times of minima determined from observations received by the AAVSO Eclipsing Binaries Section from February 2020 through July 2020 are presented.

1. Recent observations

The accompanying list contains times of minima calculated from recent CCD observations made by participants in the AAVSO's eclipsing binary program. These observations were reduced by the observers or the writer using the method of Kwee and van Woerden (1956).

The linear elements in the *General Catalogue of Variable Stars* (GCVS; Kholopov *et al.* 1985) were used to compute the O–C values for most stars. For a few exceptions where the GCVS elements are missing or are in significant error, light elements from another source are used: CD Cam (Baldwin and Samolyk 2007), AC CMi (Samolyk 2008), DV Cep (Frank and Lichtenknecker 1987), Z Dra (Danielkiewicz-Krosniak and Kurpińska-Winiarska 1996), DF Hya (Samolyk 1992), DK Hya (Samolyk 1990), EF Ori (Baldwin and Samolyk 2005), GU Ori (Samolyk 1985).

The light elements used for EK Aqr, HV Aqr, IN Boo, LM Boo, EH Cnc, CX CMa, BM CMi, AV CrB, LS Del, MR Del, V728 Her, WZ Leo, XY LMi, HI Mon, V2612 Oph, V351 Peg, DS Psc, DV Psc, DZ Psc, AS Ser, V1123 Tau, BS UMa, HT Vir, and PY Vir are from Kreiner (2004).

The light elements used for XX Ant, BV Ant, DD Aqr, GK Aqr, AH Aur, XY Boo, DN Boo, IK Boo, IL Boo, FV CVn, CW CMi, V1297 Cas, V2181 Cyg, V1065 Her, V1097 Her, V1167 Her, V470 Hya, XX Leo, GV Leo, HI Leo, VW LMi, AE LMi, V502 Oph, V2610 Oph, SW Pyx, GR Vir, and IR Vir are from Paschke (2014).

The light elements used for V407 Peg are from Nelson (2014).

The light elements used for NY Boo, V804 Cep, V425 Dra, V409 Hya, EV Lyr, and SU Pyx are from the AAVSO VSX site (Watson *et al.* 2014). O–C values listed in this paper can be directly compared with values published in the AAVSO *Observed Minima Timings of Eclipsing Binaries* monographs. The standard error is included when available. Column F indicates the filter used. A "C" indicates a clear filter.

This list will be web-archived and made available through the AAVSO ftp site at ftp://ftp.aavso.org/public/datasets/gsamj482eb244.txt. This list, along with the eclipsing binary data from earlier AAVSO publications, is also included in the Lichtenknecker Database administrated by the Bundesdeutsche Arbeitsgemeinschaft für Veränderliche Sterne e. V. (BAV) at: http://www.bav-astro.de/LkDB/index.php?lang=en.

References

Baldwin, M. E., and Samolyk, G. 2005, *Observed Minima Timings of Eclipsing Binaries No. 10*, AAVSO, Cambridge, MA.

Baldwin, M. E., and Samolyk, G. 2007, *Observed Minima Timings of Eclipsing Binaries No. 12*, AAVSO, Cambridge, MA.

Danielkiewicz-Krosniak, E, Kurpińska-Winiarska, M., eds. 1996, *Rocznik Astron.* (SAC 68), **68**, 1.

Frank, P., and Lichtenknecker, D. 1987, *BAV Mitt.*, No. 47, 1.

Kholopov, P. N., *et al.* 1985, *General Catalogue of Variable Stars*, 4th ed., Moscow.

Kreiner, J. M. 2004, *Acta Astron.*, **54**, 207 (http://www.as.up.krakow.pl/ephem/).

Kwee, K. K., and van Woerden, H. 1956, *Bull. Astron. Inst. Netherlands*, **12**, 327.

Nelson, R. 2014, Eclipsing Binary O–C Files (http://www.aavso.org/bob-nelsons-o-c-files).

Paschke, A. 2014, "O–C Gateway" (http://var.astro.cz/ocgate/).

Samolyk, G. 1985, *J. Amer. Assoc. Var. Star Obs.*, **14**, 12.

Samolyk, G. 1990, *J. Amer. Assoc. Var. Star Obs.*, **19**, 5.

Samolyk, G. 1992, *J. Amer. Assoc. Var. Star Obs.*, **21**, 111.

Samolyk, G. 2008, *J. Amer. Assoc. Var. Star Obs.*, **36**, 171.

Watson, C., Henden, A. A., and Price, C. A. 2014, AAVSO International Variable Star Index VSX (Watson+, 2006–2014; http://www.aavso.org/vsx).

Table 1. Recent times of minima of stars in the AAVSO eclipsing binary program.

Star	*JD (min) Hel. 2400000 +*	*Cycle*	*O–C (day)*	*F*	*Observer*	*Standard Error (day)*	*Star*	*JD (min) Hel. 2400000 +*	*Cycle*	*O–C (day)*	*F*	*Observer*	*Standard Error (day)*
RT And	59055.6757	28483	–0.0126	V	G. Samolyk	0.0001	RU Cnc	58988.4709	3572	–0.1622	V	S. Cook	0.0018
WZ And	58884.3422	25892	0.0856	V	T. Arranz	0.0002	TU Cnc	58957.5267	3040	–0.0187	V	S. Cook	0.0008
BX And	58890.6157	36652	–0.1094	V	G. Samolyk	0.0002	WY Cnc	58904.3328	39249	–0.0477	V	X. Miret	0.0002
XX Ant	58944.7797	23088.5	–0.0013	V	S. Cook	0.0050	WY Cnc	58904.3330	39249	–0.0476	V	L. Corp	0.0004
BV Ant	58993.6791	1543	–0.0925	V	S. Cook	0.0009	WY Cnc	58923.4080	39272	–0.0481	V	T. Arranz	0.0001
SU Aqr	58763.6999	22422	0.0054	C	G. Frey	0.0003	XZ Cnc	58903.3440	8086	0.0198	V	X. Miret	0.0005
CX Aqr	59058.8609	40658	0.0190	V	G. Samolyk	0.0001	XZ Cnc	58923.3536	8114	0.0186	V	T. Arranz	0.0001
CZ Aqr	59058.8545	18183	–0.0705	V	G. Samolyk	0.0001	EH Cnc	58900.3679	15310	–0.0092	V	X. Miret	0.0005
DD Aqr	58762.6853	15168	–0.0020	C	G. Frey	0.0002	FV CVn	58936.4796	18680	–0.0106	V	G. Coates	0.0001
EK Aqr	58787.6787	20512.5	0.0259	C	G. Frey	0.0003	R CMa	58930.6321	12889	0.1340	V	G. Samolyk	0.0002
GK Aqr	58768.6994	37030	0.0269	C	G. Frey	0.0003	RT CMa	58904.3778	24950	–0.7806	V	T. Arranz	0.0001
HV Aqr	59049.4640	17490	0.0033	V	L. Corp	0.0007	TZ CMa	58898.6074	16623	–0.2305	V	G. Samolyk	0.0002
HV Aqr	59057.5115	17511.5	0.0000	V	L. Corp	0.0004	TZ CMa	58904.3943	16626	–0.1779	V	T. Arranz	0.0002
KO Aql	59054.7251	5994	0.1070	V	G. Samolyk	0.0003	CX CMa	58956.6698	6763	0.0049	V	S. Cook	0.0004
KP Aql	59006.8428	5526.5	–0.0244	V	G. Samolyk	0.0001	XZ CMi	58908.6436	28445	0.0057	V	G. Samolyk	0.0001
OO Aql	58947.9314	40124.5	0.0748	V	R. Sabo	0.0001	XZ CMi	58930.6381	28483	0.0054	V	G. Samolyk	0.0001
OO Aql	59014.8282	40256.5	0.0756	V	G. Samolyk	0.0001	XZ CMi	58932.3750	28486	0.0059	V	T. Arranz	0.0001
OO Aql	59044.4764	40315	0.0766	V	L. Corp	0.0002	YY CMi	58933.5988	28254	0.0192	V	G. Samolyk	0.0002
OO Aql	59063.4798	40352.5	0.0755	V	T. Arranz	0.0001	AC CMi	58915.6219	7999	0.0052	V	G. Samolyk	0.0002
V343 Aql	59015.8152	16574	–0.0519	V	G. Samolyk	0.0002	AK CMi	58915.6531	27945	–0.0245	V	G. Samolyk	0.0001
V343 Aql	59050.8634	16593	–0.0512	V	G. Samolyk	0.0002	AK CMi	58943.3812	27994	–0.0254	V	T. Arranz	0.0001
RY Aur	58912.6192	7567	0.0225	V	G. Samolyk	0.0001	AK CMi	58945.6448	27998	–0.0254	V	G. Samolyk	0.0001
TT Aur	58886.6781	28246	–0.0111	V	G. Samolyk	0.0002	BH CMi	58539.6919	10799	0.0018	C	G. Frey	0.0002
AH Aur	58907.3917	68015.5	–0.0229	V	T. Arranz	0.0002	CW CMi	58540.6864	20160.5	–0.0622	C	G. Frey	0.0001
AP Aur	58915.6052	28930	1.7856	V	G. Samolyk	0.0002	AB Cas	58891.5590	11835	0.1449	V	G. Samolyk	0.0001
AP Aur	58916.4622	28931.5	1.7886	V	T. Arranz	0.0003	IR Cas	59055.8381	24522	0.0167	V	G. Samolyk	0.0001
AP Aur	58934.3985	28963	1.7916	V	T. Arranz	0.0002	V364 Cas	59047.8215	16016.5	–0.0251	V	G. Samolyk	0.0002
CL Aur	58922.4047	20858	0.1880	V	T. Arranz	0.0001	V1297 Cas	59024.4912	6092	–0.0017	V	S. Dufoer	0.0003
EP Aur	58894.6290	55135	0.0209	V	G. Samolyk	0.0002	SU Cep	59041.8243	36295	0.0064	V	G. Samolyk	0.0001
EP Aur	58896.4028	55138	0.0217	V	T. Arranz	0.0002	WZ Cep	59047.6829	74278.5	–0.2175	V	G. Samolyk	0.0002
HP Aur	58894.6812	11342.5	0.0750	V	G. Samolyk	0.0002	ZZ Cep	59018.8019	14516	–0.0179	V	G. Samolyk	0.0002
HP Aur	58904.6447	11349.5	0.0788	V	S. Cook	0.0008	DK Cep	59044.7240	25818	0.0296	V	G. Samolyk	0.0001
HP Aur	58905.3521	11350	0.0748	V	T. Arranz	0.0001	DV Cep	59011.7242	10541	–0.0052	V	G. Samolyk	0.0002
SS Boo	58973.8654	5032	7.5311	V	G. Samolyk	0.0001	DV Cep	59033.7999	10560	–0.0070	V	G. Samolyk	0.0006
TU Boo	58924.8680	79740	–0.1654	V	G. Samolyk	0.0003	EG Cep	59014.7379	30150	0.0072	V	G. Samolyk	0.0004
TU Boo	58956.6477	79838	–0.1658	TG	G. Conrad	0.0005	V804 Cep	59023.3782	21993.5	–0.0185	V	A. Beck	0.0005
TY Boo	58891.8194	76971.5	0.0602	V	G. Samolyk	0.0003	TT Cet	58811.6935	54050	–0.0854	C	G. Frey	0.0002
TY Boo	58949.6985	77154	0.0599	V	G. Samolyk	0.0001	RW Com	58886.9219	79481	0.0161	V	G. Samolyk	0.0002
TY Boo	58955.7250	77173	0.0605	TG	G. Conrad	0.0003	RW Com	58943.4106	79719	0.0165	V	X. Miret	0.0001
TY Boo	59006.6267	77333.5	0.0600	V	G. Samolyk	0.0003	RZ Com	58908.8109	71110.5	0.0573	V	G. Samolyk	0.0001
TY Boo	59021.3730	77380	0.0590	V	T. Arranz	0.0004	RZ Com	58973.6354	71302	0.0579	V	G. Samolyk	0.0001
TY Boo	59021.5313	77380.5	0.0587	V	T. Arranz	0.0001	RZ Com	58996.4844	71369.5	0.0578	V	T. Arranz	0.0002
TZ Boo	58893.9004	64816.5	0.0578	V	G. Samolyk	0.0001	RZ Com	59008.6707	71405.5	0.0579	V	G. Samolyk	0.0001
TZ Boo	58941.8929	64978	0.0587	V	G. Samolyk	0.0002	SS Com	58893.9168	82100.5	0.9854	V	G. Samolyk	0.0002
TZ Boo	59033.4174	65286	0.0573	V	T. Arranz	0.0001	SS Com	58900.9357	82117.5	0.9869	V	K. Menzies	0.0005
VW Boo	58898.8899	80992.5	–0.2980	V	G. Samolyk	0.0001	SS Com	58972.7661	82291.5	0.9915	V	G. Samolyk	0.0003
VW Boo	58957.7678	81164.5	–0.3000	V	G. Samolyk	0.0001	CC Com	58908.8129	87795.5	–0.0324	V	G. Samolyk	0.0001
VW Boo	59017.6722	81339.5	–0.3025	V	G. Samolyk	0.0002	CC Com	58954.3837	88002	–0.0333	V	X. Miret	0.0002
XY Boo	58599.7012	50317	0.0204	C	G. Frey	0.0001	CC Com	58966.6325	88057.5	–0.0326	V	G. Samolyk	0.0002
ZZ Boo	57494.6882	3792	0.0758	V	N. Simmons	0.0003	CC Com	58989.3625	88160.5	–0.0333	V	T. Arranz	0.0004
ZZ Boo	58949.7882	4083.5	0.0824	V	G. Samolyk	0.0003	CC Com	58989.4721	88161	–0.0340	V	T. Arranz	0.0001
AD Boo	58970.6929	16953	0.0380	V	G. Samolyk	0.0001	CC Com	59012.6442	88266	–0.0340	V	G. Samolyk	0.0001
AD Boo	59000.6901	16982	0.0375	V	G. Samolyk	0.0004	U CrB	58985.8031	12235	0.1480	V	G. Samolyk	0.0002
AQ Boo	58978.4144	19446	–0.0163	V	X. Miret	0.0001	RW CrB	58949.7925	25052	0.0039	V	G. Samolyk	0.0001
AQ Boo	58989.4087	19479	–0.0155	V	X. Miret	0.0002	TW CrB	58970.6693	35784	0.0601	V	G. Samolyk	0.0001
DN Boo	58605.6888	8280	0.0050	C	G. Frey	0.0003	AV CrB	58253.8362	18669.5	0.0028	V	V. Petriew	0.0001
IK Boo	58601.6839	17218	–0.0279	C	G. Frey	0.0002	AV CrB	58254.7609	18672.5	0.0030	V	V. Petriew	0.0002
IK Boo	58956.6305	18389	–0.0324	TG	G. Conrad	0.0006	AV CrB	58254.9130	18673	0.0010	V	V. Petriew	0.0003
IL Boo	58601.6839	20618.5	–0.0624	C	G. Frey	0.0002	W Crv	58901.8340	49613.5	0.0197	V	G. Samolyk	0.0003
IN Boo	59062.3523	22964	–0.0023	V	A. Beck	0.0001	V Crt	58949.6374	25002	–0.0015	V	G. Samolyk	0.0002
LM Boo	58907.5255	19539	0.0012	V	G. Coates	0.0001	V Crt	58982.6334	25049	–0.0012	V	G. Samolyk	0.0002
NY Boo	59062.3895	23427	0.0452	V	A. Beck	0.0003	Z Crt	58953.8204	9092	–0.0521	V	S. Cook	0.0014
i Boo	58999.7226	71493.5	0.1362	V	N. Simmons	0.0002	RV Crt	58972.7166	14041	0.1016	V	S. Cook	0.0011
SV Cam	58990.6878	27646	0.0608	V	G. Samolyk	0.0002	ZZ Cyg	59000.8228	22272	–0.0796	V	G. Samolyk	0.0001
AL Cam	58959.6520	24503	–0.0231	V	G. Samolyk	0.0001	ZZ Cyg	59058.6551	22364	–0.0800	V	G. Samolyk	0.0001
CD Cam	58908.6348	8042.5	–0.0157	V	G. Samolyk	0.0006	AE Cyg	58972.8392	14844	–0.0043	V	G. Samolyk	0.0002

Table continued on following pages

Table 1. Recent times of minima of stars in the AAVSO eclipsing binary program, cont.

Star	JD (min) Hel. 2400000 +	Cycle	O–C (day)	F	Observer	Standard Error (day)
BR Cyg	59014.7129	13114	0.0012	V	G. Samolyk	0.0001
BR Cyg	59058.6878	13147	0.0015	V	G. Samolyk	0.0001
DK Cyg	58970.8628	44554	0.1322	V	G. Samolyk	0.0001
KR Cyg	59035.7977	35413	0.0275	V	G. Samolyk	0.0004
V387 Cyg	58960.8787	48354	0.0194	V	G. Samolyk	0.0001
V387 Cyg	58985.8619	48393	0.0193	V	G. Samolyk	0.0001
V387 Cyg	59055.6865	48502	0.0189	V	G. Samolyk	0.0002
V388 Cyg	59006.8051	19852	–0.1387	V	G. Samolyk	0.0001
V401 Cyg	59025.7540	26068	0.0979	V	G. Samolyk	0.0003
V456 Cyg	58970.8541	15776	0.0530	V	G. Samolyk	0.0001
V466 Cyg	58981.8219	21707.5	0.0077	V	G. Samolyk	0.0001
V466 Cyg	59041.6593	21750.5	0.0077	V	G. Samolyk	0.0001
V477 Cyg	59008.8216	6314.5	–0.5144	V	G. Samolyk	0.0004
V477 Cyg	59012.8146	6316	–0.0419	V	G. Samolyk	0.0001
V488 Cyg	59035.7369	53238	–0.2652	V	G. Samolyk	0.0005
V548 Cyg	59033.7745	8075	0.0222	V	G. Samolyk	0.0004
V704 Cyg	59017.8299	36934	0.0394	V	G. Samolyk	0.0003
V1034 Cyg	59016.8144	16458	0.0250	V	K. Menzies	0.0004
V2181 Cyg	59035.7194	14437	–0.009	V	G. Samolyk	0.0011
YY Del	59018.8493	20249	0.0133	V	G. Samolyk	0.0002
LS Del	59049.5004	18000	–0.0076	V	L. Corp	0.0009
MR Del	59035.5118	12527	–0.0125	V	L. Corp	0.0002
Z Dra	58891.7049	6665	–0.0050	V	G. Samolyk	0.0001
Z Dra	58944.6451	6704	–0.0048	V	G. Samolyk	0.0001
Z Dra	58982.6531	6732	–0.0050	V	G. Samolyk	0.0001
RZ Dra	58901.9332	26729	0.0719	V	G. Samolyk	0.0001
RZ Dra	58949.8596	26816	0.0723	V	G. Samolyk	0.0001
RZ Dra	59012.6596	26930	0.0727	V	G. Samolyk	0.0001
TW Dra	59057.4311	5316	–0.0626	V	T. Arranz	0.0001
UZ Dra	59011.7317	5348	0.0035	V	G. Samolyk	0.0001
AI Dra	58981.7536	13088	0.0411	V	G. Samolyk	0.0001
AI Dra	59017.7178	13118	0.0409	V	N. Simmons	0.0001
BH Dra	58991.7623	10440	–0.0066	V	K. Menzies	0.0003
V425 Dra	58996.6974	814	–0.0157	V	S. Cook	0.0009
TZ Eri	58895.3822	6324	0.3622	V	T. Arranz	0.0001
YY Eri	58890.5568	53838.5	0.1700	V	G. Samolyk	0.0002
YY Eri	58901.3262	53872	0.1693	V	T. Arranz	0.0001
RW Gem	58863.7728	14155	0.0049	V	G. Samolyk	0.0003
WW Gem	58907.5809	26598	0.0269	V	G. Samolyk	0.0003
AF Gem	58897.6946	25521	–0.0672	V	S. Cook	0.0008
AF Gem	58901.4254	25524	–0.0669	V	T. Arranz	0.0001
AF Gem	58916.3477	25536	–0.0667	V	T. Arranz	0.0001
AY Gem	58962.6008	7313	–0.0662	V	S. Cook	0.0007
SZ Her	59001.7920	20948	–0.0359	V	G. Samolyk	0.0001
SZ Her	59048.4236	21005	–0.0359	V	T. Arranz	0.0001
TT Her	58990.8358	20826	0.0443	V	K. Menzies	0.0003
TU Her	58966.7198	6575	–0.2705	V	G. Samolyk	0.0004
TU Her	59032.4603	6604	–0.2730	V	T. Arranz	0.0003
UX Her	59006.8099	12483	0.1630	V	G. Samolyk	0.0001
UX Her	59042.4337	12506	0.1633	V	T. Arranz	0.0001
UX Her	59059.4720	12517	0.1643	V	T. Arranz	0.0001
AK Her	58658.7166	39078	0.0195	C	G. Frey	0.0002
AK Her	59042.5145	39988.5	0.0216	V	L. Corp	0.0003
CC Her	58638.6944	10940	0.3290	C	G. Frey	0.0003
CC Her	58976.8400	11135	0.3434	V	G. Samolyk	0.0002
CC Her	59044.4698	11174	0.3470	V	T. Arranz	0.0001
CT Her	59014.7548	9232	0.0106	V	G. Samolyk	0.0002
CT Her	59034.4053	9243	0.0110	V	T. Arranz	0.0002
CT Her	59050.4828	9252	0.0112	V	T. Arranz	0.0003
HS Her	59019.6455	8464	–0.0383	V	G. Samolyk	0.0007
V728 Her	59043.6754	13884	0.0257	V	G. Samolyk	0.0005
V1065 Her	58655.7359	18498	–0.0144	C	G. Frey	0.0002
V1097 Her	58657.7369	17166	0.0131	C	G. Frey	0.0002
V1167 Her	58998.3898	17471.5	–0.0135	V	X. Miret	0.0002
SY Hya	58949.5267	7856	–0.169	V	S. Cook	0.0006
TY Hya	58967.6081	5254	–0.160	V	S. Cook	0.0019
WY Hya	58912.5983	25616.5	0.0423	V	G. Samolyk	0.0001
AV Hya	58912.6574	32542	–0.1232	V	G. Samolyk	0.0002
AV Hya	58953.6632	32602	–0.1217	V	G. Samolyk	0.0004
DF Hya	58907.6074	48758.5	0.0162	V	G. Samolyk	0.0001
DF Hya	58907.7726	48759	0.0161	V	G. Samolyk	0.0001
DF Hya	58918.3528	48791	0.0170	V	T. Arranz	0.0001
DF Hya	58933.3949	48836.5	0.0165	V	T. Arranz	0.0001
DF Hya	58944.6347	48870.5	0.0157	V	G. Samolyk	0.0003
DI Hya	58941.6307	45139	–0.0394	V	G. Samolyk	0.0003
DK Hya	58943.4058	30847	0.0000	V	T. Arranz	0.0001
GK Hya	58938.7630	12258	–0.1834	V	S. Cook	0.0014
V409 Hya	58543.6388	11411	0.0723	C	G. Frey	0.0003
V409 Hya	58551.6644	11428	0.0693	C	G. Frey	0.0002
V470 Hya	58912.6782	15708.5	0.0187	V	G. Samolyk	0.0005
AR Lac	59047.7342	8801	–0.0512	V	G. Samolyk	0.0002
Y Leo	58933.6237	8005	–0.0738	V	G. Samolyk	0.0001
RT Leo	58960.9038	4715	–0.0100	V	S. Cook	0.0012
UU Leo	58924.6393	8053	0.2298	V	G. Samolyk	0.0002
UU Leo	58936.3977	8060	0.2300	V	T. Arranz	0.0002
UV Leo	58902.4648	34098	0.0476	V	L. Corp	0.0002
UV Leo	58902.4649	34098	0.0477	V	X. Miret	0.0007
UV Leo	58924.6685	34135	0.0482	V	G. Samolyk	0.0003
UV Leo	58978.6751	34225	0.0472	V	G. Samolyk	0.0001
UZ Leo	58902.5424	30907.5	0.0116	V	L. Corp	0.0007
VZ Leo	58542.7083	25120	–0.0464	C	G. Frey	0.0001
VZ Leo	58966.6856	25509	–0.0426	V	G. Samolyk	0.0005
VZ Leo	58975.4056	25517	–0.0418	V	T. Arranz	0.0002
VZ Leo	59002.6507	25542	–0.0444	V	S. Cook	0.0015
WZ Leo	58907.7764	4550	–0.0003	V	G. Samolyk	0.0002
XX Leo	58983.6465	10599	–0.0279	V	S. Cook	0.0006
XY Leo	58959.6316	48874	0.1891	V	G. Samolyk	0.0002
GV Leo	58653.7026	22117	–0.0529	C	G. Frey	0.0002
HI Leo	58567.7223	18701	0.0164	C	G. Frey	0.0001
T LMi	58941.4190	4485	–0.1332	V	T. Arranz	0.0001
VW LMi	58936.3763	21853.5	0.0341	V	T. Arranz	0.0001
XY LMi	58911.4426	14675	–0.0091	V	G. Coates	0.0002
AE LMi	58901.3906	14038	0.0157	V	X. Miret	0.0005
RR Lep	58885.3756	31142	–0.0452	V	T. Arranz	0.0002
RR Lep	58896.3596	31154	–0.0463	V	T. Arranz	0.0003
SS Lib	59018.6596	12422	0.1847	V	G. Samolyk	0.0003
RY Lyn	58930.5917	11180	–0.0171	V	G. Samolyk	0.0001
UZ Lyr	59018.6533	8105	–0.0534	V	G. Samolyk	0.0002
UZ Lyr	59056.4767	8125	–0.0555	V	T. Arranz	0.0001
EV Lyr	58058.3065	3380	0.0015	V	T. Arranz	0.0001
EW Lyr	59006.6500	16681	0.3046	V	G. Samolyk	0.0001
EW Lyr	59043.6766	16700	0.3055	V	G. Samolyk	0.0001
FL Lyr	58972.8279	9527	–0.0016	V	G. Samolyk	0.0002
RU Mon	58893.6862	4784.5	–0.7401	V	G. Samolyk	0.0002
TU Mon	58954.7136	4929	–0.0739	V	S. Cook	0.0011
AT Mon	58917.6259	15924	0.0114	V	G. Samolyk	0.0003
BB Mon	58917.3756	43996	–0.0036	V	T. Arranz	0.0002
BO Mon	58901.6563	6918	–0.0078	V	G. Samolyk	0.0001
HI Mon	58945.6026	4093.5	–0.0059	V	S. Cook	0.0007
U Oph	58985.8099	8686	–0.0053	V	G. Samolyk	0.0005
SX Oph	59046.4217	12430	–0.0015	V	T. Arranz	0.0002
SX Oph	59054.6742	12434	–0.0022	V	G. Samolyk	0.0002
V456 Oph	58671.7130	16510	0.0276	C	G. Frey	0.0001
V501 Oph	58985.8199	29004	–0.0085	V	G. Samolyk	0.0002
V501 Oph	59050.6715	29071	–0.0096	V	G. Samolyk	0.0001
V502 Oph	58999.4265	23157.5	–0.0019	V	L. Corp	0.0004
V502 Oph	59001.4696	23162	0.0009	V	L. Corp	0.0009
V508 Oph	59011.7730	40399	–0.0272	V	G. Samolyk	0.0001
V508 Oph	59047.4593	40502.5	–0.0269	V	T. Arranz	0.0001
V508 Oph	59058.4931	40534.5	–0.0265	V	T. Arranz	0.0001
V839 Oph	59051.4963	45484	0.3403	V	T. Arranz	0.0001
V1010 Oph	59025.7265	30371	–0.2155	V	G. Samolyk	0.0001

Table continued on next page

Table 1. Recent times of minima of stars in the AAVSO eclipsing binary program, cont.

Star	*JD (min) Hel. 2400000 +*	*Cycle*	*O–C (day)*	*F*	*Observer*	*Standard Error (day)*	*Star*	*JD (min) Hel. 2400000 +*	*Cycle*	*O–C (day)*	*F*	*Observer*	*Standard Error (day)*
V2610 Oph	59042.4691	15644.5	–0.0479	V	L. Corp	0.0008	CT Tau	58917.6030	20265	–0.0720	V	G. Samolyk	0.0002
V2612 Oph	59057.4558	17472	–0.0097	V	L. Corp	0.0009	EQ Tau	58908.5950	54769	–0.0449	V	G. Samolyk	0.0002
EF Ori	58891.5514	4039	0.0114	V	G. Samolyk	0.0003	HU Tau	58891.6788	8567	0.0374	V	G. Samolyk	0.0003
ER Ori	58899.3261	40795.5	0.1494	V	T. Arranz	0.0001	V781 Tau	58883.3189	43514	–0.0488	R	L. Corp	0.0005
ER Ori	58903.3497	40805	0.1507	V	T. Arranz	0.0001	V1123 Tau	58805.6573	15766	0.0171	C	G. Frey	0.0027
ET Ori	58890.5659	33868	–0.0040	V	G. Samolyk	0.0002	W UMa	58901.5925	39372	–0.1213	V	G. Samolyk	0.0001
ET Ori	58894.3696	33872	–0.0040	V	T. Arranz	0.0001	W UMa	58901.7587	39372.5	–0.1219	V	G. Samolyk	0.0003
FH Ori	58911.6122	15346	–0.4762	V	G. Samolyk	0.0002	W UMa	58901.9259	39373	–0.1215	V	G. Samolyk	0.0002
FL Ori	58884.3803	8728	0.0414	V	T. Arranz	0.0001	W UMa	58971.6550	39582	–0.1226	TG	G. Conrad	0.0001
FT Ori	58893.3677	5569	0.0235	V	T. Arranz	0.0001	TX UMa	58911.6383	4542	0.2629	V	G. Samolyk	0.0001
FT Ori	58915.4205	5576	0.0234	V	T. Arranz	0.0001	TY UMa	58911.6646	54659	0.4428	V	G. Samolyk	0.0002
FZ Ori	58900.3361	37191	–0.0238	V	T. Arranz	0.0002	TY UMa	58933.6458	54721	0.4426	TG	G. Conrad	0.0005
FZ Ori	58902.3380	37196	–0.0219	V	T. Arranz	0.0001	TY UMa	58988.4250	54875.5	0.4456	V	T. Arranz	0.0001
GU Ori	58891.5380	33614.5	–0.0715	V	G. Samolyk	0.0003	TY UMa	58998.7087	54904.5	0.4476	V	S. Cook	0.0004
GU Ori	58898.3643	33629	–0.0700	V	T. Arranz	0.0001	UX UMa	58898.8985	109147	–0.0021	V	G. Samolyk	0.0001
GU Ori	58902.3640	33637.5	–0.0711	V	T. Arranz	0.0002	UX UMa	58941.5765	109364	–0.0018	V	G. Samolyk	0.0002
U Peg	59068.4625	60187	–0.1762	V	L. Corp	0.0005	UX UMa	58941.7729	109365	–0.0020	V	G. Samolyk	0.0002
TY Peg	58772.7208	5925	–0.4667	C	G. Frey	0.0001	UX UMa	59005.4941	109689	–0.0023	V	T. Arranz	0.0005
BB Peg	59055.8370	42300	–0.0352	V	G. Samolyk	0.0003	VV UMa	58971.6962	19140	–0.0935	TG	G. Conrad	0.0004
BN Peg	58747.6667	34840	–0.0016	C	G. Frey	0.0002	XZ UMa	58935.4024	10445	–0.1560	V	T. Arranz	0.0002
BO Peg	58774.6754	22677	–0.0610	C	G. Frey	0.0001	XZ UMa	58975.7385	10478	–0.1565	TG	G. Conrad	0.0004
BX Peg	59013.7960	52844	–0.1379	V	K. Menzies	0.0006	BS UMa	58940.4271	14736.5	–0.0069	V	G. Coates	0.0001
DI Peg	58783.6616	19088	0.0145	C	G. Frey	0.0002	W UMi	59015.7385	14892	–0.2235	V	G. Samolyk	0.0003
DK Peg	58777.6827	8118	0.1693	C	G. Frey	0.0003	RU UMi	58924.6609	33011	–0.0137	V	G. Samolyk	0.0001
V351 Peg	58749.7009	17276	0.0520	C	G. Frey	0.0002	VV Vir	58966.7963	62191	–0.0514	V	G. Samolyk	0.0004
V407 Peg	57748.5327	1284.5	0.0809	V	K. Menzies	0.0002	VV Vir	58990.4405	62244	–0.0524	V	T. Arranz	0.0001
V407 Peg	58708.6766	2792	0.1259	C	G. Frey	0.0003	AG Vir	58953.7694	21040	–0.0170	V	G. Samolyk	0.0002
XZ Per	58903.6003	13369	–0.0737	V	K. Menzies	0.0001	AH Vir	58949.7043	32231.5	0.3062	V	G. Samolyk	0.0003
UV Psc	58810.6517	17890	–0.0231	C	G. Frey	0.0001	AK Vir	58941.7881	13711	–0.0434	V	G. Samolyk	0.0002
DS Psc	58775.7004	18323	–0.0011	C	G. Frey	0.0002	AW Vir	58953.6950	39353.5	0.0310	V	G. Samolyk	0.0004
DV Psc	58780.6807	20356	0.0116	C	G. Frey	0.0002	AW Vir	58998.4768	39480	0.0322	V	T. Arranz	0.0001
DZ Psc	58779.6956	17151	0.0291	C	G. Frey	0.0003	AW Vir	59006.6191	39503	0.0326	V	G. Samolyk	0.0004
UZ Pup	58933.3285	18015.5	–0.0116	V	T. Arranz	0.0002	AW Vir	59015.6463	39528.5	0.0329	V	G. Samolyk	0.0001
AV Pup	58895.7504	49821	0.2591	V	G. Samolyk	0.0002	AX Vir	58955.8307	44675	0.0287	V	G. Samolyk	0.0001
SU Pyx	58963.6312	2446	–0.0816	V	S. Cook	0.0011	AZ Vir	58899.8774	42679	–0.0198	V	K. Menzies	0.0001
SW Pyx	58974.6691	3926	0.0207	V	S. Cook	0.0019	AZ Vir	58955.8241	42839	–0.0195	V	G. Samolyk	0.0002
TV Pyx	58963.6312	37941.5	0.0910	V	S. Cook	0.0011	AZ Vir	58990.4417	42938	–0.0188	V	T. Arranz	0.0001
U Sge	59053.4965	12401	0.0248	V	T. Arranz	0.0001	BH Vir	58641.6946	18866	–0.0142	C	G. Frey	0.0002
V1968 Sgr	59055.7319	37701	–0.0216	V	G. Samolyk	0.0004	BH Vir	58957.8249	19253	–0.0132	V	G. Samolyk	0.0002
RS Sct	59043.6800	40328	0.0372	V	G. Samolyk	0.0001	BH Vir	58999.4832	19304	–0.0154	V	L. Corp	0.0003
AO Ser	59030.4172	28313	–0.0112	V	T. Arranz	0.0001	GR Vir	58640.7012	38978	0.0217	C	G. Frey	0.0004
AO Ser	59050.6425	28336	–0.0108	V	G. Samolyk	0.0001	GR Vir	59023.4178	40081	0.0270	V	T. Arranz	0.0001
AS Ser	58992.4405	13925	–0.0002	V	X. Miret	0.0001	HT Vir	58252.7164	14110.5	0.0003	C	G. Frey	0.0001
CC Ser	58949.8839	41602.5	1.1660	V	G. Samolyk	0.0003	IR Vir	58600.6783	23756	–0.0070	C	G. Frey	0.0001
CC Ser	58956.8507	41616	1.1667	V	K. Menzies	0.0002	PY Vir	58994.3857	20865	0.0083	V	L. Corp	0.0003
CC Ser	59015.6774	41730	1.1687	V	G. Samolyk	0.0003	AW Vul	59012.8457	15782	–0.0355	V	G. Samolyk	0.0001
CC Ser	59041.4806	41780	1.1716	V	T. Arranz	0.0002	BE Vul	59041.7665	12197	0.1048	V	G. Samolyk	0.0001
RZ Tau	58900.5982	51059	0.0967	V	G. Samolyk	0.0001	BO Vul	59018.7791	11835	–0.0115	V	G. Samolyk	0.0001
AM Tau	58898.5893	6676	–0.0777	V	G. Samolyk	0.0001	BS Vul	59033.8132	33116	–0.0360	V	G. Samolyk	0.0002
AQ Tau	58913.5967	24063	0.5247	V	G. Samolyk	0.0003	BT Vul	59054.6965	20726	0.0053	V	G. Samolyk	0.0001
CT Tau	58909.6009	20253	–0.0722	V	K. Menzies	0.0001	BU Vul	59041.6521	44830	0.0129	V	G. Samolyk	0.0001

Abstracts of Papers Presented at the Joint Meeting of the Society for Astronomical Sciences (SAS) and the American Association of Variable Star Observers (AAVSO 108th Spring Meeting), Held as an "Online Only" Event, May 30, June 13, 14, 20, and 21, 2020

Gaia Data Enables New Methods of Analysis and Discovery

John E. Hoot
SSC observatories, 1303 S. Ola Vista, San Clemente, CA 92672; jhoot@ssccorp.com

Abstract The release of highly precise parallax astrometry, proper motion, photometry, and spectral data from the European Space Agency's Gaia satellite makes possible a paradigm shift in the way we can target, analyze, and exploit small telescope spectroscopic and photometric observation. This paper explores employing data from ESA's Global Astrometric Interferometer for Astrophysics [Gaia] mission in conjunction with small telescope photometric and spectroscopic observations to develop several new and novel methods for exploring our galaxy, classifying and modeling stars, modeling the evolution of star clusters, and identifying candidate unique or variable stars for observation.

Beyond the Milky Way: Comparison Stars for Photometry in M31 and M33

John C. Martin
Henry R Barber Observatory, University of Illinois Springfield, Springfield, IL; Jmart5@uis.edu

Abstract At the start of the 20th century, professional astronomers had not imaged individual stars in the great spiral nebulae of Andromeda (M31) and Triangulum (M33). Present day, non-professional astronomers have the capability to regularly image individual luminous stars in both galaxies, attempting science that Edwin Hubble himself would have only dreamed of a century earlier. But obtaining calibrated photometry from images of M31 and M33 is significantly hindered by having too few reliable faint photometric comparison stars. We present an updated list of comparison stars fainter than 12th magnitude that the University of Illinois Springfield Luminous Stars Survey uses to measure photometry for luminous stars in M31 and M33. The list is derived from the AAVSO Photometric All Sky Survey (data release 10) and checked for accuracy and stability over the eight years of imaging in our survey. The list reliably yields ensemble photometry with better than 0.1 magnitude error for 20 × 20 arcminute fields covering the spiral arms of both galaxies.

Towards the Flux Calibration of Small Telescope Spectra

Wayne Green
Boulder Astronomy and Space Society, Boulder CO

Anthony Rodda
British Astronomical Society, London, United Kingdom

Clarke Yeager
Boulder Astronomy and Space Society, Boulder CO

Abstract We present a set of reference resources and machine-ready spectral data covering optical bands from UVA through 8000+ Angstroms, based on our literature/informatics search of bright spectro-photometric calibration sources suitable for small telescope investigations. These data are made available as ".dat" ASCII whitespace/column data with absolute units of ergs s^{-1} cm^{-2} Å. These catalogs have been translated and augmented for small telescope spectroscopy using additional data from SIMBAD, GAIA, and other references to produce a PostgreSQL database. We include a generic telluric line table and files suited to popular planning/operational planetarium programs. We discuss the salient aspects of each library reviewed. We include methodology to acquire spectral measurements of filters and lamp sources common with photometry and spectroscopy. These data and scripts are available through an MIT open source license via GitHUB/Docker and, to the extent possible, are platform agnostic.

The Role of 3D Printing in Spectrograph and Small Telescope Science

Anthony Rodda
British Astronomical Society, London, United Kingdom

Jerry Foote
Society for Astronomical Sciences, Ontario, CA, USA

Wayne Green
Society for Astronomical Sciences, Ontario, CA, USA, and Boulder Astronomy and Space Society, Boulder CO

Thomas Smith
AAVSO, Cambridge, MA, and Society for Astronomical Sciences, Ontario, CA, USA

Clarke Yeager
Society for Astronomical Sciences, Ontario, CA, USA, and Boulder Astronomy and Space Society, Boulder CO

Contributions from

Forrest Sims
Society for Astronomical Sciences, Ontario, CA, USA, and British Astronomical Society, London, United Kingdom

Robert Buchheim
AAVSO, Cambridge, MA, and Society for Astronomical Sciences, Ontario, CA, USA

Paul Gerlach

Abstract Anthony Rodda, following Paul Gerlach's LowSpec design, introduced this team to the power of 3D printing for astronomical purposes at the AAVSO Fall Conference in 2018. This was reinforced at the Sacramento Mountain Spectroscopy Workshop (SMSW-2) in Las Cruces, NM, in February 2019. We have created a shared repository which contains results, videos, and other resources in support of 3D spectroscopy located on GitHub. This paper offers considerations about calibration lamps, thermal expansion issues related to ABS, PETG, and other 3D media, optics, automation, telemetry, communications, and adapting to other focal-lengths.

Applying a Comprehensive, High-precision Catalog to Asteroid Light Curves

Eric Dose
New Mexico Mira Project, 3167 San Mateo Boulevars NE, #329, Albuquerque, NM 87110; astro@ericdose.com

Abstract The recently published ATLAS Reference Catalog 2 contains Gaia astrometry, including proper motions and neighboring-star flags, as well as high-precision photometric data, cross-calibrated over the entire sky, on 105 million stars to 16th magnitude. In the present approach to asteroid light curve generation from raw images, we gather all ATLAS comparison star candidates within a telescope's field of view, then automatically screen them for: magnitude range, magnitude uncertainty, color range, and absence of neighboring stars. The implementing software generates simple statistical plots to help the observer identify and optionally exclude: outlier comp stars, outlier individual comp observations, image-to-image zero-point fluctuations, and comp stars suspected of variability. This approach uses every fully qualified comp star in the asteroid's field of view—these typically number 30–80. The approach is rapid and so far has yielded light curves of high quality and has eliminated most need to adjust nightly zero-points.

Vetting The MOTESS-GNAT 1 Catalog

John E. Hoot
SSC Observatories, 1303 S. Ola Vista, San Clemente, CA 92672; jhoot@ssccorp.com

Abstract This paper presents a summary of the results of a five years study by SSC Observatories [SSCO] of short period variable star candidates in the MOTESS-GNAT 1 Catalog. It presents confirmation, light curves, and classification of 73 previously unconfirmed variable stars. Additionally, it merges SSCO's confirmations with other observers' confirmations to develop statistics on the predictive quality of MG1. It also presents a revised version of the catalog that includes updated periods, confirmation, and classification information from SSCO and other published sources designated as the Vetted-MOTESS-GNAT Candidate Variables Catalog [VMGC 2020].

An Array Photo-Polarimeter for Blazar Measurements

Gary M. Cole
Starphysics Observatory, Reno, NV, and Visiting Scholar, UC San Diego Center for Astrophysics and Space Sciences; garycole@mac.com

Andrew Friedman
Assistant Research Scientist, UC San Diego Center for Astrophysics and Space Sciences; asf@ucsd.edu

Abstract This paper describes the ongoing development of an automated array of small telescopes (APPOL) for the multicolor, time series measurement of polarized light from Blazars and similar cosmological sources. At 14th magnitude and below, and often exhibiting rapid variation, these objects are challenging polarimetric targets with relatively few published multicolor observations.

The observing system is distributed across two piers located 2 m apart. It contains two 35-cm optical telescopes equipped with self-guiding dual beam polarimeters and two 20-cm co-mounted photometric imagers. These are supplemented with instruments to measure the polarization, brightness, clarity, and spectra of the target sky region. Observations can be made across the optical spectrum from 400 nm to 900 nm. Target acquisition, data reduction, and the time synchronized operation of 12 cameras is coordinated by a custom software system.

One of the polarimeters features a novel optical assembly that provides simultaneous two-color dual beam polarimetry within a single imager. This technique may also be useful for two color photometry of transient objects.

This work has been done in conjunction with the Ax Center for Experimental Cosmology at UCSD. It is envisioned as a pathfinder experiment for a future large telescope test of Lorenz Invariance across cosmological distances.

APPOL achieved first light in late 2017. The first paper based upon this work appeared in Physical Review D in early 2019.

More Glass for Optical SETI

Bruce Howard

Owl Observatory, 131 Vaquero Road, Santa Fe, NM 87508; UBVRI@hotmail.com

Abstract In 2018 I reported to the SAS on a new Optical SETI Camera incorporating evolutionary improvements to the

original instrumentation used at the Owl Observatory. This device represented the last cycle of improvement available without incorporating newer solid-state single photon detectors still not available to the amateur at a reasonable price point. So I decided the next improvement would necessarily be a significantly larger telescope optimized for Optical SETI. This paper will detail the design and construction of a 24" Cassegrain reflector designed for Optical SETI using a combination of novel and traditional design elements. As of this writing the telescope is 95% complete and is scheduled for deployment at a new location in New Mexico in October of this year.

Observation and Investigation of NGC 1662

Talia Green
Sebastian Dehnadi
Connor Espenshade
Kalée Tock
Stanford Online High School, Academy Hall Floor 2 8853, 415 Broadway, Redwood City, CA 94063; tgreen@ma.org, sebastian@dehnadi.com, cjespenshade@icloud.com, kaleeg@stanford.edu

Abstract We observed and investigated the open cluster NGC 1662. Images of NGC 1662 were requested in multiple filters from the Las Cumbres Observatory and reduced using aperture photometry from the Our Solar Siblings Pipeline. We queried the stars' proper motions and parallaxes from Gaia Data Release 2 to ascertain cluster membership, and looked up their APASS catalog magnitudes. Using the ADU counts of the stars in our images, we calibrated the blue and visual counts of NGC 1662's stars relative to reference stars. These calibrated magnitudes were used to create a Color Magnitude Diagram (CMD) consisting of the visual magnitudes on the vertical axis and the difference between the blue and visual magnitudes on the horizontal axis. The bluest star in the cluster was in the Type A spectral class, implying that any hotter stars with shorter lifespans had already died. Based on the life span of A type stars, we determined that the open cluster NGC 1662 is less than 400 million years old, which confirms the findings of a previous study of this cluster.

Measurements of Neglected Double Stars

Brandon Bonifacio
Calla Marchetti
Ryan Caputo
Kalée Tock
Stanford Online High School, Academy Hall Floor 2 8853, 415 Broadway, Redwood City, CA 94063; bonifaciobrandon@gmail.com, calla.marchetti@gmail.com, ryanjc314@gmail.com, kaleeg@stanford.edu

Abstract Double stars with a dim, high delta-magnitude companion are difficult to resolve and measure, and are therefore often neglected despite their high abundance in the galaxy. We measured fourteen of these dim, high delta-magnitude doubles, some from the WDS and some discovered by Gaia but never studied before. Although all of our systems' components have similar parallax and proper motion, many have only a few observations other than what is presented here, making them historically neglected. To resolve the systems, we use PixInsight and AstroImageJ to perform image stacking. Using the measurements from Gaia Data Release 2, we present an escape velocity estimate to assess the likelihood of a system being gravitationally bound. A Monte Carlo method is employed to characterize the error associated with this calculation.

Tycho Tracker: A New Tool to Facilitate the Discovery and Recovery of Asteroids Using Synthetic Tracking and Modern GPU Hardware

Daniel Parrott
tychotracker@gmail.com

Abstract Approximately 2100 Near Earth Objects (NEOs) are discovered each year. Nine out of ten are discovered at magnitude 19 and fainter. The conventional wisdom for those interested in discovering such objects has been that aperture is king. However, a relatively new concept—synthetic tracking—enables the discovery and recovery of such objects even with amateur-class telescopes. At the time of its introduction in 2013, it was largely dismissed as impractical due to the required computing power. Fast-forward seven years later to 2020, and graphics processing unit (GPU) hardware is now 10 times faster at half the cost. Furthermore, the amateur astronomer now has access to full frame CMOS cameras that permit short exposures with low read-out noise. Finally, the new Rowe-Ackermann Schmidt Astrograph (RASA) telescopes offer an optimal pairing with the smaller pixels commonly encountered in modern CMOS cameras. Combining all three of these recent advancements leads to an exciting new frontier in the world of minor planet research and discovery.

Astronomy Will Not Trail Off: Novel Methods for Removing Satellite Trails From Celestial Images

Owen M. Dugan
Stanford Online High School, Academy Hall Floor 2 8853, 415 Broadway, Redwood City, CA 94063; odugan@ohs.stanford.edu

Abstract SpaceX's Starlink satellite network promises worldwide high-speed internet access. With up to 42,000 satellites to be deployed, however, the Starlink satellite network may significantly degrade ground-based astronomical research and imaging due to trails (e.g., light reflections or emissions) from passing satellites. The difficulty of removing the effects of satellite trails on night sky images is recognized because accurately identifying satellite trails is challenging and satellite trails effect not only the brightness measurements of stars they pass in front of but also the brightness measurements of stars in the vicinity of the satellite trails. Novel algorithms were developed and coded to accurately identify and remove satellite trails and reduce their effects on photometry. Platesolving is used to identify stars within an image, and an algorithm is used

to determine the radius of each star identified. Identified star brightnesses are replaced with median nearby image brightness values. Satellite trails are identified by examining each possible line traversing the image, with recursive sizing using area interpolation implemented for large images to reduce processing time. Area and/or cubic interpolation is employed to optimize satellite trail modeling. The code returns to the original image with stars, and a Gaussian brightness profile is developed for the satellite trail to account for satellite trail effects across the entire image. The satellite trail is removed by applying the additive inverse of the fitted Gaussian to every pixel in the image. Significant reductions in the effects of satellite trails on images captured using Earth-based equipment are observed while improving image photometric accuracy. Additional novel solutions for preserving star brightnesses directly under the satellite trails are explored.

Exoplanet Watch: Utilizing Small Telescopes Operated by Citizen Scientists for Transiting Exoplanet Follow-up

Robert T. Zellem
Jet Propulsion Laboratory, California Institute of Technology, M/S 169-237, 4800 Oak Grove Drive, Pasadena, CA 91109; robert.t.zellem@jpl.nasa.gov

and The Exo-planet Watch Team

Abstract Due to the efforts by NASA's Kepler and TESS and numerous ground-based surveys, there will be hundreds, if not thousands, of transiting exoplanets ideal for follow-up spectroscopic atmospheric characterization. However, over time their ephemerides could become so increasingly uncertain that significant overhead would need to be added to an observing run to ensure the detection of the entire transit. As a result, follow-up observations to characterize the atmospheres of these exoplanets would necessitate less-efficient use of an observatory's time —particularly for large platforms such as JWST, ARIEL, Astro2020 Decadal mission, and any other large observatory where minimizing observing overheads is a necessity. Here we demonstrate the power of citizen scientists operating smaller observatories ($\leq$1-m class) to keep ephemerides "fresh," defined here as when the uncertainty in the mid-transit time is less than half the transit duration. We advocate for the creation of a community-wide effort to perform ephemeris maintenance on transiting exoplanets by citizen scientists. Such observations can be conducted with even a 6-inch telescope, which has the potential to save up to 358.66 days for a 1000-planet survey. A network of small telescopes dedicated to ephemerides maintenance (rather than exoplanet discovery) could rapidly observe high-priority targets, freeing up time on larger observatories to monitor, e.g., Earth-sized objects transiting dim M-dwarf stars. Observations with this network could also provide the opportunity to resolve stellar blends, follow-up long-period transits in short-baseline TESS fields, and search for new planets or measure the masses of known planets with transit timing variations. This presentation is based on work performed as part of the NASA's Universe of Learning project and is supported by NASA under cooperative agreement award number NNX16AC65A. The NASA's Universe of Learning (NASA's UoL) project creates and delivers science-driven, audience-driven resources and experiences designed to engage and immerse learners of all ages and backgrounds in exploring the universe for themselves. The competitively-selected project represents a unique partnership between the Space Telescope Science Institute, Caltech/IPAC, NASA Jet Propulsion Laboratory, Smithsonian Astrophysical Observatory, and Sonoma State University, and is part of the NASA Science Mission Directorate Science Activation program.

Data Analysis of Bright Main-Sequence A- and B-type Stars Observed Using the TESS and BRITE Spacecraft

Joyce A. Guzik
Los Alamos National Laboratory, MS T082, Los Alamos, NM 87547; joy@lanl.gov

Jason Jackiewicz
Department of Astronomy, New Mexico State University, Las Cruces, NM

Andrzej Pigulski
Instytut Astronomiczny, Uniwersytet Wrocławski, Wrocław, Poland

Giovanni Catanzaro
INAF—Osservatorio Astrofisico di Catania, Via S. Sofia 78, I-95123 Catania, Italy

Michael S. Soukup
Los Alamos National Laboratory (retired), Albuquerque, NM 87111

Patrick Gaulme
Max-Planck-Institut für Sonnensystemforschung, Justus-von-Liebig-Web 3, 37077, Göttingen, Germany

Gerald Handler
Nicolaus Copernicus Astronomical Center, Bartycka 18, 00-716 Warsaw, Poland

The BRITE Team
https://brite-constellation.at

Abstract During the last two years we have received long time-series photometric observations of bright (V mag < 8) main-sequence A- and B-type stars observed by the NASA TESS spacecraft and the Austria-Poland-Canada BRITE satellites. Using TESS observations of metallic-line A (Am) stars having peculiar element abundances, our goal is to determine whether and why these stars pulsate in multiple radial and nonradial modes, as do the δ Scuti stars in the same region of the H-R diagram. The BRITE data were requested to investigate pulsations in bright (V around 6 mag) A- and B-type stars in the Cygnus-Lyra field of view that had been proposed for observations during the now-retired NASA Kepler mission.

Of the 21 (out of 62 proposed) Am stars observed by TESS so far, we find one δ Sct star and two δ Sct / γ Dor hybrid candidates. Of the remaining stars, we find three γ Dor candidates, six stars showing photometric variations that may or may not be associated with pulsations, and eight stars without apparent significant photometric variability. For the A- and B-type stars observed by BRITE, one star (HR 7403) shows low amplitude low frequency modes that likely are associated with its B (emission) star properties; one star (HR 7179) shows SPB variability that is also found in prior Kepler data, and two stars (HR 7284 and HR 7591) show no variability in BRITE data, although very low amplitude variability was found in TESS or Kepler data. For the TESS and BRITE targets discussed here, follow-up ground- and space-based photometric and spectroscopic observations combined with stellar modeling will be needed to constrain stellar parameters and to understand the nature of the variability.

Comparing the Ages of NGC 1513 and NGC 2420

Sahana Datar
Cindy Wang
Connor Espenshade
Kalée Tock
Stanford Online High School, Academy Hall Floor 2 8853, 415 Broadway, Redwood City, CA 94063; sahanald@gmail.com, cindersw23@gmail.com, cjespenshade@icloud.com, kaleeg@stanford.edu

Abstract We compared two star clusters, NGC 1513 and NGC 2420, using images of each cluster taken by the Las Cumbres Observatory 0.4-meter telescopes in blue and visual filters. We reduced the images using AstroImageJ and Our Solar Siblings pipeline photometry, and looked up the magnitudes of the stars, where available, from the SIMBAD and APASS catalogs. Color-Magnitude Diagrams (CMD's) were created using the magnitudes of reference stars in each cluster. The diagrams were corrected for reddening that occurred due to dust or other particles. The lowest B–V values in each CMD were then used to determine the spectral type of the hottest stars in each cluster. NGC 2420's hottest stars were type A, while NGC 1513's hottest stars were type O. Because the stars in NGC 1513 are hotter than the stars in NGC 2420, we can conclude that NGC 1513 is younger than NGC 2420.

The Prairie View Observatory: First Light

Brian Cudnik
Mahmudur Rahman
Gary M. Erickson
Premkumar Saganti
Department of Physics, Prairie View A&M University, P. O. Box 519, MS 2230, Prairie View, TX 77446; bmcudnik@pvamu.edu (Presenter) and pbsaganti@pvamu.edu (Technical Lead and PI)

S. Douglas Holland
Holland-Space, LLC, Houston, TX 77058

Abstract The Prairie View Observatory complex (PVOc) was completed early this year, 2020. The PVOc consists of two separate piers aligned east-west. A dedicated solar observatory is located just to the south (Prairie View Solar Observatory (PVSO) which began operation in 1999 and was renovated in 2017). The west (18-ft) and south (16-ft) domes are Ash domes, while the east dome (20-ft) is an Astrohaven clamshell dome. The two new piers reach 24 ft above ground level and have a vibration amplitude not to exceed 0.485 arc sec, allowing for high (pixel) resolution imaging. The current primary instruments of PVOc include a PlaneWave 24-in CDK telescope in the west dome, a Meade 16-in Cassegrain in the east dome, and PVSO's 35-cm Vacuum Solar Telescope in the south dome. In addition, an observing pad providing power and internet is located on the east end of the complex. The observatory building features a two-story visitor's center, flanked on both the east and west sides by workrooms on the ground level and control rooms and access to the domes on the mezzanine level. The solar observation program that had been carried out for so many years with the PVSO has resumed, and since January of this year we have been conducting routine solar observations from the east dome with our 16-in telescope as well. In addition to daytime solar observations, the east dome has seen many evenings of activity as we work to test and build the capabilities of the instruments and imaging system. Once the PVOc is fully online, it will be capable of a wide array of astronomical projects that will involve faculty, students, and the public. We have one additional 16-in Meade and one 14-in Meade, along with several other telescopes for outside, ground-level viewing. Finally, in collaboration with NASA-JSC over the past ten years we developed cameras for advanced astro-imaging. We are also equipped with a state-of-the-art, low-light calibration source manufactured by LabSphere. This system provides an extremely uniform low-light source for calibrating imaging systems.

We present our first light images from our PVOc along with a few calibrated images with our cameras developed for astro-imaging.

Confirmation of Short Period Pulsating Variables Using an Array of Robotic Telescopes

Eric G. Hintz
Jarrod L. Hansen
Jacob S. Jensen
Elizabeth E. Banks
Brigham Young University, Department of Physics and Astronomy, Provo, UT, 84602; hintz@byu.edu

Abstract With the large number of surveys currently in operation there are many new potential variable stars discovered. These include programs such as TESS, KELT, ATLAS, ASAS-SN, and others. Each of these has a different cadence which might impact the classification assigned to each potential new variable star. Using our current group of robotic telescopes, we are able to obtain high cadence follow-up observations to check the published period and classification of these targets. The current group of telescopes consists of four telescopes on our campus observation deck: 0.13-m, 0.2-m, 0.25-m, and the

0.3-m. Recently we have added a 0.61-m PlaneWave CDK24 telescope to our campus dome which will provide high density data and data on fainter targets. This group allows us to follow-up on pulsating variables from about 4th to 14th magnitude. We will show a range of variables and a comparison of the periods from the original surveys with periods from our high-density light curves.

Analysis of HAT-P-23 b, Qatar-1 b, WASP-2 b, and WASP-33 b with an Optimized EXOplanet Transit Interpretation Code

Sujay Nair
Stanford Online High School, Academy Hall Floor 2 8853, 415 Broadway, Redwood City, CA 94063

Jonathan Varghese
Vista Del Lago High School, 1970 Broadstone Pkwy, Folsom, CA 95630

Kalée Tock
Stanford Online High School, Academy Hall Floor 2 8853, 415 Broadway, Redwood City, CA 94063

Robert Zellem
Jet Propulsion Laboratory, California Institute of Technology 4800 Oak Grove Drive, Pasadena, California, 91109

Abstract The ability for citizen scientists to analyze image data and search for exoplanets using images from small telescopes has the potential to greatly accelerate the search for exoplanets. Recent work on the Exoplanet Transit Interpretation Code (EXOTIC) enables the generation of high-quality light curves of exoplanet transits given such image data. However, on large image datasets, the photometric analysis of the data and fitting light curves can be a time-consuming process. In this work, we first optimize portions of the EXOTIC codebase to enable faster image processing and curve fitting. Specifically, we limited repetitive computation on fitting centroids with various apertures and annuli. Moreover, this speedup is scaled linearly based on the number of FITS files. After testing on existing HAT-P-32 b data and newer HAT-P-23 b data, our best demonstration was approximately a 5x speedup, though that factor increases given a larger number of FITS files. Utilizing the accelerated code, we analyzed transits of HAT-P-23 b, Qatar-1 b, WASP-2 b, and WASP-33 b using data captured by the 16" SRO telescope operated by Boyce-Astro.

Assessing Habitability of Exoplanet Targets

Elias Koubaa
Lian E
Greta Olson
Ivan Altunin
Kalée Tock
Stanford Online High School, Academy Hall Floor 2 8853, 415 Broadway, Redwood City, CA 94063; ekoubaa1@gmail.com, lian.e.smws@gmail.com, greta.l.olson@gmail.com, vaa.space@gmail.com, kaleeg@stanford.edu

Abstract Images of exoplanet hosts KPS-1 and Qatar-8 were requested from Las Cumbres Observatory Global Telescope Network. Light curves were generated by performing differential photometry and fit using the EXOplanet Transit Interpretation Code. KPS-1 b has a well-defined transit midpoint, despite the fact that the observations did not fully sample the planet's egress from the eclipse of its host. The light curves from Qatar-8 b are too noisy to draw a definitive conclusion, even after applying six different photometric reduction methods. Lastly, pre-existing scientific definitions are used to define a new "Habitability Index," quantifying the habitability of an exoplanet based on its properties. Predictions based on this habitability index are compared to those of existing metrics.

Studies of Exoplanets with Candidate TOI 717.01 and Confirmed HAT-P-3b

Sujay Nair
Krithi Koodli
Elliott Chalcraft
Kalée Tock
Stanford Online High School, Academy Hall Floor 2 8853, 415 Broadway, Redwood City, CA 94063; sujaynr@ohs.stanford.edu, krithik@ohs.stanford.edu, elliottchalcraft@gmail.com, kaleeg@stanford.edu

Abstract Images of the exoplanets TOI 717.01, Qatar-8 b, and HAT-P-3 b were requested in the w-filter from the Las Cumbres Observatory 0.4-meter telescopes. Of these requests, images were taken of TOI 717.01 and HAT-P-3 b and were reduced using the EXOplanet Transit Interpretation Code (EXOTIC) software, as well as 6 photometric algorithms from the Our Solar Siblings pipeline. HAT-P-3 b's transit midpoint was found to be 2458907.6205, which is 20.2 minutes different from its expected midpoint that night. For TOI 717.01, the transit was not discernible, likely due to its low transit depth of 0.1%. It is possible that one of the comparison stars in the TOI 717.01 field is variable.

Looking for Transit Timing Variations in TrES-1

Quinn Perian
Paige Yeung
Peyton Robertson
Kalée Tock
Stanford Online High School, Academy Hall Floor 2 8853, 415 Broadway, Redwood City, CA 94063; pcy@ohs.stanford.edu

Abstract For exoplanets that transit between their host star and Earth, periodic variations in mid-transit time can indicate another planet's gravitational influence. We investigate 31 transits of TrES-1 b observed from 6-inch telescopes in the MicroObservatory network. The EXOplanet Transit Interpretation Code (EXOTIC) is used to fit light curves and find transit midpoints. Our analysis did not indicate the existence of other planets affecting the orbit of TrES-1 b.

Observation of Gaia (DR2) Red and White Dwarf Binary Stars in the Solar Neighborhood

Rick Wasson
Orange County Astronomers; ricksshobs@verizon.net

Abstract The Gaia satellite combines astrometric, parallax, photometric, and spectroscopic measurements of stellar properties—with greater accuracy than ever before. In 2018 Gaia Data Release 2 (DR2) made preliminary but consistent data available for an extraordinary number of stars: 1.3 Billion! Red and White Dwarf stars are intrinsically very faint—only the nearest and brightest are visible in the eyepiece of a small telescope. Although many can be recorded in long exposure images, they are less well studied than brighter stars. Red Dwarfs are the most common type, but are faint because of their small size, slow nuclear fusion, and cool red color; White Dwarfs are hot but very small and relatively rare. Even in the Solar Neighborhood, between 10 and 100 parsecs (33–326 light-years), all the stars of these two types have not yet been found. In 2019 a campaign was begun to identify and observe "new Gaia binary" candidate systems containing a red or white dwarf star. Binaries offer the chance to define stellar properties more completely by deriving masses from their orbit. The Orange County Astronomers' 22-inch Kuhn Telescope was used, together with Speckle Interferometry techniques, to achieve higher resolution than either the Gaia satellite or large deep surveys. The goals of this project were:

1. Confirm new binary systems discovered by Gaia and add measurements of their orbit.

2. Discover possible new red dwarf components in multiple star systems.

New red dwarf binary candidates are defined as not listed in the Washington Double Star (WDS) catalog. A "data mining" search of DR2 was made with the following Gaia parameters: two stars with separation $<10°$, parallax greater than 10 mas (i.e., within 100 parsecs of the Sun), similar proper motion, and at least one component with Gaia color index (Bp-Rp) >2.0 (i.e., late K or M spectral type). More than 800 Gaia candidate binaries have been identified within 100 parsecs in the northern sky; about three-quarters of them have a Red Dwarf component, and a handful of White Dwarfs are also included. Thirty-five of the brighter systems have been observed so far; about half of these do not appear in the WDS Catalog and are thus believed to be "new" Gaia binaries. Observation methods and results are presented and discussed.

New Life for the Bright Star Monitors

Arne A. Henden
ahenden@gmail.com

Abstract In 2009, the AAVSO created the Bright Star Monitor (BSM), an inexpensive CCD system optimized for stars brighter than 8th magnitude. Over the next few years, several more of these robotic systems were installed at urban sites around the world. Thanks to long-term equipment loans from the Tzec Maun Foundation and the availability of low cost CMOS cameras, we have upgraded this network and expanded its capabilities. Free to AAVSO members, this network contributes about a half-million images per year to the astronomical community. I will describe the new hardware configuration and some upcoming software improvements, as well as some photometric results from the network.

Identification and Analysis of Pulsating Red Giants Misclassified by ASAS and ASAS-SN

Kristine Larsen
Central Connecticut State University, 1615 Stanley Street, New Britain, CT 06050; larsen@ccsu.edu

Abstract Pulsating red giant stars (PRG) pose a particular challenge for automated classification algorithms due to their complex and quasiperiodic behavior, leading to their possible erroneous designation as "miscellaneous" class variables (MISC). A subset of variable stars identified as MISC by the All-Sky Automated Survey (ASAS) with extremely long period (over 1000 days) was analyzed. The AAVSO's VSTAR statistics program was applied to the stars' data from ASAS and the All-Sky Automated Survey for Supernovae (ASAS-SN). Examples of several types of PRG behavior were identified, and limitations of several automated classification algorithms made apparent.

The Photometric and Spectroscopic Development of the 2019 Eruption of the Recurrent Nova V3890 Sgr Followed with Small Telescopes

Forrest Sims
forrest@simsaa.com

Abstract V3890 Sgr is one of four known symbiotic-like recurrent novae (Red Giant donor and White Dwarf gainer). Detection of the most recent eruption was reported on August 27th, 2019, by A. Pereira at a visual magnitude of 6.7. In less than 21 days V3890 Sgr dropped to magnitude 12; after another 40 days it had reached near magnitude 16. Previous outbursts occurred in 1990 and 1962. We present the development of this outburst from photometric and spectroscopy measurements obtained with amateur equipment. Shortly after discovery, the visible spectrum at low resolution ($R\sim500$) showed only weak emission features for Hα and Hβ, but with FWZI indicating Hα velocities in excess of 8,000 km/sec. Increases in the strengths and changes in the line profiles were recorded on a near daily basis. V-filter data derived from AAVSO observations were used to flux calibrate spectra. We highlight how the spectral changes reveal the passage of the ejecta through the wind of the companion red giant through its shock dynamics and radiative precursor and ionization front.

Photometry of Betelgeuse Through Its Recent Faint Minimum

Tom Polakis
Command Module Observatory, 121 W. Alameda Drive, Tempe, AZ 85282; tpolakis@cox.net

Abstract Betelgeuse is nominally one of the ten brightest stars in the sky, known to vary irregularly between roughly magnitude 0.3 and 0.8. During December of 2019, it became apparent that it was approaching a historically faint minimum, and at a faster than usual rate of descent. V-band observations at Command Module Observatory commenced on January 12, 2020, and were carried out on 40 nights through April 19, 2020. Since the star is far too bright for measurement with the 32-cm telescope and sensitive CCD detector, an aperture mask and defocusing were required to achieve acceptable ADU counts. Errors associated with shutter timing and scintillation due to the necessarily short integrations were combated by taking multiple exposures of the target, comparison, and check stars. The resulting light curve captured not only the time of minimum, but also showed nightly fluctuations in brightness whose validity appears to be supported by the stability of check star magnitudes.

Index to Volume 48

Author

Subject

CATALOGUES, DATABASES, SURVEYS

SPECTROSCOPIC ANALYSIS

STATISTICAL ANALYSIS

NOTES